NUMERICAL MODELLING OF THE TIME DEPENDENT BEHAVIOUR OF CLAYS

by

Teresa Maria Bodas Freitas

Dipl.(Eng.), MSc, DIC

submitted January 2008

Thesis submitted to the University of London (Imperial College of Science, Technology & Medicine) in partial fulfilment of the requirements for the degree of Doctor of Philosophy in the Faculty of Engineering

ABSTRACT

In the last two decades extensive research has been undertaken to characterize the time and rate dependent response of soils and to describe it by means of a constitutive model. However, most of these constitutive equations have been developed for a single stress point and limited stress paths, and in engineering practice the time dependent nature of soils is still commonly reduced to a single coefficient of secondary consolidation obtained from a 24h oedometer test.

This thesis describes the development and implementation, in the Imperial College Finite Element Program (ICFEP), of two elastic visco-plastic models based on the overstress theory to describe the stress-strain-time/rate behaviour of clayey soils. The models differ essentially in the adopted law to describe the variation of the creep deformation with time. The first model - Creep Model 1 – incorporates a linear logarithmic law to describe the variation of the creep deformation with time, while the second model – Equivalent Time (ET) Model - incorporates a non-linear logarithmic creep law, with a limit to the amount of volumetric creep strain that can occur.

The implementation and performance of the models is validated through a series of simple finite element analyses that mimic common laboratory stress paths and show that the models are able to reproduce the phenomena of primary and secondary compression, stress relaxation, primary and secondary creep and persistent rate effects on the stress-strain response under K_0 and triaxial stress conditions.

The ET model is then used to investigate the increase in bearing capacity of pre-loaded footings on soft clay, taking into account both the effects of consolidation and soil hardening due to creep with time. Finally, a series of finite element analyses are presented that mimic the loading tests performed on two instrumented rigid footings at the Bothkennar test site. These analyses highlight the importance of considering the soil viscous effects in engineering practice and the need to account for the soil creep non-linearity if good predictions of the long-term settlements of geotechnical structures are to be made.

ACKNOWLEDGEMENTS

First, I would like to thank my supervisor Prof. D.M. Potts for guiding and assisting me during the period of this work. I will take with me his enthusiasm and eagerness to find the *why* of things and combat all the *fudges* in numerical analysis. I would like to thank Dr. L. Zdravkovic for her continuous help, advice and support.

The research presented in this thesis was sponsored by the Fundação Ciência e Tecnologia. Their financial support is greatly acknowledged.

I would like to mention Prof. M Coop that first seeded in me the idea of doing a PhD and helped me through the process applying for a scholarship.

For the last four years I have been (as a rule after 11 am) at the Imperial College, Soil Mechanics Section. I would like to thank all the staff, researchers and students for having taught me so much and made my stay so enjoyable. In particular, I would like to mention Vicky with whom I shared the computer room - and with the room came the frustrations of non-convergence and a wonderful friendship - our giggling sessions are still a legend! Stavroula friend and colleague of old wars, from the MSc to flatmate, Angeliki with whom I often shared the frustrations of constitutive modelling and the dilemmas of (PhD) life and Jian who brought a smile to my life in the last few months. Although they are unlikely to ever see this I would like to thank Vania and Rita who were my first family in London, and over the other side of the sea, in the mainland, Rita, Filipa, Iria and Victor.

I would like to thank Peter for his unconditional help, love and support.

Finally, I would like to remember my parents and my sister Isabel for their love, patience and immense capacity of understanding, giving and forgiving. Throughout my life you have always been there for me and believed I could do this right from the start, even before I would dare to consider it.

And to my own surprise, this day has finally arrived, the day that I put an end to my leisure days of a research student and finally say, "*Have I told you? I have been to the binders today!*" I planted the tree, wrote the book, what is out there for me now?

To my grand parents Maria and Agostinho

I miss you so much…

TABLE OF CONTENTS

LIST OF FIGURES

LIST OF TABLES

SYMBOLS AND ABBREVIATIONS

Symbol

A	Singh and Mitchell's model parameter
A	Tavenas' model parameter
B	Tavenas' model parameter
[B]	matrix of the derivatives of the shape functions N_i
c_v	coefficient of consolidation
C_{ce}	compression index in terms of void ratio
C_k	permeability change index (= $\Delta e/\Delta \log (k)$)
C_{re}	coefficient of recompression in terms of void ratio
C_α	coefficient of secondary consolidation
$C_{\alpha e}$	coefficient of secondary compression defined in terms of void ratio
$C_{\alpha \varepsilon}$	coefficient of secondary compression defined in terms of strain
$[D]$	constitutive matrix
$[D]$	elastic constitutive matrix
$[D]$	total constitutive matrix
$[D']$	effective constitutive matrix
$[D_f]$	pore fluid stiffness matrix
$\{\Delta d\}_{Gnodes}$	global nodal displacement vector
$\{\Delta d\}^T$	displacement vector
$\{\Delta d\}_{nodes}$	vector of the incremental nodal displacements
d	dilatancy (the ratio of volumetric to deviatoric strain increments)
D*	footing equivalent diameter
e	void ratio
e_0	initial void ratio
e_i	initial void ratio
Δe	change in void ratio
E	error in the stress changes in the non-linear solver
E	total potential energy
E	Young's modulus
E'	drained Young Modulus
E_u	undrained Young Modulus
ΔE_d^T	deviatoric total strain increment

ΔE_d^{vp}	deviatoric visco-plastic strain increment
f_d	dynamic loading surface
f_s	static yield surface
F	overstress
$\{\Delta F\}^T$	vector of the body forces
g	plastic potential function
g(θ)	inclination of the critical state line in p'-J stress space
G	shear modulus
G_{max}	elastic shear modulus at very small strains
h	sample height
H	layer thickness
ΔH	settlement
$\{i_G\}$	unit vector parallel but in the opposite direction to that of gravity
J	deviatoric stress
|J|	Jacobian determinant
$J_{2\eta}$	stress ratio squared
$J_{2\eta,failure}$	stress ratio at failure squared
k	permeability
k	hardening parameter
k_h	horizontal permeability
k_v	vertical permeability
k_v	soil permeability in the direction of the flow
$[k]$	permeability matrix
K	elastic bulk modulus
K_0	coefficient of earth pressures at rest
K_0^{NC}	coefficient of earth pressure at rest in the normally consolidated range
K_e	constant related to K_f
K_f	bulk modulus of the pore fluid
K_{skel}	soil skeleton bulk stiffness
$[K_G]$	global stiffness matrix
$[K_E]$	element stiffness matrix
L	work done by the applied forces
L_f	current mobilized load factor

m	Singh and Mitchell's creep parameter
m_v	coefficient of volume compressibility
M	gradient of the critical state line in p'-q space under triaxial compression
M_f	stress ratio at critical state
M_f	the value of M for the loading surface
M_g	the value of M for the plastic potential surface
[N]	matrix of the displacement interpolation/shape functions
$\lfloor N_p \rfloor$	matrix of the pore pressure interpolation/shape functions.
P	plastic potential function
p'	(current) mean effective stress
p_i'	initial mean effective stress
p_i'	mean effective stress at a generic stress point i
p_{ref}'	mean effective stress on the reference line
p_{0ref}'	mean effective stress on the reference line
p_{m0}'	mean effective stress at zero volumetric strain on the reference time line of the natural soil
p_{mi0}'	mean effective stress at zero volumetric strain on the intrinsic reference time line
p_{s0}	initial increase in p_{mi0}' due to soil structure
p_s	current increase in p_{mi0}' due to soil structure
$p_{natural}'$	mean effective stress on the reference time line of the natural material
$p_{Intrinsic}'$	mean effective stress on the intrinsic reference time line
p_{mc}'	size of the loading surface correspondent to the largest normally consolidated stress state that the soil element have experienced
p_{0c}'	size of the current loading surface
p_m'	size of the current loading surface
$\Delta p_m'$	mean effective stress change
$\{\Delta p\}$	pore pressure change
$\{\Delta p\}_n$	vector of the pore pressure change at the nodes
q	deviator stress
q_L	the current bearing pressure.

q_L^{max}	ultimate bearing capacity
q_{max}	soil strength at the beginning of the undrained creep process
$\overline{q}$	current stress ratio
$\overline{q}_0$	initial stress ratio
Q	sources or sinks
Q	ultimate bearing capacity
Q_i	initial undrained bearing capacity
$Q_{6months}$	undrained bearing capacity at 6 months
r_k	permeability anisotropy ratio (= k_{h0}/k_{v0})
R	relative error in the non-linear solver
$\{\Delta R_E\}$	element right hand side load vector
$\{\Delta R_G\}$	global right hand side load vector.
s	Lacerda & Houston's model parameter
s_{EOP}	settlement at the end of primary consolidation
s_t	settlement at an instant t
S	stress level
S	isoparametric coordinate
S_u	undrained strength
t	time
t_0	the real time associated with the reference time line
t_e	equivalent time
t_i	time origin
Δt	time increment
T	isoparametric coordinate
ΔT	ratio between the sub-step and the incremental strains in the non-linear solver
$\{\Delta T\}^T$	vector of the surface tractions
u	displacement value in the x direction
u	pore water pressure
u_b	pore water pressure at the base
Δu_{dev}	deviatoric part of the excess pore water pressure
Δu_{sph}	spherical part of the excess pore water pressure
$\overline{U}_s$	degree of settlement
$\overline{U}_{PWP}$	degree of pore water dissipation

v	displacement value in the y direction
v_x	superficial velocity of the pore fluid in the x-direction
v_y	superficial velocity of the pore fluid in the y-direction
$\{v\}$	vector of the pore fluid superficial velocities
V	(current) specific volume
V_0	initial specific volume
V_i	initial specific volume
V_{1i}	specific volume at unit mean effective stress
V_{1ref}	specific volume at unit mean effective stress on the reference time line
ΔV	change in specific volume
W	work done by the internal forces
X	parameter of the yield/plastic potential surface in the deviatoric plane
Y	parameter of the yield/plastic potential surface in the deviatoric plane
z	distance from the drainage boundary
Z	constants input parameter
α	Singh and Mitchell's model parameter
α	dilatancy parameter
α_f	value of α for the loading surface
α_g	value of α for the plastic potential function
β	time function
β	integration parameter for coupled consolidation analyses
δ	settlement
δ_{max}	maximum settlement
ε	strain
ε_1	major principal strain
ε_2	intermediate principal strain
ε_3	minor principal strain
ε_x	strain in the x-direction
ε_y	strain in the y-direction
ε_z	strain in the z-direction
ε_v	vertical strain
ε_∞	volumetric strain attained at infinite creep time
ε^e	elastic strain
ε^v	viscous strain

ε^{c}	creep strain
ε^{tot}	total strain
ε_{vol}	current total volumetric strain
ε_{d}	sum of the absolute values of incremental volume strain
$\varepsilon_{vol,m}$	volumetric strain at the equivalent isotropic stress state
$\varepsilon_{vol,m}^{vp}$	visco-plastic volumetric strain at the equivalent isotropic stress state
$\varepsilon_{vol,m,Limit}^{vp}$	limit volumetric visco-plastic strain
$\varepsilon_{vol,mu}^{el}$	volumetric strain at a reference mean effective stress $p_u^{'}$ on the current instant line
$\varepsilon_{vol,m}^{ref}$	volumetric strain on the reference time line at the equivalent isotropic effective stress $p_m^{'}$
$\varepsilon_{vol,m0}^{ref}$	volumetric strain on the reference time line at the isotropic effective stress $p_{m0}^{'}$
$\Delta\varepsilon^{el}$	incremental elastic strain
$\Delta\varepsilon^{vp}$	incremental visco-plastic strain
$\Delta\varepsilon^{T}$	incremental total strain
$\Delta\varepsilon_{ij}^{vp}$	incremental visco-plastic strain vector
$\Delta\varepsilon_{i}^{vp}$	incremental visco-plastic strain in the i direction
$\Delta\varepsilon_{vol}^{T}$	incremental total volumetric strain
$\Delta\varepsilon_{vol}^{vp}$	incremental visco-plastic volumetric strain
$\Delta\varepsilon_{vol,m}^{el}$	incremental elastic volumetric strain at the equivalent isotropic stress state
$\Delta\varepsilon_{vol,m}^{vp}$	incremental visco-plastic volumetric strain at the equivalent isotropic stress state
$\{\Delta\varepsilon^{el}\}$	incremental elastic strain vector
$\{\Delta\varepsilon^{vp}\}$	incremental viscous-plastic strain vector
$\{\Delta\varepsilon_{inc}\}$	incremental strain vector
$\{\Delta\varepsilon_{ss}\}$	sub-step incremental strain vector
$\dot{\varepsilon}_{a}$	axial strain rate
$\dot{\varepsilon}^{el}$	elastic strain rate
$\dot{\varepsilon}^{c}$	creep strain rate.

$\dot{\varepsilon}_v$	vertical strain rate
$\dot{\varepsilon}^{vp}$	visco-plastic strain rate
$\dot{\varepsilon}^{total}$	total strain rate
$\dot{\varepsilon}^{i}_{vol}$	current volumetric strain rate
$\dot{\varepsilon}^{ref}_{vol}$	volumetric strain rate on the reference time line
$\dot{\varepsilon}^{el}_{vol}$	elastic volumetric strain rate
$\dot{\varepsilon}^{vp}_{vol}$	visco-plastic volumetric strain rate
$\{\dot{\varepsilon}^{vp}_{ij}\}$	visco-plastic strain rate vector
$\{\dot{\varepsilon}^{el}_{ij}\}$	elastic strain rate vector
$\{\dot{\varepsilon}_{ij}\}$	total strain vector
$\{\dot{\varepsilon}^{Tot}_{ij}\}$	total strain vector
φ'_{cs}	critical state angle of shearing resistance
φ'	angle of shearing resistance
$\Phi(F)$	function of the overstress F
Φ	visco-plastic scalar multiplier
γ	fluidity parameter
γ	bulk unit weight of the soil
γ_f	bulk unit weight of the pore fluid
γ_w	bulk unit weight of the pore water
η	stress ratio
η	viscosity
$\overline{\eta}$	generalized normalized stress ratio
κ	slope of the instant time line in V-lnp' space
κ/V	slope of the instant time line in ε_v – ln p' space;
λ	slope of the reference time line in V-lnp' space
λ/V	slope of the reference time line in ε_v – ln p' space;
Λ	visco-plastic multiplier in the non-stationary flow surface theory
μ	Poisson's ratio
μ'	drained Poisson's ratio
μ_u	undrained Poisson's ratio
μ	dilatancy parameter

μ_f	value of the dilatancy parameter μ for the loading surface
μ_g	value of the dilatancy parameter μ for the loading surface
θ	Lode's angle
ρ_s	parameter that controls the rate of destructuration
σ	direct stress
σ'_1	major principal effective stress
σ'_2	intermediate principal effective stress
σ'_3	minor principal effective stress
σ_x	stress in the x-direction
σ_y	stress in the y-direction
σ_z	stress in the z-direction
σ'_c	isotropic pre-consolidation pressure
σ_v'	vertical effective stress
σ_v	total vertical stress
σ'_{v0}	in-situ vertical effective stress
σ'_{h0}	in-situ horizontal effective stress
σ'_{vi}	initial vertical effective stress
σ'_{vy}	vertical effective stress at large scale yielding
σ'_{hy}	horizontal effective stress at large scale yielding
$\sigma'_{v,eq}$	equivalent vertical effective stress
σ'_{vp}	pre-consolidation vertical effective stress
σ_y	yield stress
$\Delta\sigma_v$	total vertical stress increment
{Δσ}	vector of the incremental total stresses
{Δσ'}	vector of the incremental effective stresses
$\{\Delta\sigma_f\}$	vector of the incremental pore fluid pressure
$\{\dot{\sigma}_{ij}\}$	stress rate tensor
τ	intrinsic time
τ	shear stress
τ_{xy}	shear stress in the x-direction action of y facet
τ_{xz}	shear stress in the x-direction action of z facet

τ_{yz}	shear stress in the y-direction action of z facet
ψ	creep parameter, change in void ratio per natural logarithmic cycle of time
ψ_0	model parameter ψ at the reference time, t_0
ψ/V	creep parameter of the equivalent time model
ψ_0/V	creep parameter ψ/V at the reference time t_0
Ψ^1	residual load vector for iteration 1 during the solution of the global equations matrix

Abbreviation

1 D	one-dimensional
CRD	constant rate of displacement
CRS	constant rate of strain
CSL	critical state line
EOP	end of primary consolidation
ESP	effective stress path
ET	equivalent time
FE	finite element
ICL	intrinsic compression line
IL	incremental load
MCC	modified Cam-Clay
NC	normally consolidated
NCL	normal compression line
OC	overconsolidated
OCR	overconsolidation ratio
PI	plasticity index
pwp	pore water pressure
RF	restricted flow tests
SRS	step-wise change in the rate of strain
TESRA	temporary effect of strain rate and strain acceleration
YSR	yield stress ratio

1 INTRODUCTION

1.1 Background

The first aspect of the time dependent behaviour of soils to have attention from the engineering community was the creep time delayed deformation of soils under a given load. Observations were reported since the early decades of the 20th century and Buisman (1936) first noticed that the creep deformation of soil was mathematically well described by a semi-logarithmic law. Since the 1950s the time dependent behaviour of soils has been studies in a more systematic manner. The focus then was the time-delayed deformation behaviour of soft clays and its creep characteristics with the aim of predicting the long-term settlement of foundations on soft ground, as presented by Bjerrum (1967) in the seventh Rankine lecture. Since then various studies have been carried out on time dependent deformation and the time dependent structuration of soils (concepts that are defined in Chapter 2).

Until a decade ago it was thought that viscous effects gave rise to predictable patterns, which were essentially the same for all soil types. Tatsuoka et al. (1998), based on experimental work carried out in the late 1990's, showed that soils of varying nature might exhibit very different viscous effects, constituting a major advance in the characterization of the viscous behaviour of geomaterials. However, over the same period nothing seemed to have changed in engineering practice, and time effects on geomaterials are still often reduced to an add on secondary settlement, or a strain rate correction factor applied to the undrained strength.

During the last two decades there has been an increase in the development and use of numerical methods in the design of geotechnical structures. This has been boosted by increased construction in urban areas and pressure to engineer in locations were the geotechnical conditions are less favourable, requiring accurate calculations of stresses and ground movements around geotechnical structures, both at failure and at working loads, both in the short and long term.

Although numerical analysis is a powerful tool, the predictions obtained are highly dependent on the constitutive soil models adopted. In the analysis of many geotechnical problems (e.g. staged embankment construction, engineering in soft soil in general, long

term behaviour of geotechnical structures), it is important to use constitutive soil models that are able to incorporate the viscous nature of soils. This is particularly the case when modelling clayey soils as they are observed to be more susceptible to viscous effects, i.e. larger delayed settlements and strain rate effects on strength and stiffness.

It is apparent from the literature that there are various formulations available to describe the time dependent behaviour of clays. However, the majority of these have only been validated under very limited stress paths and there is very little experience in their use in the analysis of full boundary value problems. The work described in this thesis aims to fill these gaps.

1.2 Objectives

The aim of this research is to improve the knowledge of using time dependent constitutive models, i.e. models that are able to mimic soil viscous effects, to model clayey soils. In particular:

a) Based on available formulations, to develop and implement in a finite element program constitutive models that are able to mimic the main features of the time dependent behaviour of normally and overconsolidated clays;

b) To validate the above models against laboratory test data;

c) To use the models to analyse boundary value problems, so that the performance of the models may be fully appreciated, and any problems in their application identified.

1.3 Layout of the thesis

During this research two constitutive soil models were developed, and they are described in this thesis. The two constitutive models are based on the overstress theory and they differ essentially in the law adopted to describe the variation of the creep deformation with time. The constitutive models were implemented in ICFEP (Imperial College Finite Element Program) and validated by means of finite element analyses simulating common laboratory stress paths. The models were then used to analyse the behaviour of a generic foundation problem and finally to simulate the Bothkennar footing tests, for which there is a large amount of data regarding both the footings

performance during the tests and soil characterization. The outline of the thesis is given in detail below:

Chapter 2 presents a review of the published literature concerning the time dependent behaviour of soils associated with soil viscosity, such as creep, stress relaxation and rate effects on the stress-strain-strength soil response. References to other time effects that lead to soil ageing or structuration are also included to illustrate the approximations involved by their non-consideration. The review concentrates on the behaviour of saturated clays, but for clarity and completeness, data on other soil types is also included.

Chapter 3 presents a review of the available constitutive soil models, which attempt to incorporate the viscous nature of soils. It is noted that, most of these have been developed based on experimental work on clay soils, and therefore, reproduce the so-called isotach viscosity, described in Chapter 3. This review covers empirical relations, rheological models and selected full general stress-strain-time models.

Chapter 4 gives a brief description of the finite element (FE) method and discusses some basic modifications necessary to allow the method to be used in geotechnical engineering, namely to tackle the two phase nature of soils and their strong non-linear stress-strain behaviour.

Chapter 5 presents an elastic visco-plastic model based on the overstress theory, which incorporates a linear law between creep strain and the logarithm of time to evaluate the visco-plastic volumetric strain rate. The model is referred to as Creep Model 1. The model is initially formulated under isotropic stress conditions and is then extended to general stress space. Based on the experimental work by Tavenas et al. (1978) the extension to general stress space is initially done assuming that the visco-plastic volumetric strain rate is constant on a given loading surface (which, as explained in more detail in Chapter 5, is essentially a surface homothetic to the state boundary surface that passes through the current stress state, and it is assumed to have the ellipse shape of the Modified Cam Clay model) and the remaining strain components are calculated from a plastic potential surface. However, when adopting the above assumption, it is found that the model is not able to correctly predict critical state conditions. The formulation of the model in general stress space is modified such that a

given loading surface becomes a locus of constant visco-plastic scalar multiplier. The model is implemented in ICFEP and is then validated by means of finite element analyses that mimic common laboratory tests.

Chapter 6 presents an elastic visco-plastic model based on the overstress theory, which incorporates a non-linear logarithmic law between creep strain and time, derived based on the concept of Equivalent Time by Yin et al. (2002), to evaluate the visco-plastic volumetric strain rate. This model is called the Equivalent Time model and one of the main advantages of this model over Creep model 1 is that it incorporates a limit to the amount of creep volumetric strain, and therefore predicts a non-linear creep law. Based on the results presented in the Chapter 6 the model is extended to general stress space by assuming that a given loading surface is a locus of constant visco-plastic scalar multiplier. The validation of the model is divided into three parts: a) simulation of common laboratory tests; b) predictions of the one-dimensional consolidation of samples of various thickness and c) simulation of a set of laboratory tests on Hong Kong marine deposits. To conclude the Equivalent Time model is compared with Creep Model 1.

Chapter 7 presents a parametric study on the bearing capacity of a pre-loaded 2 m wide strip footing. Following from the study presented by Zdravkovic et al. (2003) which investigated the increase in bearing capacity of a pre-loaded strip footing due to consolidation, this study aims to evaluate the bearing capacity of the same pre-loaded strip footing when the soil hardening associated with the development of creep strains is also included. The study considers different values of the coefficient of secondary compression, the effect of creep non-linearity and the effect of the adopted loading rate.

Chapter 8 describes the numerical analyses of the loading tests performed on two rigid footings at the Bothkennar test site (Jardine et al., 1995; Lehane & Jardine, 2003). In 1990 two instrumented footings were constructed. One footing (A) was taken to failure over four days giving an undrained bearing capacity of about 138kPa, while the other (B) was loaded to two thirds of this bearing capacity and then left to consolidate under constant applied load for about 11 years, at which point it was then loaded to failure, indicating an undrained bearing capacity in excess of 204kPa. The foundation soil is modelled using the Equivalent Time model; The model parameters are derived based on the large amount of laboratory and in-situ test data available in the literature, and the

adopted values are validated by the ability of the analysis to mimic the behaviour of footing A. The results of the analyses are compared with the monitoring data published in the literature.

Finally, Chapter 9 gives a summary of the work presented in this thesis, the conclusions reached and recommendations for further research.

The remaining part of this chapter introduces the definitions of stress and strain variables used in this thesis.

1.4 Definition of stress and strain variables

A constitutive model is essentially a relationship between increments of stress and strain. Given that there are various options to characterize the stress and strain state of a soil element it is important to declare how it is done within this thesis.

A stress state in general stress space can be characterized by the magnitudes of the individual components of the stress tensor, which will depend on the chosen directions for the coordinate axes x, y and z. The second order effective stress tensor is given by the following equation:

Equation 1.1

$$\left[\sigma'\right]=\begin{bmatrix}\sigma'_x & \tau_{xy} & \tau_{xz}\\ \tau_{yx} & \sigma'_y & \tau_{yz}\\ \tau_{zx} & \tau_{zy} & \sigma'_z\end{bmatrix}$$

where $\tau_{xy}=\tau_{yx}$, $\tau_{xz}=\tau_{zx}$ and $\tau_{yz}=\tau_{zy}$.

Alternatively, the stress state can be described by the value of the three principal stresses σ'_1, σ'_2, σ'_3 and the orientation of the planes on which these principal stresses act. In either case, six independent quantities are required to fully characterize a stress state in general stress space.

The effective stress tensor can be divided into two components, a volumetric and a deviatoric component as follows:

Equation 1.2

$$[\sigma'] = \begin{bmatrix} \sigma'_x & \tau_{xy} & \tau_{xz} \\ \tau_{yx} & \sigma'_y & \tau_{yz} \\ \tau_{zx} & \tau_{zy} & \sigma'_z \end{bmatrix} = \begin{bmatrix} p' & 0 & 0 \\ 0 & p' & 0 \\ 0 & 0 & p' \end{bmatrix} + \begin{bmatrix} \sigma'_x - p' & \tau_{xy} & \tau_{xz} \\ \tau_{yz} & \sigma'_y - p' & \tau_{yz} \\ \tau_{zx} & \tau_{zy} & \sigma'_z - p' \end{bmatrix}$$

Volumetric component *Deviatoric component*

where p' is the mean effective stress defined as:

Equation 1.3 $$p' = \frac{1}{3}\left(\sigma'_x + \sigma'_y + \sigma'_z\right)$$

Equation 1.2 can be rewritten as:

Equation 1.4 $$\sigma'_{ij} = p' \cdot \delta_{ij} + s_{ij}$$

where σ'_{ij} is the component *ij* of the effective stress tensor, p' is the mean effective stress, s_{ij} is the component *ij* of the deviatoric stress tensor and δ_{ij} is the Kronecker's delta.

For materials that are isotropic, in which the material properties are the same in all directions, it is sufficient and also more convenient to consider only certain aspects of the stress tensor. In particular the stress state may be characterized by stress invariants. Within this thesis the stress state is represented by three invariants: the mean effective stress p' defined by Equation 1.3, the deviatoric stress J (or the deviator stress q) and the Lode's angle θ, which are defined below:

Equation 1.5 $$J = \left[\frac{1}{2}(s:s)\right]^{1/2}$$

$$J = \left[\frac{1}{2}\left[\left(\sigma'_x - p'\right)^2 + \left(\sigma'_y - p'\right)^2 + \left(\sigma'_z - p'\right)^2 + 2\tau_{xy}{}^2 + 2\tau_{yz}{}^2 + 2\tau_{zx}{}^2\right]\right]^{1/2}$$

Equation 1.6 $$q = \sqrt{3} \cdot J$$

Equation 1.7 $$\theta = \frac{1}{3}\sin^{-1}\left[\frac{3\sqrt{3}}{2} \cdot \frac{\det(s)}{\left[\left(\frac{1}{2}(s:s)\right)^{1/2}\right]^3}\right]$$

where *det(s)* is the determinant of the deviatoric stress tensor s_{ij}.

The above three invariants can be expressed in terms of the principal effective stresses σ'_1, σ'_2 and σ'_3, as follows:

Equation 1.8
$$p' = \frac{1}{3}\left(\sigma'_1 + \sigma'_2 + \sigma'_3\right)$$

Equation 1.9
$$J = \frac{1}{\sqrt{6}}\sqrt{\left(\sigma'_1 - \sigma'_2\right)^2 + \left(\sigma'_2 - \sigma'_3\right)^2 + \left(\sigma'_3 - \sigma'_1\right)^2}$$

Equation 1.10
$$\theta = \tan^{-1}\left[\frac{1}{\sqrt{3}}\left(2\frac{\sigma'_2 - \sigma'_3}{\sigma'_1 - \sigma'_3} - 1\right)\right]$$

The choice of the invariants is not arbitrary as the above quantities have a geometric meaning in principal effective stress space as shown in Figure 1.1. The mean effective stress *p'* is a measure of the distance of the current deviatoric plane to the stress origin, along the space diagonal ($\sigma'_1 = \sigma'_2 = \sigma'_3$), noting that a deviatoric plane is any plane perpendicular to the space diagonal. The value of *J* is related to the distance of the current stress state to the space diagonal, on the deviatoric plane. The angle θ gives the orientation of the current stress state on the deviatoric plane and given the condition that $\sigma'_1 \geq \sigma'_2 \geq \sigma'_3$ stress states are confined to lie between the lines θ=-30° and θ=+30° that correspond to triaxial compression and extension, respectively.

It is noted that the three stress invariants p', J and θ are able to give information on the overall magnitude of the stress state, but provide no information on the orientation of the principal directions. If the material is considered to be isotropic, i.e. the material properties are the same in all directions, and information on the orientation of the principal directions is not required. However, if the material is assumed to be anisotropic then the use of the three stress invariants is not sufficient and the whole stress tensor (6 pieces of information) needs to be involved in the calculation procedures.

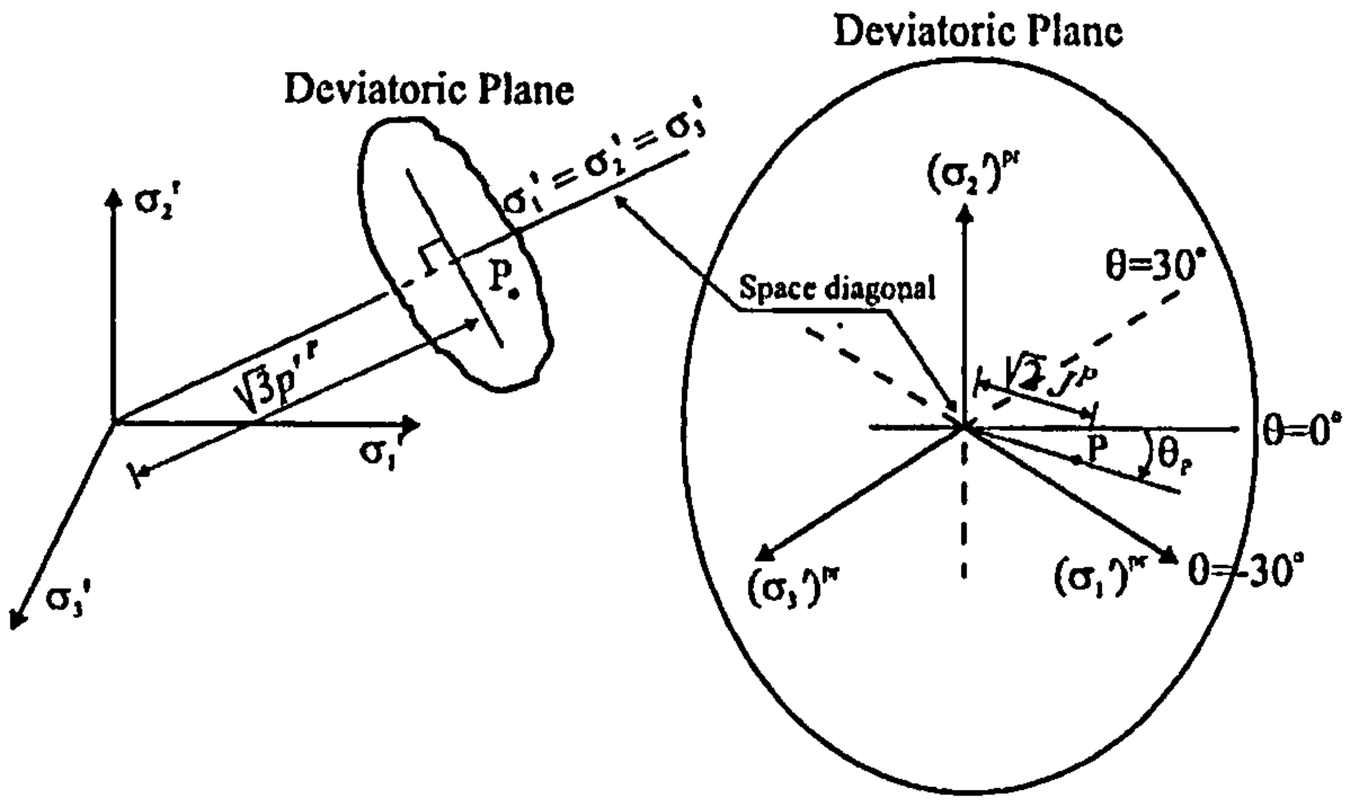

Figure 1.1: Stress invariants in principal effective stress space (after Potts & Zdravkovic, 1999).

As with the stress state, the strain state is a tensor characterized by six components, i.e. ε_x, ε_y, ε_z, γ_{xy}, γ_{xz}, γ_{yz}:

Equation 1.11

$$[\varepsilon]=\begin{bmatrix} \varepsilon_x & \gamma_{xy}/2 & \gamma_{xz}/2 \\ \gamma_{yx}/2 & \varepsilon_y & \gamma_{yz}/2 \\ \gamma_{zx}/2 & \gamma_{zy}/2 & \varepsilon_z \end{bmatrix}$$

where $\gamma_{xy}=\gamma_{yx}$, $\gamma_{xz}=\gamma_{zx}$ and $\gamma_{yz}=\gamma_{zy}$.

The strain tensor can be divided into two components, the deviatoric and volumetric components:

Equation 1.12

$$[\varepsilon]=\begin{bmatrix} \varepsilon_x & \gamma_{xy}/2 & \gamma_{xz}/2 \\ \gamma_{yx}/2 & \varepsilon_y & \gamma_{yz}/2 \\ \gamma_{zx}/2 & \gamma_{zy}/2 & \varepsilon_z \end{bmatrix}=\begin{bmatrix} e_v & 0 & 0 \\ 0 & e_v & 0 \\ 0 & 0 & e_v \end{bmatrix}+\begin{bmatrix} \varepsilon_x-e_v & \gamma_{xy}/2 & \gamma_{xz}/2 \\ \gamma_{yx}/2 & \varepsilon_y-e_v & \gamma_{yz}/2 \\ \gamma_{zx}/2 & \gamma_{zy}/2 & \varepsilon_z-e_v \end{bmatrix}$$

Volumetric component *Deviatoric component*

where e_v is defined as:

Equation 1.13

$$e_v=\frac{1}{3}(\varepsilon_x+\varepsilon_y+\varepsilon_z)=\frac{1}{3}\varepsilon_{vol}$$

where ε_{vol} is the volumetric strain. Equation 1.12 can be rewritten as:

Equation 1.14 $$\varepsilon_{ij} = \frac{1}{3}\varepsilon_{vol} \cdot \delta_{ij} + e_{ij}$$

where ε_{ij} is the component *ij* of the strain tensor, ε_{vol} is the volumetric strain, δ_{ij} is Kronecker's delta and e_{ij} is the component *ij* of the deviatoric strain tensor. Within this thesis the strain state is characterized by two invariants: the volumetric strain ε_{vol} given by 1.13 and the deviatoric strain E_d, which is defined as follows:

Equation 1.15 $$E_d = [2(e_s : e_s)]^{1/2}$$

$$E_d = \left[2\left[(\varepsilon_x - e_v)^2 + (\varepsilon_y - e_v)^2 + (\varepsilon_z - e_v)^2 + \frac{1}{2}\gamma_{xy}{}^2 + \frac{1}{2}\gamma_{yz}{}^2 + \frac{1}{2}\gamma_{zx}{}^2\right]\right]^{1/2}$$

The strain invariants can be written in terms of the principal strains ε_1, ε_2 and ε_3:

Equation 1.16 $$\varepsilon_{vol} = \varepsilon_1 + \varepsilon_2 + \varepsilon_3$$

Equation 1.17 $$E_d = \frac{2}{\sqrt{6}}\left[(\varepsilon_1 - \varepsilon_3)^2 + (\varepsilon_2 - \varepsilon_3)^2 + (\varepsilon_1 - \varepsilon_2)^2\right]$$

A basic assumption of elastic behaviour is that the directions of principal effective stress increments and incremental strains coincide. The general constitutive equation gives a relationship between increments of effective stress and increments of strain:

Equation 1.18 $$\{\Delta\sigma'_{ij}\} = [D'] \cdot \{\Delta\varepsilon_{ij}\}$$

where $\{\Delta\sigma'_{ij}\}$ is the vector containing the effective stress tensor components, $\{\Delta\varepsilon_{ij}\}$ is the vector containing the strain tensor components and $[D']$ is the effective stress constitutive matrix. If the material is assumed to be isotropic elastic then the matrix $[D']$ can be shown to be symmetric and in addition the behaviour is fully defined by two independent elastic parameters. In geotechnical engineering the elastic behaviour of materials (i.e. soils) is often characterized in terms of the elastic shear modulus, G and the elastic bulk modulus, K. If the material is assumed to be isotropic linear elastic then the quantities G and K are constant and Equation 1.18 can be written as:

Equation 1.19

$$\begin{Bmatrix} \Delta\sigma'_x \\ \Delta\sigma'_y \\ \Delta\sigma'_z \\ \Delta\tau_{xz} \\ \Delta\tau_{yz} \\ \Delta\tau_{xy} \end{Bmatrix} = \begin{bmatrix} K+4/3G & K-2/3G & K-2/3G & 0 & 0 & 0 \\ & K+4/3G & K-2/3G & 0 & 0 & 0 \\ & & K+4/3G & 0 & 0 & 0 \\ & & & G & 0 & 0 \\ & sym & & & G & 0 \\ & & & & & G \end{bmatrix} \cdot \begin{Bmatrix} \Delta\varepsilon_x \\ \Delta\varepsilon_y \\ \Delta\varepsilon_z \\ \Delta\gamma_{xz} \\ \Delta\gamma_{yz} \\ \Delta\gamma_{xy} \end{Bmatrix}$$

In an elastic isotropic material, the volumetric and shear components are decoupled and the above elastic parameters, G and K, can be calculated from any stress path as:

Equation 1.20

$$G = \frac{\partial J}{\partial E_d}$$

Equation 1.21

$$K = \frac{\partial p'}{\partial \varepsilon_{vol}}$$

Moreover, for an isotropic linear elastic material the elastic parameters G and K can be related to Young's Modulus, E and the Poisson's ratio, μ by the following equations:

Equation 1.22

$$G = \frac{E}{2 \cdot (1+\mu)}$$

Equation 1.23

$$K = \frac{E}{3 \cdot (1-2\mu)}$$

2 OBSERVED VISCOUS BEHAVIOUR OF SOILS

2.1 Introduction

As mentioned in Chapter 1, the aim of this thesis is to develop, implement and validate constitutive models that are able to reproduce the time dependent behaviour of clays that derive from the soil viscosity.

This Chapter gives a review of the published literature concerning the viscous time dependent behaviour of soils, focusing on the behaviour of saturated clays. The time dependent behaviour of soils is usually divided into viscous effects (such as creep, stress relaxation, strain rate effect) and ageing effects. However the interaction between the two types of effects and the interaction with other aspects of soil behaviour like natural soil structure and anisotropy considerably complicates their characterization and quantification.

2.2 Definition of common time effects

From the literature review, it became apparent that there is some confusion in the terminology regarding the subject of time dependent behaviour of soils. Therefore, it seems important to define the terminology as it is used in this thesis. Nowadays, most researchers appear to agree that aspects of the time dependent behaviour such as creep, stress relation and strain rate effects can be grouped into what can be called the viscous effects, where:

Creep – the continued deformation of a soil element at constant effective stress; can be applied to either the deviatoric and volumetric component of stress/strain.

Stress relaxation - the continued decrease in effective stresses acting on a soil element under constant strain conditions

Rate effects - the change in the stress-strain-strength soil response due to the rate of applied load/strain.

The viscous effects observed in soils are believed to result mainly from sliding at interparticle contacts and associated particle re-arrangement, with the presence or absence of (free) water having only a minor influence (Mitchell, 1993). In fluid

mechanics, viscosity is "the resistance a gaseous or liquid system offers to flow when it is subjected to a shear stress" (Matešić & Vucetic, 2003), noting that an increase in the fluid viscosity gives rise to a higher resistance to flow at a given shear stress.

If the term is extended to soil mechanics, one could say that granular materials are in general more viscous than clays, as they tend to give rise to a higher resistance to shearing at a given shearing rate. However, the viscous effects as defined above, that can be quantified by the magnitude of creep strains at constant stress or the increase in shear stress produced by an increase in strain rate, are in general greater in clayey soils than in granular materials. In a material such as clay there is a continuous increase in the resistance to flow with increasing strain rate, but the coefficient of viscosity is found to decreases with strain rate. It is apparent that mathematically, viscous flow alone cannot explain the behaviour of soils, and one needs also to consider additional elastic and plastic components.

Some aspects of the observed time and rate dependent behaviour of soils cannot be explained by viscous effects. They include for example, the time-dependent *structuration* associated with physico-chemical processes such as thixotropy, bonding and cementation. For *structuration* or *ageing* the author means the process (es) by which the soil acquires structure, giving the additional components of strength and stiffness of the natural soil, in relation to the reconstituted one, which cannot be accounted for by void ratio and stress history alone.

The term *thixotropy* was first employed to describe the mechanisms of aggregation and dispersion occurring in colloidal suspensions and gels. In soil mechanics the term *thixotropy* has been used to describe "an isothermal, reversible, time-dependent process occurring under conditions of constant composition and volume whereby a material stiffens while at rest and softens or liquefies upon remoulding" (Mitchell, 1960). Consequently, some authors have suggested that the term *thixotropy* should not be applied to the process of time dependent strength increase of soils, and instead a term such as *age hardening* should be used. Skempton & Northey (1952) suggest that thixotropy in soils results "from the gradual rearrangement of particles, under the action of bonding forces, into positions of increasing mechanical stability". Sorensen (2006) classifies the processes of thixotropy, bonding and cementation as *inherent ageing effects*, based on the fact that they require little interaction with the surrounding

environment (the exception may be significant cementation) and cause, in principle, no significant changes in the intrinsic properties of the soil. By "intrinsic properties" the author refers to the properties of a given soil that are evaluated on reconstituted samples, as defined by e.g. Burland (1990), Leroueil and Vaughan (1990).

Time dependent changes to the soil structure may also occur as a result of weathering, chemical changes in the pore water (e.g. leaching) and heat and pressure variations. Sorensen (2006) classified these phenomena as *environmental ageing effects*, since they require significant interaction with the surrounding environment. These effects produce, in principle, changes in the soil composition, and consequently are likely to produce changes in the intrinsic properties of the soil.

It is often difficult to distinguish between the components in the soil behaviour that are due to viscous effects and those that derive from ageing, as both are time dependent and in principle may occur simultaneously. In addition, viscous effects often give rise to *apparent* structuration; i.e. on loading after a period of drained creep an increase in stiffness, yield stress and undrained shear strength is often observed. However, there are fundamental differences between the apparent structuration that often occurs associated with viscous effects and true ageing. In addition, in clayey soils one also needs to consider the delayed dissipation of excess pore pressure and its interaction with the viscous effects, i.e. the role of viscous deformation during primary consolidation.

A review of the mechanical behaviour of soils that derives from changes in the soil state only, and is independent of time and rate of strain is beyond the scope of this thesis, and the reader should refer elsewhere (e.g. Grammatikopoulou, 2004; Gasparre, 2005; Cotecchia, 1996). The literature review presented subsequently will concentrate on the time dependent behaviour of clays that arise from viscous effects. For clarity and completeness, data on other soil types is also included. Such a review will allow the evaluation of the applicability of the constitutive models presented in this thesis, which have primarily been developed for clays, to other soil types. Throughout this chapter, and whenever relevant, reference is made to ageing effects on soils so that the limitations of their non-consideration may be fully appreciated.

Given the viscous nature of soil behaviour it is not surprising that the stress-strain-strength soil response is also affected by temperature. Although the consideration of the

effect of temperature is beyond the scope of this thesis, a brief account of the effect of temperature on the soil behaviour is included in Section 2.6.

2.3 Creep and strain relaxation

2.3.1 Characterization of the phenomena of creep and stress relaxation

Creep is defined as the soil deformation that occurs at constant effective stresses, during which the rate of deformation is controlled by the viscous properties, or the viscous resistance, of the soil. The phenomena of creep follows qualitatively similar trends for all soil types but, in general, the amount of creep deformation is found to increase with increasing soil plasticity, water content and stress level, noting that larger creep deformations imply a decrease of the soils viscous resistance.

From the definition of creep, *creep tests* are defined as tests performed at constant effective stress conditions, but due to the difficulties in keeping constant effective stress conditions, this term is often inappropriately applied to a broader range of tests. For example, in a drained triaxial test constant effective stress conditions can only be achieved if the applied load is continuously corrected to account for the change in the sample cross-section area, and the descriptor *constant load* or *constant stress* is usually added.

Some researchers refer to *undrained creep tests* (or *undrained creep* phenomenon) during which the applied stresses are kept constant and there is an increase of shear deformation (creep deformation) at constant volume with time. However, according to the definition presented above, these tests are not true creep tests as during the tests there are changes in pore water pressure and consequently, changes (reduction) in the soil's effective stress. Undrained creep is found to follow the same trends, qualitatively and quantitatively, as drained creep. Therefore when analysing laboratory test data one should be well aware of the testing procedures.

The process of creep can be characterized by three phases: primary, secondary and tertiary as shown in Figure 2.1. However, there is some confusion in the literature regarding the terms primary, secondary and tertiary creep defined in connection with creep tests performed in a triaxial apparatus, and primary, secondary and tertiary

compression defined in connection with step load tests performed in an oedometer apparatus.

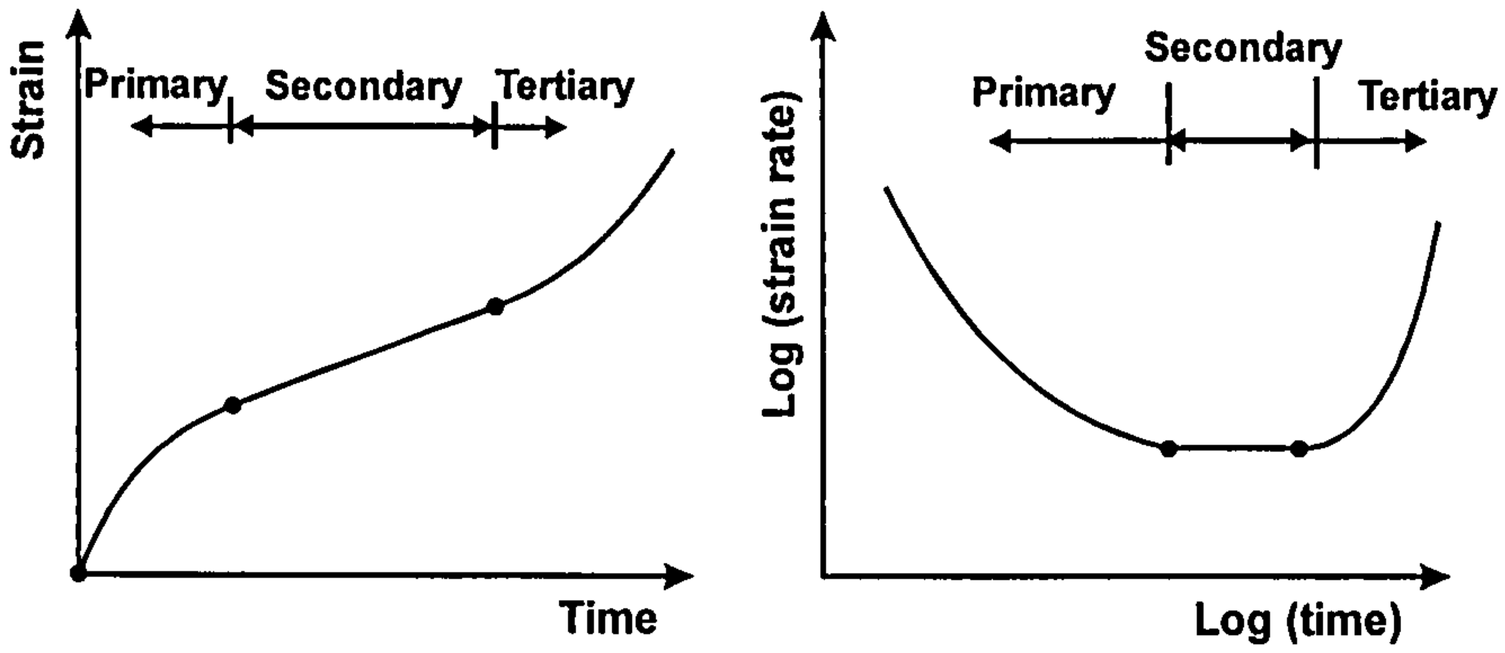

Figure 2.1: Definition of creep phase's characteristics (after Augustesen at al., 2004).

During primary consolidation, the soil deformation is associated mainly with the dissipation of excess pore water pressure, and during this period the strain rate decreases rapidly with time. After the end of primary consolidation (EOP), deformation continues at a reducing rate, and the deformation over this period – denominated secondary compression - is controlled by the soil skeleton viscosity, and is usually characterized by a linear relationship between creep strain and the logarithm of time. Sometimes a tertiary consolidation phase may be subsequently observed. The tertiary consolidation phase is characterized by an acceleration of creep strain with the logarithm of time, as schematically shown in Figure 2.2. This phenomenon has been reported by e.g. den Haan (1994) on oedometer tests on Portage peat.

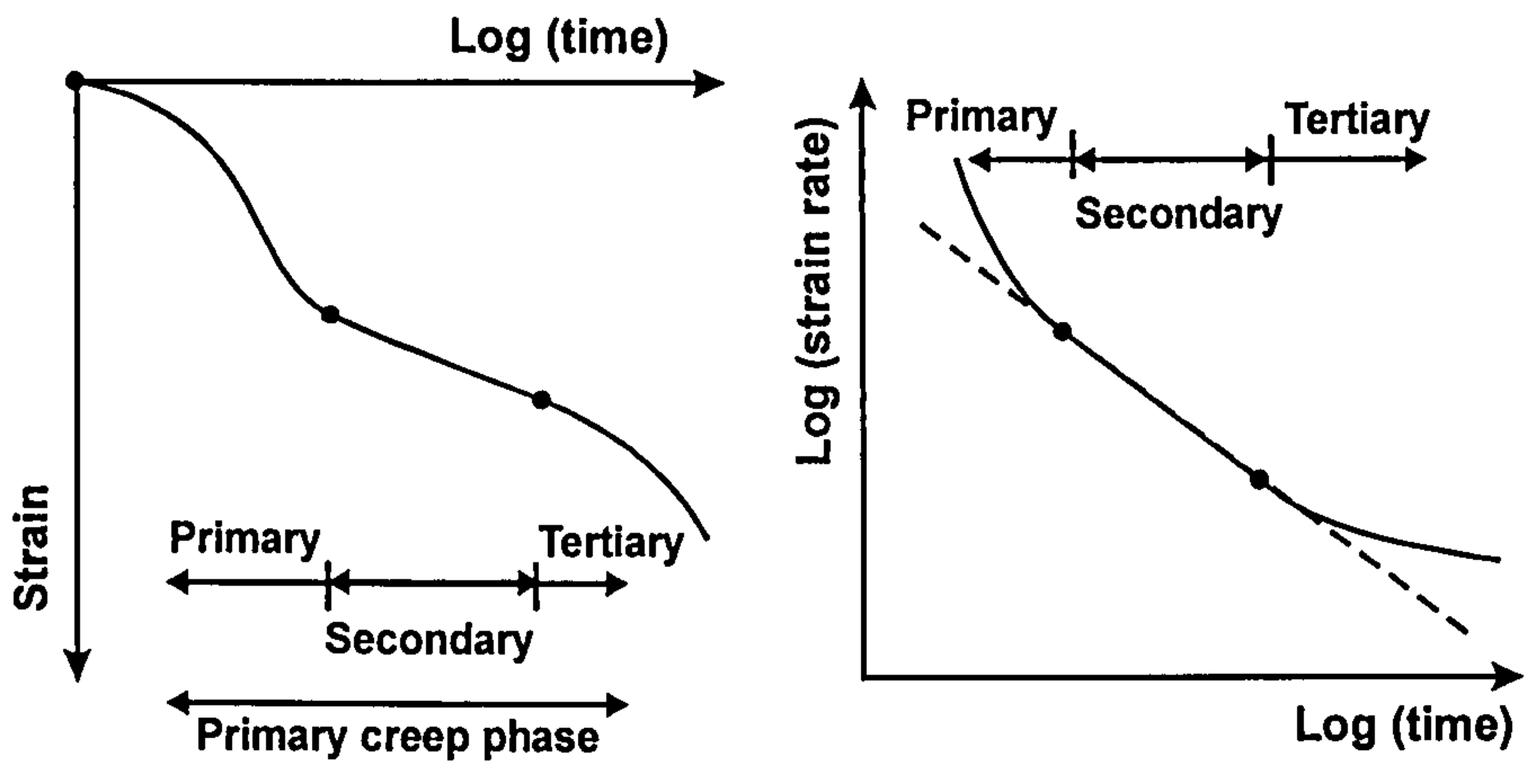

Figure 2.2: Definition of consolidation phases during a 1D oedometer compression test (after Augustesen at al., 2004).

This behaviour corresponds closely to that observed in one-dimensional (1D) oedometer tests (or triaxial tests at stress states far from failure), where the creep behaviour is characterized by reducing strain rates with time, corresponding to the primary creep (see Figure 2.1).

During creep triaxial tests, depending on the imposed stress state in relation to the failure envelope, secondary and tertiary creep phases may be observed. They are characterized by constant and accelerating strain rates with time, respectively. The tertiary creep phase leads eventually to failure, commonly known as *creep rupture*. It is noted that the creep phases described above are appropriate for deformations occurring after loading stages i.e. they are associated with an increase in the soil's mean effective stress. Creep behaviour following a significant unloading stage is usually characterized by an initial phase of creep recovery, where creep strains give rise to further swelling, reversing to compression deformation after a period of time.

Stress relaxation is defined as a time dependent change in effective stress at constant deformation. Limited information has been found in the literature concerning stress relaxation and the work of Lacerda & Houston (1973) remains the basis of the current understanding of this phenomenon. Lacerda & Houston (1973) performed undrained relaxation tests (in which the axial strain remained constant with time) on a wide range of materials, including an undisturbed soft marine clay (San Francisco Bay Mud), kaolinite, a clean quartz sand (Monterey sand) and compacted Ygnacio Valley Clay, under various testing conditions. They found that the stress relaxation phenomenon was identical in all the materials tested and followed common trends that are schematically shown in Figure 2.3:

a) Following an initial time delay the deviator stress was found to vary linear with the logarithm of time;

b) The strain rate applied prior to the stress relaxation phase influences the time at which the stress starts to decrease; an increase in the strain rate was found to decrease the time delay prior to deviator stress decay.

Lacerda & Houston (1973) show that the parameters that describe the stress relaxation process are related to the creep parameters determined from creep tests, implying that the two phenomena result from the same mechanism. Further, the influence of the

applied strain rate on the subsequent relaxation phase suggests that, at least for the materials tested, there is a correspondence between relaxation and strain rate effects. Leroueil & Marques (1996) suggest a relationship between creep and stress relaxation. They assume that the total strain rate, $\dot{\varepsilon}^{total}$ is the sum of the elastic strain rate, $\dot{\varepsilon}^{el}$ and the time dependent visco-plastic strain rate, $\dot{\varepsilon}^{vp}$:

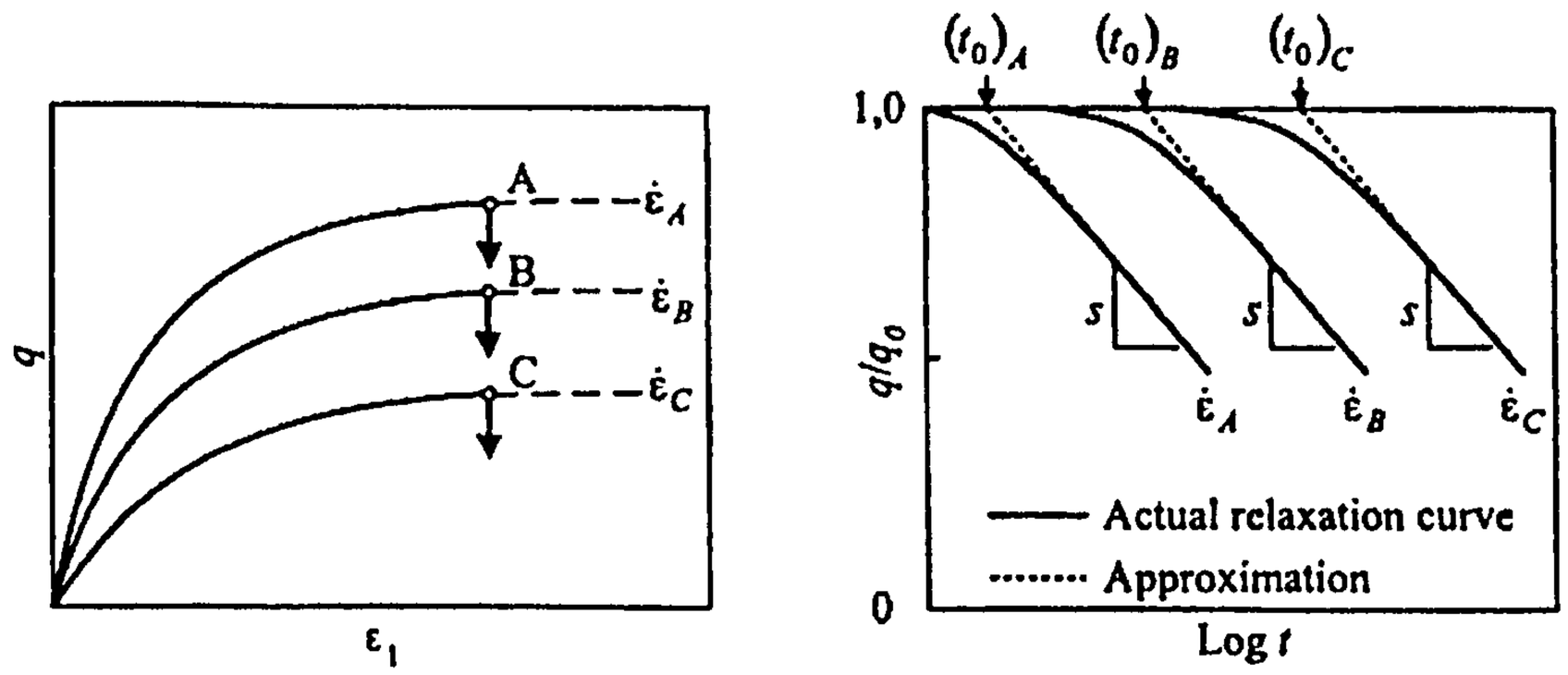

Figure 2.3: Schematic diagram of the stress relaxation model proposed by Lacerda & Houston (1973)

Equation 2.1 $$\dot{\varepsilon}^{total} = \dot{\varepsilon}^{el} + \dot{\varepsilon}^{vp}$$

A change in the current elastic strain $\Delta\varepsilon^{el}$ is uniquely related to a change in the current effective stress state, $\Delta\sigma'$ via the elastic stiffness. In a creep test, the stress is constant and consequently $\dot{\varepsilon}^{el} = 0$ and $\dot{\varepsilon}^{total} = \dot{\varepsilon}^{vp}$. During a stress relaxation test, the total strain is constant, therefore the strain rate must be zero and $\dot{\varepsilon}^{el} = -\dot{\varepsilon}^{vp}$. If $\dot{\varepsilon}^{vp}$ is positive, as it usually is after a loading stage then $\dot{\varepsilon}^{el}$ will be negative producing a reduction in effective stress σ'. In this way, the reduction in effective stress during stress relaxation is directly linked to the creep potential at the same state.

2.3.2 Uniqueness of the EOP

Possibly the subject in soil mechanics that has created the most discussion amongst researchers is the question of the uniqueness of the end of primary consolidation. The discussion revolves around whether the void ratio at the EOP under a given effective stress is unique or instead depends on the duration of primary consolidation, and

consequently on the consolidating layer thickness, which would imply the existence of viscous effects during primary consolidation.

There are two extreme approaches: one approach, the-so-called *End-Of-Primary (EOP) approach,* is particularly supported by Mesri and co-workers (1985, 1994) and assumes that the void ratio at the EOP consolidation under a given effective stress is unique and independent of the duration of the primary consolidation. Therefore, the compression curve obtained in the laboratory can be used directly for settlement analysis of thicker layers in the field. This methodology has been used to predict the settlement of various embankments and results were found to agree well with the field measurements. The second approach – or *viscous approach* - is based on the assumption that clays are viscous, and therefore influenced by strain rate and temperature, during the entire process of consolidation. Both approaches, that are apparently contradictory, have been supported by experimental data.

Leroueil (1995) has examined the data in the literature that supports both approaches, and has attempted to explain the reasons for the discrepancies. It is generally accepted, at least for strain rates encountered in the laboratory, that clays have viscous behaviour during primary consolidation and consequently when estimating the field settlements from laboratory compression curves one should account for the differences in strain rate and temperature. The value of strain rate in the field is likely to be smaller than that imposed in laboratory testing and thus, according to the viscous approach, the strain and the settlement in the field at EOP are expected to be larger. However, the effect of strain rate may be partially compensated by the fact that temperature in the ground is in general lower than in the laboratory (see section 2.6 on temperature effects). In addition the laboratory compression curve should ideally be obtained from oedometer tests on high quality samples; lower quality or disturbed samples will yield, as a rule, a smaller pre-consolidation pressure, causing an over prediction of the estimated settlement.

Another phenomenon that may complicate considerably the interpretation of field settlements is the development of structure that may occur while the clay is compressing, at sufficiently low strain rates. This has been reported by several researchers, e.g. Leroueil et al. (1985) on CRS oedometer tests on intact Batiscan clay. However, the strain rate at which structuring effects may become noticeable vary from soil to soil. The development of structure has the effect of strengthening the soil and

thus reduces the amount of in-situ settlement, in relation to that estimated on the basis of the viscous approach. The combination of the above factors causes the long-term field settlement curves to fall between those predicted by the EOP and the viscous approach (Leroueil, 1995; Aboshi, 2004).

2.3.3 Quantification of the observed creep behaviour

During secondary compression the development of creep strain / deformation with time can be approximated by a semi-logarithmic law, as first suggested Buisman (1936). The 1D compressibility of the soil during secondary compression can then be characterized by the coefficient of secondary consolidation, C_α. The coefficient of secondary consolidation can be expressed either in terms of changes in void ratio, $C_{\alpha e}$ (Equation 2.2) or changes in vertical strain, $C_{\alpha\varepsilon}$ (Equation 2.3), and in this thesis if nothing is said to the contrary, the author refers to the former.

Equation 2.2
$$C_{\alpha e} = \frac{\Delta e}{\log(t + \Delta t) - \log t} = \frac{\Delta e}{\Delta \log t}$$

Equation 2.3
$$C_{\alpha\varepsilon} = \frac{\Delta \varepsilon_v}{\Delta \log t}$$

The value of C_α is usually determined from incremental load (IL) 24-hour oedometer tests (in which the load increments are applied in 24 hour intervals). In natural soils, in particular, the value of C_α has been found to be highly dependent on the current stress level, in relation to the pre-consolidation pressure. Mesri & Castro (1987), based on tests on a wide range of natural soils, have shown that the ratio between $C_{\alpha\varepsilon}$ and the compression index, $C_{c\varepsilon}$ was constant and independent of stress level, where $C_{c\varepsilon}$ is defined by Equation 2.4 in the normally consolidated stress range. They suggest that the ratio is about 0.04±0.01 for inorganic soft clays and slightly higher for organic soft clays.

Equation 2.4
$$C_{c\varepsilon} = \frac{\Delta \varepsilon_v}{\log(\sigma_v^{'} + \Delta \sigma_v^{'}) - \log \sigma_v^{'}} = \frac{\Delta \varepsilon_v}{\Delta \log \sigma_v^{'}}$$

More generally, the relationship between creep strain and the logarithm of time is non-linear (Mitchell, 1993). Nevertheless the creep behaviour of soils seems to be characterized by a linear relationship between the logarithm of creep strain rate and

logarithm of time (i.e. Tavenas et al, 1978). Singh & Mitchell (1968) have defined the parameter m to characterize the creep behaviour of soils, where:

Equation 2.5

$$m = -\frac{\log \dot{\varepsilon}_2 - \log \dot{\varepsilon}_1}{\log t_2 - \log t_1} = -\frac{\Delta \log \dot{\varepsilon}}{\Delta \log t}$$

Figure 2.4 shows the relationship between the parameter m and the corresponding evolution of creep strains with the logarithm of time. It is noted that the special case of m=1 corresponds to a linear law between creep strain and the logarithm of time, and therefore to a constant C_α with time.

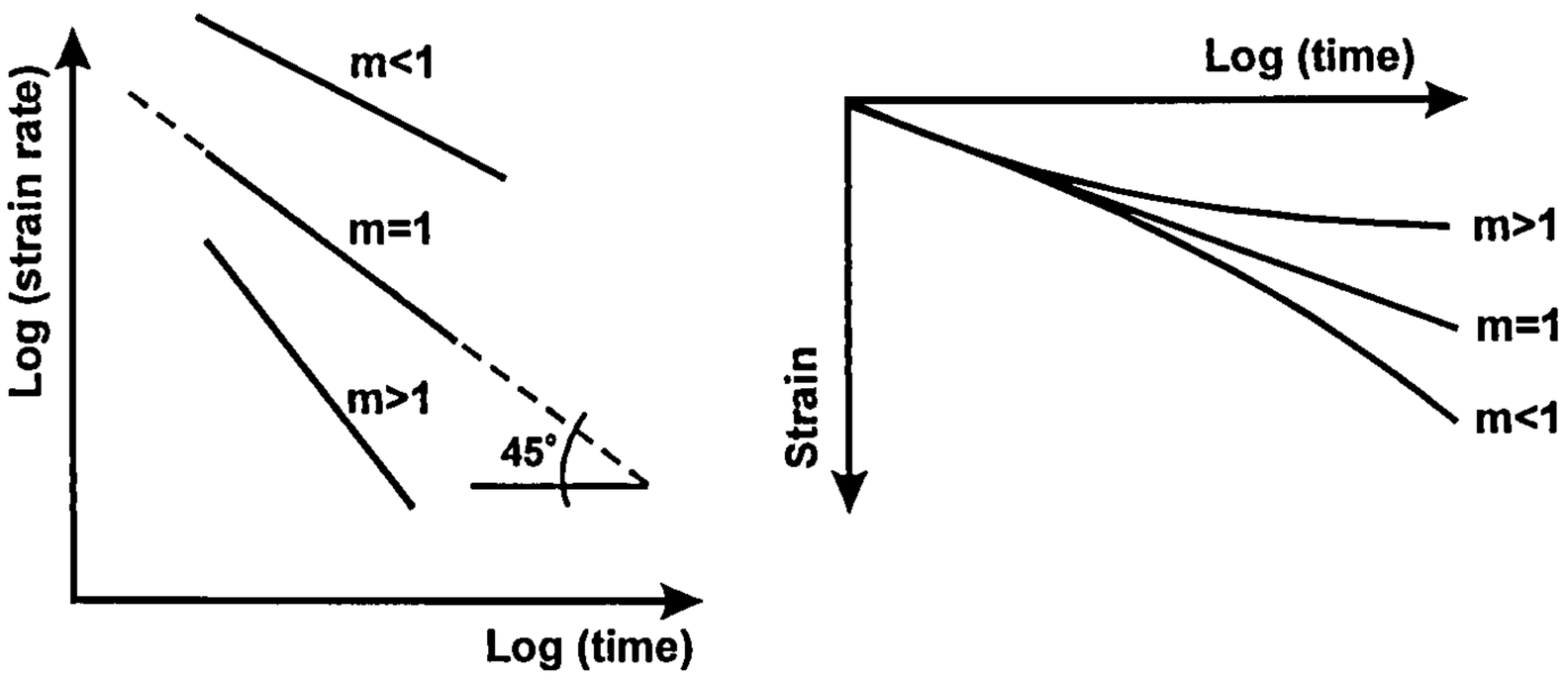

Figure 2.4: Relationship between the parameter m and the evolution of creep strain with time.

The creep behaviour described above is associated with secondary compression where the creep strain rate decreases steadily with time and the stress state is not approaching failure. Figure 2.5 shows results of undrained constant stress creep tests presented by Vaid & Campanella (1977) on intact samples of Haney clay in $\log \dot{\varepsilon} - \log t$ space. During the creep tests carried out at stress states far from the peak strength envelope, the creep strain rates are found to decrease steadily with time, and there is a linear relationship between the logarithm of creep rate and the logarithm of time. The curves are found to move upwards with increasing deviatoric stress but to maintain roughly the same slope m. For stress states close to the peak failure envelope, an increase in pore water pressure in undrained conditions may eventually bring the sample to failure. Failure is identified as a deviation from the above mentioned linear relationship and a subsequent increase in creep rate. Murayama et al. (1984), based on drained creep tests at various stress levels, have reported the same behaviour on Toyoura sand.

Several studies have investigated the problem of identifying the stress conditions that lead to the occurrence of failure during creep. Vaid & Campanella (1977), based on undrained triaxial tests on Haney Clay, suggested the existence of an upper *yield stress* below which creep rupture could not occur. For stress states above that *yield stress,* the time to failure was found to be related to the magnitude of the applied deviatoric stress, while for applied stresses below the *yield stress* the samples showed a steady decrease in creep rate with time. Tavenas & Leroueil (1977), based on undrained triaxial tests on undisturbed Saint-Alban clay, suggested that the condition for the occurrence of creep rupture was for the applied stress state to be located between the critical state line and the peak strength envelope in J-p' space.

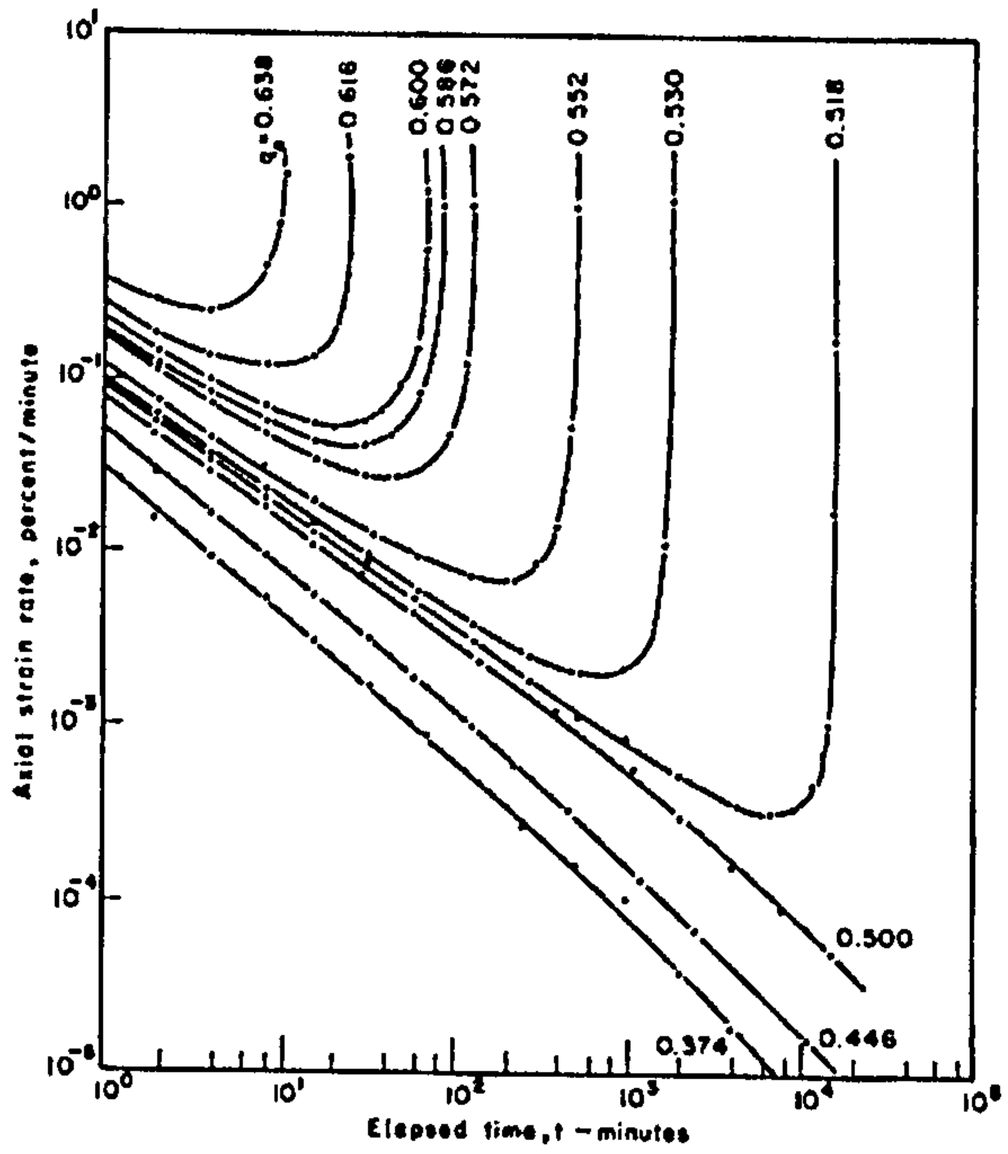

Note: the number next to each curve refers to the applied stress level $q = (\sigma_1 - \sigma_3)/\sigma_c^{'}$ *where* $\sigma_c^{'}$ *the isotropic pre-consolidation pressure.*

Figure 2.5: Variation of axial strain rate with time during constant stress creep tests (Vaid & Campanella, 1977).

2.3.4 Influence of creep on the yield locus and subsequent stress paths

From observations of creep (secondary compression) on soft clays in 1D compression, Bjerrum (1967) proposed a model for the 1D behaviour of soils based on the concept of *isochrones* or *lines of equal time*, schematically shown in Figure 2.6. According to Bjerrum (1967), the soil deformation can be decomposed into an instant and a delayed component. The isochrones plot as parallel lines in *e-log*σ_v' space and represent the

positions (void ratio) of equilibrium at the respective times of sustained load at the various stress values. Under sustained stress, the void ratio reduces with time as a result of creep (delayed compression); on applying further load the soil exhibits a yield pressure or an apparent pre-consolidation pressure higher than the stress that the soil had been subjected to previously. In addition, the undrained strength is found to increase as a result of drained creep. Both phenomena could be explained by the reduction of void ratio, or changes in state, during creep.

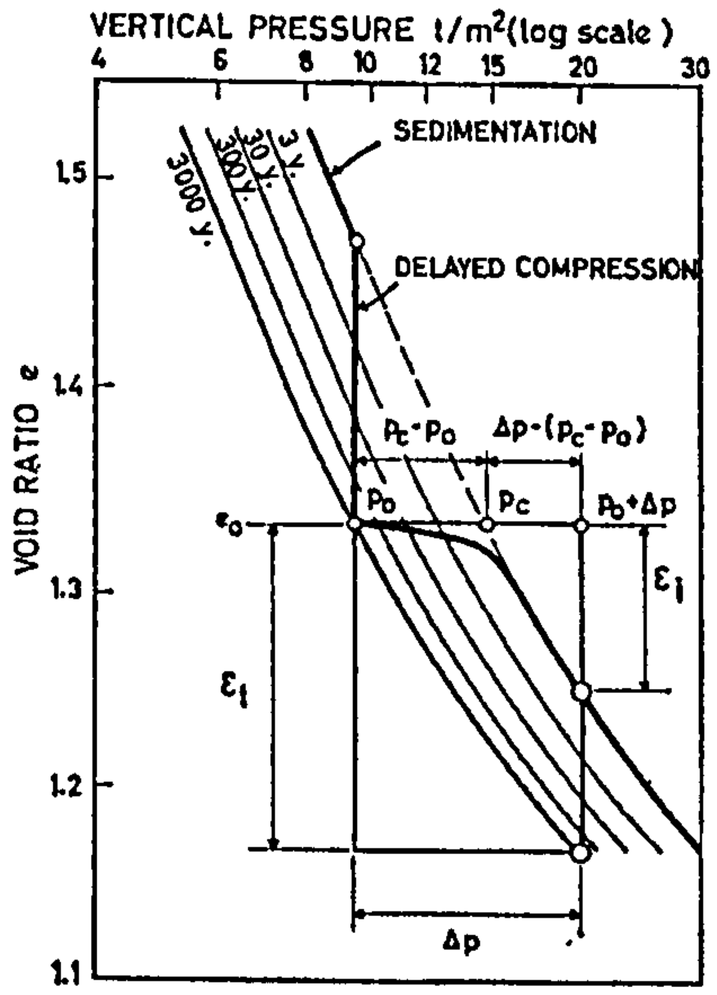

Figure 2.6: Concept of isochrones or time lines for the 1D compression of soft clays, Bjerrum (1967).

Arulanandam et al. (1971) carried out undrained triaxial creep tests on San Francisco Bay Mud at various stress ratios and observed that there was an increase of pore water pressure with time, and thus a decrease in effective stress. Figure 2.7 shows the stress locus at different creep times, showing that with increasing time the effective stress conditions move progressively towards smaller stresses, but that they form a surface with approximately the same shape. The data suggests that the isochrone concept proposed by Bjerrum (1967) for 1D compression can be extended to the entire yield surface in triaxial stress space.

The concept of isochrones or time lines was later replaced by the concept of constant rate of strain curves, which describes the rate effects on the stress-strain behaviour of soils in more general terms, and is presented in detail in Section 2.4.1. This is supported

by the work of Tavenas et al. (1978) who performed an extensive programme of drained and undrained triaxial creep tests on intact lightly overconsolidated St. Alban clay.

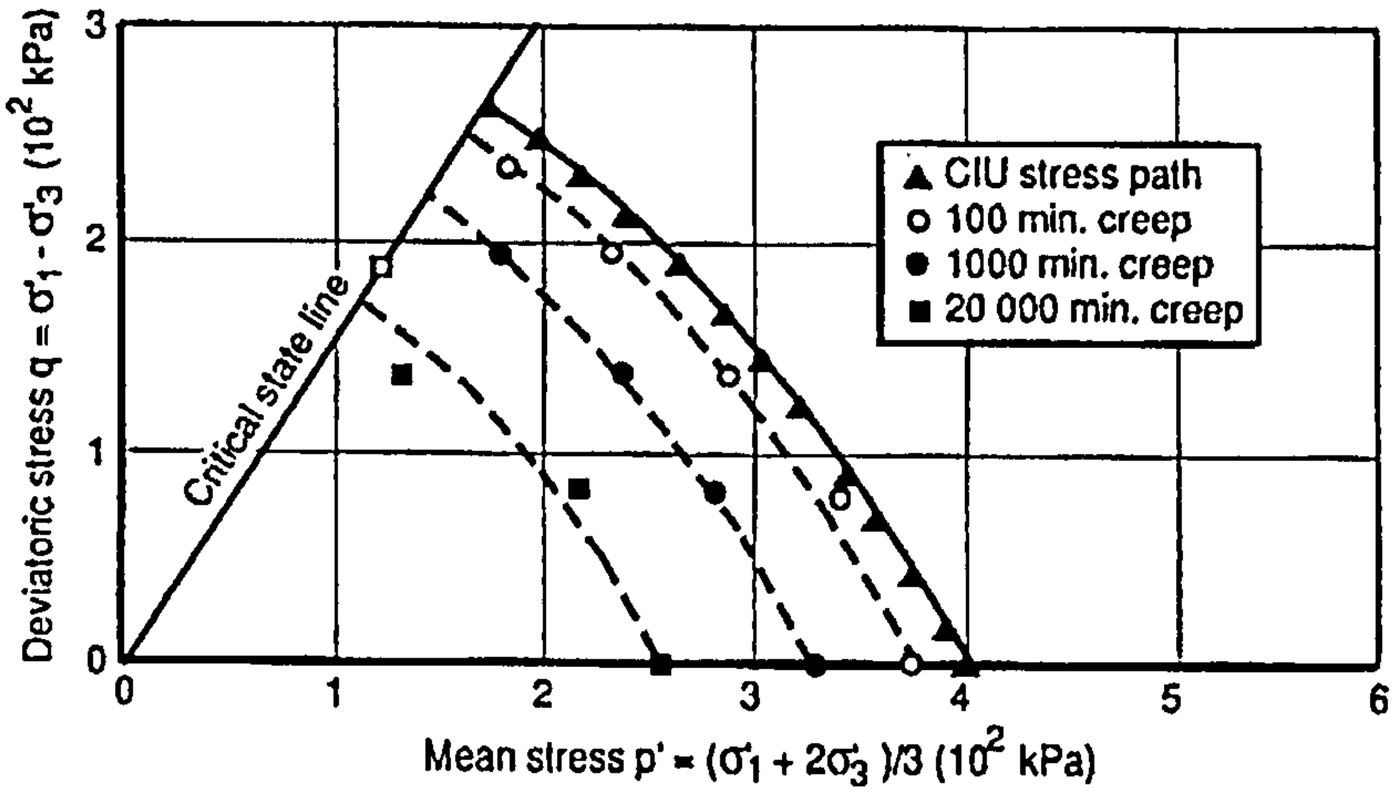

Figure 2.7: Variation of the effective stress state with time during undrained triaxial creep tests (after Arulanandam et al., 1971).

Drained creep tests were carried out at stresses located on the lines 0 to 5 as shown in Figure 2.8 and at various stress levels progressively closer to the limit state surface, monitoring both the shear and the volumetric creep deformation with time. Figure 2.8 show contours of equal volumetric strain rate at a creep time equal to 100 minutes, in other words, the contours consist of the locus of the stress states that yield the same volumetric strain rate after 100 minutes.

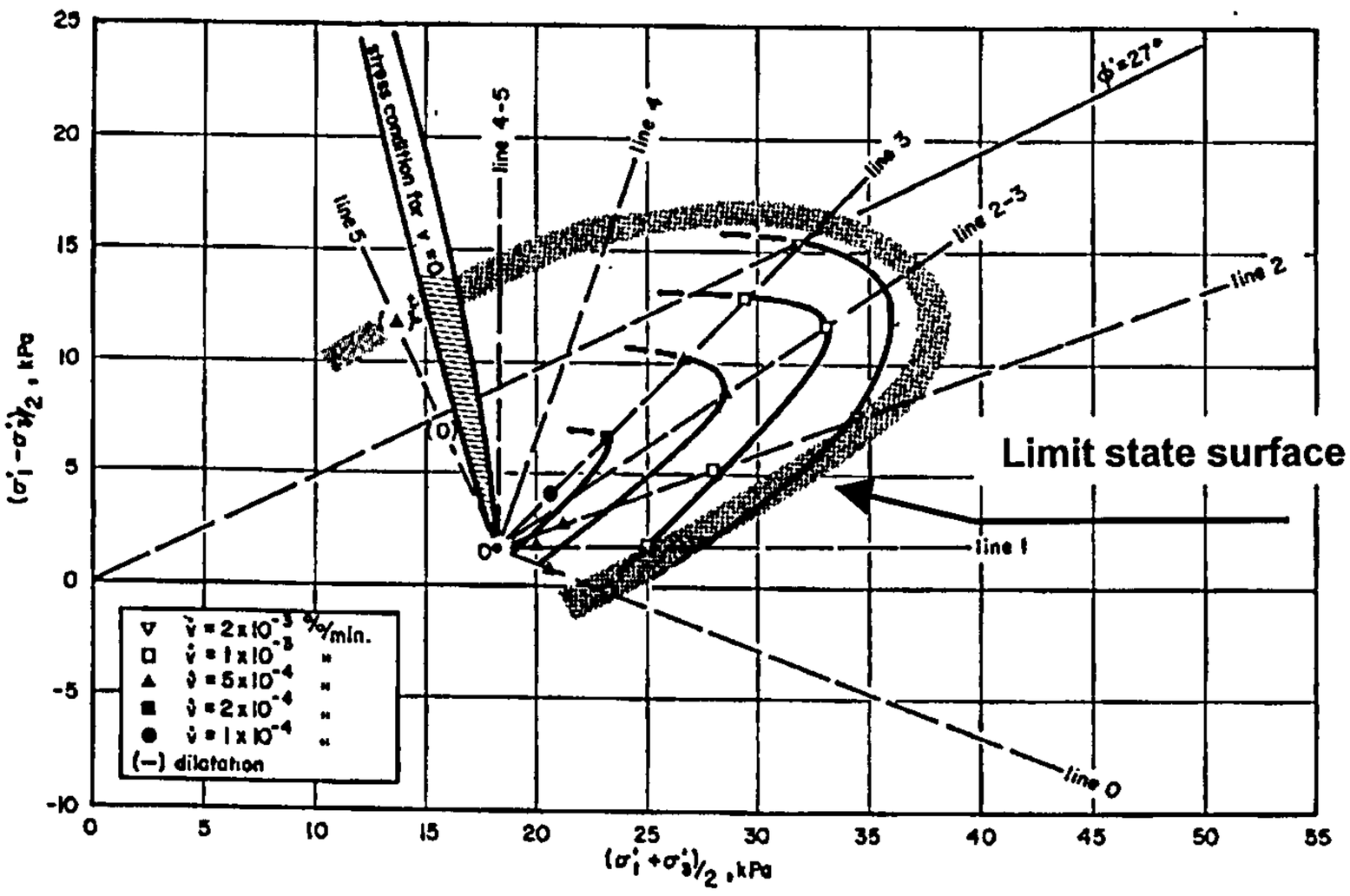

Figure 2.8: Contours of constant volumetric strain rate from drained tests on St. Alban clay (after Tavenas et al., 1978).

Between lines 0 to 3 the lines of equal volumetric strain rate have the same shape as the limit state surface, but move progressively inwards towards smaller effective stresses with reducing strain rate, and therefore the strain rate at a generic stress point is directly related to its distance to the limit state surface, which is itself a contour of constant volumetric strain rate. Between lines 5 to 4 the volumetric strains were very small or nearly zero, such that it was not possible to derive reliable values of the volumetric strain rate. In this range of stress states, the limit state line was found to be a contour of constant shear strain rate.

Creep was in general characterized by a linear relationship between the logarithm of strain rate (whatever components of strain) and logarithm of time, such that the parameter *m* for the St. Alban clay was consistently between 0.7 and 0.8, for both the volumetric and shear strain component. Based on the extensive laboratory data Leroueil et al. (1978) have proposed a general model for the effect of time on the soil's yield envelope, which is schematically shown in Figure 2.9. A soil element is assumed to be loaded in the normally consolidated range to point B on the Y_0 yield envelope, then the soil element is left to rest at stress state B for a period of time, during which it undergoes volumetric creep deformation, resulting in an expansion of the current yield envelope to Y_1.

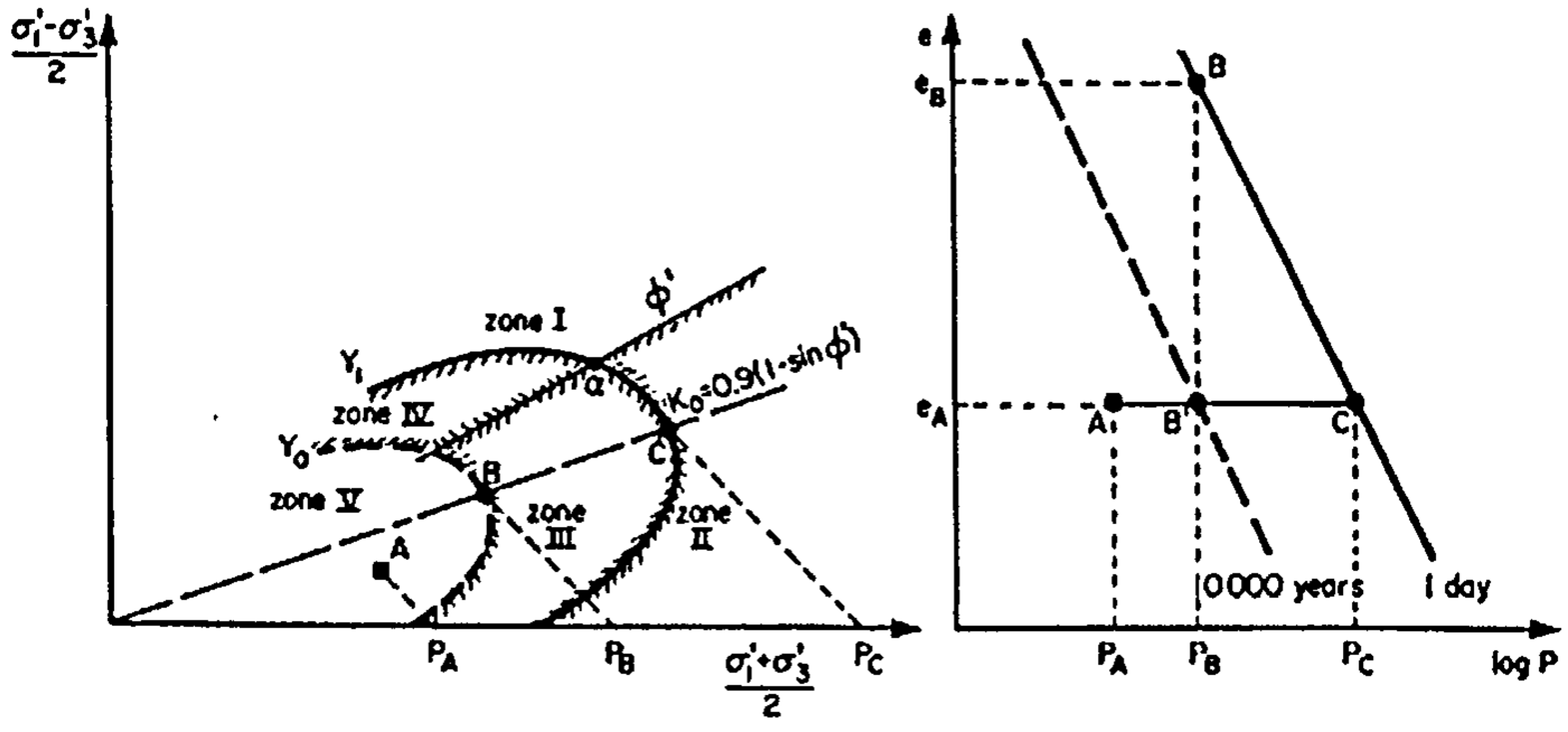

Figure 2.9: General model of the effect of time on the yield envelope of clays (after Tavenas et al., 1978).

According to the isochrone concept, on subsequent loading after a creep period the soil element will have an initial stiff response, followed by a gradual yielding until the stress path rejoins the normal compression line (NCL) corresponding to the current strain rate.

This is schematically shown in Figure 2.10(a) and corresponds to pure viscous behaviour. However, some studies reported in the literature have observed that on subsequent loading after a creep period, the stress path overshoots the NCL, as shown in Figure 2.10(b), rejoining the NCL with large straining. This behaviour could be attributed to either the development of structure or temporary effects of strain rate changes, as described later in Section 2.4.2. It is noted that if structuration occurs during the creep period then on subsequent loading the overshooting above the original NCL is in general quite persistent with continued straining, and significant straining is required to produce sufficient destructuration for the stress path to rejoin the original NCL. Similar behaviour has been identified in shearing.

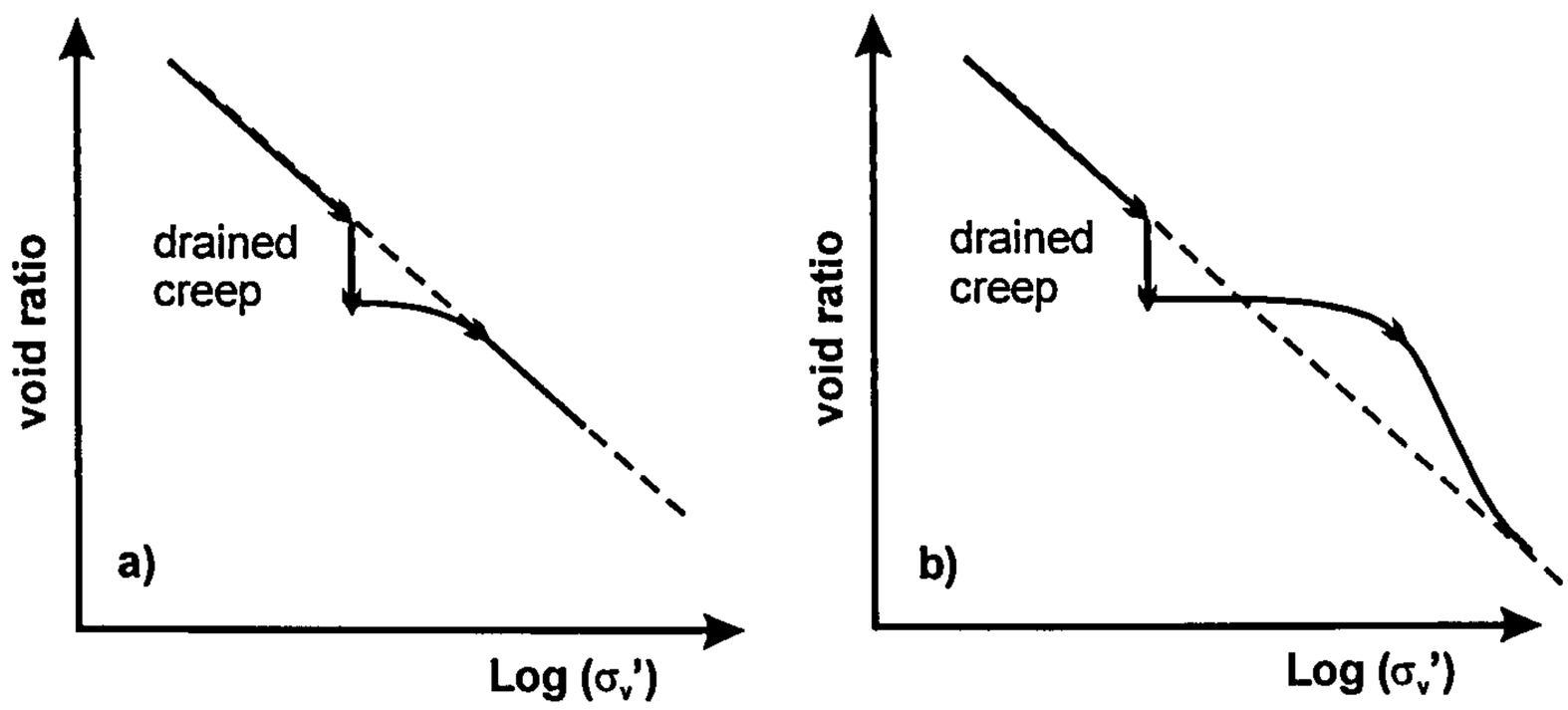

Figure 2.10: Schematic diagram of the behaviour of a soil element following a drained creep period; a) pure viscous behaviour; b) viscous and structure effects.

Various studies have been conducted to investigate the evolution of the coefficient of earth pressure at rest, K_0 with time during a creep period, where K_0 is given by the following equation:

Equation 2.6 $$K_0 = \sigma'_{h0} / \sigma'_{v0}$$

Where σ'_{h0} and σ'_{v0} are the in-situ horizontal and vertical effective stresses, respectively.

Leroueil & Marques (1996) have summarized data available in the literature and concluded that with the exception of heavily overconsolidated clays that showed a constant K_0 value with time, normally consolidated and lightly overconsolidated clays develop an increase of K_0 with time during secondary compression, this increase being between 0.003 and 0.05 per logarithmic cycle of time.

2.4 Strain rate effects

2.4.1 Introduction

The effect of strain rate on soil behaviour is generally investigated by means of constant rate of strain (CRS) tests, in which the relevant strain rate component – as a rule the vertical strain rate in oedometer tests and the axial strain rate in triaxial tests - is kept constant throughout the test. Given that, in general, small displacement theory is used in laboratory test interpretation, CRS tests are equivalent to constant rate of displacement (CRD) tests. The effect of strain rate is then evaluated by comparing the stress – strain response at different values of constant rates of straining.

Another type of laboratory test used to investigate the effect of strain rate is the step-wise change in the rate of strain (SRS) tests in which during a single test various strain rate values are applied in a step-wise manner. This procedure reduces the time of testing and eliminates sample variability. However it was soon noticed that the results from SRS and CRS tests did not agree in some cases.

Conceptually the effect of the loading or strain rate on the stress-strain response of soils is quite simple. If the rate of loading is reduced there is more time for the soil to relax and creep, allowing the development of larger deformations at a given load value, or in a displacement controlled test smaller stress at a given deformation value. The application of a larger strain rate causes, in general, the soil to yield a higher yield pressure and undrained strength. However this does not apply to all soils. According to Tatsuoka (2006) three types of viscosity can be identified in geomaterials: isotach, TESRA and Positive and negative viscosity and they are described subsequently.

2.4.2 A unique stress-strain-strain rate relationship or isotach behaviour

Until the late 1990's most of the work on the effect of strain rate on soil behaviour had concentrated on soft clays, which appeared to behave, in general, in an isotach manner. According to the isotach concept, the stress state of a soil element under any stress path is uniquely defined by the current strain and strain rate (Leroueil et al., 1985, Vaid & Campanella, 1977). Soon it was realized that it is more rigorous to state that the current stress is a unique function of the visco-plastic (or non-recoverable) strain and the respective strain rate. In this manner, the isotach model is able to explain the behaviour

during stress relaxation where the total strain rate remains zero. Tatsuoka (2006) states that the isotach behaviour is only valid during monotonic loading and cannot be applied during cyclic loading.

Sorensen (2006) has constructed a database of the viscous behaviour of various geomaterials under shearing, isotropic and 1D compression, found in the literature. The isotach behaviour is found to be applicable for a wide range of soils including soft clays in their natural and reconstituted states, undisturbed natural stiff clays and soft rocks (pre-peak), in which the stress is uniquely defined by the plastic strain and plastic strain rate and independent of the strain history. This has been observed under both 1D compression in oedometer tests and more general stress paths in the triaxial apparatus, in both drained and undrained conditions.

Several studies have investigated the strain rate dependency of the 1D and isotropic compression behaviour of soft clays. Figure 2.11 shows data from CRS 1D oedometer tests on Batiscan clay presented by Leroueil et al. (1985).

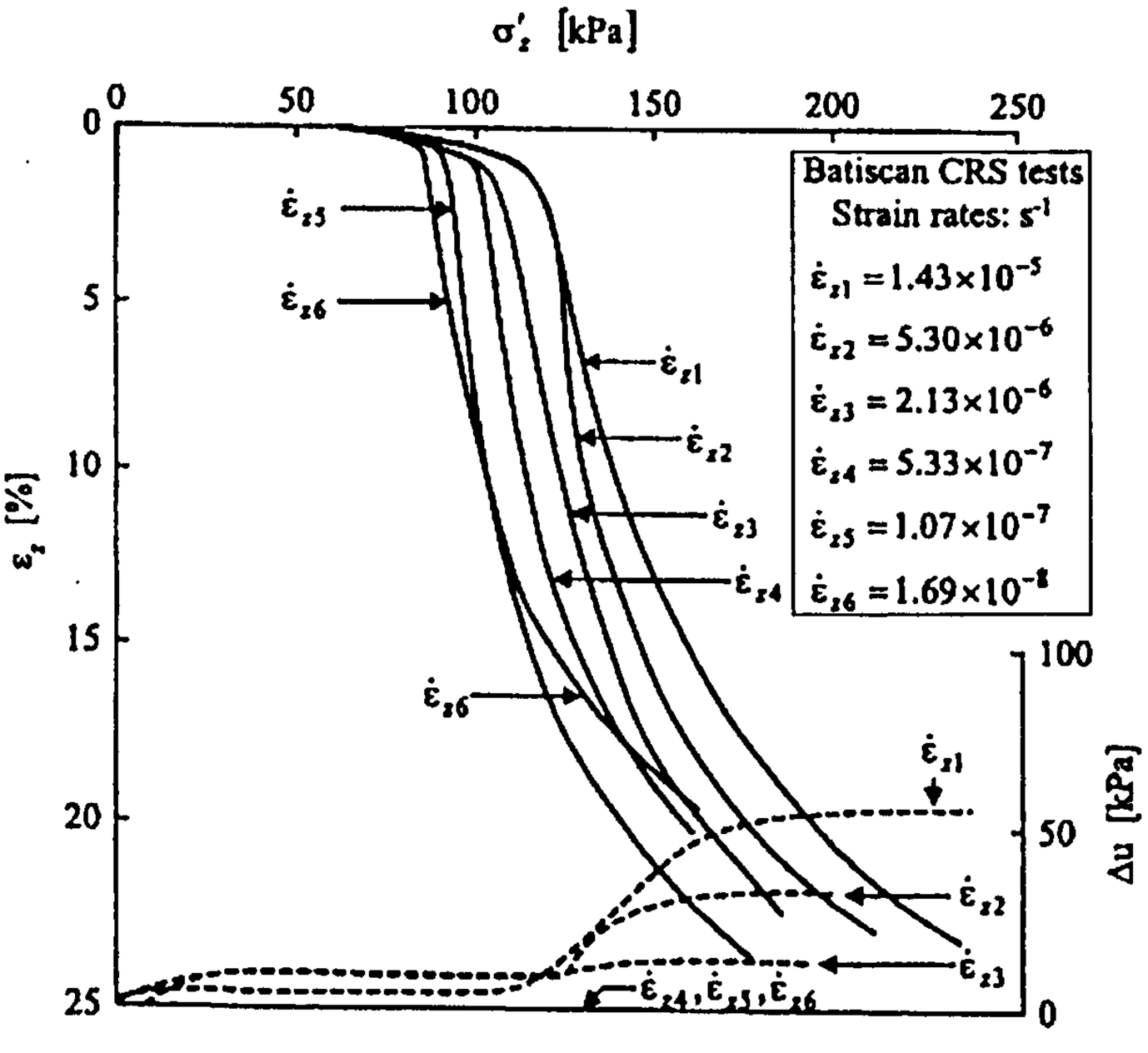

Figure 2.11: Constant rate of strain oedometer tests on Batiscan clay (after Leroueil et al., 1996).

It can be seen that following yielding there is a near linear relationship between vertical strain and effective stress for each given value of strain rate. However, with increasing

strain rate the value of pre-consolidation pressure increases causing the normal compression curves to move to the right, such that for a given vertical strain the soil element is able to sustain higher stress.

It is noted that the compression line corresponding to the slowest vertical strain rate of $1.69x10^{-8}$/s (test n.6) significantly deviates from the trend described above for the higher strain rates. Leroueil et al. (1985) interpreted this as being due to the development of structure, which occurred when the applied strain rate was sufficiently slow. With the exception of this data set, the data suggest the existence of a unique stress-strain-strain rate relationship.

Leroueil et al. (1985) suggest that the compression curves could be normalized by the correspondent yield stress, and in this case the compression behaviour could be reduced to two independent equations, one giving the relationship between the applied strain rate and the yield stress, σ_{vy}' and other giving the variation of vertical strain with normalized stress σ_v'/σ_{vy}'. This further implies that the CRS curves plot parallel in the *vertical strain – log σ_v' plane*, such that at any given vertical strain, the ratio of effective stresses measured at two different strain rates is constant.

Leroueil et al. (1983) and Leroueil et al. (1985) based on 1D compression tests on clay samples from the Champlain Sea have shown that the yield stress increased almost linearly with the logarithm of strain rate, between 7% and 15% per logarithmic cycle of strain rate. They noted that the effect of strain rate decreased at smaller strain rates, and as proposed later by other authors (i.e. Soga & Mitchell, 1996; Leroueil & Marques, 1996) it is more appropriate to consider a linear relationship between the logarithm of the YSR and the logarithm of strain rate.

Figure 2.12 shows SRS 1D oedometer tests performed on Batiscan clay by Leroueil et al. (1985). It can be seen that following an increase in the applied strain rate the soil is initially stiff and then gradually yields to join the compression curve corresponding to the current strain rate value. The compression curve is uniquely defined by the current strain rate value and the effects of strain rate are found to be persistent, which is a characteristic of isotach behaviour.

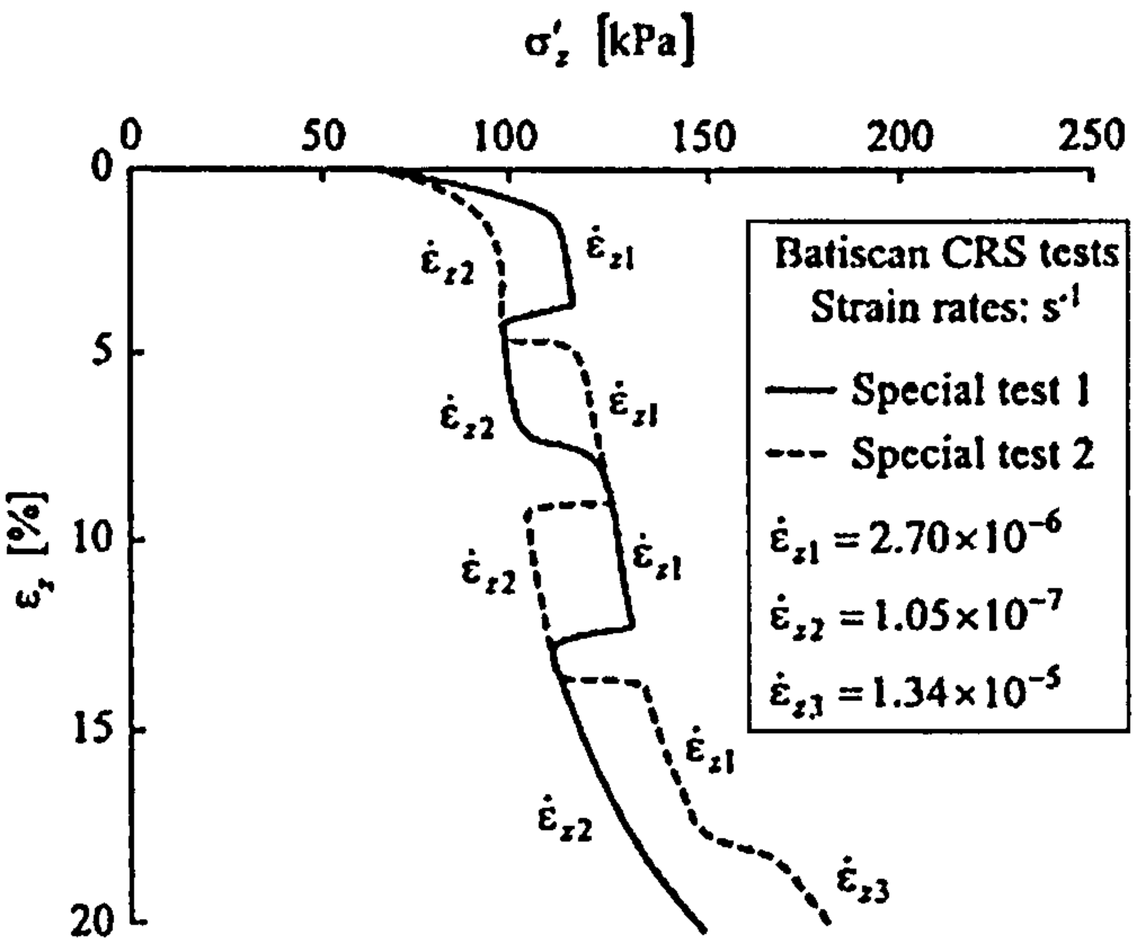

Figure 2.12: Step-wise change of strain rate and constant strain rate oedometer tests on Batiscan clay (after Leroueil et al., 1996).

Vaid & Campanella (1977) have performed undrained triaxial tests on undisturbed Haney clay (a sensitive marine soft clay) under a variety of loading conditions. After comparing the data from the various test types they identified a unique stress – strain – strain rate relationship independent of the test type, both pre and post peak. From the CRS undrained triaxial compression tests they observed that for strain rates higher than about $5x10^{-5}$ /min the undrained strength increased almost linearly with the logarithm of strain rate, about 10% per logarithmic cycle of strain rate (identical to the strain rate effect on the yield stress reported above). However, at lower strain rate values no further reduction in undrained strength was observed.

It is widely accepted that while the yield envelope, the undrained stress path and the undrained shear strength are strain rate dependent, the effective stress peak strength envelope and the critical state are strain rate independent. Therefore any observed changes in undrained strength of both NC and OC clays with strain rate are due to creep pore water pressure changes. In addition, any changes to the effective stress peak strength envelope implies the action of ageing effects and the development of soil structure.

Figure 2.13 shows the stress path and the stress-strain curve of an undrained triaxial test on kaolin during which the strain rate was varied in a stepwise manner. The test results are typical of an isotach material. Following an increase in the applied strain rate the

stress-strain curve jumps until it joins the stress-strain curve appropriate for the new current applied strain rate. It is noted that although the change in total strain rate may be stepwise, the change in the non-recoverable component of strain rate is gradual because following a change in applied strain rate there is first a change in the elastic strain rate associated with the changes in effective stresses. Given that the isotach behaviour may be expressed as a unique function of stress-irrecoverable strain – irrecoverable strain rate some authors prefer to express laboratory test results in terms of the irrecoverable strain component instead of the total one, and estimating the elastic component from a small loading – swelling loop at the start of the test.

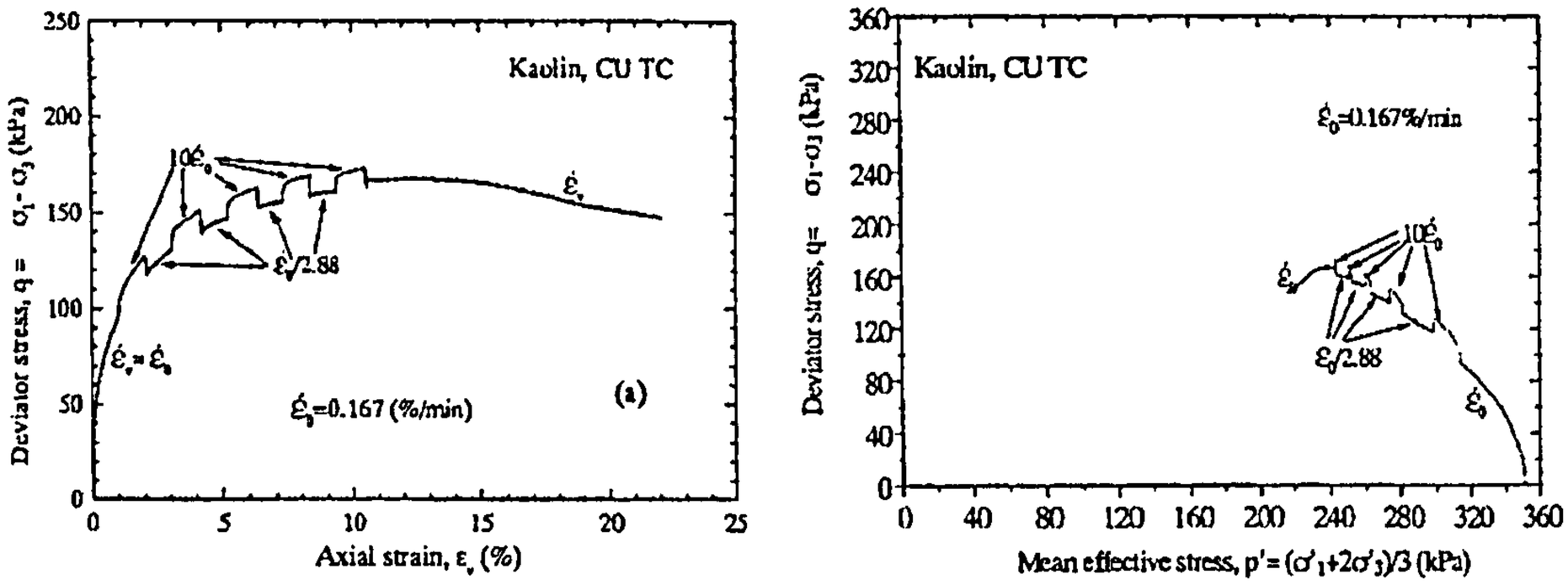

Figure 2.13: Isotach behaviour observed in an undrained triaxial compression test on Kaolin (after Tatsuoka et al., 1999).

Although the isotach model is able to explain well the facets of the time and rate dependency of soil behaviour that derive from the soil viscosity, it fails to explain other simultaneous time effects that cause the development of soil structure. It has been pointed out in relation to Figure 2.11 that the application of a sufficiently slow strain rate allowed the development of structure, such that the soil compressed less at the slowest strain rate and was able to cross the remaining CRS compression lines and sustain a higher void ratio at a given effective stress than that derived from the isotach model. However, when considering the phenomenon of structuration and the whole soil response, it is important to consider the full loading history as illustrated by the following example.

Figure 2.14 shows the compression curves from three oedometer tests performed on re-sedimented Jonquiere clay; a conventional IL 24 hours oedometer test and two CRS tests performed at 1.27×10^{-5}/s and 1×10^{-7}/s vertical strain rate. The average strain rate

for the IL oedometer test was calculated to be close to $1x10^{-7}$/s, and thus according to the isotach model the IL test would be expected to yield a compression curve close to that given by the slowest CRS test, and the faster CRS test to plot to the right, above of the other two.

The test results shown in Figure 2.14 cannot be explained by the viscous effects alone. During the slowest CRS test, soil structure has developed such that the slowest CRS test plots well above the faster one, and the distance between the two CRS compression curves increases with loading/time. In the faster CSR test, the strain rate value was such that structuration was not able to develop. In the IL 24 hour oedometer test, although the average strain rate was identical to that in the slower CRS test, the structure that may have developed during one loading stage was destroyed when the new load increment was applied, and the difference between this test and the faster CRS test is thought to be due to strain rate dependency (thus explainable by the isotach model).

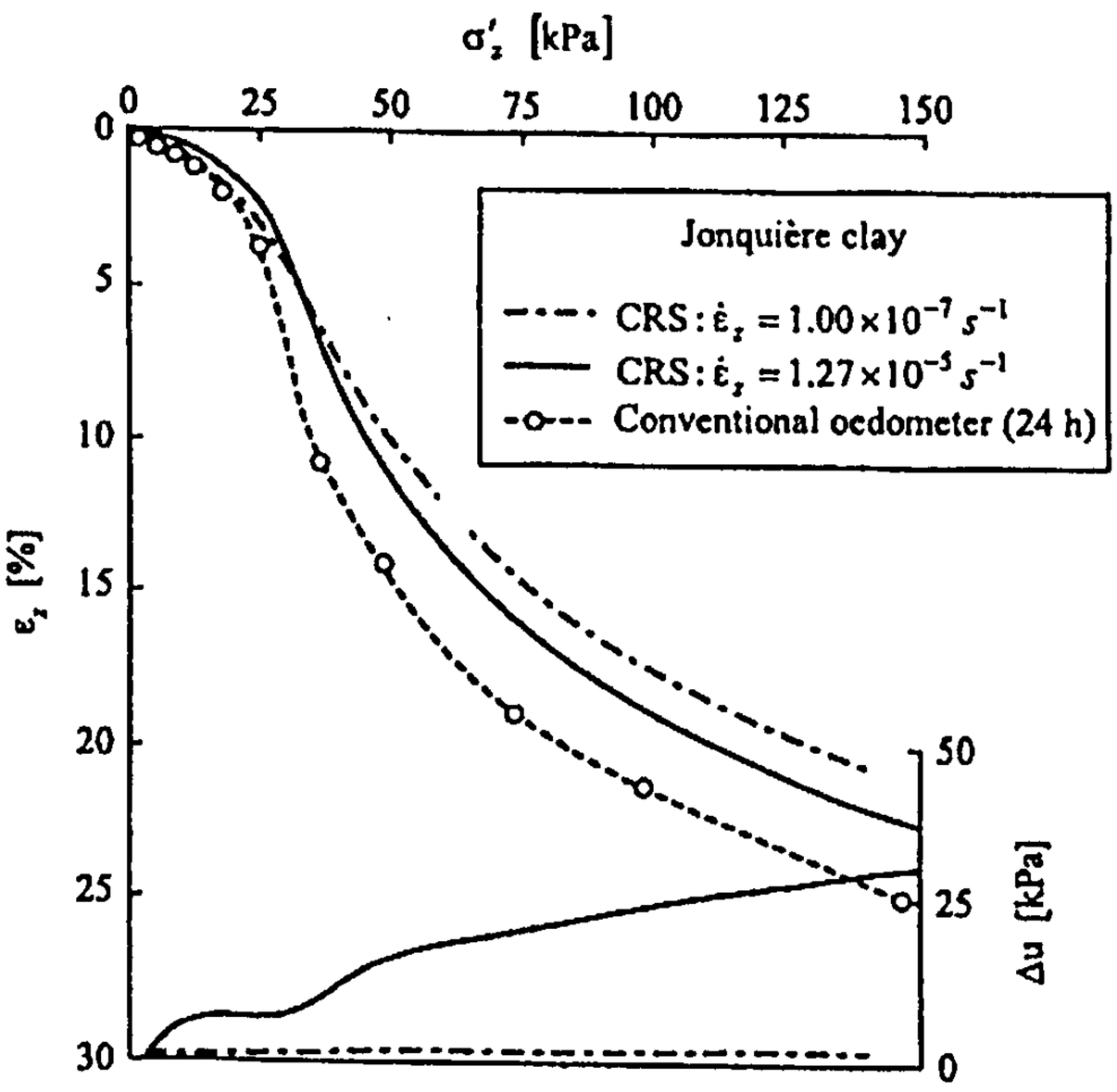

Figure 2.14: 1D oedometer tests on re-sedimented Jonquiere clay (after Leroueil et al, 1996).

Leroueil et al. (1996) suggest that for the Jonquiere clay low strain rates - that allow significant soil structuration to occur - correspond to rates below 10^{-7}/s. However, for other clays it is difficult to predict this threshold strain rate, as the potential for the development of structure is influenced, amongst other factors, by the environment and

age of the clay. It is noted that in clays structuration is mainly associated with the strengthening of the contacts between particles or aggregates, known as bonding.

Various researchers have investigated the influence of structure and geological age on the magnitude of strain rate effects on clays. Soga & Mitchell (1996) found that the rate dependency of various NC clays increased with the degree of soil structure (or sensitivity). This is corroborated by the fact that tests on reconstituted Bothkennar clay yield a value of $C_{\alpha e}$ of about 0.011 (Allman & Atkinson, 1992) while intact Bothkennar clay was found to have an average value of $C_{\alpha e}$ of about 0.028 (Nash et al., 1992b) - this value corresponding to partial to full destructuration - and thus has a much higher potential for developing creep deformations. Identically, Sorensen et al. (2007) have studied experimentally the time dependent behaviour of intact and reconstituted London Clay and have noted that when applying a strain rate change, during an otherwise constant rate of strain test, the intact samples showed a large stress jump.

In contrast, Komoto et al. (2003), based on drained triaxial compression tests on reconstituted and undisturbed samples of stiff plastic clays, suggest that rate effects are significantly smaller in undisturbed samples than in reconstituted ones, and that the difference increases with increasing geological age. However, the reconstituted samples were consolidated from slurry to the respective in-situ effective stresses (OCR=1.0), and the full stress history was not mimicked, what certainly contributed to the contradictory trend observed in the test results. It seems that more research is needed to clarify the role of soil structure and geological age on the magnitude and type of observed rate effects. In any case, the rule is that the rate effects and creep behaviour of a natural soil cannot be derived from tests on reconstituted samples.

This thesis considers the time effects associated with the soil viscosity only, however it is important to be aware that in some cases the contribution of the ageing effects may dominate the soil response.

2.4.3 Temporary effect of strain rate and strain acceleration

In the late 1990's various new aspects of the time and rate dependent behaviour of soils was observed, especially in sands, cemented soils and some stiff clays that could not be explained by the isotach concept.

Santucci de Magistris & Tatsuoka (1999) studied the time dependent behaviour of Metramo silty sand, by means of undrained triaxial compression tests on reconstituted compacted samples, during which the strain rate was changed step-wise. They observed that at small strains the behaviour followed the isotach model but changed at larger strains close to and post peak strength. At small strains, an increase in the applied strain rate caused the stress-strain curve to shift to the unique stress-strain relationship corresponding to the new strain rate and the effect of strain rate changes were found to be permanent. As the strain level increases, the change in deviatoric stress following a change in strain rate becomes temporary, and the stress-strain curve is found to decay to a unique curve independent of strain rate. This behaviour has been termed TESRA – temporary effect of strain rate and strain acceleration.

It has been shown by Tatsuoka and co-workers that the TESRA behaviour is characteristic of various clean sands over the full shearing range, until failure. Figure 2.15 shows the behaviour of Hostun sand in undrained triaxial compression tests during which the strain rate was changed stepwise. The data show that there is a unique stress-strain relationship independent of the applied strain rate. Following a change in the applied strain rate, the stress–strain response initially overshoots or undershoots the otherwise time independent stress-strain curve, but with continuing straining the path rejoins the unique CRS curve.

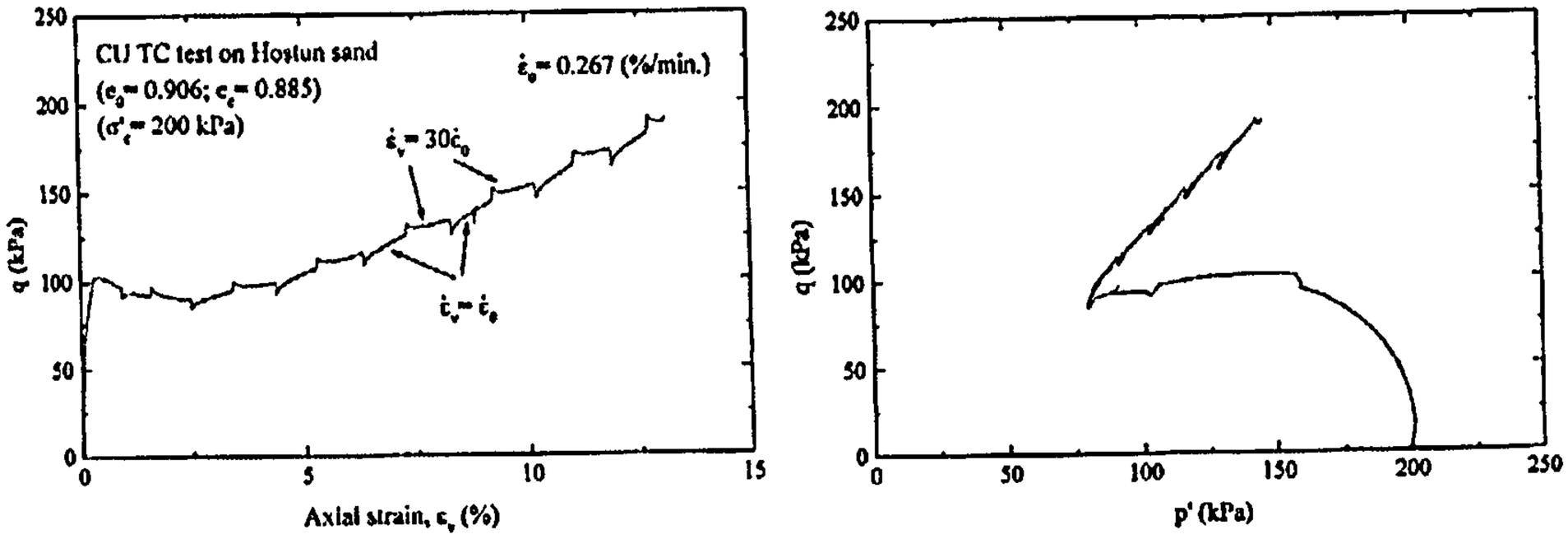

Figure 2.15: Consolidated undrained triaxial tests on Hostun sand (Tatsuoka, et al., 2002).

Materials that have pure TESRA viscosity can misleadingly be thought to be time and rate independent, because CRS tests performed at different strain rates yield the same stress-strain relationship. Their behaviour is independent of the absolute value of strain

rate and it is only affected by rate acceleration. In addition, Di Benedetto et al. (1999) have shown that Hostun sand undergoes significant creep and stress relaxation.

Figure 2.16 shows the stress path and the stress-strain relationship from undrained triaxial compression tests on reconstituted Fujinomori clay, two CRS and one SRS tests. During the SRS test, the strain rate was changed step-wise to investigate the temporary and immediate viscous effects. At low strain values, the viscous behaviour can be defined as isotach, given that the effects of strain rate are permanent and the soil response seems to be defined by a unique stress-strain-strain rate relationship (defined in terms of the plastic components of strain as discussed above). At large strain values, the effect of strain rate becomes more temporary with the stress path and stress-strain curve overshooting or undershooting the persistent CRS curves following a change in strain rate. This feature becomes more important as failure is approached. However, in contrast to the behaviour observed for clean sands (Figure 2.15), the stress path and stress-strain curve do not decay completely to a single time independent CRS curve, and instead rejoins the CRS stress-strain response that corresponds to the current strain rate value, which is well defined even at large stresses. This behaviour has been termed General TESRA behaviour (Tatsuoka, 2006).

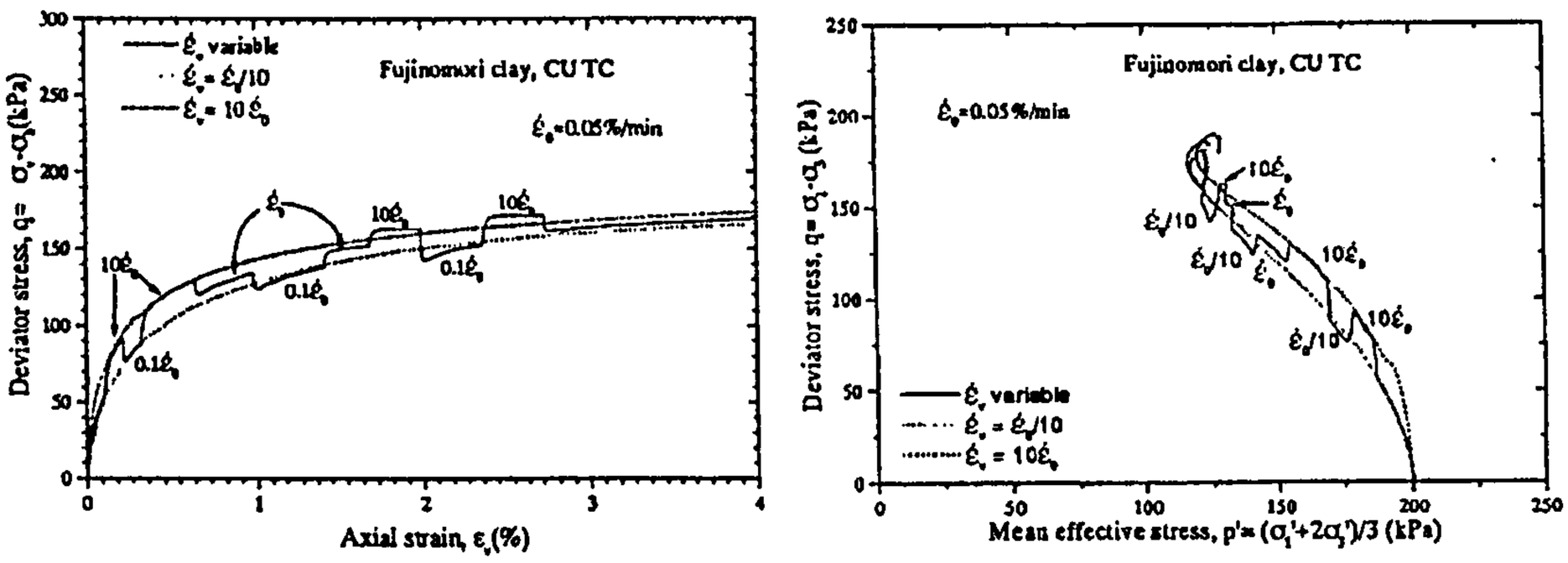

Figure 2.16: Consolidated undrained triaxial compression tests on reconstituted Fujinomori clay (after Tatsuoka et al., 1999).

In addition, the CRS effective stress paths are found to approach a unique critical state line such that the observed differences in undrained strength are due to differences in the accumulated pore water pressures. Similar behaviour has been identified by other authors i.e. Sorensen et al. (2007) on reconstituted London Clay. Generally, in soils that show a combination of temporary and persistent viscous effects, the temporary effects are found to increase with strain level (Tatsuoka, 2006).

2.4.4 Positive and Negative viscosity

Positive and negative (P&N) viscosity behaviour was found recently and has been characterized by Tatsuoka (2006) based on drained triaxial compression tests on three types of granular materials consisting of relatively round and rigid particles, namely: Albany silica sand, corundum A and Hime gravel. As an example, Figure 2.17 shows the stress-strain curves from drained triaxial compression tests performed at different constant axial strain rates on Albany sand. It can be observed that the strength decreases with an increase in the applied strain rate value. This behaviour is opposite to that of the usual isotach viscosity in which strength (or the deviatoric stress at a given value of axial strain) increases with increasing strain rate. Tatsuoka (2006) has termed the classical isotach viscosity as described in section 2.4.2 as *positive isotach viscosity* and this one as *negative isotach viscosity*. Therefore it can be said that in Figure 2.17 only the negative isotach viscosity is active.

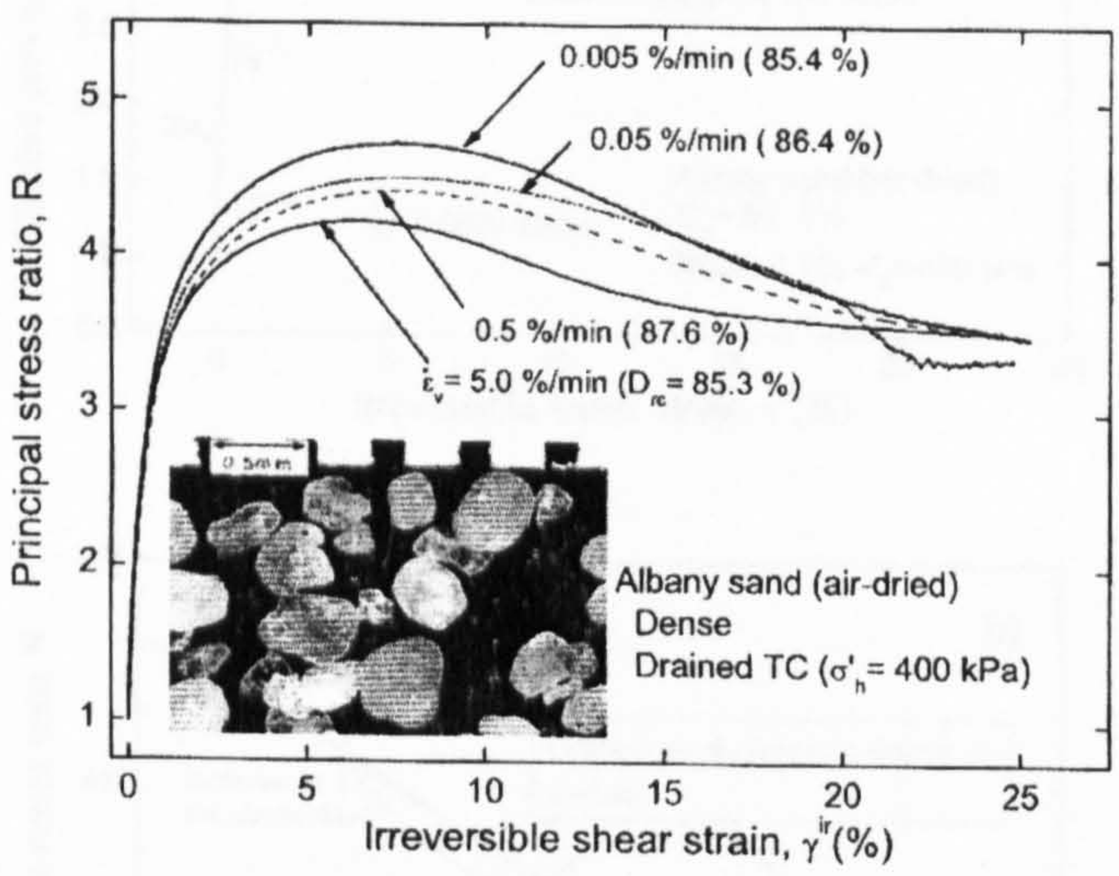

Figure 2.17: Consolidated drained triaxial compression tests at constant strain rates on air-dried dense Albany silica sand (after Tatsuoka, 2006).

Figure 2.18 shows the stress – strain curve obtained from a drained triaxial compression test performed on Albany sand during which the strain rate was changed in a stepwise manner. Following a step increase in the applied strain rate, there is a positive stress jump similar to those observed with the (positive) Isotach and the TESRA viscosity. Subsequently the stress is found to decrease relatively quickly until it joins the stress-strain curve that corresponds to the current applied strain rate (i.e. that obtained in a CRS test at that strain rate value). Conversely, when the applied strain rate is stepwise

reduced there is an immediate reduction on the stress but it then increases relatively fast until it joins the appropriate stress-strain curve that corresponds to the current strain rate, which lies above the previous one.

Therefore this type of behaviour has been termed Positive & Negative, as during a change in strain rate the soil expresses initially *positive viscosity* and then with time develops *negative viscosity*, as they have been termed above. This type of behaviour has also been observed in Toyoura and Hostun sands in the post – peak strain softening and residual regime from drained triaxial compression tests (while during the pre-peak regime it had been found to be of the TESRA type as described in Section 2.4.3).

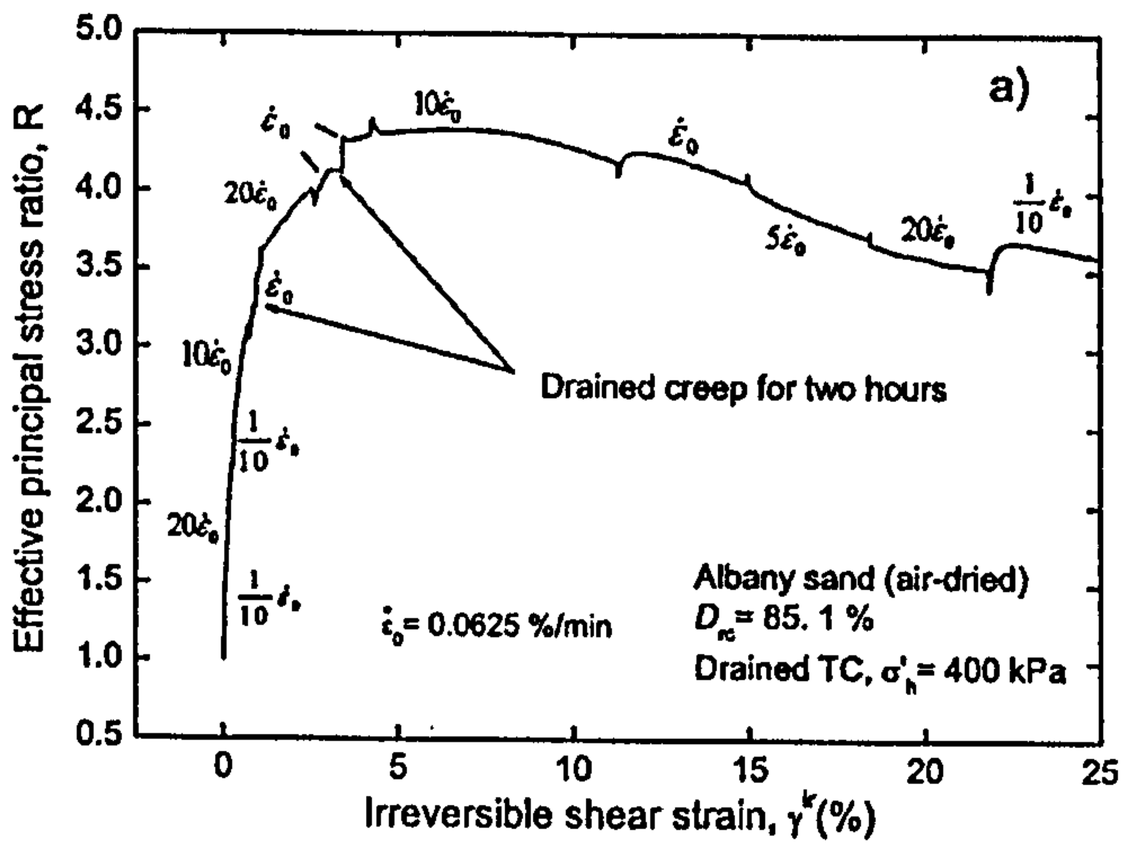

Figure 2.18: Consolidated drained triaxial compression test with stepwise change in strain rate performed on Albany sand (after Tatsuoka, 2006).

2.4.5 Transition of viscosity type

Based on an extensive number of tests Tatsuoka (2006) made a preliminary attempt to summarize the various factors that appear to influence the viscous behaviour of geomaterials (see Table 2.1). A change in each of the given factors while keeping all the other factors unchanged appeared to have the effect of progressively changing the viscous behaviour from Isotach to generalized TESRA, and then to TESRA, and finally to P&N. From the data presented in the previous two sections, it is clear that an increase in strain level, and consequent damage to any bonding at inter-particle contacts, is responsible for a change in viscosity type.

Tatsuoka (2006) suggests that the global viscous stress-strain behaviour of a geomaterial results from the balance between two mechanisms at the interparticle contact points:

c) The load-deformation relationship at the interparticle contacts becomes stiffer and stronger with an increase in the deformation rate, which corresponds to higher global strain rates;
d) There is an increase in the number of interparticle contact points with time and creep deformation, i.e. lower global strain rate, which results in a more stable and stronger behaviour.

Table 2.1: Summary of the factors affecting the viscosity type (after Tatsuoka, 2006)

Viscosity type **Influencing factors**	**Isotach**	**Intermediate or generalized TESRA**	**TESRA**	**Positive and Negative**
Particle shape (in case of stiff particles)	More angular → more round			
Grading characteristics	Better graded → more poorly graded			
Particle size	Smaller (clay) → Larger (sand/gravel)			
Particle crushability	More crushable → less crushable			
Inter-particle bonding	Stronger → Weaker → Null e.g. rock/cement-mixed soil)		Unbond granular materials	
Strain level	Pre peak → Post peak (in particular at residual state)			
Inter-particle contact points	More stable (better bond, better interlocking & → larger coordination numbers)		Less stable (less bond, less → interlocking & smaller coordination numbers)	

Mechanism a) causes any geomaterial to undergo a sudden increase in shear stress following a step increase in the global shear strain rate. The importance of mechanism b) on the response of the geomaterial is found to depend on the geomaterial type, but it seems to decrease as the particles become more stable, either due to interparticle bonding, interlocking, particle angularity or a larger number of interparticle contact points. Depending on the balance between the two mechanism mentioned above the viscosity type of the geomaterial will be of the Isotach, TESRA, generalized TESRA or P & N type.

2.5 Influence of creep and strain rate on the soil stiffness

As mentioned in Section 2.3.4, on loading a soil element after a creep period the soil exhibits an initial stiff response. Several studies have been carried out to investigate the influence of creep on the elastic shear stiffness modulus, G_{max} using dynamic tests of the resonant column or bender element types (i.e. Anderson & Stokoe, 1978; Lo Presti et al., 1996, Lohani et al., 2001), or simply using a triaxial apparatus with high resolution strain/stress measurement/control system (i.e. Santucci de Magistris et al., 1998).

These studies have observed an increase in the small strain / elastic shear stiffness with time during creep both in clayey and granular materials, however it is not clear if the observed increase in G_{max} is due to viscous effects only.

Anderson & Stokoe (1978) have presented the results of an oedometer test on a sample of kaolinite, which was step loaded and left to consolidate at constant stress for about seven days. Figure 2.19 shows the variation of the sample height and the elastic shear modulus G_{max}, measured using resonant column tests, with the logarithm of time (where the origin of time coincides with the application of the step load). The results are typical of the behaviour observed on clayey soils. During primary consolidation, the variation of elastic shear modulus follows the variation of the sample height, increasing towards the EOP consolidation.

After the EOP, given that the pore water pressure has dissipated, the variation of the sample height is controlled by creep only, and the sample height and the elastic shear stiffness modulus are seen to increase linearly with the logarithm of time. In this case the increase in elastic shear modulus during secondary compression is found to be

significantly larger than that due to the reduction of void ratio alone (i.e. see Lohani et al., 2001). However, no information is presented regarding the subsequent loading of this soil element after the seven days of maintained load, so that the possibility of the development of structure could be investigated, although due to the inactive nature of kaolinite, the development of structure over this time period is unlikely.

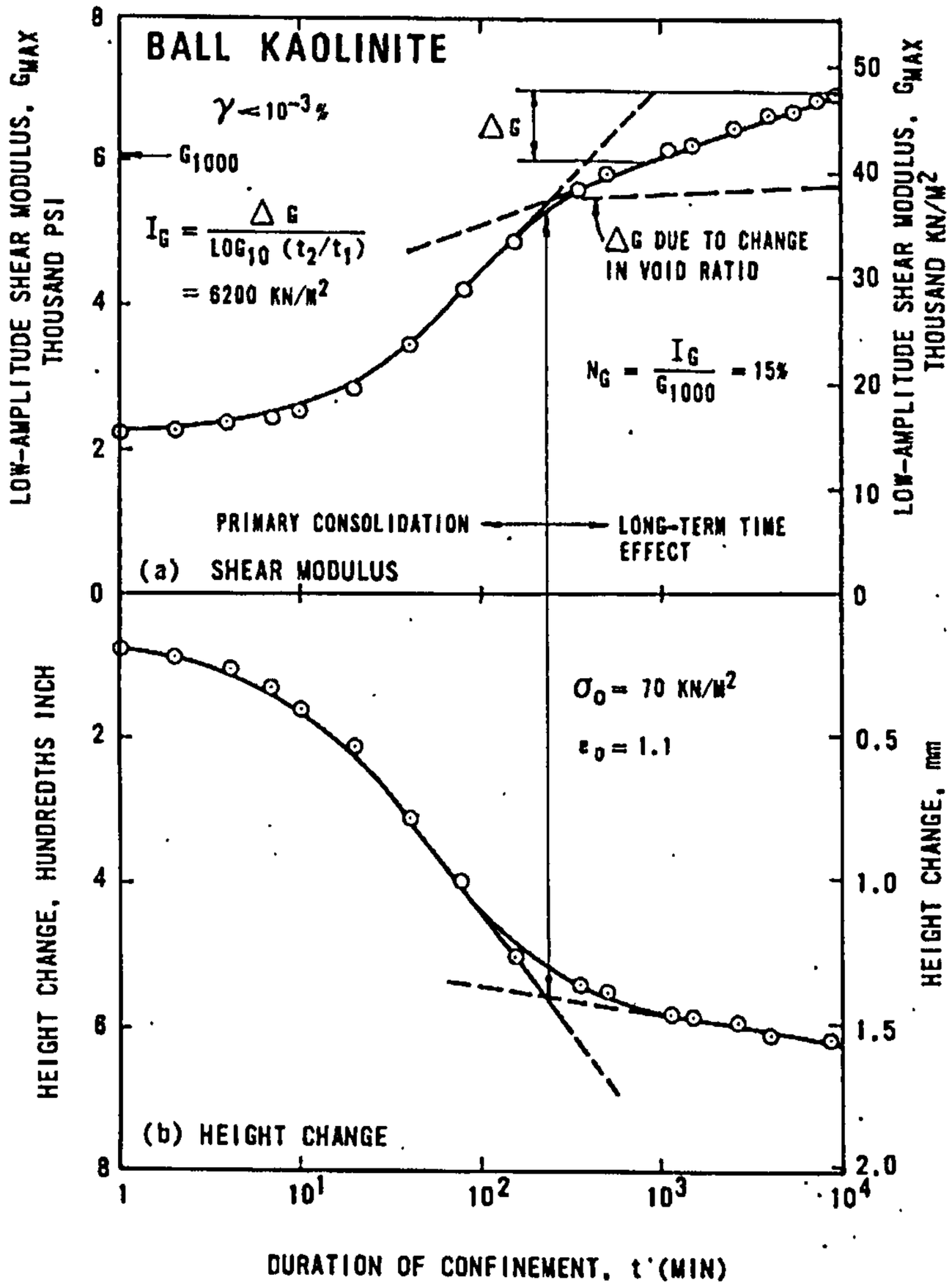

Figure 2.19: Typical behaviour of the variation of sample height and Gmax with time for a kaolinite sample at constant confining pressure (after Anderson & Stokoe, 1978).

The behaviour of a sample of granular material would be similar to that shown in Figure 2.19, with the difference that the primary consolidation phase would be very short or more likely, nonexistent, and the long-term phase would be characterized by a smaller change in both the sample height and the elastic shear stiffness with time, when compared with clayey samples.

The increase in elastic shear stiffness per logarithmic cycle of time is found to be more important in fine-grained soils, varying between 2% and 40% for a wide range of natural clays, and between 1% and 17% for granular materials.

Lohani et al. (2001) has performed drained triaxial creep tests under K_0 stress conditions for periods up to 15 days, on reconstituted samples of four clays of different origin and plasticity. The samples were subjected to incremental loading and then subjected to sustained load at various stress levels. Throughout the tests, the elastic shear modulus was determined using bender elements. Similarly to Anderson & Stokoe (1978), they found that during the creep period the elastic shear stiffness increased by an amount well in excess of that due to the change in void ratio only, which was suggested to be due to ageing or structuring effects. However, on applying further load after the creep period the stress path in *e-log*σ'_v *space* was found to rejoin the original NCL with no overshooting, indicating that during the creep period there was no significant structuration. It is proposed that either the increase in elastic shear stiffness is in fact due to viscous effects alone or the soil stiffness is dependent on subtle components of soil structure that cause no significant changes to the large scale yielding properties such as the yield stress and undrained shear strength.

Various studies have investigated the influence of the applied strain rate on the soil's elastic shear stiffness (i.e. Lo Presti et al., 1996; Shibuya et al., 1996) and it is generally accepted that the elastic shear stiffness is independent of the applied strain rate, and a function of the soil state only. Shibuya et al. (1996) have studied the influence of strain rate on the small strain stiffness of reconstituted NSF clay (an artificial clay constituted mainly of pyrophyllite and quartz; LL=56%, I_p=27%) isotropically consolidated to a mean effective stress of 300 kPa. The study included undrained monotonic loading tests at a constant rate of axial strain, fixed in each test, varying between 0.01%/min and 1%/min, and cyclic loading tests with varying strain amplitude. They concluded that the (pseudo) elastic shear stiffness (the initial slope of the stress-strain curves), did not appear to vary with axial strain rate for the range of strain rate values considered, but there was an increase in the elastic limit strain - the strain beyond which the stress-strain curve exhibits non-linear and irrecoverable behaviour, assumed to coincide with limit of the elastic region – with increasing strain rate. Lo Presti et al. (1996) based on Resonant Column / Torsional shear tests on two undisturbed clays (Pisa and Augusta Clays) have

noted that due to the soil viscosity some strain rate dependency of the secant shear stiffness will in general be observed, even at very small strains. They further report that the dependency of the soil shear stiffness increases with increasing strain level. The main implication of this finding is that the $G/G_{max} - \gamma$ *curves* are rate dependent.

In contrast Matešić & Vucetic (2003) have performed cyclic simple shear tests on six soils (three clays and three sands) and based on the test results they suggest that the $G/G_{max} - \gamma$ *curves* are not strain rate dependent. However it is the author's opinion that there were errors in the interpretation of the test results and the curves may not in fact be normalized as G_{max} is strain rate independent. In addition, the data shows that beyond the linear range the secant shear stiffness is strain rate dependent in clayey soils and virtually strain rate independent in sands. This behaviour is in agreement with the observed isotach and TESRA behaviour of clays and sands, respectively, during monotonic loading.

2.6 Temperature effects

Leroueil & Marques (1996) present a review of the available data on the literature regarding the "*importance of strain rate and temperature effects in geotechnical engineering*". Temperature seems to have two major effects on soils: thermal expansion of the solid particles and the pore water, and thermally induced changes of the contacts between the particles or aggregates. The combined effect of these two components is for an increase in the soil compressibility with increase of temperature: the soil becomes more compressible in the overconsolidated range, the pre-consolidation pressure decreases and the entire compression curve moves towards smaller effective stresses, similar to the effect of reducing strain rate. Therefore in general an increase in temperature during a drained creep test causes the creep rates to increase, and in relaxation tests the effective stress at a given value of strain decreases (Mitchell, 1993).

Leroueil & Marques (1996) propose that the model of Leroueil et al (1985) for strain rate effects should be extended to include temperature effects, such that the pre-consolidation pressure is now a function of the applied strain rate and temperature.

Similarly to strain rate effects, viscous effects associated with temperature are found to affect the limit state curve, the undrained shear strength and the pre-consolidation

pressure, on average by about 10% for a temperature change of 12°C (equivalent to a logarithmic cycle of strain rate). Viscous effects on the critical state line and residual strength envelope may be considered nonexistent. Therefore one should be aware when extrapolating laboratory test results to engineering practice, as the strain rates in-situ are in general lower than those applied in the laboratory (according to Leroueil & Marques, 1996 typically 2 to 4 orders of magnitude smaller) and the temperature is typically 10°C less, and in many situations they may partially compensate each other. Leroueil & Marques (1996) suggest that strain rate and temperature effects should be considered simultaneously as they are two facets of the viscous behaviour of soils.

2.7 Concluding remarks

This Chapter aimed to give a review of the current state of art regarding the observed time dependent viscous behaviour of geomaterials, and in particular of clayey soils. Viscous effects include phenomena such as creep, stress relaxation and strain rate effects, and are the aspects of the time dependent behaviour that are primarily intended to be reproduced by the constitutive models presented in this thesis. Ageing or structuration corresponds to a gain of additional components of strength and stiffness of the natural soil, in relation to the reconstituted soil, that cannot be accounted for by void ratio and stress history alone. However it is often difficult to distinguish between the components in the soil behaviour that are due to viscous effects and those that derive from ageing, as both are time dependent and in principle may occur simultaneously.

Most soils show qualitatively identical behaviour under creep and stress relaxation, showing a reduction in a component of strain or in effective stress, respectively with time. This variation, for stress states far from failure, can be approximated by a linear logarithmic law, or more generally by a non-linear logarithmic law. However when considering the strain rate effects on geomaterials three types of viscosity have been identified: Isotach, TESRA and Positive & Negative. The transition between the viscosity types has been identified with a reduction in the number of inter-particle contact points. The viscous behaviour of soft and stiff clays, in their natural state, can be described by an isotach viscosity, such that the soil response can be expressed by a single *stress-delayed strain-delayed strain rate* relationship. Due to the interaction between viscous and ageing effects the rate effects and creep behaviour of a natural soil cannot be evaluated from tests on reconstituted samples.

3 CONSTITUTIVE MODELS TO DESCRIBE THE TIME DEPENDENT BEHAVIOUR OF SOILS

3.1 Introduction

This Chapter presents a review of the constitutive models currently available in the literature to describe the time dependent viscous effects of soils such as creep, stress relaxation and strain rate effects. Following the methodology by Adachi et al. (1996) and Liingaard et al. (2004) the constitutive models are divided into three categories: empirical, rheological and general stress-strain-time models.

Empirical models are usually obtained by fitting experimental data with simple mathematical expressions. The constitutive relations are, in general, expressed by means of closed form solutions and their applicability is restricted to the boundary conditions from which they have been derived. Though they express a single aspect of the soil behaviour, e.g. stress decay during stress relaxation or the soil compression under K_0 stress conditions, they may be used as a basis for developing constitutive laws for generalized stress space.

Rheological models are typically employed to describe the behaviour of metals and fluids, but they may be used to obtain a conceptual understanding of the time dependent behaviour of geomaterials. They are often used to describe uniaxial loading conditions and the constitutive relations are usually expressed by means of closed form solutions or in differential form. The terminology "rheological models" is often used to describe linear viscoelastic behaviour, however when applied to soils it may include plastic behaviour as well.

In principal general stress-strain-time constitutive laws extend the models developed for rate independent behaviour to include viscous effects. They are often expressed in incremental form for direct numerical implementation in a finite element procedure. Herein only elastic visco-plastic models are considered, which are based on the assumption that viscous effects are negligible within the soil's elastic range. Two main types of elastic visco-plastic models are discussed: those based on the overstress theory and those based on the non-stationary flow surface theory.

All the general stress-strain-time models known to the author are based on a form of a stress – strain – strain rate relationship and are therefore suitable to reproduce isotach viscosity, which as shown in Chapter 2 is appropriate to describe the rate dependent behaviour of most clays in their natural state. The first attempt to develop an equation capable of expressing all viscosity types from Isotach to Positive & Negative viscosity, including all the intermediate behaviour types, was presented by Tatsuoka and co-workers (Tatsuoka et al., 2003, Tatsuoka, 2006). This equation provides a relationship between the stress ratio and a single component of strain and strain rate, during shearing. For further details on this formulation please refer to e.g. Tatsuoka (2006).

It is noted that this review is not exhaustive and focuses on the constitutive relations that have contributed to the author's understanding of the problems involved in modelling the viscous behaviour of clays, and are thus relevant to the work presented in this thesis.

3.2 Empirical models

This Section presents a review of empirical constitutive relations developed to mimic observed viscous effects in soils. Despite their simplicity the empirical models reflect real soil behaviour and they may be used either as a basis for more sophisticated general constitutive models or to provide a practical solution to engineering problems, provided that the boundary conditions are similar to those from which the relations have been derived.

3.2.1 Semi-Logarithmic creep law

It is common practice to plot the deformation during secondary compression, as observed from oedometer tests, against the logarithm of time. This is because the secondary compression is found to be, in general, well approximated by a semi-logarithmic law using the following equation:

Equation 3.1
$$\Delta e = C_{\alpha e} \cdot \log\left(\frac{t_2}{t_1}\right)$$

where $C_{\alpha e}$ is the coefficient of secondary compression expressed in terms of void ratio, Δe is the change in void ratio during secondary compression between a time t_1 and a time t_2.

In its simplest form, the coefficient of secondary compression $C_{\alpha e}$ may be considered constant for a specific soil, in which case the vertical strain due to creep, in boundary value problems in which the stress conditions are close to 1D compression, can be quantified as:

Equation 3.2

$$\varepsilon_v = \frac{C_{\alpha e}}{1+e_i} \cdot \log\left(1+\frac{t}{t_i}\right)$$

where ε_v is the vertical strain; e_i is the initial void ratio; t is the time and t_i is a reference time, that corresponds to the start of the creep deformation.

However, the assumption that the value of $C_{\alpha e}$ is constant for a given soil is an oversimplification as in natural soils the value of $C_{\alpha e}$ has been shown to be influenced by the magnitude of the vertical effective stress in oedometer tests and time.

Mesri & Godlewski (1977) note that $C_{\alpha e}$ depends on the current vertical effective stress, and essentially how this relates to the pre-consolidation pressure. It is noted that both the compression index, C_{ce} defined by Equation 3.3 and $C_{\alpha e}$ increase as the vertical effective stress approaches the pre-consolidation pressure reaching their maximum at or just beyond the pre-consolidation pressure and remaining reasonably constant thereafter, such that the ratio of $C_{\alpha e}/C_{ce}$ remains approximately constant throughout.

Equation 3.3

$$C_{ce} = \frac{\Delta e}{\Delta \log\left(\sigma_v^{'}\right)}$$

where Δe is the change in void ratio and $\sigma_v^{'}$ is the vertical effective stress. Mesri & Castro (1987) note that the value of the ratio $C_{\alpha e}/C_{ce}$ for a variety of soils, including peat, organic silt, highly sensitive clay as well as granular materials, falls in a very narrow range between 0.02 and 0.10. For a large number of inorganic soft clays the ratio of $C_{\alpha e}/C_{ce}$ was reported to be very consistent and about 0.04±0.01.

The uniqueness of the ratio $C_{\alpha e}/C_{ce}$ is based on the assumption that $C_{\alpha e}$ and C_{ce} remain constant with time. However, it is observed that $C_{\alpha e}$ may not in fact remain constant with time. The assumption of a constant $C_{\alpha e}$ implies that there is a linear relationship between the creep strain and the logarithm of time during a creep period, under constant effective stresses. This assumption may overestimate considerably the long-term creep settlements as it implies that creep volumetric strains are predicted even when there are

no voids left in the soil. Yin (1999) presents an equation to describe the soil secondary compression that introduces a variation of the coefficient of secondary compression with time and in which there is a limit to the amount of creep volumetric strain that is attained at infinite creep time:

Equation 3.4
$$\varepsilon_z = \frac{\psi}{V} \cdot \ln\left(\frac{t + t_i}{t_i}\right)$$

where
$$\frac{\psi}{V} = \frac{\psi_0 / V}{1 + \left(\frac{\psi_0}{V \cdot \varepsilon_\infty}\right) \cdot \ln\left[\left(t - t_i\right)/t_i\right]}$$

where ε_∞ is the volumetric strain attained at infinite creep time (being by definition an asymptotic value) and ψ/V is the creep parameter with V =*1*+*e*. If the quantity ψ/V is set as a constant then the above equation predicts a linear logarithmic creep law. It is noted that instead of the parameter $C_{\alpha e}$, Yin (1999) describes the creep behaviour by means of the parameter ψ/V however the two parameters are related as follows:

Equation 3.5
$$\frac{\psi}{V} = \frac{C_{\alpha\varepsilon}}{\ln 10}$$

where $C_{\alpha\varepsilon}$ is the coefficient of secondary consolidation defined in terms of strain and is equal to $C_{\alpha e}$/V, where V is the specific volume.

The semi-logarithmic creep law is only able to describe the behaviour during primary creep (as defined in Chapter 2) as it predicts a continuous reduction of the rate of compression with time. The main advantage of the semi-logarithmic creep law is the fact that there is a large database of $C_{\alpha e}$ values and of the ratio $C_{\alpha e}/C_{ce}$ for various soils, which can be used to estimate the value of $C_{\alpha e}$ when there is not enough test data. However, Equation 3.2 can only be used to evaluate the vertical strain developed during secondary compression in boundary value problems in which the stress conditions are close to those in an oedometer test (1D compression). In addition, the application of Equation 3.2 requires the definition of a time origin for the start of the creep t_i (that corresponds to the time at EOP) and which in itself is not straightforward, as discussed in Chapter 2.

3.2.2 Singh and Mitchell's creep model

Based on drained and undrained triaxial creep tests on various clays Singh and Mitchell (1968) noted that during both drained and undrained creep there is a linear relationship between the logarithm of the axial or the volumetric strain rate (depending on the test type) and the logarithm of time. Based on this observation they have defined the parameter *m*:

Equation 3.6
$$m = -\frac{\Delta \log \dot{\varepsilon}}{\Delta \log t}$$

The parameter *m* is found to vary between 0.7 and 1.3 for geomaterials. The particular case when m=1 yields a linear logarithmic creep law for the relationship between the creep strain and creep time. Singh and Mitchell (1968) proposed an equation to describe the relationship between the axial strain rate, $\dot{\varepsilon}_a$ and time, *t* of clayey soils during an undrained creep period under constant deviator stress, q:

Equation 3.7
$$\dot{\varepsilon}_a = A \cdot \exp(\overline{\alpha q}) \cdot \left(\frac{t_i}{t}\right)^m$$

$$\text{with } \overline{\alpha} = \alpha \cdot q_{\max} \text{ and } \overline{q} = q / q_{\max}$$

where *A*, α and *m* are model parameters that can be evaluated from a few creep tests on a given soil, *q* is the applied deviator stress, t_i is the time origin, and q_{max} is the soil strength at the beginning of the undrained creep process. The parameter A reflects the soil composition, structure and stress history, α gives a measure of the effect of the deviator stress on the creep rate and *m* controls the rate of decay of the strain rate with time. It is noted that the above equation has been derived from laboratory tests in which the samples were subjected to a deviatoric stress that is between 30% and 90% of the soil strength, and should therefore be used under similar stress conditions. The equation is not able to reproduce the phenomenon of undrained creep rupture, when the soil sample is subjected to a sufficiently high stress ratio.

One of the main limitations of Equation 3.7 is that it describes the creep behaviour under constant deviator stress only. In addition, identically to the semi-logarithmic law, the model only describes the behaviour during the primary creep phase, as it predicts a continuous reduction of axial strain rate with time.

3.2.3 Lacerda & Houston's Relaxation model

Lacerda & Houston (1973) derived an equation to describe the change in effective stress with time, observed during relaxation triaxial tests:

Equation 3.8

$$\frac{q}{q_0} = \frac{\overline{q}}{\overline{q}_0} = 1 - s \log\left(\frac{t}{t_i}\right) \qquad for \quad t > t_i$$

where $\overline{q}$ is the current stress ratio, $\overline{q}_0$ is the stress ratio at t=t_i, t is the time since the beginning of the relaxation test, t_i is the time delay between the start of the relaxation test and any decay in the deviator stress and s is the slope of the relaxation curve in q/q_0 – $log\ t$ space.

The equation predicts that the deviator stress decreases linearly with the logarithm of time after an initial period of time t_i has been exceeded. For a given soil, the value of t_i (also called *delay time*) was found, experimentally, to decrease with increasing applied strain rate prior to the stress relaxation period. Equation 3.8 was derived based on the three parameter creep equation proposed by Singh & Mitchell (1968), such that the parameter s in Equation 3.8 can be related to the parameters $\overline{\alpha}$ and m in Equation 3.7 as follows:

Equation 3.9

$$s = \frac{1}{\overline{q}_0} \cdot \frac{2.3 \cdot (1 - m)}{\overline{\alpha}}$$

The above relation between the creep and relaxation parameters has been demonstrated experimentally by Lacerda & Houston (1973) and show that the two phenomena result from the same mechanism. However, from the definition of the parameter s in Equation 3.9, Equation 3.8 is only valid for values of m lower than unity. In addition, Equation 3.8 predicts that there is stress decay for an infinite period of time, which can lead to unrealistic and non-stable values of q after a long finite period of time.

3.2.4 Strain Rate Approach

The strain rate approach is based on the assumption that there is a unique relationship between the current stress state, the strain and the applied strain rate, which is independent of the previous loading history. This concept was first proposed by Sukjle (1957) and it was later investigated in detail and demonstrated experimentally by Leroueil et al. (1985). Leroueil et al. (1985) performed an extensive laboratory testing

programme on the 1D compression behaviour of Champlain Clays and noted that the effective stress rate had no significant effect on the time dependent behaviour of clays. The 1D behaviour of soils could then be completely described by a unique effective stress-strain-strain rate relationship, which could be decomposed into two independent functions deducted from CRS tests at different strain rates; one, Equation 3.10, giving the variation of the pre-consolidation pressure with the strain rate and the other, Equation 3.11, expressing the relationship between the normalized effective stress and strain.

Equation 3.10 $$\sigma'_{vp} = f(\dot{\varepsilon}_v)$$

where σ'_{vp} is the vertical pre-consolidation effective stress and $\dot{\varepsilon}_v$ is the vertical strain rate;

Equation 3.11 $$\frac{\sigma'_v}{\sigma'_{vp}} = g(\varepsilon_v)$$

where σ'_v is the vertical effective stress and ε_v is the vertical strain. Once the above two equations are known it is possible to reconstruct any stress-strain-strain rate relationship. The above equations imply that in ε_v-$\log\sigma'_v$ space the distance between two compression curves corresponding to different strain rates is constant, and the compression curves are therefore parallel.

This model has been derived based on oedometer tests, mainly on normally consolidated soils, and during which the strains are always increasing. Therefore the model cannot reproduce soil rebound during unloading stages and gives very poor predictions in the overconsolidated range, where the elastic strains dominate the soil behaviour. In addition, because Equation 3.10 and 3.11 are formulated in terms of the total strain component and the respective total strain rate the model is not able to reproduce stress relaxation. During stress relaxation, the total strain rate remains zero and so the uniqueness of the stress-strain-strain rate relationship implies that there would be no stress change. To reproduce the strain relaxation phenomena the strain should be decomposed into an elastic and a plastic component, and the uniqueness of the stress-strain-strain rate relationship should be applied to the plastic strain component only.

Leroueil and Marques (1996) have suggested that Equation 3.10 can be approximated by a double logarithmic function, as follows:

Equation 3.12

$$\log\left(\frac{\sigma'_{vp}}{\sigma'_{vp0}}\right) = A + \frac{1}{m'}\log\left(\frac{\dot{\varepsilon}_v}{\dot{\varepsilon}_{v0}}\right)$$

where A and m' are model parameters and σ'_{vp0} and $\dot{\varepsilon}_{v0}$ are reference values. They show that the value of the parameter m' can be related to the compression parameters as follows:

Equation 3.13

$$\frac{1}{m'} = \frac{C_{ce}}{C_{\alpha e}}$$

The above equation implies that the strain rate approach and the $C_{\alpha e}/C_{ce}$ = constant concept (discussed in Section 3.2.1) are equivalent for describing the viscous behaviour of soils during secondary consolidation.

3.2.5 Bjerrum's Model

Bjerrum (1967) noted that, as a result of secondary compression, the 1D compression behaviour of clays could not be described by a single curve in *e-log* σ'_v space (where e is the void ratio and σ'_v is the vertical effective stress), but was instead characterized by a family of curves called *time lines*. Each *time line* was the locus of the equilibrium soil states after a specific period of sustained load, and the time lines were postulated to be equally spaced per logarithmic cycle of time. Bjerrum (1967) stated that a "*given value of overburden pressure and void ratio corresponded to an equivalent time of sustained loading and a certain rate of delayed compression, independent of the way the clay has reached these values*".

In addition the deformation of a clay sediment could be decomposed into an instant and a delayed component. The definition of the instant and delayed components of soil compression is shown schematically in Figure 3.1. The instant compression is the deformation that takes place simultaneously with the increase in the effective stress, if there is no hydro-dynamic lag and the delayed compression corresponds then to the reduction in volume at constant effective stress associated with the soil viscosity.

The terminology *instant* and *delayed* should not be confused with the expressions *primary* and *secondary*, which are used to separate the compression developed during and after the excess pore water pressures have dissipated. The dashed line in the lower diagram in Figure 3.1 corresponds to the reaction of the soil structure if the applied stress was transferred immediately to the soil structure as an effective stress. Due to the development of excess pore water pressures and the subsequent process of consolidation the effective stress will increase gradually and compression will occur along the solid line.

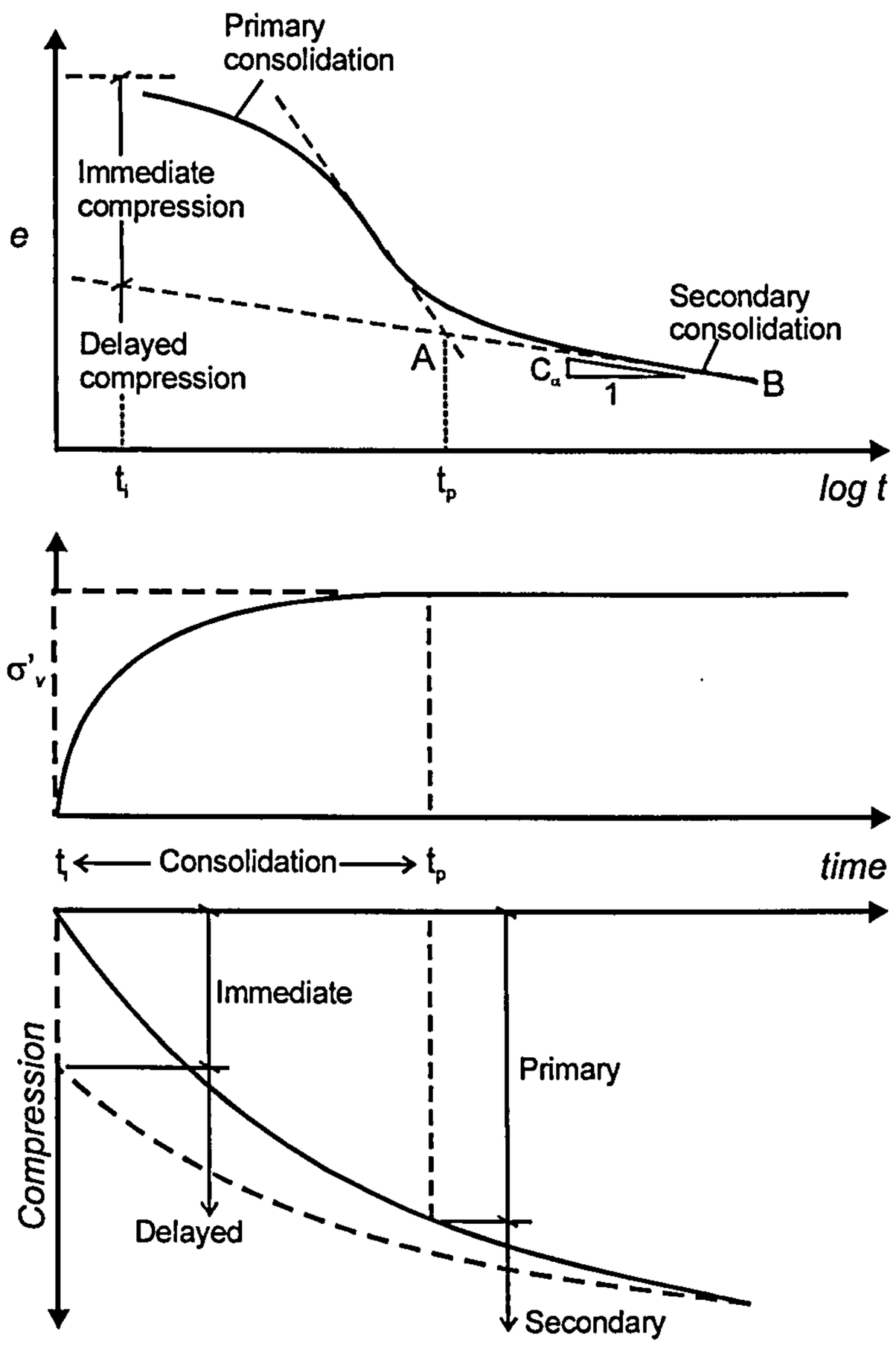

Figure 3.1: Definition of the concepts of instant and delayed compression (after Bjerrum, 1967)

Based on the above model Bjerrum (1967) introduced the concept of *aged* normally consolidated clay, as on loading a normally consolidated clay sample, after a period of delayed compression, the sample may show a pre-consolidation pressure in excess of the largest stress it had been subjected to previously. Bjerrum presented an equation to

evaluate the total settlement of an *aged* sediment when subjected to an increase in the applied vertical stress, e.g. due to the construction of a building, in which the model parameters are the compression index, C_{ce} and the coefficient of secondary compression, $C_{\alpha\varepsilon}$.

Garlanger (1972) has written the Bjerrum concept in terms of the coefficients of compression, recompression and secondary compression. Consider an aged normally consolidated (NC) soil sediment subjected to an initial vertical effective stress σ'_{v0} and with an initial void ratio e_0. The sediment is subjected to an increase in the vertical effective stress to a value σ'_v. The current void ratio at a time t after the application of the load increment can be determined as:

Equation 3.14

$$e = e_0 - C_{re} \cdot \log\frac{\sigma'_{vp}}{\sigma'_{v0}} - C_{ce} \cdot \log\frac{\sigma'_v}{\sigma'_{vp}} - C_{\alpha e} \log\frac{t_i + t}{t_i}$$

where e is the current void ratio; e_0 the initial void ratio; C_{re}, C_{ce} and $C_{\alpha e}$ are coefficients of recompression, virgin compression and secondary compression defined in terms of void ratio, respectively; t_i is the time associated with the start of the secondary compression and σ'_{vp} is the vertical pre-consolidation pressure.

Based on this formulation it is possible to derive a relationship between the vertical effective stress σ'_{v0} acting on a NC soil element and its current pre-consolidation vertical stress $\sigma'_{vp(t)}$ after a time of secondary compression t:

Equation 3.15

$$\frac{\sigma'_{vp(t)}}{\sigma'_{v0}} = \left(\frac{t_i + t}{t_i}\right)^{C_{\alpha e}/C_{ce} - C_{re}}$$

where t is the duration of the period of secondary compression and C_{re}, C_{ce} and $C_{\alpha e}$ are defined above. Equation 3.15 is very similar to Equation 3.12 (which was derived based on CRS oedometer tests) if the parameter m' is instead taken equal to $C_{\alpha e}/C_{ce} - C_{re}$.

3.2.6 Kavazanjian and Mitchell's Model

Kavazanjian and Mitchell (1977) have made one of the first attempts to develop a stress-strain-time constitutive model for triaxial stress space for clayey soils. They

decompose the soil stress state into volumetric and deviatoric stress components, each having a corresponding strain component, as expressed by the following equations:

Equation 3.16 $$\{\varepsilon\} = \{\varepsilon_V\} + \{\varepsilon_D\}$$

Both the volumetric and the deviatoric strain components are divided into an instant and a delayed component:

Equation 3.17 $$\{\varepsilon_V\} = \{\varepsilon_V\}_i + \{\varepsilon_V\}_d \quad ; \{\varepsilon_D\} = \{\varepsilon_D\}_i + \{\varepsilon_D\}_d$$

where the subscript *i* and *d* denote instant and delayed components, respectively.

The above decomposition for the volumetric component is done based on Bjerrum's concepts of instant and delayed compression. In one-dimensional compression the instant component is given by a line with slope C_{ce} in *e-log p'* space. The delayed component is evaluated by means of a logarithmic law, and assuming that the coefficient of secondary compression is constant, and independent of the stress level. The delayed volumetric strain $\{\varepsilon_V\}_d$ is then:

Equation 3.18 $$\{\varepsilon_V\}_d = \frac{C_{\alpha e}}{1+e_0} \cdot \log\left(\frac{t}{t_i}\right)$$

where t_i is the time required for the instant compression to occur.

For clays of low sensitivity and within the normally consolidated range the value of C_{ce} is found to remain approximately constant and so the assumption that $C_{\alpha e}/C_{ce}$=constant is equivalent to $C_{\alpha e}$=constant.

The instant deviatoric strain component is evaluated assuming that *deviatoric stress-strain* curves have a hyperbolic shape and are normalized by the isotropic consolidation pressure. The delayed deviatoric strain component is evaluated using the general equation proposed by Singh and Mitchell (1968) given by Equation 3.7.

Kavazanjian and Mitchell (1977) have employed the model to estimate the increase in the coefficient of earth pressure with time during secondary compression of San Francisco Bay Mud, and found that the results agreed well with the available experimental data. This model was later developed into a general elasto-viscoplastic model for generalized stress space by Borja & Kavazanjian (1985).

3.2.7 Tavenas Model

Tavenas et al. (1978) have conducted a series of drained and undrained triaxial creep tests on intact samples of lightly overconsolidated St. Alban clay and based on the test results have concluded that both the shear and the volumetric strain components could be expressed by an equation of the form proposed by Singh & Mitchell (1968):

Equation 3.19
$$\dot{\varepsilon}_v = A \cdot f\left(\sigma'_{ij}\right) \cdot \left(\frac{t_i}{t}\right)^m$$

Equation 3.20
$$\dot{\varepsilon}_q = B \cdot g\left(\sigma'_{ij}\right) \cdot \left(\frac{t_i}{t}\right)^m$$

where A and B are soil parameters that reflect the soil composition, structure and stress history, m is the parameter defined by Singh & Mitchell (1968) which controls the rate of decay of the creep strain rate with time and f and g are functions of the current stress state and replace the exponential function in Equation 3.7. Tavenas et al. (1978), based on contours of creep strain rate at a time t=100 minutes obtained from drained and undrained creep triaxial tests on St. Alban clay (see Figure 2.8), suggest that the above functions could be expressed in terms to the distance to the limit state surface.

If the parameter m is assumed to have the same value for the volumetric and the shear strain components then Equations 3.19 and 3.20 can be rewritten as:

Equation 3.21
$$\frac{\dot{\varepsilon}_v}{\dot{\varepsilon}_q} = \frac{A \cdot f\left(\sigma'_{ij}\right)}{B \cdot g\left(\sigma'_{ij}\right)} = C \cdot h\left(\sigma'_{ij}\right)$$

where C is a constant and h is a function of the current stress state and corresponds to a flow rule for the creep deformation. Although the value of m may not be the same for the volumetric and shear creep strain components Equation 3.21 is still largely used in the development of viscoplastic constitutive models that are discussed in more detail in Section 3.4.

3.2.8 Equivalent Time Concept

The concept of Equivalent Time was first introduced by Yin & Graham (1989). Yin & Graham (1989) postulate that the deformation of a soil element associated with an effective stress change can be decomposed into an instant and a delayed component. However this decomposition differs from that suggested by Bjerrum (1967) as in Yin &

Graham (1989) the instant deformation corresponds to the elastic time independent soil response and in Bjerrum's model the instant deformations corresponds to the deformation that would take place simultaneously to the application of the effective stress increment assuming that no hydro-dynamic lag occurs (see Figure 3.1). The time dependent behaviour of soils under isotropic stress conditions is then described by a series of parallel lines in $\varepsilon_{vol} - lnp'$ space (where ε_{vol} is the volumetric strain and p' is the mean effective stress*)* which are lines of constant *Equivalent Time.*

The model requires the definition of an instant time line (defining the soils instant elastic behaviour), a reference time line and ideally a limit time line (that defines a region of pure elastic behaviour). The Equivalent Time, t_e of a soil state (ε_{vol}-p') is then defined as the time it would take that soil element to creep from the reference time line to the current state, under constant effective stresses.

When considering a soil sample subjected to a constant load, such as in a oedometer test, for NC stress state the equivalent time t_e is very similar to the duration of loading, however for overconsolidated stress states, the equivalent time t_e will be considerably different from the loading time. They also assume that the equivalent time is directly related to a unique creep strain rate. Therefore by mathematical manipulation they are able to express the creep strain rate as a function of the vertical distance of the current soil state to the reference time line in ε_{vol}-p' space. Yin & Graham (1989) present an equation for the 1D compression of soils based on the above concepts and assuming that there a linear relationship between the creep strain and the logarithm of time. This means that an infinite creep strain is predicted at an infinite creep time and consequently time dependent (creep) strains are always predicted (i.e. there is no zone of pure elastic behaviour).

Later, Yin (1999) proposed a non-linear logarithmic law to describe the secondary compression of soils, which assumes that there is a limit time line and thus a limit to the volumetric creep strain. The limit time line is the locus of the soil's states associated with a creep strain rate equal to zero and defines a region of pure elastic behaviour.

The above 1D compression models have been extended to general models based on the overstress theory (see Section 3.4). The Equivalent Time model formulation is

described in more detail in Chapter 6, being the basis for one of the models investigated within this thesis.

Den Haan (1994) and den Haan and van den Berg (2001) have developed a model for the time dependent 1D compression behaviour of soils following a very similar formulation, the differences concerning mainly the choice and definition of the model parameters. The model assumes that the 1D compression behaviour of soils can be defined with reference to a set of parallel lines in ε_{vol}-p' space which are lines of constant *intrinsic time* τ. Den Haan and van den Berg (2001) define intrinsic time as "*the geological time necessary to attain the present degree of compression, under the present effective stress, if that stress was applied at the moment of formation of the soil*". Again the value of intrinsic time is uniquely related to a value of delayed strain rate.

3.2.9 Discussion

Most of the empirical models described in this Section are based on the understanding that the phenomena of creep, stress relaxation and rate dependency are due to the same basic mechanism and consequently, the observed behaviour of one of the above phenomena, for example creep, may be derived from CRS tests, or vice-versa. This is emphasized by the relationship between the parameters of the various models presented, and is valid for geomaterials that show isotach viscosity.

The simplest empirical models discussed above aim to provide a solution for a time dependent component of the soil behaviour, under particular boundary conditions, being able to give either an estimate of the secondary compression (e.g. semi-logarithmic law, Singh & Mitchell model) or the stress decay during stress relaxation (e.g. Lacerda & Houston model). In either case, the models only provide information regarding one component of stress or strain. Based on the work by Singh & Mitchell, Tavenas' model considers both volumetric and shear strain components, having the merit of implying that the creep deformation could be obtained with reference to a flow rule. The resulting model still considers the time delayed component of soil behaviour only.

Bjerrum's and the *Equivalent Time concept* models combine one or more of the previous simple empirical relationships and add this creep law to a basic time

independent model, so that the full soil deformation is considered. However, they only provide a solution for stress conditions close to 1D compression.

The empirical models are often divided into two main categories depending on whether they are time or strain hardening. Time hardening models are characterized by relations that include the time *t* as the hardening parameter, such that they can be written as:

Equation 3.22 $$\varepsilon^c = f(\sigma) \cdot g(t)$$

where ε^c is the creep strain and *f* and *g* are functions of stress and time, respectively, or as:

Equation 3.23 $$\dot{\varepsilon}^c = f(\sigma) \cdot g(t)$$

where $\dot{\varepsilon}^c$ is the creep strain rate.

The above two equations incorporate the time as the hardening parameter, but more often Equation 3.22 is referred to as a *total strain model*. An example is the semi-logarithmic creep law, in which case the function *f* is either constant ($C_{\alpha e}$ constant) or varies with confining pressure ($C_{\alpha e}/C_{ce}$ constant) and the function *g* is a logarithmic function. In the literature it is recommended that Equation 3.22 should only be used when the applied stresses remain constant or varies very slowly with time. Equation 3.23 is referred to as *time hardening model* and given its incremental form can take stress changes into account. Examples are the Singh & Mitchell and the Lacerda & Houston models. Because the time *t* is introduced explicitly, time hardening models require the definition of a time origin that establishes the onset of creep strains.

Strain hardening models are characterized by relations that include the creep strain as the hardening parameter, and can be written as:

Equation 3.24 $$\dot{\varepsilon}^c = f(\sigma) \cdot g(\varepsilon^c)$$

where *g* is now a function of the creep strain. Equation 3.24 corresponds to the strain rate approach model if the hardening equation is instead formulated in terms of the total strain and its respective rate.

3.3 Rheological models

Rheological models are typically employed to describe the behaviour of metals and fluids, but they may be used to obtain a conceptual understanding of the time dependent behaviour of geomaterials. Within the rheological models, three main categories can be identified:

a) *The differential approach*, in which the constitutive relations are constructed by combining elementary material models such as the Hookean spring, the Newtonian dashpot and the Saint Vernant's slider;

b) *Engineering theories of creep*, which are general theories for determining the creep response of solids (mainly concrete and metals). In their structure they are very similar to the empirical relations described in the previous Section, however while the phenomena of creep was originally studied on plastic normally consolidated clays, the engineering theories of creep have been developed and are valid for materials in which the stress states are below the yield limit;

c) *The hereditary approach*, which postulates that the current strain at a given stress point may be obtained by integration over the entire loading history. The general opinion is that the hereditary approach is to complex to be applied in soil mechanics. For further details please refer to Feda (1992).

The differential approach is probably the one of more interest to the subject of soil mechanics as it is often used to describe and obtain a conceptual understanding of the time dependent behaviour of geomaterials. In the differential approach, the behaviour of a material is represented by a composition of elementary models such as the elastic spring, the plastic slider and the viscous dashpot, which are illustrated in Figure 3.2.

Three models are frequently used for geomaterials: the Maxwell model, the Kelvin-Voigt model and the Bingham model, and they are described subsequently.

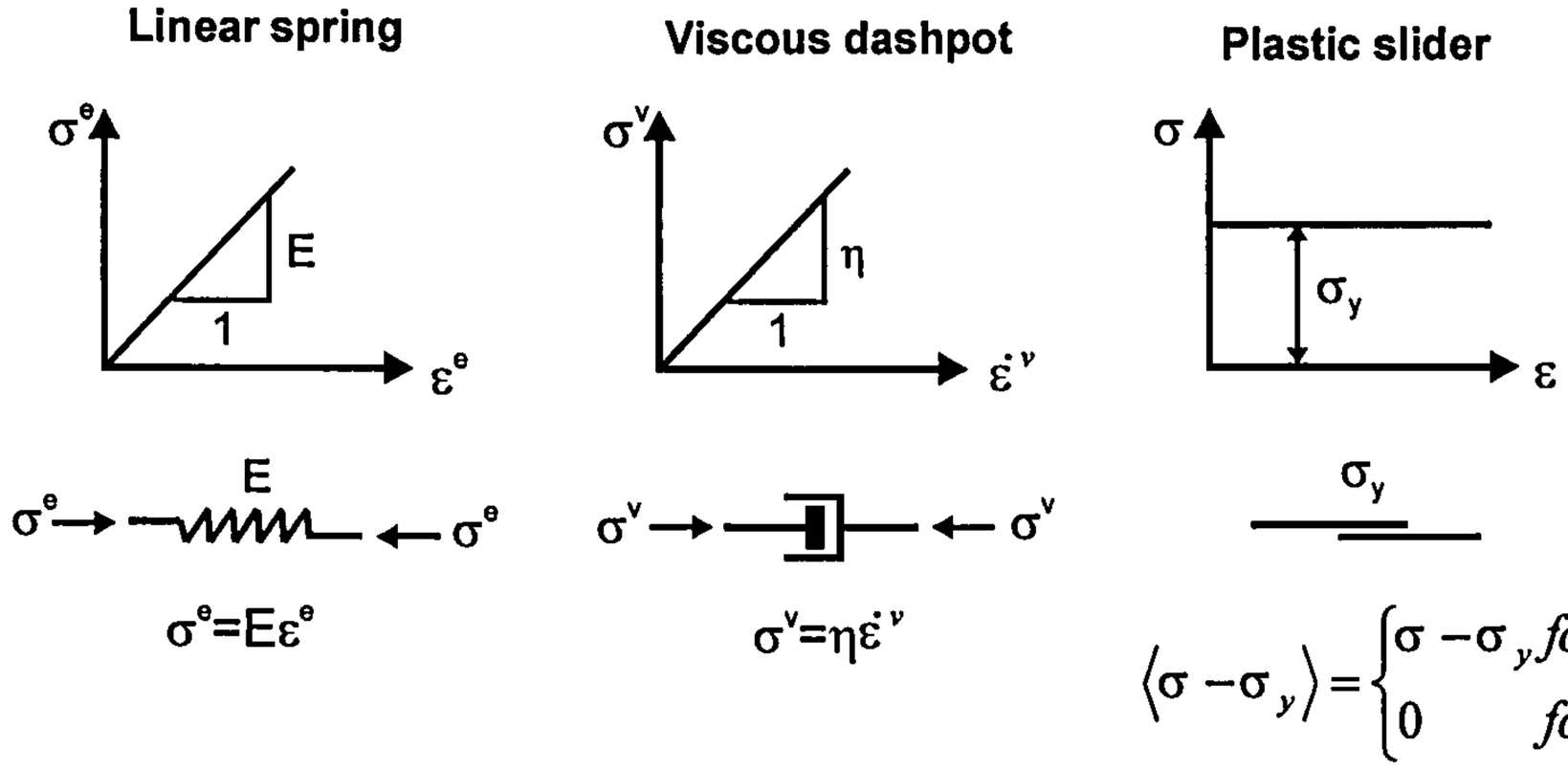

Figure 3.2: Schematic representation of the elementary material models; the Hookean spring, the Newtonian dashpot and the Saint Vernant's slider.

The Maxwell model consists of an elastic spring, characterized by a modulus E and a viscous dashpot, characterized by a constant viscosity η, arranged in series. The total strain ε^{tot} (or deformation) is then the sum of the elastic ε^{e} and the viscous ε^{v} components:

Equation 3.25 $$\varepsilon^{tot} = \varepsilon^{e} + \varepsilon^{v}$$

while the following condition $\sigma^{e} = \sigma^{v} = \sigma$ is still verified. Writing Equation 3.25 in terms of strain rate and substituting the respective elemental constitutive equations it becomes:

Equation 3.26 $$\dot{\varepsilon}^{tot} = \frac{\dot{\sigma}}{E} + \frac{\sigma}{\eta}$$

During creep at constant stress Equation 3.26 reduces to:

Equation 3.27 $$\dot{\varepsilon}^{tot} = \dot{\varepsilon}^{v} = \frac{\sigma}{\eta}$$

which means that during creep at constant stress the Maxwell model predicts a constant strain rate, which corresponds to the secondary creep phase, as defined in Chapter 2. During stress relaxation, the total strain rate is equal to zero and so Equation 3.26 can be rewritten as:

Equation 3.28 $$\dot{\sigma} = -\frac{\sigma}{\eta}\frac{1}{E} = -\frac{\dot{\varepsilon}^{v}}{E}$$

The Maxwell model predicts that during stress relaxation there is a reduction in the applied stresses, at a rate linearly proportional to the viscous strain rate.

The Kelvin-Voigt model consists of an elastic spring, with a modulus E and a dashpot characterized by a constant viscosity η, placed in parallel. The governing equation of this system can be written as:

Equation 3.29 $$\sigma^{Tot} = \sigma^{e} + \sigma^{v} = E \cdot \varepsilon^{e} + \eta \cdot \dot{\varepsilon}^{v}$$

while the deformation of the spring and the dashpot are, for compatibility, required to be equal, such that $\varepsilon^{Tot} = \varepsilon^{e} = \varepsilon^{v} = \varepsilon$ or in terms of strain rate $\dot{\varepsilon}^{Tot} = \dot{\varepsilon}^{e} = \dot{\varepsilon}^{v} = \dot{\varepsilon}$. During creep at constant applied stress, Equation 3.29 can be rewritten as:

Equation 3.30 $$\dot{\varepsilon} = \frac{\sigma - E \cdot \varepsilon}{\eta}$$

which implies that the Kelvin-Voigt model predicts that during a creep period the total strain rate decreases with increasing values of accumulated strain, which corresponds to a decreasing strain rate with creep time. During a stress relaxation period, the total strain remains constant, or in other words the total strain rate is equal to zero:

Equation 3.31 $$\dot{\varepsilon}^{tot} = \dot{\varepsilon}^{e} = \dot{\varepsilon}^{v} = 0$$

In that case Equation 3.29 can be rewritten as:

Equation 3.32 $$\sigma^{tot} = E \cdot \varepsilon^{e} + 0$$

Equation 3.32 implies that the Kelvin-Voigt model predicts that the stress remains constant when the total deformation is restrained, i.e. when stress relaxation boundary conditions are applied.

The Bingham model consists of a parallel unit composed of a dashpot characterized by a constant viscosity η and a plastic slider characterized by a yield stress σ_y, connected in series to an elastic spring with a modulus E. The governing equations of this system can be written as:

Equation 3.33 $$\dot{\varepsilon}^{Tot} = \begin{cases} \dot{\varepsilon}^{el} + \dot{\varepsilon}^{vp} = \dfrac{\dot{\sigma}}{E} + \dfrac{(\sigma - \sigma_y)}{\eta} & for \quad \sigma > \sigma_y \\ \dot{\varepsilon}^{el} = \dfrac{\dot{\sigma}}{E} & for \quad \sigma \le \sigma_y \end{cases}$$

The concept of the Bingham model corresponds very closely to that of the overstress theory, which is presented in Section 3.4. The model predicts pure elastic behaviour below the yield stress σ_y, but above this threshold value the model predicts viscous flow. The model can be divided into two components connected in series; one a time independent component consisting of the elastic spring and the other a time dependent component consisting of the dashpot and the slider combined in parallel. The viscoplastic elements are inactive provided that $\sigma < \sigma_y$. The viscous behaviour of the Bingham model is very similar to the Maxwell model; the only difference is that the quantity σ in Equation 3.26 is here replaced by the quantity $(\sigma-\sigma_y)$. Therefore the model predicts constant creep rate under constant stress (i.e. secondary creep), decay in stress during stress relaxation and the effect of strain rate on the material stress-strain response.

The models presented above are able to mimic a viscoelastic material only, because the element constitutive relations are very simple, and the behaviour of the spring, the dashpot and the slider are all described by linear relationships. However, soils are in general highly non-linear (even within a pseudo-elastic range), show plastic behaviour and in addition the assumption of a linear viscosity is found not to be suitable for soils. It has been shown that the models above are able to mimic either primary or secondary creep (but not both), while soils may exhibit both primary and secondary creep stages during a creep process.

While the adoption of more complex element constitutive relations (e.g. a non-linear elastic spring, a plastic slider with a varying yield stress) and the extension of the rheological models to generalized stress space may improve the potential of the rheological models to mimic real soil behaviour, it would considerably complicate the mathematic manipulation of the governing equations, and the models would lose one of their main attractions that is to provide a straightforward visualization of soil behaviour.

3.4 General stress-strain-time models

This section covers general constitutive laws that are able to describe both the viscous effects and the inviscid rate – independent aspects of soil behaviour (e.g. critical state), in principle, under any loading conditions. Given that soils, in particular clayey soils, are strongly plastic, the models are required to combine elastic, plastic and viscous

components of behaviour. Based on the literature review presented in Chapter 2, which showed that within the elastic range, soil behaviour might be considered time and rate independent, viscoelastic-viscoplastic models are not included here, and the discussion will focus on elastic-viscoplastic models.

Elastic visco-plastic models can be divided into three categories, depending on whether they are based on: a) the overstress theory, b) the concept of a nonstationary flow surface or c) others. The underlying assumption of all elastic visco-plastic models is that the elastic behaviour is time and rate independent, while the plastic behaviour is time dependent.

3.4.1 Overstress theory

The following description of the overstress theory is based on the work by Perzyna (1963). The total strain rate $\{\dot{\varepsilon}_{ij}\}$ is decomposed into an elastic $\{\dot{\varepsilon}_{ij}^{el}\}$ and a visco-plastic $\{\dot{\varepsilon}_{ij}^{vp}\}$ component:

Equation 3.34 $$\{\dot{\varepsilon}_{ij}\} = \{\dot{\varepsilon}_{ij}^{el}\} + \{\dot{\varepsilon}_{ij}^{vp}\}$$

The elastic strains are assumed to be time independent while the viscoplastic strains are time dependent, and represent combined viscous and plastic effects. The elastic strain rate is calculated by inverting the following equation:

Equation 3.35 $$\{\dot{\sigma}_{ij}\} = [D] \cdot \{\dot{\varepsilon}_{ij}^{el}\}$$

where $[D]$ is the elastic constitutive matrix and $\{\dot{\sigma}_{ij}\}$ is the stress rate tensor. The visco-plastic strain rate is obtained from a flow rule, such that:

Equation 3.36 $$\{\dot{\varepsilon}_{ij}^{vp}\} = \gamma \langle \Phi(F) \rangle \cdot \frac{\partial f_d}{\partial \sigma_{ij}}$$

where $$\langle \Phi(F) \rangle = \Phi(F) \qquad \text{if } F > 0$$

$$\langle \Phi(F) \rangle = 0 \qquad \text{if } F \leq 0$$

where γ is a fluidity parameter, f_d is the plastic potential function (and corresponds to the dynamic loading surface) and $\Phi(F)$ is a function of the overstress F, which is defined as:

Equation 3.37 $$F = \frac{f_d}{f_s} - 1$$

where the function f_d depends on the current stress state and viscoplastic work and describes the *dynamic* loading surface on which the current stress state is located. The function f_s is the hardening parameter and from Equation 3.37, f_s corresponds to the *static* yield surface, i.e. the surface associated with loading at a plastic strain rate equal to zero. From Equation 3.36 it can be inferred that the *static* loading surface is equivalent to the yield surface in classical plasticity, being the threshold for the development of irrecoverable deformations.

Comparing Equation 3.33 with Equations 3.34 to 3.36 shows that the overstress theory is a three dimensional version of the Bingham model; the plastic potential function derivative is omitted in the Bingham model as the model applies to one dimensional cases only, the overstress stress function $\Phi(F)$ can be interpreted as a function of the distance of the current loading surface from the static yield surface, and is the three dimensional equivalent of the quantity $(\sigma - \sigma_y)$ in the Bingham model and the parameter γ is essentially the inverse of the viscosity parameter η.

The overstress theory differs from the plasticity theory in the sense that it does not invoke the consistency rule to derive the equations that govern the deformation behaviour of a soil element. Consequently, in plasticity theory, the plastic strains are related to the stress rate; whereas in the overstress theory, the time dependent visco-plastic strains are a function of the current stress state only, and independent of the stress rate or stress history. In addition, because the consistency rule is not invoked in overstress theory, the stress state can lie, on, above or below the current static yield surface.

It can be shown that the overstress theory is able to mimic strain rate effects in a material's stress-strain response and is able to simulate the phenomena of creep and stress relaxation provided that the processes start from a stress state outside (above) the static yield surface f_s. Adachi et al. (1987) show that elasto visco-plastic models based on the overstress theory cannot mimic acceleration creep processes and therefore cannot reproduce appropriately undrained creep rupture. When loading a soil element at a very high strain rate, the theory will predict that the material response is identical or very

close to pure elastic behaviour, as there is no time for the development of the time delayed visco-plastic strains.

Some authors suggest that the function $\Phi(F)$ may be evaluated from laboratory tests. However the main difficulty in applying the overstress theory in the form described above is to define the static yield function, as by definition, it is associated with loading at a plastic strain rate equal to zero. Therefore many authors have replaced the static yield function f_s in Equation 3.37, with a reference loading surface, f_{ref} associated with a finite visco-plastic strain rate value, in which case the function $\Phi(F)$ is then evaluated for stress states on, above and below f_{ref} (for values of F larger, smaller or equal to zero). This is the approach used by e.g. Adachi & Oka (1982), Adachi et al. (1987), Kutter and Sathialingam (1992), Yin et al. (2002), den Haan & van den Berg (2001).

If no *static* or *limit* loading surface is specified then $\Phi(F)$ is evaluated for all values of F and the model predicts an infinite visco-plastic strain at infinite creep time under constant effective stresses (e.g. Kutter and Sathialingam, 1992, den Haan & van den Berg, 2001). If instead, a limit loading surface is specified then it defines the stress region of pure elastic behaviour, which corresponds now to a value of F<0 (e.g. Yin et al., 2002).

The models proposed by e.g. Kutter and Sathialingam (1992), Yin et al. (2002), den Haan & van den Berg (2001) are overstress models that use an empirical law of the type described in Section 3.2 to determine the volumetric viscoplastic strain rate under isotropic or K_0 stress conditions. To extend the models to generalized stress space further assumptions regarding the ratio between the volumetric and the deviatoric visco-plastic strain increments are required. In this respect the work of Tavenas et al. (1978) is often invoked, and it is assumed that the visco-plastic volumetric strain rate is constant on a given loading surface (e.g. Yin et al., 2002; Vermeer & Neher, 1999). It will be shown later in this thesis that this assumption prevents the soil from reaching critical state conditions, and it is preferable to assume that the function $\Phi(F)$ is constant on a given loading surface as assumed by den Haan & van den Berg, (2001).

3.4.2 Non-stationary Flow Surface theory

The non-stationary flow surface (NSFS) theory is based on the inviscid time independent classical plasticity theory. As in the overstress theory, the total strain rate $\{\dot{\varepsilon}_{ij}\}$ is decomposed into an elastic $\{\dot{\varepsilon}_{ij}^{el}\}$ and a visco-plastic $\{\dot{\varepsilon}_{ij}^{vp}\}$ component, as expressed by Equation 3.34. The main difference between the plasticity and the NSFS theory lies in the definition of the yield condition. In plasticity theory, the yield condition for an isotropic hardening material is given by:

Equation 3.38 $$f(\sigma_{ij}^{'}, k) = 0$$

where $\sigma_{ij}^{'}$ is the effective stress tensor and k is a state or hardening parameter that is a function of the plastic strains. It is noted that according to the above equation the yield condition does not change with time provided that the plastic strains (or the hardening parameter k) remains constant, and therefore the yield surface is called "stationary". In contrast in the NSFS theory the yield condition is also a function of time and can be written as:

Equation 3.39 $$f(\sigma_{ij}^{'}, k, \beta) = 0$$

where k is now a function of the viscoplastic strains and β is a function of time. Therefore, even if the visco-plastic strains are held constant, the yield surface is able to change with time, and is referred to as "non-stationary". The elastic strain rate is determined by inverting Equation 3.35 and the viscoplastic strain rate is determined according to a flow rule:

Equation 3.40 $$\dot{\varepsilon}_{ij}^{vp} = \Lambda \cdot \frac{\partial g}{\partial \sigma_{ij}^{'}}$$

where g is the plastic potential function and Λ is a positive visco-plastic multiplier that is evaluated only when loading from a plastic state. The viscoplastic multiplier can be determined by invoking the consistency rule, such that loading from a state lying on the current yield surface must lead to a stress state on the new yield surface:

Equation 3.41

$$\Lambda = \frac{\left[\frac{\partial f}{\partial \sigma_{ij}^{'}}\right]^{T}[D]\cdot\left\{\dot{\varepsilon}_{ij}^{Tot}\right\}+\left[\frac{\partial f}{\partial k}\right]\cdot\dot{k}+\left[\frac{\partial f}{\partial \beta}\right]\cdot\dot{\beta}}{\left[\frac{\partial f}{\partial \sigma_{ij}^{'}}\right]^{T}[D]\left[\frac{\partial g}{\partial \sigma_{ij}^{'}}\right]}$$

where $[D]$ is the elastic constitutive matrix and $\left\{\dot{\varepsilon}_{ij}^{Tot}\right\}$ the total strain tensor, k is a function of the viscoplastic strains and β is a function of time. The above parameter Λ is similar to the plastic scalar multiplier defined within the classical plasticity theory, with the exception that the latter does not contain the term $\left[\frac{\partial f}{\partial \beta}\right]\cdot\dot{\beta}$, the term that includes the time and rate dependency.

As mentioned above, visco-plastic strains are only evaluated when the stress state is being loaded from a state on the current yield surface (i.e. f=0). Therefore it is important to set up the criteria for loading, unloading and neutral loading, which are defined as:

Equation 3.42

$$L = \frac{\partial f}{\partial \sigma_{ij}^{'}}\cdot\dot{\sigma}_{ij}^{'}+\frac{\partial f}{\partial k}\cdot\dot{k}+\frac{\partial f}{\partial \beta}\cdot\dot{\beta}$$

L>0 loading

L=0 neutral loading

L<0 unloading

It is noted that time influences the loading criterion and a given stress increment may be considered loading if applied at a given rate, but unloading if applied at a lower rate.

It can be shown that models based on the NSFS are not able to reproduce the phenomena of creep and stress relaxation when the processes are initiated from stress states within the yield surface. This implies that this theory cannot reproduce time effects within the overconsolidated stress region. When the processes of stress relaxation and creep are initiated from a stress state on the yield surface the model should, in principle, be able to describe them.

The NSFS theory is able to mimic the rate dependency of soils over a wide range of strain rate values. When loading a soil element at a very fast strain rate the time dependent term containing β in Equation 3.41 will be very small and the model

response will correspond to the time independent elasto-plastic response. In contrast in the overstress theory, loading at a very fast strain rate will yield an elastic response.

It is noted that both the overstress and the NSFS theories are based on the assumption that all aspects of the viscous effects are due to the same basic mechanism and the same fundamental equation is used to predict the phenomena of creep, stress relaxation and strain rate effects. It is the appropriate boundary conditions used in each case that ensure a different soil response.

Also in both theories the viscoplastic strain rate component $\dot{\varepsilon}_{ij}^{vp}$ is treated as a single quantity combining both plastic and viscous effects. Tatsuoka et al. (2006) have noted that it is not possible to decompose the above quantity $\dot{\varepsilon}_{ij}^{vp}$ into a plastic and a viscous part. Nevertheless, Borja & Kavazanjian (1985) have developed a time dependent constitutive model for normally and lightly overconsolidated clays in which they assume that the total strain rate is decomposed into three components: the elastic and plastic components are assumed to be time-independent and the creep or viscous component is time dependent. For more details please refer to Borja & Kavazanjian (1985).

3.5 Concluding remarks

This Chapter presents a review of some of the constitutive laws available in the literature to describe time dependent viscous effects in soils. It has been noted that this review is not exhaustive and has focused on the constitutive relations that have contributed to the author's understanding of the problems involved in modelling the time dependent viscous behaviour of clays and are relevant for the work presented in this thesis. The constitutive relations presented herein, and the majority of those available in the literature, are based on isotach viscosity, as they have primarily been developed based on experimental observation of clayey soils.

The aim of this thesis is to develop, implement and validate general constitutive laws that are able to mimic the viscous nature of clayey soils. In this respect empirical and rheological models may be used to improve one's conceptual understanding of the time dependent behaviour of geomaterials and help to devise the requirements that general stress-strain-time equations have to obey.

Based on experimental data, viscous effects may be neglected within the elastic range, and so the time dependent behaviour of geomaterials may be appropriately described using elastic visco-plastic models. From the discussion on elastic visco-plastic formulations presented in Section 3.4, it can be concluded that the overstress theory presents some advantages in relation to the NSFS theory: it has a simpler mathematical formulation and presents the possibility of mimicking the time dependent behaviour of soils both in the normally consolidated and overconsolidated stress range. However, the overstress theory is not able to mimic: a) the tertiary compression phase - corresponding to an increase of the current coefficient of secondary consolidation with time during a drained creep period at constant effective stress and b) tertiary creep, which implies that undrained creep rupture cannot be appropriately predicted. In addition, when using the overstress theory it is not possible to determine the soil response that would be found from an equivalent time independent elasto-plastic formulation, which in the NSFS theory can be obtained by applying an infinitely fast strain rate.

4 FINITE ELEMENT METHOD APPLIED TO GEOMECHANICS

4.1 Introduction

The finite element method is a complex form of numerical analysis that has been used for the last forty years to solve boundary value problems in many fields of engineering (e.g. structural engineering, fluid mechanics, geotechnics). The main advantage of the finite element method, in relation to other analytical methods is that it is able to satisfy the four requirements of a true theoretical solution: equilibrium, compatibility, the material constitutive behaviour and the boundary conditions. In coupled consolidation analysis there are two additional requirements: continuity of flow and the generalized Darcy's law.

The analyses presented in this thesis have been carried out with the finite element program ICFEP. ICFEP is a program that has been developed specifically for the analysis of geotechnical structures and uses a displacement based finite element method. ICFEP is able to perform two-dimensional (axi-symmetric, plane strain, plane stress), three-dimensional and Fourier series aided three-dimensional analyses. The work shown in this thesis only includes axi-symmetric and plane strain analyses.

This Chapter gives a brief description of the basic fundamentals of the finite element method, with particular reference to the approach followed in ICFEP and the features that are used in this thesis. A detailed description of the finite element theory formulation and the full range of ICFEP features can be found in Potts & Zdravkovic (1999).

4.2 Finite element theory

The formulation of the finite element (FE) method consists essentially of six phases: a) element discretisation; b) primary variable approximation; c) formulation of the element equations; d) assembly of the global equations; e) formulation of the boundary conditions and f) solution of the global equations. The formulation of the finite element method for a single phase continuum material is presented in the following paragraphs. Section 4.3 describes how the finite element theory may be extended to account for the two phase nature of soils.

When the soil behaviour is described by non-linear constitutive relationships the solution strategy for the global equations becomes complex and this aspect is discussed separately in Section 4.2.8.

4.2.1 Element discretisation

The first step in a FE procedure is to approximate the geometry of the problem under consideration by an equivalent FE mesh, which comprises small discrete regions, called finite elements. For two-dimensional problems, the finite elements have in general triangular or quadrilateral shapes. The elements are defined by the nodes at the corners, though they can also have additional nodes at the mid sides, resulting in 6-noded triangular and 8-noded quadrilateral elements. The number of elements in a finite element mesh controls the accuracy and the computational time of the analysis. Therefore the ideal FE mesh should have as few elements as possible, to reduce the computational cost and be refined in the areas where large stress and strain gradients are expected, to ensure the accuracy of the analysis.

4.2.2 Primary variable approximation

In the displacement based finite element method the primary unknown is the displacements at the nodes and the main approximation is to assume the displacement field to vary in a particular way across the element. Stresses and strains are treated as secondary quantities and are calculated once the displacement field has been determined. It is assumed that the displacement field across an element can be expressed as a polynomial function of the displacement values at the nodes, where the polynomial order depends on the number of the nodes in the element. For three and four noded elements the displacement field varies linearly across the element, while for the higher order six and eight noded elements, the displacement field varies quadratically across the element.

In two-dimensional analyses the displacement field is characterized by two displacement values u and v in the x and y direction, respectively and is given by Equation 4.1.

Equation 4.1

$$\begin{Bmatrix} u \\ v \end{Bmatrix} = [N] \cdot \{u_1, v_1, u_2, v_2, ..., u_n, v_n\}^T = [N] \cdot \begin{Bmatrix} u \\ v \end{Bmatrix}_{nodes}$$

Where [N] is the matrix of the displacement interpolation functions also known as the shape functions, and the subscript *n* indicates the number of nodes in the element.

In this way the number of degrees of freedom becomes finite and equal to the number of nodal displacements, and the displacement of any point within the element can be determined from the shape function and the displacement values at the nodes.

In the analyses reported in this thesis 8-noded isoparametric elements are employed, and an example is shown in Figure 4.1. For an isoparametric element the global element as it appears in the finite element mesh is derived from the parent element, which has the same number of nodes but is defined in relation to the natural coordinate system, in terms of the coordinates *S* and *T* such that $-1 \leq S \leq 1$ and $-1 \leq T \leq 1$.

The denomination *isoparametric* derives from the fact that the interpolation functions N_i that are used to describe the displacement field in terms of the nodal displacements are also used to map the geometry of the element from the global to the natural coordinate system. The global coordinates *x*, *y* of a point within an element can be expressed as a function of the global nodal coordinates x_i, y_i by means of Equation 4.2.

Equation 4.2

$$x = \sum_{i=1}^{n} N_i x_i \qquad y = \sum_{i=1}^{n} N_i y_i$$

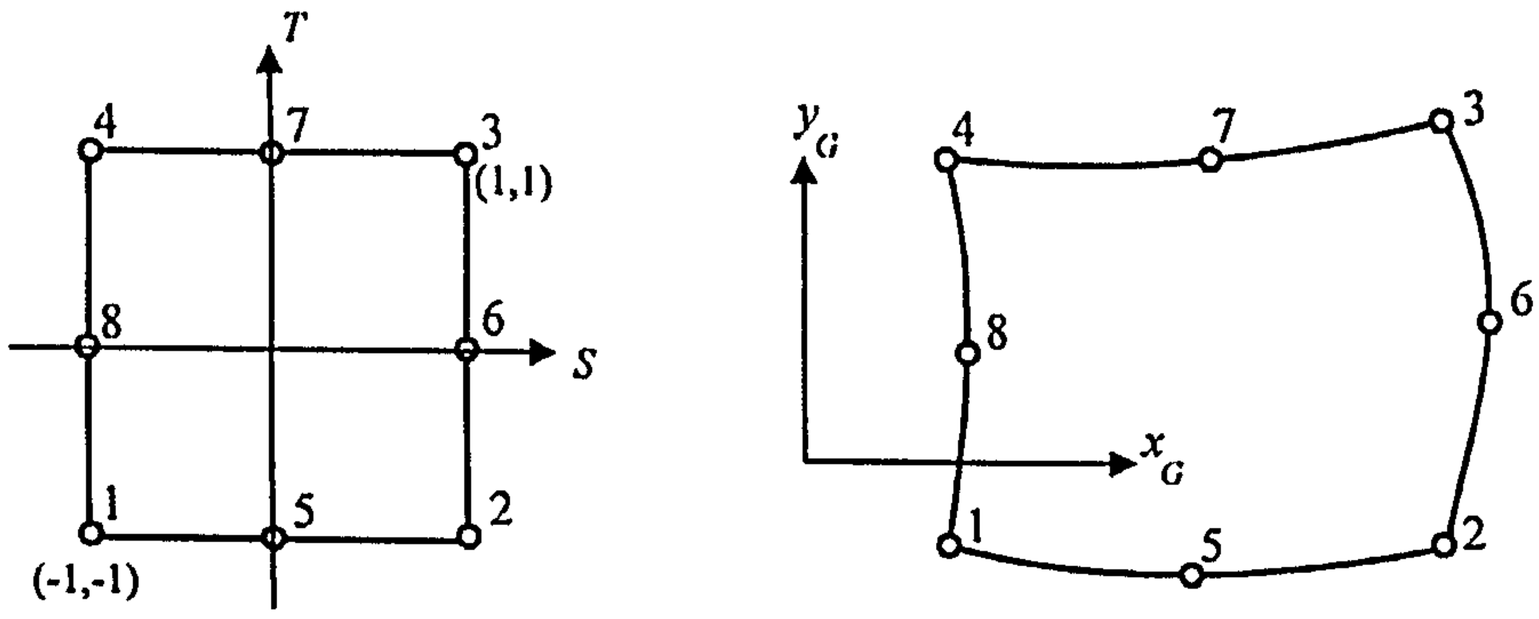

a) Parent Element

b) Global Element

Figure 4.1: Eight-noded isoparametric element (after Potts and Zdravkovic, 1999).

The main advantage of using the isoparametric finite element formulation is that the interpolation functions N_i that are used to define the displacement field and map the element geometry are expressed in terms of the natural coordinates S and T. The interpolation functions of an eight-noded quadrilateral element as shown in Figure 4.1 are given by Equation 4.3.

Equation 4.3

Mid-side nodes

$$N_5 = \frac{1}{2}(1-S^2)(1-T)$$

$$N_6 = \frac{1}{2}(1+S)(1-T^2)$$

$$N_7 = \frac{1}{2}(1-S^2)(1+T)$$

$$N_8 = \frac{1}{2}(1-S)(1-T^2)$$

Corner nodes

$$N_1 = \frac{1}{4}(1-S)(1-T) - \frac{1}{2}N_5 - \frac{1}{2}N_8$$

$$N_2 = \frac{1}{4}(1+S)(1-T) - \frac{1}{2}N_5 - \frac{1}{2}N_6$$

$$N_3 = \frac{1}{4}(1+S)(1+T) - \frac{1}{2}N_6 - \frac{1}{2}N_7$$

$$N_4 = \frac{1}{4}(1-S)(1+T) - \frac{1}{2}N_7 - \frac{1}{2}N_8$$

4.2.3 Formulation of the element equations

The derivation of the equations that govern the deformational behaviour of each element is based on the conditions of compatibility, equilibrium and the constitutive relations. Given that the soil is, in general, non-linear the equations are formulated in incremental form, and the displacement field across an element can then be written in the form of Equation 4.4. Equation 4.5 defines the strains corresponding to these displacements assuming plane strain conditions. It is noted that throughout this thesis (if nothing is stated to the contrary) positive stresses and strains are compressive.

Equation 4.4

$$\{\Delta d\} = \begin{Bmatrix} \Delta u \\ \Delta v \end{Bmatrix} = [N] \begin{Bmatrix} \Delta u \\ \Delta v \end{Bmatrix}_n = [N]\{\Delta d\}_n$$

Equation 4.5

$$\{\Delta \varepsilon\} = \begin{Bmatrix} \Delta \varepsilon_x \\ \Delta \varepsilon_y \\ \Delta \varepsilon_z \\ \Delta \varepsilon_{xy} \end{Bmatrix} = \begin{Bmatrix} -\dfrac{\partial(\Delta u)}{\partial x} \\ -\dfrac{\partial(\Delta v)}{\partial y} \\ 0 \\ -\dfrac{\partial(\Delta u)}{\partial y} - \dfrac{\partial(\Delta v)}{\partial x} \end{Bmatrix}$$

Combining Equation 4.4 and 4.5 the strains across an element can be expressed in terms of the nodal displacements by means of Equation 4.6.

Equation 4.6

$$\{\Delta \varepsilon\} = [B]\{\Delta d\}_{nodes}$$

Where [B] contains the derivatives of the shape functions N_i in relation to the global coordinates x and y, and $\{\Delta d\}_{nodes}$ contains the nodal displacements.

As mentioned above in an isoparametric element the shape functions N_i are dependent on the natural coordinates S and T only. In this case the derivatives of the functions N_i

in relation to the global coordinates can not be determined directly, but require the use of the chain rule of differentiation and some mathematical manipulation to be expressed as:

Equation 4.7 $$\begin{Bmatrix} \frac{\partial N_i}{\partial x} \\ \frac{\partial N_i}{\partial y} \end{Bmatrix} = \frac{1}{|J|} \begin{bmatrix} \frac{\partial y}{\partial T} & -\frac{\partial y}{\partial S} \\ -\frac{\partial x}{\partial T} & \frac{\partial x}{\partial S} \end{bmatrix} \begin{Bmatrix} \frac{\partial N_i}{\partial S} \\ \frac{\partial N_i}{\partial T} \end{Bmatrix}$$

Where |J| is the Jacobian determinant, $|J| = \frac{\partial x}{\partial S}\frac{\partial y}{\partial T} - \frac{\partial y}{\partial S}\frac{\partial x}{\partial T}$

The constitutive law that describes the material behaviour provides a relationship between stresses and strains, which can be expressed by Equation 4.8, where [D] is the constitutive matrix and in plane strain conditions $\{\Delta\sigma\}^T = \{\Delta\sigma_x, \Delta\sigma_y, \Delta\sigma_z, \Delta\tau_{xy}\}$

Equation 4.8 $$\{\Delta\sigma\} = [D]\{\Delta\varepsilon\}$$

The element equations are then determined by invoking the principle of minimum potential energy, that states that the static equilibrium position of a loaded body is that which minimizes the total potential energy. The total potential energy (E) is the sum of the strain energy or the work done by the internal forces (W) and the work done by the applied forces (L) during deformation of the body. The equilibrium of an element *E* can be expressed in incremental form as:

Equation 4.9 $$\Delta E_E = \Delta W_E + \Delta L_E$$

where the incremental strain energy ΔW and the incremental work done by the applied loads ΔL during an increment of deformation of the body are given by Equation 4.10 and 4.11, respectively.

Equation 4.10 $$\Delta W = \frac{1}{2}\int_{Vol}\{\Delta\varepsilon\}^T\{\Delta\sigma\}\cdot dVol = \frac{1}{2}\int_{Vol}\{\Delta\varepsilon\}^T[D]\{\Delta\varepsilon\}\cdot dVol$$

Equation 4.11 $$\Delta L = \int_{Vol}\{\Delta d\}^T\{\Delta F\}\cdot dVol + \int_{surface}\{\Delta d\}^T\{\Delta T\}\cdot dSurface$$

Where $\{\Delta d\}^T = \{\Delta u, \Delta v\}$ is the displacement vector; $\{\Delta F\}^T = \{\Delta F_x, \Delta F_y\}$ is the vector of the body forces and $\{\Delta T\}^T = \{\Delta T_x, \Delta T_y\}$ is the vector of the surface tractions.

The volume integrals are performed over the volume of the element and the surface integral is done over that part of the element boundary on which surface tractions are being applied. Substituting Equations 4.10 and 4.11 into Equation 4.9, expressing the displacement variation over the element in terms of the nodal values (Equation 4.6) and then summing the potential energies of the various elements, leads to Equation 4.12.

Equation 4.12

$$\Delta E = \sum_{i=1}^{N}\left[\frac{1}{2}\int_{vol}\left(\{\Delta d\}_n^T[B]^T[D][B]\{\Delta d\}_n - 2\{\Delta d\}_n^T[N]^T\{\Delta F\}\right)dVol - \int_{surface}\{\Delta d\}_n^T[N]\{\Delta T\}dSrf\right]$$

where the volume and the surface integrals refer to that over the element *i*.

To mathematically obtain the state that corresponds to the minimum potential energy, Equation 4.12 is differentiated and the result set to zero. This expression can then be reworked such that it can take the form of Equation 4.13 that represents the governing equation of the finite element method.

Equation 4.13

$$\sum_{i=1}^{N}[K_E]_i(\{\Delta d\}_n)_i = \sum_{i=1}^{N}\{\Delta R_E\}$$

Where $[K_E] = \int_{vol}[B]^T[D][B]\cdot dVol$ is the element stiffness matrix and

$\{\Delta R_E\} = \int_{Vol}[N]^T\{\Delta F\}\cdot dVol + \int_{Surface}[N]^T\{\Delta T\}\cdot dSurface$ is the right hand side load vector.

The problem is thus reduced to determining and summing the separate element equilibrium equations. The integrals in Equation 4.13 are formulated in terms of the global coordinates x and y, but using the isoparametric coordinate transformation they can be evaluated using the natural coordinate system and reduced to an integral over a square with S and T varying between –1 and 1, and for example the element stiffness matrix becomes:

Equation 4.14

$$[K_E] = \int_{-1}^{1}\int_{-1}^{1}[B]^T[D][B]\,|J|\cdot t\cdot dS\cdot dT$$

Noting that $dVol = t\cdot dx\cdot dy = t\cdot|J|\cdot dS\cdot dT$ and in a plane strain problem the thickness t is assumed equal to unity.

4.2.4 Numerical integration

In general it is not possible to evaluate the integrals in Equation 4.13 and 4.14 explicitly and instead numerical integration is employed. The most common integration scheme is Gaussian integration and this is the method used in ICFEP. Gaussian integration consists of a weighted sum of the value of the function to be integrated at a discrete number of points, denominated as *integration points* or in this case *Gauss points*. The number of integration points determines the *integration order*, and Figure 4.2 shows the location of the *Gauss points* for an 8-noded isoparametric element for a 2x2 and 3x3 integration order, usually referred to as reduced and full integration, respectively. The accuracy of the integration improves with the integration order, however this is at the expense of longer computational time/cost since the function needs to be evaluated at a greater number of points.

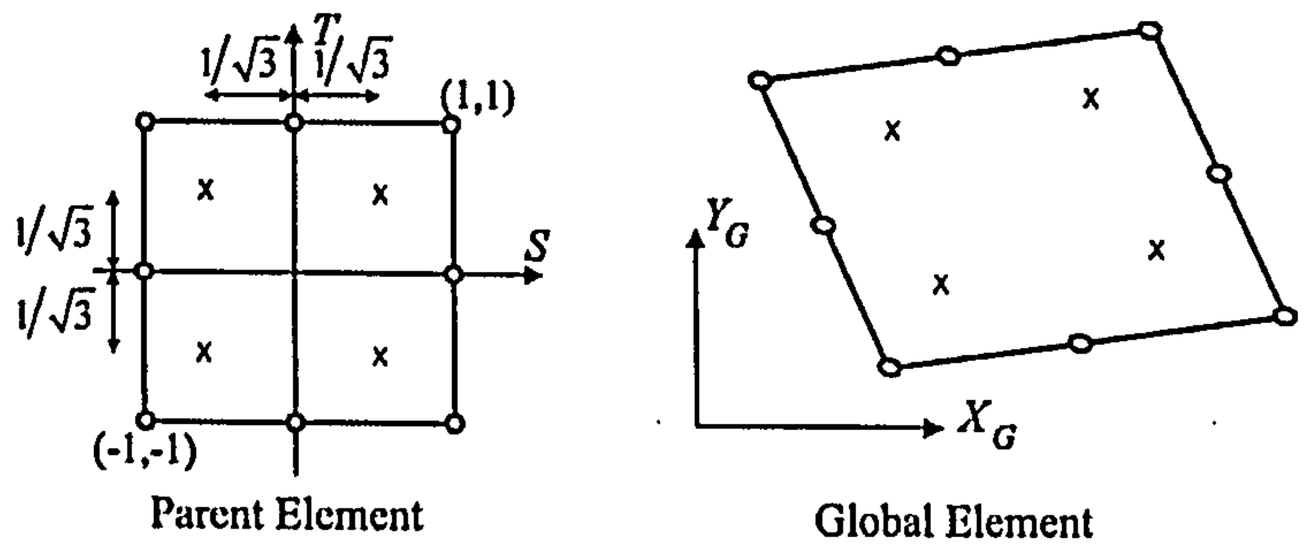

Figure 4.2: Location of the Gauss points for an 8-noded isoparametric element (after Potts and Zdravkovic, 1999).

4.2.5 Assembly of the global equations

The next step in the finite element formulation is to assemble the separate element equations into a set of global equations in the form of Equation 4.15.

Equation 4.15 $$[K_G]\{\Delta d\}_{Gnodes} = \{\Delta R_G\}$$

Where $[K_G]$ is the global stiffness matrix, $\{\Delta d\}_{Gnodes}$ is the vector containing the nodal displacements (unknowns) for the entire finite element mesh and $\{\Delta R_G\}$ is the global right hand side load vector.

The terms of the global stiffness matrix are obtained by summing the individual element contributions taking into account the degrees of freedom that are common between elements. From Equation 4.14 it can be inferred that if the constitutive matrix [D] is symmetric – a situation that arises frequently - the element stiffness and the global stiffness matrix will also be, and this may be used to reduce the amount of information being stored. In addition, zero entries in the global stiffness matrix arise if two degrees of freedom are not connected, and so from the geometry of the finite element mesh there will be a large number of zero terms. There are techniques to reduce the non-zero terms to a diagonal band by means of careful renumbering of the element nodes, in order to reduce the memory requirement.

The terms in the right hand side vector are obtained in a similar way by adding the individual loads acting at each node in a given direction.

4.2.6 Formulation of the boundary conditions

To fully define the boundary value problem being analysed, all that remains is to specify appropriate boundary conditions along the boundary of the FE mesh and incorporate them in the global system of equations.

The boundary conditions can be broadly divided into three types according to their influence on the global system of equations. One group of boundary conditions affects the right hand side vector and are loading conditions such as point load, surcharge pressures, body weight and excavation/construction.

The second group of boundary conditions affects the vector of the unknown nodal displacements, i.e. prescribed degrees of the freedom. It is noted that sufficient displacement conditions need to be specified in order to prevent any rigid body modes of deformation (e.g. rotation, translation) otherwise the global stiffness matrix will be singular and the equations cannot be solved.

There is a third group of more complex boundary conditions that affect the whole structure of the system of equations; included in this group are *tied degrees of freedom,* which affect the numbering of the degrees of freedom and the stiffness matrix assembly. The *tied degrees of freedom* boundary condition allows the user to specify that two or more nodal displacements are equal, but the magnitude of that displacement is unknown and a result of the analysis.

4.2.7 Solution of the global equations

The global equations form mathematically a large system of simultaneous equations, which need to be solved in order to obtain the value of the unknown nodal displacements. There are several techniques for solving such large systems of equations; a popular scheme adopted by many finite element programs, including ICFEP is the Gaussian elimination method (Potts & Zdravkovic, 1999). However, for three-dimensional problems the large size of the equation system means that iterative techniques may be preferable.

Once the nodal displacements have been determined, the secondary quantities such as stresses and strains may be calculated by application of Equations 4.6 and 4.8.

4.2.8 Non-linear finite element theory

In the previous sections, it has been implicitly assumed that on applying a change in the boundary conditions either in terms of displacements $\{\Delta d\}$ or loads $\{\Delta R\}$ the constitutive matrix and therefore the stiffness matrix remains constant throughout. However this is valid for a linear elastic material only.

If soil behaviour is to be simulated more accurately it is likely that non-linear elastic or elastic-plastic constitutive models must be used, and in this case the constitutive matrix is no longer constant but varies with stress and/or strain during the analysis. To deal

with this the boundary conditions are applied in a series of increments and Equation 4.15 takes the incremental form of Equation 4.16 (where the subscript *i* indicates the increment number) and the final solution is obtained by summing the results of each increment.

Equation 4.16 $$[K_G]^i \{\Delta d\}^i_{Gnodes} = \{\Delta R_G\}^i$$

However, the global stiffness matrix varies over each increment, and unless very small increments are used the results will be in error. The solution of Equation 4.16 is not straightforward and there are several solution strategies that can be employed e.g. tangent stiffness method, visco-plastic method, Newton-Raphson method. The analyses presented in this thesis are carried out using the modified Newton-Raphson method and thus this is explained in more detail below.

Modified Newton-Raphson method

The Newton-Raphson method solves Equation 4.16 for each increment using an iterative procedure, as schematically shown in Figure 4.3. In the first iteration, Equation 4.16 is solved using a global stiffness matrix $[K_G]^0$ calculated using the current stress and strain state at the beginning of the increment. The method recognizes that due to the dependency of the stiffness matrix on the stress and/or strain state and their variation over the increment the solution is in error, and uses the predicted displacements from the first iteration Δd^1 to evaluate a measure of the error and the residual load vector Ψ^1. Equation 4.16 is then solved again using the residual load vector Ψ^1 as the new right hand side vector, such that it can be rewritten in the following form:

Equation 4.17 $$[K_G]^i \left(\{\Delta d\}^i_{Gnodes}\right)^j = \{\psi\}^{j-1}$$

Notes: i denotes the increment number and j the iteration number.

The process is repeated until the residual load is smaller than a pre-set tolerance. In ICFEP, the convergence criteria involves setting a limit to the size of the iterative displacement vector and the iterative residual load vector, expressed in terms of the scalar norms obtained by Equation 4.18 and 4.19 respectively.

Equation 4.18 $$\left\|\left(\{\Delta d\}^i_{Gnodes}\right)^j\right\| = \sqrt{\left(\left(\{\Delta d\}^i_{Gnodes}\right)^j\right)^T \cdot \left(\{\Delta d\}^i_{Gnodes}\right)^j}$$

Equation 4.19 $$\left\|\{\psi\}^j\right\| = \sqrt{\left(\{\psi\}^j\right)^T \cdot \{\psi\}^j}$$

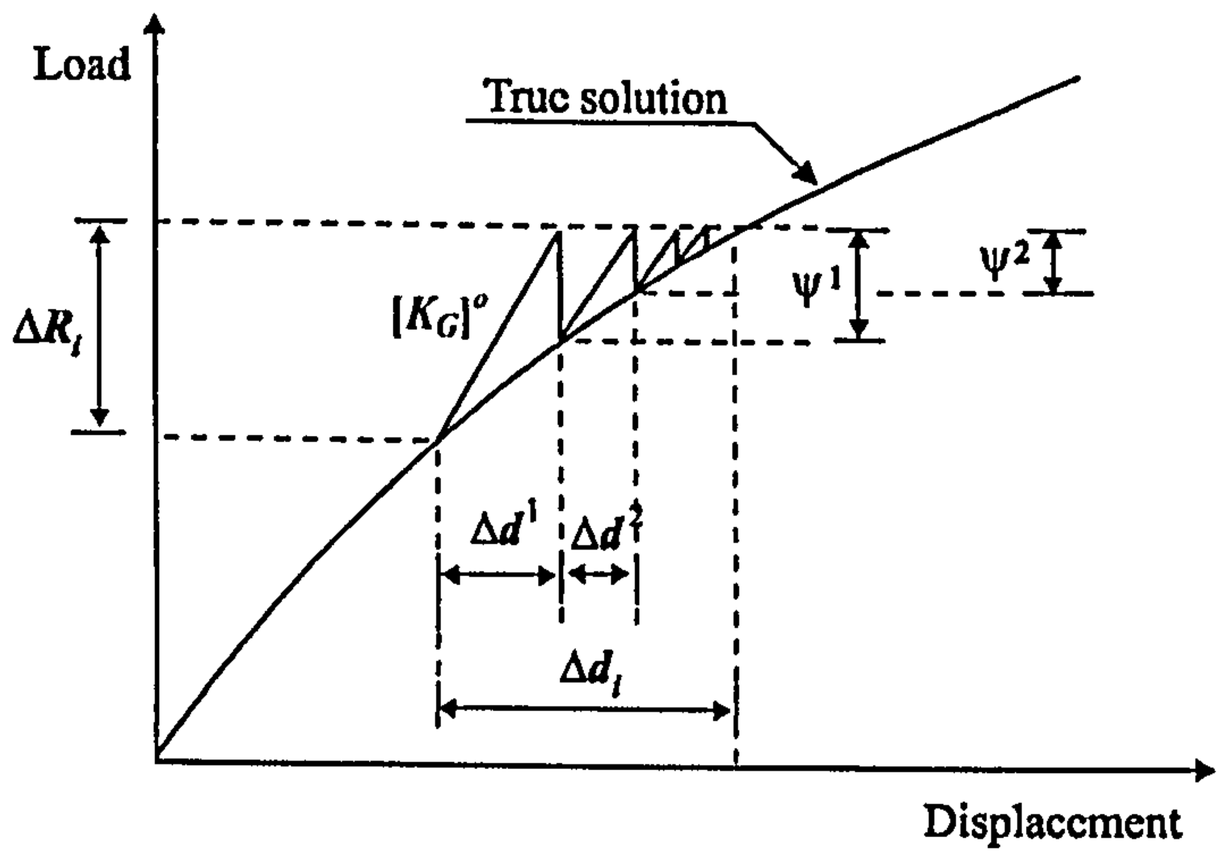

Figure 4.3: Schematic representation of the modified Newton-Raphson method for a one-dimensional problem (Potts & Zdravkovic, 1999).

The iterative quantities are compared with the respective accumulated and incremental values, and the default convergence settings in ICFEP (that are used in the analyses presented in this thesis) are that the iterative quantity is less than 2% of both the accumulated and incremental ones. When convergence is achieved, the incremental displacements are then obtained by summing the iterative displacements.

In the original Newton-Raphson method, the incremental global stiffness matrix $[K_G]^i$ is recalculated and inverted at the beginning of each iteration, based on the stresses and strains estimated at the previous iteration. However, the modified Newton-Raphson method only calculates and inverts the global stiffness matrix at the beginning of the increment and uses it for all the iterations within that increment. This works because the method recognizes that the solution is in error and it is the iterative procedure that ensures that the constitutive equations are satisfied and the solution obtained is correct (or more correctly, contains an acceptable error).

An important step in this method is the evaluation of the residual load vector. At the end of each iteration, the current estimate of the incremental displacements are used to evaluate the incremental strains at each integration point, after which the constitutive model is integrated along the strain path to obtain an estimate of the stress changes. The stress changes are added to the accumulated stresses at the start of the increment, which are then used to calculate the equivalent nodal forces. The residual load vector is the

difference between these forces and the nodal forces derived from the externally applied loads (boundary conditions).

Given that the constitutive behaviour changes over the increment the evaluation of the stress change is not straightforward and there are several methods available in the literature to perform this integration, termed stress point algorithms. In the analyses presented in this thesis, a substepping algorithm with a modified Euler integration scheme has been used and therefore this is explained in more detail below.

Having determined the incremental strains $\{\Delta\varepsilon\}$ for each integration point, the objective of the stress point algorithm is to evaluate the associated incremental stresses. In a substepping algorithm the incremental strains are split into a number of smaller sub-steps and the main assumption is that the strains in each sub-step $\{\Delta\varepsilon_{ss}\}$ are a proportion, ΔT, of the incremental strains $\{\Delta\varepsilon_{inc}\}$ as expressed by Equation 4.20.

Equation 4.20 $$\{\Delta\varepsilon_{ss}\} = \Delta T\{\Delta\varepsilon_{inc}\}$$

This implies that the ratio between the strain components in each sub-step is the same as that for the incremental strains. The strains are therefore assumed to vary in a proportional manner over the increment, which in general may not be true, and consequently introduces, potentially, small errors in the calculation.

The calculation procedure starts by identifying any linear elastic region over which the determination of the stress changes could be performed by direct integration. The remaining incremental strains are then split into smaller sub-steps. To integrate the constitutive equation over a strain step $\{\Delta\varepsilon_{ss}\}$ a modified Euler integration scheme is employed. Initially, the size of the sub-step, ΔT is assumed to be equal to one. The stress changes $\{\Delta\sigma_1\}$ are evaluated using a constitutive matrix based on the stresses and strains at the start of the sub-step. Subsequently the stress changes $\{\Delta\sigma_1\}$ and respective change in the hardening parameters are used to evaluate the constitutive matrix at the end of the sub-step and the corresponding stress changes, $\{\Delta\sigma_2\}$. The true stress changes are assumed to be the average of the two values, and it can be shown that the error in the stress changes, E can be approximated by Equation 4.21 and the relative error, R by Equation 4.22.

Equation 4.21 $$E \approx \frac{1}{2}\left(\{\Delta\sigma_1\} - \{\Delta\sigma_2\}\right)$$

Equation 4.22 $$R = \frac{\|E\|}{\|\{\sigma + \Delta\sigma\}\|}$$

Where σ is the stress state at the start of the sub-step and $\Delta\sigma$ is the estimated stress change.

Usually, the relative error R is checked against a pre-defined tolerance and if the error is larger than the tolerance, the size of the sub-step is reduced. The new size of the sub-step can be estimated based on the value of the relative error, R and the procedure is repeated until the sub-step is accepted.

4.3 Pore pressures considerations

In general terms it can be said that soil has two phases: the solid phase that constitutes the soil skeleton and the fluid phase, which fills the pores within the soil skeleton. If the soil is fully saturated the pore fluid is water, while if the soil is fully dry the fluid will be air. In an intermediate situation in which the soil is partially saturated the fluid is a mixture of air and water, but the consideration of such a case goes beyond the scope of the present work.

If the soil is fully saturated, the stresses acting in the two phases can be related using the principle of effective stresses (Equation 4.23), and in the majority of the available constitutive models the soil deformation is related to the effective stress changes.

Equation 4.23 $$\{\Delta\sigma\} = \{\Delta\sigma'\} + \{\Delta\sigma_f\}$$

The finite element method as presented in the previous section can only be applied to single phase continuous media, as it only provides information on one stress component. In Section 4.2.3, the constitutive behaviour was expressed in terms of total stresses by the following equation:

Equation 4.24 $$\{\Delta\sigma\} = [D]\{\Delta\varepsilon\}$$

Where in plane strain conditions $\{\Delta\sigma\} = \{\Delta\sigma_x, \Delta\sigma_y, \Delta\sigma_y, \Delta\tau_{xy}\}$ is the incremental total stress vector, $\{\Delta\varepsilon\} = \{\Delta\varepsilon_x, \Delta\varepsilon_y, 0, \Delta\gamma_{xy}\}$ is the incremental total strain vector and $[D]$ is the constitutive matrix that provides a relationship between these two vectors.

This formulation can therefore be used in the following two cases only:

a) In fully drained problems in which there is no change in pore fluid pressure $\Delta\sigma_f$ and consequently changes in effective and total stress are the same i.e. $\{\Delta\sigma\}=\{\Delta\sigma'\}$. In this case the matrix $[D]$ is expressed as a function of the effective stress stiffness parameters, e.g. in the case of an isotropic linear elastic model the drained Young's Modulus E' and drained Poisson's ratio, μ', or two other equivalent elastic parameters (see section 1.4). When employing the creep models described in the following chapter the matrix $[D]$ is expressed as a function of the elastic bulk modulus K and a second elastic parameter either the elastic shear stiffness, G or the Poisson's ratio, μ that is input by the user.

b) In fully undrained problems in which the constitutive matrix $[D]$ is expressed as a function of the total stress parameters, e.g. in the case of an isotropic linear elastic model the constitutive matrix would be derived from the undrained Young's Modulus E_u and undrained Poisson's ratio, μ_u.

In a fully undrained analysis, if the material is saturated there will be no volume change, which would be ideally modelled in an isotropic elastic soil by setting the Poisson's ratio equal to 0.5. However, this causes some terms of the constitutive matrix to be evaluated as infinite, and so a value smaller than 0.5 needs to be specified. Potts and Zdravkovic (1999) show that once the Poisson's ratio exceeds 0.499 the value has little effect on the analysis predictions.

When analysing fully undrained problems in this manner no information on the pore fluid pressures are obtained, and in addition the formulation puts a limitation on the constitutive model that can be used to reproduce the soil behaviour. In the following section, a more general methodology to perform the analysis of fully undrained problems considering the two phase nature of the soil is presented.

4.3.1 Undrained effective stress analysis

If information regarding the pore fluid pressure is required and/or it is required to specify the constitutive model in terms of effective stress (as happens in the models presented in this thesis and with most advanced constitutive models), it is necessary to express the changes in effective stress and pore fluid pressure separately. This can be

achieved by invoking the principle of effective stress (Equation 4.23) and using $\left[D^{'}\right]$ to express the relationship between effective stresses and strains, such that:

Equation 4.25 $$\{\Delta\sigma\}=\{\Delta\sigma^{'}\}+\{\Delta\sigma_f\}=\left[D^{'}\right]\{\Delta\varepsilon\}+\{\Delta\sigma_f\}$$

Where $\{\Delta\sigma\}$ is the vector that contains the incremental total stresses, $\{\Delta\sigma'\}$ the vector of the incremental effective stresses and $\{\Delta\sigma_f\}$ is the vector of the incremental pore fluid pressure that corresponds to an isostatic stress state, i.e. in plane strain conditions $\{\Delta\sigma_f\}=\{\Delta u,\Delta u,\Delta u,0\}$.

In undrained conditions it is assumed that there is no flow of water and so the solid and fluid phase deform together. Assuming that the two phases undergo the same strain increment Equation 4.24 implies that the total constitutive matrix $[D]$ is the sum of the effective constitutive matrix $\left[D^{'}\right]$ and the pore fluid stiffness matrix $\left[D_f\right]$ as shown in

Equation 4.26 $$[D]=\left[D^{'}\right]+\left[D_f\right]$$

Where the effective constitutive matrix $\left[D^{'}\right]$ is fully characterized by the elastic soil parameters e.g. for the creep models described in the following chapters the elastic bulk modulus K and a second elastic parameter either the elastic shear stiffness, G or the Poisson's ratio, μ that is input by the user.

Noting that the fluid phase cannot transmit shear the pore fluid stiffness matrix $\left[D_f\right]$ has the form of Equation 4.27 in plane strain conditions, where K_e is a constant and its value is related to the bulk modulus of the pore fluid, K_f.

Equation 4.27 $$\left[D_f\right]=K_e\begin{bmatrix}1&1&1&0\\1&1&1&0\\1&1&1&0\\0&0&0&0\end{bmatrix}$$

Potts and Zdravkovic (1999) show that in analysis involving saturated soils the analyses results are not sensitive to the actual magnitude of K_e provided it is considerably larger than the soil skeleton bulk stiffness K_{skel} and they recommend setting K_e as a multiple of the soil skeleton bulk modulus, such that $K_e=\beta\cdot K_{skel}$ with β assuming a value between 100 and 1000.

Equation 4.26 can be combined with the finite element theory presented previously. The required input parameters enable the calculation of the effective constitutive matrix and the equivalent bulk modulus K_e separately, which are then combined to obtain the total constitutive matrix $[D]$ of each element. After that, the calculation of the element stiffness matrix, the global stiffness matrix assembly and the solution of the equation system follows the procedure described in Section 4.2. Once the (unknown) nodal displacements have been calculated, the effective stresses can be evaluated using Equation 4.28 and the pore fluid pressures by using Equation 4.29. The total stresses can be calculated either by replacing $[D']$ with the total constitutive matrix $[D]$ in Equation 4.28 or through Equation 4.25.

Equation 4.28 $$\{\Delta\sigma'\}=[D']\{\Delta\varepsilon\}$$

Equation 4.29 $$\{\Delta\sigma_f\}=[D_f]\{\Delta\varepsilon\}$$

4.3.2 Coupled consolidation analyses

The formulation presented so far in this chapter deals with the situations when the soil behaviour is fully drained or undrained. Some geotechnical problems can be analysed using either of these extreme conditions, but in others it may be important to account for the time dependent pore pressure response, which is affected by the soil permeability, the rate of loading and the hydraulic boundary conditions. In this case, in addition to the equilibrium equations that govern the deformation of the soil skeleton due to loading, it is necessary to consider the equations governing the flow of the pore fluid through the soil skeleton, namely the equation for the continuity of flow and the generalized Darcy's law. The analysis is then said to be *coupled,* as in effect it couples or combines the pore fluid flow with the stress-strain soil behaviour.

To model such behaviour the pore fluid pressure must be incorporated as a primary unknown, together with the displacements. In a similar manner to the displacement variation (Equation 4.4), the pore fluid pressure variation across an element can be expressed in terms of the nodal values by means of Equation 4.30.

Equation 4.30 $$\{\Delta p\}=[N_p]\{\Delta p\}_n$$

where $\{\Delta p\}$ is the pore pressure change, $\{\Delta p\}_n$ is the pore pressure change at the nodes and $[N_p]$ is a matrix of the shape functions.

If each node of a consolidating element is attributed an incremental pore pressure degree of freedom, the matrix $[N_p]$ is identical to $[N]$. In an 8-noded element this implies that both the displacements and the pore fluid pressure vary quadratically. However, if the displacements vary quadratically, the strains and therefore the effective stresses (for a linear elastic material) vary linearly, causing an inconsistency between the variation in effective stress and pore pressure across the element, which are linked by the principle of effective stresses. Although this is theoretically acceptable it is in general preferable that effective stresses and pore fluid pressures vary in the same way. In an eight noded quadratic element this can be achieved by assigning pore pressure degrees of freedom at the corner nodes only, and this is the approach used in the analyses presented in this thesis.

To derive the equations that govern coupled consolidation analyses, the first step is to formulate the equations that describe the deformation of the soil allowing the solid and the fluid phases to deform independently. It has been shown above that the constitutive behaviour can be written as a relationship between increments of total stress and strain:

Equation 4.31 $$\{\Delta\sigma\} = [D]\{\Delta\varepsilon\}$$

Invoking the principle of effective stress the equation can be rewritten as:

Equation 4.32 $$\{\Delta\sigma\} = [D']\{\Delta\varepsilon\} + \{\Delta p_f\}$$

Where $\{\Delta p_f\} = \{\Delta p_f, \Delta p_f, \Delta p_f, 0\}$ in plane strain conditions and Δp_f is the change in pore fluid pressure.

In a similar way to the procedure described in Section 4.2.3 for the uncoupled formulation, the principle of minimum potential energy is employed. The incremental potential energy ΔE_E is the sum of the incremental strain energy ΔW given now by Equation 4.33 and the incremental work done by the applied forces ΔL, which remains the same and is still given by Equation 4.11.

Equation 4.33 $$\Delta W = \frac{1}{2}\int_{Vol}\left[\{\Delta\varepsilon\}^T[D']\{\Delta\varepsilon\} + \langle\Delta p_f\rangle\cdot\{\Delta\varepsilon\}\right]\cdot dVol$$

The principle of minimum potential energy states that the static equilibrium position of a loaded body is that which minimizes the total potential energy and so, to obtain the minimum of the quantity ΔE_E the potential energy is differentiated and the result set

equal to zero, as outlined in Section 4.2.3. The element equations for all elements in the analysis domain are then assembled to form the global equilibrium equation.

Equation 4.34 $$[K_G]\{\Delta d\}_{Gnodes} + [L_G]\{\Delta p_f\}_{Gnodes} = \{\Delta R_G\}$$

$$\textit{Where}\quad [K_G] = \sum_{i=1}^{N}[K_E]_i = \sum_{i=1}^{N}\left(\int_{Vol}[B]^T[D'][B]\cdot dVol\right)$$

$$[L_G] = \sum_{i=1}^{N}[L_E]_i = \sum_{i=1}^{N}\left(\int_{Vol}\{m\}[B]^T[N_p]\cdot dVol\right)$$

$$\{\Delta R_G\} = \sum_{i=1}^{N}\{\Delta R_E\}_i = \sum_{i=1}^{N}\left[\left(\int_{Vol}[N]^T\{\Delta F\}\cdot dVol\right)_i + \left(\int_{Surface}[N]^T\{\Delta T\}\cdot dSurface\right)_i\right]$$

$$\{m\}^T = \{1 \quad 1 \quad 1 \quad 0\}$$

The subscript E indicates element quantities, i the element number and N the total number of elements in the analysis domain.

However Equation 4.34 cannot be solved because it contains two unknowns the nodal displacements and the nodal pore pressure changes. Another equation is needed, which can be obtained by combining the equation of continuity of flow (which in plane strain conditions is given by Equation 4.35) and the generalized Darcy's law (Equation 4.36).

Equation 4.35 $$\frac{\partial v_x}{\partial x} + \frac{\partial v_y}{\partial y} - Q = \frac{\partial \varepsilon_v}{\partial t}$$

where v_x and v_y are the components of the superficial velocity of the pore fluid in the directions x and y, respectively and Q represents any sources or sinks. Darcy's law assumes the soil to be fully saturated and that both the pore fluid and the soil grains are incompressible.

Equation 4.36 $$\{v\} = -[k]\{\nabla h\}$$

where $\{v\}$ is the vector of the pore fluid superficial velocities, $[k]$ is the matrix that contains the permeability properties of the material (if the material has an isotropic permeability, k then $k_{xx}=k_{yy}=k$ and $k_{xy}=0$) and h is the hydraulic head given by:

Equation 4.37 $$h = \frac{p_f}{\gamma_f} + \left(x \cdot i_{Gx} + y \cdot i_{Gy}\right)$$

where γ_f is the bulk unit weight of the pore fluid, x and y are the global coordinates and the vector $\{i_G\}=\{i_{Gx}, i_{Gy}, 0\}$ is a unit vector parallel but in the opposite direction to that of gravity.

Applying the principle of virtual work, the continuity equation can be rewritten as:

Equation 4.38
$$\int_{Vol}\left[\{v\}^T\{\nabla(\Delta p_f)\}+\frac{\partial \varepsilon_v}{\partial t}\{\Delta p_f\}\right]\cdot dVol=\{Q\}\cdot\{\Delta p_f\}$$

Substituting Equations 4.36 and 4.37 into Equation 4.38 and approximating $\frac{\partial \varepsilon_v}{\partial t}$ as $\frac{\Delta \varepsilon_v}{\Delta t}$ one obtains:

Equation 4.39
$$\int_{Vol}\left[\int_{t_k}^{t_k+\Delta t}-[k]\cdot\left(\frac{1}{\gamma_f}\{\nabla p_f\}+\{i_G\}\right)\{\nabla(\Delta p_f)\}\cdot dt+\Delta\varepsilon_v\{\Delta p_f\}\right]\cdot dVol=\{Q\}\cdot\{\Delta p_f\}\cdot\Delta t$$

Rearranging Equation 4.39 by expressing the pore pressures changes $\{\Delta p_f\}$ in terms of the nodal values $\{\Delta p_f\}_{nodes}$ and adding the equations for each element into a global equation, the following global equation is obtained:

Equation 4.40
$$[L_G]^T\{\Delta d\}_{Gnodes}-\int_{t_k}^{t_k+\Delta t}[\Phi_G]\{p_f\}_{Gnodes}\cdot dt=([n_G]+\{Q\})\Delta t$$

where
$$[\Phi_G]=\sum_{i=1}^{N}[\Phi_E]_i=\sum_{i=1}^{N}\left(\int_{Vol}\frac{[E]^T[k][E]}{\gamma_f}\cdot dVol\right)_i$$
$$[n_G]=\sum_{i=1}^{N}[n_E]_i=\sum_{i=1}^{N}\left(\int_{Vol}[E]^T[k]\{i_G\}\cdot dVol\right)_i$$
$$[E]^T=\left[\frac{\partial N_p}{\partial x}+\frac{\partial N_p}{\partial y}\right]$$

E indicates element quantities, G global quantities, i the element number and N the total number of elements in the analysis domain.

The integral in Equation 4.40 can be approximated by:

Equation 4.41

$$\int_{t_k}^{t_k+\Delta t}[\Phi_G]\{p_f\}_{Gnodes}\cdot dt=[\Phi_G]\cdot\Delta t\cdot\left[\beta\left(\{p_f\}_{Gnodes}\right)_{t_k+\Delta t}+(1-\beta)\left(\{p_f\}_{Gnodes}\right)_{t_k}\right]$$

Where β is an integration parameter that is introduced to indicate how the pore fluid pressure varies over the increment Δt. Booker and Small (1975) suggest that β should be larger than 0.5 to ensure the stability of the analysis process. In the analyses presented in this thesis, a value of β equal to 0.8 is employed. Coupled consolidation analyses can be computed by using a time marching process and the following system of simultaneous equations, which combines Equations 4.34 and 4.40:

Equation 4.42

$$\begin{bmatrix}[K_G] & [L_G]\\ [L_G]^T & -\beta\Delta t[\phi_G]\end{bmatrix}\cdot\begin{Bmatrix}\{\Delta d\}_{Gnodes}\\ \{\Delta p_f\}_{Gnodes}\end{Bmatrix}=\begin{Bmatrix}\{\Delta R_G\}\\ \{[n_G]+\{\Delta Q\}+[\Phi_G]\{p(t_k)\}_{Gnodes}\}\cdot\Delta t\end{Bmatrix}$$

In coupled analysis, in addition to load or displacement boundary conditions it is necessary to specify the hydraulic boundary conditions along the mesh boundary. This takes the form of either nodal flow values that are included in the term ΔQ, and/or nodal pore pressures that affect the vector of the global nodal pore pressures $\{\Delta p_f\}_{Gnodes}$ reducing the number of unknowns. Once the boundary conditions have been specified, Equation 4.42 can be solved using the formulation described in Sections 4.2.7 and 4.2.8.

4.4 Summary

This chapter has described the main steps required in the formulation of the finite element method for static analysis: element discretisation, primary variable approximation, formulation of the element equations, assemblage of the element equations into a global equation, formulation of the boundary conditions and solution of the system of global equations.

In addition, when the soil is described by a non-linear elastic or elastic-plastic constitutive model that causes the constitutive relations to be stress/strain dependent, and thus causes the stiffness matrix to change over an increment, the solution of the global equations becomes more complex. The non-linear solution method used in the analyses presented in this thesis consists of a modified Newton-Raphson method with a

substepping stress point algorithm and an error controlled modified Euler integration scheme, which has been shown to be robust, accurate and computationally cost effective when dealing with non-linear problems.

The two phase nature of soil means that for a fully saturated soil three types of response are possible: a) the fully drained case in which there is no change in the pore fluid pressure; b) the fully undrained case (no volume change) and c) an intermediate case in which the pore pressure response results from combining the equations of the flow of the pore fluid with the equations that govern the soil skeleton deformability due to loading. The finite element method is able to deal with the above three situations and the procedures involved have been described.

5 A TIME DEPENDENT CONSTITUTIVE MODEL BASED ON A LINEAR LOGARITHMIC CREEP LAW

5.1 Introduction

This Chapter describes the derivation, implementation and validation of a constitutive model that reproduces the time dependent behaviour of clays that derive from viscous effects. From the literature review presented in Chapter 2 it became apparent that most clays in the undisturbed state have isotach viscosity. The isotach viscosity is also appropriate to describe the rate dependent behaviour of soft reconstituted clays over the full stress range, and stiff overconsolidated clays and various transition soils in the small to medium stress range.

The model presented subsequently results from the first steps that the author undertook in understanding the requirements of a constitutive model, in general, and those specific to a constitutive model that reproduces isotach viscosity, in particular. The model is based on an extension of the overstress theory by Perzyna (1963) and assumes that the soil deformation associated with a stress increment $\Delta\sigma$ is divided into an instantaneous and a delayed component. The instantaneous component is assumed to coincide with the elastic response and it is, in this case, characterized by a stress dependent bulk modulus and a second elastic parameter that is specified by the user, either the Poisson's ratio or the elastic shear stiffness. The delayed component is determined assuming that the soil response follows a unique stress-strain-strain rate relationship that corresponds to a linear logarithmic law. Hereafter, the constitutive model is referred to as Creep Model 1.

The constitutive equations are first derived under isotropic stress state conditions. The extension to general stress space is then done assuming that the visco-plastic volumetric strain rate is constant on a given loading surface. This means that the volumetric visco-plastic strain rate at a stress state (p', J) is equal to that at the stress state (p'_0, 0) where p'_0 is the mean effective stress at zero deviatoric stress on the loading surface that passes through the current stress point, which is assumed to have the Modified Cam Clay (MCC) model elliptical shape. The remaining strain components are obtained from a plastic potential surface, which is assumed to coincide with the current loading surface. In this form the model is found to correspond very closely to the model

described by Kutter & Sathialingam (1992) and to that employed by Gnanendran et al. (2006) to analyse the behaviour of the Sackville test embankment, the differences concern mainly the choice and definition of the model parameters and the calculation of the creep scalar multiplier when the model is extended to generalized stress space.

The Modified Cam Clay (MCC) model ellipse has been adopted to describe the loading and the plastic potential surfaces of Creep Model 1 essentially for its mathematical simplicity allowing an easy manipulation of the model equations. This was especially relevant during the early stages of this research when the main focus was to obtain a conceptual understanding of time dependent models and their main requirements. It is noted that the choice of a surface rotated in relation to the K_0 stress axis, even without evolving anisotropy, would present benefits when modelling the behaviour of real soils e.g. predicting well the K_0 value during 1D compression.

The model has been implemented in the finite element program ICFEP and the model performance assessed by means of single element analyses reproducing typical laboratory stress paths. The model is found to reproduce well the phenomena of creep, stress relaxation and strain rate effects under 1D compression. However when simulating undrained triaxial compression tests the model fails to predict critical state conditions – shearing at constant stresses and constant volume – even at very large strains. The model is then improved to reproduce the behaviour of soils at large stress levels, in particular the critical state condition. This is achieved by considering that a given loading surface is a locus of constant creep multiplier and not a surface of constant visco-plastic volumetric strains as assumed previously by the author and other researchers.

5.2 Derivation of the constitutive equations

Creep Model 1 assumes that the soil response can be divided into an instantaneous and a delayed component, such that a total strain increment $\Delta\varepsilon^T$ is given by:

Equation 5.1 $$\Delta\varepsilon^T = \Delta\varepsilon^{el} + \Delta\varepsilon^{vp}$$

where the elastic strain component $\Delta\varepsilon^{el}$ is instantaneous and thus time independent, and the visco-plastic strain component $\Delta\varepsilon^{vp}$ is time dependent and irreversible. The

elastic strain component associated with an effective stress increment $\{\Delta\sigma'\}$ can be evaluated by inverting Equation 5.2, where $[D]$ is the elastic constitutive matrix.

Equation 5.2 $$\{\Delta\sigma'\} = [D] \cdot \{\Delta\varepsilon^{el}\}$$

In the present case, the elastic response of the model is characterized by a stress dependent bulk modulus, K given by Equation 5.3, and a second elastic parameter, which can be either the Poisson's ratio μ or the elastic shear stiffness, G.

Equation 5.3 $$K = \frac{V \cdot p'}{\kappa}$$

where V is the specific volume, p' is the mean effective stress and κ is the slope of the instant (elastic) line in *V-lnp' space*.

According to the visco-plastic theory proposed by Perzyna (1963), the visco-plastic strain component can be expressed as:

Equation 5.4 $$\Delta\varepsilon_{ij}^{vp} = \langle\Phi(F)\rangle \cdot \Delta t \cdot \frac{\partial f_d}{\partial \sigma_{ij}}$$

where $$\langle\Phi(F)\rangle = \Phi(F) \qquad \text{if } F > 0$$

$$\langle\Phi(F)\rangle = 0 \qquad \text{if } F \le 0$$

Δt is the time increment, $\Phi(F)$ is a function that represents the effects of strain rate on the material behaviour, and is a function of the quantity F, which is essentially the distance between the current *dynamic* loading surface f_d and the *static* yield surface f_s (see Section 3.4.1) and the *dynamic* loading surface f_d is used as the plastic potential surface.

In Creep Model 1, the quantity F and $\Phi(F)$ are calculated in relation to a *reference* loading surface, that is characterized by a finite value of plastic strain rate, and the function $\Phi(F)$ is evaluated, and visco-plastic strains are predicted, for stress states located on, above or below that *reference* loading surface. The visco-plastic strain increment can then be written as:

Equation 5.5 $$\Delta\varepsilon_{ij}^{vp} = \Phi \cdot \Delta t \cdot \frac{\partial P}{\partial \sigma_{ij}}$$

where Φ is a visco-plastic scalar multiplier, Δt is the time increment and P is the plastic potential function, which is, in principle, different to the current loading surface. In Creep Model 1 no limit line is defined and consequently, visco-plastic strains are always engaged and there is no region of pure elastic soil behaviour.

The derivation of the creep strain vector $\Delta\varepsilon_{ij}^{vp}$ or the visco-plastic scalar multiplier Φ is initially done for isotropic stress conditions, in which case the soil deformation is completely defined by the volumetric strain component.

It is assumed that under isotropic compression at a constant volumetric strain rate the compression curve in the normally consolidated (NC) range plots as a straight line in *V - ln p' space* (where V is the specific volume and *ln p'* is the natural logarithm of the mean effective stress), with a slope λ. When compressing a soil element at a different strain rate it is assumed that a compression line parallel to the previous one is obtained. The offset between the two compression lines is assumed to vary linearly with the logarithm of the applied strain rate.

This is in agreement with experimental observation that the pre-consolidation pressure increases with the logarithm of the applied strain rate as shown by Leroueil et al. (1985) and corresponds to the Equation 3.12 proposed by Leroueil and Marques (1996). It can be shown that this assumption implies that there is a linear relationship between the creep deformation and the logarithm of time. The formulation of the model is schematically shown in Figure 5.1, noting that the reference compression line is the compression line obtained when the soil element is strained at the reference volumetric strain rate value, $\dot{\varepsilon}_{vol}^{ref}$.

Consider a soil element isotropically consolidated under a mean effective stress p_i' with a specific volume, V_i, which is being consolidated at a constant volumetric strain rate $\dot{\varepsilon}_{vol}^{I}$. The mean effective stress at the intersection between the instant line that passes through the current stress state and the reference compression line is denoted p_{ref}'. The current specific volume V_i can then be written by means of Equation 5.6.

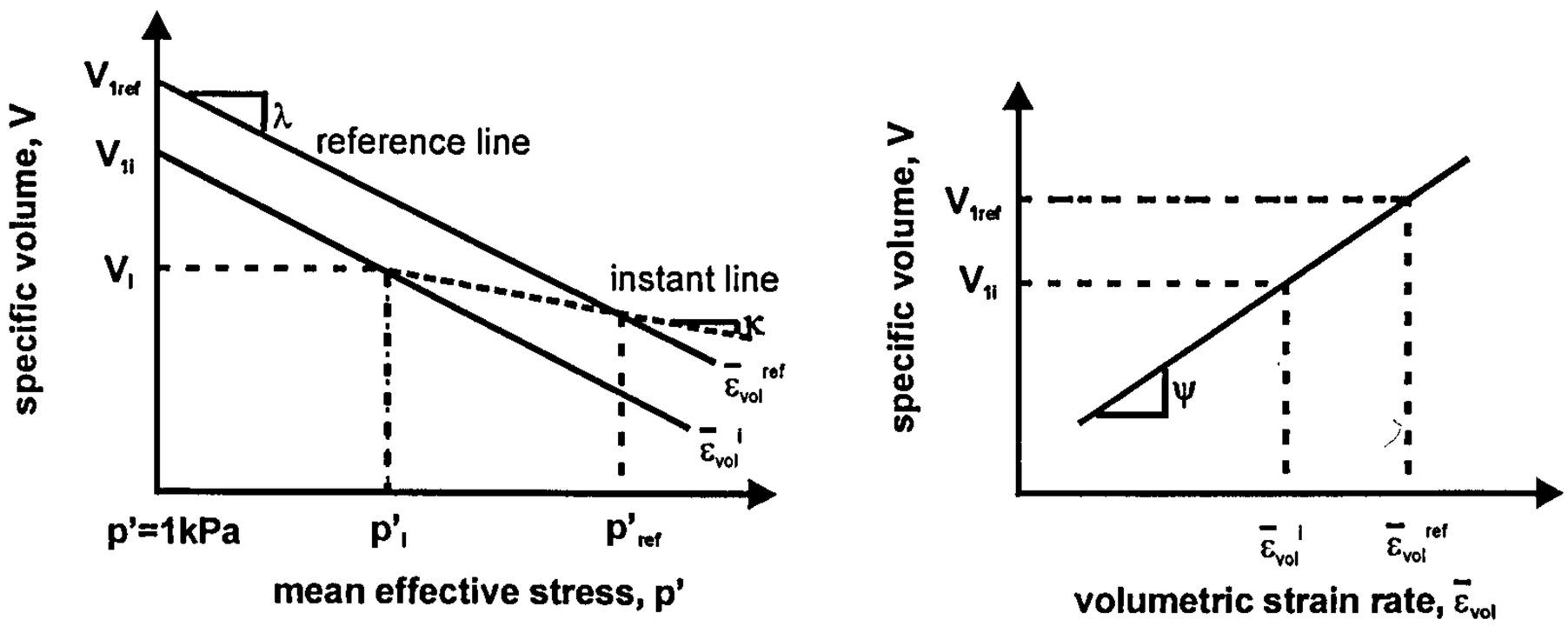

Figure 5.1: Schematic time dependent behaviour under isotropic compression.

Equation 5.6 $$V_i = V_{1i} - \lambda \cdot \ln p_i^{'}$$

where V_{1i} is the specific volume at unit mean effective stress on the compression line that corresponds to the strain rate value $\dot{\varepsilon}_{vol}^{i}$. From Figure 5.1, the current specific volume V_i can alternatively be written as:

Equation 5.7 $$V_i = V_{1ref} - \lambda \cdot \ln p_{ref}^{'} + \kappa \cdot \left[\ln p_{ref}^{'} - \ln p_i^{'}\right]$$

where V_{1ref} is the specific volume at unit mean effective stress on the reference compression line. Combining the two above equations:

Equation 5.8 $$V_{1i} - V_{1ref} = (\lambda - \kappa) \cdot \ln\left(\frac{p_i^{'}}{p_{ref}^{'}}\right)$$

Alternatively, V_{1ref} and V_{1i} can be written as a function of the reference strain rate $\dot{\varepsilon}_{vol}^{ref}$ and the current strain rate $\dot{\varepsilon}_{vol}^{i}$:

Equation 5.9 $$V_{1i} - V_{1ref} = \psi \ln\left(\frac{\dot{\varepsilon}_{vol}^{i}}{\dot{\varepsilon}_{vol}^{ref}}\right)$$

Substituting Equation 5.8 into Equation 5.9 (or vice-versa), it is possible to write the current strain rate value $\dot{\varepsilon}_{vol}^{i}$ in terms of the distance of the current stress state to the reference line:

Equation 5.10 $$\dot{\varepsilon}_{vol}^{i} = \dot{\varepsilon}_{vol}^{ref} \cdot \left(\frac{p_i^{'}}{p_{ref}^{'}}\right)^{\frac{\lambda-\kappa}{\psi}}$$

And the visco-plastic volumetric strain component $\Delta\varepsilon_{vol}^{vp}$ can be evaluated as:

Equation 5.11 $$\Delta\varepsilon_{vol}^{vp} = \Delta t \cdot \dot{\varepsilon}_{vol}^{i}$$

where Δt is the time interval.

According to the model formulation, following an effective stress increment $\{\Delta\sigma'\}$ the stress path moves instantaneously along the current elastic line (κ – line in Figure 5.1) with an associated strain increment $\Delta\varepsilon^{el}$ (Equation 5.2). With time, under constant effective stresses, the soil element develops delayed visco-plastic strains $\Delta\varepsilon^{vp}$, the magnitude of which is evaluated by means of Equation 5.11, bringing the stress state to the appropriate compression curve.

The extension of Equation 5.10 to general stress state is initially done, based on the experimental observations by Tavenas et al. (1978), assuming that the creep volumetric strain rate is constant on a given loading surface. The loading surface is a surface that passes through the current stress state *(p', J)* and it is characterized by the quantity $p_{0c}^{'}$ - the mean effective stress at zero deviatoric stress on the current loading surface. The loading surface is assumed to have the elliptical shape of the MCC yield surface, given by the following equation:

Equation 5.12 $$f = \left(\frac{J}{p^{'} g(\theta)}\right)^2 - \left(\frac{p_{0c}^{'}}{p^{'}} - 1\right) = 0$$

Where the function *g(θ)* is the inclination of the critical state line in *p'-J space* and is a function of the Lode's angle, θ to account for the intermediate principal stress and to express the failure criterion in the deviatoric plane. In order to obtain a Mohr-Coulomb hexagon for the failure surface in the deviatoric plane, g(θ) is:

Equation 5.13 $$g(\theta) = \frac{\sin\varphi_{cs}}{\cos\theta + \frac{\sin\theta \cdot \sin\varphi_{cs}^{'}}{\sqrt{3}}}$$

Where $\varphi_{cs}^{'}$ is the critical state angle of shearing resistance and θ is the Lode's angle. ICFEP offers the user the alternative to specify the failure and plastic potential surfaces in the deviatoric plane by the general expression given by Equation 5.14, which has the advantage of simulating a wide range of shapes:

Equation 5.14 $$g(\theta)=\frac{X}{(1+Y\sin 3\theta)^{-Z}}$$

where Y and Z are constants and input parameters and $X=\sin\varphi'_{CS}$.

The creep volumetric strain rate is now given by Equation 5.15, where the quantities p'_i and p'_{ref} in Equation 5.10 are replaced by the values of the current loading surface p'_{0c} and the reference loading surface p'_{0ref}, respectively.

Equation 5.15 $$\dot{\varepsilon}^{i}_{vol}=\dot{\varepsilon}^{ref}_{vol}\left(\frac{p'_{0c}}{p'_{0ref}}\right)^{\frac{\lambda-\kappa}{\psi}}$$

Noting that $\Delta\varepsilon^{vp}_{vol}=\dot{\varepsilon}^{i}_{vol}\cdot\Delta t$ and $\Delta\varepsilon^{vp}_{vol}=\Phi\cdot\Delta t\cdot\frac{\partial P}{\partial p'}$ the creep strain components can be quantified as:

Equation 5.16 $$\Delta\varepsilon^{vp}_{ij}=\Phi\cdot\Delta t\cdot\frac{\partial P}{\partial\sigma_{ij}}=\frac{\dot{\varepsilon}^{ref}_{vol}\cdot\left(\frac{p'_{0c}}{p'_{0ref}}\right)^{\frac{\lambda-\kappa}{\psi}}}{\left|\frac{\partial P}{\partial p'}\right|}\cdot\Delta t\cdot\frac{\partial P}{\partial\sigma_{ij}}$$

In the denominator of the above equation, the introduction of the absolute value of the quantity $\partial P/\partial p'$ ensures that the visco-plastic scalar multiplier Φ is always a positive number, even for stress states that are on the dry side of the critical state.

Assuming that the virgin compression line in the MCC model corresponds to the reference compression line, the changes in the parameter p'_{0ref} (used in Equation 5.15) can be quantified with reference to the hardening rule of the MCC model and the change in p'_{0ref} can be evaluated as:

Equation 5.17 $$\Delta p'_{0ref}=p'_{0ref}\cdot\frac{V}{\lambda-\kappa}\cdot\Delta\varepsilon^{vp}_{vol}$$

where V is the current specific volume, $\Delta\varepsilon^{vp}_{vol}$ the visco-plastic volumetric strain increment and λ and κ are the slope of the reference and instant time line, in *V-lnp'* space, respectively.

5.3 Modification of the visco-plastic scalar multiplier

The model described in the previous section was implemented in the finite element program ICFEP. The model performance was investigated by means of single element analyses simulating typical laboratory stress paths. The model was found to simulate well the phenomena of creep, stress relaxation and strain rate effects under 1D compression. However, the behaviour under undrained triaxial compression was somewhat anomalous. Figure 5.2 shows the stress paths predicted by Creep Model 1 under undrained triaxial compression at three values of constant axial strain rate, on normally consolidated samples isotropically consolidated to 100 kPa. Figure 5.3 shows the respective stress strain curves. For comparison Figure 5.2 and Figure 5.3 also show the prediction given by the time independent MCC model.

During undrained shearing of a reconstituted normally consolidated clay sample the response is expected to be contractive (reduction in mean effective stress) and the deviatoric stress is expected to increase steadily up to critical state (CS), where the peak undrained strength is attained. Once critical state is attained further shearing occurs at constant effective stress state (and volume, in drained conditions). Such behaviour is recovered well by the MCC model.

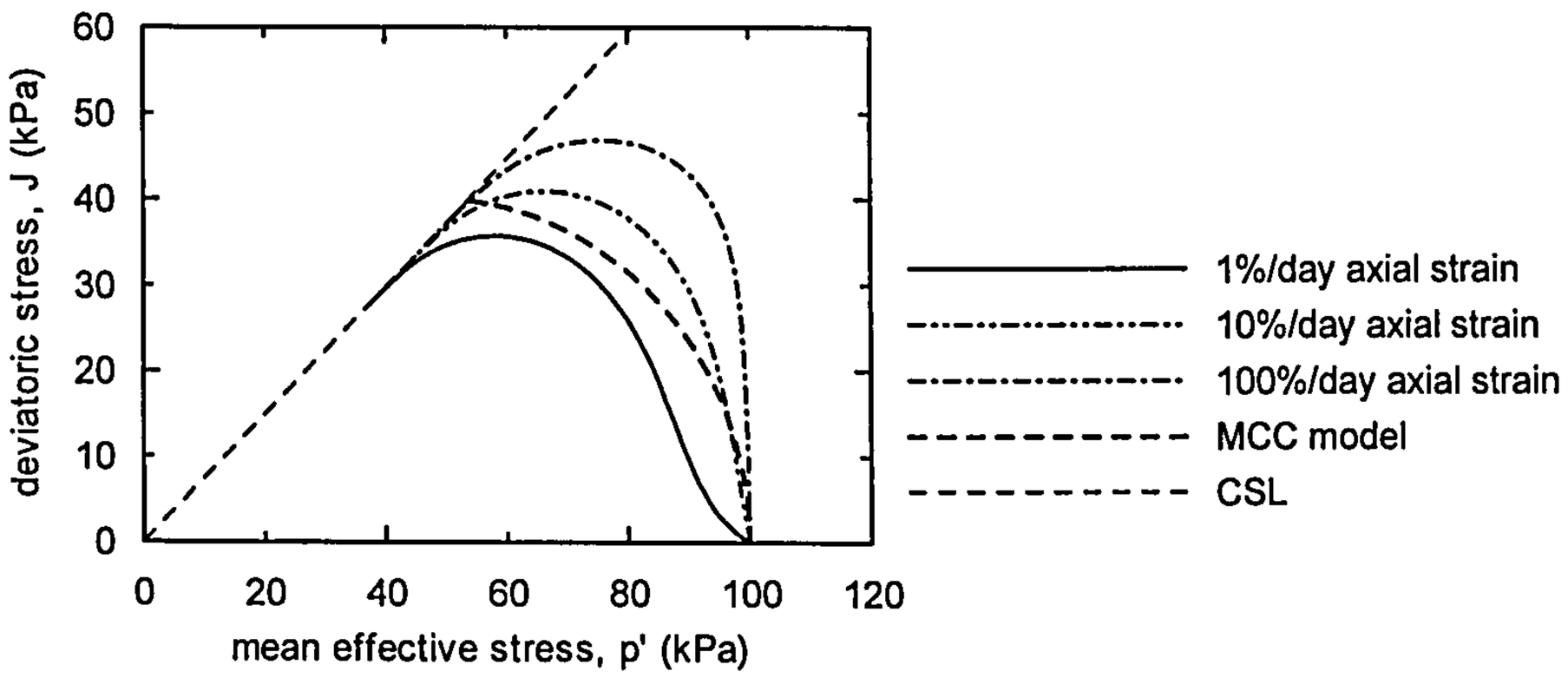

Figure 5.2: Stress paths predicted by Creep Model 1 under undrained triaxial compression at various values of constant axial strain rate, on normally consolidated samples (CSL = critical state line).

Creep Model 1 is able to capture some rate dependency as the predicted peak undrained strength is found to increase with increasing strain rate. However, the peak deviatoric stress is reached at stress ratios, η (where $\eta=J/p'$) considerably lower than the stress

ratio at critical state M_f. After peak, the stress paths tend asymptotically to the critical state line with reducing mean effective stress and deviatoric stress, converging towards the stress origin (p'=0, J=0). The analyses were extended up to 40% axial strain at which point true critical state conditions had not been reached and the stress path was still heading towards the stress origin.

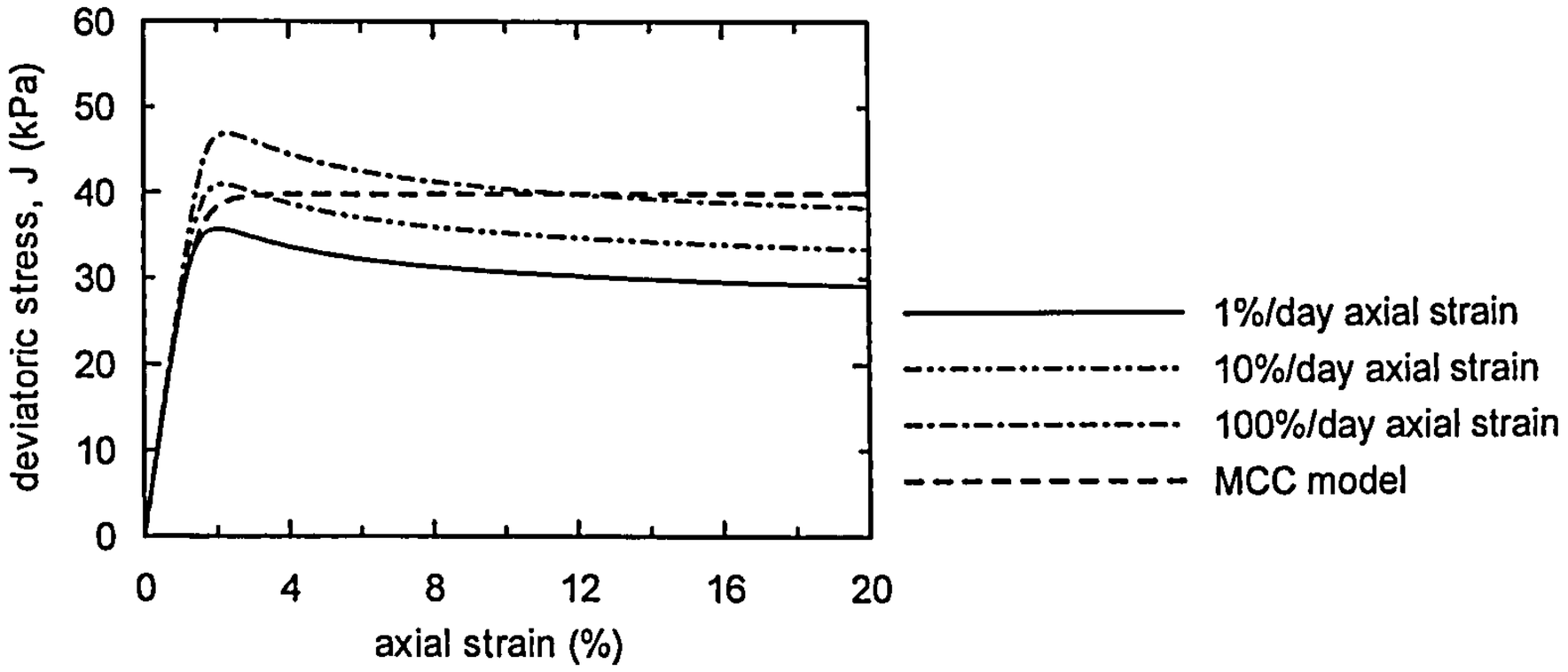

Figure 5.3: Stress – strain curves predicted by Creep Model 1 under undrained triaxial compression at constant axial strain rate.

The results shown in Figure 5.2 and 5.3 correspond to undrained triaxial compression tests at constant axial strain rate, during which the volumetric and deviatoric strain rate components can be evaluated as:

Equation 5.18
$$\dot{\varepsilon}_{vol}^{total} = \dot{\varepsilon}_{vol}^{el} + \dot{\varepsilon}_{vol}^{vp} = 0 \Rightarrow \dot{\varepsilon}_{vol}^{el} = -\dot{\varepsilon}_{vol}^{vp}$$

Equation 5.19
$$\dot{E}_d^{total} = \dot{E}_d^{el} + \dot{E}_d^{vp}$$

In the normally consolidated range the elastic deviatoric component is much small than the visco-plastic one, and the following approximation can be made:

Equation 5.20
$$\dot{E}_d^{total} \cong \dot{E}_d^{vp} = \sqrt{3} \cdot \dot{\varepsilon}_a$$

where $\dot{\varepsilon}_a$ is the axial strain rate that is constant during the tests under discussion. On the other hand, based on Equation 5.16 the volumetric and the deviatoric visco-plastic strain rate can be written as:

Equation 5.21
$$\dot{\varepsilon}_{vol}^{vp} = \Phi \cdot \frac{\partial P}{\partial p'} = \frac{\dot{\varepsilon}_{vol}^{ref} \cdot \left(\frac{p'_{0c}}{p'_{0ref}} \right)^{\frac{\lambda-\kappa}{\psi}}}{\left| \frac{\partial P}{\partial p'} \right|} \frac{\partial P}{\partial p'} = \dot{\varepsilon}_{vol}^{ref} \cdot \left(\frac{p'_{0c}}{p'_{0ref}} \right)^{\frac{\lambda-\kappa}{\psi}}$$

Equation 5.22

$$\dot{E}_d^{vp} = \Phi \cdot \frac{\partial P}{\partial J} = \frac{\dot{\varepsilon}_{vol}^{ref} \cdot \left(\frac{p'_{0c}}{p'_{0ref}} \right)^{\frac{\lambda-\kappa}{\psi}}}{\left| \frac{\partial P}{\partial p'} \right|} \frac{\partial P}{\partial J}$$

Combining Equation 5.21 with Equation 5.22 gives:

Equation 5.23

$$\dot{E}_d^{vp} = \frac{\dot{\varepsilon}_{vol}^{vp} \cdot \frac{\partial P}{\partial J}}{\frac{\partial P}{\partial p'}}$$

It can be shown that the partial derivatives of the plastic potential function P (given by Equation 5.12) in relation to the mean effective stress, p' and the deviatoric stress, J can be evaluated as:

Equation 5.24

$$\frac{\partial P}{\partial p'} = \frac{1 - S^2}{p'}$$

Equation 5.25

$$\frac{\partial P}{\partial J} = \frac{2S}{p' \cdot g(\theta)}$$

where S is the stress level, $S = \frac{J_i}{p' \cdot g(\theta)}$ and $g(\theta)$ is the slope of the critical state line in *p'-J space* and *p'* is the mean effective stress. Substituting Equations 5.24 and 5.25 into Equation 5.23 gives:

Equation 5.26

$$\dot{E}_d^{vp} = \frac{2S}{\left(1 - S^2\right) \cdot g(\theta)} \cdot \dot{\varepsilon}_{vol}^{vp}$$

From Equation 5.20 the deviatoric visco-plastic strain rate, $\dot{E}_d^{vp}$ remains constant during the test due to the applied boundary conditions. However from Equation 5.26 the ratio between the visco-plastic deviatoric and volumetric strain rate increases with increasing stress level, S and for $\dot{E}_d^{vp}$ to remain constant $\dot{\varepsilon}_{vol}^{vp}$ is forced to decrease. From inspection of Equation 5.21, and the underlying assumption that a loading surface is a locus of constant visco-plastic volumetric strain rate, a reduction in the volumetric visco-plastic strain rate is only achieved if the stress state moves inwards to a smaller loading surface (away from the reference line) such that the quantity p'_{0c} / p'_{0ref} decreases.

At a critical state condition there is no effective stress change, which means from Equation 5.18 that the visco-plastic volumetric strain rate is zero. From Equation 5.21 this condition is attained when the quantity p'_{0c} is zero, and the current stress state is located at the stress origin.

In this form, the model is now called *Basic Creep Model* 1. Gnanendran et al. (2006) describe the analysis of the Sackville test embankment employing two time dependent constitutive models, one of which they claim as being the model presented by Kutter & Sathialingam (1992). In the constitutive model description, they state that the quantity $\partial P/\partial p'$ is calculated at the current stress condition, as in the *Basic* Creep Model 1, which is also the assumption employed by other researchers (e.g. Yin & Graham, 1999; Yin et al., 2002; Vermeer & Neher, 1999, 2006; Borja & Kavazanjian, 1985).

However, in their original paper Kutter & Sathialingam (1992) state that the quantity $\partial P/\partial p'$ is instead evaluated at K_0 stress conditions, as their reference line is defined from 1D oedometer tests, but note that to determine the stress state that corresponds to K_0 stress conditions is not straightforward.

In *Basic* Creep Model 1, the reference time line is assumed to correspond to an isotropic stress path and so it is more appropriate (and also convenient) to evaluate the quantity $\partial P/\partial p'$ at the current equivalent isotropic stress state (p'_{0c}, J=0). The visco-plastic scalar multiplier can then be evaluated as:

Equation 5.27

$$\Phi = \frac{\dot{\varepsilon}_{vol}^{ref} \cdot \left(\frac{p'_{0c}}{p'_{0ref}} \right)^{\frac{\lambda-\kappa}{\psi}}}{\left| \frac{\partial P}{\partial p'} \right|_{\substack{p=p'_{0c} \\ J=0}}}$$

In this form the model becomes very similar to the compression model for soft clays presented by den Haan & van den Berg (2001), the difference in the governing equations concerning the choice and definition of the model parameters. Noting that the plastic potential function P has the shape of the MCC model ellipse and is described by Equation 5.12, the partial derivative $\partial P/\partial p'$ can be evaluated as:

Equation 5.28

$$\frac{\partial P}{\partial p'} = \frac{1}{p'}\left(1 - \frac{J^2}{p'^2 \cdot g(\theta)^2}\right)$$

At the current equivalent isotropic stress state (p'_{0c}, J=0) this becomes:

Equation 5.29

$$\left.\frac{\partial P}{\partial p'}\right|_{\substack{p=p'_{0c} \\ J=0}} = \frac{1}{p'_{0c}}$$

and Equation 5.16 can be rewritten as:

Equation 5.30

$$\Delta\varepsilon_{ij}^{vp} = \dot{\varepsilon}_{vol}^{ref} \cdot \left(\frac{p'_{0c}}{p'_{0ref}}\right)^{\frac{\lambda-\kappa}{\psi}} \cdot p'_{0c} \cdot \Delta t \cdot \frac{\partial P}{\partial \sigma_{ij}}$$

which implies that a given loading surface is a locus of constant visco-plastic scalar multiplier Φ. In this form, the model is referred to as *Modified* Creep Model 1 and an extensive investigation of the models performance is presented in Section 5.5. Figure 5.4 shows the model predictions of an undrained triaxial compression test at 10%/day axial strain rate on a NC sample. It can be seen that the two formulations yield nearly identical predictions up to about 40 kPa deviatoric stress, after which the stress paths diverge. The *Basic* formulation attains peak strength at a stress ratio lower than that at critical state, and then moves leftwards and downwards with decreasing deviatoric and mean effective stress, moving asymptotically towards the critical state line and the stress origin. The *Modified* formulation on the other hand predicts a steady hardening up to the critical state line.

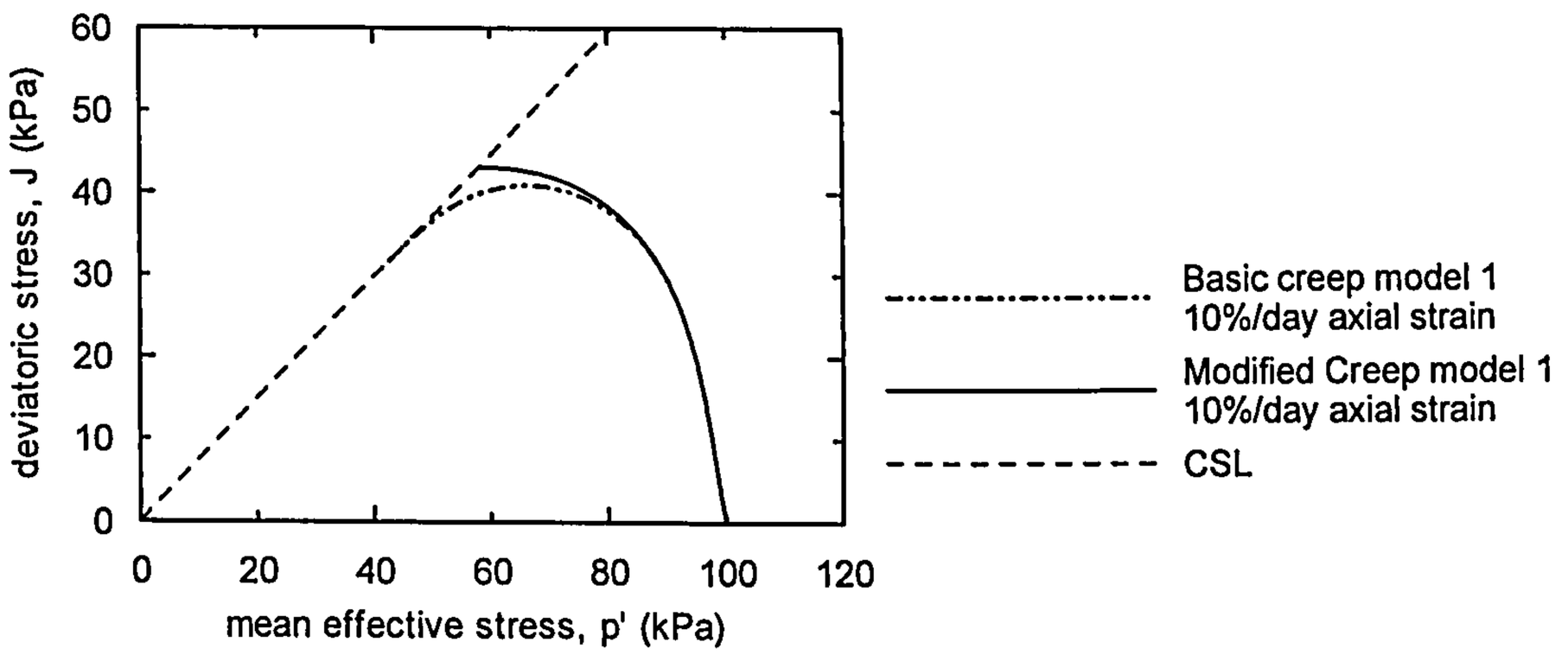

Figure 5.4: Comparison between the stress paths predicted by the Basic and the Modified Creep Model 1 under undrained triaxial compression at constant axial strain rate.

The difference between the two formulations is quantified subsequently. Simplistically the visco-plastic scalar multiplier Φ can be expressed as:

Equation 5.31 $$\Phi = A \cdot B$$

where $A = \dot{\varepsilon}_{vol}^{ref} \cdot \left(\frac{p'_{oc}}{p'_{0ref}} \right)^{\frac{\lambda-\kappa}{\psi}}$ and $B = \frac{1}{\left| \frac{\partial P}{\partial p'} \right|}$. The difference between the two formulations consists in the choice of the stress condition where the quantity B is evaluated. According to the *basic* formulation, B is evaluated at the current stress state $\left(p'_i, J_i\right)$ such that a given loading surface is a locus of constant visco-plastic volumetric strain rate. Substituting the current stress state into Equation 5.28 gives:

Equation 5.32 $$\left. \frac{\partial P}{\partial p'} \right|_{\substack{p'=p'_i \\ J=J_i}} = \frac{1}{p'_i} \cdot \left(1 - S^2\right)$$

where S is the stress level, $S = \frac{J_i}{p'_i \cdot g(\theta)}$ and $g(\theta)$ is the slope of the critical state line in *p'-J space*. The value of B is then:

Equation 5.33 $$B_{basic} = \frac{p'_i}{1 - S^2}$$

In the *modified* formulation, B is evaluated at the current equivalent stress state (p'_{0c}, J=0). Substituting in Equation 5.28 gives:

Equation 5.34 $$\left. \frac{\partial P}{\partial p'} \right|_{\substack{p'=p'_{0c} \\ J=0}} = \frac{1}{p'_{0c}}$$

However from Equation 5.12 the value of p'_{0c} can be written as:

Equation 5.35 $$p'_{0c} = p'_i \cdot \left(1 + S^2\right)$$

And the value of B can then becomes:

Equation 5.36 $$B_{Modified} = p'_i \cdot \left(1 + S^2\right)$$

Figure 5.5a) shows the variation of the quantity B with stress level S at an arbitrary mean effective stress p'_i=1kPa according to the basic and the modified formulation.

Figure 5.5b) shows the difference in B_{basic} in relation to $B_{Modified}$ with the stress level S, the logarithmic scale being employed to amplify the behaviour at small values of stress level. It can be seen that up to a stress level of about 0.7 the two formulations yield very similar values of B and consequently of visco-plastic scalar multiplier Φ, in agreement with the results shown in Figure 5.4. It can be concluded that for stress states far from failure both formulations could potentially be used as they yield very similar predictions. However, the failure condition is only correctly captured by the *modified* formulation.

The similarity between the predictions of the two formulations at stress levels less than 0.7 leads the author to believe that the experimental data by Tavenas et al. (1978) that has been used to postulate that the limit state surface (and any homothetic loading surface) is a locus of constant volumetric strain rate may fit identically well the assumption that the limit state surface is instead a surface of constant visco-plastic scalar multiplier. This is especially true if one bears in mind the errors involved in any experimental work. In particular in this data set, estimated apparatus leakage that could cause significant errors during undrained tests, the reduced number of data points used to draw the isochrones of volumetric strain rate in triaxial stress space (p', J) and the fact that these isochrones correspond to a relatively short creep time (100 minutes) all combine to give potential errors in the measured strain rates.

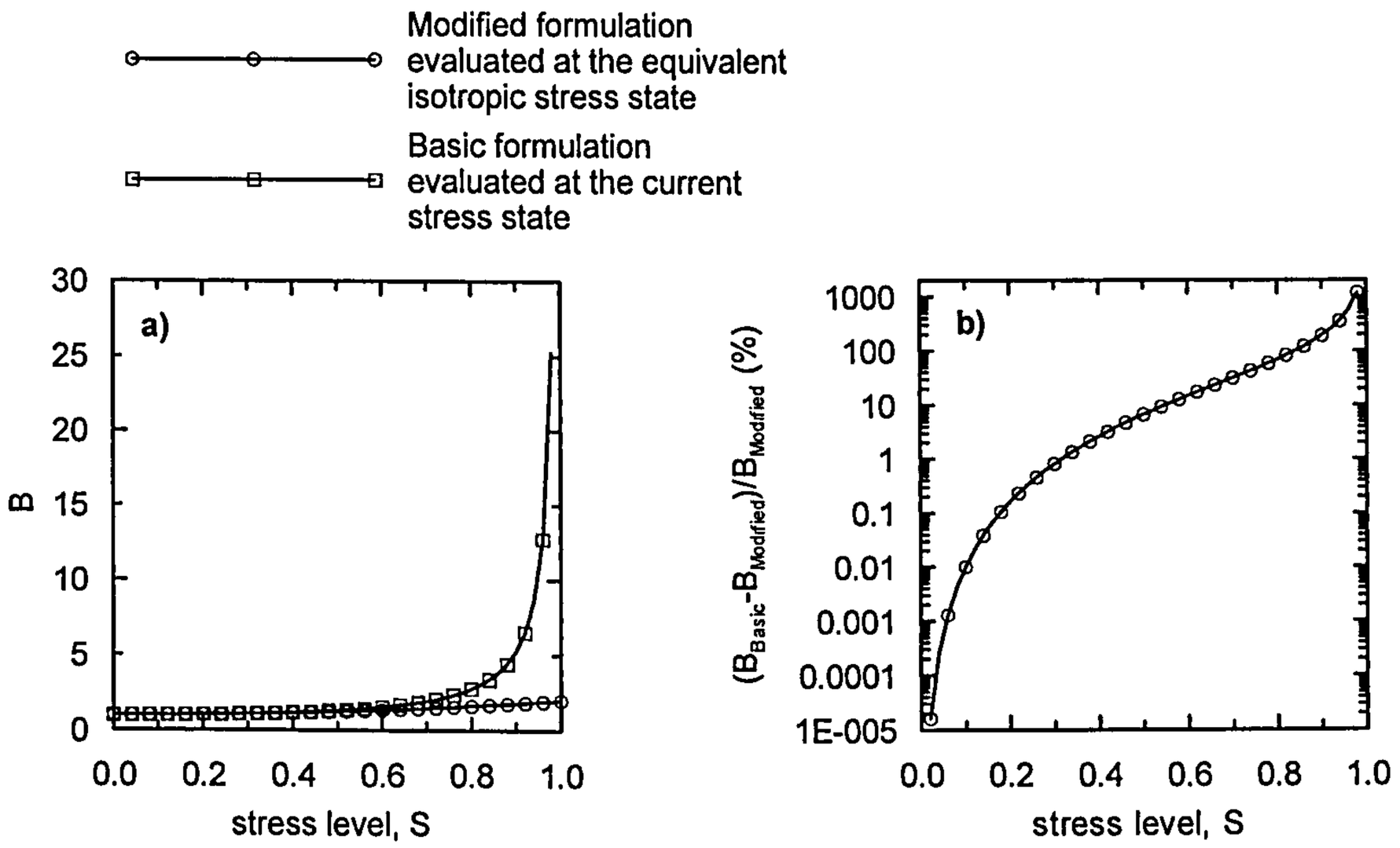

Figure 5.5: Variation of the quantity B with stress level for the basic and modified formulations.

5.4 Considerations regarding the model parameters

To fully define the model in triaxial stress space seven parameters are required, two in addition to those required for the modified Cam-Clay model, as follows:

V_{1ref} - the specific volume at unit pressure on the reference isotropic compression line (V_{1ref} >0.0);

λ – the slope of the reference time line in *V-lnp' space* (λ >0.0);

κ – the slope of the instant time line in *V-lnp' space* (κ >0.0), which is assumed to coincide with the swelling line;

μ, G or $G/p_0^{'}$ - an elastic parameter that can be either the Poisson's ratio μ (-1.0 μ < 0.5), the elastic shear modulus G (G>0.0) or the quantity $G/p_0^{'}$ ($G/p_0^{'}$>0.0), in which case the elastic shear modulus varies linearly with $p_0^{'}$;

$\varphi_{CS}^{'}$ - angle of shearing resistance at the critical state;

ψ - a creep parameter that defines the vertical spacing between compression lines per logarithmic cycle of strain rate ($\psi \geq 0.0$) in $V-lnp'$ *space*;

$\dot{\varepsilon}_{vol}^{ref}$ - Volumetric strain rate on the reference compression line ($\dot{\varepsilon}_{vol}^{ref}$ >0).

To define the model in general stress space, it is necessary to specify the shape of the failure and plastic potential surfaces in the deviatoric plane and consequently two to four additional parameters are required. As mentioned above in ICFEP the user has various options to perform this. The failure surface in the deviatoric plane can take the shape of a Mohr Coulomb hexagon in which case no additional parameters are required and the slope of the critical state line in *p'-J plane* (the value of the function g(θ)) is calculated using Equation 5.13. Alternatively the shape of the failure surface in the deviatoric plane can be described by a general equation in the form of Equation 5.14 in which case two parameters are required. The shape of the plastic potential in the deviatoric plane is defined by Equation 5.14, which is a flexible expression that can describe a wide range of shapes by choosing appropriate values for the two constants.

In addition, the user is required to input the overconsolidation ratio (OCR), which together with the initial stress conditions define the initial value of the hardening

parameter p'_{0ref}. The OCR is defined in relation to the reference compression line and it can be input either as a ratio of mean effective stresses or vertical effective stresses. In the first case the value of the hardening parameter p'_{0ref} is calculated directly:

Equation 5.37 $$p'_{0ref} = OCR \cdot p'_i$$

where p'_i is the initial mean effective stress. More commonly, the value of OCR is defined in terms of vertical effective stress:

Equation 5.38 $$OCR = \frac{\sigma'_{vy}}{\sigma'_{vi}}$$

Where σ'_{vi} is the initial vertical effective stress and σ'_{vy} is the vertical effective stress at large scale yielding. It is then assumed that the coefficient of earth pressure at rest in the NC range can be evaluated by Equation 5.39, as proposed by Jaky (1944).

Equation 5.39 $$K_0^{NC} = 1 - \sin \varphi'_{CS}$$

where φ'_{CS} is the angle of shearing resistance at the critical state. The direct stress in the horizontal direction can then be evaluated as:

Equation 5.40 $$\sigma'_{hy} = K_0^{NC} \cdot \sigma'_{vy}$$

Assuming that the direct stresses acting in the two horizontal cartesian directions are the same and the vertical and horizontal directions are principal directions, the values of p' and J associated with that NC stress state can be evaluated. These values are then used in Equation 5.12 to obtain the size of the corresponding loading surface, which is then the initial value of p'_{0ref}. Once the value of p'_{0ref} is known, the initial void ratio e_i is calculated from Equation 5.41.

Equation 5.41 $$e_i = \left(V_{1ref} - \kappa \ln p'_i - (\lambda - \kappa) \ln p'_{0ref}\right) - 1$$

Before describing the derivation of the model parameters, it is of interest to note that the two time dependent parameters ψ and $\dot{\varepsilon}_{vol}^{ref}$ are related and in some circumstances may become redundant. From Equation 5.9 ψ is defined as:

Equation 5.42 $$\psi = \frac{\Delta V_1}{\ln \dot{\varepsilon}_{vol2} - \ln \dot{\varepsilon}_{vol1}} = \frac{\Delta e_1}{\Delta \ln \dot{\varepsilon}_{vol}}$$

If it is assumed that the value of the coefficient of secondary consolidation $C_{\alpha e}$ is constant with time and thus that there is a linear relationship between void ratio (or strain) and the logarithm of time (see Chapter 2). Then the parameter m proposed by Singh & Mitchell (1968) is equal to unity.

Equation 5.43
$$m = \frac{\Delta \log \dot{\varepsilon}}{\Delta \log t} = \frac{\Delta \ln \dot{\varepsilon}}{\Delta \ln t} = 1$$

Substituting Equation 5.43 into Equation 5.42 and invoking the definition of the coefficient of secondary consolidation $C_{\alpha e}$ (Equation 2.3) the value of ψ can be written as:

Equation 5.44
$$\psi = \frac{\Delta e}{\Delta \ln t} = \frac{\Delta e}{\ln 10 \cdot \log_{10} t} = \frac{C_{\alpha e}}{\ln 10}$$

which gives a relationship between the model parameter ψ and the coefficient of secondary consolidation $C_{\alpha e}$. The volumetric creep strain predicted by a logarithmic law, at an instant t during secondary compression under K_0 stress conditions can be evaluated as:

Equation 5.45
$$\varepsilon_{vol} = \varepsilon_v = \frac{C_{\alpha e}}{1 + e_0} \log\left(\frac{t}{t_i}\right)$$

where t_i is the time corresponding to the beginning of secondary compression. Differentiating Equation 5.45 with respect to time we obtain the volumetric strain rate:

Equation 5.46
$$\dot{\varepsilon}_{vol} = \frac{C_{\alpha e}}{1 + e_0} \cdot \frac{1}{\ln 10} \cdot \frac{1}{t} = \frac{\psi}{1 + e_0} \cdot \frac{1}{t}$$

Equation 5.46 implies that for a given value of $C_{\alpha e}$ or ψ there is a unique relationship between the strain rate and time. Consequently, to characterize the reference time line either $\dot{\varepsilon}_{vol}^{ref}$ or a reference time value, t_0 can be specified. The set of parameters (ψ, $\dot{\varepsilon}_{vol}^{ref}$) is equivalent to the more common set of parameters ($C_{\alpha e}$, t_0). Essentially the parameter $C_{\alpha e}$ or ψ defines the amount of creep deformation per logarithmic cycle of time and the parameter $\dot{\varepsilon}_{vol}^{ref}$ or t_0 characterizes the reference line, which has been defined by the input parameters V_{1r} and λ.

However the value of $C_{\alpha e}$ is, in general, calculated from IL 24-hour oedometer tests, which are also used to define the normal compression line in engineering practice. If the reference compression line is specified to be an IL 24-hour oedometer compression curve then the value of t_0 is by default always equal to 1 day = 24 hours, and the time dependent part of the model requires only one additional parameter in relation to the MCC model.

It is noted that according to the model derivation the reference compression line that is characterized by the input parameters λ and V_{1ref} corresponds to the compression of a soil element under isotropic stress conditions at the reference volumetric strain rate $\dot{\varepsilon}_{vol}^{ref}$. However, in engineering practice the soil compressibility characteristics are more often investigated by means of 1D oedometer tests, which are found to yield compression curves with, theoretically, the same slope λ in *V - lnp' space.* The 1D compression curves are found to be offset in relation to those obtained under isotropic stress conditions, but according to the model formulation the absolute position of the reference compression line is not of primary importance, and so it is appropriate to evaluate the parameters λ and V_{1ref} from 1D oedometer tests.

In addition, the axial strain rate at the end of each of the 24-hour load increments is found to be fairly constant for a given material and typical loading sequence (i.e. a load increment ratio equal to unity), such that the IL 24 hour compression curve may be assumed to be approximately a locus of constant volumetric strain rate.

It is of interest to quantify the error that is introduced when the reference compression line and the reference volumetric strain rate are estimated based on oedometer tests, as Modified Creep Model 1 assumes the same compression line to correspond to an isotropic stress path. For a reference line corresponding to a 1D compression the parameter B in Equation 5.31 should be evaluated at K_0 stress conditions, and the visco-plastic scalar multiplier Φ would then be:

Equation 5.47

$$\Phi = \dot{\varepsilon}_{vol}^{ref} \cdot \left(\frac{p'_{0c}}{p'_{0ref}} \right)^{\frac{\lambda-\kappa}{\psi}} \cdot \frac{1}{\left| \frac{\partial P}{\partial p'} \right|_{K_0}}$$

During 1D compression $\varepsilon_2 = \varepsilon_3 = 0$ so the following condition applies:

Equation 5.48

$$\frac{\Delta E_d^T}{\Delta \varepsilon_{vol}^T} = \frac{2}{\sqrt{3}}$$

where ΔE_d^T and $\Delta \varepsilon_{vol}^T$ are the deviatoric and the volumetric total strain increments, respectively. The stress state under K_0 stress conditions $\left(p'_{K_0}, J_{K_0}\right)$ can be estimated assuming that the elastic incremental strains are much smaller than the visco-plastic ones and:

Equation 5.49

$$\frac{\Delta E_d^T}{\Delta \varepsilon_{vol}^T} = \frac{2}{\sqrt{3}} \cong \frac{\Delta E_d^{vp}}{\Delta \varepsilon_{vol}^{vp}}$$

Where ΔE_d^{vp} and $\Delta \varepsilon_{vol}^{vp}$ are the deviatoric and volumetric visco-plastic strain increments, respectively. Invoking Equation 5.30 the above equation can be rewritten as:

Equation 5.50

$$\frac{\Delta E_d^{vp}}{\Delta \varepsilon_{vol}^{vp}} = \frac{\partial P / \partial J}{\partial P / \partial p'} = \frac{2}{\sqrt{3}}$$

Where $\partial P/\partial J$ and $\partial P/\partial p'$ are the partial derivatives of the plastic potential function P in relation to the deviatoric stress J and the mean effective stress p'. The above equation can be reworked such that it gives the value of the stress ratio at K_0 stress conditions $\eta_{K_0} = \frac{J_{K_0}}{p'_{K_0}}$ as a function of the stress ratio at critical state $g(\theta)$.

Equation 5.51

$$\eta_{K_0} = \frac{-\sqrt{3} \pm \sqrt{3 + 4 \cdot g(\theta)^2}}{2}$$

For an angle of shearing resistance φ'=32° – the value used in the analyses presented subsequently in Section 5.5 – the stress ratio at critical state is 0.7431 giving a value of $\eta_{K_0} = 0.2751$, this in turn corresponds to a stress level S of about 0.37. Figure 5.5b) shows that for a stress level of 0.37 the difference in evaluating the quantity $\partial P/\partial p'$ in Equation 5.47 at the current stress state or at the equivalent isotropic stress state results in an error of only 2% in the value of the visco-plastic scalar multiplier Φ. This error is considered to be negligible when compared with the scatter of any soil parameters measured experimentally, such as λ, κ, $C_{\alpha e}$ or $\dot{\varepsilon}_{vol}^{ref}$ in Equation 5.47.

Based on the above discussion, the model parameters can be derived from conventional laboratory tests: one IL oedometer test and one, ideally two, consolidated undrained triaxial tests, one in compression and one in extension. The oedometer test will enable the direct determination of the values of λ and κ, noting that the determination of the value of κ requires the assumption that the value of the coefficient of earth pressures remains constant, while this is known to change during a swelling stage. From the undrained triaxial compression tests it is possible to calculate the angle of shearing resistance, φ' at the critical state and by having data both in compression and extension it is possible estimate roughly the shape of the failure surface on the deviatoric plane. In addition, the stress-strain curves from the undrained triaxial tests can be used to calculate the variation of the shear stiffness with shear strain, and a value of G should be selected having in mind the range of strains being attained in the particular boundary value problem being analysed. Assuming that the compression line obtained from the IL oedometer tests corresponds to the reference time line, the parameter V_{1ref} can be extrapolated from the compression line and the parameter $\dot{\varepsilon}_{vol}^{ref}$ can be either measured directly in the laboratory or evaluated using Equation 5.46 with $t=t_0=24$ hours. The parameter ψ or C_α, can be evaluated from the consolidation *settlement-time curves* of the various load increments.

5.5 Validation by means of single element analyses

The validation of Modified Creep Model 1 consists of a series of finite element analyses to investigate the model performance under a variety of stress and strain paths. For simplicity, the analyses mimic common laboratory tests and the analysis results are then compared with observed trends, as reported in Chapter 2. The following stress paths will be considered:

e) Incremental load 24 hours oedometer;

f) Constant rate of strain oedometer tests at different values of strain rate;

g) Step-wise change of strain rate oedometer test;

h) A CRS oedometer test with a long creep and relaxation period;

i) Isotropically consolidated undrained triaxial compression tests on normally and overconsolidated samples at constant axial strain rate.

The FE analyses are performed using the model parameters given in Table 5.1. These are justified below.

Table 5.1: Model parameters for the validation analyses.

φ'	κ	λ	V_{1ref}	$\dot{\varepsilon}_{vol}^{ref}$	ψ	G
(°)	-	-	-	h^{-1}	-	kPa
32	0.022	0.22	3.0	0.00036	0.01303	1700

Notes:
φ' = angle of shearing resistance;
κ = slope of the instant time line in V-ln p' *space;*
λ = slope of the reference time line in V-ln p' *space;*
V_{1ref} *= specific volume at unit pressure on the reference line (See Figure 5.1).*
$\dot{\varepsilon}_{vol}^{ref}$ *= visco-plastic volumetric strain rate on the reference line (see Figure 5.1).*
ψ = creep parameter that corresponds to the variation of void ratio per natural logarithmic cycle of time during creep (see Figure 5.1).
G = elastic shear modulus;

The model parameters have been given values typical of soft clay. As shown in section 5.4 the parameter ψ can be related to the coefficient of secondary consolidation, $C_{\alpha e}$ through Equation 5.44, and a value of $C_{\alpha e}$ equal to 0.03 has been assumed – a value typical for soft NC inorganic clays. The value of the total volumetric strain rate on the reference line corresponds to a realistic value of the axial strain rate measured at the end of a load increment during IL 24 hour oedometer tests ($1x10^{-7}$/s). In addition, it is assumed that in the deviatoric plane the failure surface is given by the Mohr-coulomb hexagon and the plastic potential surface is a circle.

In clayey soil, the delayed excess pore water pressure dissipation during loading, either in the laboratory or in the field, is in general significant to the overall soil response. Despite this the FE analyses (with exception of the analyses mimicking undrained triaxial compression stress paths) are carried out assuming drained conditions, as the main interest of these analyses is to investigate the performance of the effective stress constitutive relationship. In addition, this assumption considerably simplifies the analysis procedure.

Incremental load 24 hours oedometer tests

Figure 5.6 shows the model predictions of an IL 24 hour oedometer test with a load increment ratio $\Delta\sigma_v / \sigma_v$ equal to one, obtained by means of drained single element FE analyses, using the model parameters included in Table 5.1. In run 1 each load increment is simulated by a single analysis increment with a duration Δt=24 hours. In run 2 each load increment is simulated using two analysis increments; the first with a very small duration Δt=0.1 hour during which the incremental load $\Delta\sigma_v$ is applied and the stress path moves instantaneously along an instant elastic line (κ – line), and then a second increment with a duration Δt=23.9 hours during which the sample is maintained at constant applied stress. The two simulations yield the same results at the end of each load increment as would be expected, showing that the model response depends only on the overall applied strain rate and not on how this is specified.

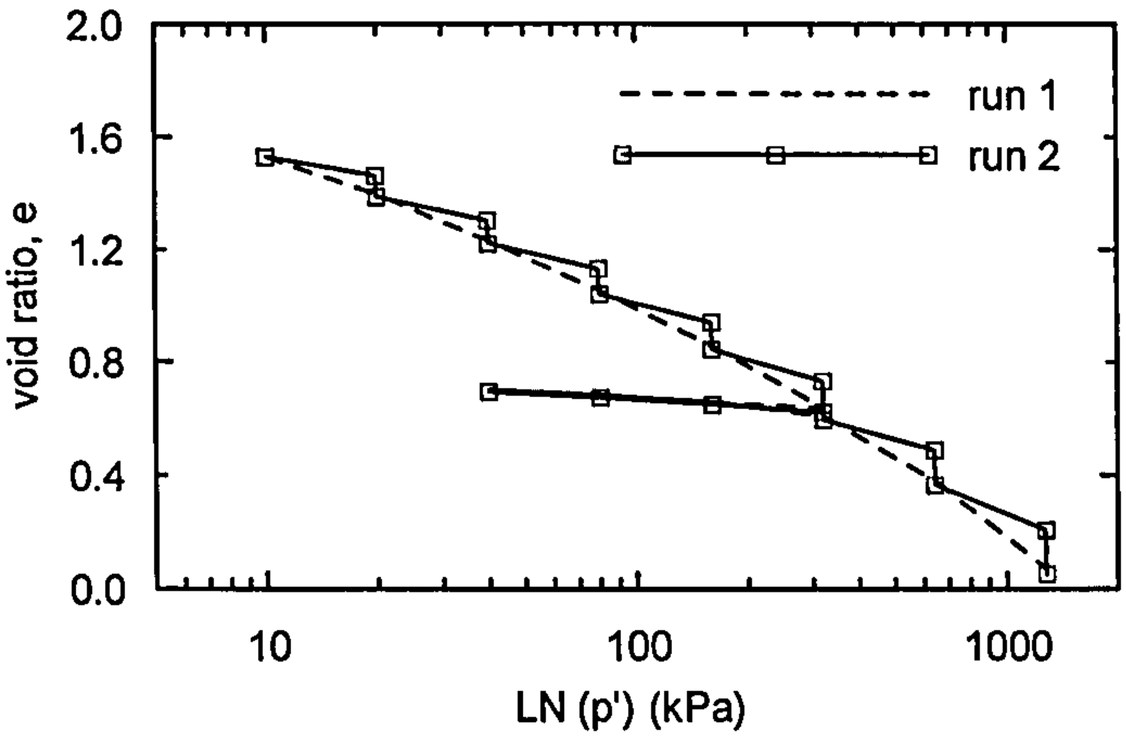

Figure 5.6: IL 24hours oedometer tests - model predictions.

Constant rate of strain tests oedometer tests

Figure 5.7 shows the Modified Creep Model 1 predictions of a set of constant rate of strain oedometer tests at four values of axial strain rate. In addition, Figure 5.7 shows the results of an analysis that simulates an oedometer test during which the strain rate was changed in a stepwise manner. The analysis results show that the model predicts a single stress-strain-strain rate relationship that is independent of the previous soil loading history.

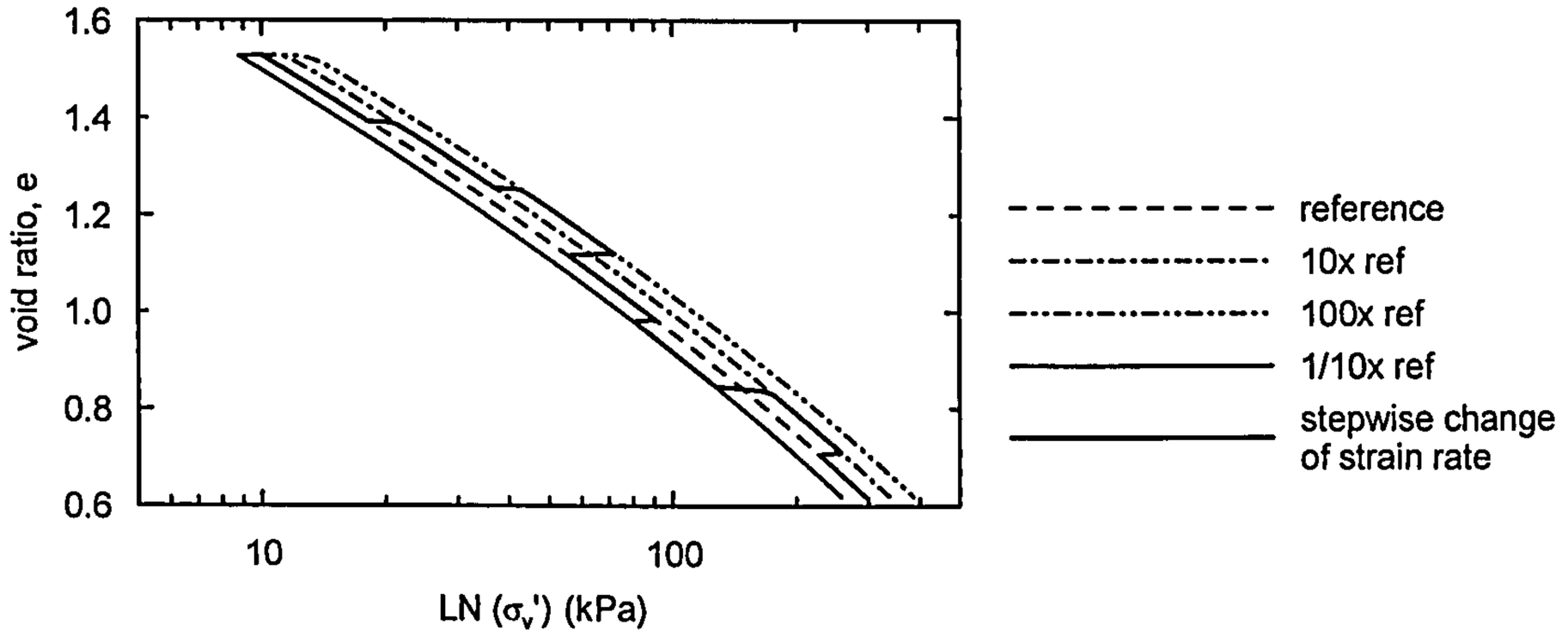

Figure 5.7: Constant rate of strain and stepwise change of strain rate oedometer tests - model predictions.

Drained creep tests under 1D conditions

Figure 5.8 shows the results of single element FE analyses of 1D oedometer tests performed at a constant rate of axial strain. During the otherwise monotonic loading, a long creep period is introduced, and the value of the maintained vertical effective stress during creep is indicated in Figure 5.8. Following the creep period the samples are reloaded at the previous value of axial strain rate and the compression curves are found to rejoin the compression curve appropriate to the current strain rate value. As observed experimentally, on reloading the soil response is initially stiff and then the soil gradually yields showing a yield stress well in excess of the stress that it has been subjected to during creep.

Figure 5.8b) shows the variation of void ratio with time during the creep period. The change in void ratio at a given creep time t is found to increase with the value of the applied strain rate prior to creep. In addition, the rate of change in void ratio is found to decrease steadily with time in all cases.

Figure 5.8c) shows the variation of void ratio with the logarithm of time, where the time origin is taken as the start of the creep period. The results show that there is a time delay between the start of the creep tests and the establishment of a linear relationship between the void ratio change and the logarithm of time, and that time delay is found to reduce for higher values of applied strain rate prior to creep.

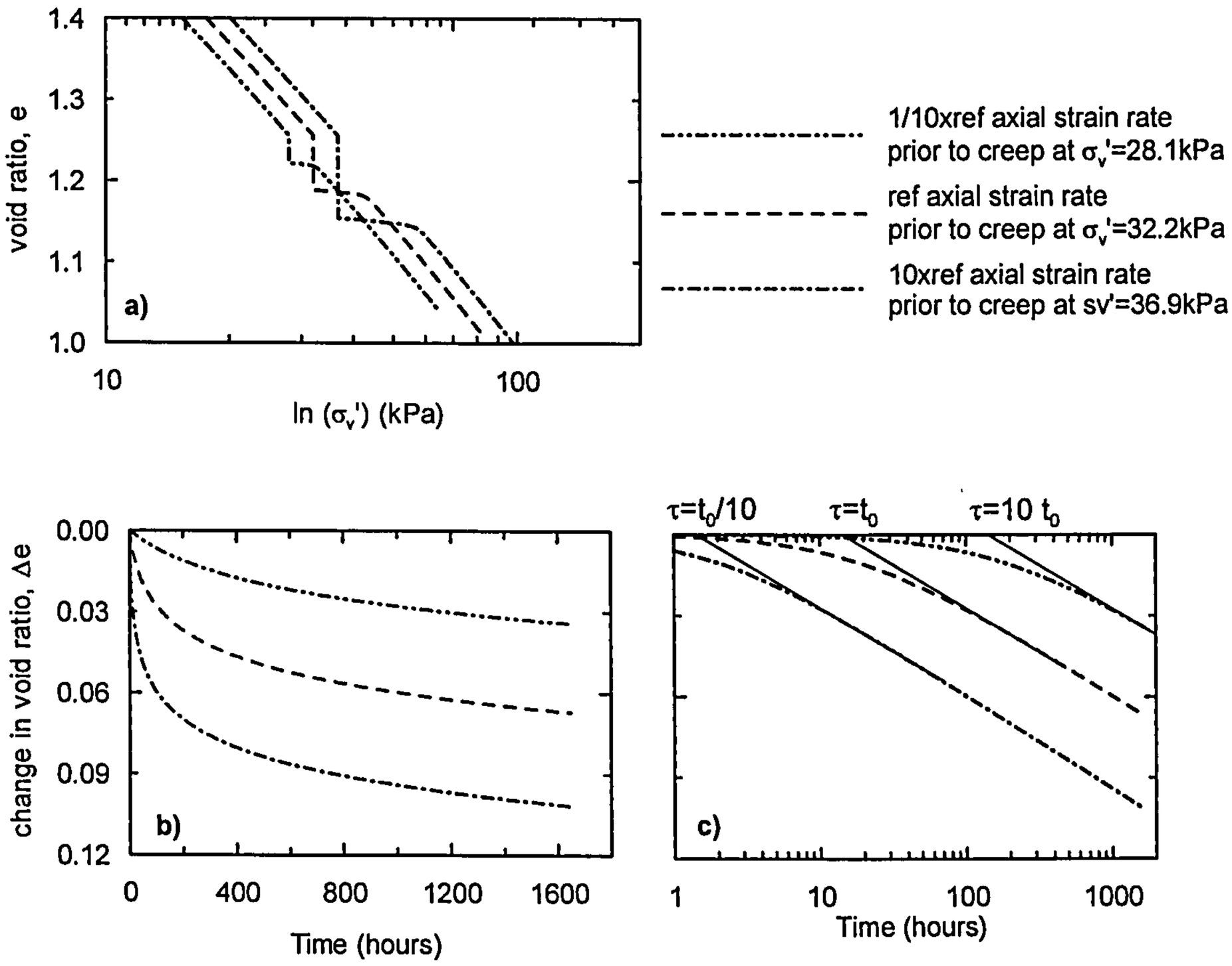

Figure 5.8: Variation of void ratio during drained creep – model predictions.

The intersection between the tangent passing through the linear part of the Δe-log t curve and the time axis gives a value of time that is often called the intrinsic time τ (den Haan, 1994), such that the change in void ratio during a creep period at a time instant t > τ can be written as:

Equation 5.52
$$\Delta e = C_{\alpha e} \cdot \log \frac{t}{\tau}$$

When creep starts from a stress state located on the reference line, the intrinsic time is then equal to the reference time t_0 and Equation 5.46 can be used to estimate its value:

Equation 5.53
$$\dot{\varepsilon}_{vol}^{ref} = \frac{\psi}{1+e_0} \cdot \frac{1}{t_0}$$

Giving a value of t_0=14.5 hours, which agrees well with the value deducted from Figure 5.8c). In the two other cases, the applied strain rate prior to creep is 10 times larger and smaller than the axial strain rate on the reference line and from Equation 5.53 the intrinsic time is 10 times smaller and larger than t_0, respectively.

Figure 5.9 shows the decay of the of axial strain rate with natural time in a double logarithmic space. The analysis results eventually converge onto a line that corresponds to m=1 (as defined by Equation 5.43), which is characteristic of a linear logarithmic creep law. The time delay to reach the line m=1 is found to increase with decreasing applied axial strain rate prior to creep, in agreement with the results in Figure 5.8c).

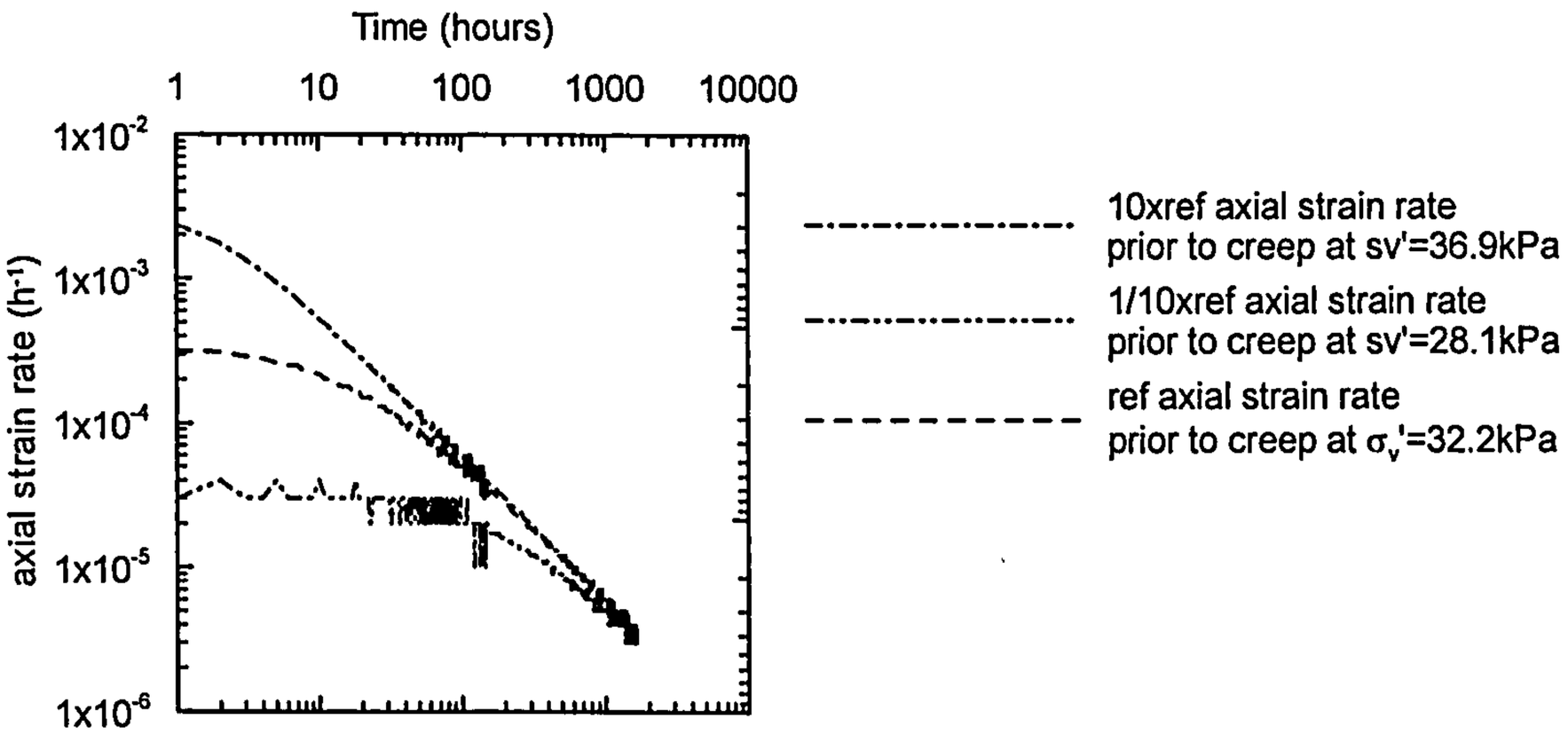

Figure 5.9: Variation of the axial strain rate with time during creep as predicted by Modified Creep Model 1.

Relaxation tests under 1D conditions

A set of analyses were carried out to investigate the model predictions during stress relaxation. The analysis details are similar to those described above, but instead of a creep period a stress relaxation period is introduced. Figure 5.10 shows the results in terms of the change (decrease) in vertical effective stress with time during the stress relaxation period. The axial strain rate value in the legend refers to the loading conditions prior to the stress relaxation period. As observed experimentally (e.g. Lacerda & Houston, 1973) there is a time delay (more obvious in the slowest test) between the start of the relaxation period and a significant reduction in effective stress. This time delay is found to increase for lower values of applied strain rate prior to the stress relaxation period. Following that, the vertical effective stress is found to decrease linearly with the logarithm of time. It is noted that during the relaxation phase the analyses consider 1-hour increments and thus the graph starts at a relaxation time equal to 1 hour. For the samples consolidated at higher strain rate values there is already significant reduction in the vertical effective stress after 1 hour.

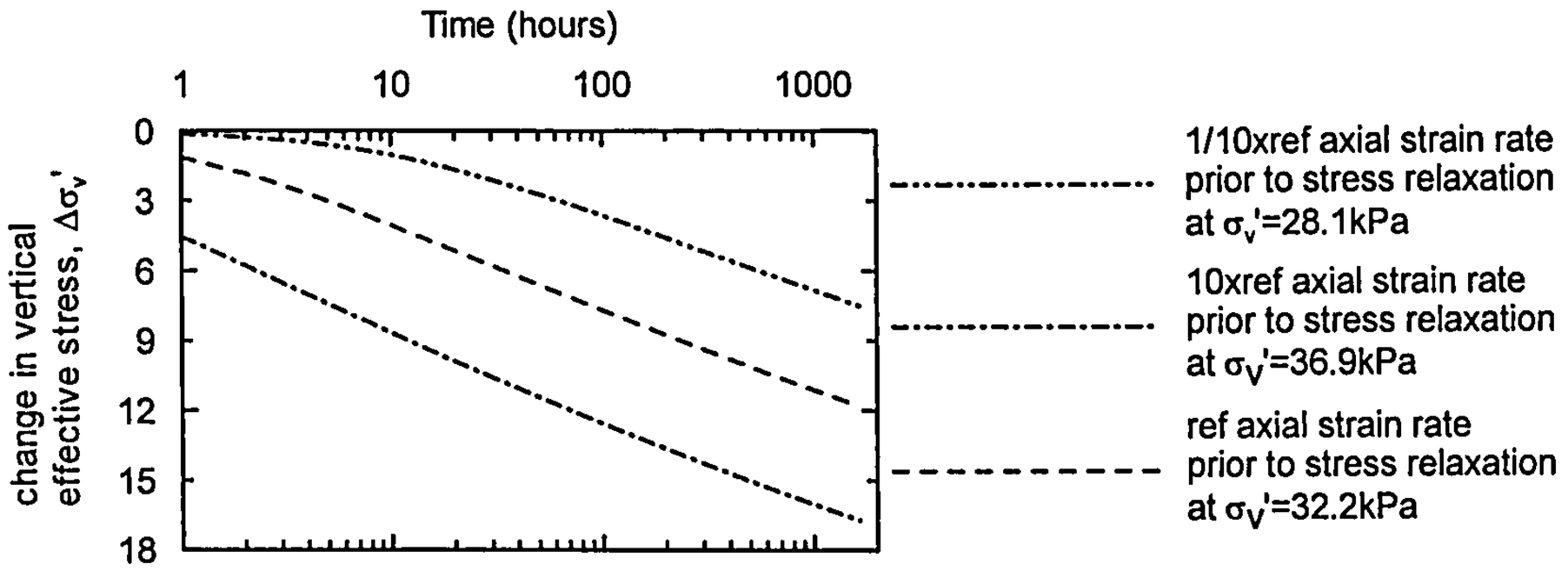

Figure 5.10: Stress relaxation tests under one-dimensional conditions – model predictions.

Consolidated undrained triaxial compression tests at constant axial strain rate

Figure 5.11 shows stress paths predicted by Modified Creep Model 1 during constant rate of strain undrained triaxial compression tests on NC samples. The samples are initially consolidated to an isotropic effective stress of 100 kPa.

Figure 5.12 shows the respective stress-strain curves and the development of excess pore water pressure with axial strain during the tests. An increase in the applied axial strain rate causes the model to predict a higher peak undrained strength. The critical state effective stress failure envelope, characterized by a stress ratio $g(\theta)=0.743$ ($\varphi'=32°$), remains unchanged in the three cases, and the observed increase in undrained strength is found to result from the fact that different excess pore water pressure are predicted.

Figure 5.13 shows the stress path predicted by Modified Creep Model 1 during undrained triaxial compression tests on NC and OC samples. Two values of overconsolidation ratio (OCR) have been considered 1.5 and 4.0, the latter value aiming to investigate the model performance at stress states that are dry in relation to the critical state, and thus are expected to undergo plastic dilation and some post-peak softening during shearing. All tests start from an isotropic stress of 100 kPa, such that the pre-consolidation pressure p'_{0i} is 100, 150 and 400 kPa for samples with an OCR equal to 1.0, 1.5 and 4.0, respectively. Figure 5.14 shows the respective stress-strain curves and the development of excess pore water pressure with axial strain during the tests, but only for samples sheared at an axial strain rate of 10%/day.

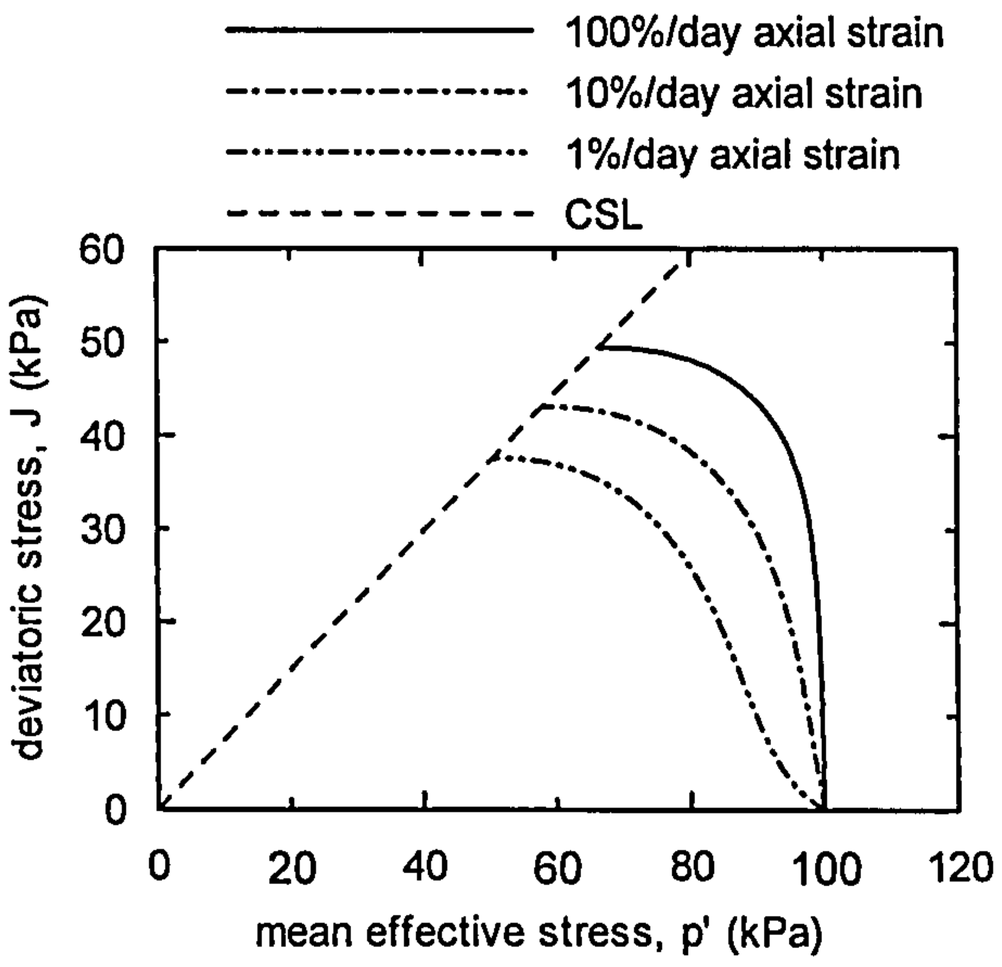

Figure 5.11: Stress paths predicted by Modified Creep Model 1 during undrained triaxial compression tests on NC samples at various values of constant axial strain rate.

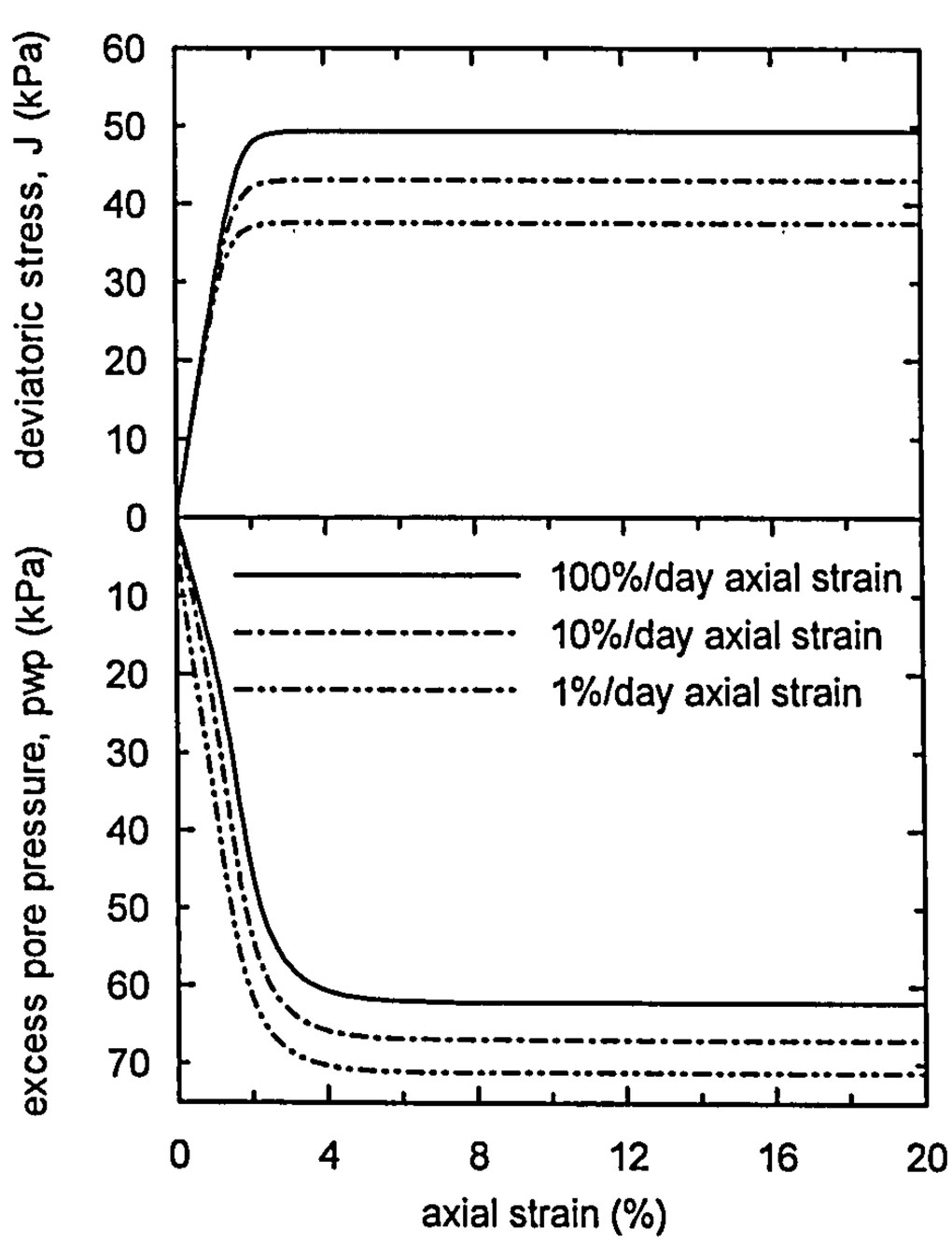

Figure 5.12: Stress-strain curves predicted by Modified Creep Model 1 during undrained triaxial compression tests on NC samples at various values of constant axial strain rate.

Figure 5.13 shows that with increasing applied strain rate there is an increase in the *pseudo-elastic* stress domain and on the peak undrained strength value. As explained above, the increase in undrained strength results from the fact that lower excess pore water pressures are predicted while the effective stress failure envelope remains unchanged. The NC and lightly OC (OCR=1.5) samples show, as expected, a steady increase in deviatoric stress, as the stress path bends leftwards with decreasing mean effective stress (increasing contractive excess pore water pressure) up to the critical state, and the critical state condition is found to coincide with the peak undrained strength.

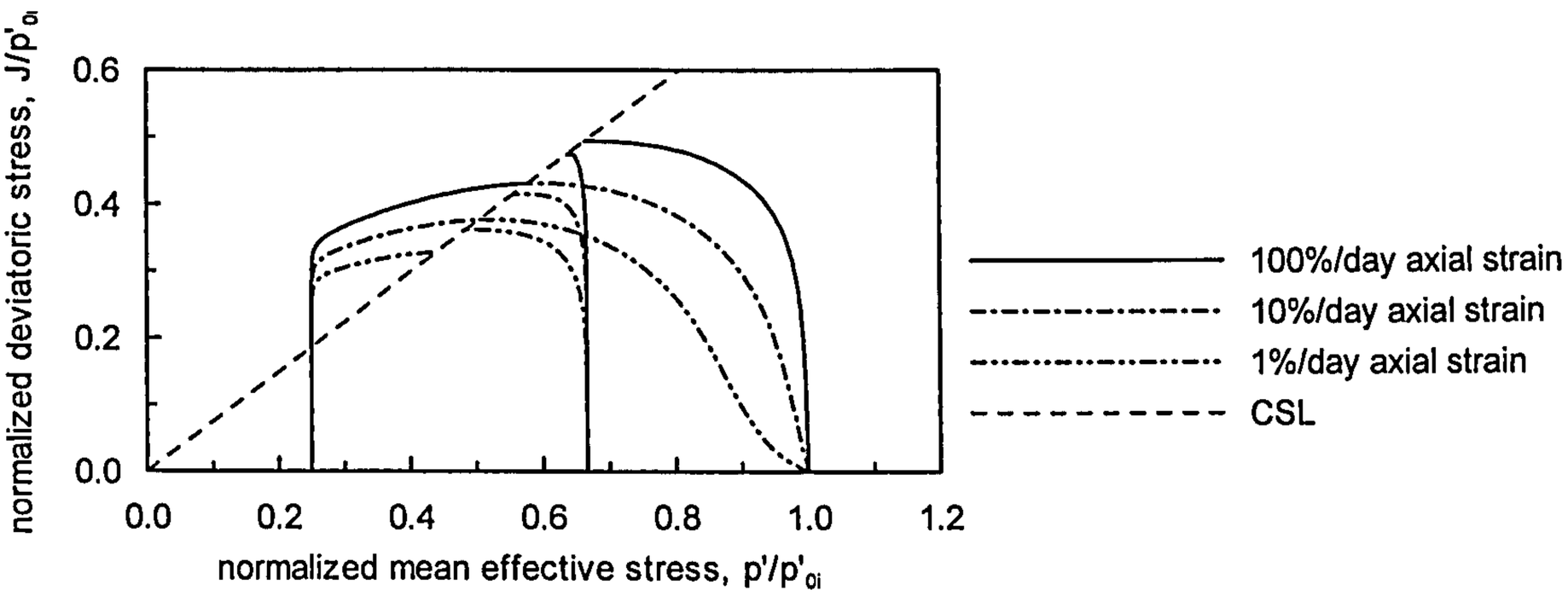

Note: in all cases the initial mean effective stress $p_i^{'}$ *=100kPa, that means that for NC samples the pre consolidation* $p_{0i}^{'}$ *=100kPa; for samples with OCR=1.5* $p_{0i}^{'}$ *=150kPa and samples with OCR=4* $p_{0i}^{'}$ *=400kPa.*

Figure 5.13: Normalized stress path of undrained triaxial tests on NC and OC samples at various values of constant axial strain rate.

The heavily OC samples (OCR=4.0) show an initial stiff response within which the soil behaviour is dominated by the elastic response and the deviatoric stress is observed to increase sharply with minimal or no change in mean effective stress (during which the sample develops contractive excess pore water pressure), reaching stress ratios well above that at critical state. The stress path then starts to bend rightwards (as the sample develops dilative pore water pressure changes), towards the critical state and the deviatoric stress is found to increase monotonically up to the critical state. The model is able to reproduce the observed fact that heavily OC samples under undrained shearing, reach stress ratios well in excess of the stress ratio at critical state. However, the model fails to predict a peak undrained strength at stress ratios higher than the critical state and subsequent post peak softening as the stress path tends to the critical state.

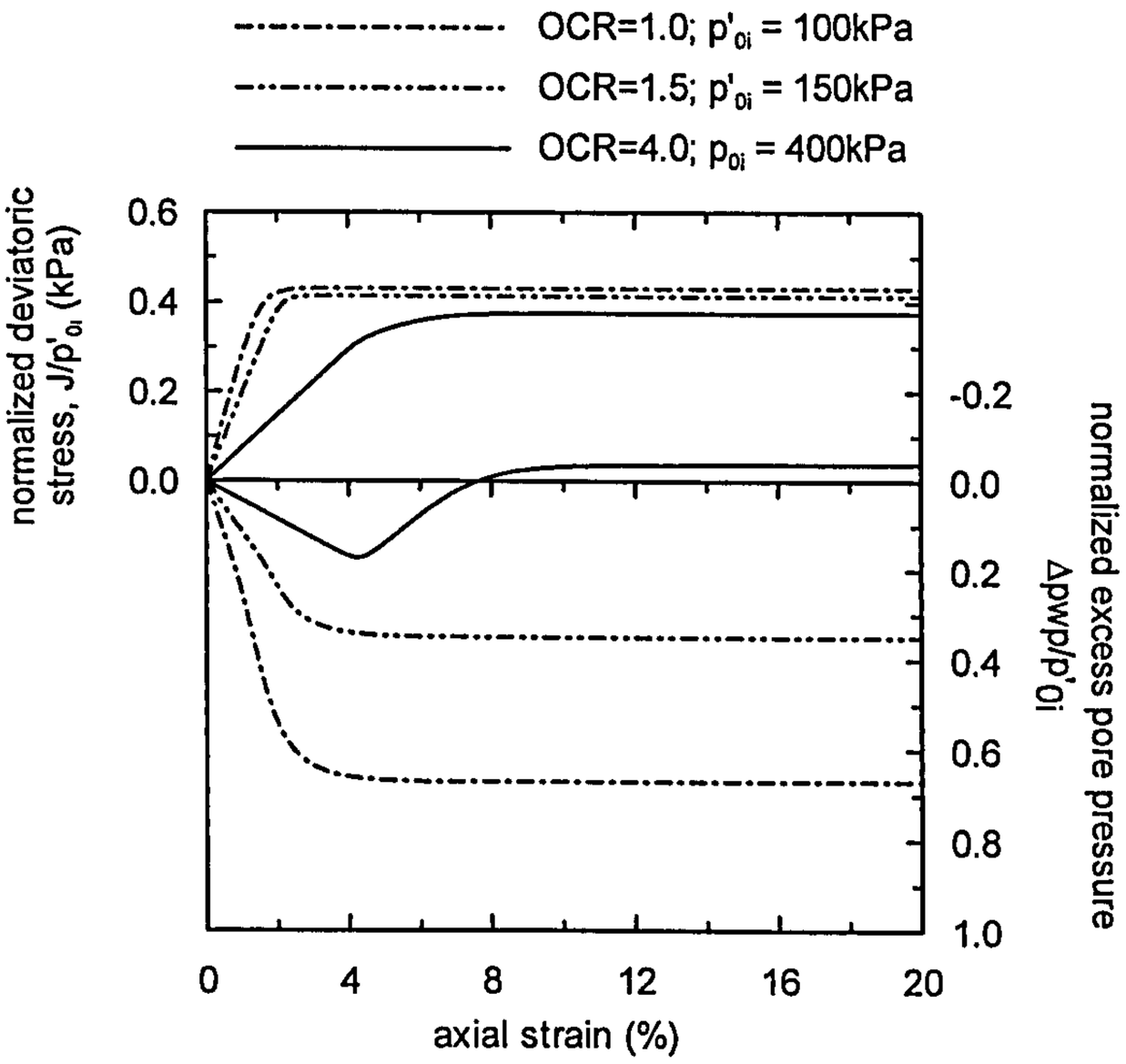

Figure 5.14: Variation of the deviatoric stress and excess pore pressures during undrained triaxial compression tests on NC and OC samples sheared at 10%/day axial strain rate.

From Figure 5.14 it seems that the soil response becomes softer with increasing OCR, however this is a distortion that results from the fact that the deviatoric stress has been normalized by the respective pre-consolidation pressure p'_{0i}. In the three cases, the elastic stiffness – that could be taken as the tangent to the initial part of the stress-strain curves – is the same, however the value of the axial strain at peak increases with OCR as the absolute value of the deviatoric stress at peak also increases.

Figure 5.15 shows the position of the quantity p'_{0c} during the undrained triaxial compression tests described above, in *specific volume – lnp' space*. The position of the current state (V_{oc}, p'_{oc}) - where p'_{oc} is the size of the current loading surface and $V_{oc} = V + \kappa \ln(p'/p'_{oc})$ is the current specific volume at the isotropic stress state - to the reference line, controls the magnitude of the visco-plastic scalar multiplier Φ, and thus of the incremental visco-plastic strains. Figure 5.15 shows that initially the stress path follows very closely an instant elastic line passing by the initial stress state until it joins the line that corresponds to the appropriate value of Φ. Failure points of samples sheared at the same axial strain rate are found to define a line parallel to the reference line (and thus of equal Φ value), and these lines move rightwards for higher values of

applied strain rate. The initial pseudo-elastic range is seen to increase with the applied axial strain rate and OCR as an increase in the OCR means that the sample is further way from the reference line, located on a line characterized by a much smaller Φ value.

The results presented in Figure 5.13 and Figure 5.15 show that the Modified Creep Model 1 predicts that the critical state line (CSL) is unique in stress space but is rate dependent in *void ratio – mean effective stress* space. While the first is well corroborated by data published in the literature there is very little information regarding the uniqueness of the CSL in terms of void ratio. Sorensen (2006) suggests that the CSL for the NC reconstituted London Clay is unique and strain rate independent both in stress space and in terms of void ratio. In any case this is consistent with the fact that NC reconstituted London Clay was observed to have pure TESRA behaviour at large stress levels, showing no persistent strain rate effects at failure.

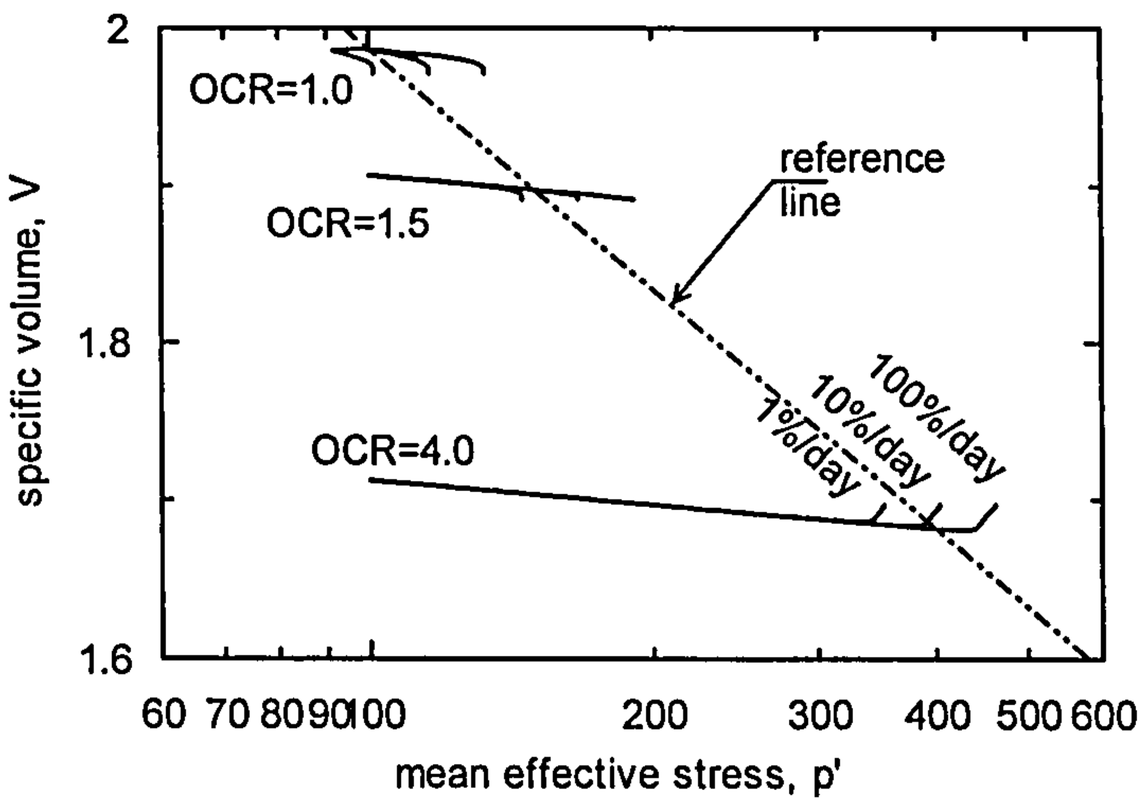

Figure 5.15: Variation of the p'_{0c} with void ratio during undrained triaxial compression of NC and OC samples.

On the other hand intact London Clay, which has isotach viscosity up to failure, is reported to have a unique CSL in stress space; nonetheless the uniqueness in terms of void ratio is not clear. Sorensen notes that the fact that the undrained strength is rate dependent (which was observed experimentally), explained by creep driven pore water pressures, would suggest that in fact the CSL is not unique in terms of void ratio, since for a given void ratio several failure stress states can be obtained during undrained shearing, depending on the applied strain rate. On the other hand it may be that such tests have been terminated prior reaching true critical state conditions and the referred

dependency of the undrained strength with strain rate corresponds instead to the rate dependency of the bounding surface rather than that of the CLS.

In any case inspection of Figure 5.15 shows that the distance between the critical state lines per logarithmic cycle of strain rate is about 0.025. This value is very small, comparable to the error involved in the calculation of the value of void ratio in a laboratory test, suggesting that the experimental verification of the rate dependency of the CSL in terms of void ratio is a matter of achieving better accuracy in laboratory testing.

5.6 Concluding comments

This Chapter has described the development, implementation and validation of a simple elasto visco-plastic model that aimed to simulate the time and rate dependent behaviour of a material with isotach viscosity. The model assumes that the soil deformation associated with an effective stress increment $\{\Delta\sigma'\}$ can be divided into an instantaneous elastic component and a time dependent visco-plastic component. The model is based on an extension of the overstress theory and visco-plastic (delayed) strains are predicted when the stress state lies on, above or below the reference loading surface. The magnitude of visco-plastic strain increment is defined by the visco-plastic scalar multiplier Φ that is essentially a function of the distance of the current loading surface to the reference surface. The quantity Φ ensures that the model response follows a unique stress-strain-strain rate relationship that is characterized by a linear logarithmic creep law.

Similar to the approach followed by other researchers, the extension to general stress space was initially carried out, based on the experimental observation by Tavenas et al. (1978), assuming that a given loading surface was a locus of constant volumetric visco-plastic strain rate. However, in this case the model was not able to predict critical state conditions. This was shown to be a consequent of the above assumption and implies that many theoretical models described in the literature, which are based on this assumption, are flawed. The model was subsequently modified such that a given loading surface was instead a locus of constant visco-plastic scalar multiplier Φ. The difference between the two approaches was shown to be significant only for stress ratio values larger than

about 0.7, but only the latter approach is able to appropriately simulate critical state conditions.

The model has been formulated such that it requires two additional parameters in relation to the MCC model, ψ and $\dot{\varepsilon}_{vol}^{ref}$. The parameter ψ defines the vertical spacing between lines of constant volumetric strain rate in *specific volume – lnp' space* and can be related to the coefficient of secondary consolidation $C_{\alpha e}$ by means of Equation 5.44, and the parameter $\dot{\varepsilon}_{vol}^{ref}$ is the volumetric strain rate associated with the reference line. The parameters ψ and $\dot{\varepsilon}_{vol}^{ref}$ are shown to be equivalent to the more common set of parameters $C_{\alpha e}$ and t_0, where t_0 is the time associated with the reference line. If the value of t_0 is set equal to 1day=24 hours, as the reference time line is usually defined based on IL 24hour oedometer tests, then the model only requires one additional parameter in relation to the MCC model.

It has been shown that a very small error is introduced when the two additional parameters are derived from an IL 24 hour oedometer test, even though in the model formulation the reference line corresponds to an isotropic stress path.

The Modified creep model 1 was shown to reproduce well the time dependent behaviour of soils associated with isotach viscosity. However, as a consequence of adopting a linear logarithmic creep law, the model would predict an infinite volumetric creep strain at an infinite creep time under constant effective stresses. The constitutive model presented in the following Chapter overcomes this problem by including a limit for the volumetric creep deformation, and the model can then reproduce a flexible non-linear creep law more in agreement with observed creep soil behaviour. The implications of the above two assumptions in practice are better demonstrated in Chapter 7 and 8 when considering the long-term settlement of preloaded footings.

6 A TIME DEPENDENT CONSTITUTIVE LAW BASED ON A NON-LINEAR LOGARITHMIC CREEP LAW

6.1 Introduction

This chapter describes the development, implementation and validation of an elastic visco-plastic constitutive model for general stress space based on the concept of equivalent time, which was first defined by Yin & Graham (1989).

The visco-plastic strain rate is evaluated using the concepts of instant and delayed compression and assuming a non-linear logarithmic creep law. Schematically the model may resemble the Bjerrum's framework for the 1D compression of clays (1967). However, as noted in Section 3.2.8, the decomposition of the soil deformation into an instant and delayed component is distinct in the two models; in Yin & Graham (1989) the instant deformation corresponds to the elastic time dependent soil response while in Bjerrum's model the instant deformations corresponds to the deformation that would take place simultaneously to the application of the effective stress increment, assuming that no hydro-dynamic lag occurs.

In addition, Bjerrum (1967) proposes that the 1D compression behaviour of clays can be described by a set of compression lines in *void ratio – vertical effective stress* space, each corresponding to a different duration of loading. The virgin compression line, i.e. the locus of the normally consolidated stress states, is then a line associated with a reference duration of loading. On the other hand, Yin & Graham (1989, 1994) have noted that more generally the compression of a soil element should be related to an *equivalent* loading *time* rather than to an absolute time or duration of loading, this being of particular significance to overconsolidated stress states.

Based on the concept of equivalent time Yin & Graham (1989, 1999) proposed a 1D constitutive equation that was able to reproduce the phenomena of creep, stress relaxation and strain rate effects under 1D compression, according to a linear logarithmic law. Yin & Graham (1999) have extended the model to triaxial stress space, assuming that the visco-plastic volumetric strain rate was constant on a given loading surface and the remaining components were evaluated from a plastic potential function. Both the plastic potential and the loading surface were identical to the MCC ellipse.

Yin (1999) notes that the linear logarithmic creep law has a theoretical limitation that at infinite time an infinite creep strain (or settlement) is predicted, and proposes a hyperbolic function with a limit for the creep strain (which is attained at infinite time) to fit the non-linear logarithmic creep behaviour of soils. Yin et al (2002) developed an elastic visco-plastic constitutive model for general stress space incorporating the above-mentioned non-linear logarithmic law The model assumes that the visco-plastic volumetric strain rate is constant on a given loading surface and the remaining strain components are evaluated from a plastic potential function. In *p'-J* stress space, the plastic potential and the loading surface are each described by two complex functions, one applicable to the dry and one to the wet side of the critical state, respectively. The failure surface in the deviatoric plane is described by a smooth shape function, implemented with the aim of removing the singularities of the Mohr-Coulomb criterion at the hexagon corners.

Within this research programme it was aimed to develop an overstress type elasto visco-plastic model, extended to general stress space, based on the equivalent time concept and incorporating the above mentioned non-linear logarithmic creep law. The equivalent time concept associated with a given creep law define completely the time dependent behaviour of a soil element under isotropic stress conditions. The extension to general stress space is done assuming that the soil deformation under a general stress state (ε_{vol}, p', J) can be evaluated from an equivalent isotropic stress state and employing still the same isotropic relationship. Assuming, based on the findings reported in Chapter 5, that a given loading surface is a locus of constant scalar creep multiplier, the only piece of information needed to define completely the model in general stress space is a function to describe the loading and the plastic potential surfaces.

The equation adopted to describe the loading and the plastic potential surfaces is that proposed by Lagioia et al. (1996) because it is very flexible and consequently can reproduce a wide range of shapes in the stress space *p'- J*. The extension to general stress space is done based on the Matsuoka-Nakai failure criterion.

It is noted that the *equivalent time equations* completely defined the soil behaviour i.e. the elastic behaviour, the ration of elastic to visco-plastic strain increments, with failure being define by the plastic potential. Therefore the *equivalent time equations* could not

be used in combination with other, more sophisticated, soil models reported in the literature and available in the ICFEP soil model's library, such as the *bubble* or kinematic yield surfaces type models (Al-Tabbaa & Wood, 1989; Stallebrass & Taylor, 1997; Grammatikopoulou, 2004) or the single and double surface Lade's models based on bounding surface plasticity (Lade, 1977; Kovacevic, 1994), the former being able to capture e.g. the small strain strong non-linearity of soils, the influence of the stress path direction on the soil response.

Amongst the models available in ICFEP is that of Lagioia & Nova (1995), which was initially developed to model the behaviour of calcarite and is able to mimic the existence of an initial soil structure and the subsequent structure loss. Therefore the inclusion of the structure mechanism described by the above authors represented limited additional work and opened the perspectives of investigating the coupling between soil structure and viscosity in the same constitutive model. However, as it will be shown later in this thesis, the destructuration mechanism presents major shortcomings when applied to simulate the behaviour of structured clayey soils as the destructuration is made to occur associated with the development of volumetric strains only, and thus no loss of structure is predicted during undrained loading. It is recognized that it would be more appropriate to employ a formulation similar to that described e.g.; Rouainia & Muir Wood, (2000), Kostinen et al., (2002) or Baudet & Stallebrass, (2004), in which the soil structure is made to decay as a function of both the deviatoric and volumetric strain components and may account for the existence of a stable soil structure component.

This chapter starts by describing the principle of equivalent time, which is then used to derive a general non-linear logarithmic creep law applicable to normally and overconsolidated stress states, as proposed by Yin (1999). The model is then extended to general stress space and the constitutive equations are presented in detail in Section 6.3. To characterize the time dependent part of the model three parameters are required, and the physical meaning of the model parameters and their derivation is discussed in Section 6.4. The performance of the model is investigated by conducting a series of finite element analyses that simulate typical laboratory stress paths and the analysis results are compared with observed trends as described in Chapter 2. In addition, a set of finite element analyses are carried out that simulate laboratory tests on soft Hong

Kong marine deposits (HKMD) and the results are compared with the experimental results (Zhu, 2000) and numerical predictions reported by Yin et al. (2002). Finally, the Equivalent Time model is compared with the *Modified* Creep Model described in Chapter 5.

6.2 The concept of equivalent time

The concept of equivalent time was first introduced by Yin & Graham (1989) to overcome the problems that arise when the soil (delayed) compression is related to the *real* loading time and the real loading time needs to be introduced explicitly, as in Bjerrum's model. The above implies that the start of secondary compression is identified with a normally consolidated stress state and thus it cannot account for loading within the overconsolidated stress range and for strain rate effects.

Yin & Graham (1989) note that the compression characteristics of a soil element can be described instead by reference to an *equivalent* loading *time*. The *equivalent time* of an isotropic state $\left(\varepsilon_{vol,m}, p_m^{'}\right)$ is defined as the time that a soil element would take to creep from a reference line to the current stress state under constant mean effective stress. In the normally consolidated range of IL oedometer tests, equivalent times are usually close to the duration of the load increments. However, in the overconsolidated range, equivalent times and load durations may be quite different. An equivalent time is related to a unique creep strain rate, with large equivalent times associated with smaller creep strain rates. The relationship between *stress –strain - equivalent time* is unique and independent of the loading history as it is shown subsequently.

Figure 6.1 shows schematically the basic elements required to define equivalent time in *volumetric strain – mean effective stress space*, namely lines of constant equivalent time, a reference time line, a limit time line and an instant time line, and where the subscript *m* denotes an isotropic stress state.

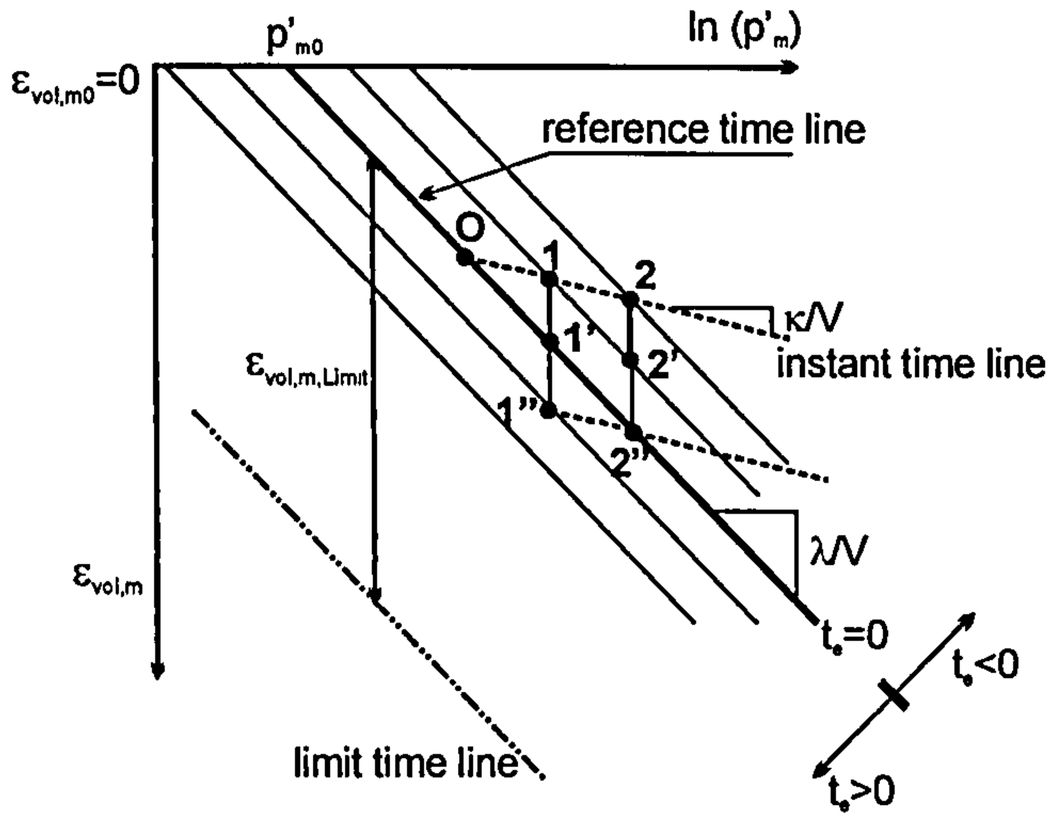

Figure 6.1: Schematic representation of equivalent time lines.

Reference time line

The reference time line is the locus of the soil states that corresponds to zero equivalent time. The equivalent time of states located below the reference time line are always positive and vary between 0 and infinity. Above the reference time line, the equivalent time varies between zero and the value $-t_0$, where t_0 is a model parameter and corresponds to the real time associated with the reference time line (which is discussed in more detail in the following sections). The reference time line is mathematically defined by the following equation:

Equation 6.1
$$\varepsilon_{vol,m}^{ref} = \varepsilon_{vol,m0}^{ref} + \frac{\lambda}{V} \ln\left(\frac{p_m^{'}}{p_{m0}^{'}}\right)$$

where the superscript *ref* denotes a quantity evaluated on the reference time line, and the subscript m denotes isotropic conditions, $\varepsilon_{vol,m}^{ref}$ is the volumetric strain at an isotropic effective stress $p_m^{'}$, $\varepsilon_{vol,m0}^{ref}$ is the volumetric strain at a reference isotropic effective stress $p_{m0}^{'}$ and is assumed here to be zero, and λ/V (where V is specific volume V=1+e) and $p_{m0}^{'}$ are two model parameters.

Limit time line

The limit time line is the locus of the soil states that are attained after drained creep for an infinite time, and it is defined by the finite value of visco-plastic volumetric strain $\varepsilon_{vol,m,Limit}^{vp}$. The value of $\varepsilon_{vol,m,Limit}^{vp}$ is by definition an asymptotic value and thus cannot

be measured or identify directly in practice. The limit time line is associated with an infinite equivalent time and a creep strain rate equal to zero. Beyond this line, the behaviour of the soil is time-independent, and pure elastic behaviour is predicted. In a linear logarithmic creep law there is no limit to the amount of creep volumetric deformation i.e. $\varepsilon^{vp}_{vol,m,Limit}$ is equal to infinity.

Instant time line

The instant time line defines the soils instant elastic deformation at any point in Figure 6.1. The instant time line can be generically expressed as:

Equation 6.2
$$\varepsilon^{el}_{vol,m} = \varepsilon^{el}_{vol,mu} + \frac{\kappa}{V}\ln\left(\frac{p'_m}{p'_u}\right)$$

where the superscript *el* denotes quantities evaluated on the instant line, $\varepsilon^{el}_{vol,m}$ is the volumetric strain at the isotropic effective stress p'_m; $\varepsilon^{el}_{vol,mu}$ is the volumetric strain at a reference mean effective stress p'_u and κ/V is a model parameter (where V is the specific volume V=1+e). There are an infinite number of instant time lines; the current instant time line is essentially a line passing through the current soil state $\left(\varepsilon_{vol,m}, p'_m\right)$ with slope κ/V in $\varepsilon_{vol,m} - ln\, p'_m$ *space*.

Consider now Figure 6.1 and point O located on the reference time line. The application of a load increment $\Delta p'_1$ causes the stress state to move instantaneously along the instant time line to point 1. Point 1 is characterized by an equivalent time t_e smaller than zero as it is located above the reference time line. With time the soil element undergoes delayed visco-plastic deformation moving to point 1' and eventually to point 1". The equivalent time at point 1" is larger than zero and equal to the time that it has taken the soil element to creep from point 1' (on the reference time line) to point 1". The equivalent time at 1" is entirely defined by its position in relation to the reference time line and independent of how that stress state was reached, and thus it would be the same if the point 1" had been attained following a loading path along 0-2-2" and then instantaneous unloading along the new instant time line from 2" to 1". It is noted that the above considerations neglect the time dependent compression associated with hydraulic pore water pressure dissipation.

6.3 Formulation of the constitutive equations

6.3.1 Derivation of an elastic visco-plastic constitutive equation for isotropic loading conditions

Using the concept of equivalent time it is possible to derive a unique relationship between $p_m^{'}$, $\varepsilon_{vol,m}$ and t_e, which is able to express the time dependent behaviour of a soil element with isotach viscosity under isotropic conditions. Under isotropic conditions, the stress state is completely defined by the mean effective stress $p_m^{'}$, and the volumetric strain, $\varepsilon_{vol,m}$. From Figure 6.1, the volumetric strain of a generic stress state can be written as:

Equation 6.3 $$\varepsilon_{vol,m} = \varepsilon_{vol,m}^{ref} + \varepsilon_{vol,m}^{vp}$$

Where $\varepsilon_{vol,m}$ is the current volumetric strain, $\varepsilon_{vol,m}^{ref}$ is the volumetric strain on the reference time line at the current mean effective stress $p_m^{'}$ and $\varepsilon_{vol,m}^{vp}$ is the creep visco-plastic volumetric strain.

Assuming that the visco-plastic strains are given by a linear logarithmic law:

Equation 6.4 $$\varepsilon_{vol,m}^{vp} = \frac{\psi}{V} \ln\left(\frac{t_0 + t_e}{t_0}\right)$$

where ψ/V is a model parameter, t_e is the current equivalent time and t_0 is the real time associated with the reference time line. The visco-plastic volumetric strain rate can then be obtained by differentiation of Equation 6.4 in relation to time *t*, where $t=t_0+t_e$:

Equation 6.5 $$\frac{d\varepsilon_{vol,m}^{vp}}{dt} = \frac{d\varepsilon_{vol,m}^{vp}}{dt_e} = \dot{\varepsilon}_{vol,m}^{vp} = \frac{\psi}{V} \cdot \frac{1}{t_0 + t_e}$$

Substituting Equation 6.4 into Equation 6.3 gives:

Equation 6.6 $$\varepsilon_{vol,m} = \varepsilon_{vol,m}^{ref} + \frac{\psi}{V} \ln\left(\frac{t_0 + t_e}{t_0}\right)$$

The above equation can be reworked to give the current equivalent time t_e as:

Equation 6.7 $$t_e = -t_0 + t_0 \cdot \exp\left[\left(\varepsilon_{vol,m} - \varepsilon_{vol,m}^{ref}\right)\frac{V}{\psi}\right]$$

Substituting Equation 6.7 into Equation 6.5 the visco-plastic volumetric strain rate can be written as:

Equation 6.8 $$\dot{\varepsilon}^{vp}_{vol,m} = \frac{\psi}{V \cdot t_0} \cdot \exp\left[\left(\varepsilon^{ref}_{vol,m} - \varepsilon_{vol,m}\right)\frac{V}{\psi}\right]$$

In numerical analysis, it is of interest to consider the constitutive equations in incremental form. Consider an infinitesimal load increment $\Delta p'_m$ over a duration of time Δt. The associated incremental volumetric strain $\Delta\varepsilon_{vol,m}$ can be decomposed into an elastic and a visco-plastic component, such that:

Equation 6.9 $$\Delta\varepsilon_{vol,m} = \Delta\varepsilon^{el}_{vol,m} + \Delta\varepsilon^{vp}_{vol,m}$$

Where $\Delta\varepsilon^{el}_{vol,m}$ and $\Delta\varepsilon^{vp}_{vol,m}$ are the elastic and the visco-plastic volumetric strain increments, respectively. If the time increment Δt is sufficiently small, the visco-plastic volumetric strain rate $\dot{\varepsilon}^{vp}_{vol,m}$ may be considered constant over that time increment and:

Equation 6.10 $$\Delta\varepsilon^{vp}_{vol,m} = \Delta t \cdot \dot{\varepsilon}^{vp}_{vol,m}$$

It remains to evaluate the incremental elastic strain component, which is instantaneous and time independent. Again, if the load increment is sufficiently small that the elastic bulk modulus may be considered constant then the elastic volumetric strain increment associated with a load increment $\Delta p'_m$ can be evaluated as:

Equation 6.11 $$\Delta\varepsilon^{el}_{vol,m} = \frac{\Delta p'_m}{K}$$

Where K is the elastic bulk modulus and can be shown to be $K = \frac{V \cdot p'_m}{\kappa}$

Combining the above two equations gives a general equation for the time dependent behaviour of soil under isotropic stress conditions:

Equation 6.12 $$\Delta\varepsilon_{vol,m} = \frac{\kappa}{V \cdot p'_m} \cdot \Delta p'_m + \frac{\psi}{V \cdot t_0} \cdot \exp\left[\left(\varepsilon^{ref}_{vol,m} - \varepsilon_{vol,m}\right)\frac{V}{\psi}\right] \cdot \Delta t$$

The above constitutive equation is identical to that presented by Yin & Graham (1994) for one-dimensional stress conditions. Yin (1999) proposed a non-linear logarithmic function to describe the creep deformation of soils, as follows:

Equation 6.13
$$\varepsilon_{vol,m}^{vp} = \frac{\frac{\psi_0}{V}\ln\left(\frac{t_0+t_e}{t_0}\right)}{1+\frac{\psi_0}{V\cdot\varepsilon_{vol,m,Limit}^{vp}}\ln\left(\frac{t_0+t_e}{t_0}\right)}$$

Replacing quantity $\frac{\psi_0}{V}\ln\left(\frac{t_0+t_e}{t_0}\right)$ by x the above equation can be rewritten as:

Equation 6.14
$$\varepsilon_{vol,m}^{vp} = \frac{x}{1+\frac{1}{\varepsilon_{vol,m,Limit}^{vp}}\cdot x}$$

This corresponds to a hyperbolic function. The visco-plastic volumetric strain rate can be obtained by differentiating Equation 6.13 with respect to time t, where $t=t_0+t_e$.

Equation 6.15
$$\frac{d\varepsilon_{vol,m}^{vp}}{dt} = \frac{d\varepsilon_{vol,m}^{vp}}{dt_e} = \dot{\varepsilon}_{vol,m}^{vp} = \frac{\frac{\psi_0}{V}}{t_0+t_e}\cdot\frac{1}{\left(1+\frac{\psi_0}{V\cdot\varepsilon_{vol,m,Limit}^{vp}}\ln\frac{t_0+t_e}{t_0}\right)^2}$$

It is of interest to consider the meaning of the parameters in Equations 6.13 to 6.15. When the equivalent time t_e tends to infinity:

Equation 6.16
$$\varepsilon_{vol,m}^{vp}\Big|_{t_e=\infty} = \varepsilon_{vol,m,Limit}^{vp}$$

The parameter $\varepsilon_{vol,m,Limit}^{vp}$ is therefore the limit to the visco-plastic volumetric strain, which is attained under constant effective stress at infinite creep time. At the equivalent time $t_e=0$, the visco-plastic volumetric strain rate becomes:

Equation 6.17
$$\left(\dot{\varepsilon}_{vol,m}^{vp}\right)_{t=t_0} = \frac{\psi_0}{V\cdot t_0}$$

Consequently the parameter ψ_0/V together with t_0 define the visco-plastic volumetric strain rate on the reference time line. The parameters ψ_0/V and $\varepsilon_{vol,m,Limit}^{vp}$ affect the variation of the visco-plastic strain with the logarithm of time. Equation 6.13 can be rewritten in the following form:

Equation 6.18

$$\varepsilon_{vol,m}^{vp} = \frac{\psi}{V} \ln\left(\frac{t_0 + t_e}{t_0}\right)$$

with

$$\frac{\psi}{V} = \frac{\frac{\psi_0}{V}}{1 + \frac{\psi_0}{V \cdot \varepsilon_{vol,m,Limit}^{vp}} \ln\left(\frac{t_0 + t_e}{t_0}\right)}$$

where the parameter ψ/V corresponds to the parameter used in the linear logarithmic law (see Equation 6.4). However, in the non-linear logarithmic model the quantity ψ/V is no longer a constant but decreases with equivalent time t_e and the parameter ψ_0/V corresponds to the value of ψ/V at time t_e=0. Substituting Equation 6.13 into Equation 6.3 gives:

Equation 6.19

$$\varepsilon_{vol,m} = \varepsilon_{vol,m}^{ref} + \frac{\frac{\psi_0}{V} \ln\left(\frac{t_0 + t_e}{t_0}\right)}{1 + \frac{\psi_0}{V \cdot \varepsilon_{vol,m,Limit}^{vp}} \ln\left(\frac{t_0 + t_e}{t_0}\right)}$$

The above equation can be reworked to give the value of equivalent time t_e as:

Equation 6.20

$$t_e = -t_0 + \exp\left[\frac{\varepsilon_{vol,m} - \varepsilon_{vol,m}^{ref}}{\frac{\psi_0}{V}\left(1 - \frac{\varepsilon_{vol,m} - \varepsilon_{vol,m}^{ref}}{\varepsilon_{vol,m,Limit}^{vp}}\right)}\right]$$

Substituting Equation 6.20 into Equation 6.15 the visco-plastic strain rate can be expressed as:

Equation 6.21

$$\dot{\varepsilon}_{vol,m}^{vp} = \frac{\psi_0}{V \cdot t_0} \cdot \left(1 + \frac{\varepsilon_{vol,m}^{ref} - \varepsilon_{vol,m}}{\varepsilon_{vol,m,Limit}^{vp}}\right)^2 \cdot \exp\left[\frac{V}{\psi_0} \frac{\varepsilon_{vol,m}^{ref} - \varepsilon_{vol,m}}{\left(1 + \frac{\varepsilon_{vol,m}^{ref} - \varepsilon_{vol,m}}{\varepsilon_{vol,m,Limit}^{vp}}\right)}\right]$$

It is now possible to write a general incremental equation for the time dependent behaviour of soils based on a non-linear logarithmic law as:

Equation 6.22

$$\Delta\varepsilon_{vol,m} = \frac{\kappa}{V \cdot p_m^{'}} \cdot \Delta p_m^{'} + \frac{\psi_0}{V \cdot t_0} \cdot \left(1 + \frac{\varepsilon_{vol,m}^{ref} - \varepsilon_{vol,m}}{\varepsilon_{vol,m,Limit}^{vp}}\right)^2 \cdot \exp\left[\frac{V}{\psi_0} \frac{\varepsilon_{vol,m}^{ref} - \varepsilon_{vol,m}}{\left(1 + \frac{\varepsilon_{vol,m}^{ref} - \varepsilon_{vol,m}}{\varepsilon_{vol,m,Limit}^{vp}}\right)}\right] \cdot \Delta t$$

6.3.2 Extension to general stress space

The previous section has presented the derivation of two constitutive equations to describe the time dependent behaviour of soil with isotach viscosity under isotropic stress conditions. The first is based on a linear logarithmic creep law, while the second is based on a non-linear logarithmic creep law. The latter has the advantage that it is able to mimic the fact that there is a physical limit to the amount of volumetric creep deformation that a soil can sustain.

This section shows how the above constitutive relationship, for isotropic stress conditions, based on the non-linear logarithmic creep law may be extended to general stress space. As noted above it is assumed that the soil deformation associated with a effective stress increment $\{\Delta\sigma'\}$ over a time increment Δt may be decomposed into an elastic and a visco-plastic part:

Equation 6.23 $$\{\Delta\varepsilon^T\} = \{\Delta\varepsilon^{el}\} + \{\Delta\varepsilon^{vp}\}$$

where the elastic incremental strains $\{\Delta\varepsilon^{el}\}$ are instantaneous and thus time independent, and the viscous-plastic incremental strains $\{\Delta\varepsilon^{vp}\}$ are time dependent and irreversible. The elastic incremental strains $\{\Delta\varepsilon^{el}\}$ can be determined by inverting the following equation:

Equation 6.24 $$\{\Delta\sigma'\} = [D] \cdot \{\Delta\varepsilon^{el}\}$$

where $\{\Delta\sigma'\}$ is the effective stress increment and $[D]$ is the elastic constitutive matrix. The elastic response is assumed to be isotropic and thus is fully characterized by two elastic parameters, a stress dependent bulk modulus (defined by Equation 6.25) and a second elastic parameter that can be either the Poisson's ratio μ or the elastic shear modulus G.

Equation 6.25 $$K = \frac{V \cdot p'}{\kappa}$$

According to the visco-plastic theory proposed by Perzyna (1963), the visco-plastic strain component can be expressed as:

Equation 6.26 $$\left\{\Delta\varepsilon_{ij}^{vp}\right\} = \left\langle \Phi(F) \right\rangle \cdot \Delta t \cdot \frac{\partial P}{\partial \sigma_{ij}}$$

where $\left\langle \Phi(F) \right\rangle = \Phi(F)$ if $F > 0$

$\left\langle \Phi(F) \right\rangle = 0$ if $F \leq 0$

$\Phi(F)$ is a function that represents the effects of strain rate on the material behaviour, and is a function of the quantity F, which is essentially the distance between the current *dynamic* loading surface to a *static* yield surface, and P is the plastic potential surface. In the present case, the quantities F and $\Phi(F)$ are evaluated in relation to a reference loading surface, characterized by a finite value of visco-plastic strain rate, and the function $\Phi(F)$ is evaluated and visco-plastic strains are predicted for stress states, on, below and above the reference loading surface, provided that the stress states lies above the limit time line (that defines the region of pure elastic behaviour). Therefore the visco-plastic incremental strain can more generally be expressed as:

Equation 6.27 $$\left\{\Delta\varepsilon_{ij}^{vp}\right\} = \left\langle \Phi \right\rangle \cdot \Delta t \cdot \frac{\partial P}{\partial \sigma_{ij}}$$

where $\left\langle \Phi \right\rangle = \Phi$ if the stress state lies above the limit line

$\left\langle \Phi \right\rangle = 0$ if the stress state lies on or below the limit line

It remains to evaluate the value of the quantity Φ. Yin et al. (2002) evaluate the visco-plastic scalar multiplier assuming that the visco-plastic volumetric strain rate is constant on a given loading surface. However, based on the results shown in Chapter 5, the current loading surface is instead assumed to be a locus of constant visco-plastic scalar multiplier. Consider a generic stress state $\left(p', J, \varepsilon_{vol}\right)$, from Equation 6.27 the incremental visco-plastic volumetric strain can be evaluated as:

Equation 6.28

$$\left\{\Delta\varepsilon_{vol}^{vp}\right\} = \Phi \cdot \Delta t \cdot \frac{\partial P}{\partial p'}$$

Comparing Equation 6.28 with Equation 6.22 the value of Φ can be evaluated as:

Equation 6.29

$$\Phi = \frac{\psi_0}{V \cdot t_0} \cdot \left(1 + \frac{\varepsilon_{vol,m}^{ref} - \varepsilon_{vol,m}}{\varepsilon_{vol,m,Limit}^{vp}}\right)^2 \cdot \exp\left[\frac{V}{\psi_0} \frac{\varepsilon_{vol,m}^{ref} - \varepsilon_{vol,m}}{\left(1 + \frac{\varepsilon_{vol,m}^{ref} - \varepsilon_{vol,m}}{\varepsilon_{vol,m,Limit}^{vp}}\right)}\right] \cdot \frac{1}{\left|\frac{\partial P}{\partial p'}\right|_{\substack{p'=p'_m \\ J=0}}}$$

where $\left|\frac{\partial P}{\partial p'}\right|_{\substack{p'=p'_m \\ J=0}}$ is the absolute value of the partial differential of the plastic potential surface function P in relation to the mean effective stress, p', evaluated at the equivalent isotropic stress state $\left(p'_m, J=0\right)$ (noting that the absolute value function is introduced to ensure that the visco-plastic scalar multiplier is always a positive quantity), the quantity $\varepsilon_{vol,m}^{ref}$ is the volumetric strain on the reference time line at the equivalent mean effective stress p'_m and the quantity $\varepsilon_{vol,m}$ is the associated volumetric strain which is evaluated as:

Equation 6.30

$$\varepsilon_{vol,m} = \varepsilon_{vol} + \frac{\kappa}{V} \ln\left(\frac{p'_m}{p'}\right)$$

where ε_{vol} is the current total volumetric strain, p' is the current mean effective stress and p'_m is the size of the current loading surface, and corresponds to the mean effective stress at zero deviatoric stress on the current loading surface (the calculation of p'_m is discussed in detail subsequently). The geometrical significance of the quantity $\varepsilon_{vol,m}$ is illustrated in Figure 6.2. The problem of evaluating the visco-plastic incremental strains at a generic stress point $\left(p', J, \varepsilon_{vol}\right)$ is reduced to evaluating the incremental volumetric visco-plastic strain, and thus the quantity Φ, at the equivalent stress point $\left(p'_m, J=0, \varepsilon_{vol,m}\right)$.

With reference to Figure 6.2 the condition for a stress point to be located above the limit line can be mathematically expressed as:

Equation 6.31

$$1+\frac{\varepsilon_{vol,m}^{ref}-\varepsilon_{vol,m}}{\varepsilon_{vol,m,Limit}^{vp}}>0$$

which implies that the limit time line is parallel to the reference time line.

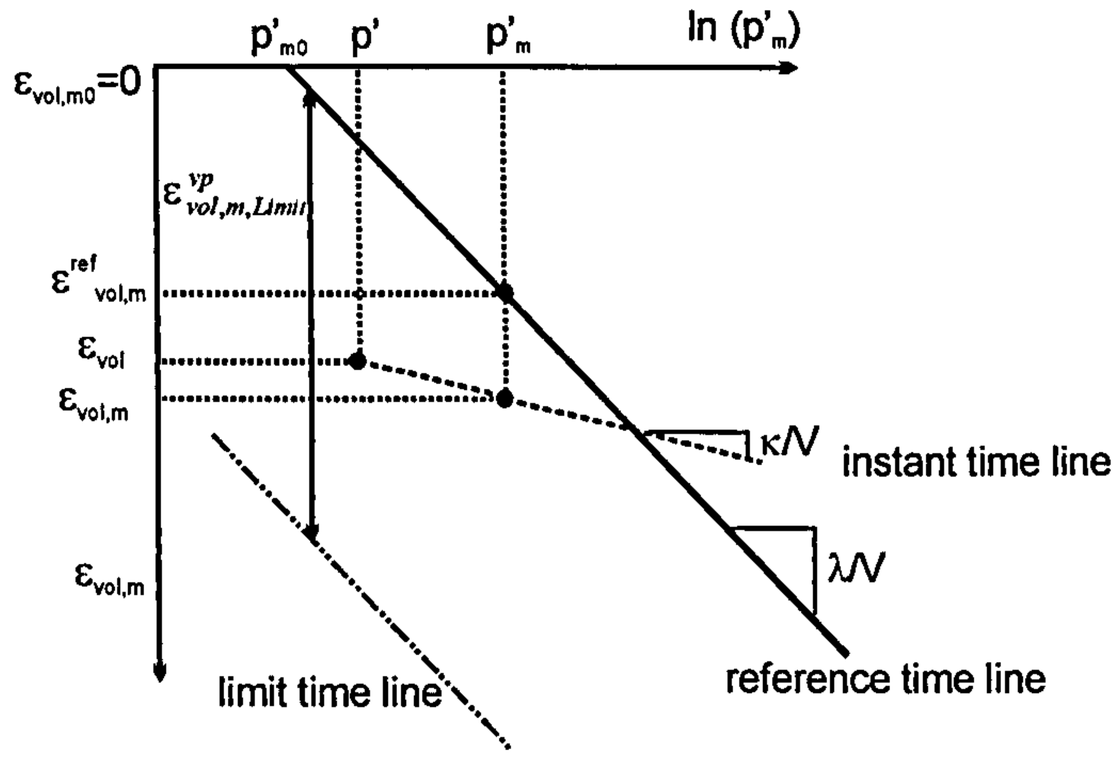

Figure 6.2: Geometrical calculation of the quantity $\varepsilon_{vol,m}$.

6.3.3 Plastic Potential and Loading surface

In triaxial stress space, the loading and the plastic potential surfaces are described by the flexible function proposed by Lagioia et al. (1996) that can simulate a wide range of shapes from the "bullet shape" used in the original Cam-Clay model to the tear shape employed in more recent models. The equation was obtained by integrating a postulated general variation of dilatancy, d (the ratio of volumetric to deviatoric plastic strain increments) with stress ratio η ($\eta = J / p'$). From plasticity theory, the dilatancy d can be written as:

Equation 6.32

$$d=\frac{\Delta\varepsilon_{vol}^{pl}}{\Delta E_d^{vp}}=\frac{\Lambda\dfrac{\partial P}{\partial p'}}{\Lambda\dfrac{\partial P}{\partial J}}=-\frac{dJ}{dp'}$$

which can be rewritten as a function of p' and η as (see e.g. Potts and Zdravkovic, 1999):

Equation 6.33

$$\frac{dp'}{p'}=-\frac{d\eta}{d+\eta}$$

An appropriate dilatancy function should ensure that at the critical state when η=g(θ) dilatancy, d is zero (where g(θ) is the stress ratio at the critical state) and that at η=0

(isotropic stress conditions) dilatancy, d is infinite and only incremental plastic volumetric strains are predicted. The variation of dilatancy, d with stress ratio can be expressed by Equation 6.34 and is schematically shown in Figure 6.3.

Equation 6.34
$$d = \mu(g(\theta) - \eta) \cdot \left(\frac{\alpha \cdot g(\theta)}{\eta} + 1 \right)$$

The parameter μ defines the slope of the d-η curve over its linear range, α defines how close to the η=0 axis the curve must start to bend towards $d = \infty$ and g(θ) is the stress ratio at critical state. The parameter μ in Equation 6.34 should not be confused with the Poisson's ratio, μ and where confusion may occur the former is often characterized by a subscript f or g denoting a loading or plastic potential surface parameter, respectively.

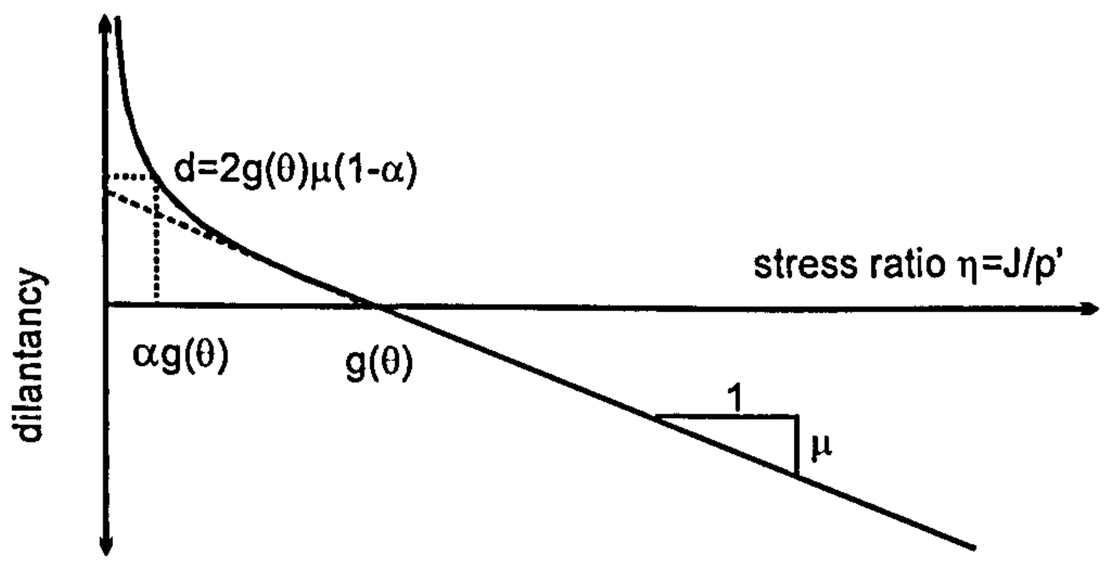

Figure 6.3: Geometrical meaning of the loading and plastic potential function parameters.

By substituting Equation 6.34 into Equation 6.33 and integrating the resultant equation, the following expression for the loading and plastic potential surface is obtained:

Equation 6.35
$$f = \frac{p'}{p'_m} - \frac{\left(1 + \frac{\overline{\eta}}{K_2}\right)^{\frac{K_2}{(1-\mu)\cdot(K_1-K_2)}}}{\left(1 + \frac{\overline{\eta}}{K_1}\right)^{\frac{K_1}{(1-\mu)\cdot(K_1-K_2)}}} = 0$$

where K_1 and K_2 are constants given by:

Equation 6.36
$$K_{1/2} = \frac{\mu \cdot (1-\alpha)}{2 \cdot (1-\mu)} \cdot \left(1 \pm \sqrt{1 - \frac{4\alpha \cdot (1-\mu)}{\mu \cdot (1-\alpha)^2}} \right)$$

And $\overline{\eta}$ is the generalized normalized stress ratio:

Equation 6.37

$$\overline{\eta} = \sqrt{\frac{J_{2\eta}}{J_{2\eta,failure}}}$$

where $J_{2\eta}$ is the stress ratio squared:

Equation 6.38

$$J_{2\eta} = \left(\frac{J}{p'}\right)^2$$

and $J_{2\eta,failure}$ is the square of the stress ratio at failure such that $g(\theta) = \sqrt{J_{2\eta,failure}}$. $J_{2\eta,failure}$ can be obtained by solving the following cubic equation, which is based on the Matsuoka-Nakai criterion (Potts & Zdravkovic, 1999).

Equation 6.39

$$\frac{2}{\sqrt{27}} \cdot \sin(3\theta) \cdot \left(J_{2\eta,failure}\right)^{3/2} + (C-3) \cdot J_{2\eta,failure} - (C-9) = 0$$

in which

$$C = \frac{9 - M^2}{\frac{2M^3}{27} - \frac{M^2}{3} + 1}$$

where M is the gradient of the critical state line in *p'-q stress space* under triaxial compression stress conditions (θ=-30°) and can be related to the angle of shearing resistance φ' as follows:

Equation 6.40

$$M = \frac{6\sin\varphi'}{3 - \sin\varphi'}$$

Four parameters are required to fully define the function given by Equation 6.35: M, μ, α and p'_m. M has been defined above and it is the slope of the critical state line under triaxial compression stress conditions in *p'-q stress space* varying between 0 and 3; p'_m is the size of the surface, that corresponds to the value of the mean effective stress at zero deviatoric stress, and is required to be larger than zero. μ and α define the dilatancy law and consequently the shape of the plastic potential surface (or loading surface) in *p'-J stress space*. There are various restrictions to the values that the parameters μ and α can take. The values of μ and α are required to be larger than zero and different from unity. In addition, if μ<1 then μ must satisfy the following condition:

Equation 6.41

$$\mu > \frac{4\alpha}{(1-\alpha)^2 + 4\alpha}$$

Theoretically Equation 6.35 is valid for any value of μ except for μ=1. However in practice this equation can be used to reproduce the condition of μ=1 by adopting values very close to unity (e.g. 0.99999 or 1.00001). More details regarding the plastic potential and the loading surface function can be found in Lagioia et al. (1996).

It is noted that two sets of parameters M, μ and α are required, one to characterize the loading surface and the other to characterize the plastic potential surface and they are denoted by the subscripts *f* and *g* respectively. If the same values are chosen for the loading surface and the plastic potential parameters such that $M_f=M_g$, $\mu_f=\mu_g$ and $\alpha_f=\alpha_g$ then there is an associated flow rule.

6.3.4 Soil Structure

This thesis deals with the time dependent effects on clays that result from viscosity. While it is recognized that soil structure may, in most cases, be quite important to the overall soil time dependent response, the consideration of structure was beyond the scope of this thesis. However, the model described by Lagioia & Nova (1995) has been implemented by previous researchers in ICFEP, and so the inclusion of the structure mechanism described by the above authors represented limited addition work and opened the perspectives of investigating the coupling between soil structure and viscosity in the same constitutive model.

According to the framework by Lagioia & Nova (1995), the contribution of structure is accounted for by considering that the quantity p'_{m0} is decomposed into an intrinsic part and a transient part associated with the existence of soil structure such that:

Equation 6.42 $$p'_{m0} = p'_{mi0} + p_s$$

where p'_{m0} is the mean effective stress on the reference time line of the natural material at $\varepsilon_{vol,m}$=0; p'_{mi0} is the mean effective stress on the intrinsic reference time line at $\varepsilon_{vol,m}$=0 and p_s is the current contribution due to soil structure. The current value of p'_{m0} is used in Equation 6.1 to evaluate the current value of $\varepsilon^{ref}_{vol,m}$ which in turn is used in Equation 6.29 to evaluate the value of the visco-plastic scalar multiplier. The value of the quantity p_s varies during the analysis procedure, from an initial value p_{s0} input by

the user to zero at a very large volumetric visco-plastic strain, according to the following hardening rule:

Equation 6.43 $$\Delta p_s = -3.0 \cdot \rho_s \cdot p_s \cdot \varepsilon_d^2 \cdot \Delta\varepsilon_d$$

where ρ_s is a model parameter; p_s is the current value of the structure contribution, $\varepsilon_d = \int \left| d\varepsilon_{vol}^{vp} \right|$ and $\Delta\varepsilon_d$ is the incremental value of the quantity ε_d. In the above equation the constant 3.0 is somewhat redundant as it could be incorporated in the scalar model parameter ρ_s.

6.3.5 Plastic hardening / softening parameters

The constitutive model, as described above, requires four plastic hardening parameters. At the start of an analysis, the plastic hardening parameters are initiated and their initial values are evaluated from the model parameters and initial stress conditions. During the analysis procedure, the values of the plastic hardening parameters are continuously up-dated, according to their respective hardening rule:

ε_d - Accumulated visco-plastic volumetric strain

It is defined as $\varepsilon_d = \int \left| d\varepsilon_{vol}^{vp} \right|$. At the start of an analysis this hardening parameter is set equal to zero and then during the analysis its change is evaluated as:

Equation 6.44 $$\Delta\varepsilon_d = \left| \Delta\varepsilon_{vol}^{vp} \right| = \left| \Delta\varepsilon_x^{vp} + \Delta\varepsilon_y^{vp} + \Delta\varepsilon_z^{vp} \right|$$

p_s - The current increase in p'_{m0} due to structure

Its initial value is set equal to the model parameter p_{s0}. Then during the analysis the value is updated according to Equation 6.43. The soil structure decay is a function of the current value of p_s, a model parameter ρ_s and the accumulated and the incremental visco-plastic volumetric strain.

V - Current specific volume

The specific volume is initiated as $V_i = 1 + e_i$, where e_i is the initial void ratio that is input in the initial stress file. The change in the current specific volume is equal to $\Delta V = \Delta e$, where e is the void ratio.

ε_{vol} - Current total volumetric strain

The calculation of the initial value of ε_{vol} is shown schematically in Figure 6.4. The quantity p'_{mc} is the size of the loading surface corresponding to the largest normally consolidated stress state that the soil element has experienced, and thus can be quantified from the initial stress state, the overconsolidation ratio and the model parameters. The time dependent nature of the model means that the apparent pre-consolidation pressure p'_{mc} or yield vertical effective stress σ'_{vy} is now a function of the applied strain rate and so, for simplicity, it is assumed that the input value of overconsolidation ratio is defined in relation to the reference time line. In ICFEP, the user has two options on how to input the OCR, either as a ratio of mean effective stresses or as a ratio of vertical effective stresses. In the first case, the value of p'_{mc} is calculated directly as:

Equation 6.45 $$p'_{mc} = OCR \cdot p'_i$$

where OCR is the overconsolidation ratio and p'_i is the initial mean effective stress. When the OCR is assumed to be the ratio of the yield vertical stress and current vertical effective stress then:

Equation 6.46 $$\sigma'_{vy} = OCR \cdot \sigma'_{vi}$$

where σ'_{vi} is the initial vertical effective stress and σ'_{vy} is the vertical effective stress at (large scale) yield. It is assumed that the coefficient of earth pressure at rest in the normally consolidated range K_0^{NC} can be evaluated using Equation 5.31 as proposed by Jaky (1944) and the effective stress acting in the horizontal direction is evaluated as:

Equation 6.47 $$\sigma'_{hy} = K_0^{NC} \cdot \sigma'_{vy}$$

The values of p' and J associated with this NC stress state are evaluated assuming that the stresses acting in the two horizontal directions are the same and that the vertical and horizontal directions are principal directions. These values are then used in Equation 6.35 to obtain the size of the corresponding loading surface, which is then the initial value of $p_{mc}^{'}$. Once the value of $p_{mc}^{'}$ is known, the initial volumetric strain $\varepsilon_{vol}^{initial}$ can be evaluated as:

Equation 6.48
$$\varepsilon_{vol}^{initial} = \frac{\lambda}{V}\ln\left(\frac{p_{mc}^{'}}{p_{m0}^{'}}\right) - \frac{\kappa}{V}\ln\left(\frac{p_{mc}^{'}}{p_{i}^{'}}\right)$$

where $p_i^{'}$ is the initial mean effective stress and $p_{m0}^{'}$ is the mean effective stress on the reference time line of the natural material at $\varepsilon_{vol,m} = 0$.

During the analysis the change in ε_{vol} is evaluated as:

Equation 6.49
$$\Delta\varepsilon_{vol} = \Delta\varepsilon_x + \Delta\varepsilon_y + \Delta\varepsilon_z$$

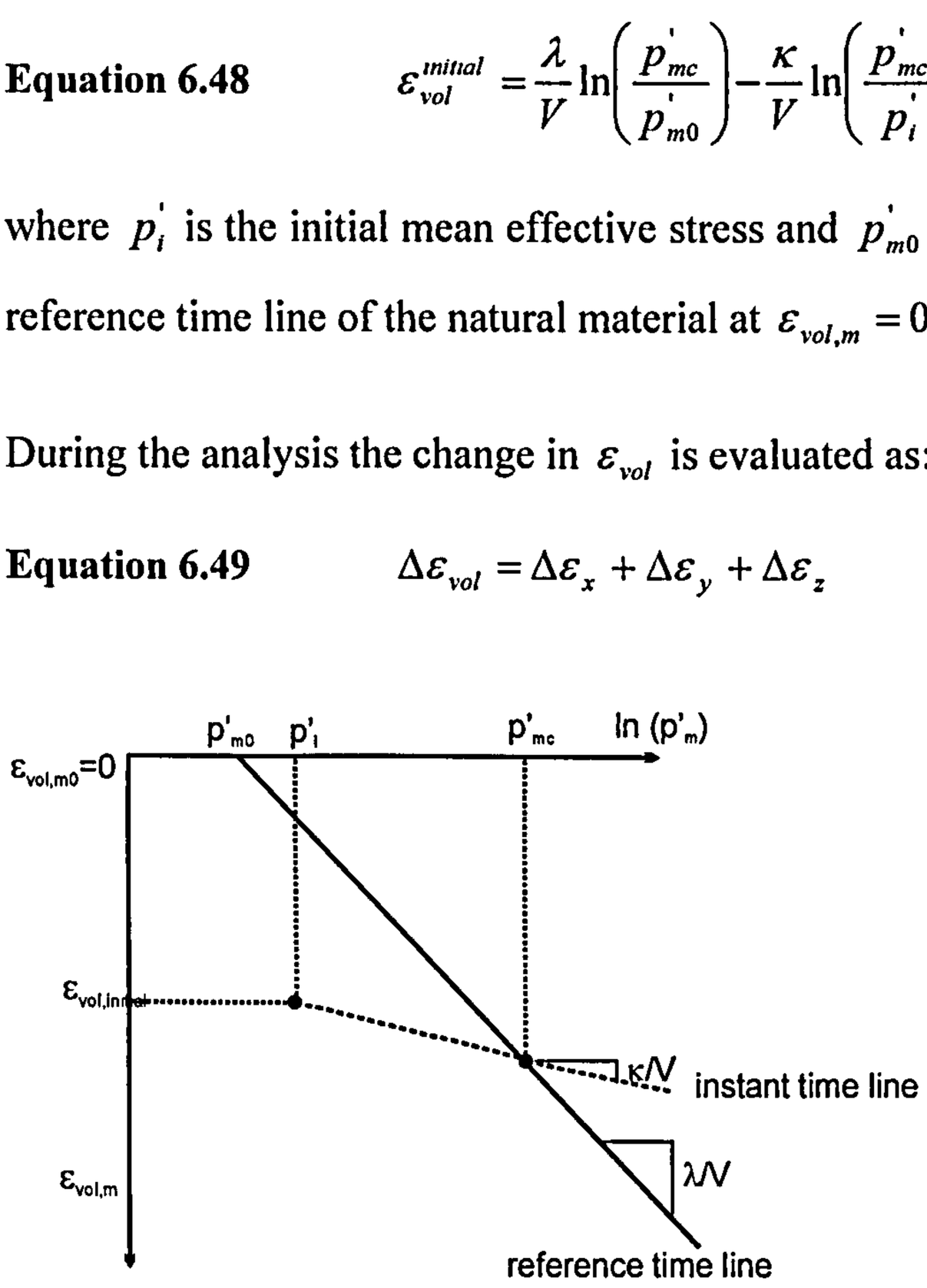

Figure 6.4: Schematic diagram of the calculation of the initial value of ε_{vol}

6.4 Model parameters

The model requires a total of 15 parameters, which are listed in Table 6.1. In addition to these model parameters, the user is required to specify the initial stress conditions, the initial void ratio, e_0 and the overconsolidation ratio, OCR so that the initial value of the plastic hardening parameters may be evaluated as described in Section 6.3.5.

In this section, the model parameters are described focusing on their physical meaning and the manner in which their values can be determined from common laboratory tests.

Table 6.1: Equivalent time model parameters.

Model Parameter	Units	Description
$p_{mi0}^{'}$	kPa	Mean effective stress at $\varepsilon_{vol,m} = 0$ on the intrinsic reference time line.
λ/V	-	Slope of the reference time line in $\varepsilon_{vol} - \ln p^{'}$ space.
κ/V	-	Slope of the instant time line on $\varepsilon_{vol} - \ln p^{'}$ space.
μ or G or $G/p^{'}$	- kPa -	A second elastic parameter that can be either the Poisson's ratio μ, the elastic shear modulus G or the normalized shear modulus $G/p_{mc}^{'}$, which results in a stress dependent shear modulus.
α_f	-	Loading surface parameter
μ_f	-	Loading surface parameter
M_f	-	Loading surface parameter
α_g	-	Plastic potential parameter
μ_g	-	Plastic potential parameter
M_g	-	Plastic potential parameter
ψ_0/V	-	Time dependent parameter
t_0	unit of time	Reference time; it should be expressed in the same units as that used to define the analysis time increments and permeability (in coupled consolidation analyses only).
$\varepsilon_{vol,m,Limit}^{vp}$	-	Limit for the amount of volumetric visco-plastic strain.
p_{s0}	kPa	Initial increase in $p_{mi0}^{'}$ due to structure, defining the position of the reference time line of the natural material.
ρ_s	-	Parameter that controls the rate of destructuration

Parameters λ/V *and* κ/V

The equivalent time constitutive model is formulated in ε_{vol}-*lnp' space*, assuming that λ/V and κ/V are model parameters and soil constants. In contrast, in many other critical state models the soil compressibility is determined in *V –lnp' space* assuming that λ and κ are constants. Therefore both options have been included during the model implementation and they are compared subsequently. Figure 6.5 and Figure 6.6 show the compression curves obtained from constant rate of strain tests on two samples with different initial specific volumes, such that $V_{0A} > V_{0B}$ for the two options, using small and large displacement theory, respectively.

Considering first the case when small displacement theory is employed. When the parameter λ/V is constant then $(\lambda/V)_A = (\lambda/V)_B = \lambda/V$ =*constant* and the compression curves of CRS oedometer tests are straight lines and coincide for the samples A and B in ε_{vol}-*lnp'* space (Figure 6.5a). The change in specific volume or void ratio is then evaluated as:

Equation 6.50 $$\Delta V = \Delta e = \Delta\varepsilon_{vol} \cdot (1 + e_0) = \Delta\varepsilon_{vol} \cdot V_0$$

where V_0 is the initial specific volume (V_0=1+e_0), and the compression curves in *V-lnp'* space are straight lines but with different slopes with $\lambda_A > \lambda_B$ as $V_{0A} > V_{0B}$ (Figure 6.5b).

If instead λ is taken as a constant then the compression curves of CRS tests on samples A and B in ε_{vol}-*lnp'* space are different, with an initial slope $(\lambda/V)_{0A} < (\lambda/V)_{0B}$ (Figure 6.5c). During compression, the void ratio decreases and the slope of the compression curves in ε_{vol}-*lnp'* space (that is mathematically the current value of λ/V) increases as shown in Figure 6.5 c). The change in specific volume is calculated using Equation 6.50 and the resulting compression lines in *V-lnp' space* are schematically shown in Figure 6.5d).

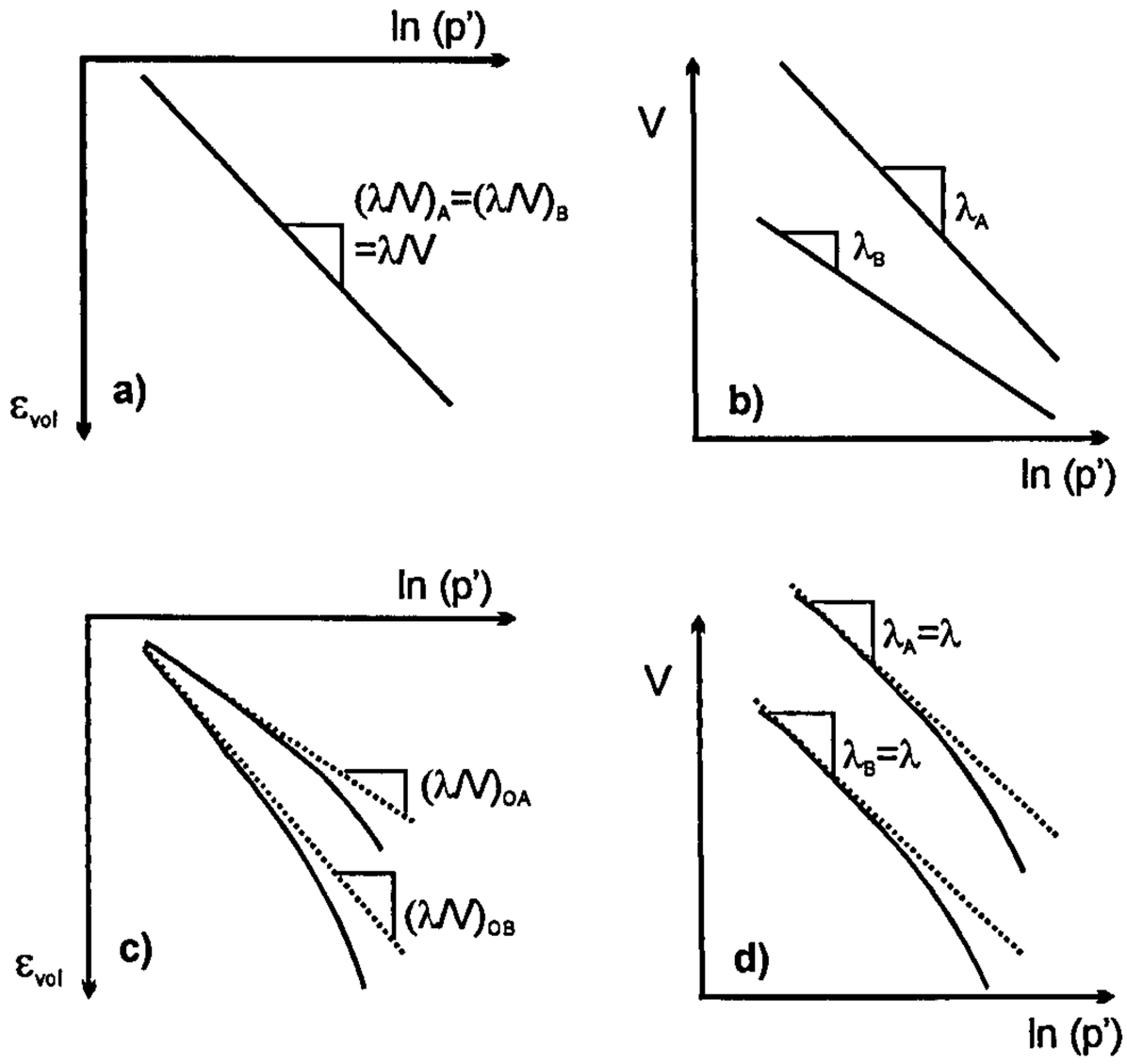

Figure 6.5: Schematic compression curves from CRS oedometer tests assuming either λ/V or λ constant – small displacement theory.

Considering now the case when large displacement theory is employed. If λ/V is taken as a constant value then the compression curves of CRS tests on samples A and B are straight lines with the same slope λ/V in ε_{vol}-*lnp'* space (Figure 6.6a). The change in specific volume is now given by:

Equation 6.51 $$\Delta V = \Delta e = \Delta \varepsilon_{vol} \cdot (1+e) = \Delta \varepsilon_{vol} \cdot V$$

where e is the current void ratio and V is the current specific volume. During compression, with increasing applied stress, the specific volume decreases and so according to Equation 6.51 the change in specific volume associated to a given volumetric strain increment $\Delta \varepsilon_{vol}$ decreases with increasing stress level. This leads to a decreasing slope of the compression curves in *V-lnp'* space as shown in Figure 6.5b). This is consistent with the fact that the condition of zero void ratio is approached asymptotically with increasing applied stress.

If λ is taken as a constant the behaviour will be qualitatively identical to that reported above when considering small displacement theory, and the compression curves of CRS tests on samples A and B will be curved concave downwards both in ε_{vol}-*lnp'* and *V-lnp'* space.

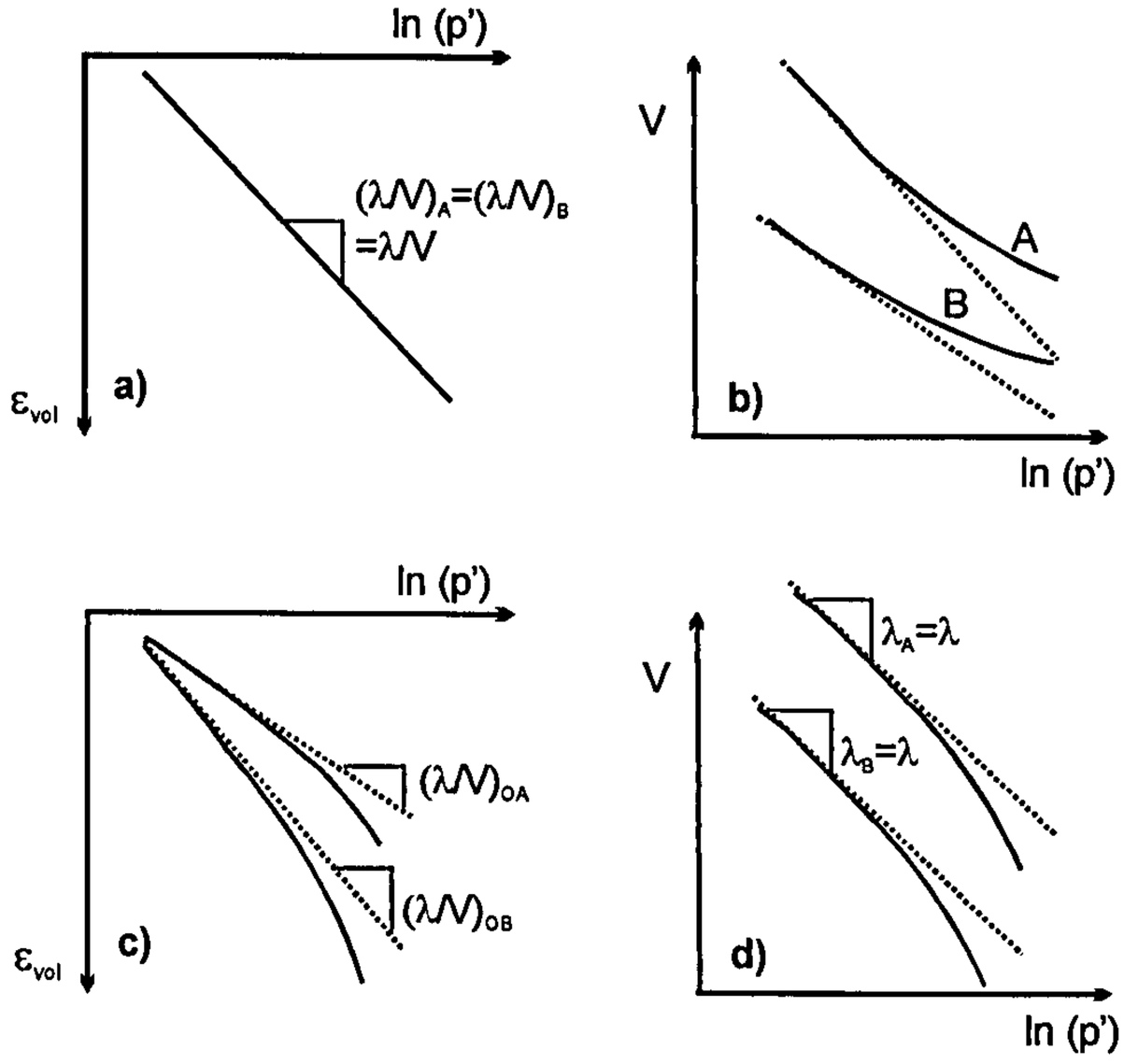

Figure 6.6: Schematic compression curves from CRS oedometer tests assuming either λ/V or λ constant – large displacement theory.

From the above discussion, it can be concluded that the option of considering λ/V constant should always be adopted, when using either small or large displacement theory, and that in the Equivalent Time model the parameter λ does not have the same meaning as in other critical state type models, where λ is the inclination of the critical state line in *V-lnp'* space. For compatibility, κ/V should also be taken as a constant.

The value of the parameters λ/V and κ/V can be evaluated from an oedometer test, either a CRS or an IL test. When deriving the parameters from a test on an undisturbed sample, the parameters can be determined directly from the compression curve in ε_{vol} - *lnp'* space. The parameter λ/V is the slope of the compression curve in ε_{vol} - *lnp'* space, in the normally consolidated range after full destructuration (i.e. the intrinsic value) and the parameter κ/V should be determined as the average slope of an unloading – reloading loop. It is unadvisable to use the recompression data at the start of the test to determine the quantity κ/V as at low stress levels the data is significantly affected by the apparatus compliance.

If the parameters have to be derived from a reconstituted sample the user should be aware that the sample's initial void ratio may be much higher than that in situ. In this case it is recommended, as a first approximation, to evaluate the value of λ and κ from

the loading / unloading / reloading compression curve in *V-lnp'* space and then compute λ/V and κ/V using a specific volume representative of that in-situ (see Figure 6.5 a) and b)).

Second elastic parameter

The elastic part of the model is characterized by a stress dependent bulk modulus, K defined by Equation 6.25. To fully characterize the isotropic elastic response of the soil a second elastic parameter is required, and the user is free to input either the Poisson's ratio μ, the elastic shear modulus G or the normalized shear modulus G/ p' (where p' is the current mean effective stress). If a value of Poisson's ratio, μ is prescribed then the current elastic shear modulus is computed as:

Equation 6.52
$$G = K \cdot \frac{3}{2} \cdot \frac{(1-2\mu)}{(1+\mu)}$$

where K is the current elastic bulk modulus.

Parameters α_f α_g, μ_f, μ_g, M_f *and* M_g

The parameters α, μ and M characterize the shape of the loading surface or plastic potential in general stress space. In principle, two sets of parameters giving a total of six parameters are required, one set referring to the loading surface and characterized by the subscript *f* and the other set for the plastic potential surface and characterized by the subscript *g*. If the parameters are set such that $\alpha_f = \alpha_g$, $\mu_f = \mu_g$ and $M_f = M_g$ then the loading surface and the plastic potential are identical and the model is said to be associated.

The parameter *M* is mathematically equal to the value of g(θ) in triaxial compression (with θ=-30°) corresponding to the stress ratio at which the tangent to the loading or plastic potential surface is horizontal and thus parallel to the mean effective stress axis. The parameter *M* can be related to the angle of shearing resistance φ' through Equation 6.40.

The parameters α and μ control the shapes of the loading and plastic potential surfaces in the *J-p'* stress space. The parameters are determined by fitting experimental

data, more specifically, the stress paths during undrained triaxial compression and extension tests, noting the restrictions to the parameter values mentioned in Section 6.3.3. By suitable selection of the values of α and μ, the model is able to reproduce a wide range of surfaces published in the literature (Lagioia et al., 1996), e.g. the MCC model ellipse is recovered by setting α=0.4 and μ=0.9.

Time dependent parameters t_0, ψ_0/V *and* $\varepsilon_{vol,m,Limit}^{vp}$

The parameter t_0 is the real time associated with the reference time line, and corresponds to the start of what is conventionally defined as secondary consolidation (see e.g. Equation 6.4 or Equation 6.18). Given that the reference time line is in general defined based on IL 24-hour oedometer tests the parameter t_0 is then set equal to 1 day = 24 hours. The parameter t_0 must be expressed in the same units as those used to describe the duration of the analysis increments and other soil properties.

The parameter ψ_0/V together with the parameter t_0 define the visco-plastic volumetric strain rate on the reference time line as follows:

Equation 6.53 $$\left(\dot{\varepsilon}_{vol,m}^{vp}\right)_{t=t_0} = \frac{\psi_0}{V \cdot t_0}$$

The above equation can be used to determine the value of the parameter ψ_0/V (once the value of t_0 has been determined) in cases when there are measurements of the strain rate at the end of the load increments in a IL oedometer test. However, given the scatter in strain rate measurements that are expected from commercial oedometer tests this procedure is not recommended, because a small scatter in terms of strain rate (maybe up to an order of magnitude) results in a wide range of values in the parameter ψ_0/V. A more accurate approach is to derive the parameter ψ_0/V from compression data obtained during a load increment in the normally consolidated range that, ideally, is extended beyond the time t=t_0. The parameter ψ_0/V is then mathematically the slope of the consolidation curve in ε_{vol} *-ln(t)* space at a time $t=t_0$.

Considering the definition of the coefficient of secondary consolidation $C_{\alpha e}$ and the fact that in engineering practice the value of $C_{\alpha e}$ is in general determined from IL 24

hour oedometer tests - and thus evaluated close to the condition $t=t_0$ - then the value of ψ_0 can be calculated as a function of $C_{\alpha e}$:

Equation 6.54
$$C_{\alpha e} = \frac{\Delta e}{\log t_2 - \log t_1} = \frac{\Delta e}{\Delta \log t} = \frac{\Delta e}{\ln 10 \cdot \Delta \ln t} = \frac{\psi_0}{\ln 10}$$

Or in a different form:

Equation 6.55
$$\frac{\psi_0}{V} = \frac{C_{\alpha e} \cdot \ln 10}{V}$$

In Chapter 2, it was noted that there is a strong interaction between viscous effects and soil structure, with the degree of soil structure affecting the magnitude and the type of viscosity. Therefore, the above time-dependent parameters should be evaluated from oedometer tests on undisturbed samples.

The parameter $\varepsilon^{vp}_{vol,m,Limit}$ is defined as the volumetric visco-plastic strain that is reached at infinite creep time under constant effective stress, and therefore ideally it should be derived from an infinite long creep test. Yin et al. (2002) suggest that in the absence of a long creep test the value of $\varepsilon^{vp}_{vol,m,Limit}$ can be evaluated as:

Equation 6.56
$$\varepsilon^{vp}_{vol,m,Limit} = \frac{e_0}{1+e_0}$$

where e_0 is the initial void ratio. The value obtained from Equation 6.56 corresponds to the volumetric strain required to reach the situation when voids no longer exist in the soil. It is noted that if the parameter $\varepsilon^{vp}_{vol,m,Limit}$ is given the value computed from Equation 6.56 then the non-linear logarithmic creep law yields predictions very similar to that of a linear logarithmic creep law, for time intervals of interest to engineering practice. To model the soil creep non-linearity the parameter $\varepsilon^{vp}_{vol,m,Limit}$ must be given values considerably lower. In ICFEP, the parameter $\varepsilon^{vp}_{vol,m,Limit}$ can be defined in two different ways, either as a proportion of the value given by Equation 6.56 or as an absolute value of volumetric strain.

Parameters p'_{mi0}, p_{s0} *and* ρ_s

The parameter p'_{mi0} is the mean effective stress at $\varepsilon_{vol,m} = 0$ on the intrinsic reference time line, i.e. the reference time line of the reconstituted unstructured soil. Given that the model response is determined by the relative position of the current stress state to the reference line and not the absolute value of volumetric strain (see Equation 6.29) then the value of p'_{mi0} may be considered arbitrary. This applies when the soil is assumed to have no structure (p_{s0} =0), in which case the reference time line of the reconstituted and natural material coincide ($p'_{mi0} = p'_{m0}$) and the position of the reference time line does not change during the analysis procedure.

When the soil is considered to have an initial structure then the position of the current reference time line is defined by the quantity $p'_{m0} = p'_{mi0} + p_s$ where the value of p_s varies during the analysis procedure (according to Equation 6.43) from the value p_{s0} at the start of the analysis to a value close to zero attained at very large visco-plastic volumetric strains. Consider a soil element being isotropically consolidated along the reference time line; during compression in the NC range the soil element develops significant visco-plastic volumetric strains and the quantity p_s decreases mimicking the soil destructuration.

The soil structure may be evaluated as the distance between the intrinsic and the natural reference compression line in ε_{vol} *-lnp'* (or *V-lnp'*) space, or more commonly by the ratio between the stress on the natural compression line and that on the reconstituted material at a given void ratio or volumetric strain value. From Figure 6.7 that ratio can be computed as:

Equation 6.57
$$\frac{p'_{natural}}{p'_{Intrinsic}} = \frac{p'_{m0}}{p'_{mi0}} = 1 + \frac{p_s}{p'_{mio}}$$

where $p'_{natural}$ is the mean effective stress on the reference time line of the natural material and $p'_{Intrinsic}$ is the mean effective stress on the intrinsic time line at the same volumetric strain. Similarly, the volumetric deformation associated with the complete

loss of structure that occurs associated with the movement of the stress point from the natural to the intrinsic reference time line can be evaluated as:

Equation 6.58

$$\Delta\varepsilon_{vol} = \frac{\lambda}{V}\ln\left(1+\frac{p_s}{p'_{mi0}}\right)$$

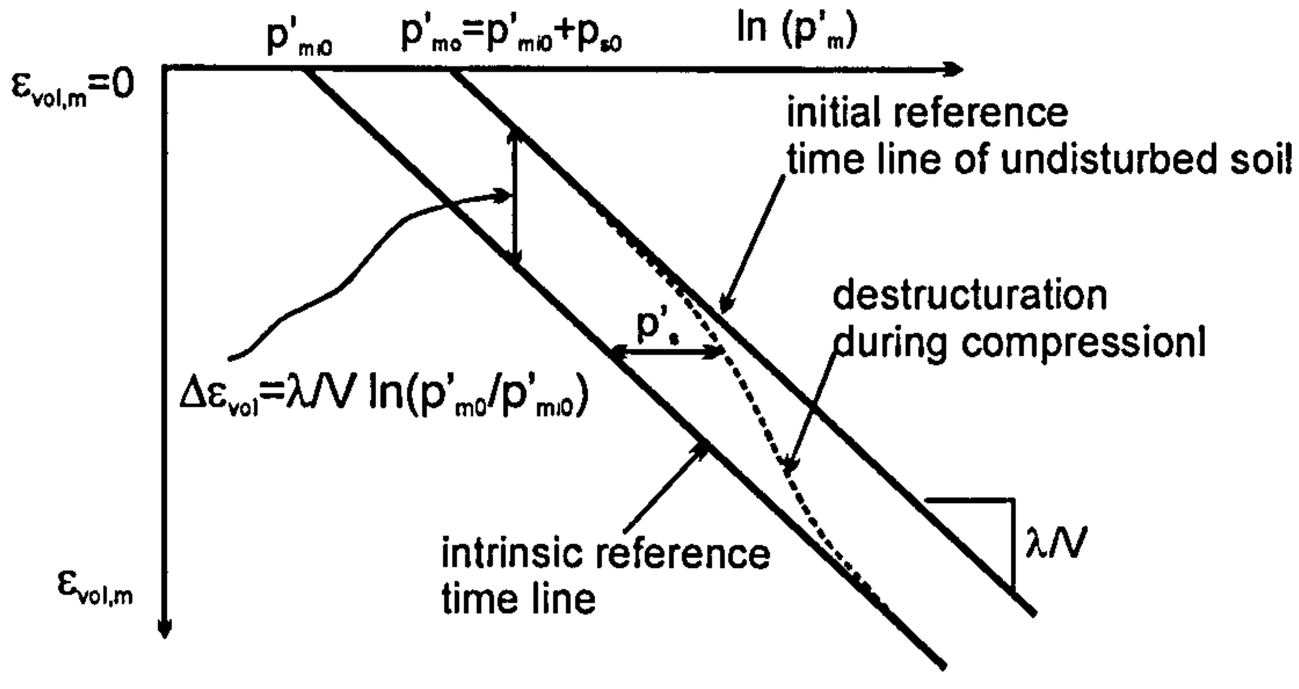

Figure 6.7: Framework for the consideration of soil structure.

Therefore, the initial soil structure is not characterized by the absolute value of p_{s0} but by the ratio p_{s0}/p'_{mi0}. If the remaining model parameters have been previously defined then the values of p_{s0} and ρ_s can be determined by curve fitting a 1D oedometer compression curve obtained from a natural sample that has been consolidated up to full destructuration.

The Equivalent Time model requires a total of 15 parameters, however if the loading surface is assumed to be identical to the plastic potential, as it is commonly done, then the number of model parameters is reduced to 12. In addition, if the soil structure is thought to be reasonably stable and/or not to dominate the soil compressibility and strength characteristics then the parameters p_{s0} and ρ_s can be set equal to zero. The model parameters can be derived from common laboratory tests preferably on undisturbed samples: one IL 24 hours oedometer test and one, ideally two, consolidated undrained triaxial tests, one in compression and one in extension.

From the compression curve of the IL 24 hours oedometer test, it is possible to compute directly the value of the parameters λ/V and p'_{mi0}. Ideally, the oedometer test should include an unloading – reloading loop from which the parameter κ/V can be evaluated

and a longer load increment to extrapolate a reliable value of $\varepsilon^{vp}_{vol,m,Limit}$. Being a IL 24 hour oedometer, the parameter t_0 may be set equal to 1day = 24 hours and the parameter ψ_0/V can be evaluated from the consolidation curves of the various load increments, and is mathematically the slope of the curve ε_{vol}-*ln t* space at $t=t_0$ (as discussed previously it would be an advantage if this load step is extended, so that an accurate evaluation of gradient can be done).

The parameter M (assuming $M=M_f=M_g$) can be determined directly from a consolidated undrained triaxial compression test and the parameters α (assuming $\alpha=\alpha_f=\alpha_g$) and μ ($\mu=\mu_f=\mu_g$) can be determined by curve fitting of the respective stress path, so that the model predicts correctly the peak undrained strength in compression. It is noted that the shape of the failure surface and plastic potential in the deviatoric plane is predefined, following the Matsuoka-Nakai criterion. Therefore, if the model parameters α and μ are calibrated to recover the peak undrained strength in compression the value of undrained strength under other shearing modes (different θ values) is then defined. Comparison between the model predictions and the laboratory data from a consolidated undrained triaxial extension test will enable the user to assess the error involved. If the constitutive model is to be employed in the analysis of a boundary value problem in which the soil is subjected mainly to unloading (e.g. excavation problem) then it is recommended to evaluate the parameter α and μ such that the model recovers well the undrained strength in triaxial extension.

When analysing a boundary value problem, the initial void ratio (or specific volume) is, in general, found to vary with depth. To evaluate the influence of adopting a varying initial void ratio, within the same soil stratum, three samples with the following characteristics are considered:

Sample A	**Sample B**	**Sample C**
e_0=1.5	e_0=2.5	e_0=2.5
λ/V =0.088	λ/V =0.062857	λ/V =0.088
κ/V =0.0088	κ/V =0.0062857	κ/V =0.0088

The remaining ET model parameters are identical for the three samples. A set of single element FE analyses was carried out during which the three samples were subjected to

.an IL 24 hour oedometer test with a load increment ratio $\Delta\sigma_v / \sigma_v$ equal to unity, and starting from a K_0 normally consolidated stress state with σ'_{vi}=10 kPa. The analysis results are shown in Figure 6.8 in ε_{vol}-lnp' and e- ln p' space. Another set of single element FE analyses was carried out during which the same three samples were subjected to undrained triaxial compression tests at a constant axial strain rate equal to 10%/day, starting from an isotropic normally consolidated stress state with p'=100 kPa. The predicted stress paths in *J-p'* space are shown in Figure 6.9. From the above results the following can be observed:

a) As the ET model is formulated in ε_{vol}-lnp' space a change in the initial void ratio of the soil has no influence on the model response (strength and stiffness) provided that the model parameters (including λ/V and κ/V) and the initial stress conditions are the same – samples A and C. If the same void ratio is adopted throughout a soil stratum, the ET model will predict an increase of the undrained strength with depth, as the initial soil state at each depth is evaluated from the initial stress conditions (that will vary with depth) and the overconsolidation ratio.

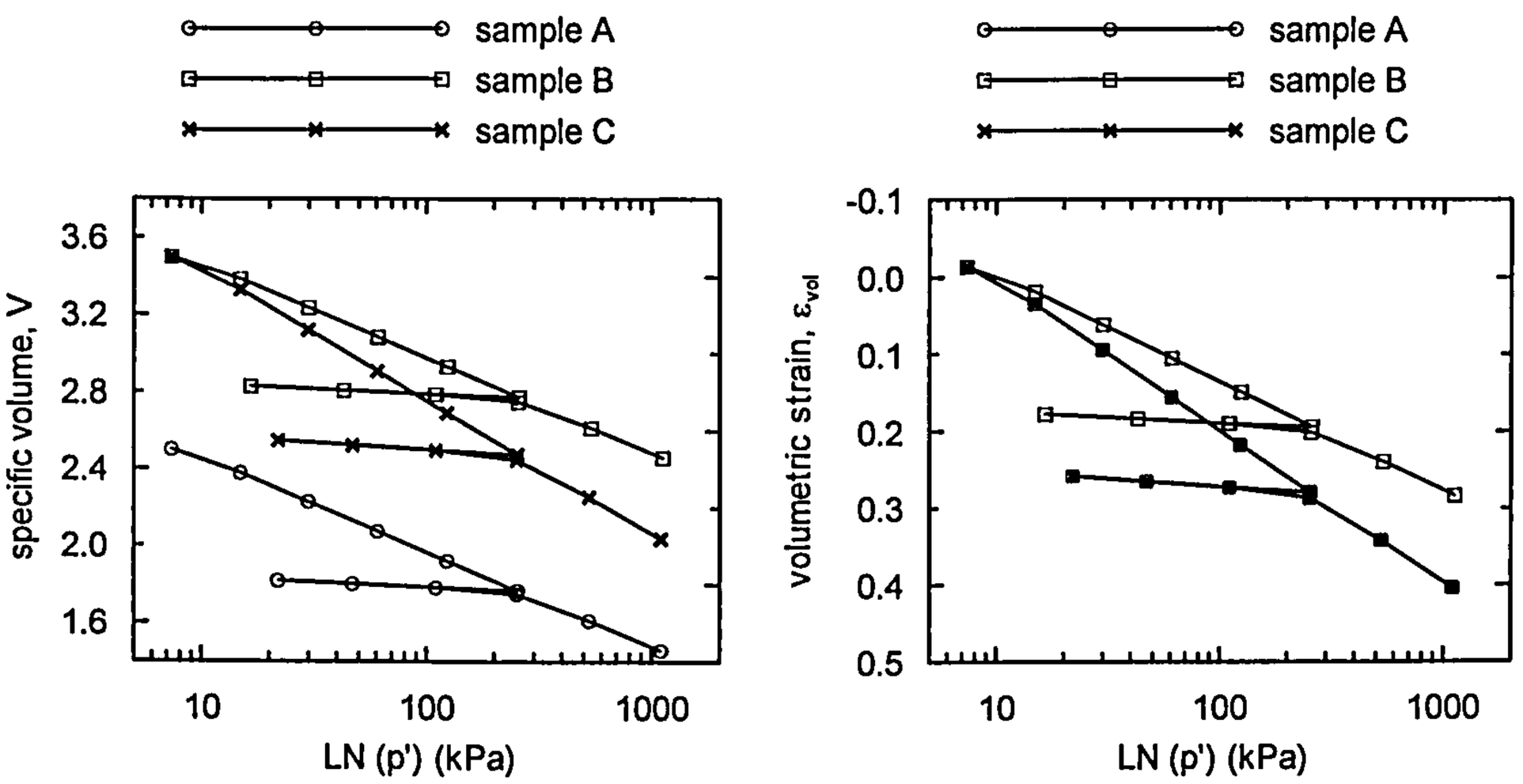

Figure 6.8: ET model predictions of IL 24hour oedometer tests on samples A to C.

b) In some situations, it may be necessary to input a specific profile of void ratio with depth, e.g. when a void ratio dependent permeability is being employed. Then there is an apparent inconsistency as the compression curves obtained from oedometer tests on samples A and C are characterized by a different slope in *V-lnp'* space, and this is the format more commonly employed in the literature to describe the soil compressibility. However, according to the ET model the slope of the compression curve in *V-lnp'* space is not a soil constant, as it happens in most of the classical critical state models e.g. Cam Clay and Modified Cam Clay models, and instead will vary with the soil initial void ratio, for a given set of model parameters.

c) The user may be tempted to change the values of the parameters λ/V and κ/V such that the slope of the virgin compression line in *e-lnp'* space is the same in samples A and B. This methodology may be appropriate to simulate samples within the same stratum with different initial void ratio under such simple stress paths as isotropic and 1D compression in *V-lnp'* space, as the compression curves predicted for samples A and B are found to be parallel and separated by the difference in initial void ratio. However, samples A and B have different model parameters and therefore will in principle yield a different response, for example when subjected to undrained triaxial compression, the sample B yields a undrained strength 10% higher than that of sample A.

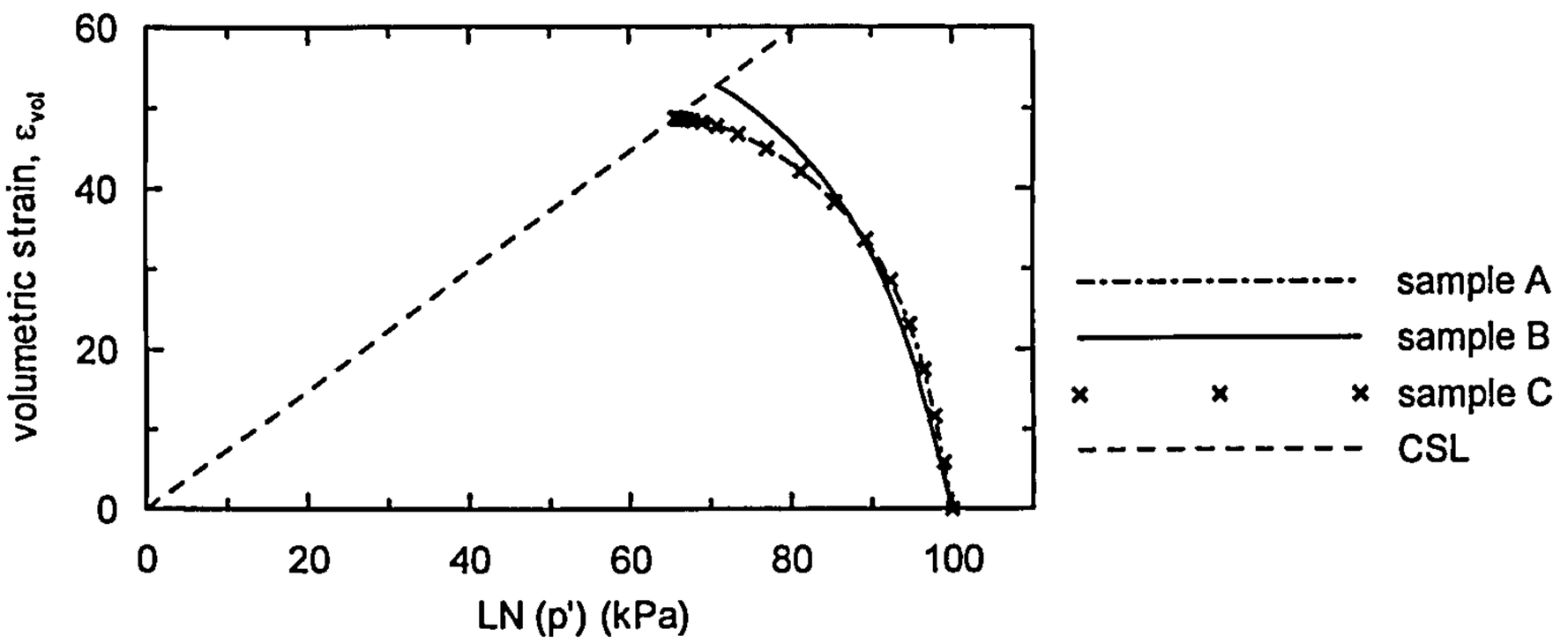

Figure 6.9: ET model predictions of the stress path in J-p' space during undrained triaxial compression tests performed with an axial strain rate of 10%/day on samples A to C.

6.5 Validation

The validation of the Equivalent Time (ET) model consists of a series of finite element analyses to investigate the model performance under a variety of stress and strain paths.

In their majority, the analyses mimic common laboratory tests and the analysis results are compared with the observed experimental trends, as reported in Chapter 2. Such a comparison enables the strengths and weaknesses of the ET model, for describing the main features of the time dependent behaviour of clays, to be identified. In Section 6.6, the ET model is used to simulate a series of laboratory tests on Hong-Kong marine deposits, and the ability of the model to mimic the behaviour of a real soil is assessed.

6.5.1 Model parameters

The FE analyses presented in Section 6.5 are performed using the model parameters listed in Table 6.2. The model parameters have been given values typical of a soft clay and as a rule are identical or equivalent to those employed in the analyses reported in Chapter 5.

Table 6.2: Model parameters for the validation analyses.

e_0	$M_f=M_g$	λ/V	κ/V	G	ψ_0/V	k (3)
-	-	-	-	kPa	-	m/s
1.5	1.2872	0.088	0.0088	1700.0	0.00521	$1x10^{-9}$
t_0	$\varepsilon^{vp}_{vol,m,Limit}$ (1)	$\alpha_g=\alpha_f$	$\mu_g=\mu_f$	p'_{mio}	p_{s0}	ρ_s
day	-	-	-	kPa	kPa	-
1.0	0.6/0.06	0.4	0.9	10.0	*(2)*	*(2)*

Notes:

(1) If nothing stated to the contrary the analyses assumed $\varepsilon^{vp}_{vmLimit}=0.6=e_0/(1+e_0)$.

(2) If nothing stated to the contrary the analyses assume $p_{s0}=0.0$ *and* $\rho_s=0.0$.

(3) Only used in the coupled consolidation analyses.

The parameter ψ_0/V was calculated using Equation 6.55 with a value of $C_{\alpha e}$ equal to 0.03 typical of soft inorganic clays. Assuming that the reference time line was defined from an IL 24 hour oedometer test the reference time t_0 is taken equal to 1 day (or 24 hours), and the visco-plastic volumetric strain rate on the reference time line (calculated

using Equation 6.53) is equal to 0.005211/day. This is the main difference in relation to the model parameters employed in the analyses presented in Chapter 5, in which the value adopted for the volumetric strain rate on the reference time line (a model input parameter) was equal to 0.00864/day corresponding to $C_{e\alpha}$ =0.03 and t_0=14.5 hours.

In the majority of the analyses presented subsequently the parameter $\varepsilon^{vp}_{vol,m,Limit}$ is set equal to 0.6, which corresponds to the quantity $e_0/(1+e_0)$ that is the volumetric strain required to reach the condition of no voids in the soil. To investigate the influence of considering the soil creep non-linearity two analyses were carried out in which $\varepsilon^{vp}_{vol,m,Limit}$ is equal to 0.06, a value ten times smaller.

The parameters p_{s0} and ρ_s characterize the initial structure of the soil and the subsequent loss of structure with volumetric visco-plastic straining, respectively. Most of the analyses presented in this section are carried out assuming these two parameters are equal to zero. In a separate set of analyses that mimic CRS oedometer tests the parameters p_{so} and ρ_s are varied independently in order to investigate the performance of the destructuration mechanism included in the ET model.

In clayey soil, delayed excess pore pressure dissipation is in general significant to the overall soil response, both in the laboratory and in the field. However in most of the analyses shown subsequently in this chapter drained conditions are assumed, as this simplifies considerably the analysis procedure and is sufficient to investigate the performance of the effective stress constitutive relationship. The FE analysis mimic *ideal* laboratory tests, in which there is no end effects, no bulging or necking of triaxial samples during shearing or stress localization. Therefore if the soil behaviour is assumed to be drained or undrained the soil sample may be modelled using a single FE element as the stresses are uniform across the sample.

In the analyses presented in Section 6.5.3, the effect of delayed pore water pressure dissipation is considered in which case coupled consolidation analyses are performed and the pore pressure response then results from the combination of the stress-strain soil behaviour and the equations that govern the pore fluid flow (Darcy's Law and the continuity equation, see Chapter 4 for details). In this case, the effective stresses across a sample will not be constant as the excess pore pressure dissipates faster closer to the

drainage boundary. The author has concluded that the analysis results become independent of the number of elements when the number of elements in the direction of flow is equal to or larger than 10 elements for a sample with a single drainage path direction. The permeability properties of the soil are characterized by an isotropic and constant permeability k equal to $1x10^{-9}$m/s.

6.5.2 FE analyses of K_0 stress paths of an unstructured soil

Incremental load 24-hour oedometer tests

Figure 6.10 shows the ET model predictions of a IL 24 hour oedometer test with a load increment ratio $\Delta\sigma_v / \sigma_v^{'}$ equal to unity, obtained by means of drained single element FE analyses using the model parameters given in Table 6.2. In run 1 each load increment is simulated by a single analysis increment with a duration Δt =24 hours. In run 2 each load increment is simulated using two analysis increments; the first with a very small duration Δt=0.1 h, during which the load increment $\Delta\sigma_v$ is applied and the stress path moves instantaneously along the instant time line, and then a second increment with a duration Δt=23.9 h during which the sample deforms at constant applied stress. As would be expected, the two simulations yield the same results at the end of each load increment, showing that the model response depends only on the overall applied strain rate and not on how this is specified in the analyses.

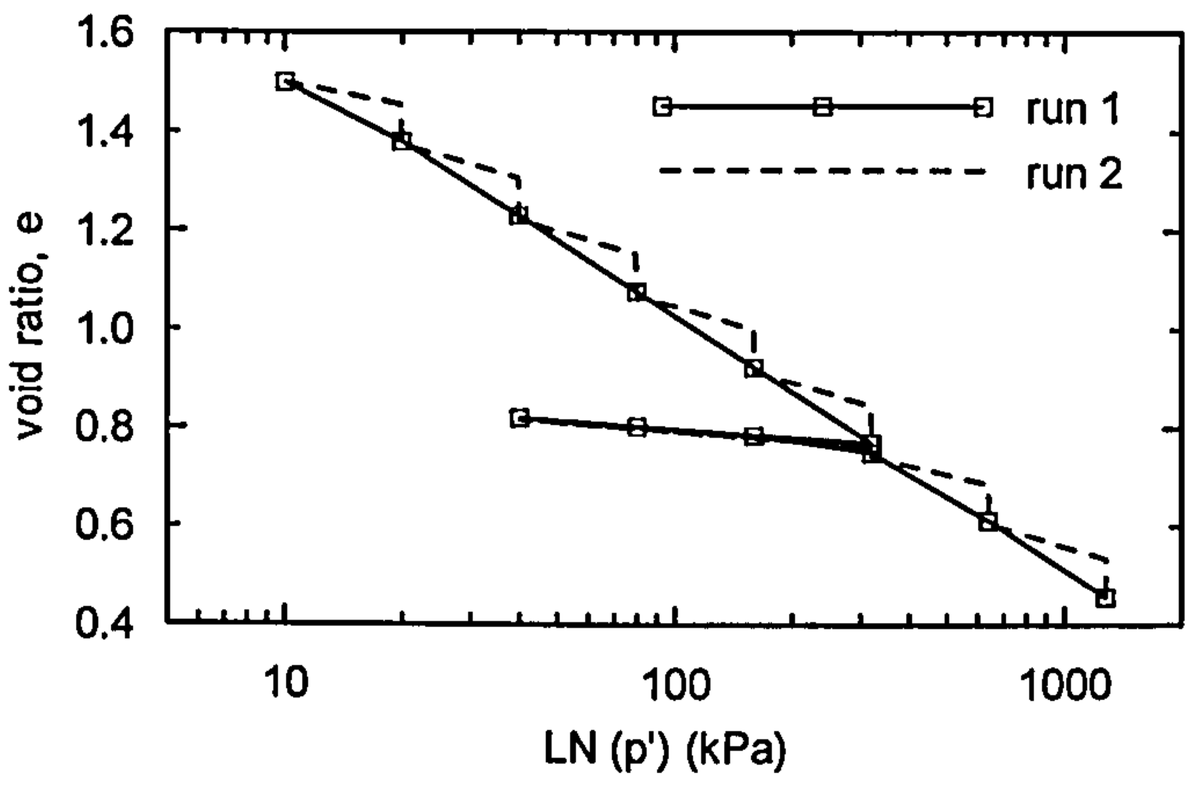

Figure 6.10: Incremental load 24-hour oedometer tests – ET model predictions.

Constant rate of strain tests

Figure 6.11 shows the ET model predictions of a set of CRS oedometer tests at four values of axial strain rate, which have been obtained by means of drained single element FE analysis, where $\dot{\varepsilon}_0$ is equal to 0.00521/day and corresponds to the value of the visco-plastic volumetric strain rate on the reference time line (see Equation 6.53). In addition Figure 6.11 shows the results of a single element FE analysis that simulates an oedometer test during which the volumetric strain rate has been changed in a stepwise manner. The analysis results show that the ET model predicts a single stress-strain-strain rate relationship that is independent of the soil's previous loading history.

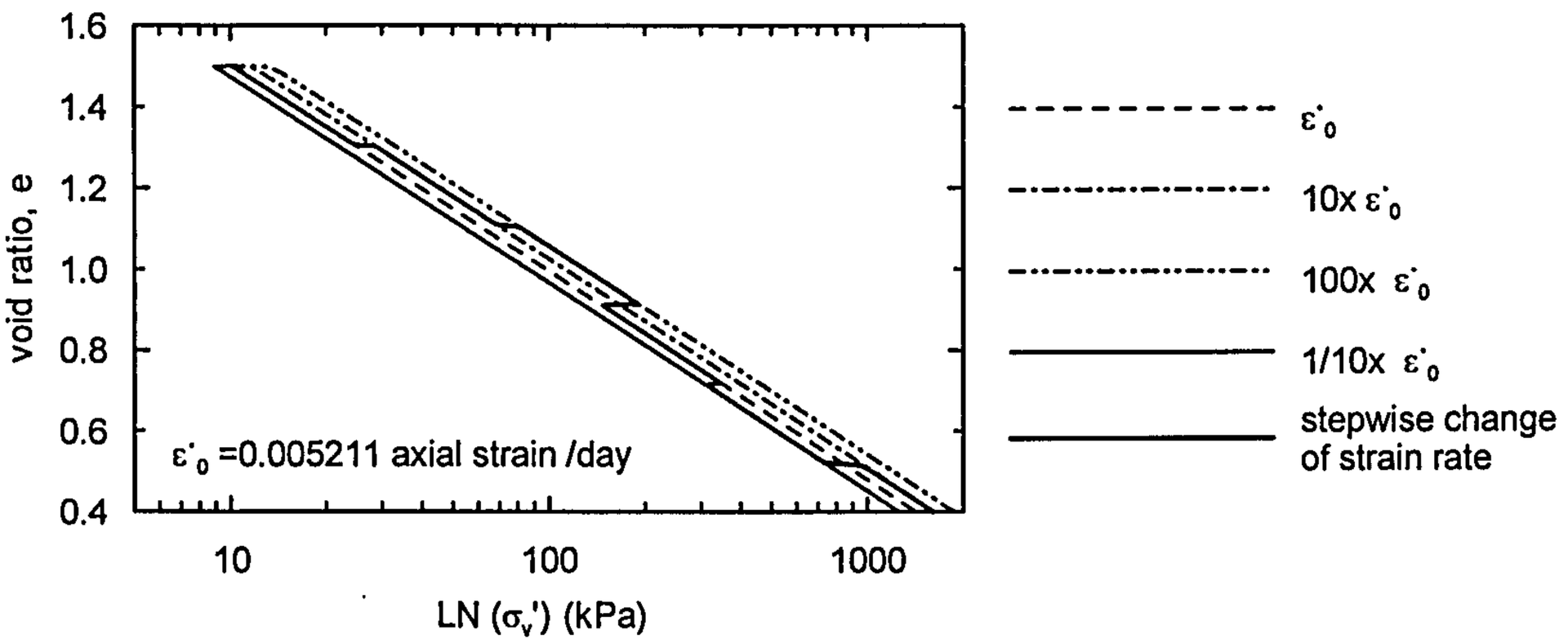

Figure 6.11: Constant rate of strain and stepwise change of strain rate oedometer tests – ET model predictions.

Drained creep tests

Figure 6.12 shows the results of a set of single element FE analyses that simulate CRS oedometer tests. During the otherwise monotonic loading, a long creep period has been introduced and the value of the maintained vertical effective stress is indicated in the legend of Figure 6.12, as well as the applied strain rate prior to the creep period. Following the creep period the samples were loaded at the previous axial strain rate, and the compression curves are found to rejoin the compression curve appropriate to the applied strain rate (Figure 6.12a). As observed experimentally, on reloading, the soil is initially stiff and then the soil gradually yields showing a yield stress well in excess of the magnitude of the stress that it had been subjected to during the creep period.

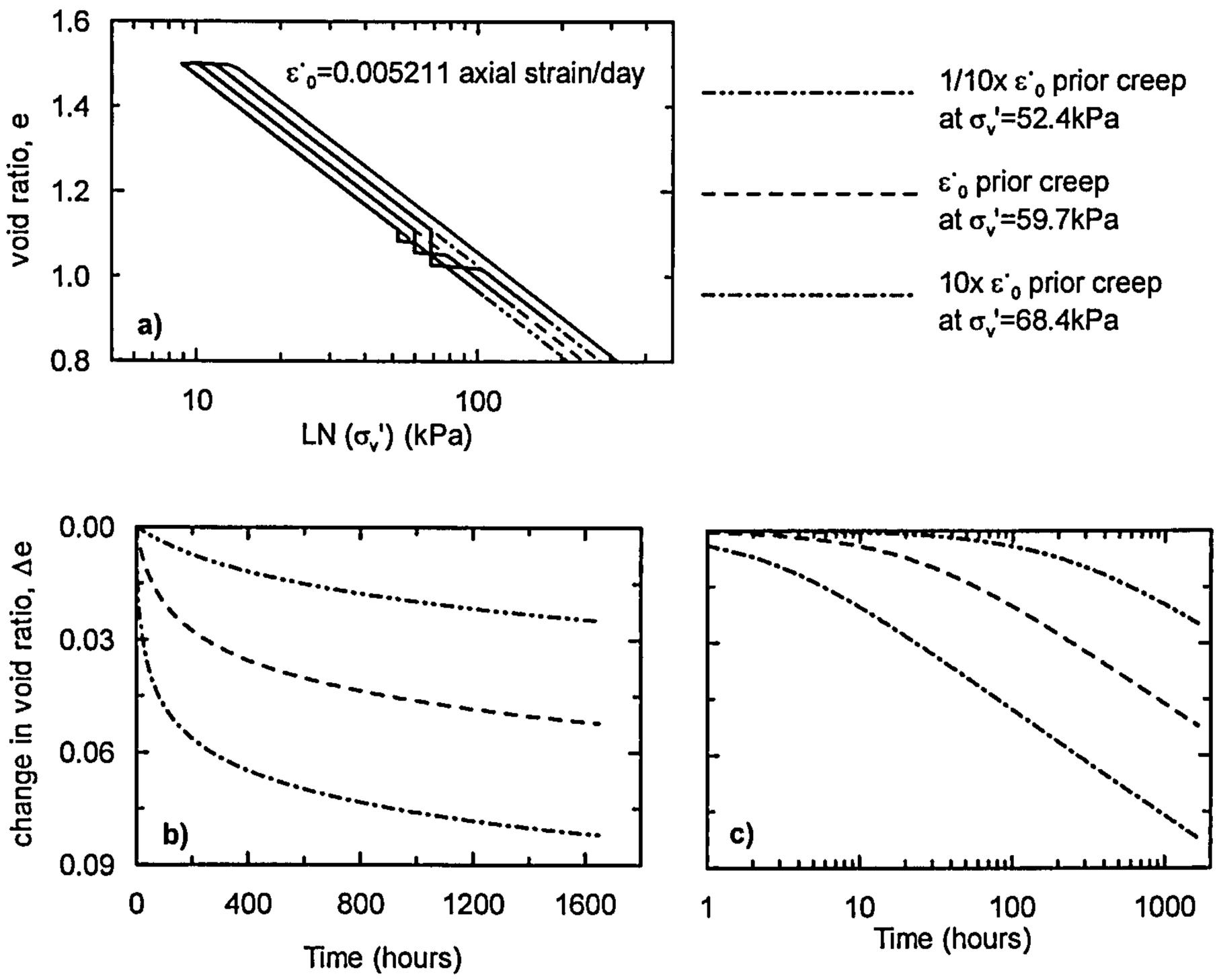

Figure 6.12: Drained creep tests under K0 stress conditions – ET model predictions.

Figure 6.12b) shows the change (decrease) in void ratio with time during the drained creep period, with the time origin being the start of the creep period. The change in void ratio at a given time t is found to increase with the value of the applied axial strain rate prior to creep. The change in void ratio increases monotonically with time, but the rate of change reduces with time. Figure 6.12c) shows the variation in void ratio with the logarithm of creep time. The results show that there is a time delay between the start of the creep period and the establishment of a linear relationship between void ratio change and the logarithm of creep time. This time delay is found to increase for lower values of applied strain rate prior to creep. It is noted that these analyses were carried out assuming $\varepsilon^{vp}_{vol,m,Limit}=e_0/(1+e_0)$ and thus the model yields predictions very close to a linear logarithmic creep law, for the range of creep time values investigated, and those of interest to engineering practice (10 to 100 years).

This can be better appreciated in Figure 6.13, which, in addition to the data of Figure 6.12c), also includes FE results obtained when $\varepsilon^{vp}_{vol,m,Limit}$ is taken equal to 0.06 (i.e. 10% of $e_0/(1+e_0)$) and the prediction of a simple linear logarithmic creep law characterized

by a coefficient of secondary consolidation $C_{\alpha e}$ equal to 0.03 and a creep time origin equal to 24 hours.

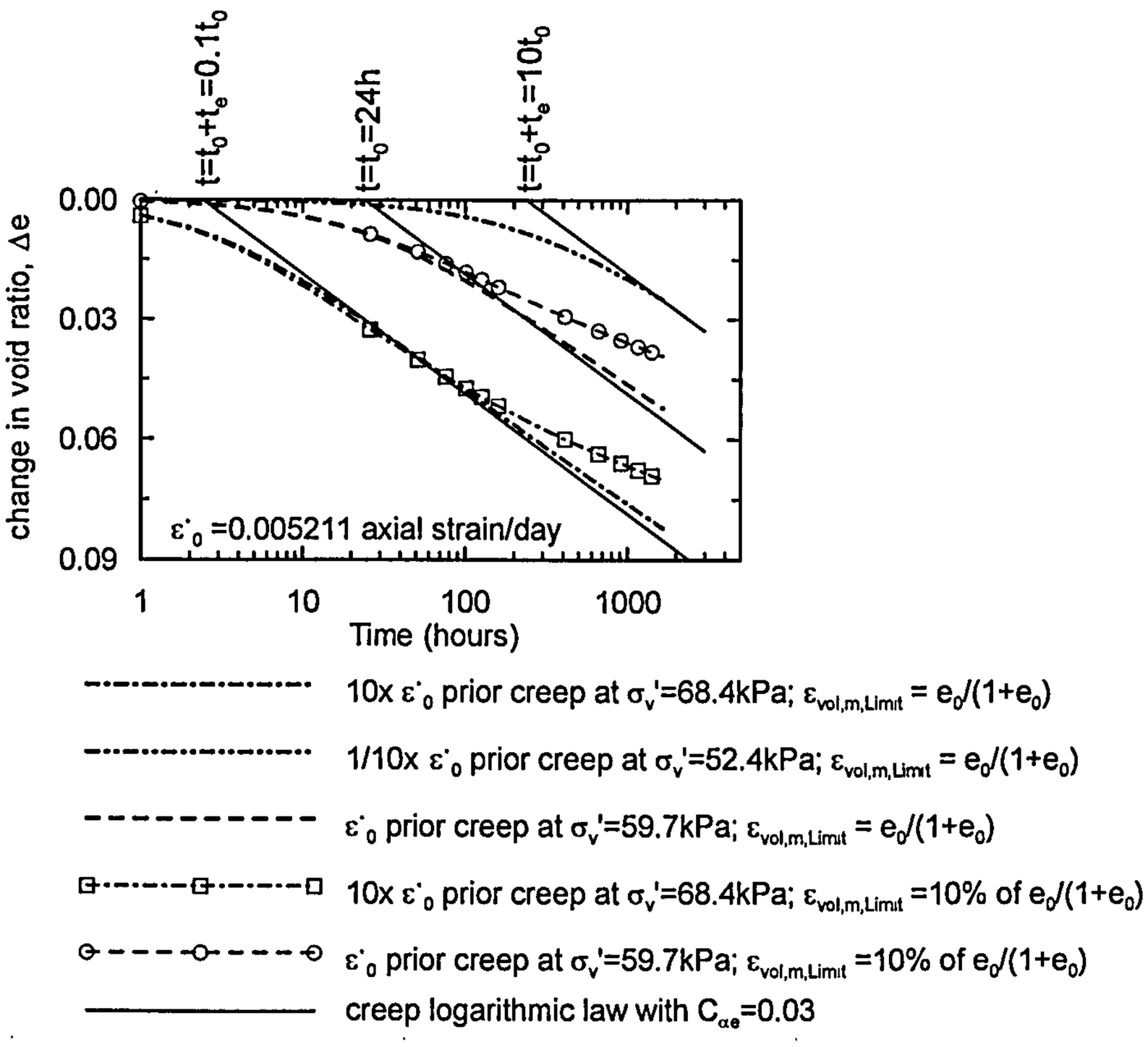

Figure 6.13: Change in void ratio with time during drained creep under K_0 stress conditions: comparison between logarithmic and non-logarithmic creep laws.

When the parameter $\varepsilon^{vp}_{vol,m,Limit}$ is set equal to 10% of $e_0/(1+e_0)$ then the model predictions are found to diverge significantly from the linear logarithmic creep law. The difference increases with increasing creep time as the current value of $C_{\alpha e}$ (or ψ/V) diverges from the value ψ_0/V on the reference time line ($t=t_0$), according to Equation 6.18.

Relaxation tests under K_0 stress conditions

A set of FE analyses was carried out to investigate the model behaviour under stress relaxation. The analyses are similar to those described previously but instead of a creep period, a stress relaxation period was introduced by preventing the vertical deformation of the sample. Figure 6.14 shows the change in vertical effective stress with time during

the stress relaxation period. In a similar manner to the behaviour observed during creep, during stress relaxation there is a time delay between the start of relaxation and the occurrence of significant changes in the soil element vertical effective stress.

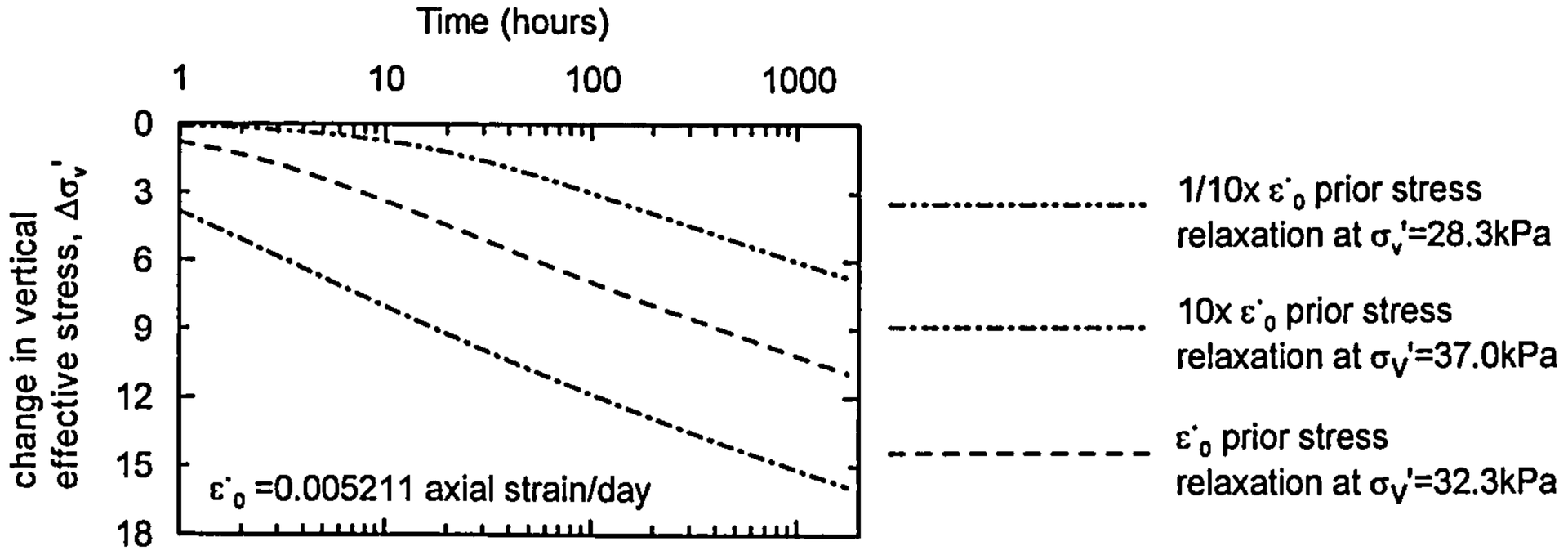

Figure 6.14: Change in vertical effective stress with time during stress relaxation.

As observed experimentally by Lacerda & Houston (1973), this time delay decreases for higher values of applied strain rate prior to stress relaxation and then, following this time delay, the effective stress changes linearly with the logarithm of time. During stress relaxation tests, the total volumetric strain and strain rate are zero, such that the following condition applies:

Equation 6.59 $$\dot{\varepsilon}_{vol}^{el} = \dot{\varepsilon}_{vol}^{vp}$$

where $\dot{\varepsilon}_{vol}^{vp}$ is the visco-plastic volumetric strain rate evaluated by means of Equation 6.27, and $\dot{\varepsilon}_{vol}^{el}$, the elastic volumetric strain rate. From Equation 6.59 the effective stress change predicted during a stress relaxation period depends both on the soil time dependent parameters and the elastic parameters. The ET model uses an elastic bulk modulus that varies linearly with mean effective stress, and correspondingly the slope of the linear portion of the $\Delta\sigma_v'$-*log t* curves are found to increase with the applied vertical effective stress at the start of the stress relaxation period.

6.5.3 Coupled consolidation FE analysis of IL 24 hour oedometer tests on unstructured soil

This section presents ET model predictions of a IL 24 hour oedometer test obtained by means of coupled consolidated FE analyses. The loading history is identical to that employed in the analyses presented in Figure 6.10. The coupled consolidation analyses

mimic an oedometer test with drainage from the top only, and the condition of no flow at the remaining boundaries, implying the existence of a porous stone at the bottom where the excess pore water pressures during the test can be monitored. As mentioned earlier, in coupled analyses the oedometer sample is simulated with 10 elements in the direction of the flow (vertically). The analyses simulate 2cm high samples– the height of conventional oedometer samples – and thicker samples 10 and 20 cm high.

In Figure 6.15, the analysis results are presented in terms of the sample's equivalent vertical effective stress and equivalent void ratio. The equivalent vertical effective stress is calculated assuming a parabolic variation of excess pore water pressure across the sample, such that:

Equation 6.60 $$\sigma'_{v,eq} = \sigma_v - 0.667 \cdot u_b$$

where $\sigma'_{v,eq}$ is the equivalent vertical effective stress, σ_v is the total vertical effective stress and u_b is the pore water pressure at the base. The equivalent void ratio is calculated from the sample's vertical deformation at the top. In the coupled analysis each load increment is simulated using a total of 11 increments; the first with a very small duration Δt=0.1 hour during which the load increment $\Delta\sigma'_v$ is applied and the remaining 10 increments each with a duration Δt=2.39 hours during which the sample consolidates and deforms under constant applied stress (making a total of 24 hours per load increment). Figure 6.15 also shows the results obtained from a drained analysis, in which case each load increment is simulated using a single analysis increment with a duration Δt=24 hours.

For the thin sample (2cm) the equivalent void ratio at the end of each load increment lies consistently very close to that predicted by the drained analysis, at the same equivalent vertical effective stress (implying full excess pore water pressure dissipation in 24 hours) and only at slightly lower void ratio. The resulting compression curve is almost identical. For the 20cm high sample the location of the end points after each load increment, in relation to the compression curve predicted by the drained analysis, varies with stress level during the test, but in general they lie above and to its left (as can be seen from the location of the unloading – reloading loop data) indicating that the excess pore water pressure dissipation is not complete when the next load increment is applied.

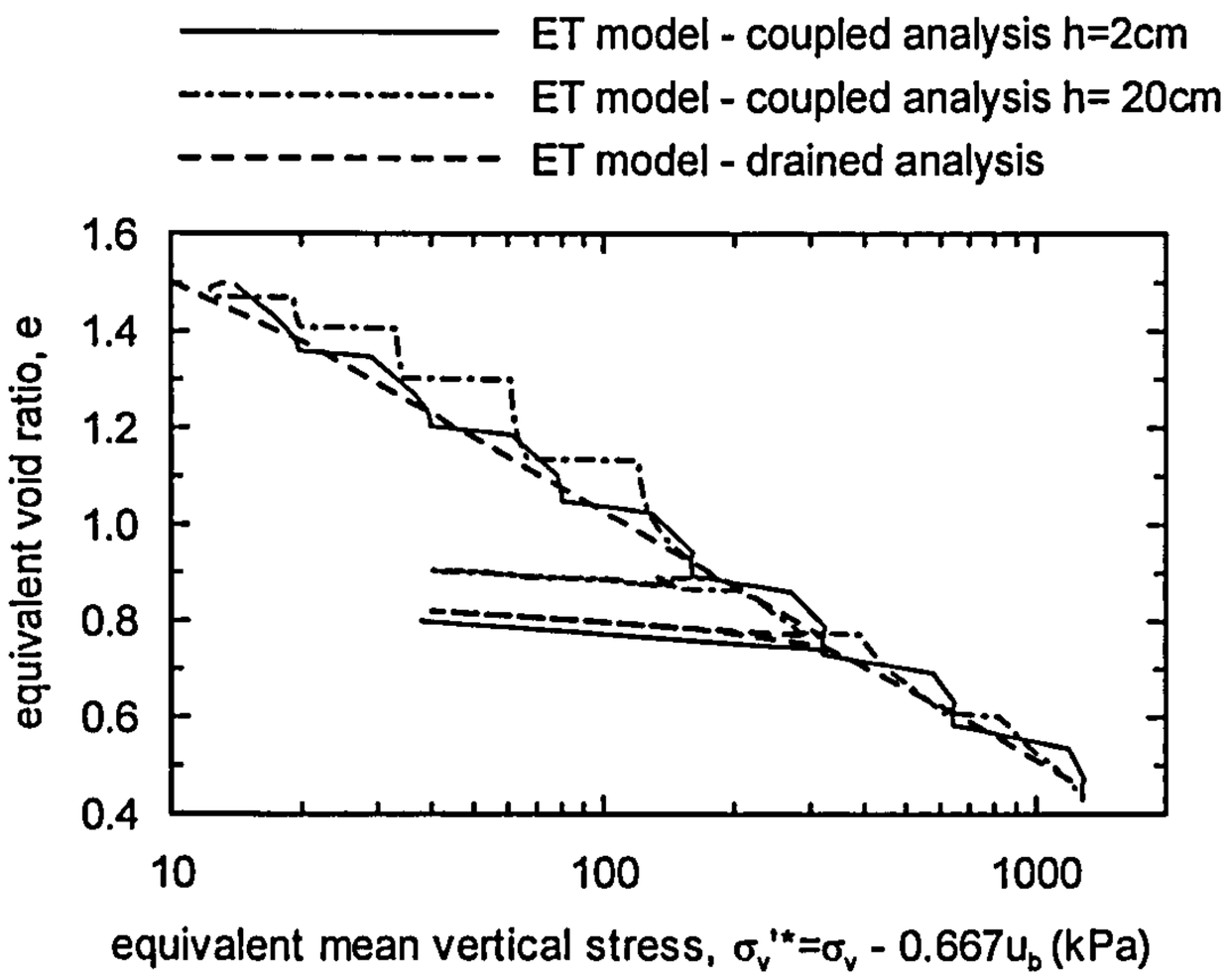

Figure 6.15: Compression curves obtained from coupled consolidated and drained analyses simulating an IL 24 h oedometer.

Figure 6.16 shows the variation of the pore water pressure predicted by the ET model at the base of the samples 2, 10 and 20 cm high, following the application of a vertical stress increment equal to 40 kPa, from a previous K_0 normally consolidated state characterized by a vertical effective stress equal to 40 kPa. Figure 6.16 also shows predictions obtained from similar coupled consolidated analyses in which the soil is modelled using the time independent MCC constitutive model, and the predictions that are obtained by application of Terzaghi's solution for one – dimensional consolidation.

The Terzaghi equation for 1D consolidation requires a single parameter, the coefficient of consolidation c_v defined as:

Equation 6.61
$$c_v = \frac{k_v}{\gamma_w \cdot m_v}$$

where k_v is the soil permeability in the direction of the flow (in this case, in the vertical direction), γ_w is the bulk unit weight of the pore water and m_v is the coefficient of volume compressibility. The results of the Terzaghi equation presented in Figure 6.16 correspond to a value of c_v equal to 5.6×10^{-8} m^2/s (=1.766 m^2/year) which has been obtained by curve fitting the MCC results. This value is however very close to the value determined from Equation 6.61 with the soil parameters used in the analyses. For details

on the Terzaghi solution of 1D consolidation please refer elsewhere e.g. Terzaghi and Peck (1967).

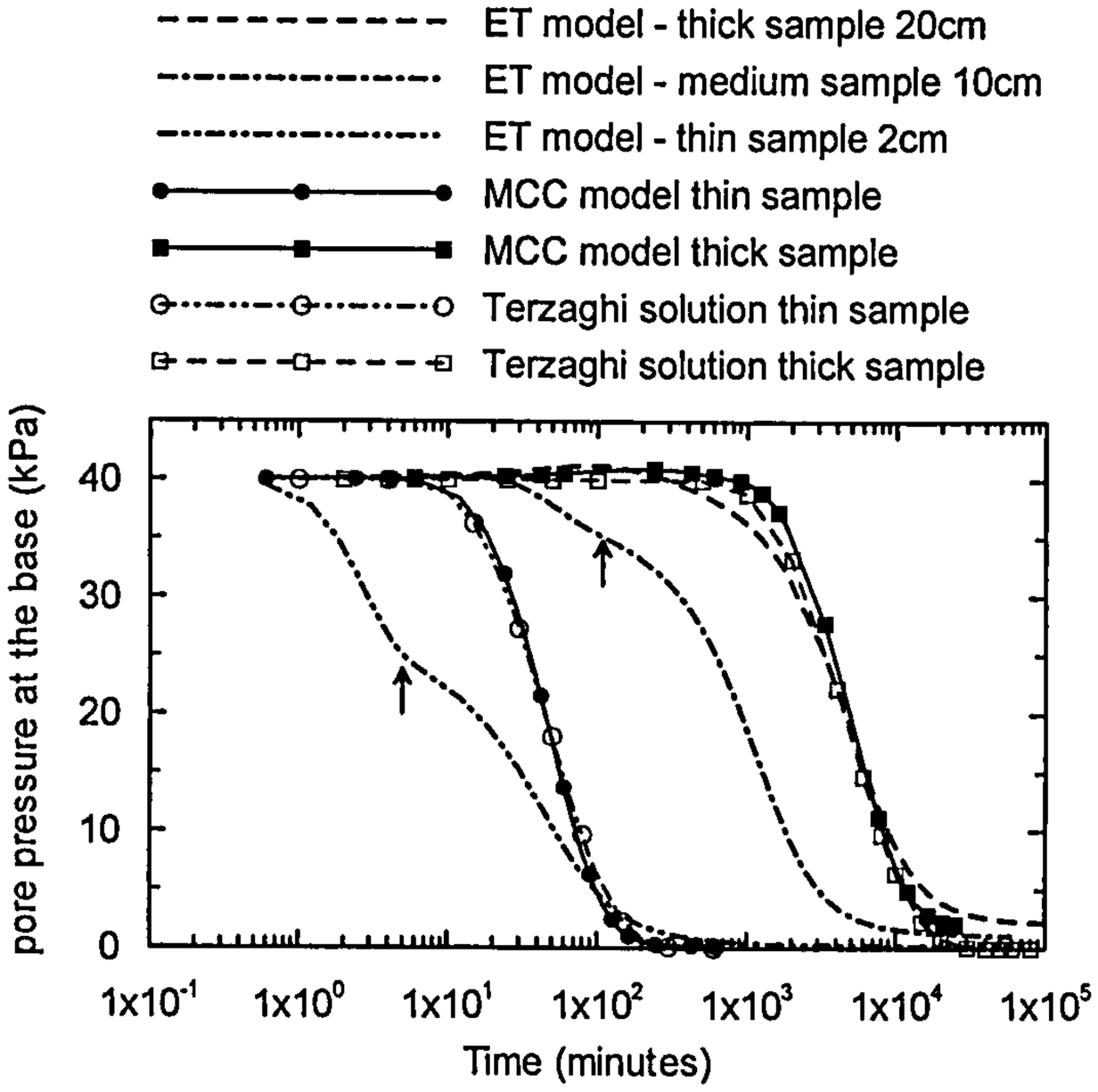

Figure 6.16: Variation of pore water pressure at the base of the sample with time following the application of a load increment $\Delta\sigma'_v$ =40kPa.

From Figure 6.16 the following observations can be made:

a) The variation of excess pore water pressure predicted by the ET model is very similar to that given by the Terzaghi solution for the 20cm sample;

b) For the 2cm sample the variation of excess pore pressure at the base predicted by the ET model is found to be quite different from that predicted by the Terzaghi solution during most of the consolidation period, except close to the end of consolidation.

c) The variation of excess pore water pressure at the base with time predicted by the ET model shows a change in curvature early on during the consolidation for the 2 and 10 cm samples (indicated by arrows in Figure 6.16), a feature that is not predicted by the Terzaghi solution or the MCC model.

d) From the analyses with the ET model, the End of primary consolidation (EOP), defined as 95% degree of pore water pressure dissipation is found to occur at

about 138 minutes (2.3 hours) for the thin sample and at 23500 minutes (about 16 days) for the 20cm sample.

e) Both the MCC and the ET model are able to predict the Mandel-Cryer effect that corresponds to an increase in pore water pressure, above that initially set up by the loading, before a subsequent decay, in an element away from the drainage boundary. Mandel (1953) and Cryer (1963) have shown that this may occur when consolidation is governed by the Biot equations (i.e. considering the equations of force equilibrium, the soil skeleton deformation and the flow continuity in three perpendicular directions). They estimate that the additional excess pore pressure can be up to 20% of the initial excess pore water pressure generated due to loading alone, for a Poisson's ratio of about 0.3, a typical value for soils. As consolidation starts, the equivalent overall Poisson's ratio at the drained boundary drops from its undrained value, close to 0.5, to a drained value. Away from the drained boundary, where excess pore pressure dissipation has not yet commenced, undrained conditions prevail and the equivalent overall Poisson's ratio remains close to 0.5. This discrepancy causes the soil away from the drained boundary to temporarily attract load, producing an increase in total mean stress and an associated increase in pore pressure. It is thought that the consideration of the time dependent nature of soils may aggravate this effect. If the soil permeability is sufficiently low such that undrained conditions (no volume change) operate at a certain distance away from the drained boundary, when the soil attempts to creep the soil is compelled to develop further contractive excess pore pressure (a phenomena also referred to as undrained creep).

Points a) to c) may be explained with reference to Figure 6.17, which shows the state path of a FE element located at the base of the oedometer sample in terms of $\varepsilon_{vol,m} - \ln p_m^{'}$ during consolidation, where $p_m^{'}$ is the size of the current loading surface (i.e. the current equivalent isotropic effective stress) and $\varepsilon_{vol,m}$ is the corresponding total volumetric strain (Equation 6.30). The distance of the current stress state $\left(\varepsilon_{vol,m}, p_m^{'}\right)$ to the reference time line determines the magnitude of the visco-plastic scalar multiplier, and therefore the visco-plastic strain rate. The FE elements located at the base of the sample are expected to be those undergoing the slowest changes in effective stress (and

thus to experience lower strain rates) as they are located further away from the drainage boundary.

In the 2cm sample, the drainage path is the shortest and a smaller period of time is required to reach full dissipation of the excess pore water pressure. Consequently the strain rate operating on the sample during consolidation is expected to be higher in the 2cm sample than in the thicker samples. This is shown in Figure 6.17 as the $\varepsilon_{vol,m} - \ln p'_m$ curve for the thin sample lies further above of the reference time line, than those of the 10 and 20 cm samples.

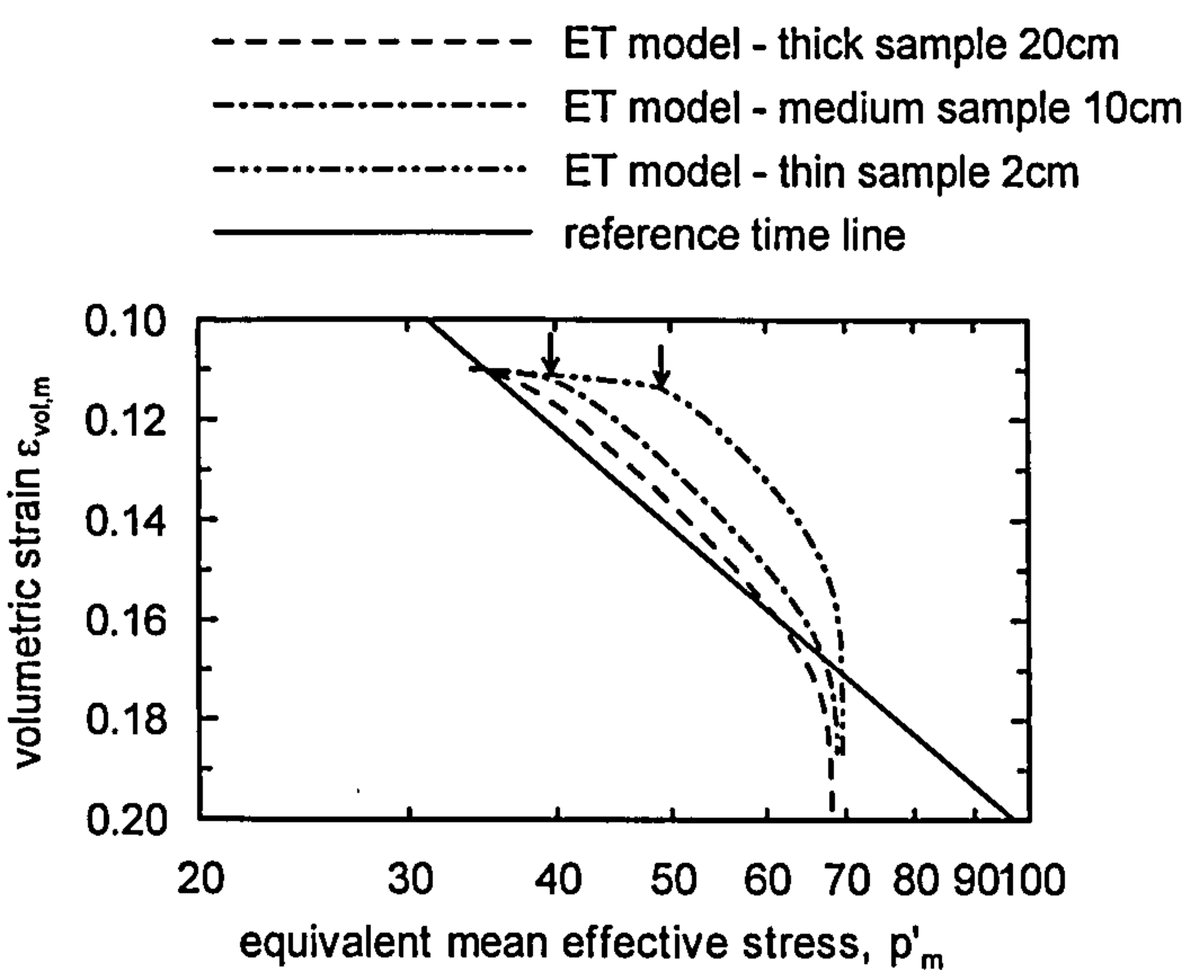

Figure 6.17: State path of an FE element at the base of the oedometer sample during consolidation in $\varepsilon_{vol,m} - \ln p'_m$ space.

The $\varepsilon_{vol,m} - \ln p'_m$ curve of the sample 20 cm high lies very close to the reference time line during most of the consolidation time, such that the strain rate acting at the base of the sample is very close to the strain rate on the reference line (see Equation 6.53). This is thought to be the reason why the predictions of the ET model for the 20cm sample are very close to those given by the MCC model and the Terzaghi solution, but not for the thinner samples.

Further, the change in curvature in the u_b - log t curves predicted by the ET model for the 2 and 10cm high samples are found to coincide with the yielding of the respective compression curves in $\varepsilon_{vol,m} - \ln p'_m$ space (i.e. indicated by the arrows in Figure 6.17),

and corresponds to a change in the soil behaviour from the domain in which its behaviour is dominated by the elastic and the visco-plastic components.

Figure 6.18 shows the variation of the equivalent vertical strain with time as predicted by the ET model for the 2, 10 and 20 cm high samples, during the same consolidation period. The equivalent vertical strain is derived from the sample settlement at the top. Figure 6.18 also includes the MCC model predictions for the 2 cm and 20 cm high samples. The MCC model being a time independent model predicts soil deformation while there is an increase in the soil effective stress. However, once all the excess pore water pressure has dissipated no further deformation is predicted. The ET model instead is able to predict both the primary and the secondary consolidation phases.

The variation of equivalent vertical strain with time predicted for the 20cm sample by the ET model and the MCC model are very similar up to about 15000 minutes. Again this is thought to result from the fact that the strain rate acting on the 20 cm high sample is very close the strain rate on the reference line. On the other hand, for the thin sample the equivalent vertical strain predicted by the ET model, at an instant t during primary consolidation, is consistently smaller than that predicted by the MCC model. As the sample is strained at an average strain rate considerably higher than that on the reference line the ET model predicts that the soil exhibits a smaller volumetric strain (or void ratio) at the same effective stress than the MCC model.

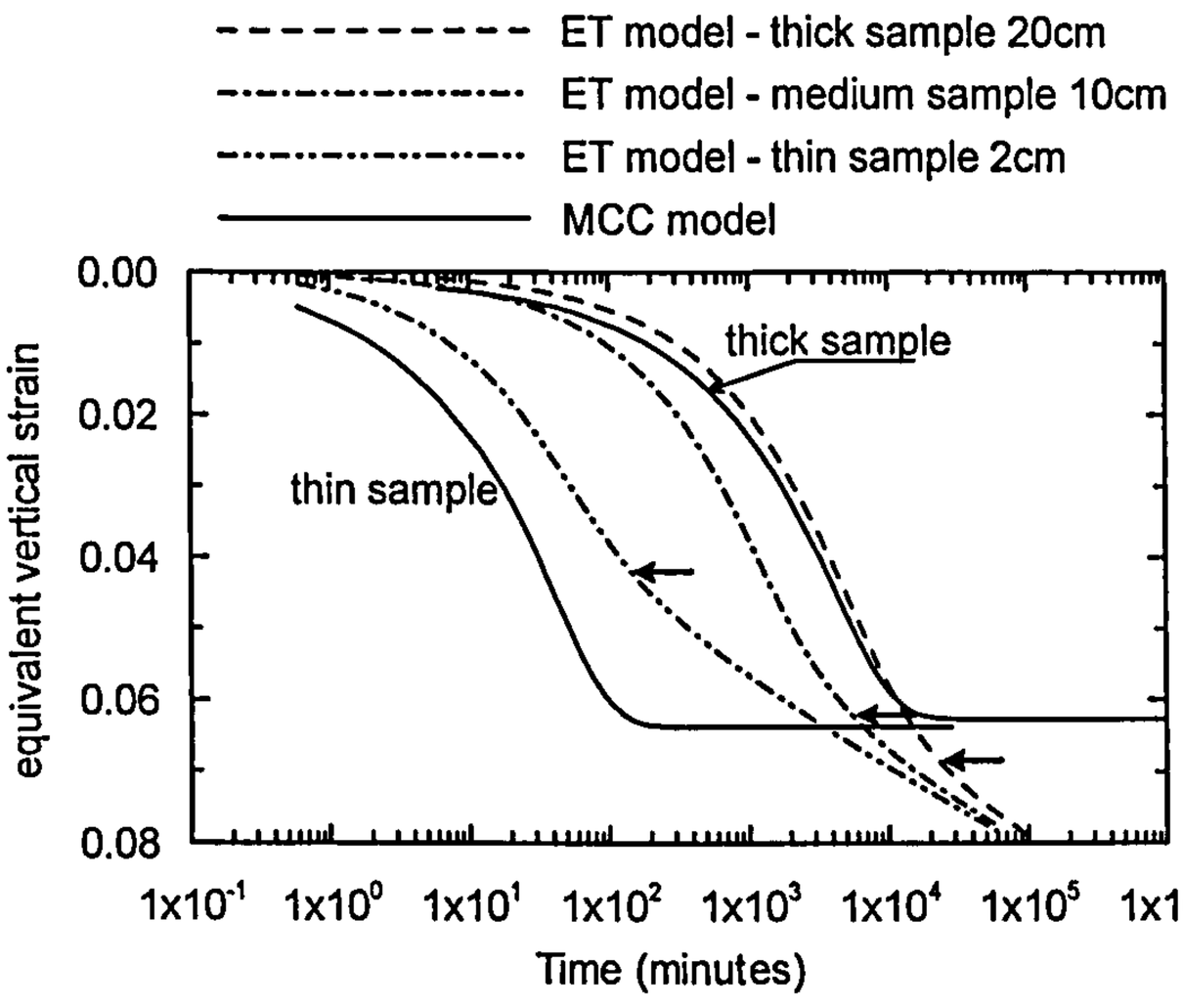

Figure 6.18: Variation of the equivalent vertical strain with time following the application of a vertical stress increment equal to 40kPa.

The points that correspond to 95% degree of excess pore water pressure dissipation (that is assumed to coincide with the EOP) are indicated by arrows in Figure 6.18. The ET model predicts that the strain at the EOP depends on the thickness of the consolidating layer, increasing with the layer thickness, as predicted by the viscous approach discussed in Chapter 2.

Figure 6.19 shows the variation of the degree of settlement and excess pore pressure dissipation with time predicted by the ET model during the same consolidation period for the 2cm and the 20 cm samples. The degree of settlement $\overline{U}_s$ is determined as:

Equation 6.62
$$\overline{U}_s(t) = \frac{s_t}{s_{EOP}}$$

where s_t is the settlement at an instant t and s_{EOP} is the settlement at the end of primary consolidation, as defined above.

The degree of pore water dissipation $\overline{U}_{PWP}$ at an instant t is calculated as:

Equation 6.63
$$\overline{U}_{PWP}(t) = \frac{\int_0^h u(t,z) \cdot dh}{\Delta\sigma_v \cdot h}$$

where h is the sample height, $\Delta\sigma_v$ is the vertical stress increment and equal to the excess pore water pressure generated in the soil immediately after the application of the load increment and $u(t,z)$ is a function that describes the variation of the excess pore water pressure at any instant t, at a distance from the drainage boundary, z.

Also included in Figure 6.19 is the variation of the degree of consolidation with time as predicted by the Terzaghi solution, according to which the degree of settlement is equal to the degree of excess pore water pressure dissipation. This is valid when the soil behaviour is time independent. For the 20 cm sample, which is strained at a strain rate very close to the strain rate on the reference line, the degree of excess pore water pressure dissipation and the degree of settlement predicted by the ET model are not that dissimilar, and they are in turn similar to the Terzaghi degree of consolidation.

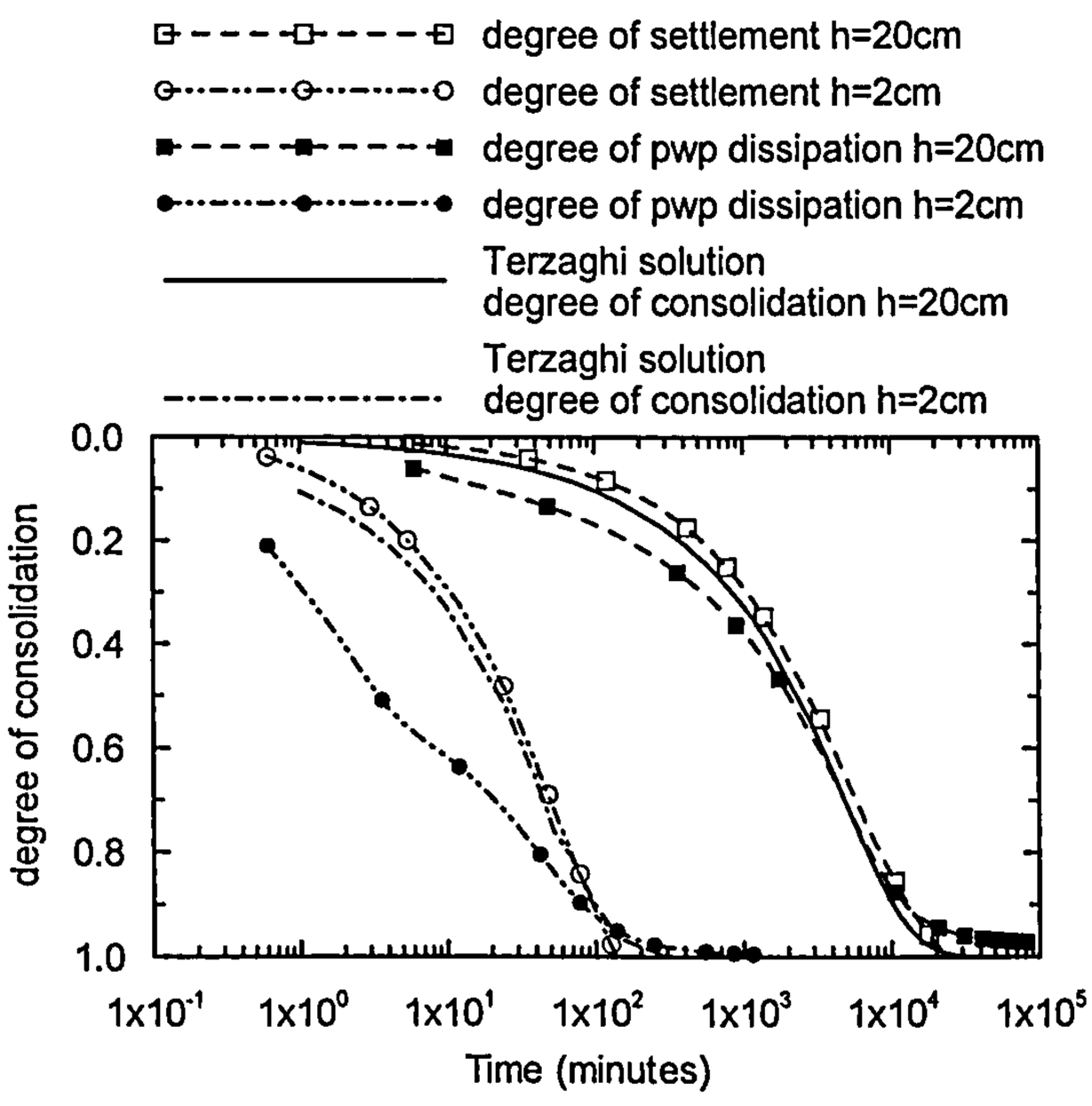

Figure 6.19: Evolution of the degree of settlement and excess pore water pressure dissipation with time.

In the more general case, as observed for the 2cm sample, the degree of settlement predicted by the viscous approach (ET model) is well recovered by the Terzaghi degree of consolidation, but the degree of excess pore water pressure dissipation is different. The difference is expected to increase as the average strain rate acting in the consolidating soil diverges from the strain rate on the reference line, and for a thick layer consolidating in the field (where due to the length of the drainage path the soil deforms at rates much lower than those experienced in the laboratory), the degree of excess pore water pressure dissipation is expected to be smaller than the degree of settlement, an issue of major importance, e.g. in staged construction of embankments.

6.5.4 FE analyses of CRS oedometer tests on structured soil

This section presents the results of single element FE analyses that mimic CRS oedometer tests on K_0 normally consolidated samples of a structure soil. The soil is simulated using the ET constitutive model and the model parameters included in Table 6.2, with the exception of the parameters p_{s0} and ρ_s which are varied as described below.

Figure 6.20 shows the results of a set of FE analyses that simulate CRS oedometer tests performed at 0.005211/day axial strain rate, in which the value of p_{s0} is set equal to 10 kPa and the value of ρ_s is varied between 500 and 4000, in terms of $\varepsilon_{vol,m} - \ln p'_m$ (Figure 6.20a) and in terms of *e-ln p'* (Figure 6.20b). Figure 6.21 shows the results of a set of similar FE analyses in which both the value of p_{s0} and ρ_s are varied.

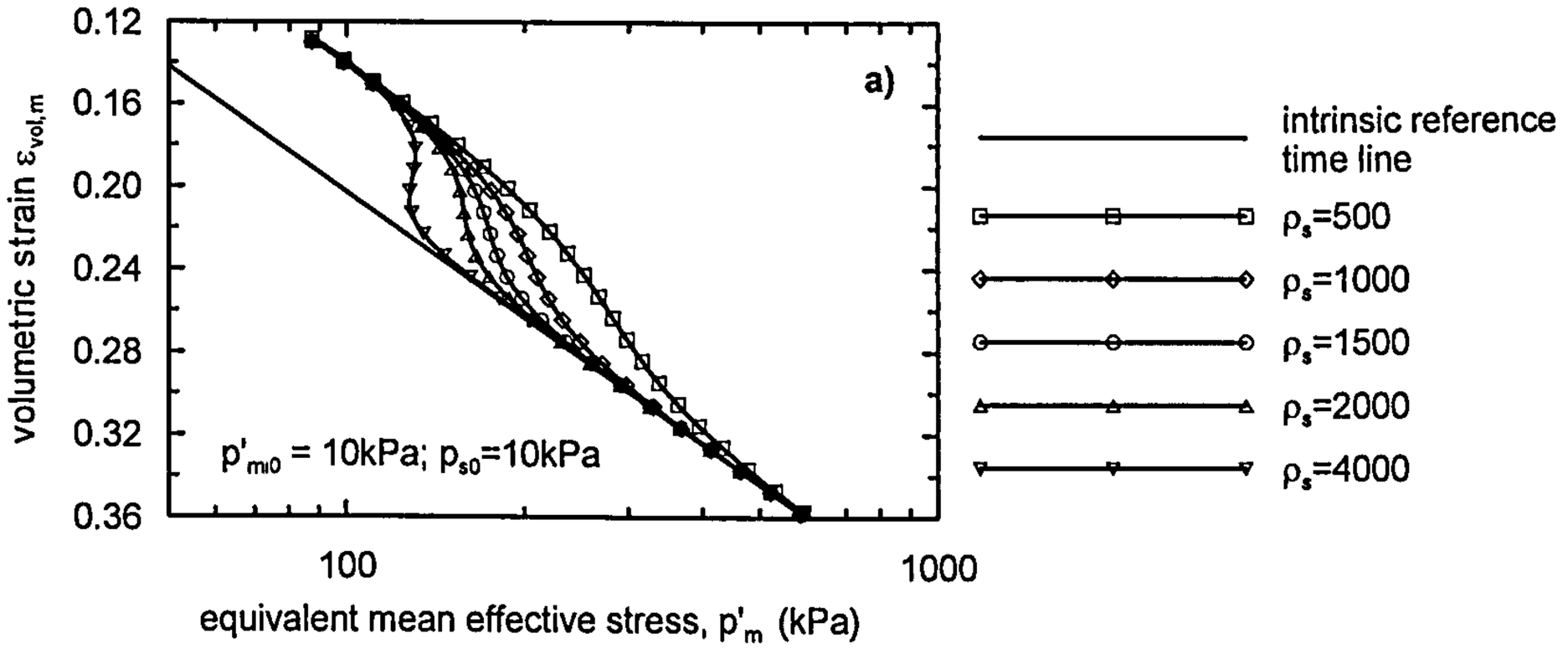

Figure 6.20: CRS oedometer compression curves of a structured soil predicted by the ET model – influence of the parameter ρ_s; a) in $\varepsilon_{vol,m} - \ln p'_m$ space and b) in $e - \ln p'$ space.

In $\varepsilon_{vol,m} - \ln p'_m$ space the location of the reference time line is defined by the value of the mean effective stress at zero total volumetric strain, such that the intrinsic reference time line is characterized by the parameter p'_{mi0} (which is kept constant and equal to 10kPa in all the analyses) and the reference time line of the natural structured soil is characterized by the quantity $p'_{m0} = p'_{mi0} + p_s$. The soil is assumed to be initially normally consolidated and thus the initial stress state is located on the appropriate

reference time line that lies above that of the reconstituted soil, the distance increasing with the value of p_{s0} (see Figure 6.21a)). In both Figures 6.20 and 6.21, in $\varepsilon_{vol,m} - \ln p'_m$ space, the compression curves start at a value of volumetric strain $\varepsilon_{vol,m}$ different from zero, which is taken as a soil state parameter. The volumetric strain developed during the analysis due to the soil compression at a given mean effective stress p' can be calculated as the difference between the current volumetric strain and the initial volumetric strain value. In the ET model, the initial void ratio is equal to the value input in the initial stress file, and has been set equal to 1.5 in all analyses, and so in *e - lnp'* space the reference time line of the natural soil is made to pass through the same initial soil state (e_0, p'_i) where e_0 is the initial void ratio and p'_i is the initial mean effective stress.

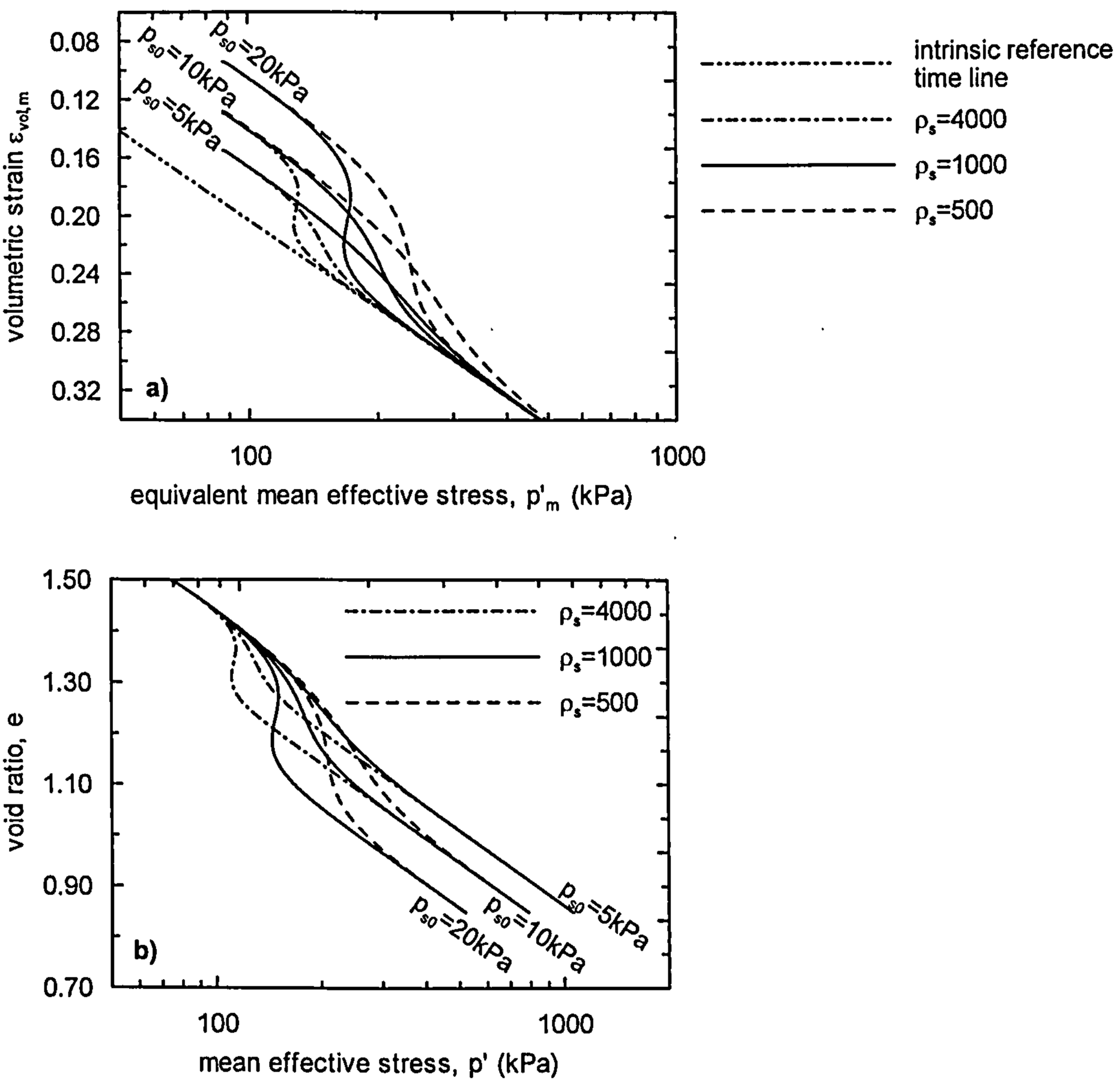

Figure 6.21: CRS oedometer compression curves of a structured soil predicted by the ET model – influence of the parameter p_{s0}; a) in $\varepsilon_{vol,m} - \ln p'_m$ space and b) in $e - \ln p'$ space.

Figure 6.20 shows that for a given value of p_{s0} the increase in the parameter ρ_s causes the loss of structure to become more abrupt, that is, the destructuration is completed over a smaller stress interval. For very large values of ρ_s, the model may even predict a temporary reduction in mean effective stress with decreasing void ratio as observed for the data corresponding to ρ_s=4000. Figure 6.21 shows that an increase in p_{s0} causes an increase in the soil structure, as it increases the distance between the reference time line of the natural structured soil and that of the reconstituted soil. In addition, an increase in the value of p_{s0}, while ρ_s is kept constant, is found to cause the destructuration process to become more abrupt.

6.5.5 FE analyses of triaxial compression stress paths of an unstructured soil

This section investigates the shearing behaviour predicted by the ET model under triaxial compression stress conditions, both for the drained and undrained case.

Undrained triaxial compression

Figure 6.22 shows the stress paths in *J-p' space* predicted by the ET model during undrained triaxial compression tests on normally consolidated samples isotropically consolidated to 100 kPa sheared at various values of axial strain rate. The data has been obtained from single element FF analysis using the model parameters given in Table 6.2 and assuming the soil to have no structure. Figure 6.23 shows the respective stress strain curves and the variation of pore water pressure with axial strain during the analyses.

As would be expected, for NC samples the behaviour during shearing is contractive and there is a monotonic increase in deviatoric stress with decreasing mean effective stress up to the critical state line, such that the peak strength is equal to the CS strength. The model is able to recover the strain rate dependency of the soil's undrained strength, with the undrained strength increasing with the applied axial strain rate. However, the effective stress critical state envelope remains unchanged with the differences in the predicted undrained strength resulting from differences in the predicted excess pore water pressure.

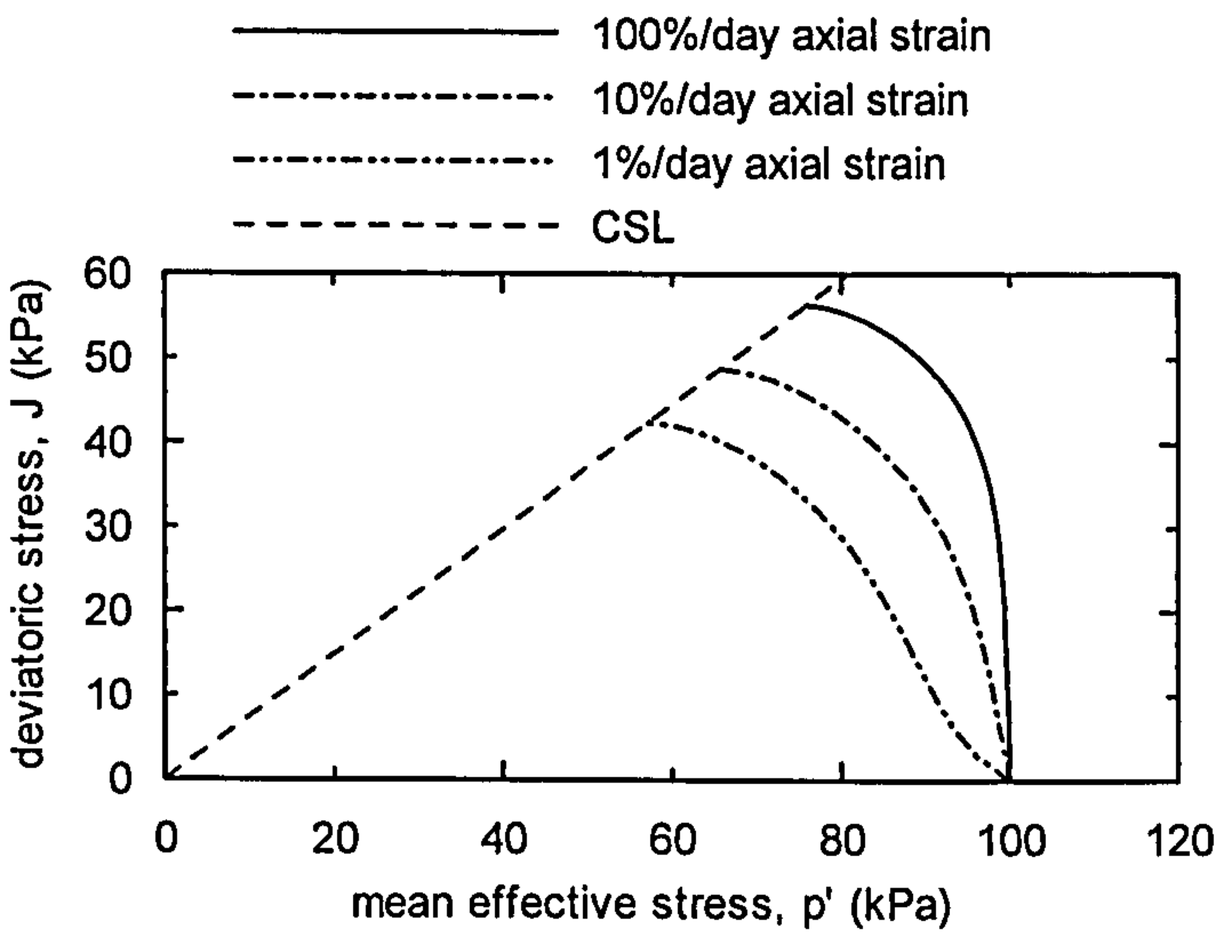

Figure 6.22: Effective stress paths during undrained triaxial compression tests on NC samples sheared at constant axial strain rate.

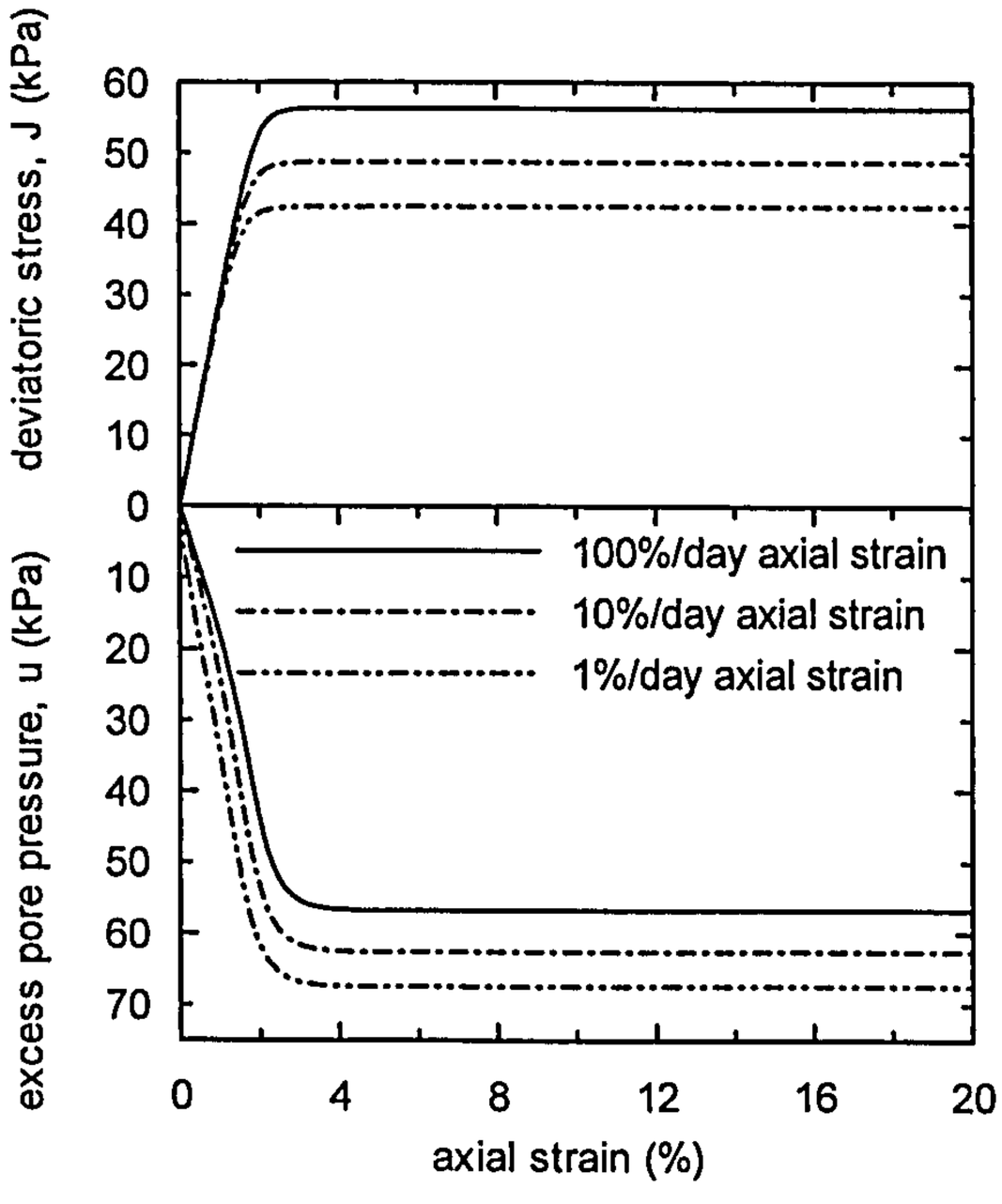

Figure 6.23: Stress – strain curves and the development of excess of pore water pressures during undrained triaxial compression tests on NC samples sheared at constant axial strain rate.

Figure 6.24 shows the normalized effective stress paths in $J / p'_{oi} - p' / p'_{oi}$ *space* predicted by a series of FE analyses that simulate undrained triaxial compression tests performed at constant axial strain rate on normally and overconsolidated samples with OCRs equal to 1.0, 1.5 and 4.0 and isotropically consolidated to 100kPa. Figure 6.25 shows the respective normalized stress – strain curves and the variation of normalized

excess pore water pressure with axial strain during the same tests, for the samples sheared at 10%/day axial strain. In both figures, the normalizing quantity is the initial pre-consolidation pressure that is equal to 100, 150 and 400 kPa, for the samples with an OCR equal to 1.0, 1.5 and 4.0, respectively.

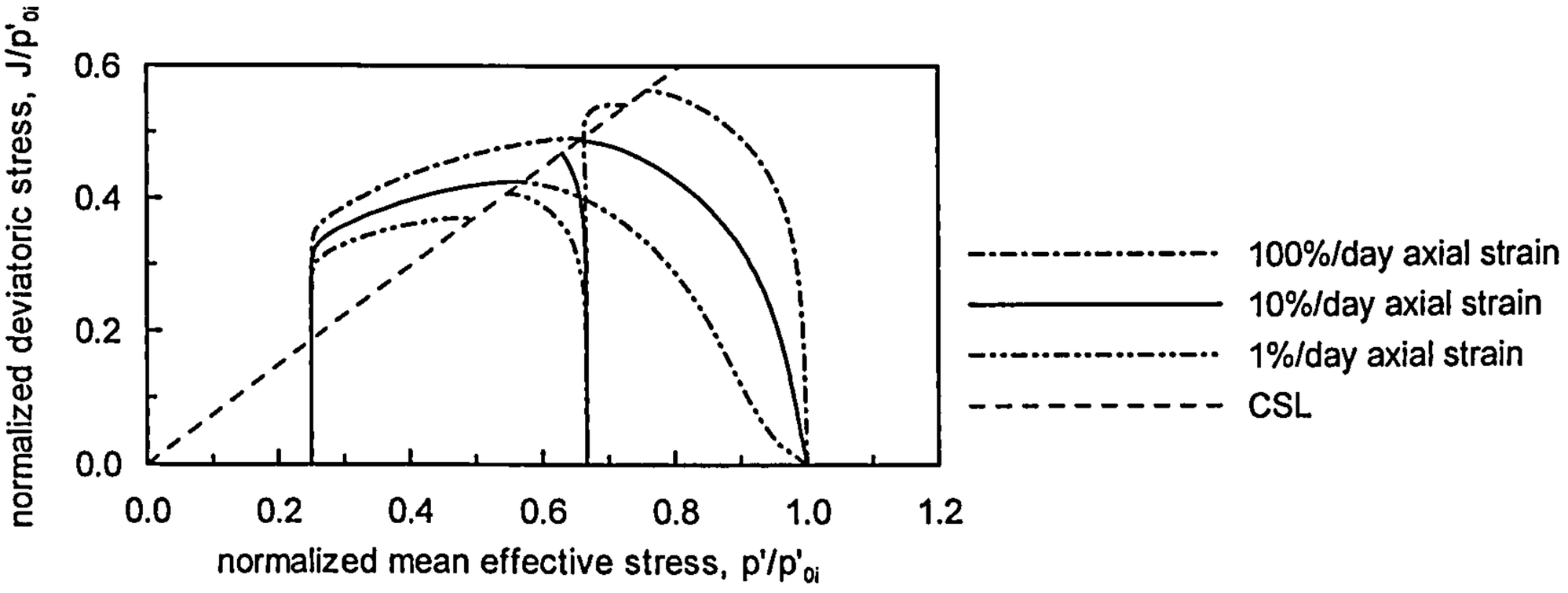

Figure 6.24: Effective stress paths of undrained triaxial test on NC and OC samples at constant axial strain rate.

As noted with reference to Figure 6.22 and Figure 6.23, during undrained shearing normally consolidated samples show a contractive behaviour with the development of positive excess pore water pressures (decrease in mean effective stress) as the deviatoric stress increases monotonically up to the critical state line.

The heavily overconsolidated samples (OCR=4.0) follow initially a vertical effective stress path, corresponding to the phase during which the behaviour is essentially elastic. During this initial phase, the soil element develops positive excess pore water pressure and the stress state reaches stress ratios well above that at critical state. The stress path then bends rightwards towards the critical state line with a monotonic increase in the deviatoric stress, and the peak undrained strength is again attained at CS. During this phase the soil develops incremental negative pore water pressures. The stress ratio at which the stress path bends to the right is found to increase with the value of the applied axial strain rate.

The behaviour of lightly overconsolidated samples (OCR=1.5) depends on the applied strain rate, with the end of the pseudo elastic stress path finishing at a stress ratio above or below the stress ratio at critical state. The samples sheared at the slowest strain rates show a behaviour similar to that of the NC samples, while the sample sheared at 100%/day axial strain follows the same pattern as the heavily overconsolidated samples.

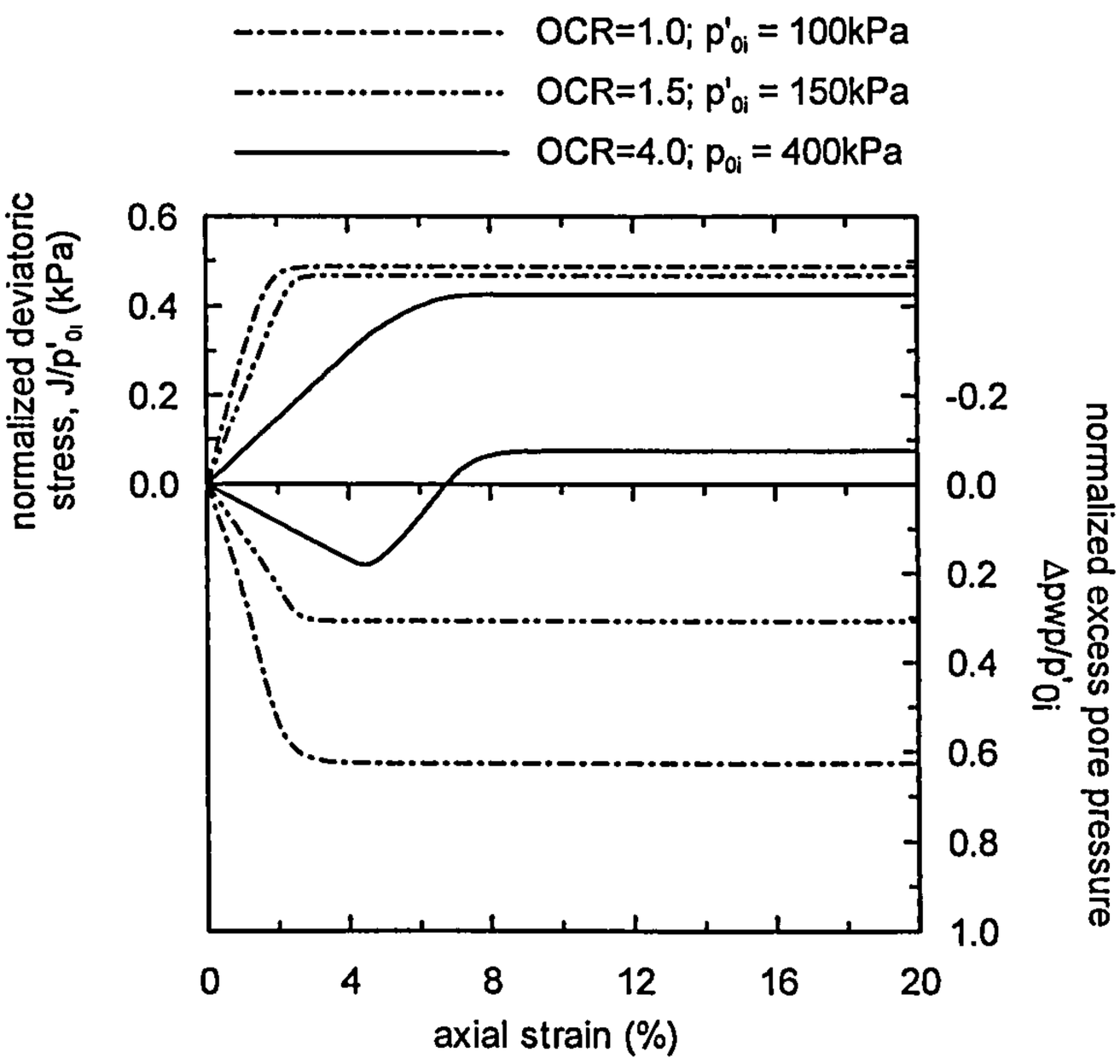

Figure 6.25: Stress – strain curves and development of excess pore pressures during triaxial compression tests on NC and OC samples sheared at 10% axial strain per day.

Figure 6.26 shows the state paths during the above undrained triaxial compression tests in $\varepsilon_{vol,m} - \ln p_m^{'}$ space, where $p_m^{'}$ is the size of the current loading surface and $\varepsilon_{vol,m}$ is the associated total volumetric strain. The position of the current state $\left(\varepsilon_{vol,m}, p_m^{'}\right)$ in relation to the reference time line defines the magnitude of the visco-plastic scalar multiplier (and thus the magnitude of the visco-plastic strain increment). Initially the stress state is seen to follow very closely the instant time line that passes through the initial state $\left(\varepsilon_{vol,m}, p_m^{'}\right)$ until it joins the line that corresponds to the appropriate value of the visco-plastic scalar multiplier for the applied strain rate. The final states of the samples sheared at the same applied strain rate are found to define a line that is parallel to the reference time line, and these lines move towards the right for higher values of applied strain rate. The initial pseudo elastic range is seen to increase with the overconsolidation ratio and the applied strain rate, noting that higher initial OCR value means that the stress state is located further away from the reference time line, and thus is characterized by a much lower value of visco-plastic scalar multiplier.

Figure 6.24 and 6.26 show that according to the ET model the CSL is unique in stress space but is rate dependent in terms of void ratio. A discussion on the experimental evidence of this has been carried out in Section 5.5.

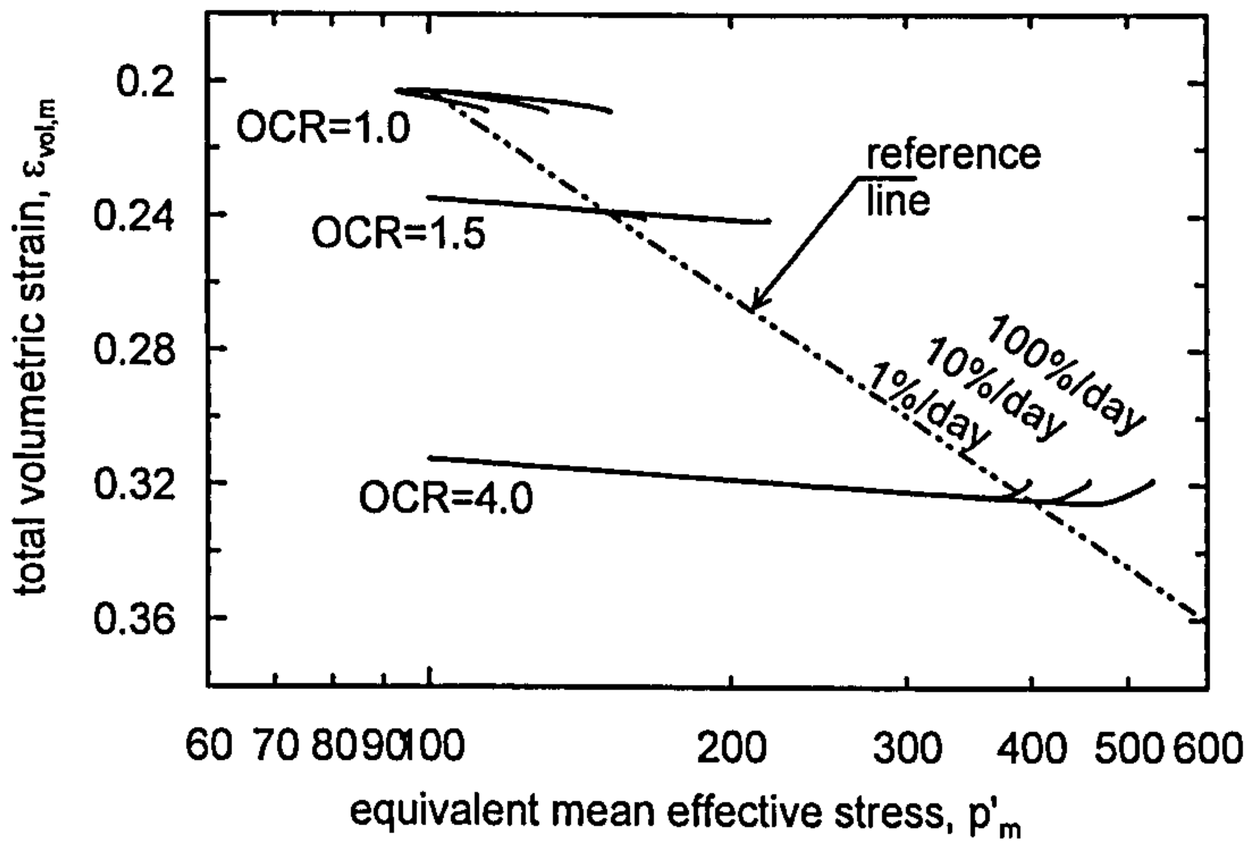

Figure 6.26: State paths predicted by the ET model during undrained triaxial compression tests on NC and OC samples in $\varepsilon_{vol,m}$ –lnp'$_m$ space.

Drained triaxial compression

Figure 6.27 shows the stress-strain curves obtained from a series of single element FE analyses that simulate drained triaxial compression tests on normally and overconsolidated samples isotropically consolidated to 100kPa, and sheared at three values of axial strain rate. Figure 6.28 shows the variation of total volumetric strain with total axial strain, for the samples sheared at 10%/day axial strain rate. The analyses show that the ET model mimics strain rate dependency during drained shearing in the pre critical state range, but that the critical state condition is time and rate independent and a function of the initial stress conditions and the angle of shearing resistance only.

Normally and lightly overconsolidated samples show a contractive behaviour with a monotonic increase in deviatoric stress up to the critical state, which is attained at very large strains (i.e. about 40% axial strain). In the pre-failure stress range, the stress-strain curves are found to move upwards with increasing applied strain rate and overconsolidation ratio, as result of an increase in the pseudo elastic range.

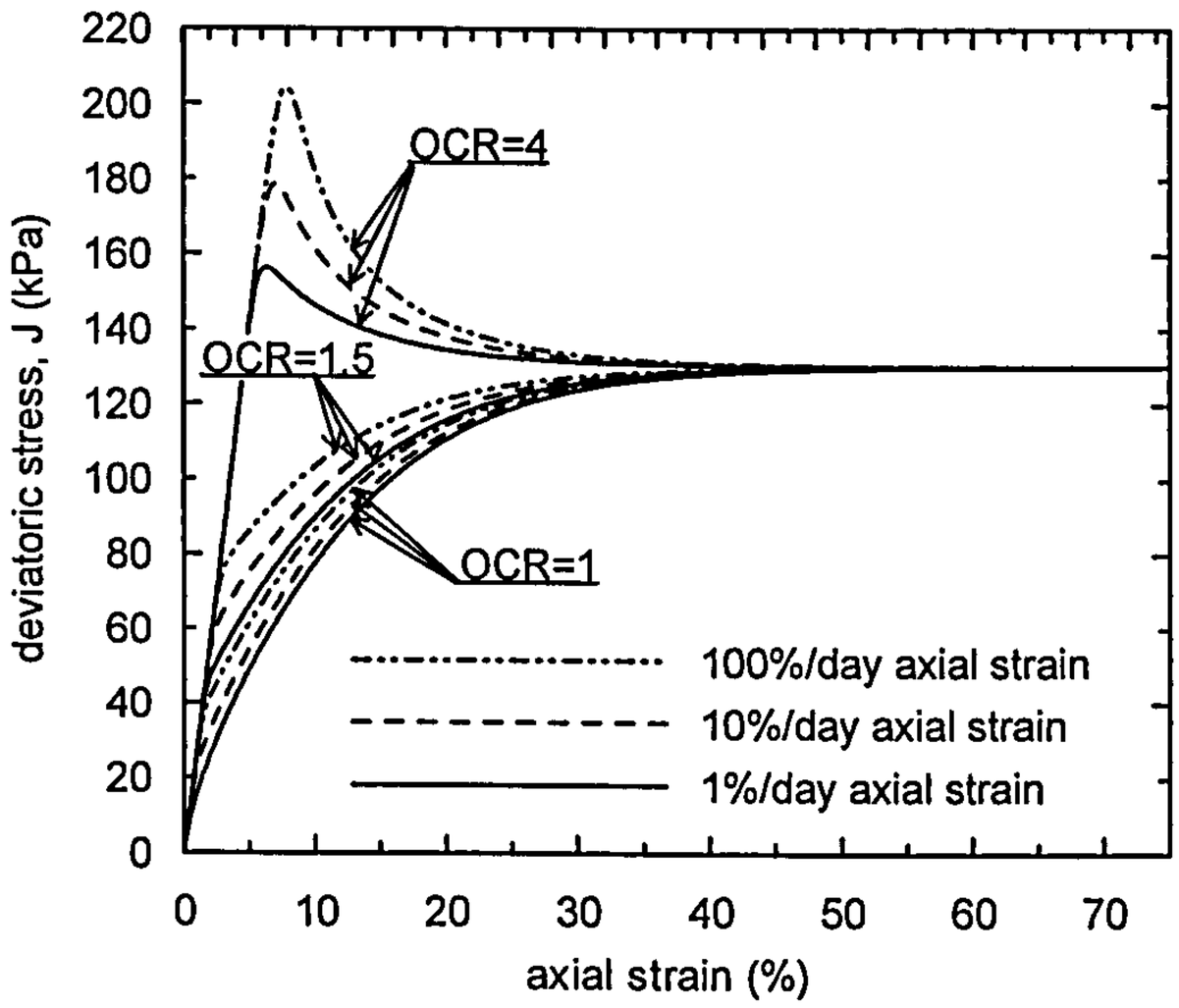

Figure 6.27: Stress-strain curves from drained triaxial compression tests on NC and overconsolidated samples sheared at constant axial strain rate.

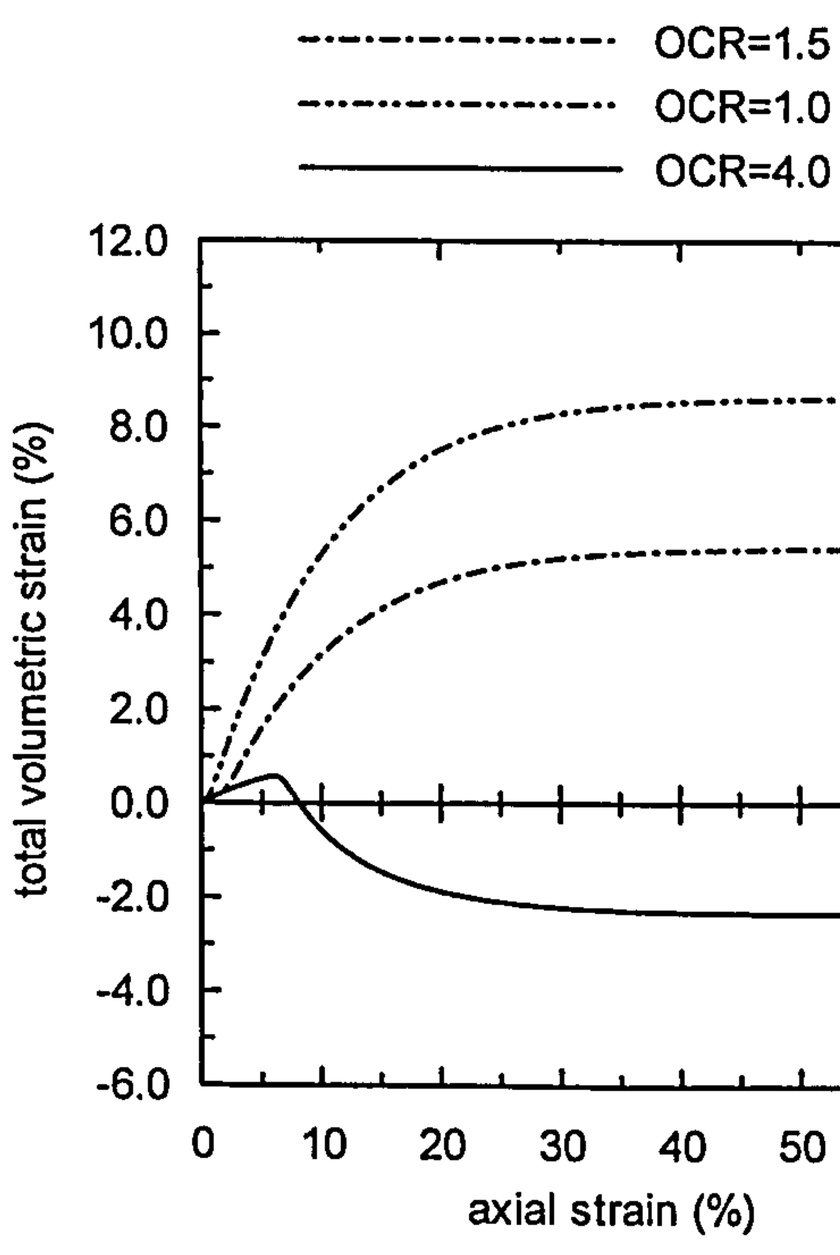

Figure 6.28: Variation of volumetric strain with axial strain during drained triaxial compression tests on NC and OC samples sheared at 10%/day axial strain rate.

The heavily overconsolidated samples (OCR=4.0) show an initial contractive phase up to peak strength, which is well in excess of the strength at critical state, and the peak strength value is found to increase with applied strain rate. After peak, the behaviour

becomes dilatant and the deviatoric stress decreases to the rate and time independent critical state strength, which is attained at very large strains.

Figure 6.29 shows the state path of the above consolidated drained triaxial compression tests in $\varepsilon_{vol,m}$ - $ln\ p'_m$ space. The ultimate states (critical state) of samples sheared at the same axial strain rate value are found to correspond to a single point in $\varepsilon_{vol,m}$ - $ln\ p'_m$ space (i.e. indicated with a small circle in Figure 6.29). Failure points associated with different strain rates lie on the same vertical (same effective stress condition) but the points move upwards, further away from the reference time line, with increasing applied strain rate.

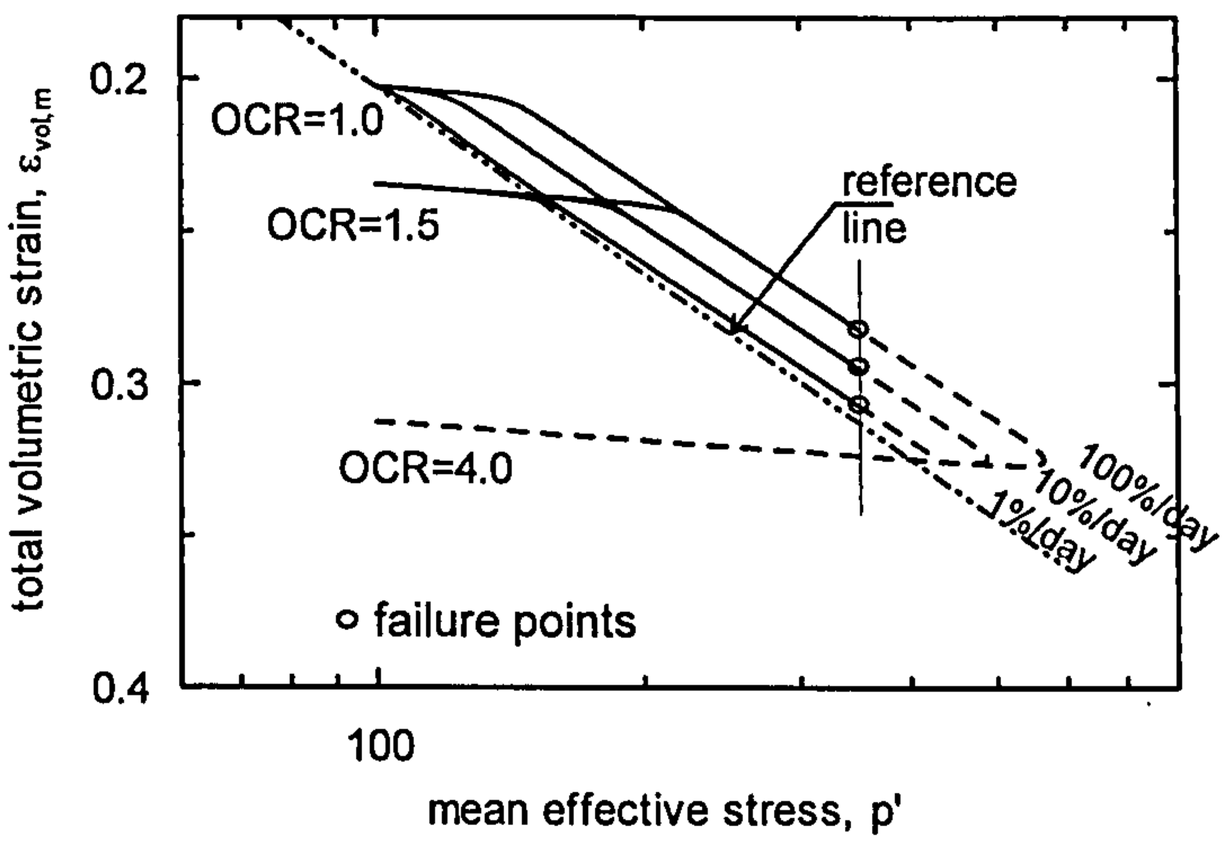

Figure 6.29: State paths predicted by the ET model during drained triaxial compression tests on NC and OC samples in $\varepsilon_{vol,m}$ –lnp'_m space.

6.6 Simulation of laboratory tests on Hong-Kong marine deposits

Yin et al. (2002) present an elasto–visco plastic constitutive model based on the equivalent time concept, and employ the model to simulate a series of laboratory tests on reconstituted samples of Hong Kong Marine Deposits (HKMD). Yin et al. (2002) derive their model parameters using test data from an isotropic consolidation test and consolidated undrained triaxial compression tests.

In this section the same laboratory test data are reproduced using the ET model described in Section 6.3 and the differences between the two models and consequent model predictions are investigated. One of the main differences concerns the definition of the creep scalar multiplier.

In the formulation described by Yin et al. (2002) the creep scalar multiplier is determined assuming that a given loading surface is a locus of constant volumetric visco-plastic strain rate; but while the results described in Chapter 5 show that such assumption implies that true critical state conditions cannot be reached, the results reported by Yin et al. (2002) suggest the model reproduces well critical state conditions (as it will be seen in validation exercises 1 and 2). The author is uncertain about the formulation employed by Yin et al. (2002) and assumes there are inaccuracies in the description of the model.

The other main differences between the two model formulations regards the function adopted to describe the loading surface and the plastic potential in *J-p'* space and in the deviatoric plane. In Yin et al. (2002), the loading surface in *J-p'* space is described by two functions, one valid for the wet side and the other for the dry side of the critical state. In the deviatoric plane, the loading surface is described by a shape function proposed by Xin (1988) that follows very closely the Mohr coulomb failure criterion but removes the singularities at the corners.

From the data presented by Yin et al. (2002), the author has understood that the shape of the loading surface adopted to characterize the HKMD under triaxial compression stress conditions is as shown in Figure 6.30. In order to produce a good match to this surface, two different sets of parameters α and μ are employed to simulate the loading surface, depending on whether the stress path being tested engages the dry or the wet side of the loading surface, as indicated in Figure 6.30. Figure 6.30 also includes the MCC ellipse associated to the same critical state stress ratio, showing that the MCC is likely to over predict the undrained strength of the soil.

The remaining parameters are the same in the two model formulations and the values derived by Yin et al. (2002) are adopted. The following paragraphs describe a series of single element FE analyses obtained using the ET model parameters given in Table 6.3. The FE analyses mimic a wide range of laboratory tests on reconstituted samples of HKMD and the analysis results are compared with the laboratory data and the numerical predictions reported by Yin et al. (2002).

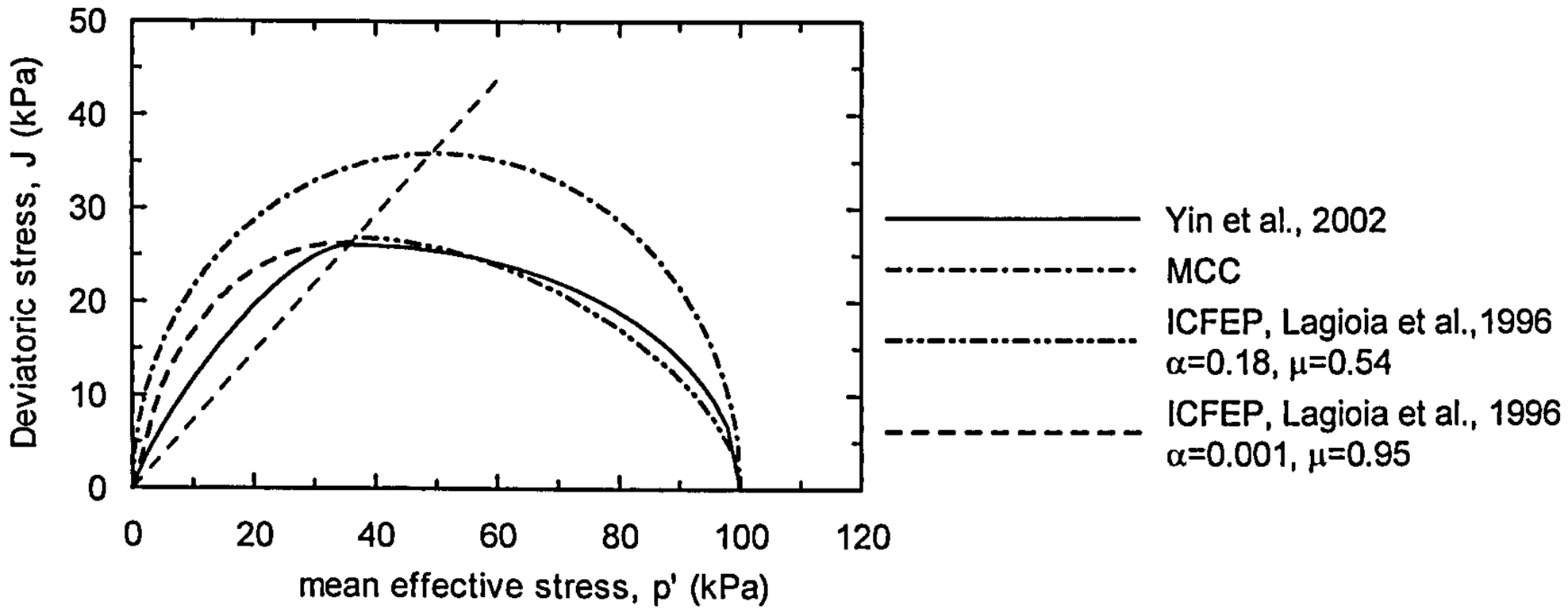

Figure 6.30: Comparison of the shape of the loading and plastic potential surfaces in J-p' space.

Table 6.3: ET model parameters for the HKMD.

e_0	M	λ/V	κ/V	μ	ψ_0/V
-	-	-	-	-	-
1.504	1.265	0.0793	0.0025	0.3	0.00521
t_0	$\varepsilon^{vp}_{vol,m,Limit}$	$\alpha_g=\alpha_f$	$\mu_g=\mu_f$	p'_{mio}	
hours	-	-	-	kPa	
24.0	0.6	0.18 0.001	0.54 0.95	15.2	

Validation test 1

The first validation exercise consists of reproducing a series of consolidated undrained triaxial compression tests on reconstituted samples of HKMD isotropically and normally consolidated to 400 kPa. The samples are sheared at values of axial strain rate of 0.15, 1.5 and 15%/hour, respectively. Figure 6.31 a) shows the effective stress paths in $q/\sigma_c^{'} - p^{'}/\sigma_c^{'}$ space obtained from the numerical simulations and experimentally in the laboratory. Figure 6.31 b) show the respective stress strain curves. In both figures, the stress quantities q and p' have been normalized by the pre-consolidation pressure $\sigma_c^{'}$ equal to 400 kPa. The agreement between the ET model predictions and the experimental data is in general good with the value of the undrained strength being well recovered, especially for the samples sheared at 0.15% and 1.5%/hour. There are however some discrepancies:

a) Experimentally the samples develop larger pore water pressures during the early stages of shearing, with the respective stress paths lying in general to the left (at a lower mean effective stress) than that predicted by the ET model.

b) The experimental stress-strain curves show a stiffer response within the small strain range than that predicted by the ET model.

c) The ET model seems to mimic a larger increase of undrained strength per logarithmic cycle of strain rate than that observed experimentally, but this may be exacerbated by the errors introduced during the data digitalisation from the original publication.

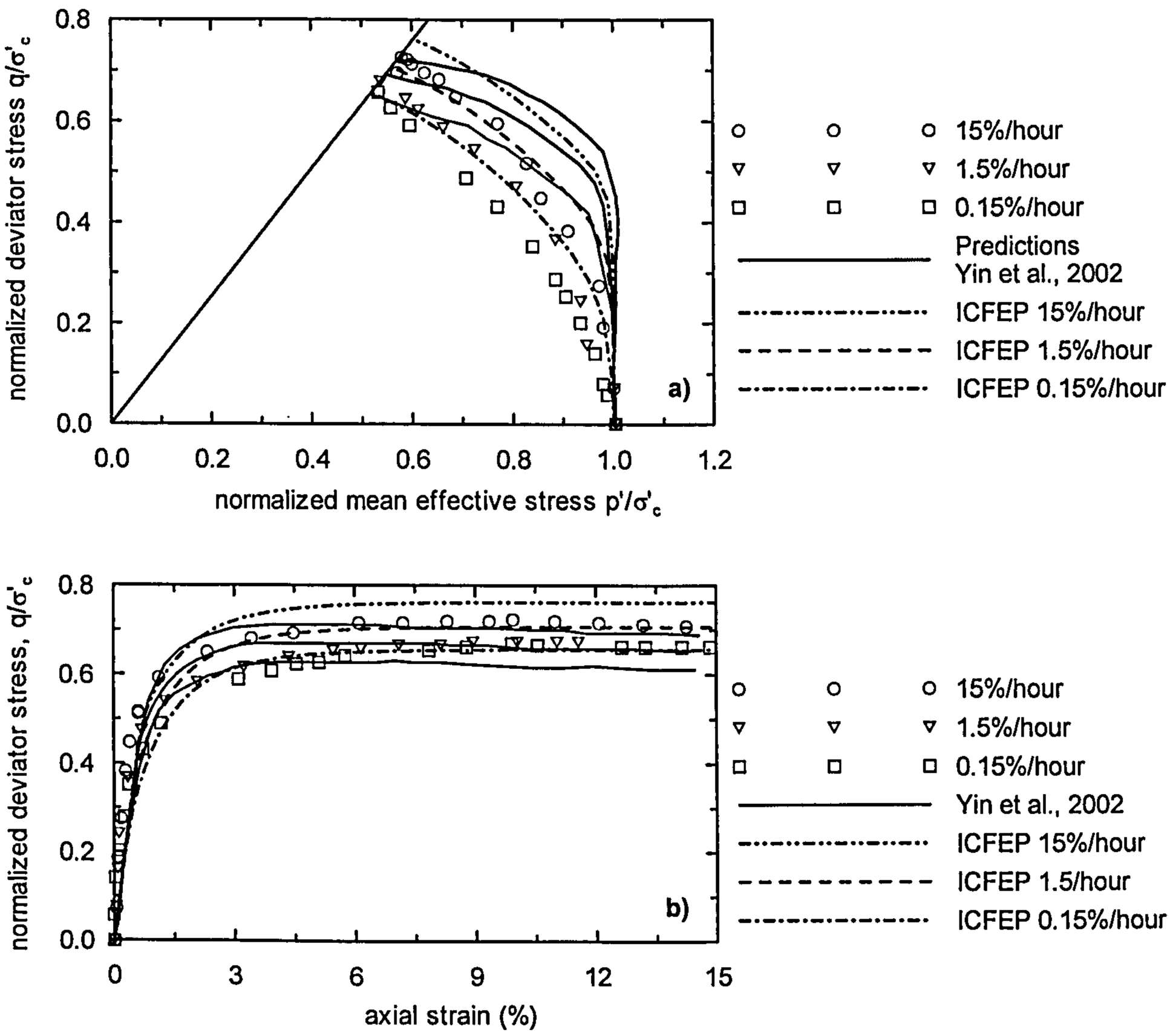

Figure 6.31: Undrained triaxial compression tests on NC samples at different values of constant axial strain rate; a) effective stress path; b) stress-strain curves.

The differences between the ET model predictions and those reported by Yin et al. (2002) are in general small, and are due to the differences in the adopted loading surfaces.

Validation test 2

The second validation exercise consists of reproducing a series of consolidated undrained triaxial compression tests on normally and overconsolidated samples of reconstituted HKMD, sheared at a constant axial strain rate equal to 1.5%/hour. The normally consolidated sample was sheared from an initial isotropic effective stress p'=400 kPa, while the overconsolidated samples with an OCR equal to 2 and 4 were sheared from an isotropic stress state p'=100kPa. Figure 6.32a) shows the effective stress paths in $q/\sigma_c^{'} - p^{'}/\sigma_c^{'}$ space obtained from the laboratory tests and predicted by the numerical simulations. Figure 6.32 b) shows the respective stress-strain curves.

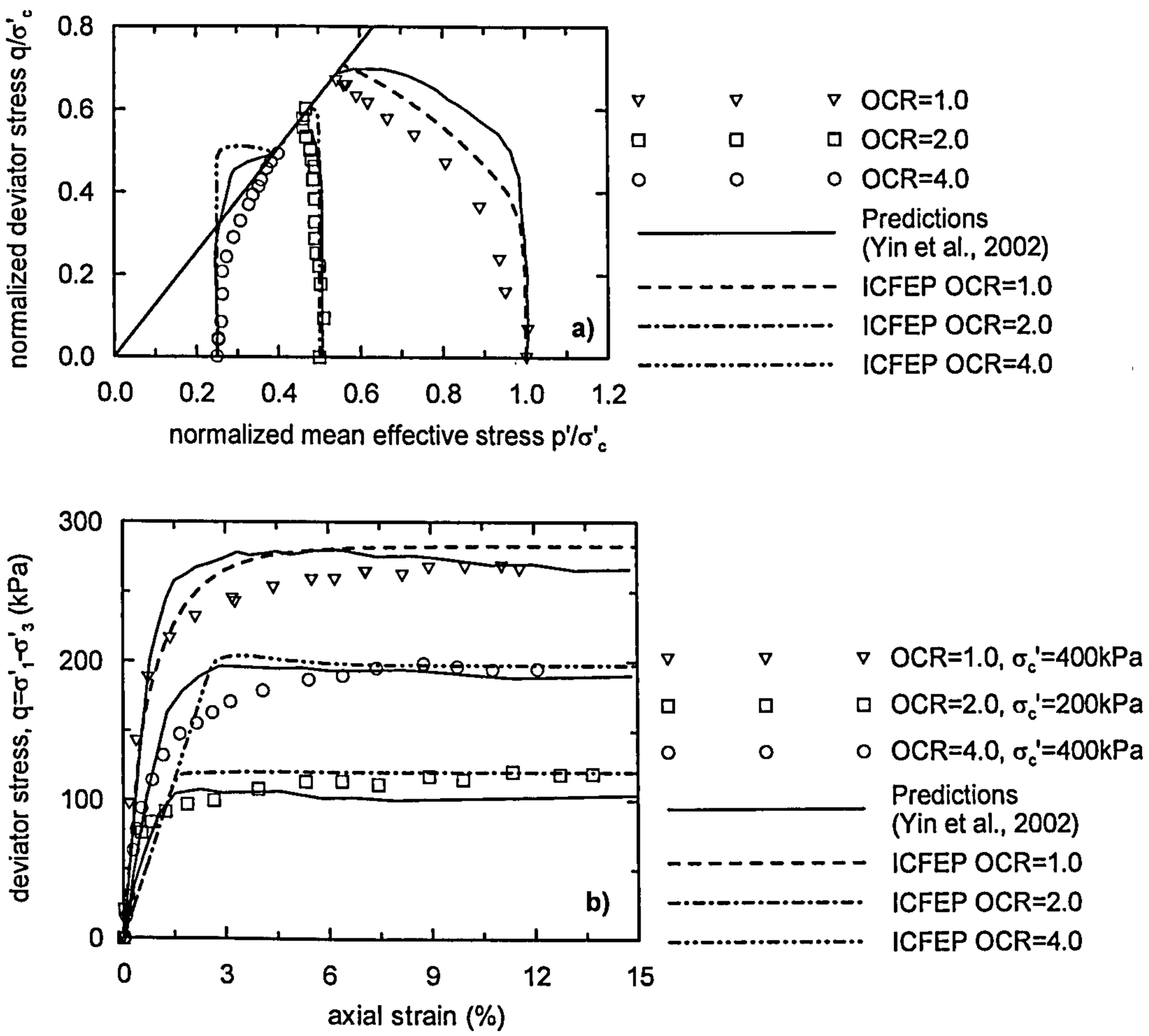

Figure 6.32: Undrained triaxial compression tests on normally consolidated and overconsolidated samples sheared at 1.5% axial strain per hour; a) effective stress path; b) respective stress-strain curves.

In both figures, the stress quantities q and p' are normalized by the respective pre-consolidation pressure, that is equal to 400, 200 and 400 kPa, for the samples with an OCR equal to 1.0, 2.0 and 4.0, respectively. The ET model is found to yield in general good predictions, in particular it recovers well the peak undrained strength of both normally and overconsolidated samples. There are however some discrepancies in the shape of the effective stress path prior to reaching the critical state, in particular for the sample with an OCR equal to 4.0.

Validation test 3

The third validation test consists of the simulation of three undrained triaxial creep tests on samples of reconstituted HKMD. The samples were initially normally consolidated to an isotropic stress state of 400kPa. The samples were then loaded instantaneously with a deviator stress q equal to 134, 189 and 243 kPa, respectively, and restrained from undergoing any volume change while the applied stresses were kept constant.

Figure 6.33 compares the experimental data with the numerical predictions in terms of the variation of the axial strain and excess pore water pressures with time, where the time origin corresponds to the application of the deviator stress. From Figure 6.33a) the ET model seems to recover reasonably well the variation of axial strain with time for all cases, including that at the highest deviatoric stress, in which case it underestimates the time that it took the sample to fail.

Figure 6.34 shows the data presented in Figure 6.33a) plotted in *axial strain – natural time* space, in which case the slope of curves is mathematically the current axial strain rate. For the samples subjected to 134 and 189 kPa deviator stress it is observed that following the application of the deviator stress there is a jump in axial strain, after which the axial strain rate decreases monotonically until the end of the test, and this behaviour is well recovered by the ET model analyses. The sample subjected to 243 kPa deviator stress, has a similar behaviour to the samples at lower deviator stress up to about t=500 hours, at which point the strain rate starts to increase, increasing monotonically until the sample failure and the end of the test. The ET analyses predicts that following the application of the deviator stress and a jump in the axial strain, the strain rate decreases monotonically, at a slower rate than observed experimentally, reaching a stable and constant value of axial strain rate just after t=500 hours.

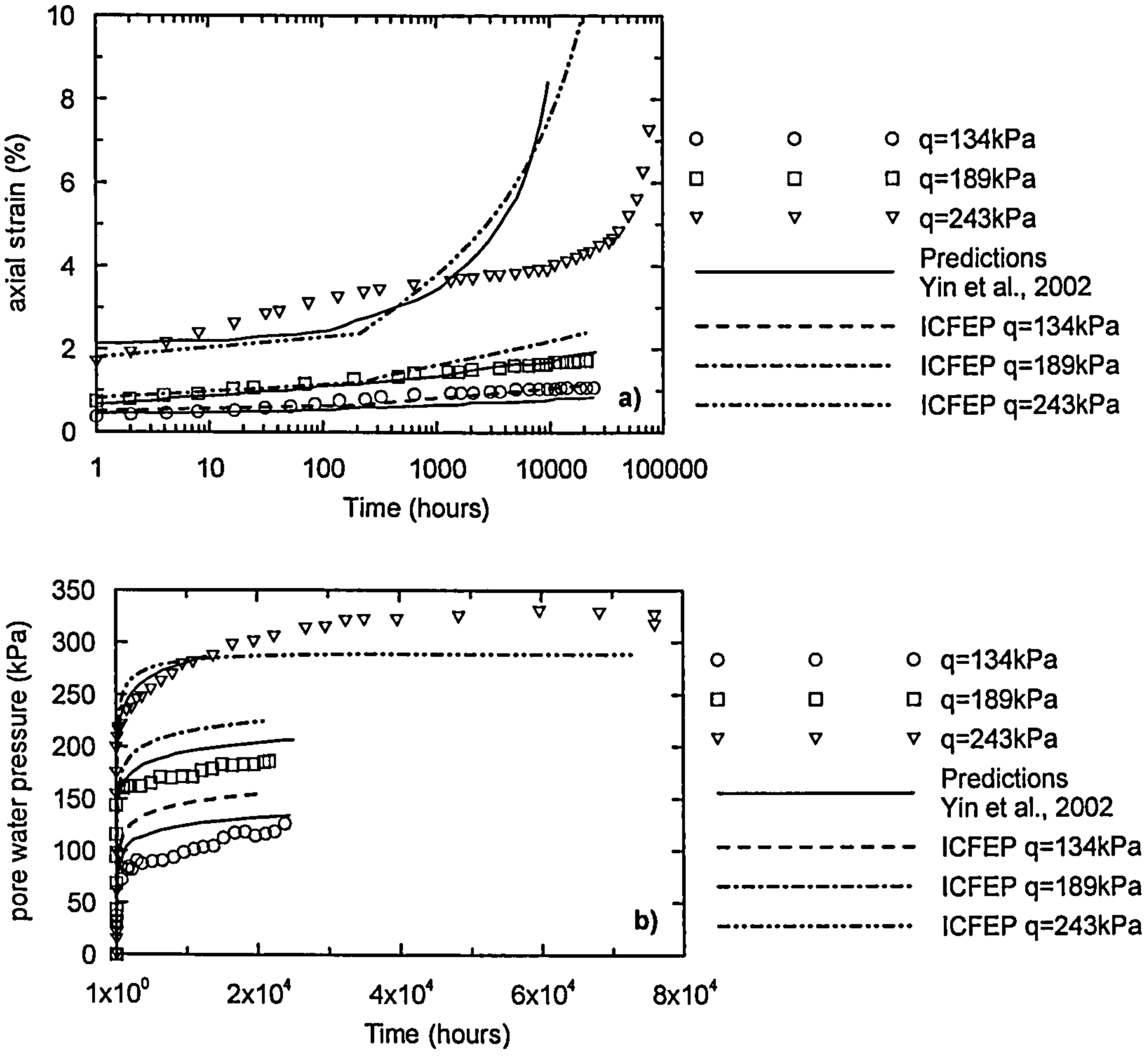

Figure 6.33: Undrained triaxial creep tests at different stress levels; a) variation of axial strain with logarithm of time; b) variation of excess pore water pressure with time.

The fact that the ET model is not able to mimic accelerating creep strain rate (tertiary creep phase) is a result of the formulation of the overstress theory, in which the model is based. According to the overstress theory an increase in the visco-plastic (creep) strain rate leads to an increase in the soil's undrained strength. During an undrained creep test the applied deviatoric stress remains constant throughout the test and at failure an increase in the axial strain rate would imply an increase in the soil's undrained strength, which would inhibit failure.

Regarding the variation of excess pore water pressure with time the ET model is found to overestimate the experimental results for the lower values of applied deviator stress and underestimate the experimental data for a deviator stress equal to 243 kPa.

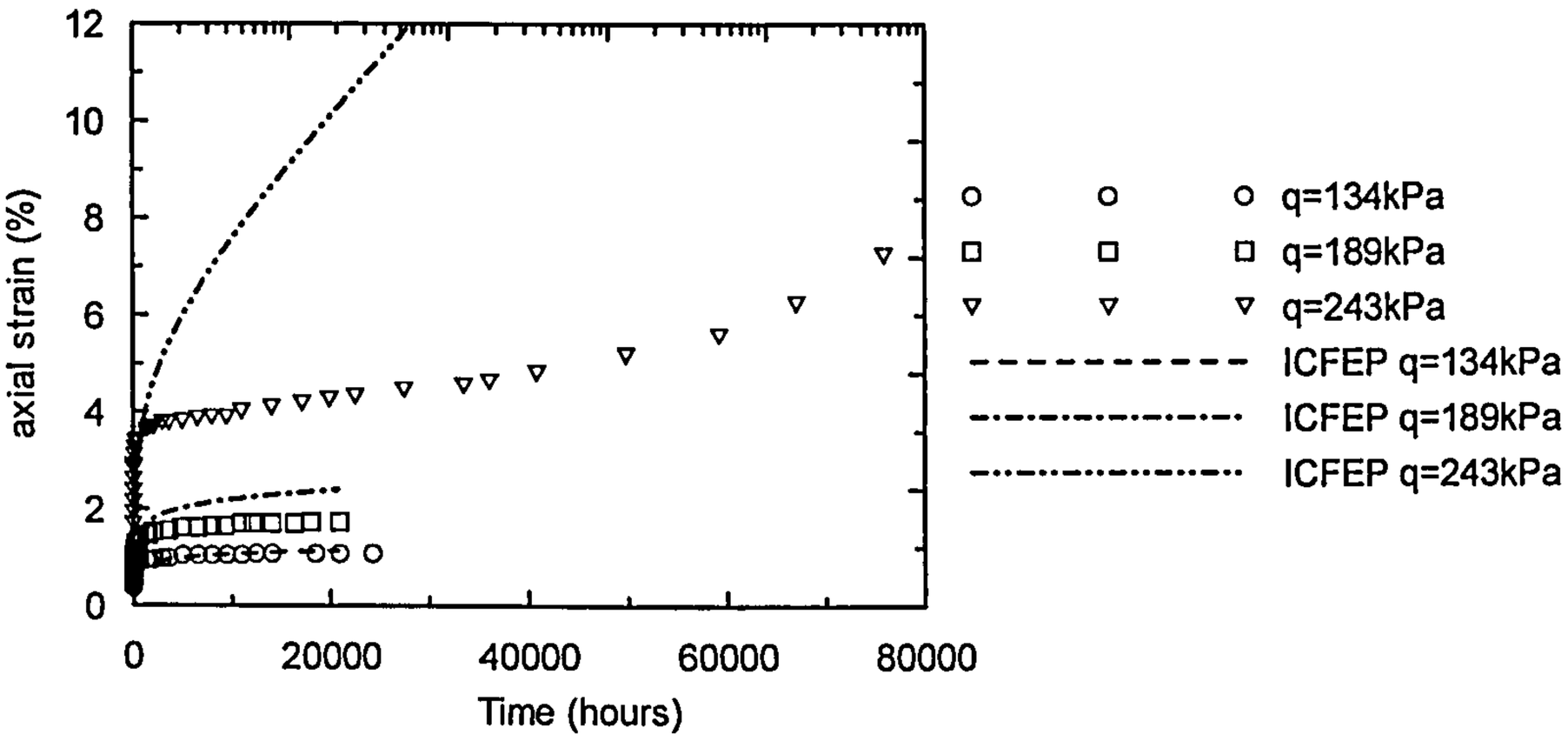

Figure 6.34: Variation of axial strain with time during undrained triaxial creep tests at different stress levels.

Validation test 4

The last validation exercise consists of predicting an undrained triaxial compression test during which the applied axial strain rate was changed in a stepwise manner and combined with stress relaxation periods. The sample was initially isotropically consolidated to 300 kPa and the test procedure is indicated in Figure 6.35. Figure 6.35 compares the experimental data with the numerical predictions in terms of the variation of the deviator stress with axial strain.

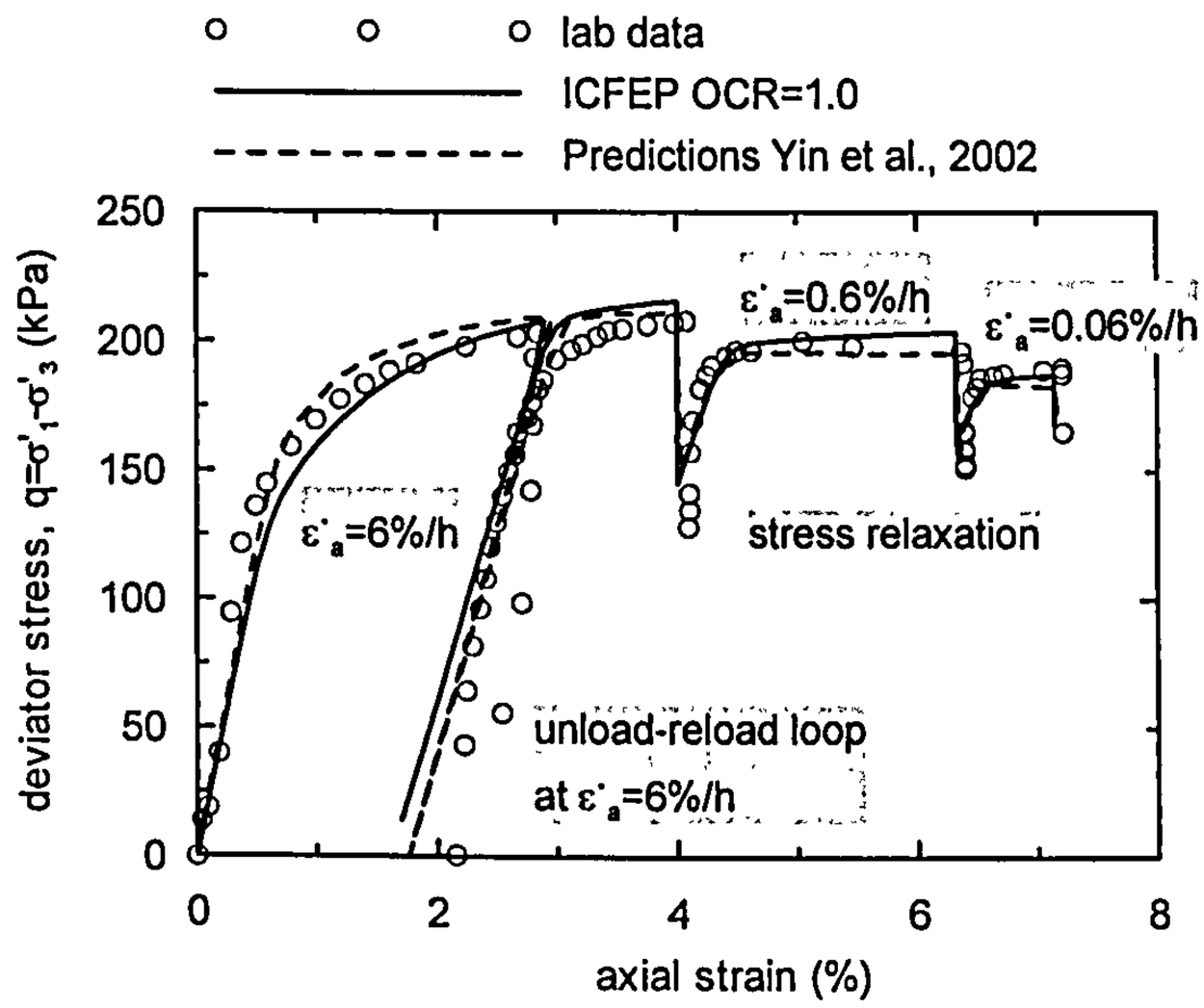

Figure 6.35: Stress – strain curve during an undrained triaxial compression test with stepwise change in strain rate combined with stress relaxation.

The ET model predictions approximate well the experimental data. However the experimental data shows a stiffer response within the small strain range and during the unloading – reloading loop, suggesting that ideally a stiffer elastic response should have been assumed. This is in agreement with the fact that the ET model slightly underestimates the stress change during stress relaxation.

Overall the ET model is found to capture well the behaviour of the HKMD under a variety of stress conditions. Most of the discrepancies may be attributed to the fact that the elastic part of the ET model is characterized by a stress dependent elastic and shear module and therefore cannot incorporate the soil's strong non-linearity at small strains, and the progressive yielding of the soil, as observed experimentally. It is noted that because the shape of the yield and plastic potential surfaces in the deviatoric plane are pre-set in the ET model, and the model parameters have been derived to reproduce the undrained strength under triaxial compression, the ET model is likely to give poor predictions of the undrained strength under other modes of shearing e.g. triaxial extension.

Differences between the ET model predictions and those reported by Yin et al. (2002) can be in general considered minor and result from the differences in the adopted loading surface and/or a misinterpretation of Yin et al. (2002) work.

6.7 Comparison between the Equivalent Time and the Modified Creep Model

This section compares the formulation of the Equivalent Time and the Modified creep model (presented in Chapter 5), and considers the differences in the model predictions under some simple stress paths. In both models, it is assumed that the soil deformation associated with a stress increment $\{\Delta\sigma\}$ over a time increment Δt may be decomposed into an elastic and a visco-plastic part:

Equation 6.23 $$\{\Delta\varepsilon^{T}\} = \{\Delta\varepsilon^{el}\} + \{\Delta\varepsilon^{vp}\}$$

where the elastic incremental strains $\{\Delta\varepsilon^{el}\}$ are instantaneous and thus time independent, and the viscous-plastic incremental strains $\{\Delta\varepsilon^{vp}\}$ are time dependent and

irreversible. The elastic incremental strains $\{\Delta\varepsilon^{el}\}$ can be determined by inverting Equation 6.24:

Equation 6.24 $$\{\Delta\sigma\} = [D] \cdot \{\Delta\varepsilon^{el}\}$$

where $\{\Delta\sigma\}$ is the stress increment and $[D]$ is the elastic constitutive matrix. The elastic response is assumed to be isotropic and thus is fully characterized by two elastic parameters, a stress dependent bulk modulus and a second elastic parameter that can be either the Poisson's ratio μ or the elastic shear modulus G. The first difference between the two models concerns the definition of the elastic bulk modulus, K that is defined by Equation 6.25:

Equation 6.25 $$K = p' \cdot \frac{V}{\kappa}$$

In the Modified Creep model both the specific volume V and the mean effective stress p' vary during an analysis. In contrast, in the ET model the quantity V/κ is a soil constant and during an analysis the elastic bulk modulus will only vary with the mean effective stress.

The visco-plastic incremental strains are in both cases calculated based on an extension of the overstress theory proposed by Perzyna (1963) and can be expressed by Equation 6.27:

Equation 6.27 $$\{\Delta\varepsilon_{ij}^{vp}\} = \Phi \cdot \Delta t \cdot \frac{\partial P}{\partial \sigma_{ij}}$$

The value of the visco-plastic scalar multiplier Φ is assumed to be constant on a given loading surface and the difference between the two models concerns the definition of Φ. In the ET model, the value of Φ is essentially a function of the vertical distance between the current volumetric strain at the equivalent isotropic stress state, $\varepsilon_{vol,m}$ and the volumetric strain on the reference line at the same mean effective stress $\varepsilon_{vol,m}^{ref}$, and how this difference compares to the limit to the amount of volumetric creep strain $\varepsilon_{vol,m,Limit}^{vp}$ and it is given by Equation 6.29:

Equation 6.29

$$\Phi = \frac{\psi_0}{V \cdot t_0} \cdot \left(1 + \frac{\varepsilon_{vol,m}^{ref} - \varepsilon_{vol,m}}{\varepsilon_{vol,m,Limit}^{vp}} \right)^2 \cdot \exp\left[\frac{V}{\psi_0} \frac{\varepsilon_{vol,m}^{ref} - \varepsilon_{vol,m}}{\left(1 + \frac{\varepsilon_{vol,m}^{ref} - \varepsilon_{vol,m}}{\varepsilon_{vol,m,Limit}^{vp}} \right)} \right] \cdot \frac{1}{\left| \frac{\partial P}{\partial p'} \right|_{\substack{p'=p'_m \\ J=0}}}$$

If the value of $\varepsilon_{vol,m,Limit}^{vp}$ is set equal to infinity – the underlying assumption in the Modified Creep model – then the above equation reduces to:

Equation 6.64

$$\Phi = \frac{\psi_0}{V \cdot t_0} \cdot \exp\left[\frac{V}{\psi_0} \left(\varepsilon_{vol,m}^{ref} - \varepsilon_{vol,m} \right) \right] \cdot \frac{1}{\left| \frac{\partial P}{\partial p'} \right|_{\substack{p'=p'_m \\ J=0}}}$$

Consider a general stress state $\left(p', J\right)$ that lies on a loading surface characterized by the quantity p'_{mc}. From Figure 6.36 the value of $\varepsilon_{vol,m}^{ref}$ and $\varepsilon_{vol,m}$ can be written as:

Equation 6.65

$$\varepsilon_{vol,m}^{ref} = \frac{\lambda}{V} \ln\left(\frac{p'_{mc}}{p'_{m0}} \right)$$

where p'_{m0} is the mean effective stress at zero volumetric strain on the reference time line.

Equation 6.66

$$\varepsilon_{vol,m} = \varepsilon_{vol} + \frac{\kappa}{V} \ln\left(\frac{p'_{mc}}{p'} \right) = \frac{\lambda}{V} \ln\left(\frac{p'_{ref}}{p'_{m0}} \right) - \frac{\kappa}{V} \ln\left(\frac{p'_{ref}}{p'_{mc}} \right)$$

where p'_{ref} is the mean effective stress at the intersection of the current elastic line with the reference time line. Substituting Equation 6.65 and Equation 6.66 into Equation 6.64, and considering the definition of the volumetric strain rate on the reference time line given by Equation 6.53 gives:

Equation 6.67

$$\Phi = \left(\dot{\varepsilon}_{vol}^{vp} \right)_{t=t_0} \cdot \left(\frac{p'_{mc}}{p'_{ref}} \right)^{\frac{\lambda-\kappa}{\psi}} \cdot \frac{1}{\left| \frac{\partial P}{\partial p'} \right|_{\substack{p'=p'_m \\ J=0}}}$$

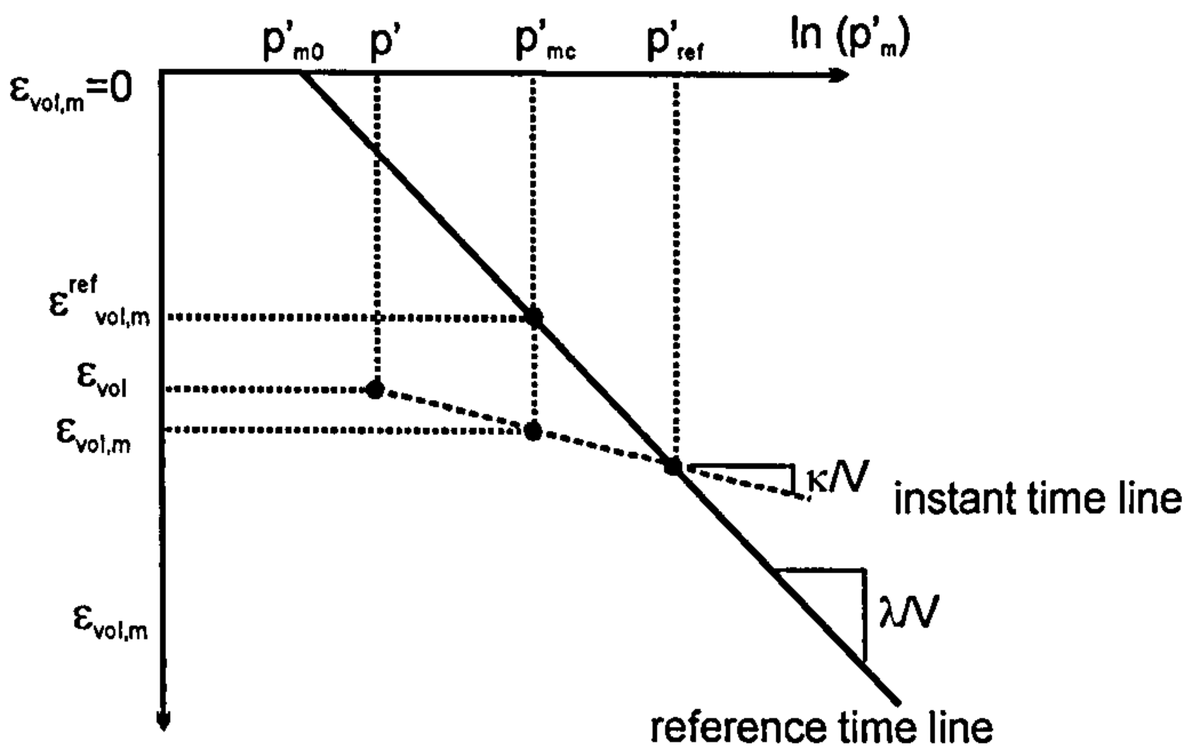

Figure 6.36: Schematic diagram of the framework of the Equivalent time model.

That is similar to Equation 5.19, used in the Modified Creep Model to evaluate the value of Φ. So in principle when the ET model is made to collapse into a linear logarithmic law, by setting the parameter $\varepsilon^{vp}_{vol,m,Limit}$ to a large value (i.e. a value equal to or larger than the volumetric strain to reach the condition when there is no longer any voids in the soil), the two formulations are identical, and provided that the same shape is adopted for the loading and plastic potential surfaces the models should yield identical predictions.

In the next paragraphs, the models performance is compared using the results of single element FE analyses that mimic common laboratory tests. The ET model predictions are obtained using the model parameters given in Table 6.2, assuming the soil to have no structure and setting $\varepsilon^{vp}_{vol,m,Limit}$ equal to 0.6. For the Modified Creep model, the model parameters are given in Table 5.1 with the exception of $\dot{\varepsilon}^{ref}_{vol}$ which is set equal to 0.005211/day so that the time dependent parameters adopted for the two models are comparable.

Figure 6.37 shows the model predictions under 1D compression in *e-lnp'* space for an IL 24 hour oedometer test with a stress increment ratio equal to unity (Figure 6.37a) and a CRS oedometer test performed at 0.005211/day axial strain rate (Figure 6.37b).

The initial void ratio is slightly different for the two models as in the Modified Creep model the initial void ratio is calculated from the initial stress state and the model parameter V_{1ref}, λ and κ, while in the ET model, the initial void ratio is input in the initial stress file. However, the more striking feature is the divergence between the two

models at large stress values. The CRS compression curve predicted by the ET model is a straight line while that predicted by the Modified Creep model curves downwards, although in the MCM the reference time line and lines of constant volumetric strain rate have been postulated to be straight in V-lnp' space. The reason for the curvature was found to be related to the hardening rule given by Equation 5.18.

Equation 5.18

$$\Delta p'_{0ref} = p'_{0ref} \cdot \frac{V}{\lambda - \kappa} \cdot \Delta \varepsilon_{vol}^{vp}$$

where the V is the current specific volume both when employing small and large displacement theory.

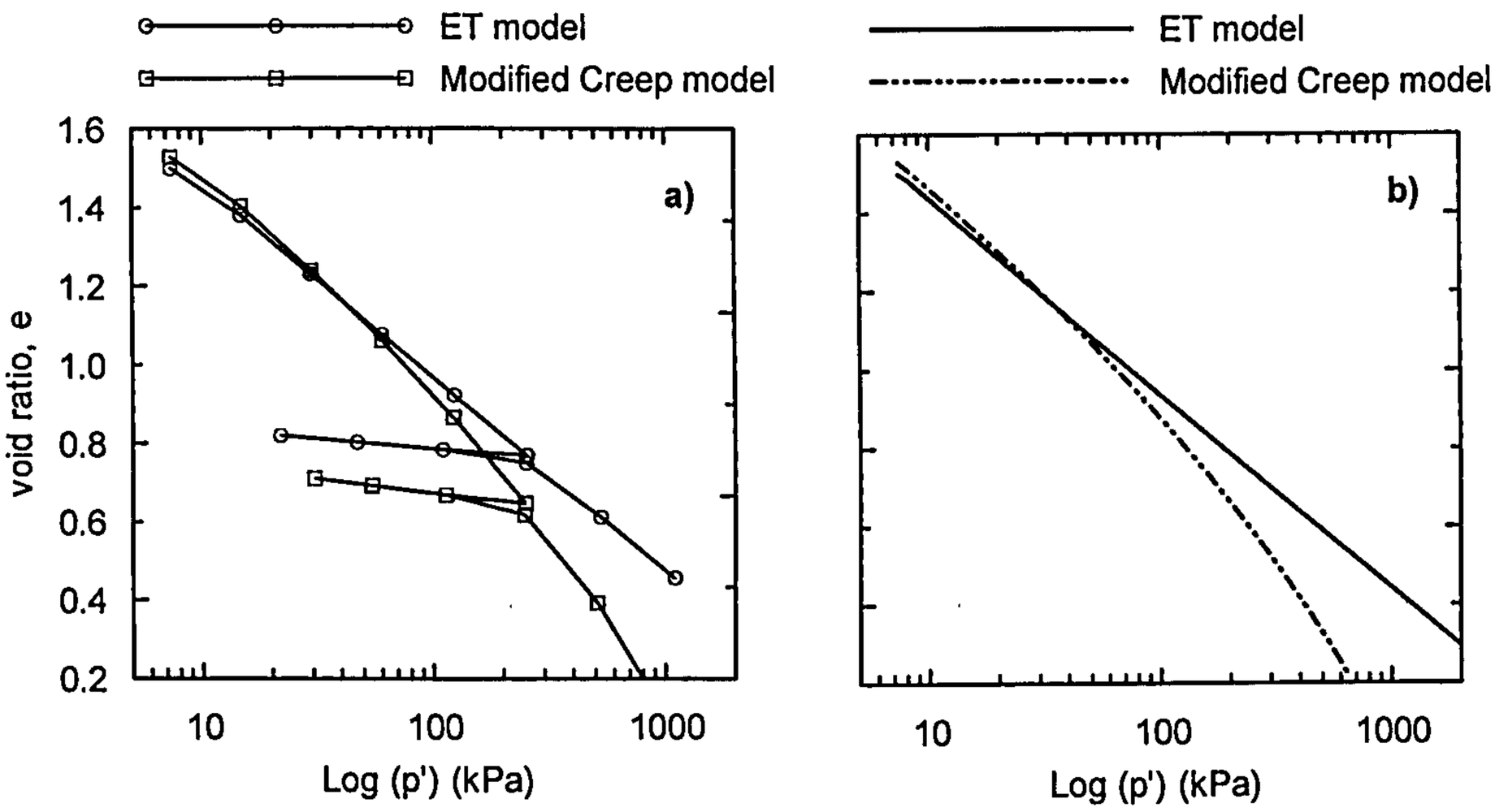

Figure 6.37: Comparison between the ET and the Modified Creep model under 1D compression a) IL 24 hour oedometer test; b) CRS oedometer test.

Therefore when employing small displacement theory a given volumetric strain increment $\Delta \varepsilon_{vol}^{vp}$ will progressively yield a smaller change in the mean effective stress on the reference line p'_{0ref} as the value of specific volume decreases, causing the reference time line (and thus any line of constant volumetric strain rate) to become curved). If the same analyses are repeated using large displacement theory it is found that the MCM model predicts that the CRS compression line is a straight line in *e-lnp'* space and the Equivalent Time model predicts that the CRS compression line is concave upwards (as shown in Section 6.4, Equation 6.6b). The two models give coinciding

predictions if the value of specific volume V in Equation 5.18 is replaced by its initial value V_i during analyses employing small displacement theory.

Figure 6.38 shows the model predictions during a drained creep period and a stress relaxation period under K_0 stress conditions, following compression at a 0.00521/day axial strain rate. Figure 6.38 a) shows the change in void ratio with time during a drained creep period predicted by the two models and that calculated using a linear logarithmic creep law with a coefficient of secondary consolidation equal to 0.03, and considering the start of the secondary compression to occur at t=24 hours.

The ET model predicts a change in void ratio very close to that given by the linear logarithmic creep law, the small difference resulting from the in-built non-linearity in the model. The Modified creep model predicts a change in void ratio larger than that predicted by the linear logarithmic law, with the difference increasing with time. This results from the curvature of the reference time line in *e-lnp'* space as discussed above, that causes the horizontal distance between the current state point and the reference line to be less than that required for the establishment of a linear logarithmic creep law.

Figure 6.38 b) shows the variation in vertical effective stress with time during a stress relaxation period and the predictions from the two models are very similar. It is noted that in this case the differences in curvature of the reference line in *e-lnp'* space does not affect the results as during undrained loading the specific volume remains constant and it is therefore irrelevant if in Equation 5.18 the current or the initial value of specific volume is employed.

From the above discussion the formulation of the two models is in the essence very similar, and the two models will yield similar predictions for the case in which the parameter $\varepsilon^{vp}_{vol,m,Limit}$ in the ET model is given a value equal to or larger than the volumetric strain required to bring the soil to a state when there are no voids left, and the yield and plastic potential functions in the ET model are set to give the shape of the ellipse of the MCC model. The difference between the predictions of the two models will increase with the magnitude in mean effective stress change prescribed during the analysis procedure.

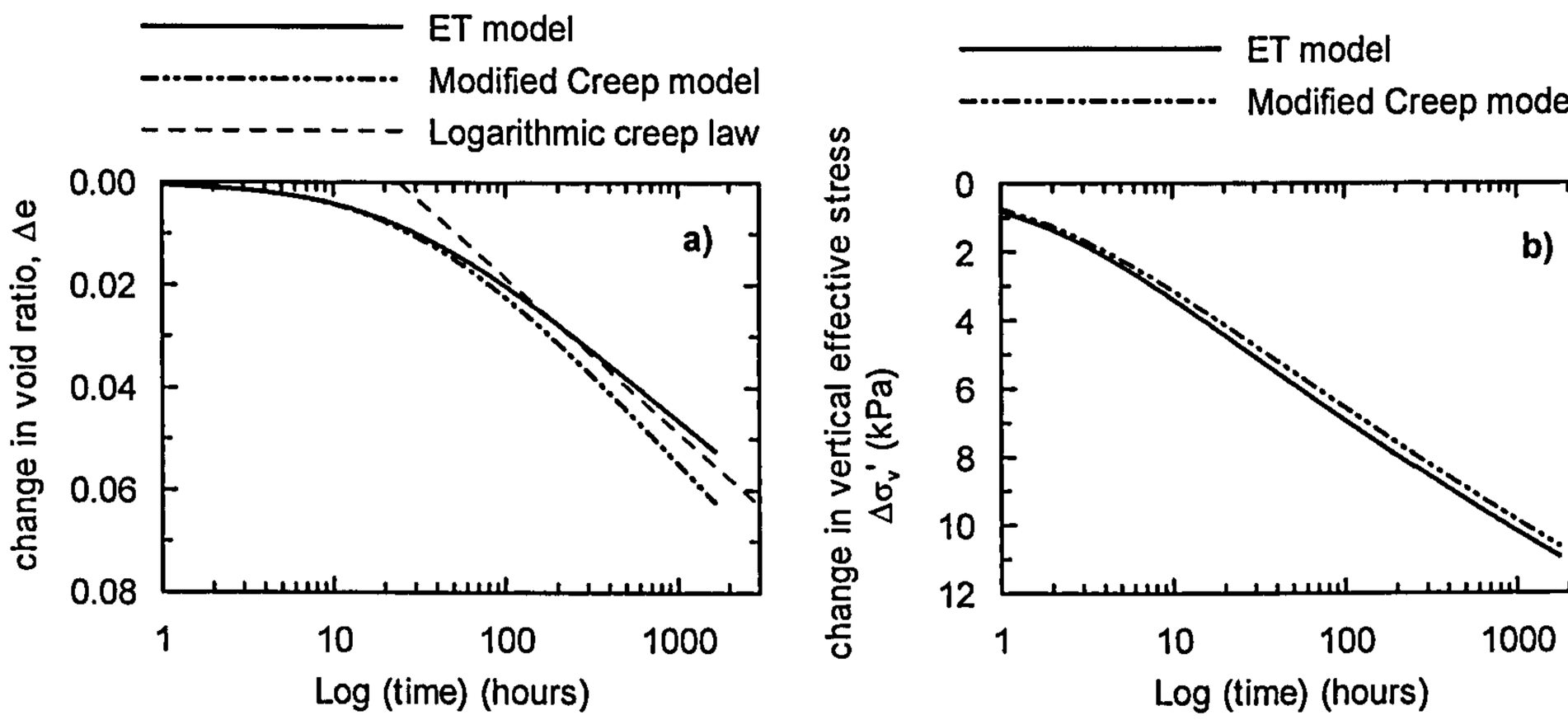

Figure 6.38: Comparison between the ET and the Modified creep model under a) a drained creep period and b) stress relaxation under K_0 stress conditions.

6.8 Concluding remarks

This Chapter has presented the development, implementation and validation of an elastic visco-plastic constitutive model based on the overstress theory that aimed to simulate the time and rate dependent behaviour of a material with isotach viscosity.

The model assumes that the soil deformation associated with an effective stress increment $\{\Delta\sigma'\}$ can be divided into an instantaneous elastic component and a time dependent visco-plastic component. The instant component is derived from the elastic model parameters, which consist of a stress dependent bulk modulus and a second elastic parameter that can be either the Poisson's ratio, μ or the elastic shear modulus, G. Under isotropic stress conditions the delayed component is calculated assuming an hyperbolic creep law, with a limit for the amount of visco-plastic volumetric strain that can be developed during creep at constant effective stress. Based on the findings reported in Chapter 5 the extension of the model to generalized stress space was done assuming that a given loading surface was a locus of constant visco-plastic scalar multiplier and the various visco-plastic strain components are given by a plastic potential function. The loading and plastic potential surfaces are described by a flexible function that can reproduce a wide range of shapes in *J-p'* stress space. The influence of the intermediate principal stress is accounted for using the Matsuoka-Nakai failure criterion.

The model was subsequently validated through a series of simple finite element analyses, and the validation procedure can be divided in three main parts:

- Single element analyses that mimic common laboratory stress paths where the analysis results are compared with observed experimental trends as described in Chapter 2. The ET model is found to reproduce the phenomena of primary and secondary compression, stress relaxation and persistent rate effects on the stress-strain soil response under K_0 and triaxial stress conditions. Due to its formulation the ET model is not able to mimic accelerating creep and thus cannot reproduce appropriately undrained creep rupture.

- A set of single element analyses that simulate laboratory tests on soft Hong Kong marine deposits (HKMD). The analysis results are compared with the experimental results (Zhu, 2000) and numerical predictions reported by Yin et al. (2002). Overall the ET model is found to capture well the behaviour of the HKMD under a variety of stress conditions, with most of the discrepancies being attributed to the fact that the elastic part of the ET model cannot reproduce the soil's strong non-linearity at small strains, and the progressive yielding of the soil, as observed experimentally. Differences between the ET model predictions and those reported by Yin et al. (2002) can be considered minor and are likely to result from the differences in the adopted loading surface.

- A series of finite element analysis that mimic the consolidation of three oedometer samples with different thickness, 20, 10 and 2 cm, respectively, when subjected to a vertical stress increment $\Delta\sigma_v$ =40 kPa. The ET model predicts that the vertical strain at the end of primary consolidation depends on the thickness of the consolidating layer, increasing with the layer thickness as predicted by the viscous approach. The implications are that when estimating vertical strain (or deformation) of a consolidating layer in the field, which will be much thicker than the element of soil investigated in the laboratory, the non-consideration of the rate effects may lead to a substantial underestimation of the magnitude of the settlement at EOP. In addition, the Terzaghi's solution for 1D consolidation is adequate to evaluate the average degree of settlement, independently of the consolidating layer thickness, however the degree of pore water pressure dissipation is in principle different, and for a consolidating layer

in the field the degree of excess pore water pressure dissipation is expected to be smaller than the degree of settlement.

When comparing the ET model with the Creep Model 1 it was concluded that the formulation of the two models was essentially very similar and that the two models would give close predictions provided that the ET model is made to collapse into a linear logarithmic creep law (by adopting a large value for the limit for the visco-plastic volumetric strain during a creep period) and setting the loading and plastic surfaces to give the ellipse of the MCC model. The predictions given by the two models will diverge as the mean effective stress change imposed by the considered stress path increases. The ET model presents advantages in relation to the Creep model 1: a) it can consider both linear and non-linear creep laws and b) incorporates a flexible function to describe the loading and plastic potential surfaces in J-p' stress space such that both the drained and undrained soil strength can be correctly captured. The above aspects make the ET model more flexible to model the behaviour of natural clays and therefore it is the model employed in the analyses of the boundary value problems presented in the subsequent chapters of this thesis.

7 BEARING CAPACITY OF PRE-LOADED FOOTINGS ON SOFT CLAYS

7.1 Introduction

The design of shallow foundations on both clay and sand soils is usually performed using well-established analytical and empirical bearing capacity formulae. These solutions can take into account the foundation shape, size and depth, the load inclination and eccentricity, and assume the soil strength parameters to be either constant or to vary in some simple way with depth. An updated summary of available solutions can be found e.g. in Randolph et al (2004). The design of new foundations is therefore relatively simple and for clay soils the short term undrained bearing capacity is the most critical (except for heavily overconsolidated clays).

However, the situation is not so clear if extra load is to be added to an existing foundation on clay, which has been in place for a period of time. This is because there has been a change in undrained shear strength due to the dissipation of the excess pore pressures, generated during construction and initial loading. The resulting distribution of undrained shear strength below the foundation will be complex, and conventional solutions for determining the current bearing capacity will be inappropriate. In practice, such a situation arises when extra load needs to be added to an existing foundation e.g. installation of additional equipment in a building, construction of new floors or the reuse of old foundations for a new building.

Bransby (2002) examined the effect of vertical preload on the capacity of surface footings under combined vertical and horizontal undrained loading, a situation of particular relevance to offshore foundations, by means of a series of finite element analyses. The foundation soil was modelled using the Cam Clay constitutive model and both a constant and a linearly increasing undrained strength with depth were considered. It was shown that larger increases occur in the horizontal capacity, compared to that in the vertical capacity.

Jackson et al (1997) and Zdravkovic et al. (2003) have investigated the increase in undrained bearing capacity under pure vertical load of pre-loaded strip foundations by means of coupled finite element analyses. In these studies, the soil foundation was

modelled using the time independent Modified Cam-Clay (MCC) constitutive model and ground profiles and model parameters, typical of both soft and stiff clays, were considered.

The general methodology was: a) define the initial undrained bearing capacity of the footing; b) pre-load footings to a percentage of the initial bearing capacity, namely, 20%, 40%, 60%, 80% and 100%; c) allow full consolidation of the foundation soil under constant applied load and d) load the footings to failure under undrained conditions.

In these analyses, the increase in undrained bearing capacity, or increase in the undrained strength of the foundation, is produced by the increase in effective stress in the foundation soil concurrent with the dissipation of the (contractive) excess pore water pressures generated during the initial loading. Therefore, once full consolidation has occurred, the increase in the undrained strength of the foundation is a direct measure of the magnitude of the contractive pore water pressures generated during first loading.

However, once all the excess of pore water pressures have dissipated and the effective stresses in the foundation are constant no further increase in undrained strength is predicted (nor secondary consolidation settlement, if the serviceability of the footing was under consideration). On the other hand, it is well documented in the literature (e.g. Bjerrum, 1967) that soils, in particular soft normally consolidated clays may experience a significant amount of secondary consolidation settlement and ageing – apparent increase in strength and stiffness characteristics with time at constant effective stresses. The mechanisms responsible for the development of ageing are not yet entirely understood but it is thought that ageing derives from the development of both creep and structure.

This Chapter presents a study of the bearing capacity, under pure vertical load, of a pre-loaded strip footing taking into account the effects of consolidation and the soil hardening associated with the development of creep strains. The foundation soil is modelled with the Equivalent Time (ET) Model described in Chapter 6, which has been shown to mimic primary and secondary consolidation, stress relaxation, persistent strain rate effects on the stress-strain response under K_0 and general stress states conditions and of particular relevancy to this study, to reproduce an increase in the yield stress and

in the pseudo elastic stress range, on subsequent loading, following a period of drained creep. It is emphasized that the development of structure is not considered in this study.

Both the MCC and the ET constitutive models predict an increase in the foundation's undrained strength due to the dissipation of the excess pore pressures generated during the initial loading. The use of the time dependent ET model in this study means that both during and after the dissipation of the excess pore pressures there will be an additional increase in the foundation's undrained strength due to the development of visco-plastic strains and associated soil hardening that occurs even under constant effective stress. The results of Zdravkovic et al. (2003), which do not account for such creep strains, are then likely to under predict the undrained bearing capacity of a pre-loaded strip foundation.

It seems appropriate to summarise the relevant outcomes of the work by Zdravkovic et al. (2003). Figure 7.1 shows the ultimate bearing capacity (Q), expressed as a proportion of the initial undrained bearing capacity (Q_i), plotted against the level of preload, for 2 m and 10 m wide strip footings on soft clay with a surface crust.

It is found that the gain in bearing capacity is highest for the 10 m wide rough footing as the condition of no horizontal displacements at the base of the footing pushes the failure mechanism deeper, involving a larger amount of normally consolidated soil. The gain for the 10 m wide smooth footing is slightly smaller because the failure mechanism is slightly shallower.

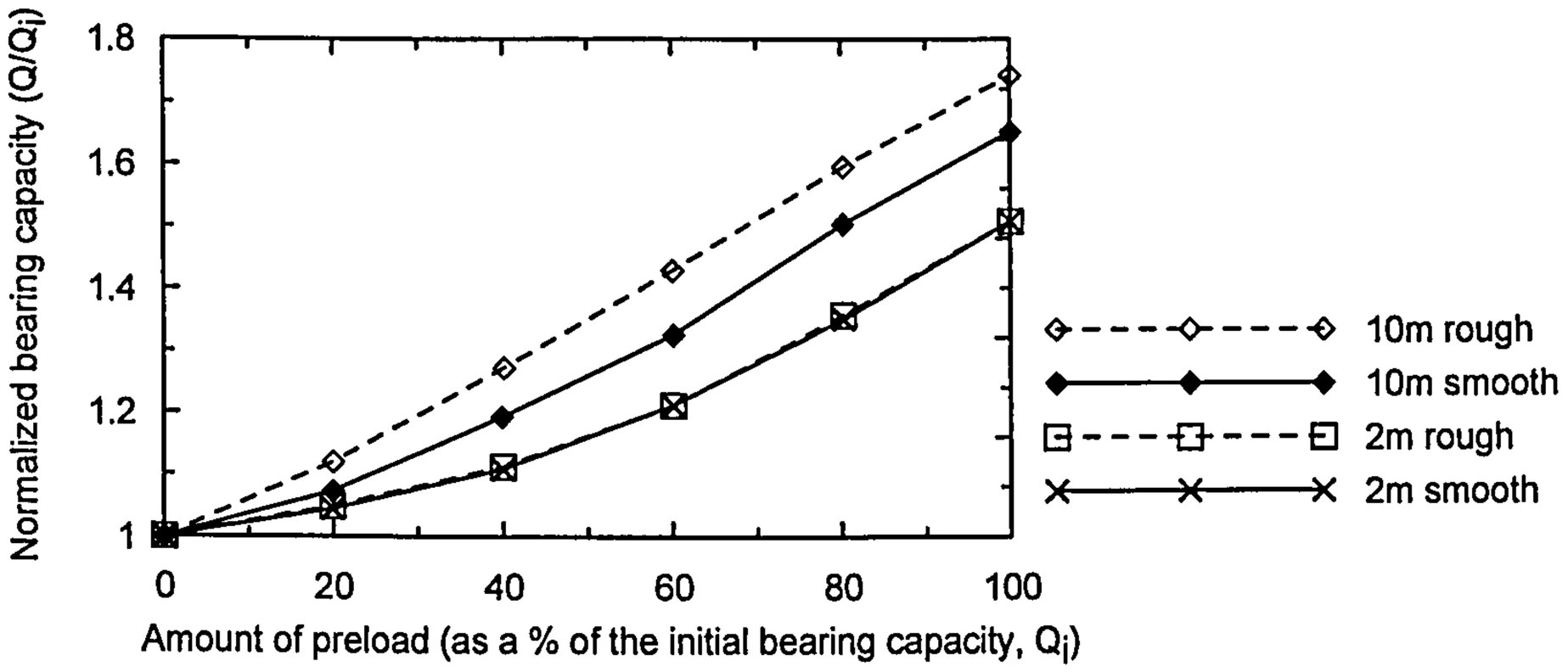

Figure 7.1: Gain in bearing capacity due to pre-load for strip footing on soft clay with a surface crust (Zdravkovic et al, 2003).

The failure mechanism of the 2 m wide footing is controlled by the presence of the 2 m deep surface crust, which has a strength reducing with depth, and the failure mechanisms of both rough and smooth footing are forced to pass through the weakest soil at the base of the crust and, consequently, yield the same bearing capacity.

In the case of the 2 m wide footings, the failure mechanisms involve a smaller proportion of the normally consolidated clay than the 10 m wide footings, and a greater proportion of the surface crust that has a higher overconsolidation ratio. Consequently for a given value of preload the contractive excess pore pressures generated will be relatively smaller for the 2 m wide footings, compared to the 10 m wide footings, and so is the gain in bearing capacity.

The gain in bearing capacity is found to increase significantly with the level of preload, for all cases considered in Figure 7.1. For a 2.0m wide footing, the gain in bearing capacity can reach about 50%, at 100% preload. In practice, given that shallow foundations are designed with a factor of safety on load of at least 2 (50% preload), the available gain in bearing capacity would be at the most 15%.

The present study examines the case of a 2 m wide rough strip footing on soft clay with a surface crust. The reasons that lead to the choice of this case are as follows:

a) Soft normally consolidated clays develop, in general, larger secondary consolidation settlements, compared with stiff clays, both in absolute value and as a proportion of the primary consolidation settlement and, therefore, the additional gain in bearing capacity to be predicted is likely to be more significant.

b) According to the results presented by Zdravkovic et al. (2003), shown in Figure 7.1, a 10 m wide footing, either smooth or rough, yields a larger increase in bearing capacity than a 2 m wide footing, for a given value of preload. It is expected that the analyses with the ET constitutive model will show a similar trend, and thus it is on the safe side to analyse a narrow footing and eventually apply those results to a wider one.

c) The condition of rough interface at the foundation base is more likely to occur in practice than that of a smooth interface.

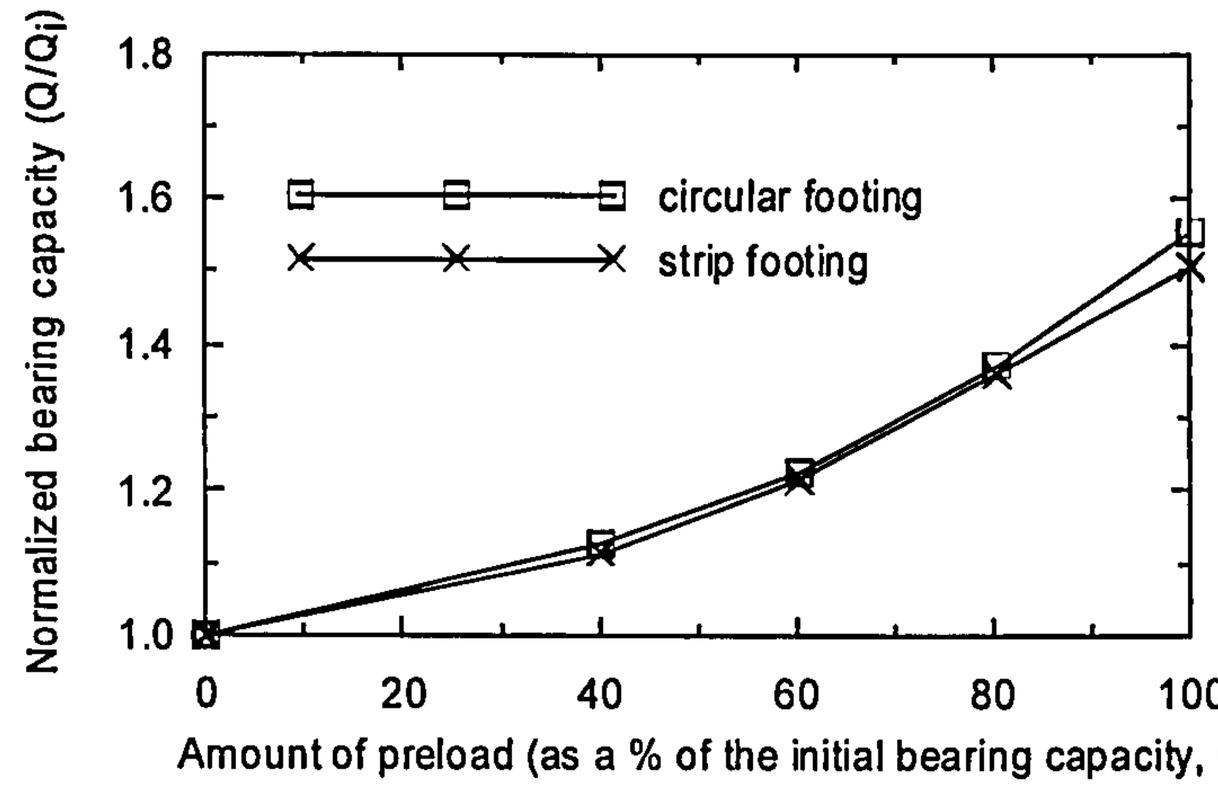

Figure 7.2: Normalized bearing capacity of a circular (D=2m) and a strip (B=2m) preloaded footing on a soft clay with a surface crust (Randolph et al., 2004)

Randolph et al. (2004), using the same methodology as that employed by Zdravkovic et al. (2003), have compared the effect of preload on the bearing capacity of circular (2 m diameter) and strip (2 m wide) surface footings for the case of a ground profile consisting of soft clay with a surface crust. The results are shown in Figure 7.2 in terms of the normalized bearing capacity against the value of preload. The effect of preload is almost identical for the circular and the strip footing, being slightly larger for the circular footing, especially at large preload values. The applicability of the results of the present study on a strip footing to circular footings is discussed later in this Chapter.

7.2 Ground profile

The ground profile adopted for this study is the "soft clay" case described by Zdravkovic et al. (2003) that corresponds to the ground conditions encountered on a site in Grimsby, Yorkshire (Mair et al., 1992). The ground conditions and the model parameters shown in Table 7.1, with the exception of the time dependent parameters t_0, ψ_0/V and $\varepsilon^{vp}_{vol,m,Limit}$, have been determined by means of in-situ and laboratory test data. The derivation of the time dependent parameters is discussed in Section 7.4.

At this site, the ground profile consists of normally consolidated clay (overconsolidation ratio of 1) below a depth of approximately 2 m, with a stronger crust at the surface. The water table is 2 m below ground level, and the soil above this level is assumed to be saturated and able to sustain tensile pore water pressures.

Table 7.1: Model parameters.

φ'	κ/V	λ/V	G	γ	k
(°)	-	-	kPa	kN/m^3	m/s
32	0.0088	0.088	1700	17.0	$5 \cdot 10^{-10}$
V_0	t_0	ψ_0/V	$\varepsilon^{vp}_{vol,m,Limit}$	$\alpha_f=\alpha_g$	$\mu_f=\mu_g$
-	day	-	-	-	-
2.5	1.0	0.00521 0.00174	0.6 0.06	0.4	0.9

Notes:

φ' = angle of shearing resistance;

κ/V= slope of the instant time line in ε_{vol}-ln p' space;

λ/V = slope of the reference time line in ε_{vol}-ln p' space;

The option of constant κ/V and λ/V has been adopted, for details please refer to Chapter 6.

G = elastic shear modulus;

k = permeability;

γ = bulk unit weight of the soil;

V_0 =initial specific volume;

t_0, ψ_0/V and $\varepsilon^{vp}_{vol,m,Limit}$ are time dependent parameters, see section 7.4.

α_f and μ_f = model parameters that define the shape of the loading surface in the p'-J space;

α_g and μ_g = model parameters that define the shape of the plastic potential function in the p'-J space.

The initial undrained strength profile has been estimated based on undrained triaxial compression tests, and is shown in Figure 7.3. The model parameters for both the MCC and the ET models are effective stress parameters and the undrained strength cannot be input directly.

In the case of the MCC model, the undrained strength can be derived from the basic model parameters, the overconsolidation ratio (OCR) and the initial stress state (Potts &Zdravkovic, 1999). Consequently the coefficient of earth pressures at rest (K_0) and the overconsolidation ratio (OCR) have been varied to give a realistic distribution of undrained strength above the water table, as shown in Figure 7.3 (a). The resulting distributions of OCR and K_0 are shown in Figure 7.3 (b).

In the ET model, the undrained strength will be, in addition, a function of the shearing rate and no closed form solution exists. It is noted that the mobilized undrained shear strength will be a function of the foundation loading rate and, as a rule, different to that predicted by the MCC model.

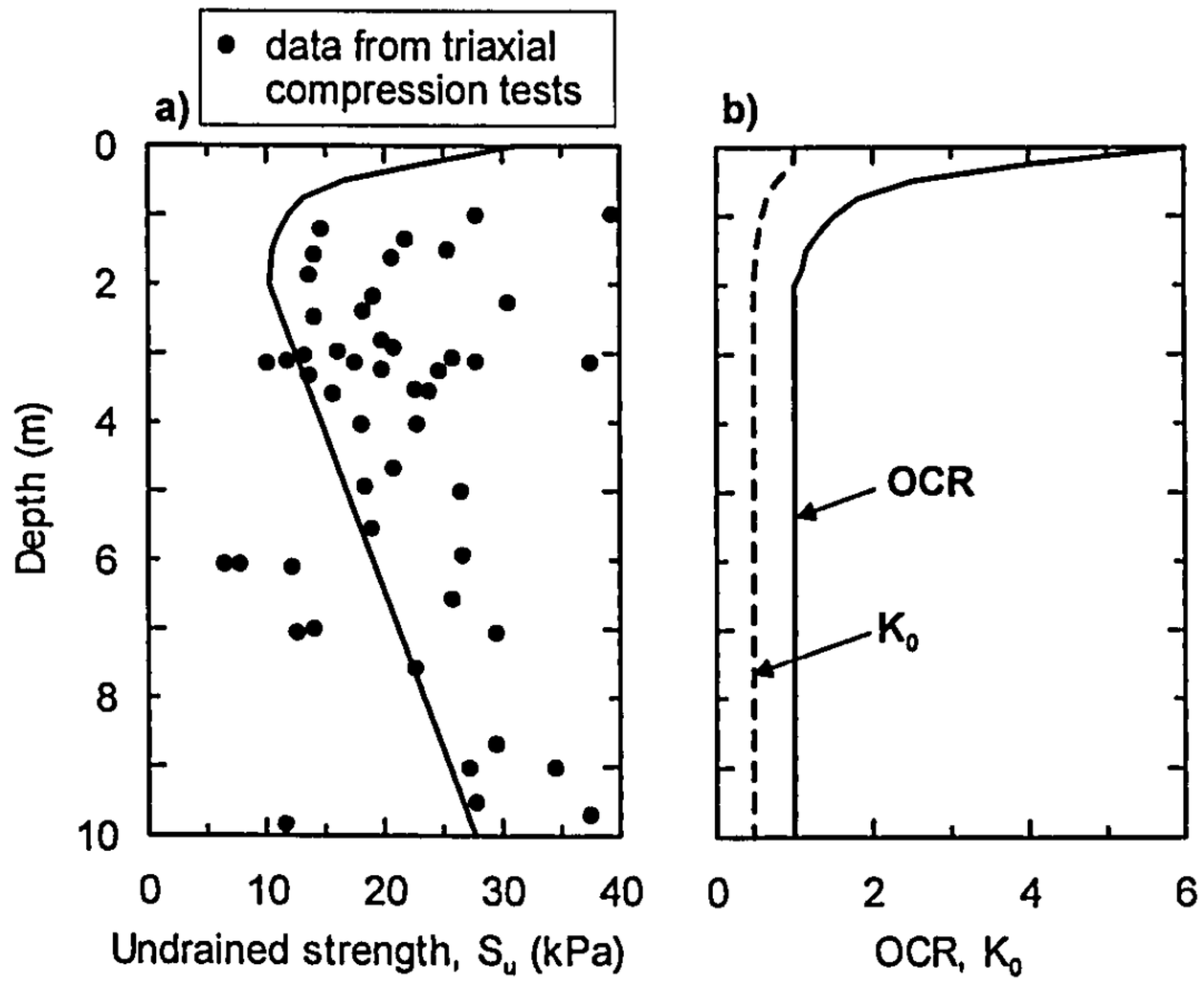

Figure 7.3: a) Undrained triaxial compression laboratory data (from Mair et al., 1992) and undrained strength profile predicted by the MCC model for triaxial compression conditions b) variation of OCR and K_0 with depth.

7.3 Problem Geometry and Boundary Conditions

Plane strain analyses modelling a 2 m wide rough strip footing have been performed. The analyses presented are, as rule, coupled consolidation analyses with full (3x3) integration, with a few exceptions when it is stated so. The finite element mesh is shown in Figure 7.4. Due to symmetry considerations only half of the problem domain needs to be discretized and considered in the analyses. The mesh consists of eight noded isoparametric elements with four pore pressure degrees of freedom at the corner nodes, and two displacement degrees of freedom at both corner and mid-side nodes.

The displacement boundary conditions are shown in Figure 7.4; the nodes at the base of the mesh are prevented from moving in the vertical and horizontal directions, while the vertical sides of the mesh are fixed in the horizontal direction only.

The footing itself was not discretized in the finite element mesh. The loading of a rough rigid footing is simulated by applying increments of equal vertical displacement and zero horizontal displacement to the nodes on the boundary below the position of the footing, and the load being carried by the footing is then the sum of the reaction forces on those nodes. During the consolidation periods, these nodes are forced to move vertically by the same amount, using the *tied degree of freedom* concept. Consequently

the resulting displacement is not prescribed but instead is a result of the analyses. During this process the total load carried by the footing remains constant.

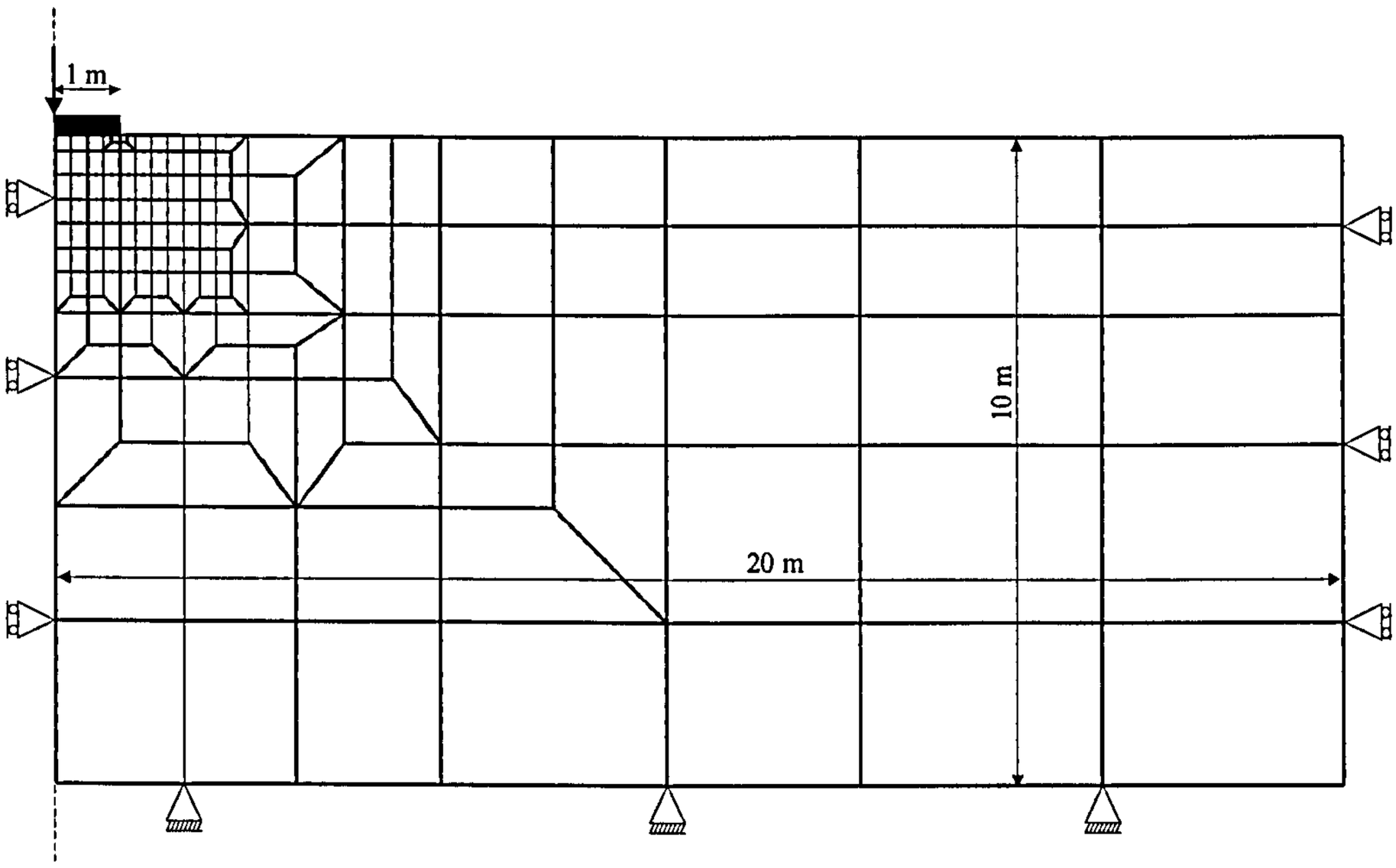

Figure 7.4: Finite element mesh and displacement boundary conditions.

The seepage boundary conditions are to allow no flow of water at the base of the mesh, immediately beneath the footing and on the left hand boundary of the mesh, which forms the vertical plane of symmetry through the footing. On the right hand boundary of the mesh, pore water pressures are kept equal to their initial values, as determined by the water table 2 m below ground level. Along the ground surface, next to the footing no flow of water was allowed during the loading stages of the analyses, aiming to maintain overall undrained conditions, while in the consolidation periods the pore water pressures have been set equal to their initial values, prior to footing construction.

7.4 Constitutive Model and Model Parameters

This chapter examines the effect of soil hardening due to the development of creep strains on the bearing capacity of pre-loaded strip footings. The foundation soil is modelled using the Equivalent Time constitutive model described in Chapter 6.

The model parameters have been derived based on in-situ and laboratory testing data and, therefore, correspond to a real soil. The model parameters are given in Table 7.1. The first six parameters are equal or equivalent to the parameters required by the MCC

model and take the values used by Zdravkovic et al. (2003). The three parameters, t_0, ψ_0/V and $\varepsilon^{vp}_{vol,m,Limit}$ describe the time and rate dependent response of the model, and they have been determined to have a practical meaning.

In engineering practice, the time dependent behaviour of soil is commonly characterized by the coefficient of secondary consolidation, $C_{\alpha e}$ calculated from IL 24h oedometer tests, and assuming a linear logarithmic creep law between time and void ratio (or settlement).

Mesri and Castro (1987) reported that the value of $C_{\alpha e}/C_c$, where C_{ce} is the compression index (defined in the normally consolidated range by Equation 7.1 and related to the value of λ by Equation 7.2), is equal to 0.04±0.01 for most inorganic soft clays. For a value of λ equal to 0.22 that corresponds to values of $C_{\alpha e}$ between 0.015 and 0.025.

Equation 7.1

$$C_{ce} = \frac{\Delta e}{\Delta \log(\sigma'_z)}$$

e =void ratio; σ_z'= vertical effective stress

Equation 7.2

$$C_{ce} = \lambda \cdot \ln 10$$

When estimating long-term settlements of foundations or other geotechnical structures, the conservative approach is to consider a high value of $C_{\alpha e}$ as this implies that larger settlements are predicted. However, when considering the ultimate bearing capacity, the use of a larger value of $C_{\alpha e}$ is non-conservative. Adopting a high value of $C_{\alpha e}$ implies that more *creep* strains are predicted, and consequently a larger increase in the soil undrained strength. In this study two values of $C_{\alpha e}$ are considered: 0.01 and 0.03.

To relate $C_{\alpha e}$ to the model parameters t_0, ψ_0/V and $\varepsilon^{vp}_{vm\lim it}$ that characterise the model time dependent response, some assumptions are required, as the parameter $C_{\alpha e}$ is based on a linear logarithmic creep law and the ET constitutive model incorporates non-linear logarithmic creep function. However, if the limit for the amount of visco-plastic volumetric strain $\varepsilon^{vp}_{vol,m,Limit}$, is prescribed a value that corresponds to the volumetric strain required to attain the condition when voids no longer exist in the soil, ($e_0/1+e_0$, where e_0 is the initial void ratio), the model yields predictions close to a linear logarithmic creep law, at least for the time intervals considered in this study. Smaller

values of $\varepsilon^{vp}_{vol,m,Limit}$ will cause the soil's creep response to be noticeably more non-linear logarithmic.

In the sets of analyses A, B and D to be described subsequently the parameter $\varepsilon^{vp}_{vol,m,Limit}$ is assumed to be equal to $e_0/1+e_0$, with an initial void ratio of 1.5. As emphasized in Chapter 2, the creep behaviour of geomaterials is in general non-logarithmic, however, in these analyses the ET model is made to collapse onto a nearly logarithmic law because that is the assumption frequently made in practice, when analysing the long-term behaviour of engineering structures. The implications of such assumption are investigated in the set of analyses C where $\varepsilon^{vp}_{vol,m,Limit}$ is set to 10% of $e_0/1+e_0$, i.e. equal to 0.06.

Given that the parameter $C_{\alpha e}$ is usually determined from 24h oedometer tests, the reference time t_0 is set equal to 24hour = 1 day.

The remaining parameter, ψ_0/V, can be determined from the condition that the volumetric visco-plastic strain rate predicted by the logarithmic law with the prescribed $C_{\alpha e}$ value and that predicted by the equivalent time model at the reference time t_0 are the same. Based on the above condition, it was shown in Chapter 6 that the value of ψ_0/V is related to the coefficient of secondary compression by the following equation:

Equation 7.3
$$\frac{\psi_0}{V}=\frac{C_{\alpha e}}{V\cdot \ln 10}$$

Using Equation 7.3 with V=2.5 the parameter ψ_0/V is evaluated equal to 0.00174 and 0.00521 for values of $C_{\alpha e}$ of 0.01 and 0.03, respectively.

In total four sets of analyses have been considered, aiming at investigating: 1) the effect of different values of C_α (sets A and B); 2) the influence of adopting a markedly non-logarithmic law (set C) and 3) the influence of the foundation loading rate (set D). A summary of the parameters adopted in each set of analyses is given in Table 7.2.

The shape of the loading and plastic potential surfaces in the *p'-q* plane are set nearly identical to the MCC model ellipse by setting the parameters α and μ equal to 0.4 and 0.9, respectively. The extension to generalized stress space is done based on the

Table 7.2: Summary of the sets of analyses

Set of analyses	Model parameters			Creep law/ Equivalent $C_{\alpha e}$
	t_0	$\varepsilon^{vp}_{vol,m,Limit}$	ψ_0/V	
A	1 day	0.6	0.00521	Nearly log law; 0.03
B	1 day	0.6	0.00174	Nearly log law; 0.01
C	1 day	0.06	0.00521	Non-log law; 0.03
D	1 day	0.6	0.00521	Nearly log law; 0.03

Matsuoka-Nakai failure criterion, as described in Chapter 6. In contrast the analyses presented by Zdravkovic et al. (2003) using the MCC model assumed that the yield and plastic potential surfaces in the deviatoric plane are given by a Mohr Coulomb hexagon and a circle, respectively. Such differences in the plastic potential in the deviatoric plane, in plane strain problems, can cause a significant discrepancy in the predicted failure loads (Potts and Gens 1984).

Due to the differences in the models formulation in the deviatoric plane any comparison between the results of this study and those of Zdravkovic et al (2003) can only be done in terms of the proportional increase in bearing capacity observed in each case.

7.5 Description of the analyses

7.5.1 Definition of the initial load-displacement curve

The time dependent nature of the ET model implies that the footing loading rate affects the soil's undrained strength and the visco-plastic strain rates operating in the foundation soil at the end of loading. While the former can be dealt with by using the same loading rate in first loading and subsequent reloading, the latter can only be accommodated by choosing a realistic loading rate.

In the absence of a specific loading history, the footing is assumed to be loaded to failure under a constant displacement rate over a period of six months, as this is believed to be the average time taken for the construction of the over-ground structure of a medium/ small building, where the choice of surface foundations on soft clay may be appropriate. This was the assumption in the set of analyses A to C. In set D, aiming at investigating the effect of the adopted footing displacement rate on the analyses

results, the footing is loaded to failure in about three days, a situation that is likely to occur during a foundation load testing, and the fastest static loading rate likely to occur in engineering practice.

Due to the development of visco-plastic strains and consolidation, which become significant when the footing is loaded over a period of six months, the load sustained by the footing does not have a well-defined limit value. Therefore, the displacement rate that causes the footing to fail within six months - hereafter referred to as the *reference displacement rate* - is defined on the basis of a pure undrained analysis, in which any increase in the load sustained by the footing at large displacements is due to the viscous component of the soil model. The reference displacement rate is chosen such that the increase in the load sustained by the footing between a foundation displacement δ, after six months, and a foundation displacement four times δ, is smaller than 5%, as schematically shown in Figure 7.5.

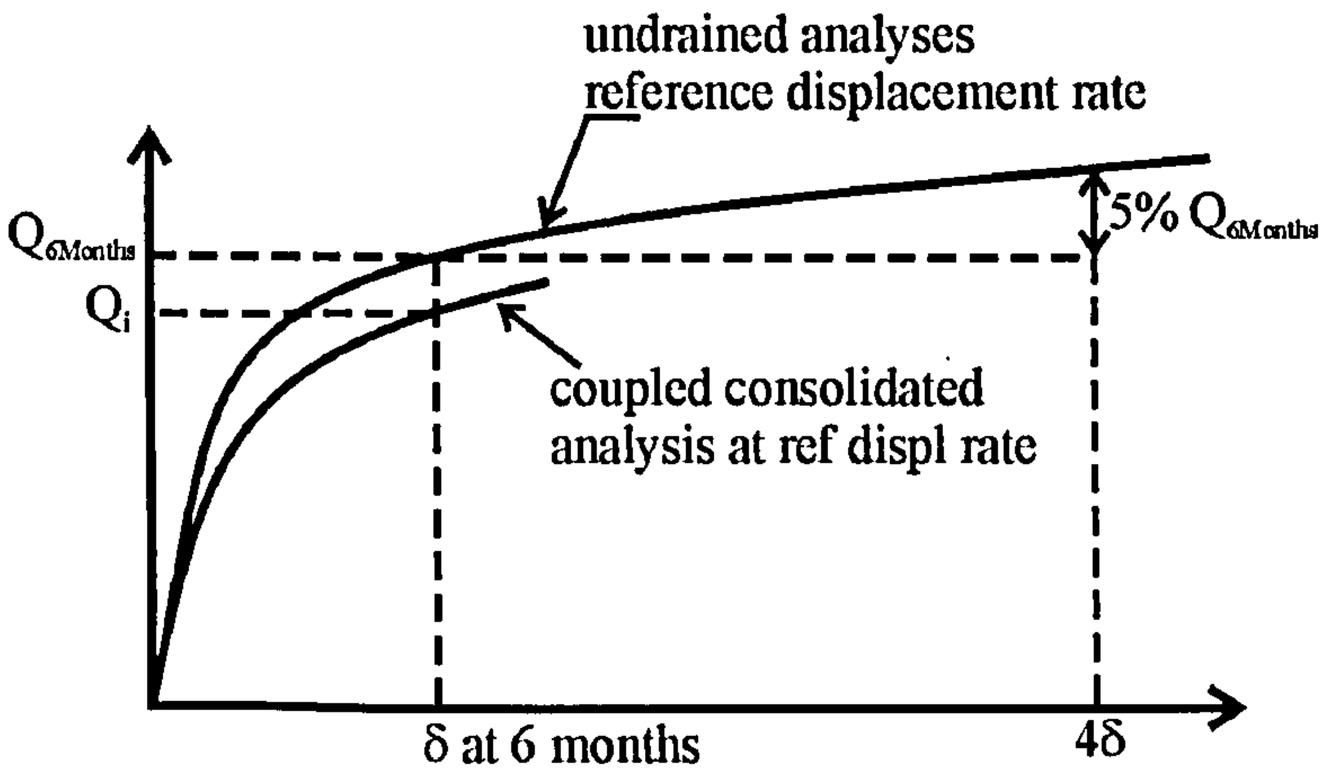

Figure 7.5: Definition of the reference displacement rate and the initial bearing capacity, Q_i.

The initial loading curve is the load–displacement curve obtained in a coupled consolidation analysis when the footing is loaded, from the initial conditions, at the reference strain rate, and the initial bearing capacity is the load sustained by the footing at the end of six months. The reference displacement rate and the initial bearing capacity are, as rule, different for each set of analyses. The values of the reference displacement rate and initial bearing capacity are included in Table 7.3, and the initial load-displacement curves are shown in Figure 7.6. Figure 7.7 shows the incremental displacements of the foundation soil predicted by undrained and coupled analyses at failure (after 6 months for sets A to C, and after 2.7 days for set D).

Table 7.3: Initial bearing capacity and reference displacement rate.

Set of analyses	$Q_{6months}$ or $Q_{2.7days}$ undrained analyses (kN/m) (*)	Reference displacement rate (m/day)	Initial bearing capacity, Q_i (kN/m)	Consolidation time before reloading
A	82	0.002	72	1, 10, 100 years & 95% PWP
B	90	0.0025	82	1, 10, 100 years & 95% PWP
C	86	0.002	74	1, 10, 100 years & 95% PWP
D	105	0.2	98	10 years and 95% PWP

(*) In set A to C failure is attained in 6 months while in set D failure is attained in 2.7 days.

The undrained analyses are found to predict a better defined failure mechanism when compared with coupled analyses (as the footing also approaches a better defined failure load). Due to the faster rate of loading in set D, coupled and undrained analyses give very similar predictions. As there are no noticeable differences between the failure mechanisms predicted by each set of analyses, the changes in bearing capacity should correspond to proportional changes in the soil's undrained strength. In set of analyses A and D, the same model parameters have been adopted, thus the difference in bearing capacity is due to the time dependent response of the ET model. This is especially true, if we consider the undrained analyses, where the effect of consolidation has been removed. Based on the bearing capacity values given by the undrained analyses, an increase in bearing capacity of about 14% per logarithmic cycle of displacement rate is predicted.

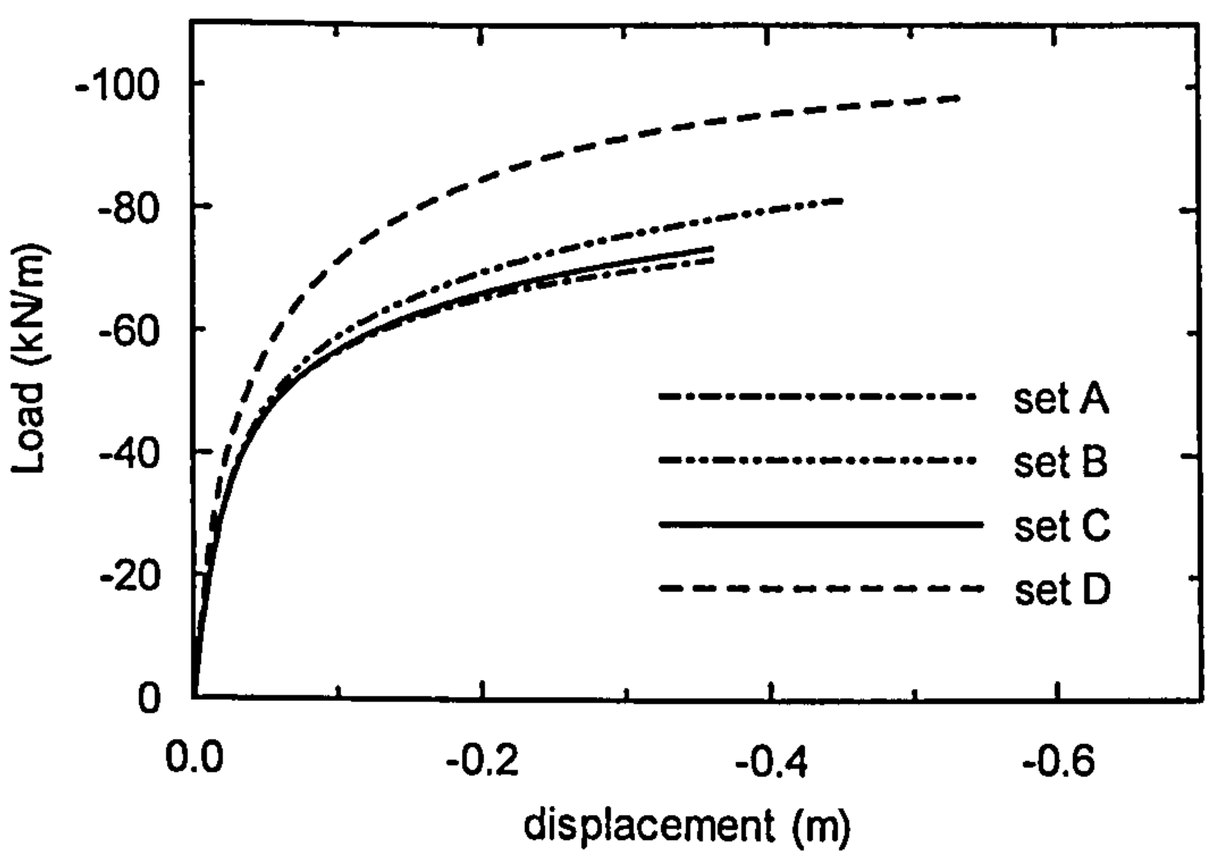

Note: ICFEP uses tension +ve sign convention; the reaction force on the nodes beneath the foundation, which corresponds to the load carried by the footing, is therefore negative. A Negative displacement is downwards.

Figure 7.6: Initial load-displacement curves for the four sets of analyses.

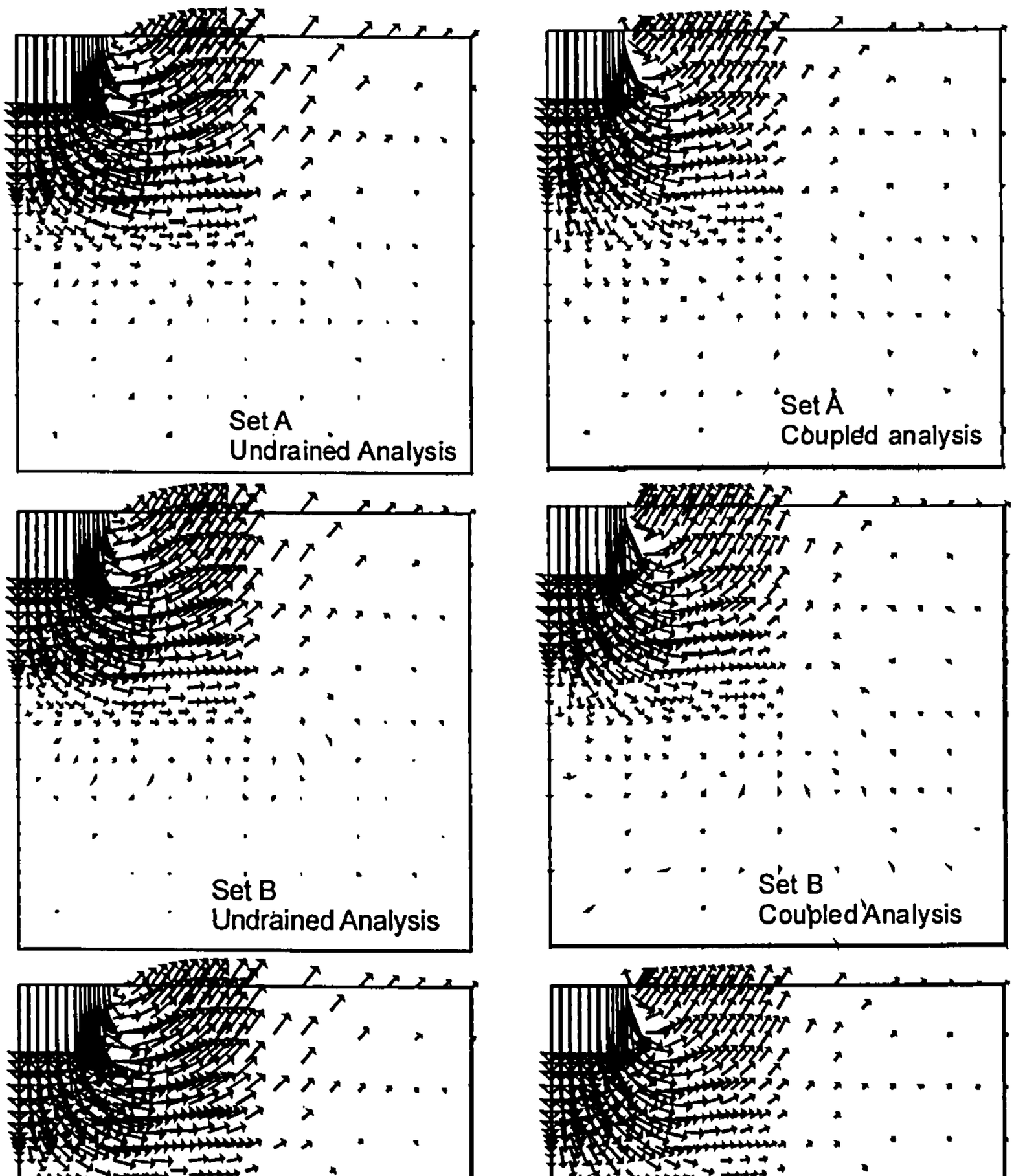

Note: The plots above are all at the same scale.

Figure 7.7: Incremental displacements at failure predicted by undrained and coupled analyses – set A to D.

The difference in the initial bearing capacity between sets A and B, from 72 to 82kN/m (or from 82 to 90 kN/m in terms of $Q_{6months}$) cannot be explained by the difference in displacement rate from 0.002m/day to 0.0025m/day, and results mainly from the differences in the adopted model parameters. Set A assumes a value of C_α of 0.03, compared to 0.01 in set B, the former corresponding to a higher volumetric visco-plastic strain rate at the reference time, t_0. Therefore, even if the same displacement rate was used in both cases, a larger bearing capacity would be predicted in set B, because the visco-plastic strain rates acting in the foundation would be, relative to the reference value, higher in set B than in set A.

Once the initial load-displacement curve, for each set of analyses, has been defined a series of analyses is performed in which the footing is loaded from initial conditions, at the respective reference displacement rate, to a percentage of the initial bearing capacity, namely 20, 40, 60, 80, and 100%.

The load is then held constant while the excess pore water pressures are allowed to dissipate. The end of consolidation is assumed to correspond to the dissipation of 95% of the excess pore water pressures developed during the first loading, based on the pore water pressure profile along the footing axis, where the largest excess pore water pressures developed. The footings are subsequently reloaded at the respective reference displacement rate, at various time intervals after the end of first loading, in general, 1, 10 and 100 years, and at the end of consolidation, as defined above.

7.5.2 Definition of the condition of failure on reloading

On reloading, similarly to the initial loading, the load - displacement curves do not give a well-defined failure load, showing a steady increase in sustained load even at large displacements, due to the continuous soil hardening associated with both the process of consolidation and the development of visco-plastic strains that would occur even at constant effective stresses. Figure 7.8 shows the load-displacement curves on reloading for consolidation times of 1, 10 and 100 years, for the set A.

From the load-displacement curves shown in Figure 7.8, a trend can be identified, that the reloading curves, at very large displacements, become steeper as the consolidation time increases.

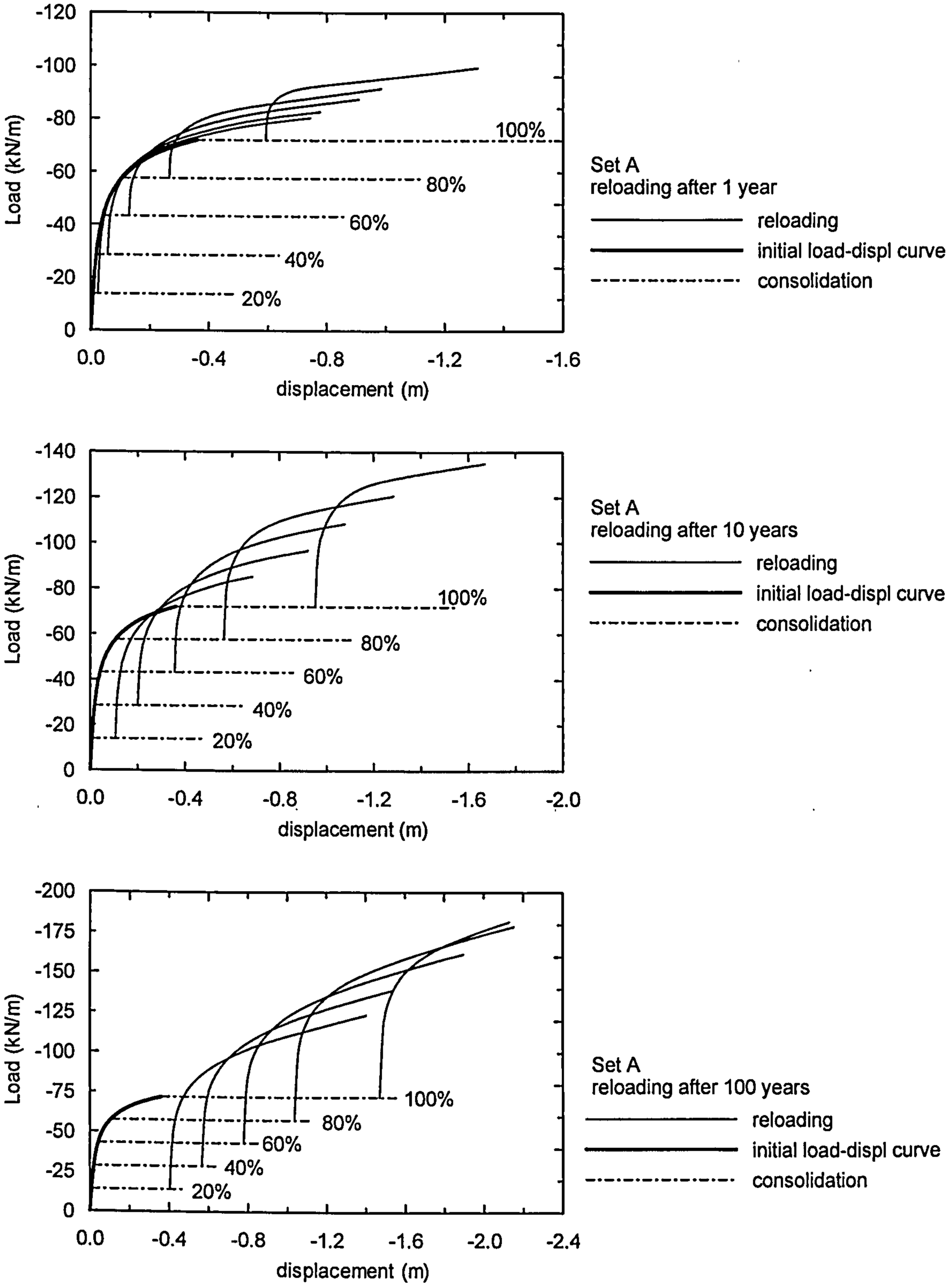

Note: ICFEP uses tension +ve sign convention; the reaction force on the nodes beneath the foundation, which corresponds to the load carried by the footing, is therefore negative. A Negative displacement is downwards.
The number next to each consolidation line indicates the amount of preload as a percentage of the initial bearing capacity.

Figure 7.8: Load-displacement curves on reloading after 1, 10 and 100 years of consolidation– set of analyses A.

To investigate if such behaviour is a consequence of the constitutive model formulation or, instead, of the interaction between the phenomenon of consolidation and shearing, the footing was reloaded under purely undrained conditions, for some combinations of preload and consolidation time values, for set of analyses A. The respective load-displacement curves are shown in Figure 7.9.

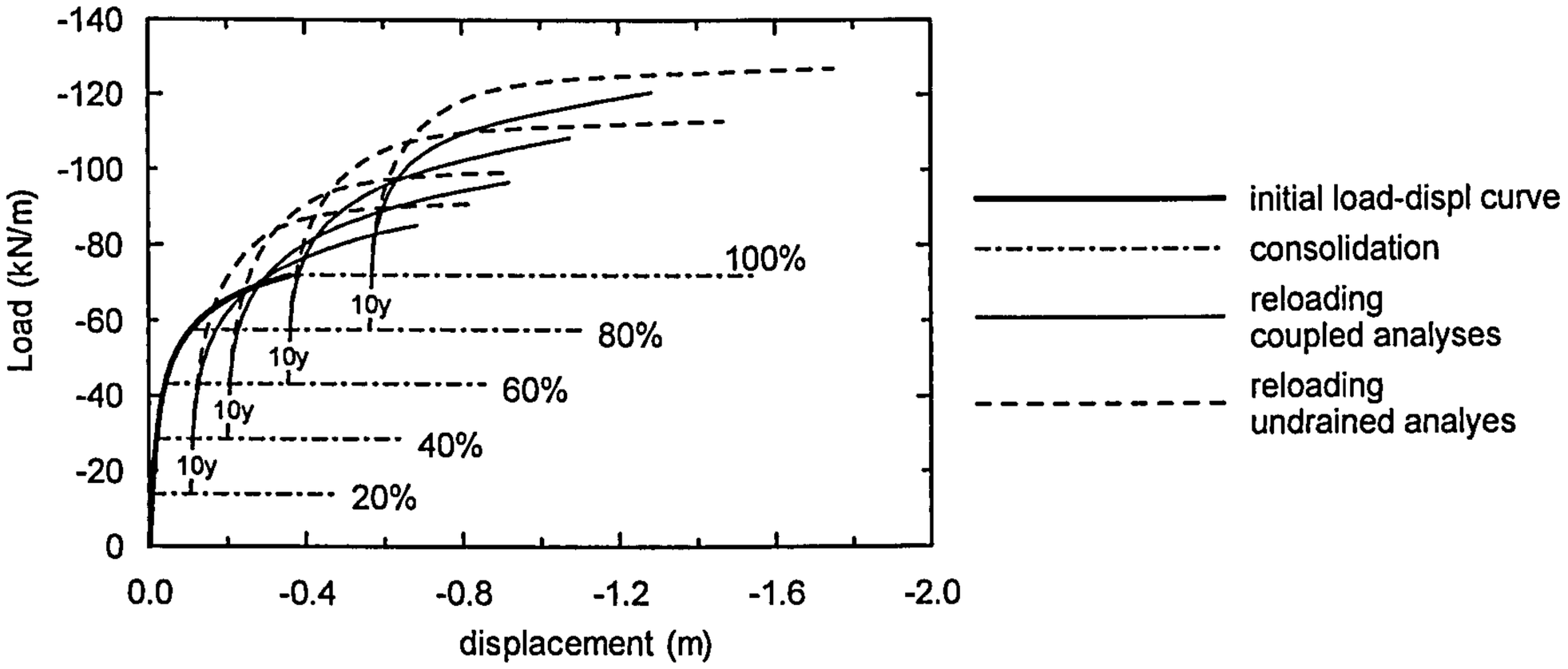

Figure 7.9: Load-displacement curves on reloading, set A: coupled consolidation versus undrained analyses; a) effect of preload; b) effect of the consolidation time.

As would be expected, when the foundation soil is considered undrained, the load-displacement curves at large displacements are flatter than those obtained from coupled consolidation analyses, as there is no soil hardening associated with pore pressure dissipation and concurrent increase of the foundation mean effective stress. In addition, the slope of the load-displacement curve at large displacements is apparently independent of the preload and consolidation time values, supporting the hypothesis that

differences in the load-displacement curve at large displacements in the coupled analyses, are a consequence of the interaction between the processes of consolidation and shearing.

To investigate this further, the stress path of a soil element is shown in Figure 7.10, for several combinations of preload and consolidation time. For clarity, only the reloading path is shown. The soil element being considered is located at the footing axis, about 1 m below ground level, within the surface crust. From Figure 7.10, the following observations can be made:

a) During undrained reloading, the effective stress path (ESP) moves initially vertically, and then bends to the left, reaching the CSL quite early on during the reloading process.

b) In the coupled consolidation analyses, the ESP initially follows that observed in the undrained analysis, but then bends to the right, away from the CSL.

c) At very large displacements, the ESP moves nearly parallel to the CSL (bending very slightly away from the CSL) and there is a continuous increase in the sustained deviatoric stress. The ESP is found to lie further to the right as the level of preload and the consolidation time increases.

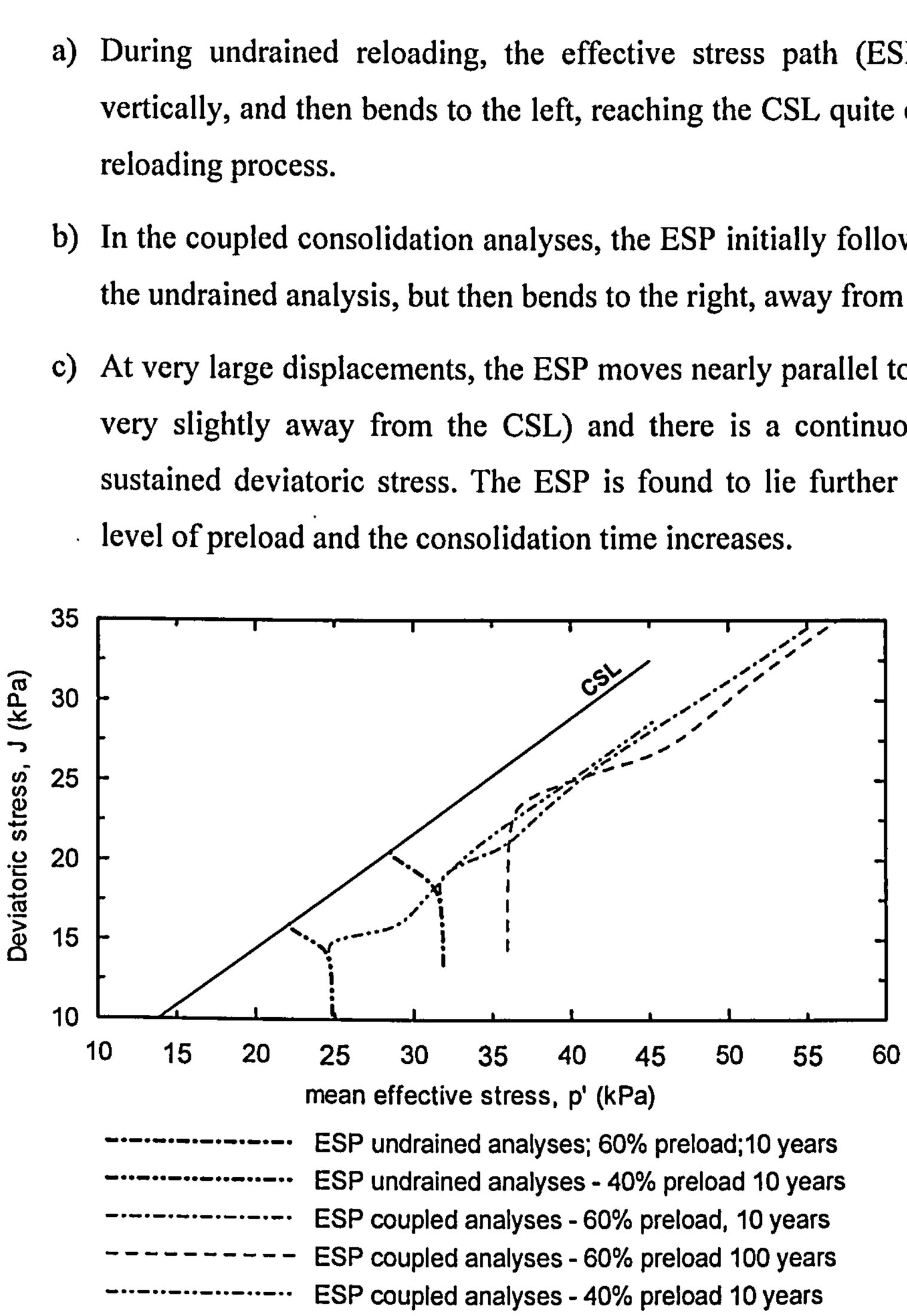

Figure 7.10: Effective stress path during foundation reloading of element 93 located at the footing axis, about 1 m below ground level.

d) Noting that the loading and plastic potential surfaces are identical and nearly equal to the MCC ellipse in the *p'-q* plane, the fact that the ESP lies further to the right, at lower stress ratios, implies a large volumetric component of strain relative to the deviatoric component which then results in larger soil hardening, and steeper load-displacement curves.

When the footing is loaded under undrained conditions excess pore water pressures are generated in the soil. These excess pore water pressures can be considered to have two components; the first component – also called the spherical part Δu_{sph} – is associated (and has the same sign) with the change in mean total stress; the second, is due to the increase in deviatoric stress, Δu_{dev}. The deviatoric component can be either positive or negative, and both its sign and magnitude depend, in general, on the stress level, the soil type and its overconsolidation ratio. For normally consolidated and lightly overconsolidated clays, in the range of OCR values present in this boundary value problem, the deviatoric component Δu_{dev} will be in general positive.

Figure 7.11 shows the excess pore water pressures plotted against the change in mean total stress developed during reloading, for a few combinations of preload and consolidation time values, at the same finite element, located at the footing axis 1 m below ground level.

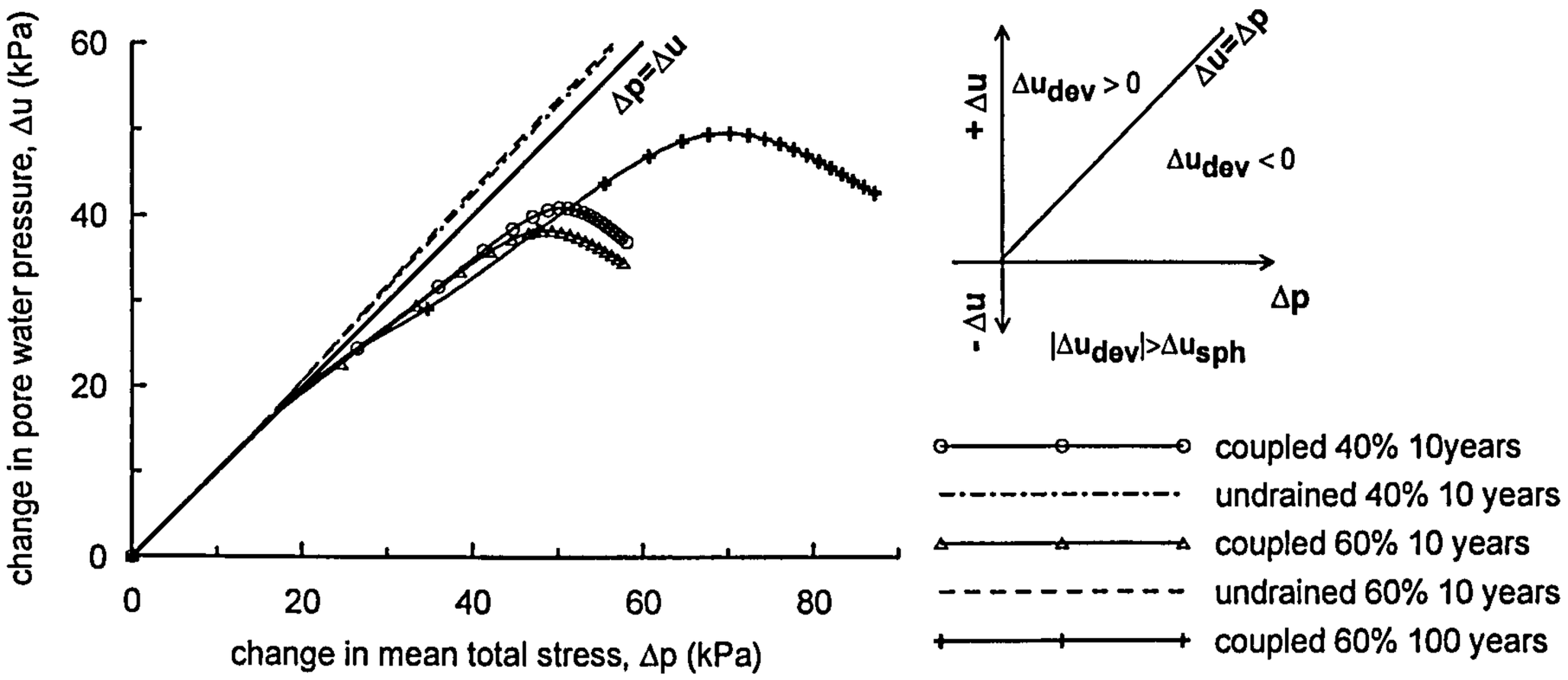

Figure 7.11: Pore water pressures developed during shearing: element 93 located at the footing axis, about 1 m below ground level.

During undrained and coupled reloading, and up to approximately a mean total stress of 20 kPa, the excess pore water pressures are equal to the change in mean total stress, indicating that the deviatoric component, Δu_{dev}, is nearly zero due to the very small plastic strains being predicted in that stress range. From then on, the behaviour of undrained and coupled analyses diverge. In the undrained analyses, the excess pore water pressures become larger than the changes in the mean total stress, indicating that the deviatoric component Δu_{dev} is also positive.

In the coupled consolidation analyses, due to the relatively slow loading rate, there is the occurrence of significant consolidation (pore water pressure dissipation) concurrent with shearing, and the resulting excess pore water pressures become smaller than the change in mean total stress.

As shearing progresses, the change (decrease) in pore pressures due to consolidation becomes larger than the positive pore pressures generated due to contractive shearing and increasing mean total stress, resulting in incremental negative pore water pressures. At this point, it is the consolidation, rather than shearing, that governs changes in pore water pressures within the foundation soil. Footing failure on reloading has been identified with the onset of incremental negative pore water pressure immediately below the footing. Figure 7.12 shows contours of the incremental pore water pressures at failure, when loading the footing from the initial conditions, for set of analyses A to D. It is found that the failure points on first load support quite well the failure condition defined for reloading.

Contour levels (Tension positive)
(kPa)
D = -0.1
E = -0.05
F = -0.01
G = -0.001
H = 0.001
I = 0.01
J = 0.05

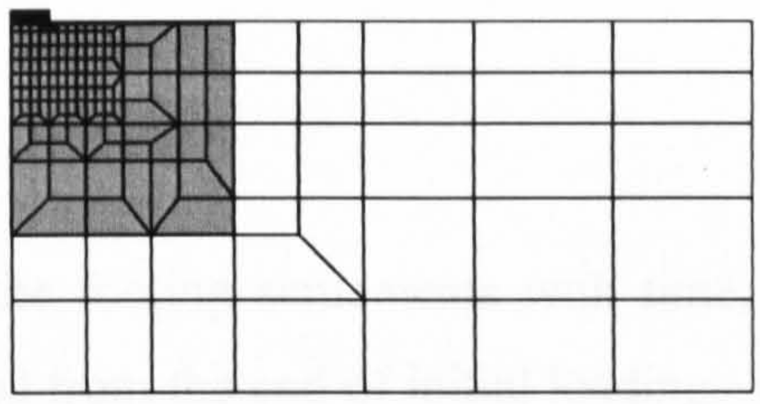

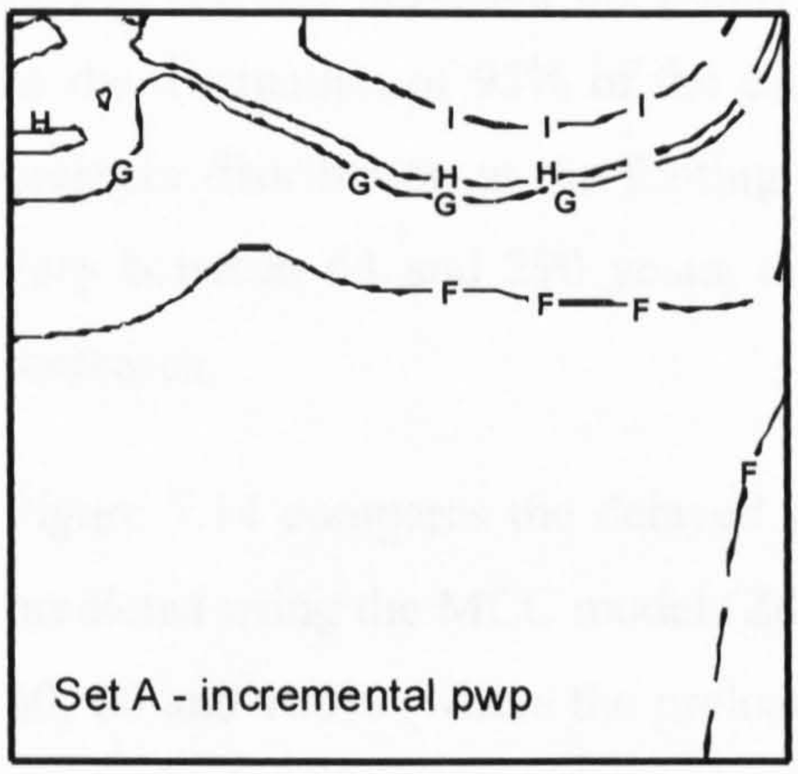

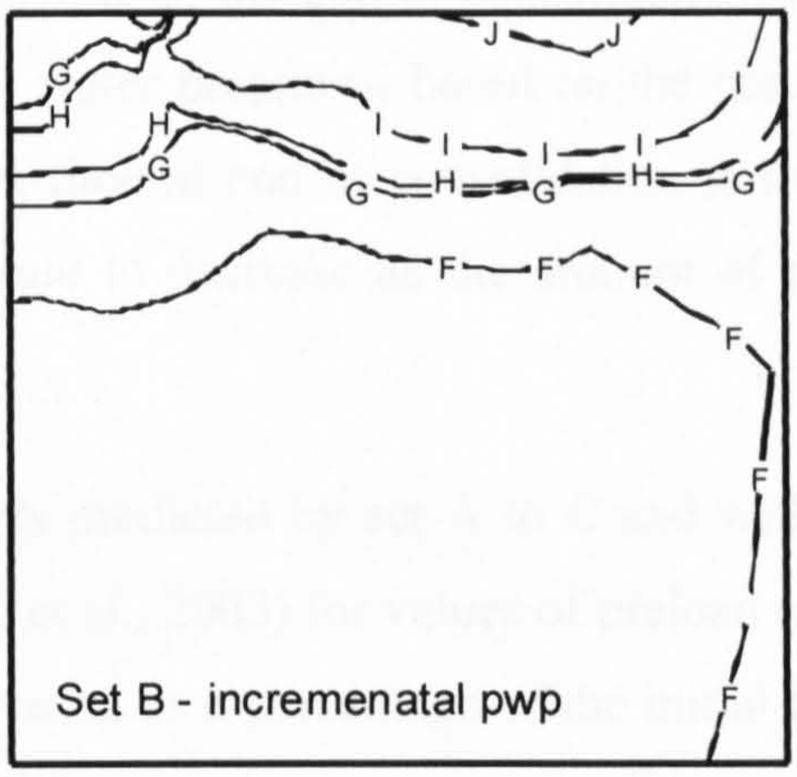

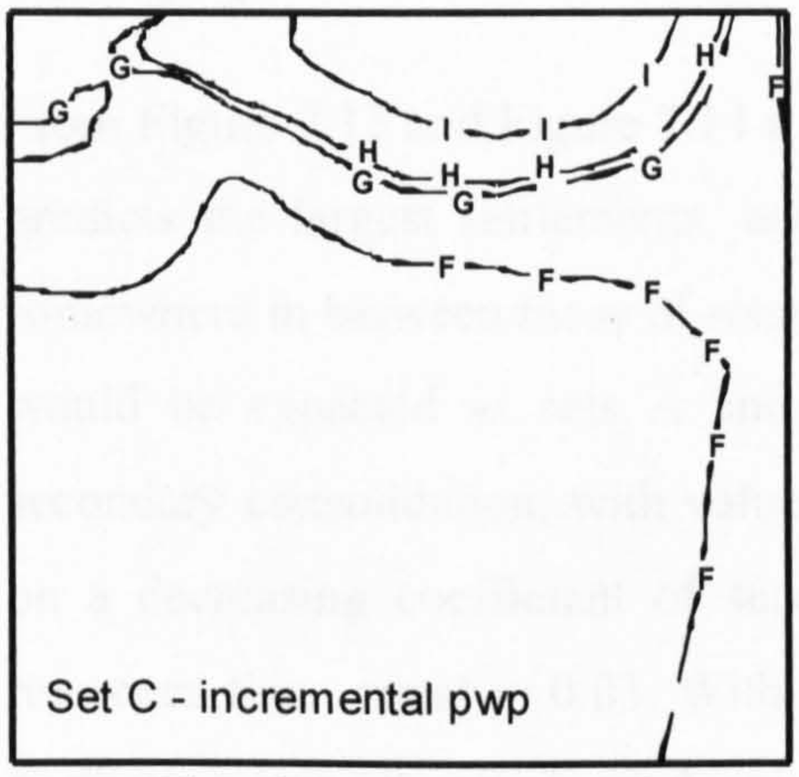

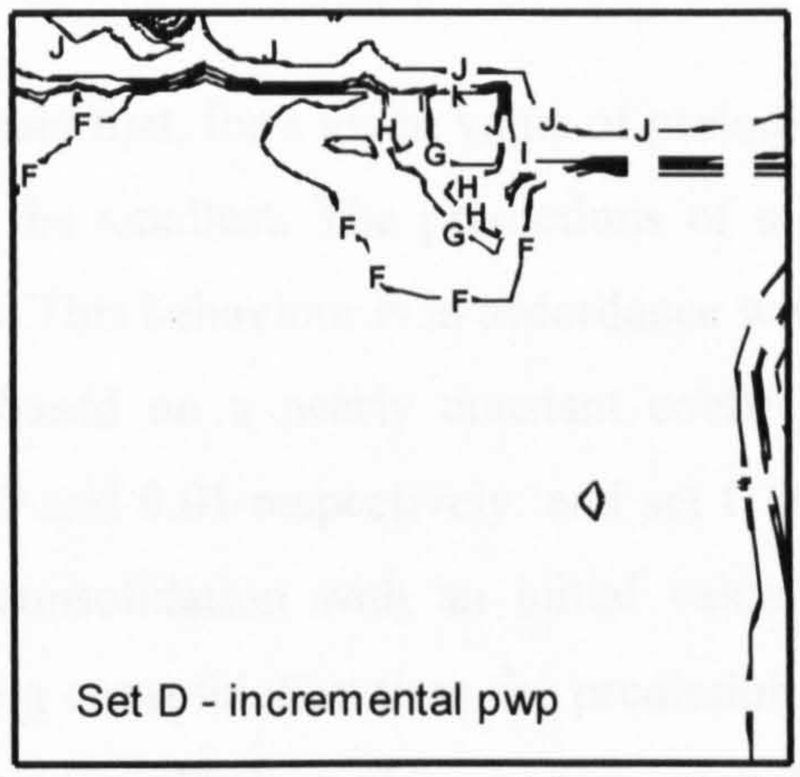

Notes: The plots above are at the same scale; they represent a portion of the mesh close to the footing, indicated in the mesh above.

Figure 7.12: Incremental pore water pressures at failure during first loading - set of analyses A to D.

7.6 Results of the analyses

7.6.1 Consolidation settlements

Figure 7.13 shows the development of the footing settlements with time, for sets of analyses A to C, where the time is counted from the end of initial loading. In the same graphs are also indicated the points corresponding to the end of consolidation, defined as the dissipation of 95% of the excess pore water pressures, based on the pore water pressure distribution at the footing axis. The time at end of consolidation is found to vary between 63 and 290 years, and as a rule to decrease as the amount of preload increases.

Figure 7.14 compares the delayed settlements predicted by set A to C and with those predicted using the MCC model (Zdravkovic et al., 2003) for values of preload equal to 40, 60 and 100% (where the preload is expressed as a percentage of the initial bearing capacity, Q_i).

From Figure 7.13 and Figure 7.14 it can be said that, for a given value of preload, set A predicts the largest settlements, and set B the smallest. The predictions of set C lie somewhere in between those of sets A and B. This behaviour is in accordance with what would be expected as sets A and B are based on a nearly constant coefficient of secondary consolidation, with values of 0.03 and 0.01 respectively, and set C is based on a decreasing coefficient of secondary consolidation with an initial value, at the reference time, equal to 0.03. With increasing consolidation time the predictions of set C diverge from those of set A, as the current coefficient of secondary consolidation diverges (decreases) from the value of 0.03. This can be better appreciated in Figure 7.14. After the dissipation of the excess pore water pressures, assuming that one dimensional conditions prevail below the footing, the current value of the coefficient of secondary consolidation, $C_{\alpha e}$, is mathematically related to the slope of the curve of the foundation settlements with time, by the following equation:

Equation 7.4

$$\Delta H = H \cdot \frac{\Delta e}{1 + e_0} \text{ and } \Delta e = C_{\alpha e} \cdot \log\left(\frac{t}{t_i}\right)$$

Notes: *ΔH= settlement*
H= layer thickness
Δe= change in void ratio
t_i= time origin

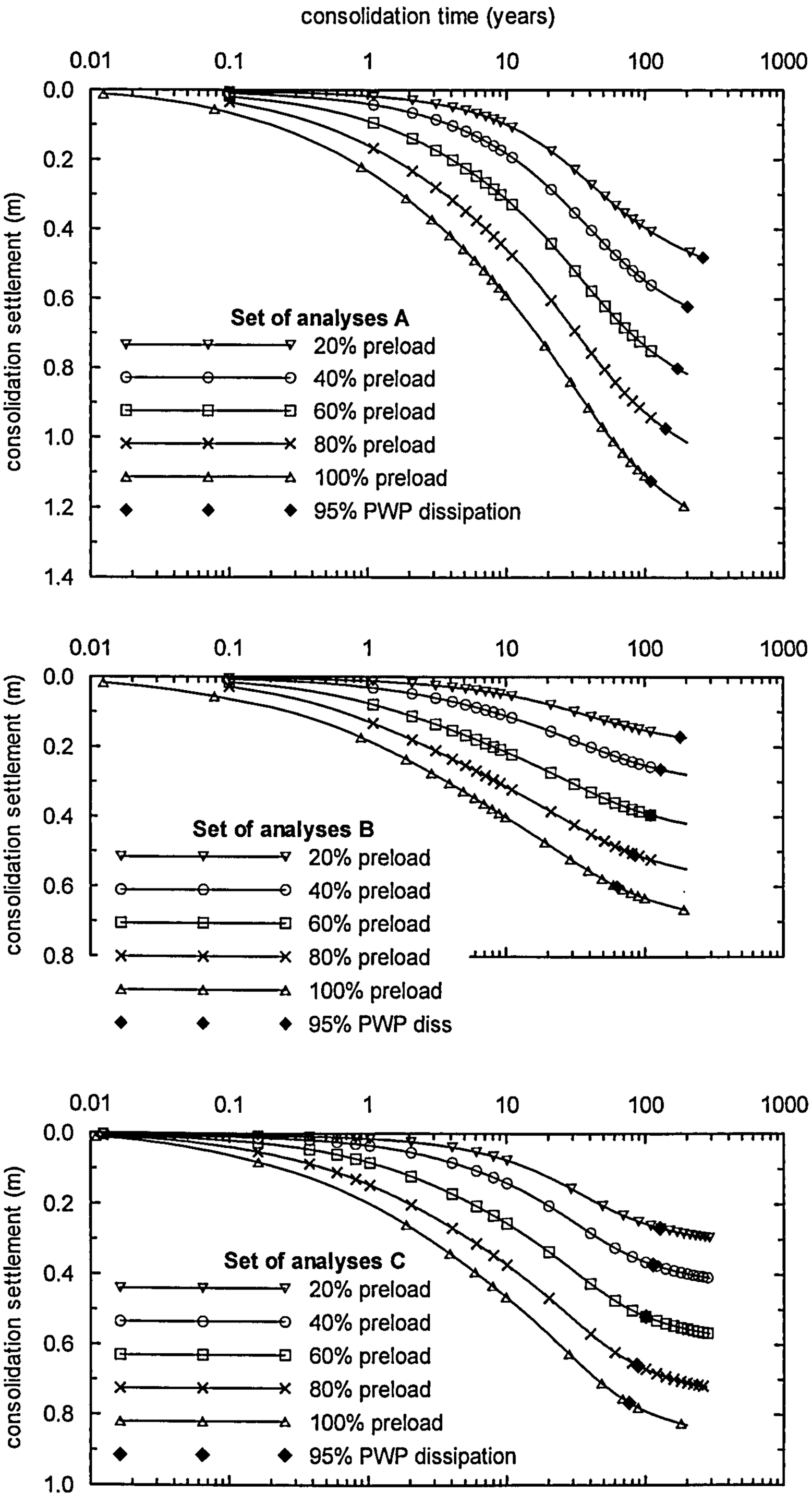

Note: The consolidation time is counted from the end of initial loading. The graphs are at the same scale.

Figure 7.13: Consolidation settlements with time for various values of preload, with indication of the end of consolidation - set A to C.

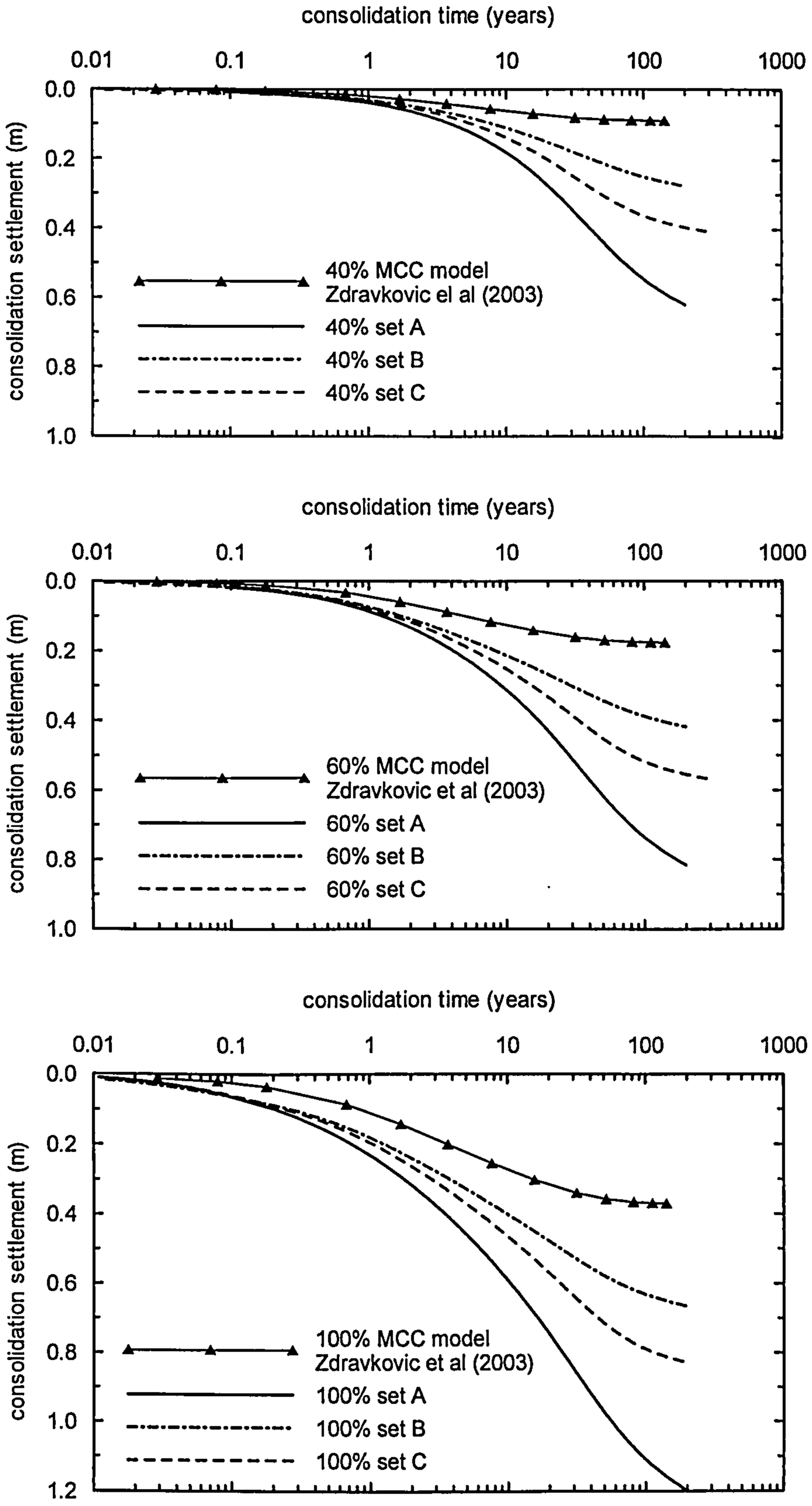

Note: The consolidation time is counted from the end of initial loading. The amount of preload is expressed as a percentage of the respective initial bearing capacity.

Figure 7.14: Comparison of the delayed settlements predicted by set A to C and Zdravkovic et al (2003) for values of preload of 40, 60 and 100%.

The last part of the settlements curves, say after 100 years of consolidation for sets A and B, are found to be linear, denoting the adoption of a near constant value of $C_{\alpha\varepsilon}$ with time, with set A showing a larger slope than that of set B. In set C, instead, no sign of a linear range can be identified and the slope of the curves of settlement *vs.* time decrease continuously, indicating the adoption of a non-linear logarithmic creep law.

In the analyses using the MCC model, the delayed settlement (or the increase in undrained bearing capacity) is a result of the increase in mean effective stress in the foundation soil, concurrent with the dissipation of the excess pore water pressures generated during first loading. Therefore, once all the excess pore water pressures have dissipated no further settlement or increase in the soil undrained strength is predicted.

In the analyses using the ET model, the increase in the footing settlement derives both from the dissipation of the excess pore water pressures and from the development of visco-plastic strains (that occur even at constant effective stress) with time.

However, due to the interaction between the processes of consolidation, creep and shearing it is not possible to separate the two components contributing to the total footing settlement. When comparing the delayed settlements predicted by each set of analyses in Figure 7.13 and Figure 7.14 it should be noted that:

a) The excess pore water pressures generated during initial loading are, in general, even for the same amount of preload, different, for each set of analyses;

b) The initial bearing capacity is different for each set of analyses, therefore the magnitude of the stresses being applied is different;

c) For a given consolidation time, the degree of excess pore water pressure dissipation is also different;

d) It is thought that the differences in displacement rate between set A, B and C are negligible, and consequently the visco-plastic strain rates acting in the foundation's soil, at a given level of preload, immediately after loading, are identical in the three sets.

Despite what was said above, it is found that for a consolidation time of 100 years (after which any contribution from the excess pore water pressure dissipation to the foundation settlement will be quite small), the additional settlement predicted by

analysis set B, in relation to that predicted by the MCC model, is between 35% and 39% of the additional settlement predicted by set A, not far from the ratio 0.01/0.03.

It is noted that preload values of 40% and 60% correspond to an initial design of the footing to a factor of safety on load between 2.5 and 1.67, respectively, and thus are cases of particular relevance for engineering practice.

At these values of preload, the consideration of secondary consolidation (or creep) using a linear logarithmic creep law increases the long-term settlements (at about 100 years) between 2.2 and 2.8 times that predicted by a time independent model for a value of C_α of 0.01 and between 6 and 4.2 times for a value of C_α of 0.03. Using a non-linear logarithmic creep law reduces the total long-term settlements by about one third.

Figure 7.15 shows the development of delayed settlements with time as predicted by set of analyses D. For comparison, the predictions from set A are also included. As mentioned above, differences between sets A and D derive from the rate dependent model response and its interaction with the process of consolidation.

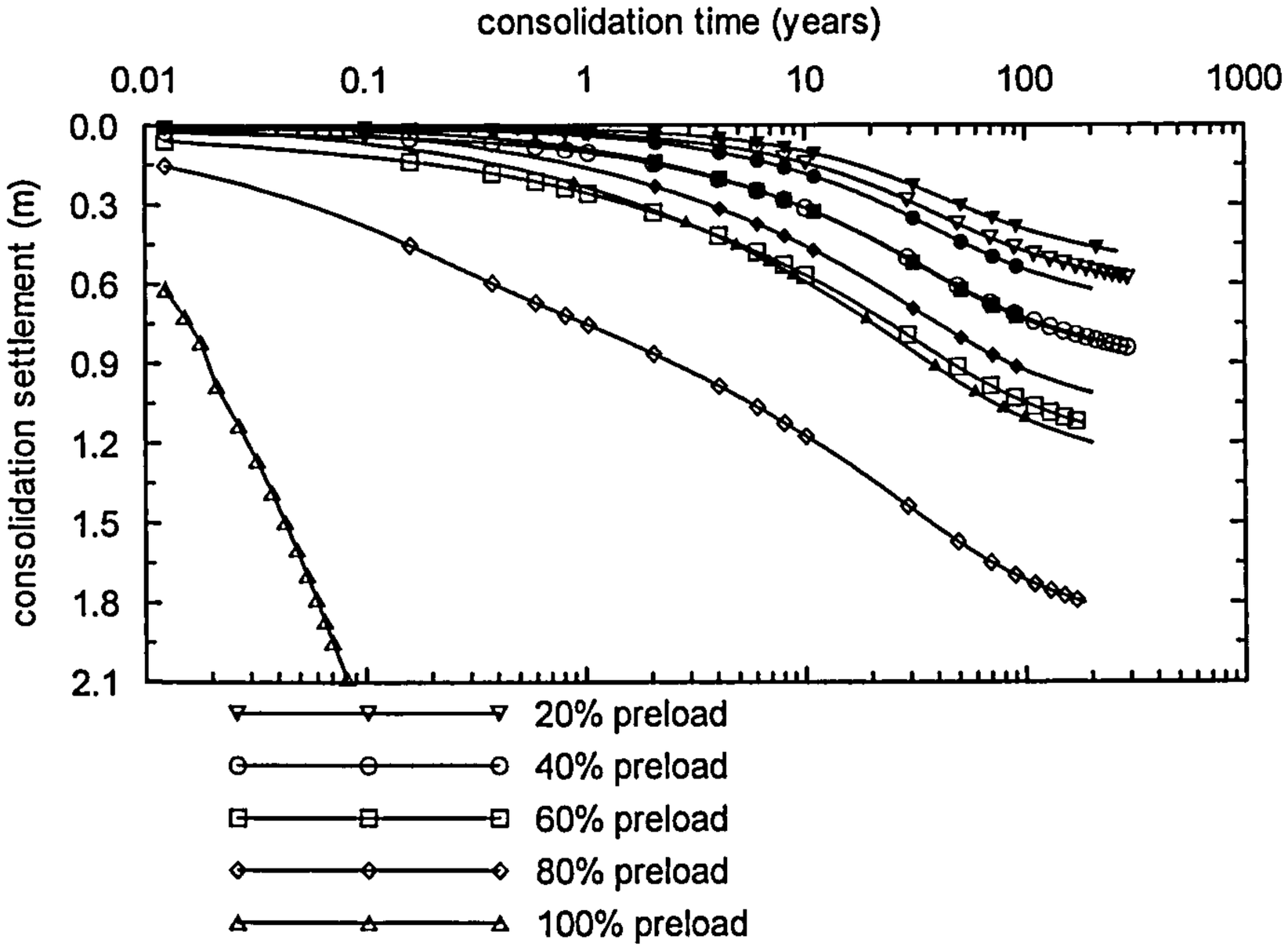

Note: open symbols are data from set D and full symbols from set A.

Figure 7.15: Consolidation settlements with time for various values of preload – set D.

In set D, the foundation is loaded at a rate 100 times faster than in set A, and thus the strain rates operating in the foundation soil at the end of first loading are much larger. This explains the larger delayed settlements predicted in set D at 20%, 40% and 60% preload.

At 80% and 100% preload, the settlement *vs.* time curves deviate from the trend observed at lower values of preload and in set A, both in terms of shape and magnitude reached. The exaggerated amount of delayed settlements predicted at 80% and 100% is thought to result from the development of large deviatoric visco-plastic strains as a large proportion of the foundation soil has failed.

7.6.2 Ultimate bearing capacity

Figure 7.16 shows the load-displacement curves on reloading for sets of analyses A to D, and a consolidation time of 10 years. In the same plots are also included the failure points defined using the criterion described in section 7.5.2. The reloading curves for all the cases considered in this study can be found in Appendix A.

Table 7.4 lists the ultimate bearing capacity, for all the cases studied.

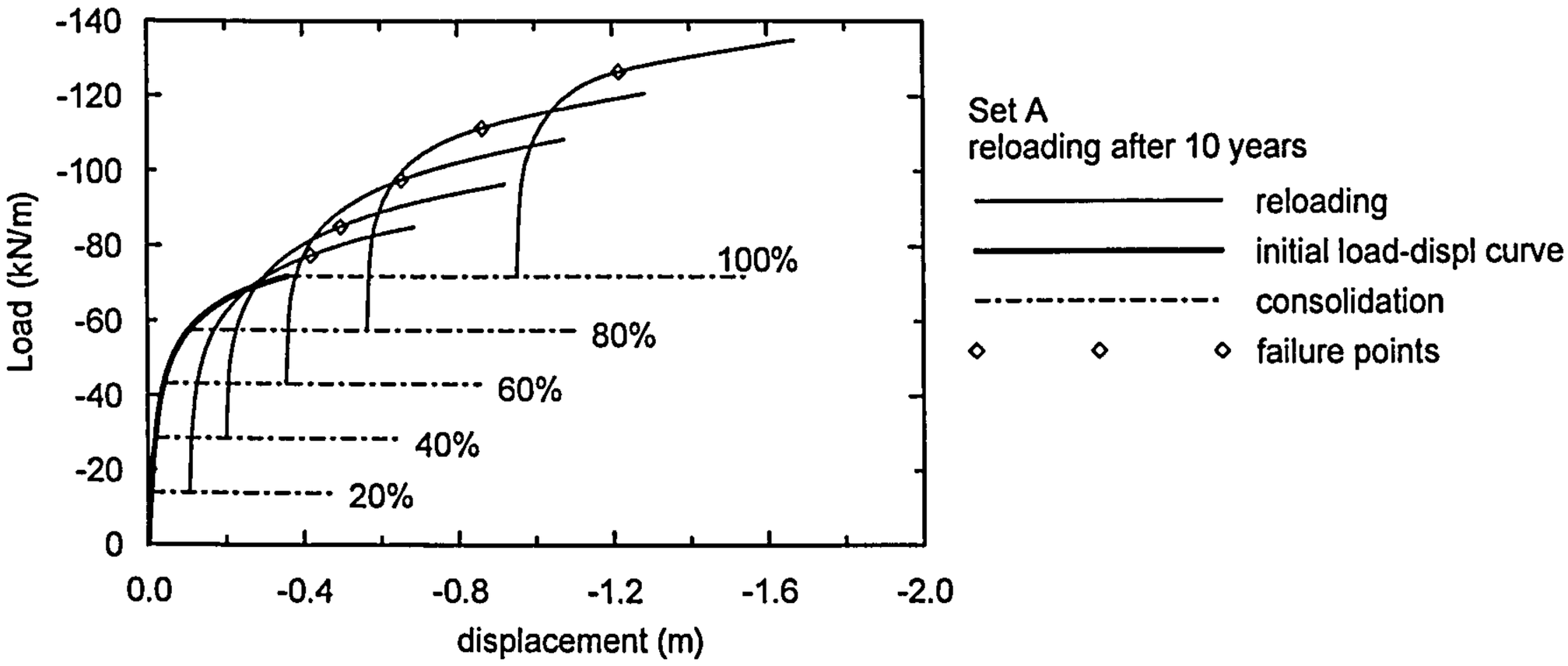

Figure 7.16: Load-displacement curves on reloading after 10 years of consolidation with indication of the failure points – set A to D.

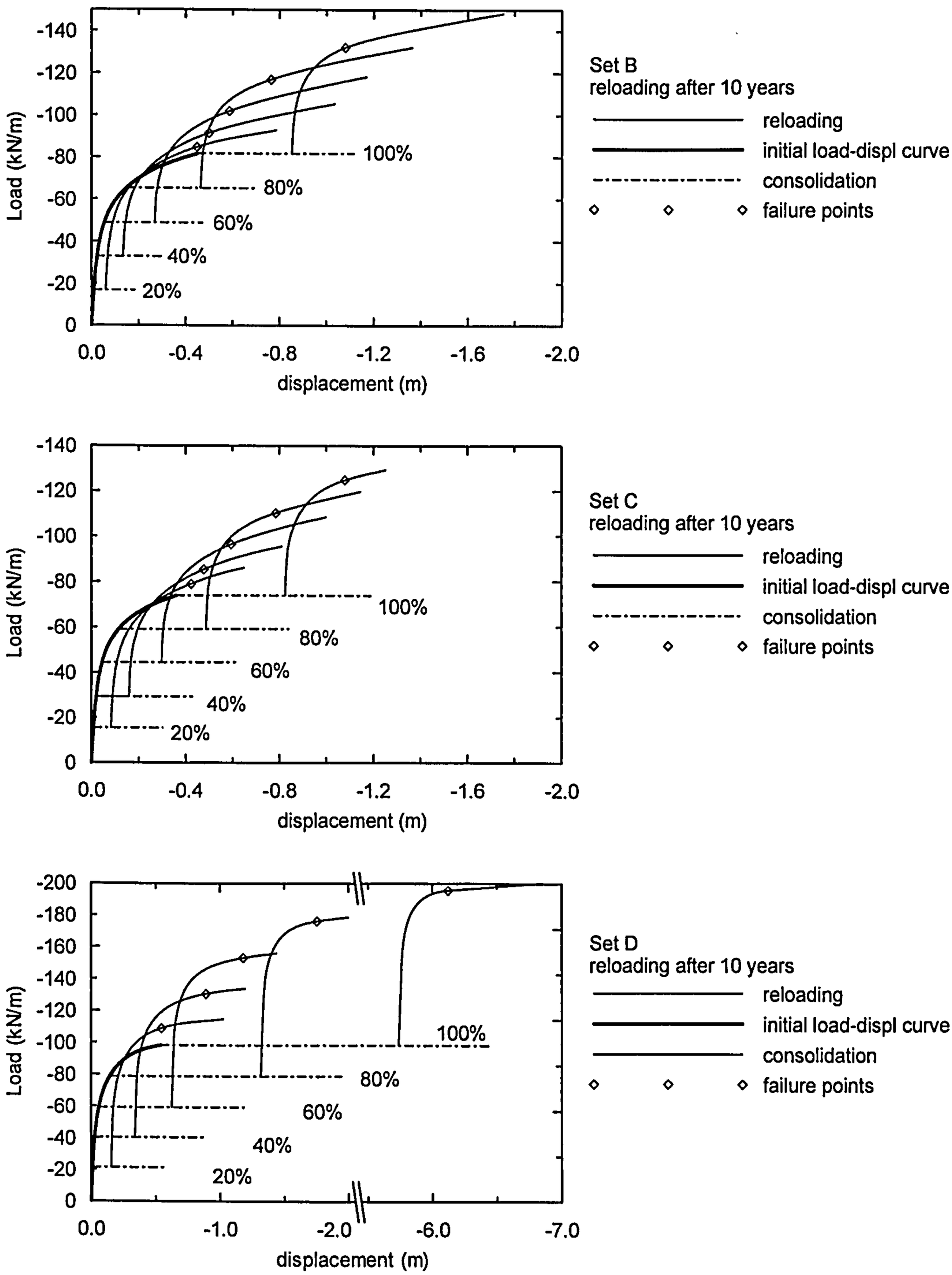

Figure 7.16: Load-displacement curves on reloading after 10 years of consolidation with indication of the failure points – set A to D. (cont.)

Table 7.4: Ultimate bearing capacity of a preloaded strip footing after different consolidation periods – set A to D.

Set A	Time between end of 1st loading and reloading			
Preload	1 year	10 years	100 years	End of cons.
20%	72.5	77.5	93.5	98.6
40%	74.7	85.2	107.6	113.3
60%	78.8	97.8	125.5	130.4
80%	84.1	111.6	143.4	147.2
100%	92.2	127.5	162.8	163.8

Note: Preload is expressed as a percentage of the initial bearing capacity, Q_i=72 kN/m.

Set B	Time between end of 1st loading and reloading			
Preload	1 year	10 years	100 years	End of cons.
20%	82.1	84.8	89.7	90.5
40%	84.2	91.4	98.7	99.4
60%	88.9	102.0	112.6	113.1
80%	94.5	117.0	130.3	129.5
100%	103.6	132.1	148.7	146.3

Note: Q_i=82 kN/m.

Set C	Time between end of 1st loading and reloading			
Preload	1 year	10 years	100 years	End of cons.
20%	74.7	78.9	87.7	88.3
40%	76.7	85.2	97.0	97.3
60%	81.0	96.3	112.4	112.4
80%	86.9	110.2	128.7	127.9
100%	94.8	124.8	145.4	143.8

Note: Q_i=74 kN/m.

Set D	Time between end of 1st loading and reloading			
Preload	1 year	10 years	100 years	End of cons.
20%	-	108.8	-	144.5
40%	-	130.7	-	173.3
60%	-	153.3	-	200.6
80%	-	*176.3*	-	*227.9*
100%	-	*195.5*	-	*247.3*

Note: Q_i=98 kN/m.

Given the differences in the initial bearing capacity for each set of analyses, the ultimate bearing capacity values shown in Table 7.4 have been normalized by the respective initial bearing capacity, Q_i. This normalization allows the results of the four sets of analyses to be compared between each other, and with the results from Zdravkovic et al. (2003).

Figure 7.17 plots the normalized ultimate bearing capacity against the level of preload, for sets of analyses A to D. In the four sets of analyses, the normalized ultimate bearing capacity is found to increase significantly with the amount of preload and consolidation time. In addition, for consolidation times equal or higher than 10 years the results of Zdravkovic et al. (2003) using the time independent MCC model are found to under predict the current bearing capacity of preloaded strip footings, for the conditions analysed.

In set D, despite the atypical settlement predictions at 80% and 100% preload, the ultimate bearing capacity on reloading at these preload values follows the trend observed at lower preload values and in the other analysis sets. This emphasizes that the large predicted settlements result from the development of large deviatoric visco-plastic strains, as a large proportion of the foundation soil has failed, and has not influenced significantly the process of soil hardening (that is related to the volumetric strain component). In any case, it is suggested to use these values with care.

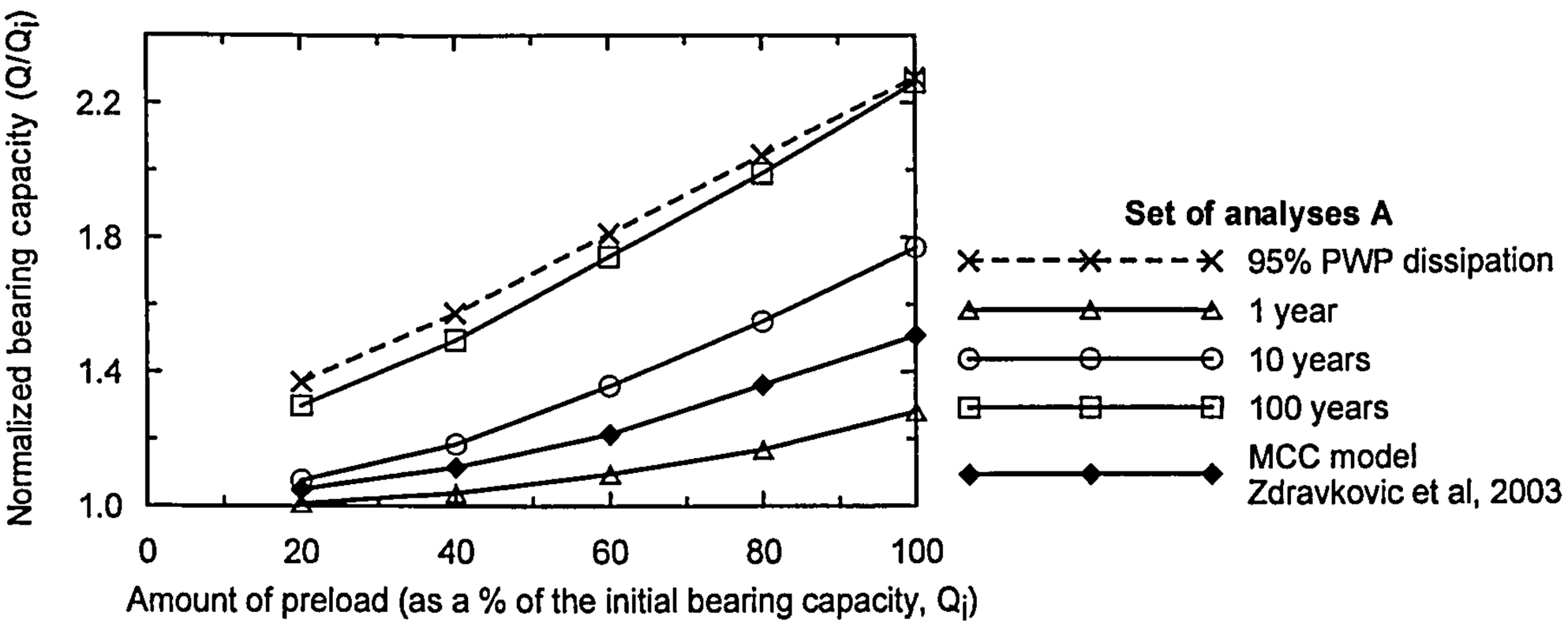

Figure 7.17: Normalized bearing capacity of a preloaded strip footing after different consolidation periods as a function of the amount of preload – set A to D.

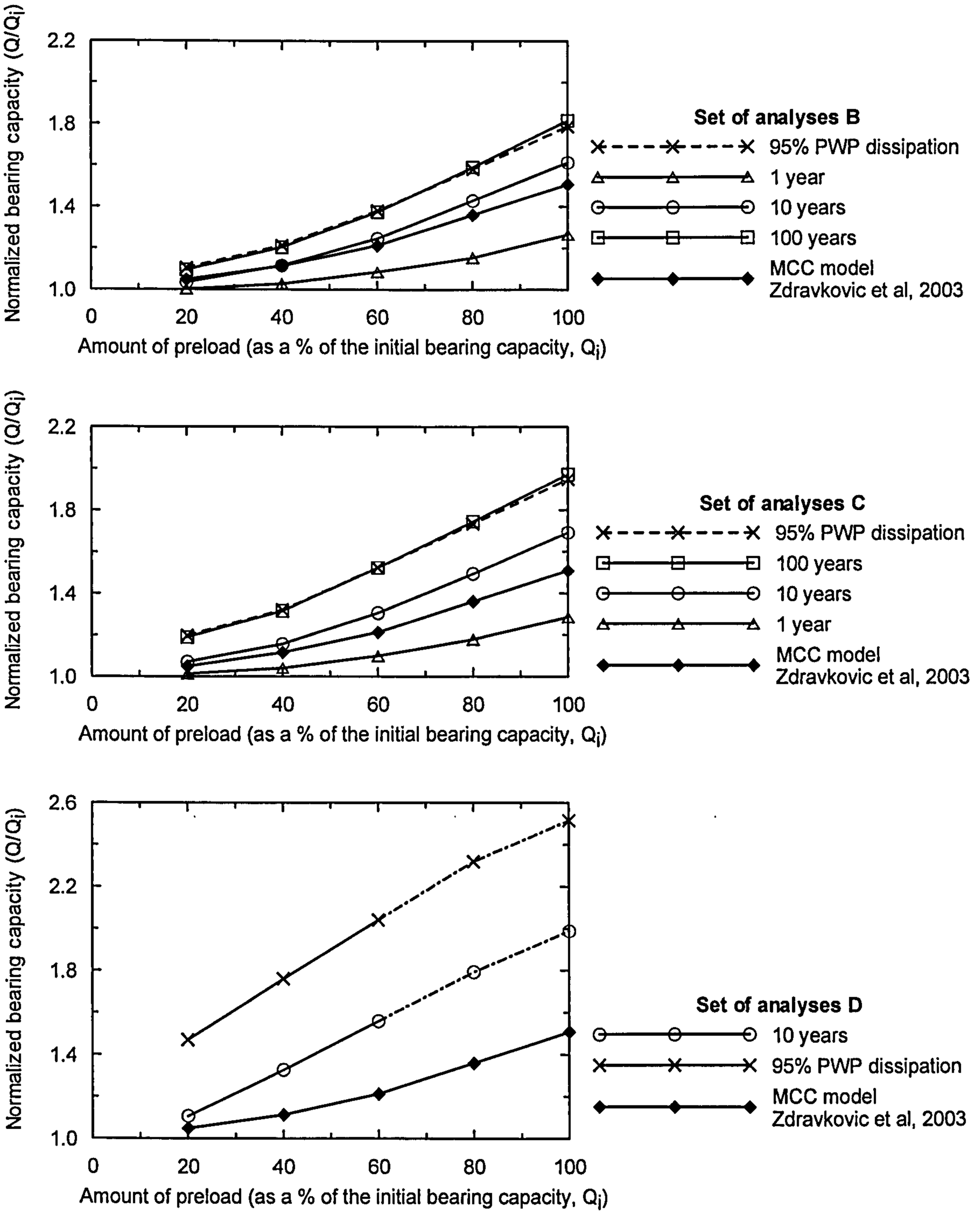

Notes: the graphs are all the same scale.

Figure 7.17: Normalized bearing capacity of a preloaded strip footing after different consolidation periods as a function of the amount of preload – set A to D.

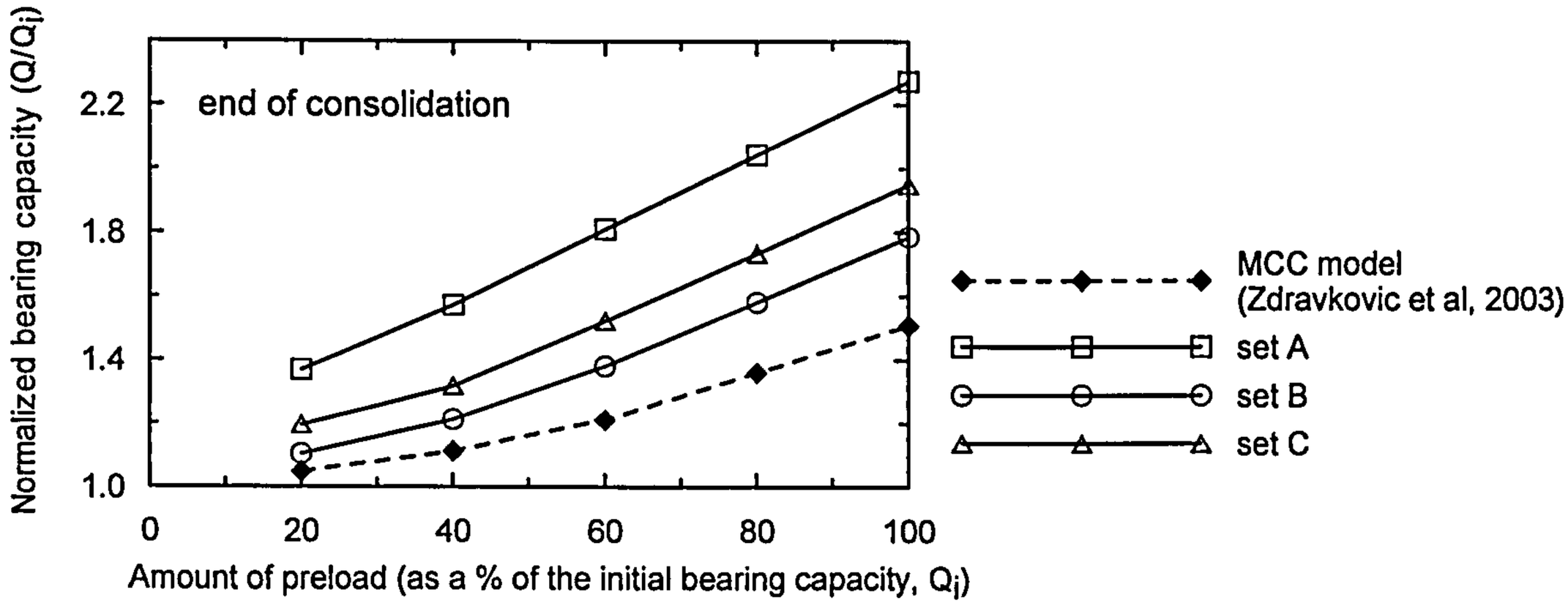

Figure 7.18: Normalized bearing capacity of a preloaded footing at the end of consolidation

Figure 7.18 presents the normalized ultimate bearing capacity of a preloaded footing at the end of consolidation for sets of analyses A to C. The main aim of determining the footing bearing capacity at the end of consolidation was to somehow quantify the effect of soil hardening due to creep by comparison with the results of Zdravkovic et al (2003), which correspond to the end of consolidation and include no secondary consolidation.

However, as mentioned in section 7.6.1, due to the interaction of the phenomena of consolidation, creep and shearing, it is not possible to separate the two components contributing to the soil hardening. In addition, it is found that the time to the end of consolidation varies from 63 to 290 years, depending on the preload value, the model parameters and the loading rate adopted, and so each data point will correspond to a different consolidation time.

In any case, the ultimate bearing capacity at the end of consolidation is, as a rule, very similar to that obtained after 100 years of consolidation. The exception is set A, where the end of consolidation gives values up to about 5% higher, with this difference decreasing at larger values of preload.

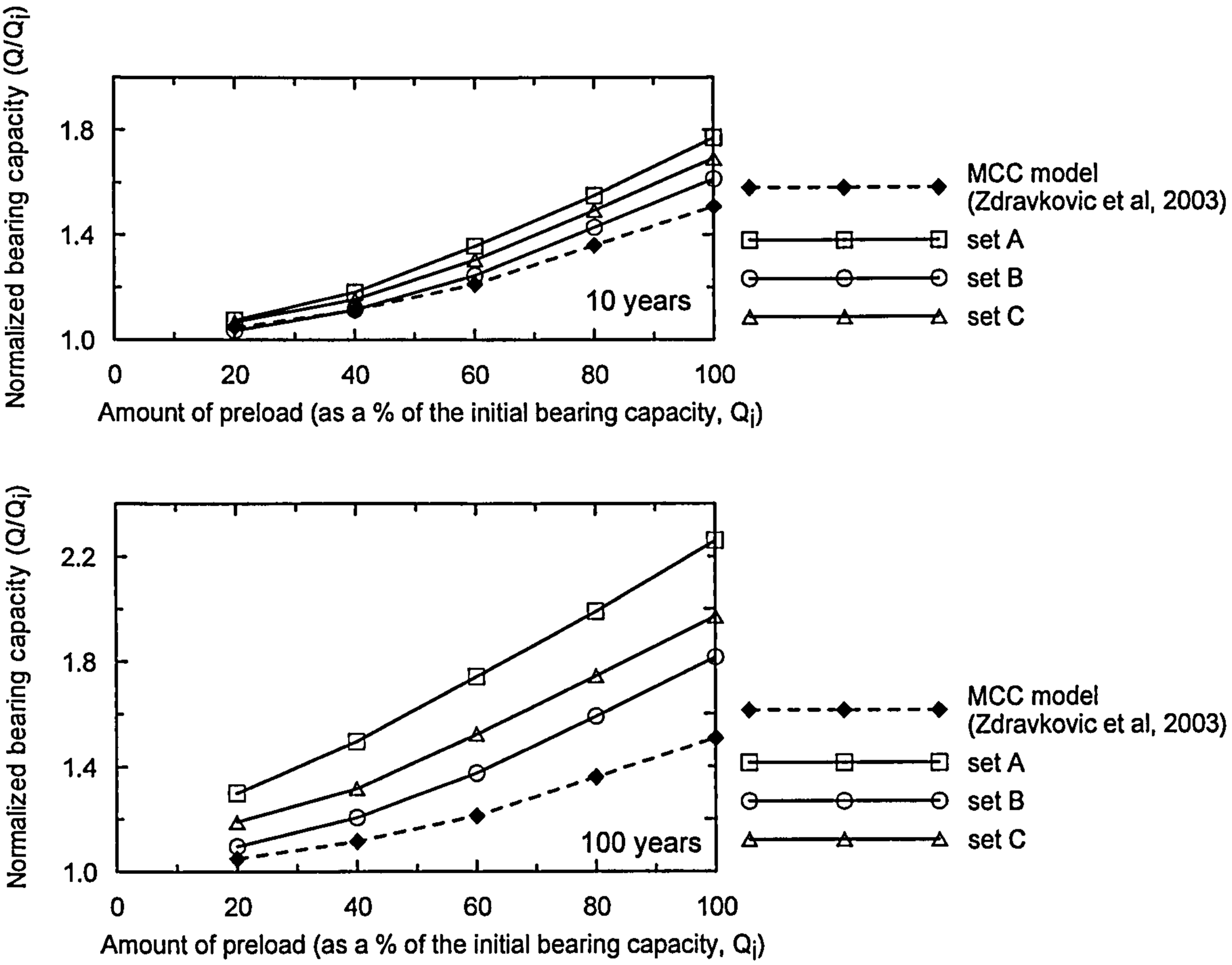

Figure 7.19: Normalized bearing capacity of preloaded strip footing after 10 and 100 years of consolidation.

It is of interest to analyse how the values of normalized bearing capacity relate to the observed footing settlements, at a given consolidation time. Both models predict that the soil's hardening – increase in soil's undrained strength and/or apparent pre-consolidation pressure - is an exponential function of the predicted plastic / visco-plastic volumetric strain, and thus the same plastic volumetric strain increment is expected to produce a larger soil's hardening at higher stress levels.

Figure 7.19 compares the normalized bearing capacity of a preloaded strip footing as predicted by sets of analyses A to C after 10 and 100 years of consolidation time.

After 100 years of consolidation, the consideration of creep given by a constant coefficient of secondary consolidation equal to 0.03 (set A) causes an additional increase in the normalized bearing capacity, in relation to that predicted using the MCC model, of 38% at 40% preload and 53% at 60% preload. This corresponds to an

additional increase of about 39% on the normalized bearing capacity as result of increasing its preload from 40% to 60%. In contrast, in terms of foundation settlements, there is an increase of about 22%, from 0.456 to 0.558 m of additional delayed settlement in relation to that predicted using the MCC model.

When comparing the relative effect of creep to the soil hardening between 60% and 100% preload it is found that there is a relative increase of about 41% (from an additional increase of 53% to 75%) in terms of bearing capacity and of about 33% in terms of delayed settlements (from 0.558 m to 0.741 m). The proportionally higher increase in footing settlements at 100% preload arises from the larger contribution of deviatoric strains to the footing settlements, but not to the soil hardening.

In any case, it is found that for a given consolidation time, the larger the predicted settlements the higher the predicted bearing capacity. Therefore, identically to the behaviour observed in terms of delayed settlements, it is found that for the analyses performed using the ET model set A predicts the highest normalized bearing capacity values and set B the smallest for a given value of preload and consolidation time. The predictions given by set C lie somewhere in between and they diverge from those of set A as the consolidation time increases. The results corroborate that the adoption of a higher value for the coefficient of secondary consolidation is conservative in terms of settlements but is unsafe when considering the ultimate bearing capacity of preloaded footings.

For a preload of 100% and C_α=0.03 the consideration of soil hardening associated with creep is found to cause the long term (say at 100 years) ultimate bearing capacity to reach a value over twice the initial one. For more practical values of preload, say at 50%, the consideration of creep may increase the normalized bearing capacity from 1.15 times Q_i (predicted using the MCC model) to a value between 1.3 and 1.6 times Q_i depending on the amount of secondary consolidation considered.

Figure 7.20 shows the evolution of the ultimate bearing capacity of a preloaded strip footing with time for 40 and 60% preload for sets A and B. It has been noted that 40% and 60% preload are cases of particular relevance in engineering practice as they correspond to an initial factor of safety on load between 2.5 and 1.67, respectively.

Figure 7.20 can be used as a design tool to do a preliminary estimate of the available bearing capacity of an existing footing.

Effect of adopting a non-logarithmic creep law

In sets of analyses A and B, the ET model is made to reproduce a linear logarithmic creep law, as this is the assumption commonly made in engineering practice when considering the long-term behaviour of soils. However, the creep behaviour of geomaterials is known to be in general non-linear in semi-logarithmic space, showing a progressive decrease in the current coefficient of secondary consolidation, $C_{\alpha e}$, with time. In set C, the effect of adopting a non-linear logarithmic creep law is examined.

As observed in Figure 7.19 the ultimate bearing capacities predicted by set C lie somewhere in between those predicted by set A and B, and deviate progressively from set A, as the consolidation time increases. The effect of the creep law non-linearity is found to be more pronounced as the consolidation time increases; for example at 40% preload (equivalent to a factor of safety of 2.5) the normalized bearing capacity decreases from 1.18 to 1.16 at 10 years, compared to a change from 1.49 to 1.32 at 100 years.

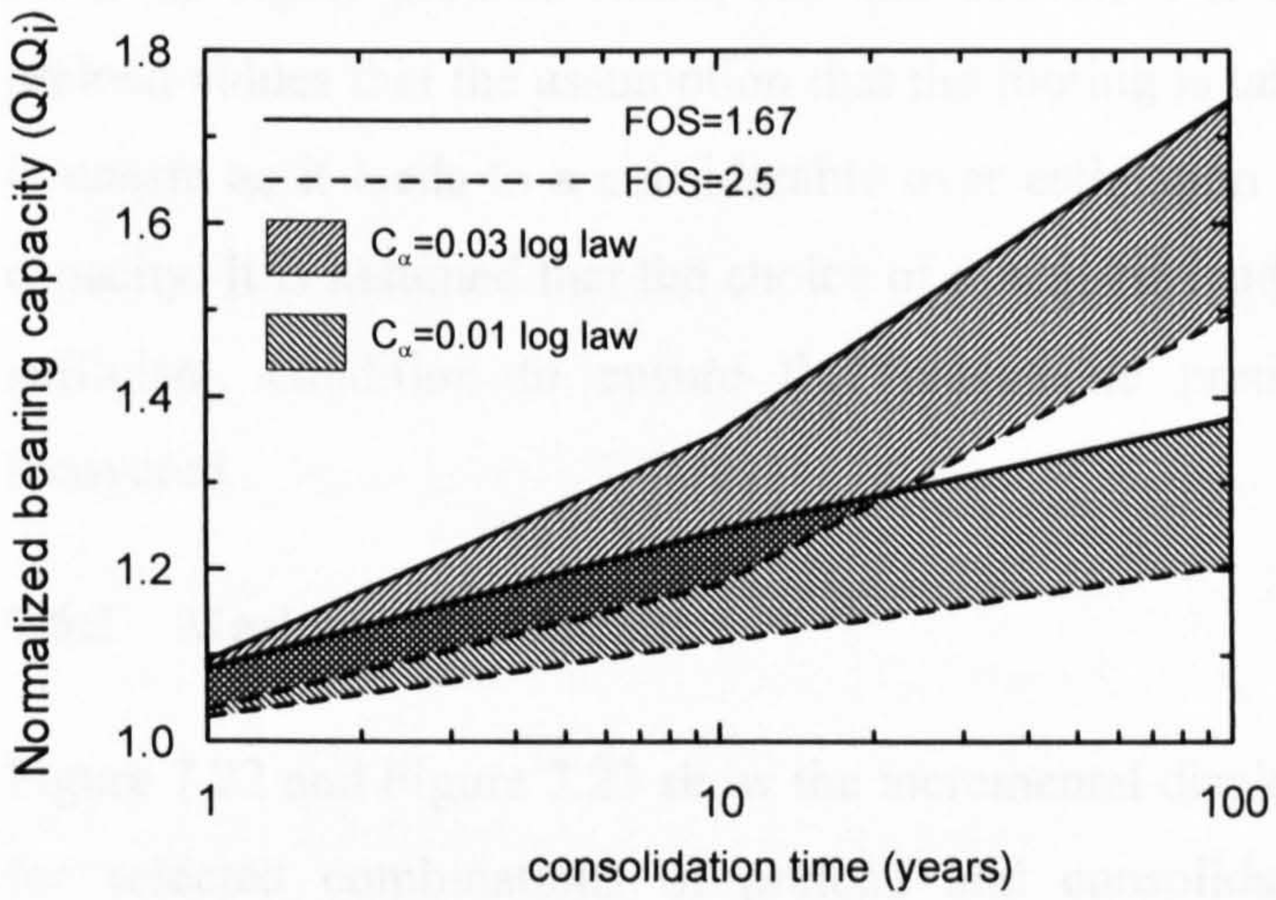

Note: the time origin is the end of loading.

Figure 7.20: Normalized bearing capacity of a preloaded strip footing *versus* consolidation time, for 40 and 60% preload.

Effect of the footing loading rate

As mentioned above the time dependent nature of the ET model causes the footing loading rate to affect both the value of soil's undrained strength and the visco-plastic strain rates acting in the foundation at the end of loading. The former has been dealt with by normalizing the ultimate bearing capacity by the respective initial value and using the same loading rate during first loading and subsequent reloading. The influence of the applied loading rate on the magnitude of the strain rates acting in the foundation at the end of the application of the preload is taken into account by choosing a realistic loading rate and in sets A to C the footing is assumed to be taken to failure under a constant displacement rate over a period of 6 months.

In set D, the footing is taken to failure in about 3 days, and it was expected that due to the higher strain rates acting in the foundation soil immediately after loading, larger settlements and gains in bearing capacity would be predicted, and in terms of bearing capacity such an assumption is obviously unsafe.

Figure 7.21 shows the predicted normalized ultimate bearing capacities after 10 years and at the end of consolidation for all sets of analyses. Even disregarding the results of set D at higher preload values (80 and 100%), it is evident from the data at lower preload values that the assumption that the footing is taken to failure over about 3 days is unsafe as it leads to a considerable over estimation of the footing ultimate bearing capacity. It is assumed that the choice of a realistic loading rate is a necessary, but also sufficient, condition to ensure that reasonable predictions of soil hardening are recovered.

7.6.3 Mechanism of failure

Figure 7.22 and Figure 7.23 show the incremental displacements at failure on reloading for selected combinations of preload and consolidation time for sets A and B, respectively. For the cases examined there are no significant changes in the failure mechanism of the preloaded footings, in relation to that observed on first loading, resulting from variations in the amount of preload or consolidation time.

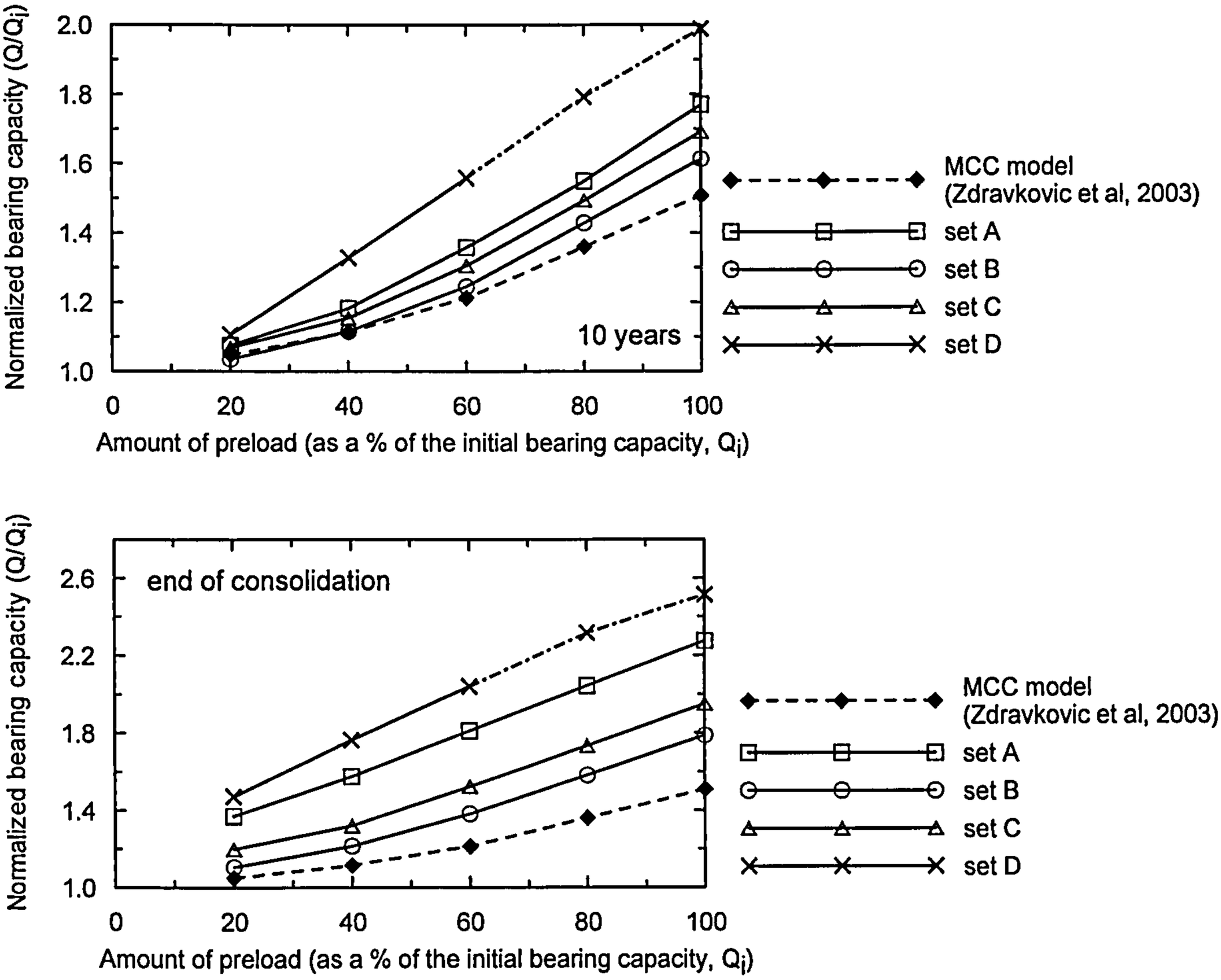

Figure 7.21: Normalized bearing capacity of a preloaded strip footing after 10 years of consolidation and at the end of consolidation.

It was initially expected that the soil hardening associated with pore pressure dissipation and creep would cause the failure mechanisms to extend deeper into the soil mass to avoid the shallower areas that have undergone more significant hardening. However, the presence of the surface crust in the top 2 m and the small dimension of the footing when compared with that of the crust create the conditions for this not to happen.

During initial loading, the larger stress changes occur within the surface crust in the top 2 m. Given that the soil at that level is medium to slightly overconsolidated the amount of contractive excess pore water pressures generated are significantly lower than if the material was normally consolidated, and the soil hardening associated with consolidation process is correspondingly limited.

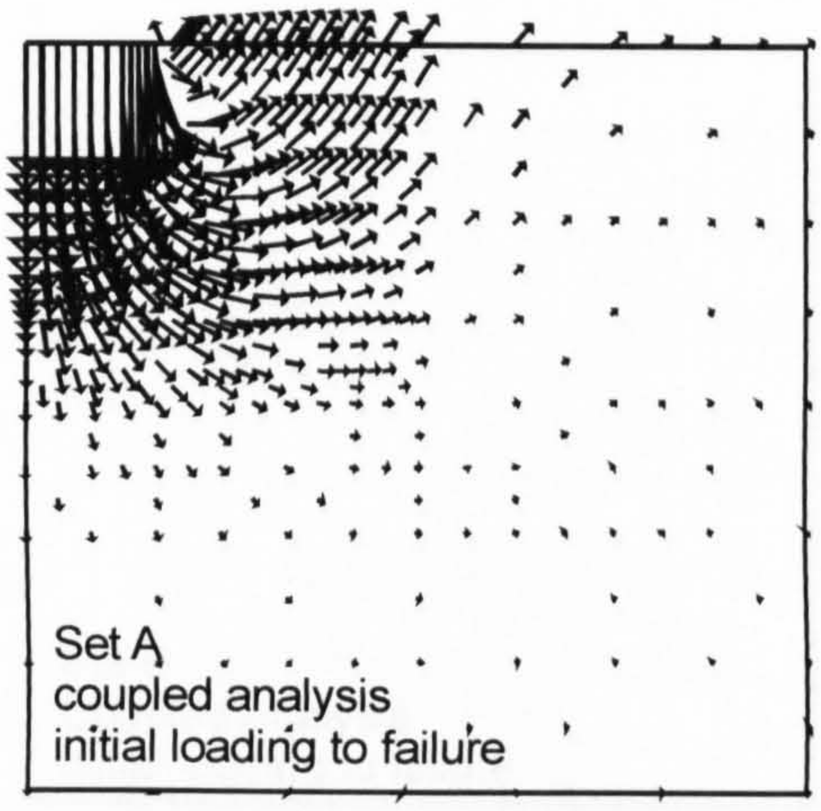

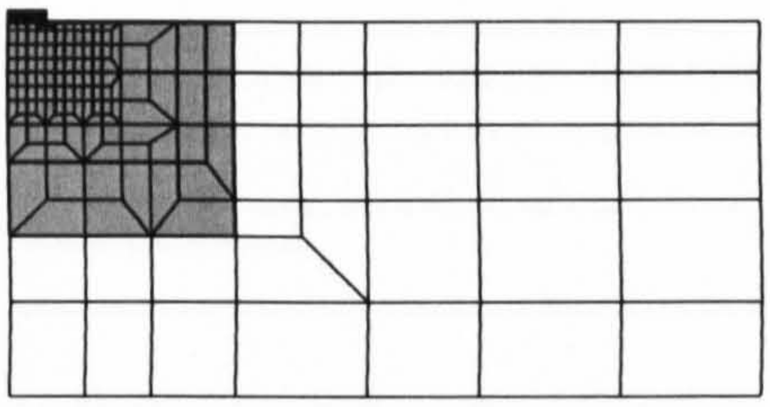

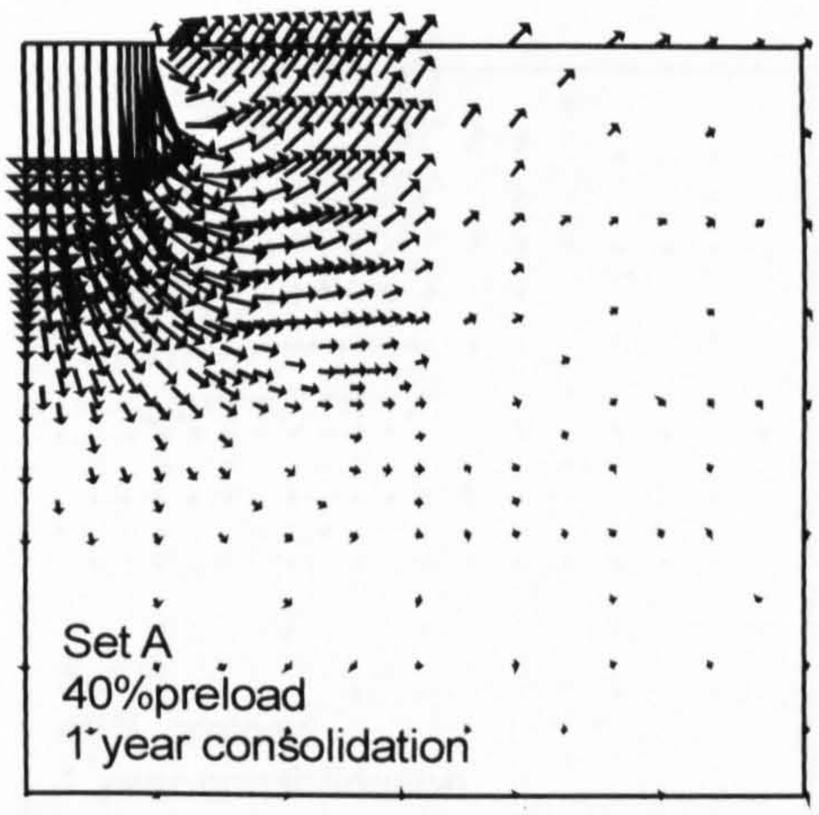

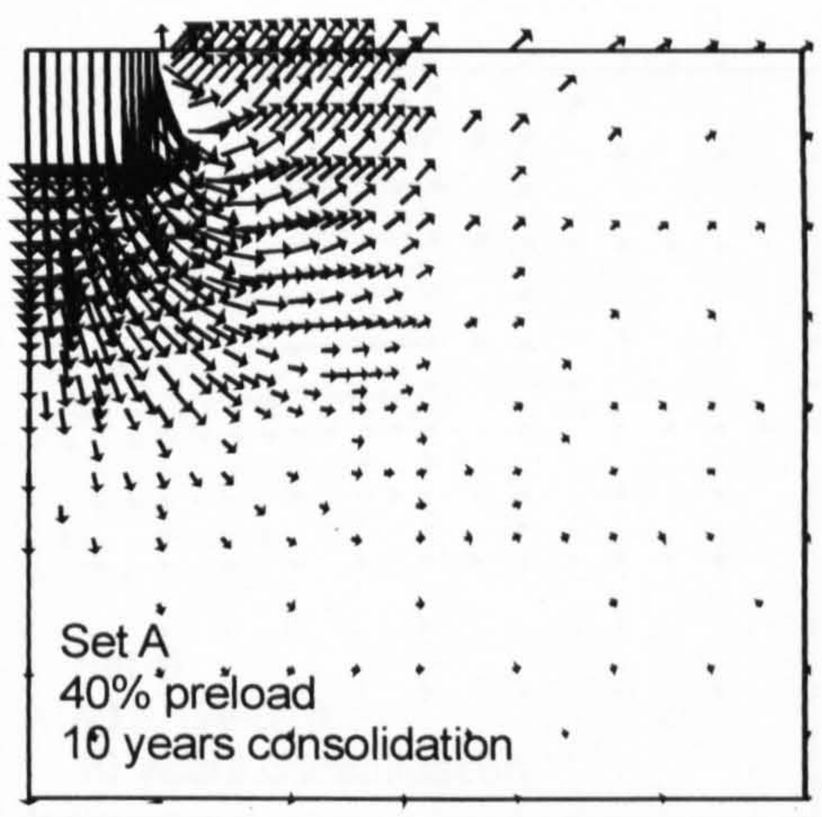

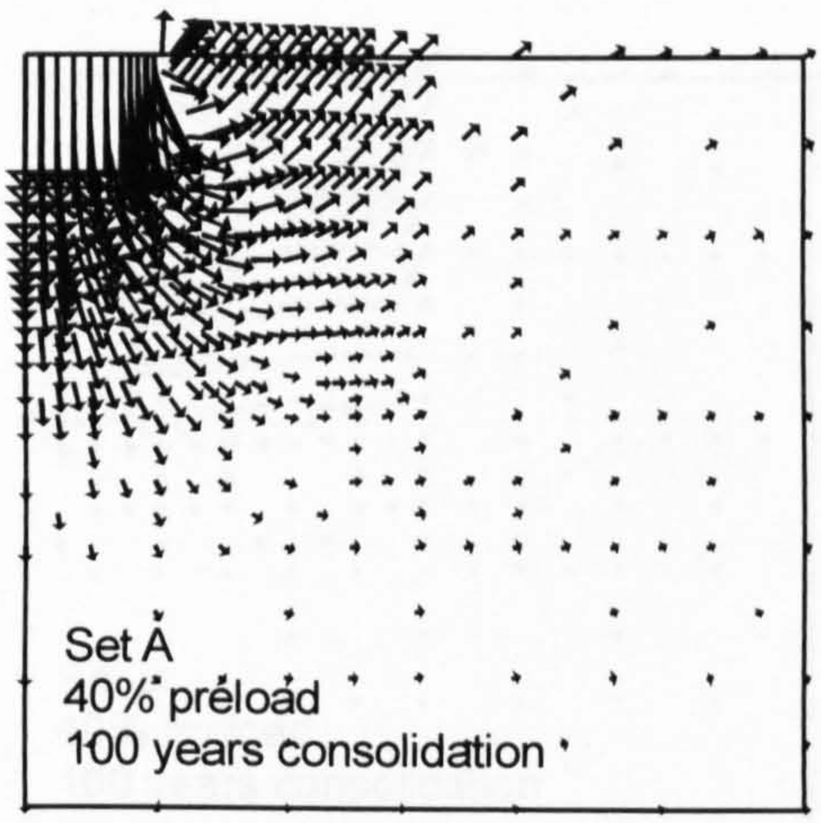

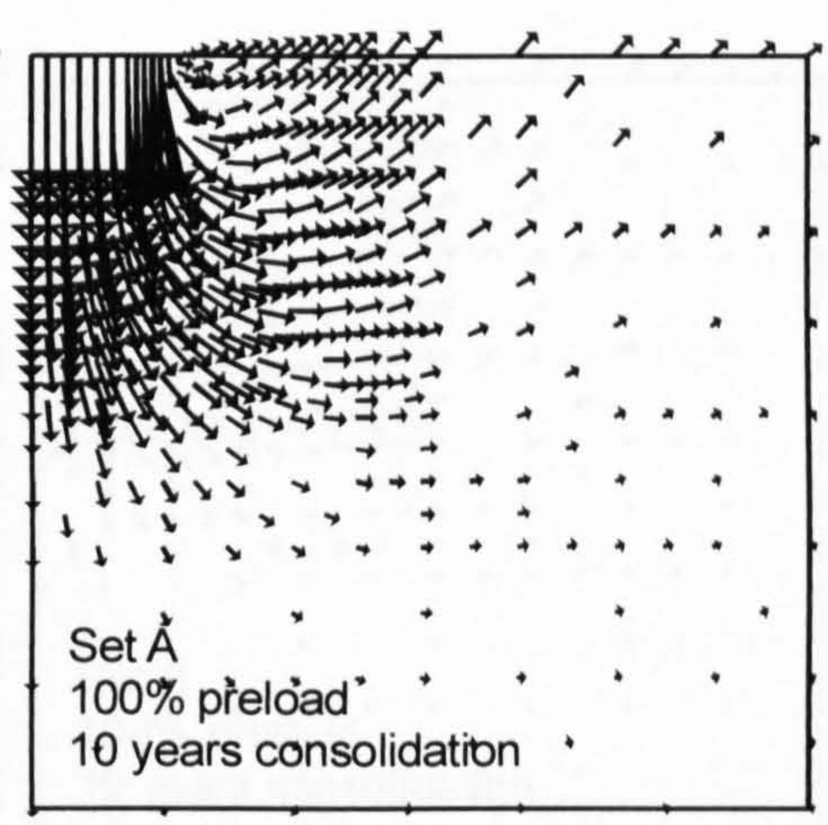

Note: the plots above are all at the same scale.
The area in the plots of incremental displacements corresponds to the area of the mesh in grey.

Figure 7.22: Incremental displacements at failure for some preload and consolidation time values – set A.

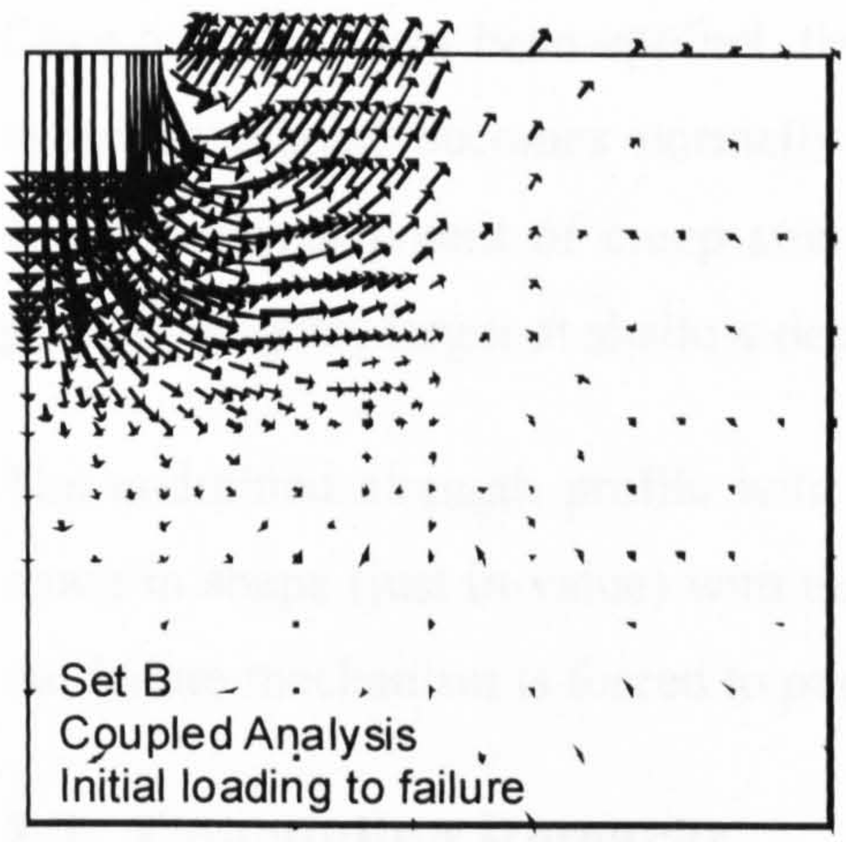

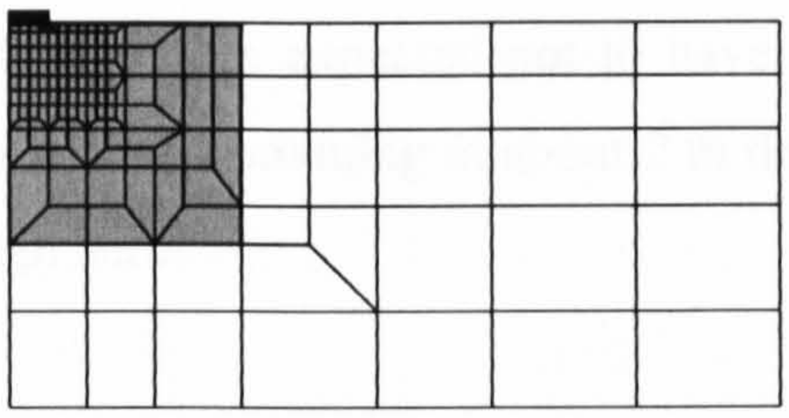

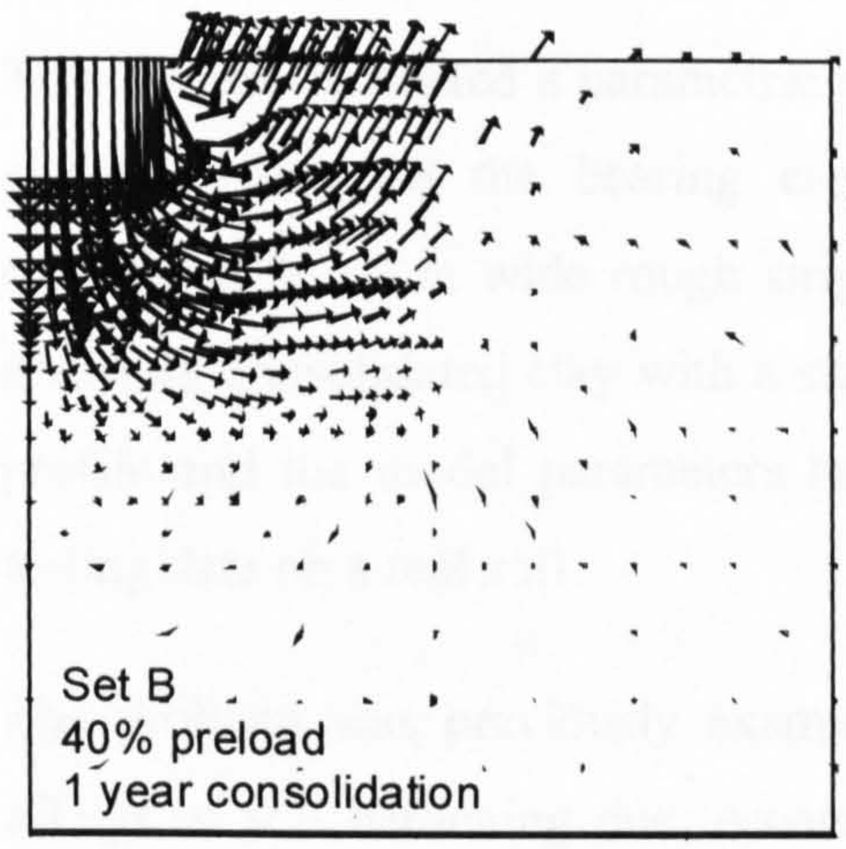

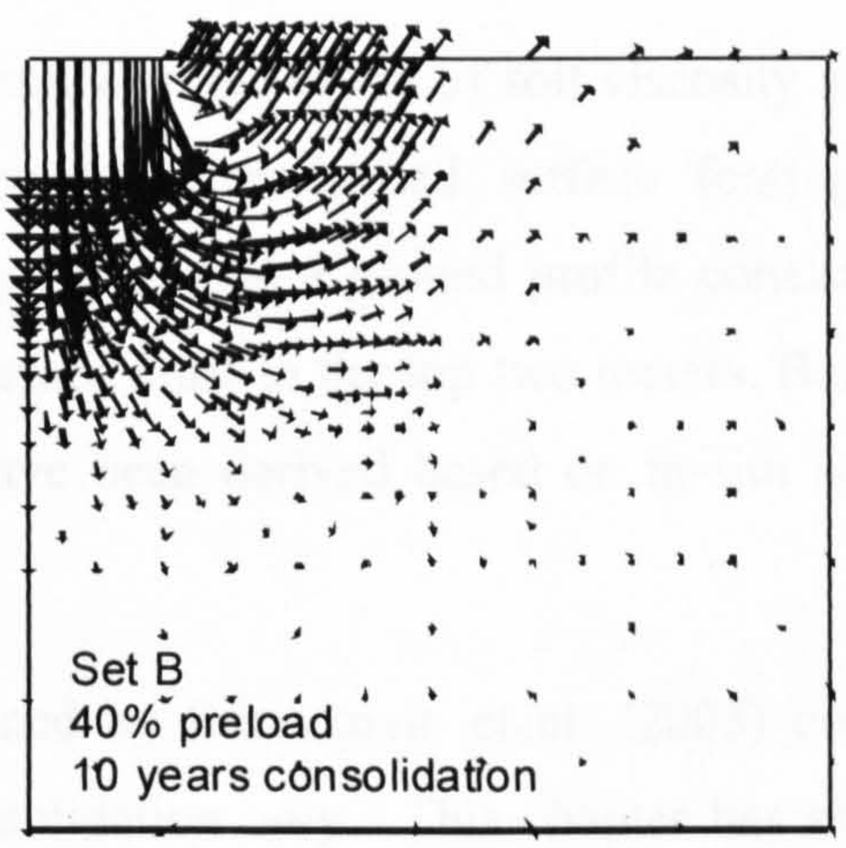

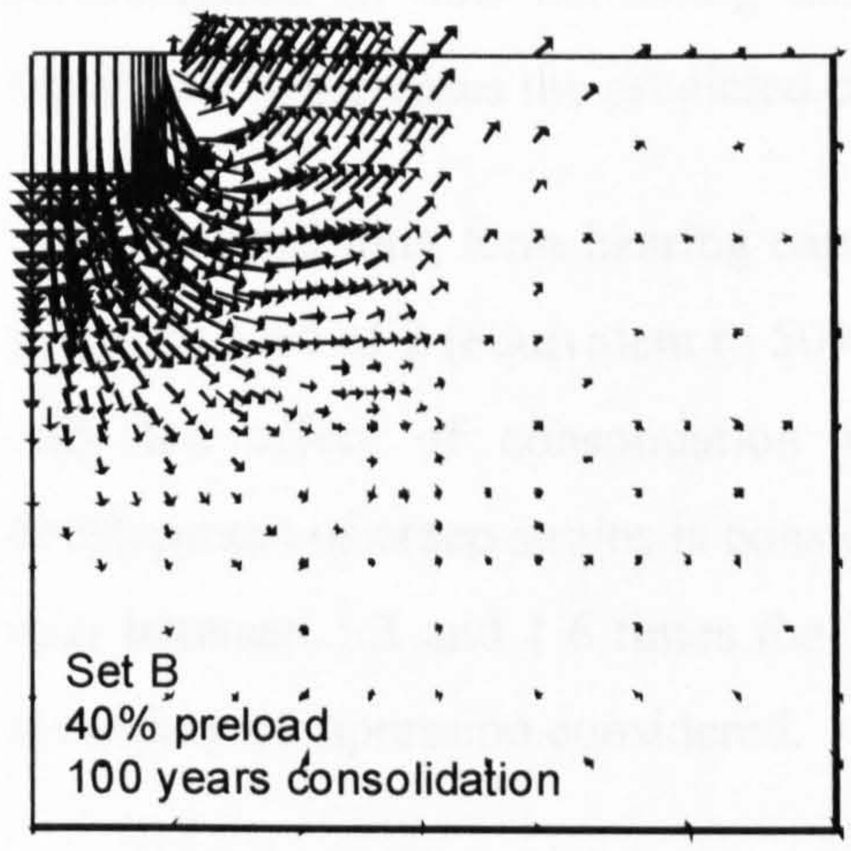

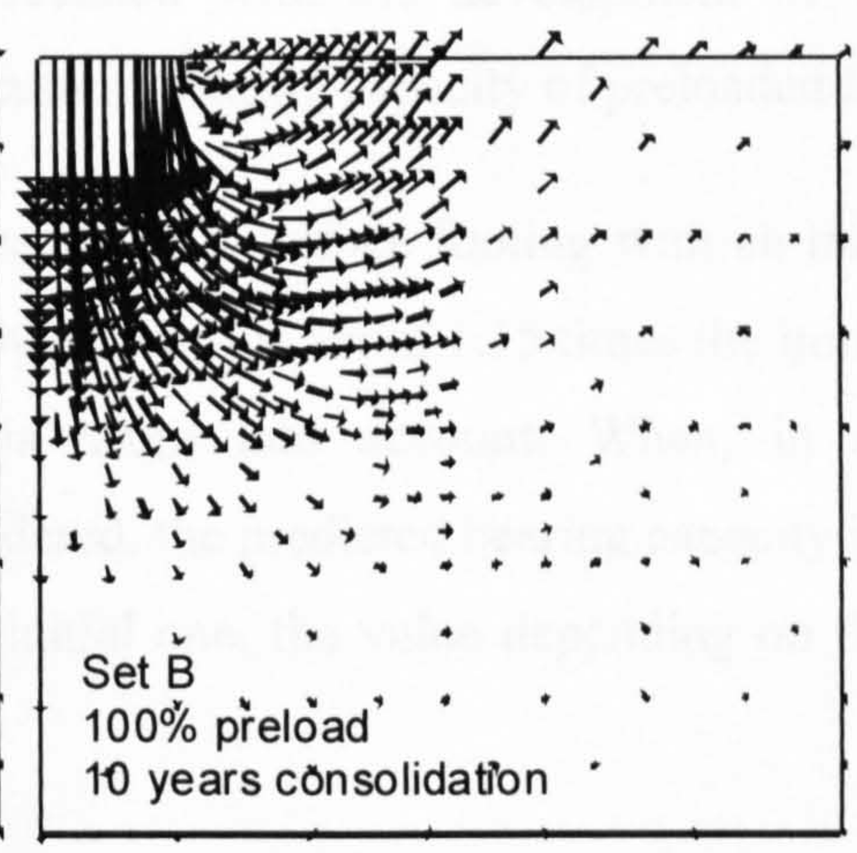

Note: the plots above are all at the same scale.
The area in the plots of incremental displacements corresponds to the area of the mesh in grey.

Figure 7.23: Incremental displacements at failure for some preload and consolidation time values – set B.

Once a preload has been applied, the soil adjacent to the footing that was previously overconsolidated becomes normally consolidated, and the soil hardening associated with the development of creep strains is expected to be almost uniform with depth, possibly slightly larger at shallow depth were larger strain rates have been imposed.

The undrained strength profile with depth is therefore expected not to have changed much in shape (just in value) with the weakest zone remaining at about 2 m depth, and the failure mechanism is forced to pass through here.

7.7 Concluding Remarks

This chapter presented a parametric study on the effect of soil viscosity and associated soil hardening on the bearing capacity of preloaded surface footings. The case considered is a 2 m wide rough strip footing on a ground profile consisting of a soft normally consolidated clay with a surface crust in the top two meters. Both the ground profile and the model parameters have been derived based on in-situ and laboratory testing data on a real soil.

The problem was previously examined by Zdravkovic et al. (2003) considering the effects of soil hardening due to consolidation only. This chapter has shown that the consideration of soil hardening associated with the development of creep strains significantly increases the predicted current bearing capacity of preloaded footings.

The predicted long term bearing capacity of a surface footing with an initial factor of safety on load of 2 (equivalent to 50% preload) is about 1.15 times the initial one, when only the effect of consolidation is taken into account. When, in addition, the development of creep strains is considered, the predicted bearing capacity is found to be then between 1.3 and 1.6 times the initial one, the value depending on the amount of secondary compression considered.

It has been shown that the adoption of a large value of secondary compression, quantified by the parameter C_α, may be conservative when estimating the long term settlement of an engineering structure, however it is unsafe when considering the soil hardening, in this study expressed as the current bearing capacity of a preloaded footing.

The adoption of a non-linear logarithmic creep law becomes more significant at larger consolidation times, and in particular when considering serviceability states. For the case examined, the total long-term settlement is found to reduce by a third when the creep behaviour non-linearity is taken into account.

How realistic it is to apply this study to engineering practice will depend mainly on how the site conditions approximate those assumed in this study, mainly in terms of the ground profile and the dimension of the footing in relation to that of the crust. Based on the work shown by Randolph et al. (2004) (see Figure 7.2) it is anticipated that the results obtained on this study on a strip footing could be applied to footings of similar dimensions but different geometry. Analyses have been carried out to examine the effect of the soil hardening associated with creep on a preloaded circular footing. A methodology identical to that presented here was followed. The results in terms of undrained bearing capacity have shown a similar pattern with the bearing capacity increasing with the amount of preload and consolidation time. However, in a circular footing the drainage path is considerably reduced and so is the time to the end of consolidation. This exacerbates the problem of defining the failure condition during the footing reloading and it has been preferred not to include this set of data.

It is noted that for the case examined, the failure mechanism is very much influenced by the presence of the surface crust, which has a reducing undrained strength with depth. Such a condition forces the failure mechanism to extend down to intercept the weakest soil at the base of the crust. This implies that the failure mechanism involves a relatively small proportion of normally consolidated clay, and consequently more soil hardening could potentially be predicted for other footing/crust dimension ratio, for which the failure mechanism intercepts a larger proportion of normally consolidated soil, as normally consolidated soils develop the largest positive (contractive) excess pore pressures.

The following chapter aims to recover the behaviour of two footings on Bothkennar Clay and given the broad similarities in the ground profiles and footing/crust dimensions it is expected to further validate this study.

8 NUMERICAL ANALYSES OF TWO SURFACE FOOTINGS ON BOTHKENNAR CLAY

8.1 Introduction

This Chapter describes the numerical analyses of the loading tests performed on two rigid footings at the Bothkennar clay test site (Jardine et al., 1995; Lehane & Jardine, 2003). Footing A, 2.2 m x 2.2 m square, was loaded to failure in July 1990 over 4 days, reaching a net bearing pressure of 138 kPa. One month later Footing B, 2.4 m x 2.4 m square, was loaded over three days to 89 kPa, about 2/3 of the bearing capacity proven in footing A, and left to consolidate under a constant applied load for about 11 years. In July 2001, due to the imminent closure of the Bothkennar research site, the preloaded footing was loaded over three days to 204 kPa, at which point severe tilting of the footing prevented the test from continuing.

Considering the two footings to have the same initial bearing capacity, the increase in bearing capacity due to the preload over 11 years of consolidation was over 48%. According to Zdravkovic et al. (2003) the expected increase in bearing capacity due to the preload would be about 25%.

The parametric study described in Chapter 7 shows that the consideration of soil hardening due to the development of creep strains may account for a significant increase in the ultimate bearing capacity of preloaded footings. Applying the results of the parametric study to the Bothkennar case, one would predict an increase in bearing capacity between 30% and 45% depending on the amount of creep strain that had developed, which is close to the value observed at Bothkennar.

From the monitoring data, it is concluded that most of the excess pore pressure generated during the application of the initial load dissipated in less than a year (Jardine et al., 1995), and consequently the settlement developed during the observation period, after the first year, is associated with creep.

In Chapter 7, the ET model was applied to study the effect of soil ageing on a generic pre-loaded strip footing resting on a soft clay stratum, and the model was shown to reproduce qualitatively well the soil ageing associated with the development of creep

strains with time and the consequent increase in the stiffness and strength characteristics.

It is therefore relevant to analyse the footings at the Bothkennar research site in order to assess the model's performance in describing the behaviour of a real soil in a boundary value problem where the consideration of the time dependent nature of the soil is important and consequently validate the outcomes of the parametric study shown in Chapter 7.

The Bothkennar case presents the additional advantage of being very well documented with a wide range of data available in the literature regarding the soil characterization and the footing's behaviour. The general methodology adopted was to derive the model parameters based on the extensive laboratory and in-situ test data available, then use the observed behaviour of footing A to confirm the model parameters and ground profile adopted, which are subsequently used to analyse footing B.

The load tests are studied by means of coupled consolidation axi-symmetric finite element analyses performed using ICFEP (Imperial College Finite Element Program) and using the Equivalent Time (ET) constitutive model, described in Chapter 6, to mimic the foundation soil behaviour.

8.2 The soft clay test site at Bothkennar, Scotland

8.2.1 Introduction

The Bothkennar soft clay test site was bought in 1987 by the former Science and Engineering Research Council (SERC, now EPSRC) with the intent of creating a site for the development of soil investigations including, sampling, laboratory testing and large to full-scale tests on soft clay. The primary intent was to support academic research but the site was also available to industry, and collaborative studies between academics and industry were encouraged.

The Bothkennar site is located approximately midway between Edinburgh and Glasgow, on the south side of the River Forth, as shown in Figure 8.1. The site has an area of approximately 11 ha and a soft clay stratum up to about 20 m deep - the main criteria set for the selection of the research site. The soil profile consists essentially of a deep soft clay stratum with a surface crust 2 to 3 m thick that enables the use of heavy

plant at the site. The relatively simple soil profile was expected to simplify the back analysis and the interpretation of field experiments.

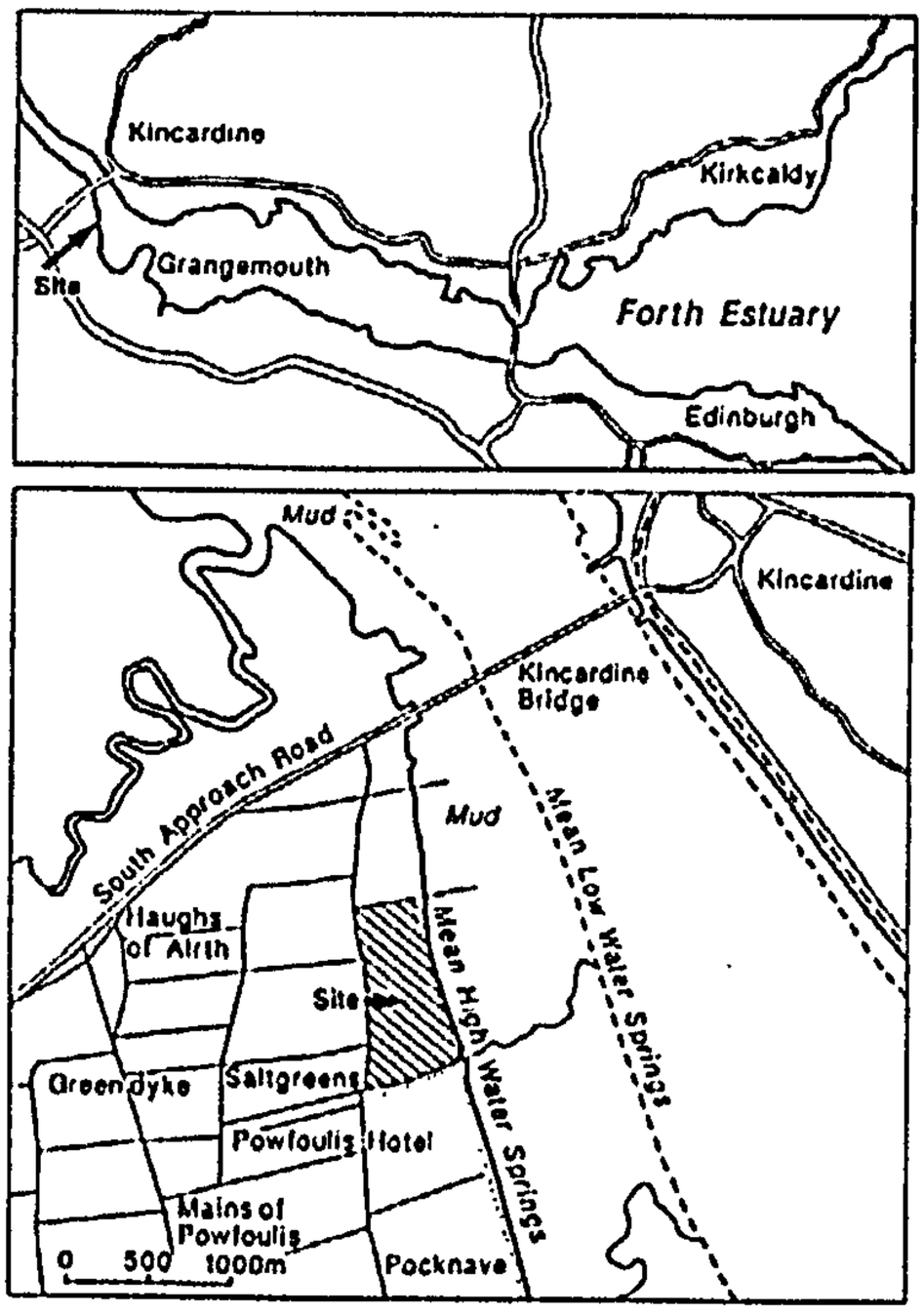

Figure 8.1: Location of the Bothkennar site.

Following the establishment of the site, the SERC launched a project for the detailed characterization of the soil properties of the clay stratum at Bothkennar. The project included a research programme on methods of field sampling and laboratory testing of soft saturated clays. Figure 8.2 shows a plan of the Bothkennar site with the indication of the site investigation undertaken. The outcomes of this project were collected and published in the Geotechnique Symposium In Print (Institution of Civil Engineers, 1992).

In addition, the SERC supported projects to improve the understanding of engineering on soft clay. In particular, tests on rigid footings (Jardine et al., 1995; Lehane & Jardine, 2003), some of them instrumented, and an instrumented pile test programme (Lehane & Jardine, 1993) have been carried out in the area indicated as *BRE test area* in Figure 8.2.

This chapter focuses on the load tests performed on two instrumented rigid footings between June 1990 and July 2001. A description of the footings construction and loading is presented in Section 8.3.

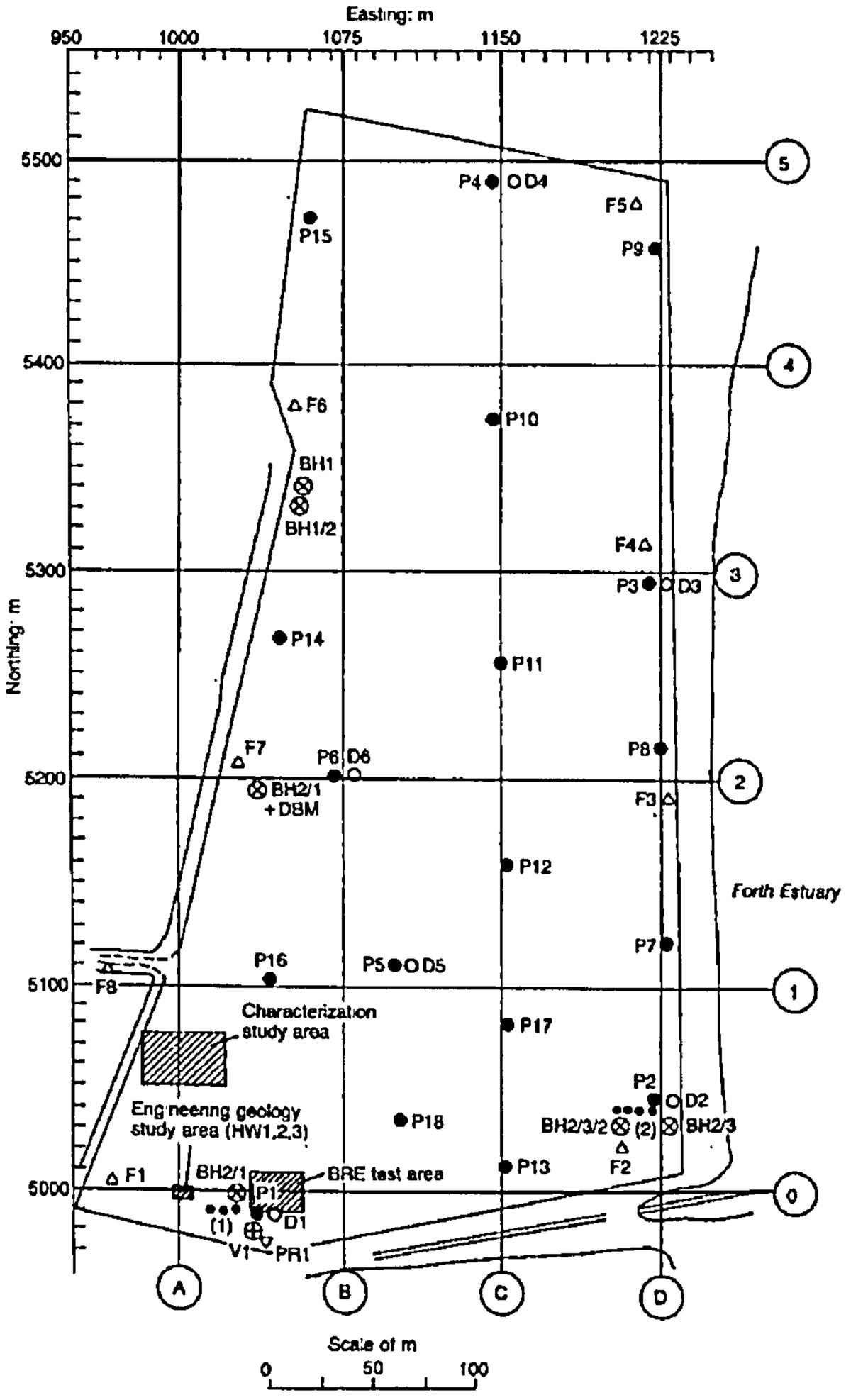

Figure 8.2: Plan of the Bothkennar site with the location of the site investigation performed during the initial investigation and subsequent characterization project (after Hight et al., 1992).

8.2.2 Local geology

The Bothkennar site is located on the south side of the Firth of Forth in Scotland as shown in Figure 8.1. The River Forth crosses the Carboniferous Coal Measures and Millstone Grit, and strata of the Lower Devonian age. The Lower Devonian consists of conglomerates, fluvial and lacustrine sandstones. The Carboniferous rocks are mostly limestones with some coals and sandstones.

The geological conditions encountered in Scottish estuaries differ from those in the Severn and the Thames regions, as during the late Devensian age, parts of the Midland Valley are thought to have been covered by 1500 to 1800 m of ice. It is thought that the area was free of ice by 13000 years before present (BP), with the exception of a minor glaciation - the Loch Lomond Readvance – that occurred between 11000 and 10300 BP.

It is thought that glacial erosion caused the excavation of a trench up to 180 m beneath the present estuary. The exposed bedrock was subsequently infilled by deposits of diverse grain sizes and under varying depositional environments. The changeable depositional conditions resulted from the simultaneous worldwide change in sea level resulting from glacial melting (eustatic rise) and the depression / elevation of the land as a result of the periodic loading and reloading of the ice (isostatic movements). This combination of eustatic and isostatic movements of differing magnitudes and rates increased the complexity of the depositional history.

The engineering geology of the Forth estuary has been studied by a number of researchers e.g. Sissons et al. (1966), Browne et al. (1984). The general Late and Postglacial Quaternary stratigraphy of the area, shown in Figure 8.3, consists of a buried gravel stratum (the Bothkennar Gravel), above which lie the clayey Letham and Claret Beds that form the soft clay sequence of the Carse Clay. This sequence is in part overlain by clayey silts of the Grangemouth Beds, and at the margins of the estuary is completed by modern intertidal deposits. The deposits below the Bothkennar Gravel consist of further silty clays, which overlie till, which in turn lies on bedrock.

The site lies within the outcrop of the Carse Clay, which comprises the main sequence at the site, and is described subsequently.

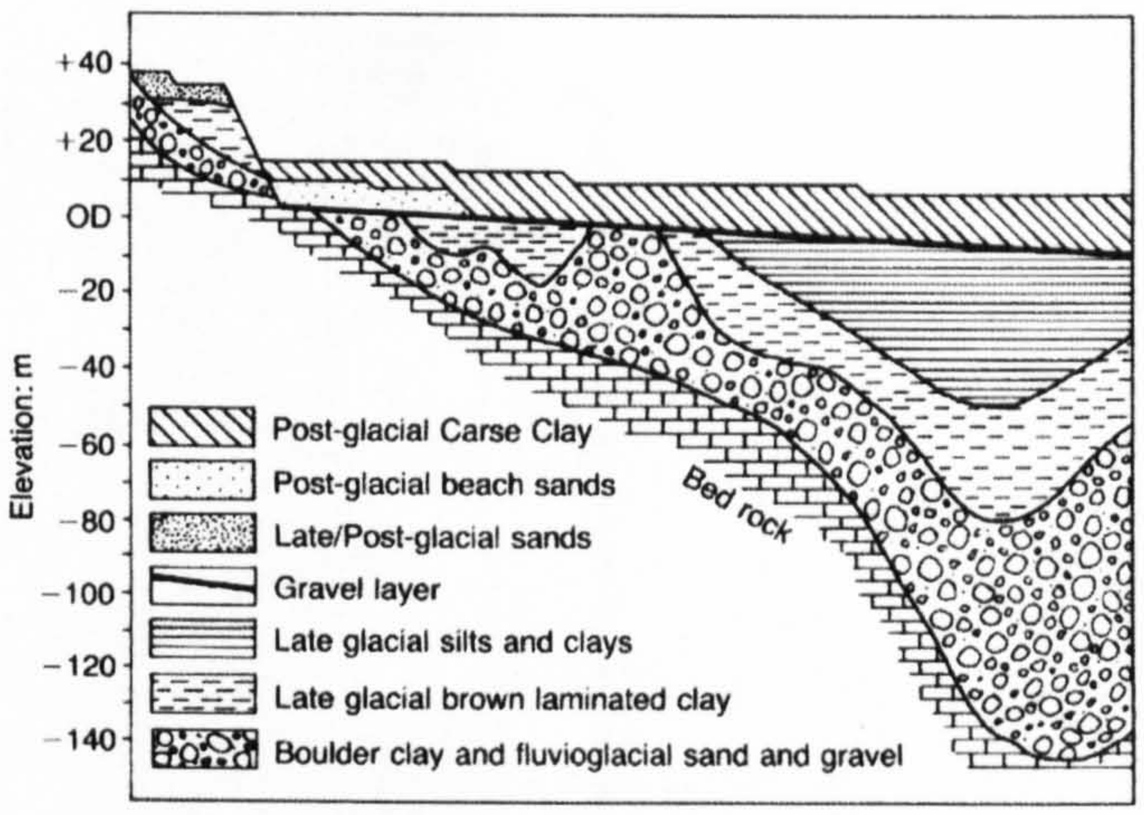

Figure 8.3: Nature of infill deposits above the bedrock the River of Forth valley (Browne et al., 1984).

a) Sediment description

The Carse clay deposits above the Bothkennar gravel show a thickness between 14 and 22 m across the site and can be subdivided into four facies: bedded, laminated, mottled and weathered. Figure 8.4 shows a generalized facies sequence at Bothkennar and a correlation with the local stratigraphy.

The bedded facies is a silty clay to clayey silt in which the original sedimentary structures from quiet water tidal deposition are still present. The laminated facies corresponds to more energetic depositional conditions giving rise to the occurrence of interbedded silt laminae typically about 1 to 2 mm thick and 30 to 50 mm apart. In general the laminated facies can be interpreted as a development from the bedded facies, in which a higher proportion of silty clay beds are separated by laminae rather than being in direct contact.

The mottled facies is mainly a silty clay in which bedding and laminations are poorly defined or even absent. The principal feature of the mottled facies is the presence of mottles varying in size from a few millimetres to 1 - 2 cm, which are thought to result from the reworking of the sediment by burrowing organisms, at times when the depositional rates were reduced.

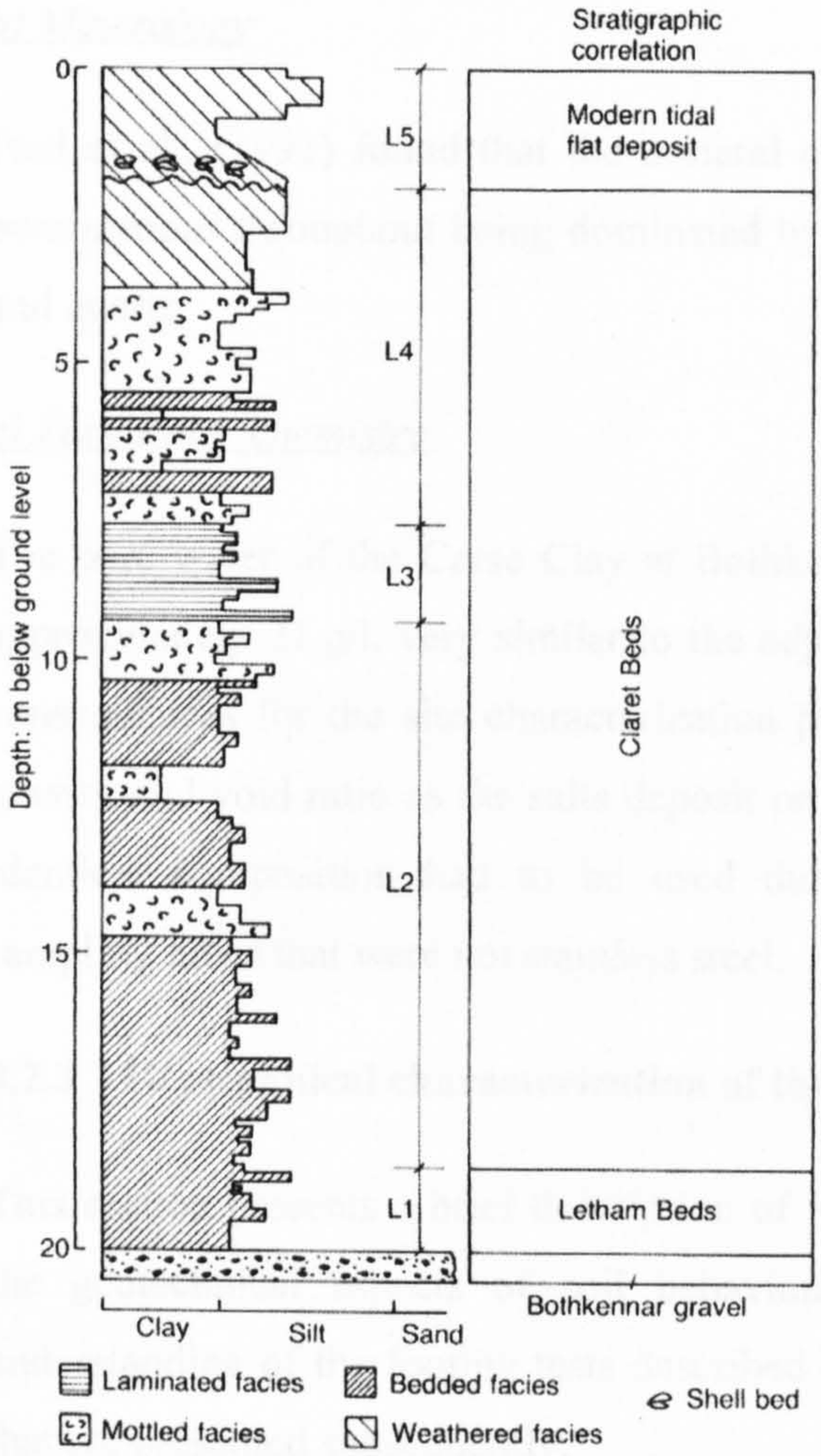

Figure 8.4: Generalized facies sequence and correlation with the local stratigraphy at Bothkennar (Paul et al., 1992)

The weathered facies occurs about 4 m from the surface and corresponds to the zone that has been affected by desiccation and oxidation. This causes the material to undergo a gradual change in colour from the characteristic very dark grey to black of the intact material to dark grey to greyish brown. This altered material corresponds to the surface crust, but also includes a sub-crust transition zone. Details on the facies persistence, stratigraphy and structure can be found in Paul et al. (1992).

The Carse Clay is overlain by modern deposits of the reclaimed tidal flats, with a marked unconformity. At the site this unconformity is identified by a bed of shells, many of which are paired and articulated, denoting that this may have been their position in life. It is thought that some limited erosion may have taken place at the surface of the Carse Clay before the deposition of the modern sediments.

b) Mineralogy

Paul et al., (1991) found that the mineral composition of the clay stratum was quite homogenous throughout being dominated by quartz and feldspar flour, kaolinite, illite, and quartz.

c) Pore water chemistry

The pore water of the Carse Clay at Bothkennar has an average total salts content of approximately 21 g/l, very similar to the adjacent estuary water. This had a number of consequences for the site characterization project: i) errors in measuring the specific gravity and void ratio as the salts deposit on the soil particles when dry; ii) water with identical composition had to be used during laboratory testing; iii) corrosion of sampling tubes that were not stainless steel.

8.2.3 Geotechnical characterization of the Carse Clay at Bothkennar

This section presents a brief description of the Carse Clay at Bothkennar, focusing on the geotechnical aspects of soil behaviour that are particularly relevant for the understanding of the footing tests described in Section 8.3 and the numerical analyses that are presented subsequently.

A detailed characterization of the Carse Clay can be found in the Symposium in Print (ICE, 1992) that summarises the outcomes of the characterization research project sponsored by the SERC.

8.2.3.1 Index tests

Figure 8.5 shows the description of the ground profile, in terms of index tests, at borehole D1 located next to the test footings. Borehole D1 was undertaken as part of an initial site investigation carried out before the purchase of the site, to ascertain its suitability. Later investigations have confirmed the findings of borehole D1.

a) Organic content

The Carse clay at Bothkennar has an organic content of between 3% and 8%, which consists mainly of the remains of marine organisms, and therefore is, in general, higher in the mottled facies.

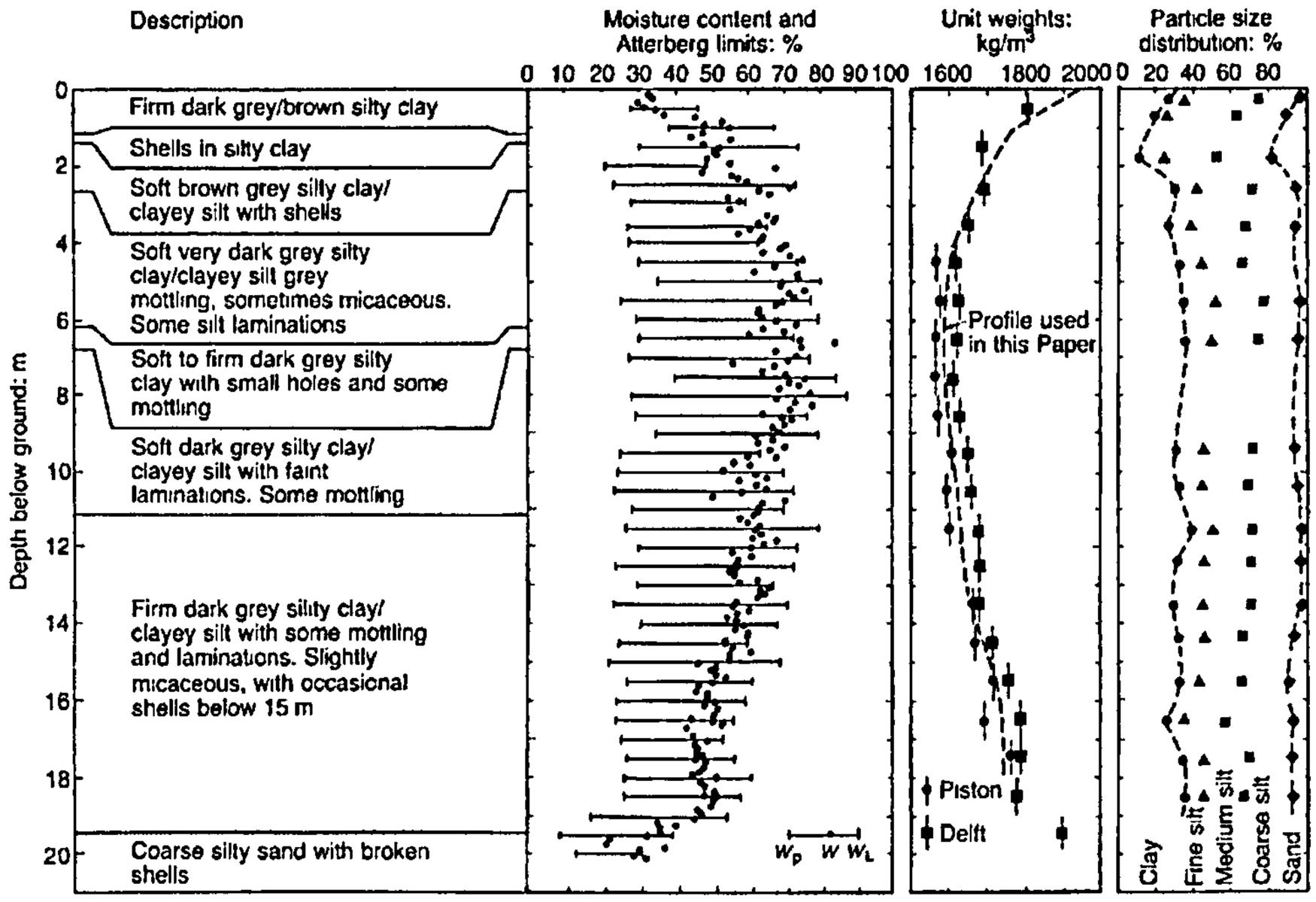

Figure 8.5: Ground profile at borehole D1 (after Nash et al., 1992a); soil description; moisture content and Atterberg limits determined on natural samples; unit bulk weight; particle size distribution.

b) Plasticity

The results of Atterberg limits on natural untreated material lead to the Carse clay to be classified as a high plasticity clay, with an average plasticity index (PI) of 40%. After removal of the organic material the PI reduces to an average value of 18% that corresponds to a clayey silt of intermediate plasticity, more consistent with the high angles of shearing resistance and turbulent shear observed in laboratory testing.

The activity of the clay after removal of the organic material lies in general between 0.5 and 0.75, consistent with the clay mineralogy of illite and kaolinite. The influence of the organic material in the determination of the Atterberg limits is discussed in detail in Paul et al. (1992).

c) Water content and bulk unit weight

The water content shows a well-defined trend with depth; the water content increases with depth up to 7 m, from about 35% at 1 m to approximately 80 % at 7 m. Below this the water content decreases with depth, reaching about 45% just above the Bothkennar Gravel.

d) Grading

In terms of particle size distribution the overall mean grain size is found to increase from bottom to top in the profile, and the clay sized fraction is, in global terms, between 35 to 50% of the material. Sediment from the bedded facies has an average size of 4-5 μm and a clay sized content of 35-40%. Sediment from the mottled facies is in general slightly finer, with an average particle size of 3 μm and a clay sized content of 40-50%. In the laminated facies the individual laminae are composed of well-sorted medium to coarse silt interbedded with mottled clayey silts. In the bottom 2 m of the Carse clay, above the Bothkennar gravel, the material is less well sorted but has a similar average size and clay content. The material above the shelly layer in the top 1.2 m of the ground profile is a rather different material formed of silt with some clay (clay fraction of 20-30%).

8.2.3.2 In-situ stresses

Piezometers placed in the clay and in the gravel indicate the piezometric profile at the Bothkennar site to be hydrostatic with the ground water level between 0.5 and 1.0m below ground level (BGL). The characterization area (and the area where the footings were constructed) is located away from the estuary and suffers minimal influence of the tides, with tidal fluctuations of only 0.01 m.

For the purposes of the analyses shown in this Chapter, the pore water pressures in the ground are calculated assuming a hydrostatic profile with the ground water level at 0.9 m BGL, in agreement with conditions encountered during summer when the loading tests took place.

The total vertical stress was estimated based on the variation of the bulk unit weight with depth shown in Figure 8.5. The horizontal effective stresses were estimated on the basis of self-boring pressumeter data, dilatometer test data and spade cells, and Figure 8.6 shows the resulting variation of the coefficient of earth pressures at rest, K_0 with depth, where K_0 is defined by Equation 8.1.

Equation 8.1 $$K_0 = \sigma'_{h0} / \sigma'_{v0}$$

where σ'_{h0} and σ'_{v0} are the in-situ horizontal and vertical effective stresses, respectively.

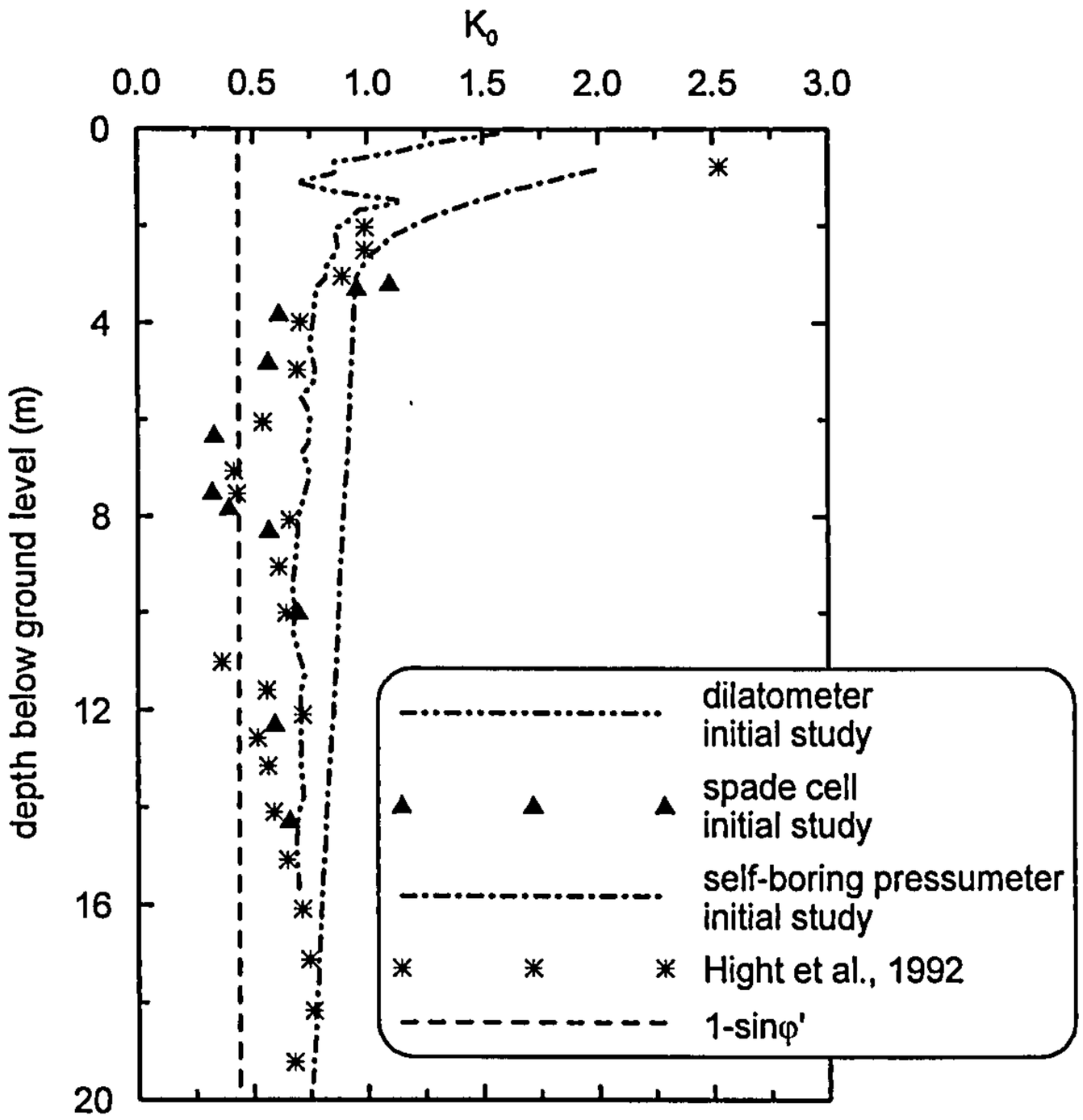

Figure 8.6: Variation of the coefficient of earth pressures at rest with depth.

Figure 8.6 also includes the value of coefficient of earth pressures at rest that is obtained by application of the expression proposed by Jaky (1944) (Equation 8.2) using an angle of shearing resistance equal to 34°.

Equation 8.2 $K_0=1-\sin\varphi'$

Note: φ' is the angle of shearing resistance at critical state.

8.2.3.3 One-dimensional compression

The one-dimensional behaviour of the intact Carse Clay was extensively investigated by means of oedometer tests of the following three types: i) conventional incremental load (IL) tests using 24 h loading stages and small load increments close the vertical yield stress; ii) continuous load tests at constant rate of strain (CRS) and iii) restricted flow tests (RF).

Figure 8.7 shows the one-dimensional compression curves from CRS tests at 0.005 mm/min on specimens from various depths. The samples from the crust, at 1.2 m, and the transition zone, at 2.3 m, show a different behaviour from the remaining samples, with an initial softer response and no well defined yield stress. The remaining

samples follow a consistent trend, with the compression curves moving to the right as the depth of the sample increases.

The stress – strain curves in one-dimensional compression are non-linear both pre and post large scale yield, and in both arithmetic and semi-logarithmic plots. Therefore it is not possible to describe the compressibility of the intact clay by means of a single value of either C_{ce} or λ, which are defined by Equations 8.3 and 8.4, respectively.

Equation 8.3
$$C_{ce} = \frac{\Delta e}{\Delta \log(\sigma_v')}$$

Equation 8.4
$$\lambda = \frac{\Delta e}{\Delta \ln(p')}$$

where e is the void ratio, σ_v' is the vertical effective stress and p' is the mean effective stress.

Equations 8.3 and 8.4 are defined in the normally consolidated (NC) range, during which the coefficient of earth pressures, K_0 is almost constant and so C_c and λ can be related approximately by Equation 8.5.

Equation 8.5
$$\lambda = \frac{C_c}{\ln 10}$$

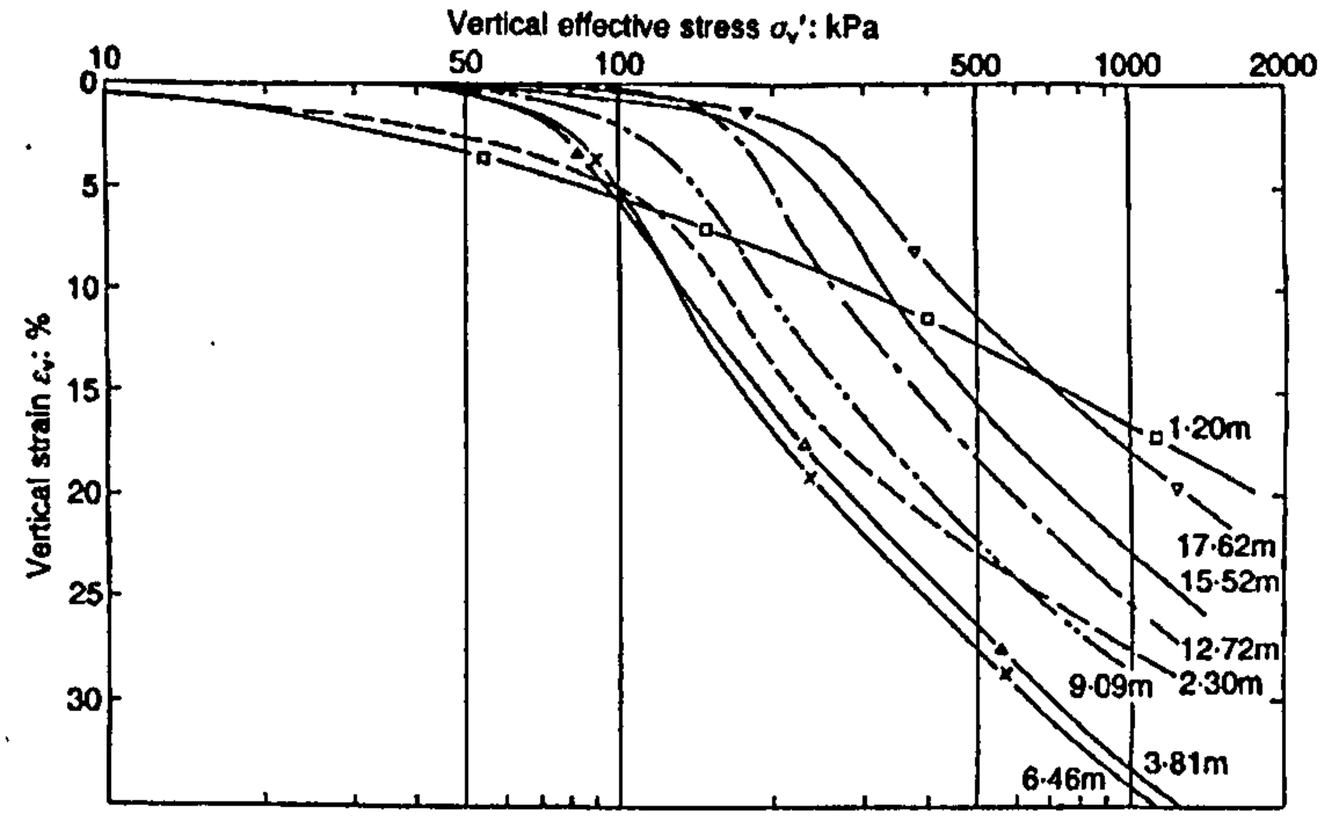

Notes: number next to the curve refers to the sample depth.

Figure 8.7: Variation in 1D compression behaviour of the intact Carse Clay with depth (CRD test at 0.005 mm/min on Laval samples), after Hight et al. (1992).

Figure 8.8 shows compression curves obtained from oedometer tests on natural and reconstituted samples. The natural state of the intact Carse clay lies, in general, well above the intrinsic compression line (ICL), indicating the existence of structure. The compressibility of the intact clay is highest immediately after large-scale yielding, decreasing progressively, until, depending on the specimen fabric, the 1-D compression line joins or remains parallel with the ICL.

Nash et al. (1992b) report average values of C_c between 1.2 and 0.8 on intact samples of Carse Clay and between 0.56 and 0.46 on reconstituted samples.

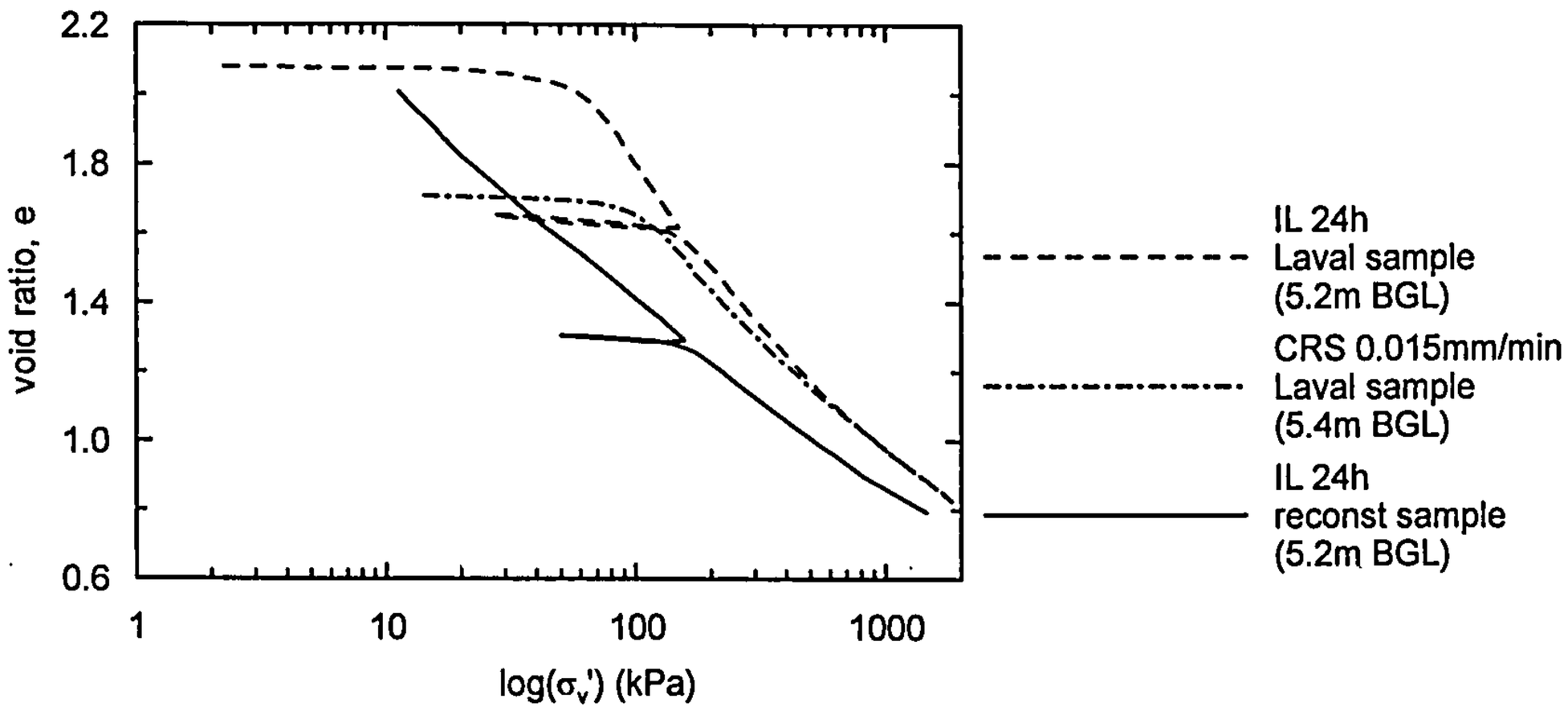

Figure 8.8: Oedometer tests on natural and reconstituted samples (Nash et al., 1992b).

a) Yield stress ratio

Figure 8.9 shows data on the variation of the yield stress ratio (YSR) with depth as determined from oedometer tests and the in-situ dilatometer test. Figure 8.9 also includes the YSR profile that would be generated by an overconsolidation of 15 kPa, a value that has been put forward as the maximum probable mechanical overconsolidation undergone by the Carse Clay over its geological history.

The oedometer tests on high quality samples indicate YSR values between 1.4 and 1.6 over the full depth of the clay (except the crust), which are significantly higher than any credible value of true overconsolidation, even considering extreme fluctuations in the ground water level.

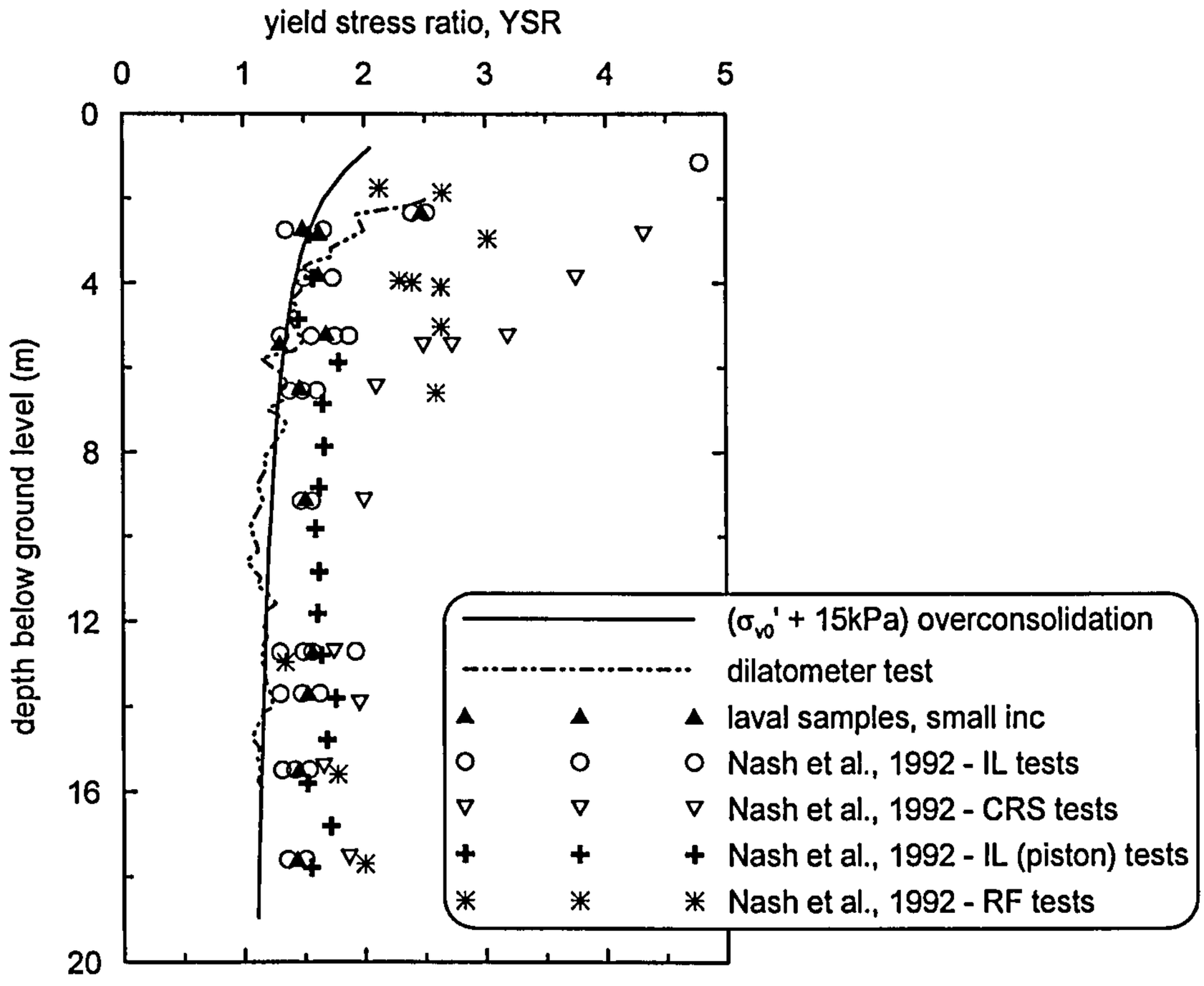

Notes: IL=incremental load tests with 24 hours loading stages; CRS= constant rate of strain tests; RF= restricted flow test;
When omitted tests were carried out on Laval samples.

Figure 8.9: Variation of the yield stress ratio with depth at the Bothkennar site.

b) Effect of strain rate

The effect of strain rate was studied by means of constant rate of displacement oedometer tests at two depths, with displacement rates varying between 0.00015 and 0.015 mm/min, which correspond to strain rates between $1x10^{-7}$ and $1x10^{-5}$/s (Nash et al., 1992b). The authors report an increase in the YSR with increasing strain rate, similar to that described by Leroueil et al. (1983) for the Champlain clays, as shown in Figure 8.10. Figure 8.10 also includes the YSR obtained from IL tests, in which case the corresponding strain rate is that occurring at the end of the relevant load increment. Nash et al. (1992b) report typical axial strain rates at the end of the load increments (in IL tests) between $5x10^{-8}$ and $1x10^{-7}$/s.

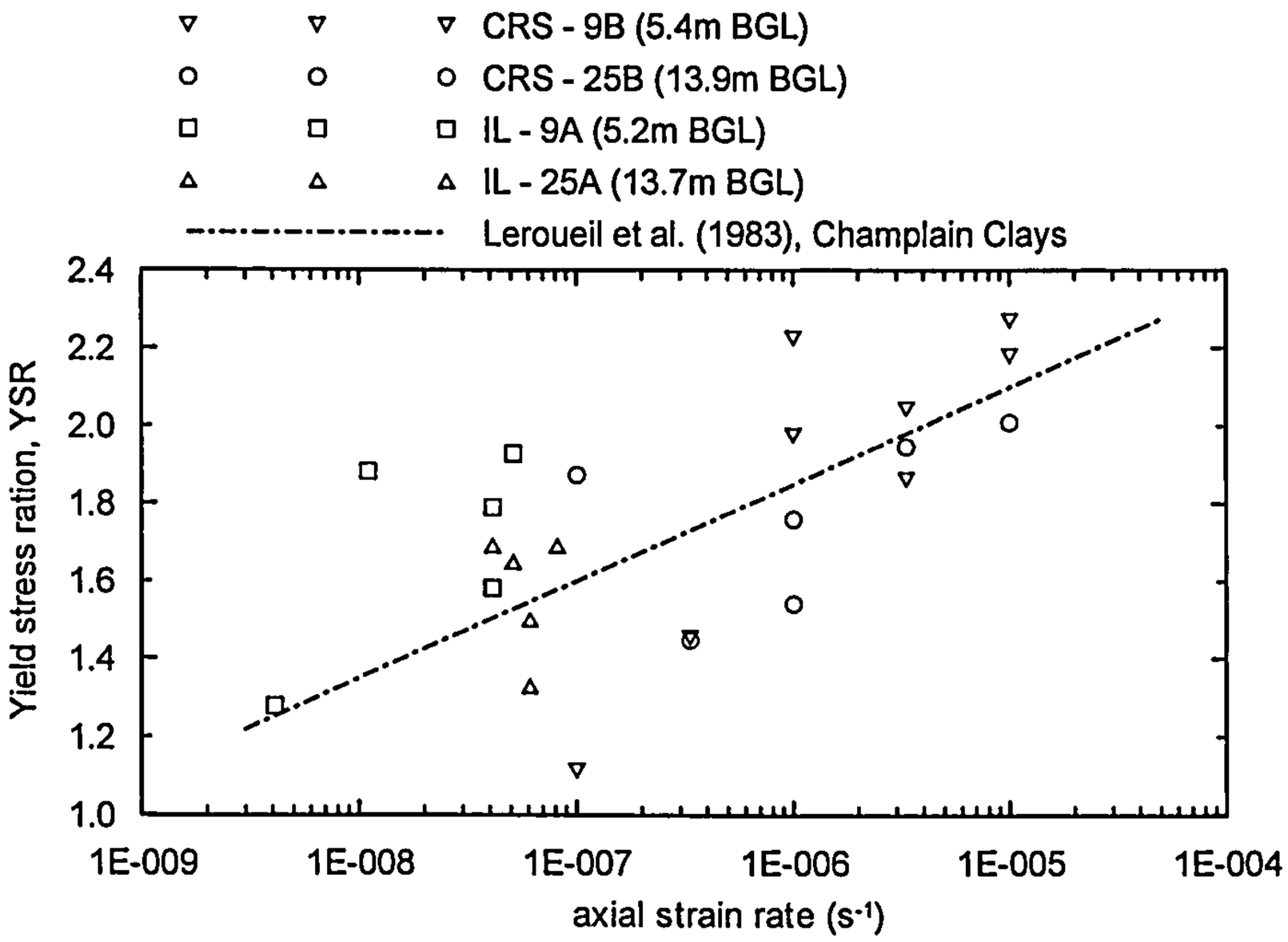

Figure 8.10: Variation of the yield stress ratio with axial strain rate in oedometer tests.

c) Creep behaviour

Nash et al. (1992b) have determined the value of the coefficient of secondary consolidation, C_α at the end of each load increment from IL oedometer tests on natural samples, where C_α is defined by Equation 8.6. The authors found that there is a linkage between creep and the structural breakdown at large scale yield, with the value of the ratio of the coefficient of primary consolidation C_c and the coefficient of secondary consolidation, C_α remaining fairly constant at about 0.03-0.05, over the whole stress range examined.

Equation 8.6

$$C_\alpha = \frac{\Delta e}{\Delta \log(t)}$$

8.2.3.4 Undrained strength

Figure 8.11 shows profiles of undrained strength estimated on the basis of in-situ vane tests and laboratory test data. The vane test data in Figure 8.11b) emphasize the soil brittleness, with the soil showing a very significant strength loss from peak to the remoulded state.

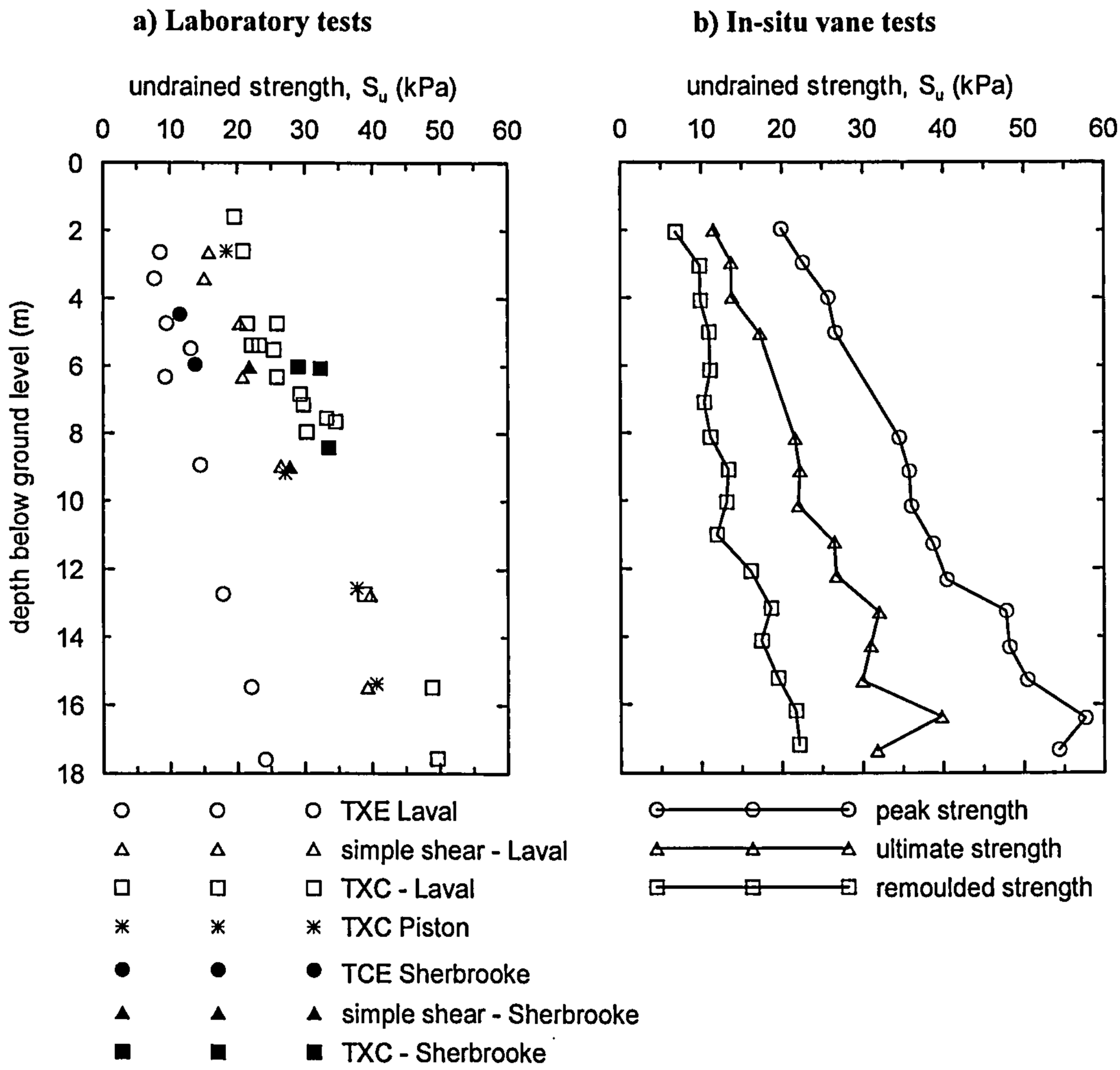

Figure 8.11: Undrained strength profile with depth at Bothkennar site based on laboratory tests and in-situ data.

The data included in Figure 8.11 a) correspond to values of undrained strength at peak obtained on samples that were previously consolidated to the estimated in-situ stress state. The data shows the influence of the intermediate principal stress on the measured undrained strength, with the ratio of the peak undrained strength in compression and in extension being well in excess of 2. Direct shear tests give undrained strength values somewhere in between those obtained in triaxial compression and extension.

For a given mode of shearing, say triaxial compression, there is a wide range of measured undrained strength values. This scatter is the result of differences in the level of structure in the sample, determined by the disturbance undergone during sampling, transport and specimen preparation, the reconsolidation stress path and the rate of shear (Smith, 1992).

8.2.3.5 Effective stress strength parameters

Allman & Atkinson (1992) report critical state angles of shearing resistance of 34° in compression and 37° in extension, based on triaxial tests on reconstituted samples. These values form the lower bound to the data at large strains for the intact material.

Smith (1992) found that for undrained triaxial compression tests on intact material the mobilized angle of shearing resistance at axial strains between 15-20% varied between 36° and 45°, being especially high in specimens from the bedded and laminated facies. In triaxial extension, the effect of necking prevents the sample from being taken to very large strains.

The peak strength values obtained in laboratory tests are strongly dependent on the level of previous disturbance undergone by the sample. The envelope to peak strengths in triaxial compression, based on high quality samples from different depths, can be approximated to c'=4 kPa and φ'=37°. In triaxial extension, the peak strength envelope corresponds to a shear angle between 42° and 60° for a c'=0. The very high angles of shearing resistance both at peak and critical state are thought to result from the high angular silt content and low clay particles content, that is corroborated by the turbulent mode of shearing.

The lowest value of φ' equal to 27° is obtained in shear box tests in which the failure is forced along the horizontal plane that on natural samples coincides with the preferred direction of the clay particles.

8.2.3.6 Small strain stiffness

a) Undrained stiffness characteristics

Figure 8.12 shows the variation of Young's Modulus with shear strain during consolidated undrained triaxial compression and extension tests on samples from 5.3 to 6.2 m depth. The data demonstrates the strong soil non-linearity prior to large scale yielding and that the small strain stiffness is influenced by:

a) The reconsolidation path: all the samples, with exception of LCU2, have been consolidated to the in-situ stresses with a small load-unloading loop to simulate the recent stress history of the sediment. The reproduction of the sediments

recent stress history prior to shearing seems to be able to erase the effects of disturbance during sampling and specimen preparation, and Sherbrooke and Laval samples are found to yield similar stiffness;

b) The shearing mode: the Carse clay is found to be stiffer in triaxial compression than extension, but the stiffness decays more quickly in triaxial compression.

c) The shearing rate: an increase in the strain rate is found to move the stiffness curves upwards, even if only by a small amount.

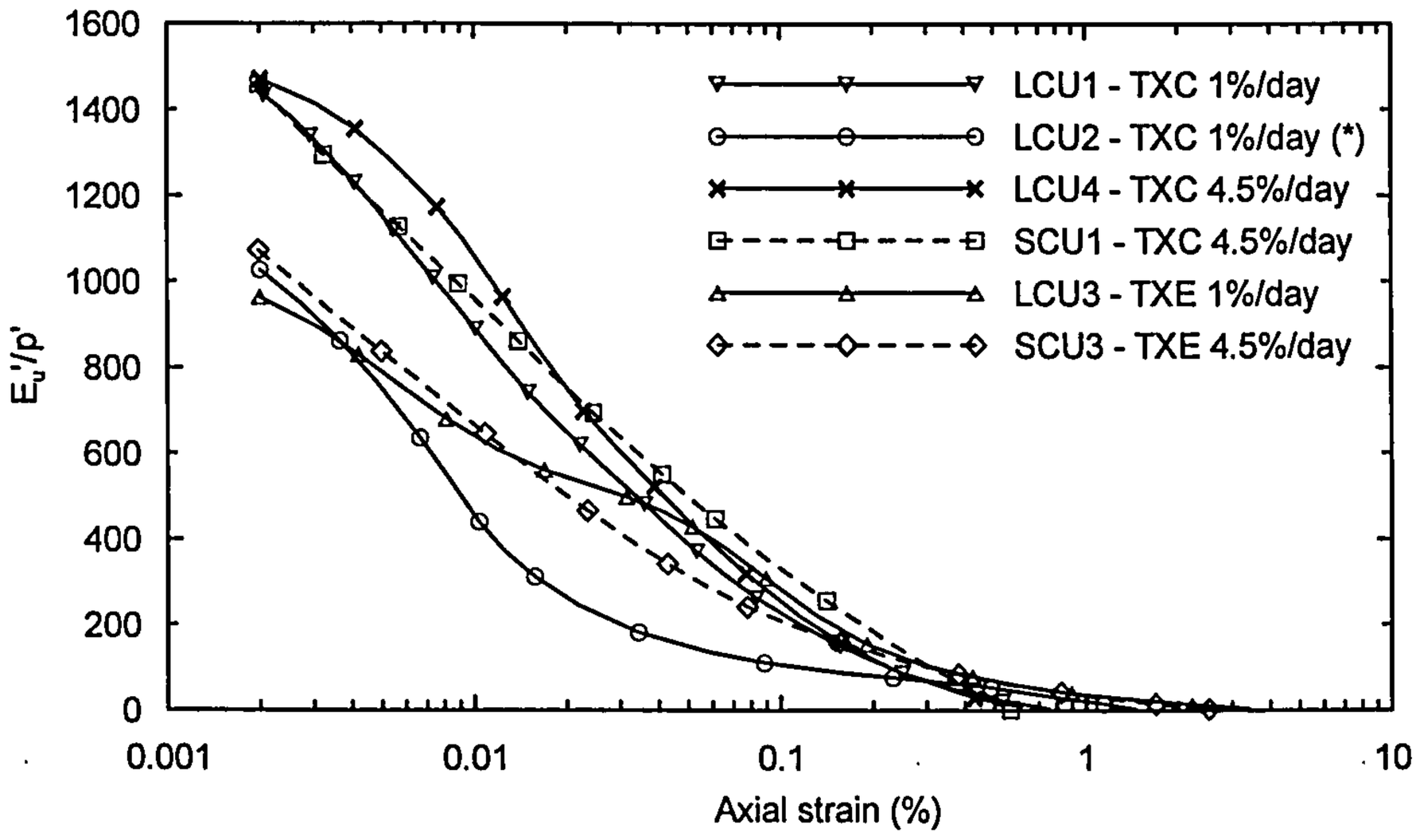

Notes: L= Laval sample; S = Sherbrooke sample; %/day refers to the applied axial strain rate during shearing. For Laval samples pi'=33.3 kPa and Sherbrooke samples pi'=36 kPa.
(*) Sample consolidated directly to in-situ stresses without swelling loop.

Figure 8.12: Variation of the normalized tangent Young's modulus with shear strain from undrained compression and extension tests (Smith et al., 1992).

Smith (1992), based on tests on samples consolidated to stresses close to or beyond the yield stress, show that there is a progressive reduction in stiffness with increasing straining and/or amount of destructuration undergone prior to shearing.

Rolo (2003) reports measurements of elastic shear stiffness at the in-situ stresses (which are reached using a load-swelling loop) on high quality samples of Carse clay from 5.9 to 6.2 m depth, obtained using bender elements. Rolo (2003) reports values of shear stiffness between 14.6 and 16.8 MPa depending on the direction considered, the higher stiffness values being found in the horizontal plane. These values correspond to a normalized shear stiffness G/p' between 409 and 470 or normalized Young's Modulus,

E_u/p' between 1230 and 1410, in good agreement with the data shown in Figure 8.12. The relationship between the shear stiffness and the Young's Modulus during undrained shearing is given by Equation 8.7.

Equation 8.7

$$G_u = G' = \frac{E'}{2 \cdot (1 + \mu')} = \frac{E_u}{2 \cdot (1 + \mu_u)} = \frac{E_u}{3}$$

Rolo (2003) found that these values agreed quite well with the shear stiffness calculated from the initial pseudo linear region of the stress – strain curves from both drained and undrained consolidated triaxial tests.

A pressumeter test gave information on the variation of the secant shear stiffness, G_p with depth. It was concluded that the values of stiffness derived from the pressumeter correspond to values of stiffness at 0.1% shear strain obtained on consolidated undrained triaxial tests. The data suggest that the shear stiffness increases proportionally with the mean effective stress, and thus varies roughly linearly with depth.

b) Drained stiffness characteristics

Smith (1992) performed a series of triaxial tests in which the samples were previously consolidated to the in-situ stress state following a load-unload cycle to retrace the soil's light overconsolidation, and then subjected to continuous drained probing tests, starting from the in-situ stress state, at different angles θ in the *p' – q plane*, θ being defined as $\theta = \tan^{-1} (\Delta q/\Delta p')$. Figure 8.13 shows the variation of the normalized shear and bulk stiffness during the drained probing tests.

The data demonstrates once again the strong non-linearity of the Carse clay prior to large scale yielding and the influence of the recent stress history and the stress path direction on the measured stiffness characteristics.

The normalized bulk modulus shows a wide scatter with the largest values of bulk stiffness occurring along paths where the deviatoric stress is constant (θ=0° or 180°) and smallest when changes in deviatoric stress dominate (θ= 70° or 110°). Regarding the shear stiffness data, the trends are not so well defined.

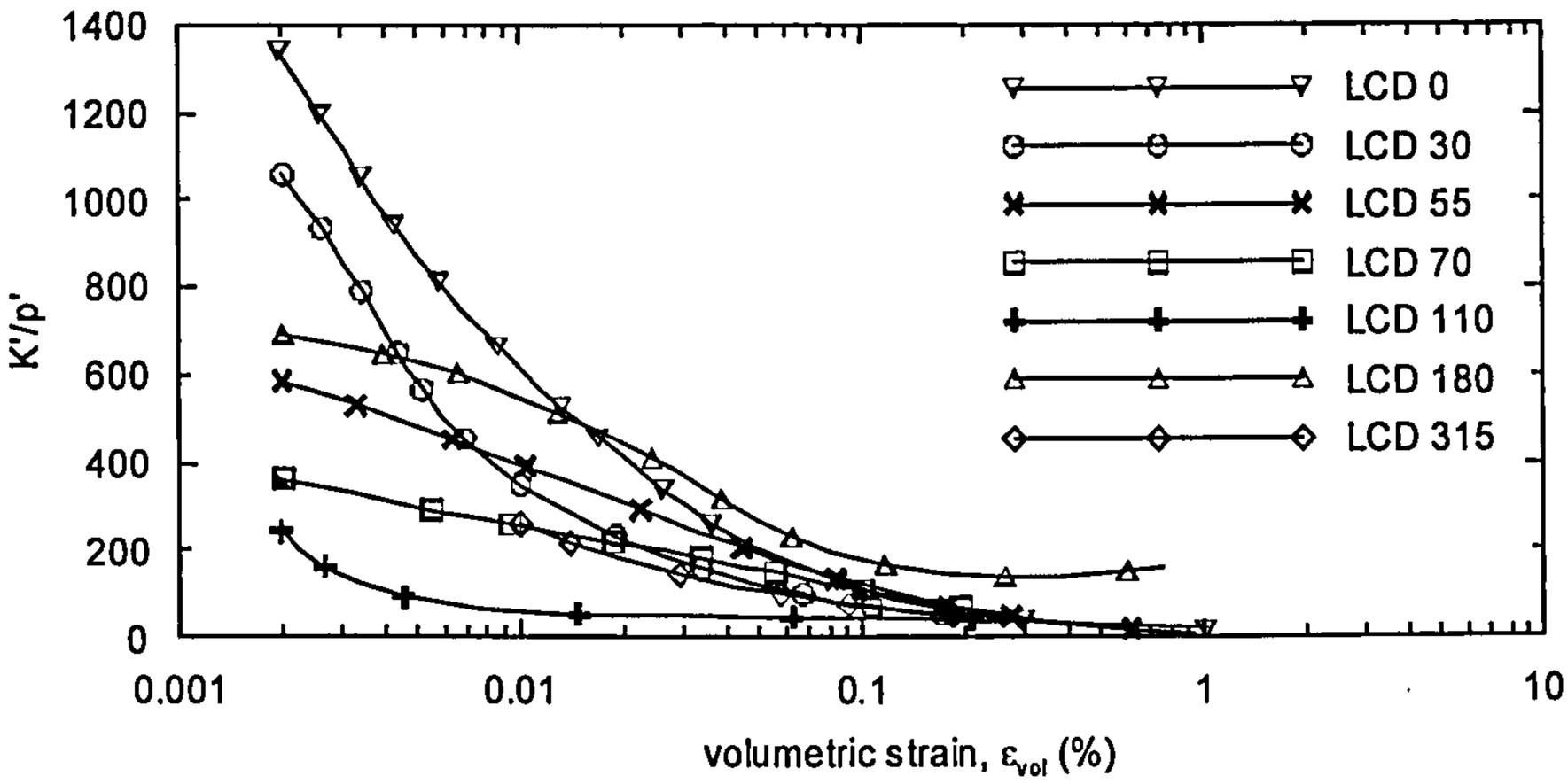

Notes: L=Laval sample; C=consolidated; D=drained; the identification number of each test corresponds to the value of the angle θ, θ being defined as $\theta = \tan^{-1}(\Delta q/\Delta p')$.

Figure 8.13: Variation of the tangent normalized shear and bulk stiffness during drained probing tests (Smith, 1992).

Rolo (2003) also gives evidence of the dependency of the elastic bulk stiffness on the adopted stress path and reports values of bulk modulus of about 23 MPa under axial straining and 15 MPa under radial straining, which correspond to values of K'/p' of about 644 and 420, respectively. Rolo (2003) derived values of Poisson's ratio between 0.22 and 0.29 with an average value of 0.26.

8.2.3.7 Soil structure

The behaviour of a natural clay is in general different from that of the same soil after it has been reconstituted because both the depositional conditions and the post-depositional processes to which both soils have been subjected are different, leading to

differences in fabric and inter-particle bonding. The term structure has been adopted in the literature to refer to the additional components of strength and stiffness of the natural soil, in relation to the reconstituted one, which cannot be accounted for by void ratio and stress history alone (Burland, 1990; Leroueil & Vaughan, 1990). The degree of structure in a natural clay can be evaluated in terms of:

a) State, by comparing the void ratio of the natural clay and reconstituted material at the same stress state (e.g. Figure 8.8);

b) Strength, by comparing the strength of intact and remoulded soil (e.g. Figure 8.11);

c) Yield stress, by comparing the apparent overconsolidation ratio or the YSR with that caused by mechanical overconsolidation (e.g. Figure 8.9).

Smith et al. (1992) have investigated the effect of destructuration on the stress – strain response of Carse clay under triaxial conditions, by testing samples that were previously consolidated to stresses close to or above the yield stress. The structural components of resistance in the Carse Clay reduce progressively with the development of volumetric and/or shear strains and destructuration causes the behaviour of the soil to shift towards that of the reconstituted material.

Clayton et al. (1992) and Smith et al. (1992) have concluded that sample disturbance during sampling was least when using the Sherbrooke sampler, followed by the Laval sampler, and in both cases samples were able to reveal the existence of structure. The Piston sampler recovered the lowest quality samples, which were not suitable for reliable measurements of the yield stress or peak strength.

In general terms the combined effect of disturbance during sampling, specimen preparation and reconsolidation was to reduce the mean effective stress in the specimen, to shrink the initial bounding surface and therefore reduce the yield stress and peak undrained strength. In terms of compressibility, the effect of sample disturbance was to increase pre large-scale yield compressibility and decrease compressibility post-yield.

The susceptibility of the Carse clay to destructuration due to sample disturbance may have increased the scatter in the laboratory testing data, especially in the peak strength and yield stress data. The other consequence of sample disturbance was to accentuate

eventual differences between the behaviour of different fabric types, as different fabrics are affected differently during sampling.

8.2.3.8 Permeability

Figure 8.14 shows the variation of the vertical and horizontal permeabilities at the in-situ void ratio with depth, based on laboratory and in-situ tests. The vertical permeability data from different laboratories and test types show very good agreement. The variation of vertical permeability, k_{v0} with depth follows the trend observed in the water content (Figure 8.5), with permeability increasing up to 7 m depth, from $1x10^{-9}$ m/s at 1 m to about $2x10^{-9}$ m/s at about 7 m. Below 7 m depth, the vertical permeability decreases with depth, reaching the value of $5x10^{-10}$ m/s at 15 m.

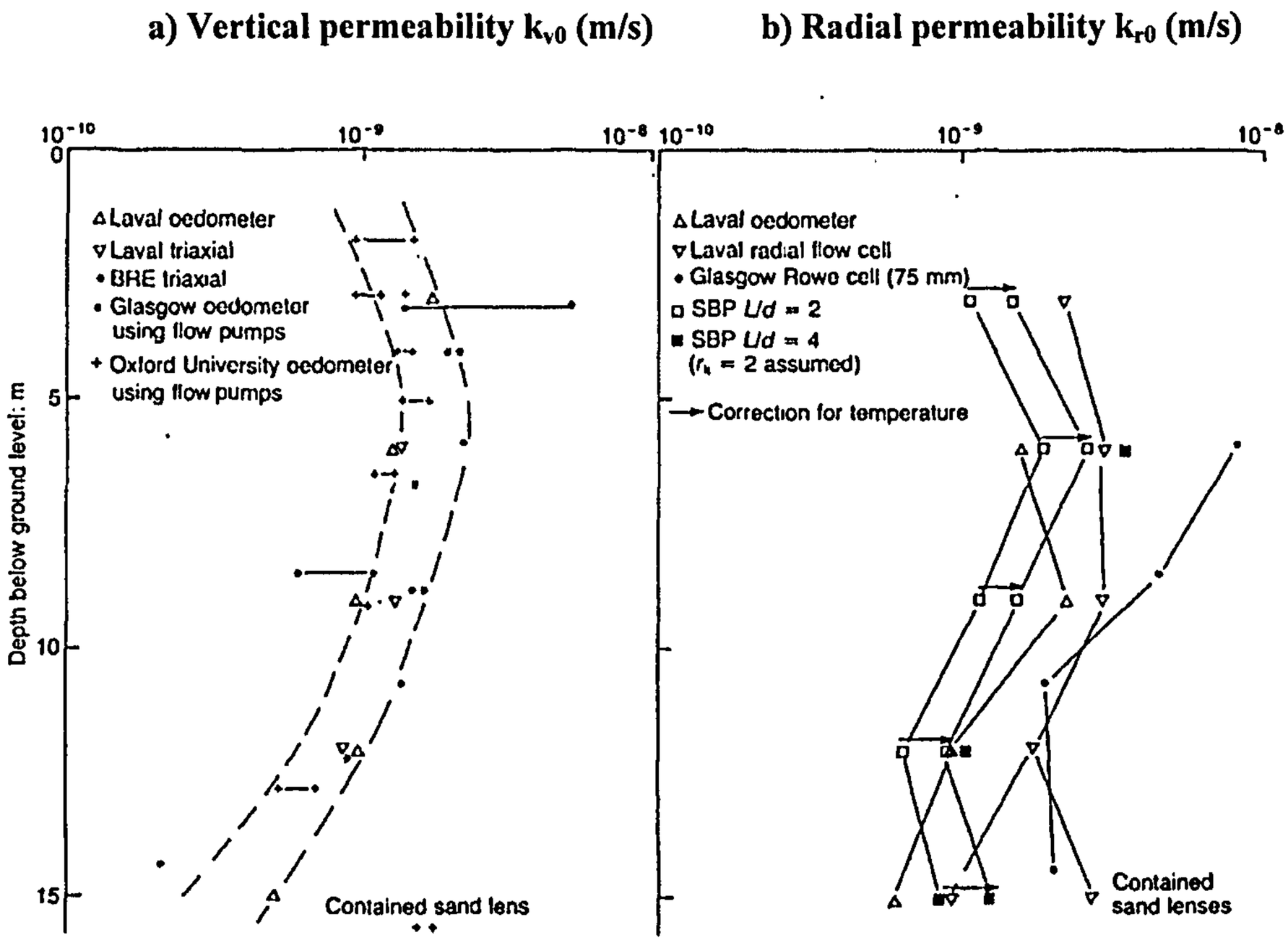

Figure 8.14: Profiles of vertical and horizontal permeability at the in-situ void ratio, (after Hight et al., 1992).

The horizontal permeability has been estimated based on laboratory and in-situ tests. Leroueil et al. (1992) showed that of the in-situ measurements those derived from the self-boring pressumeter are the most representative, as they are not so affected by smearing and reconsolidation as pushed in place devices. The in-situ measurements included in Figure 8.14 have been multiplied by a factor of 1.5 to allow for the higher

temperature (and consequently lower viscosity of the pore water) in the laboratory tests. The range of horizontal permeability values that are obtained at a certain depth depends on the size of the specimen size in relation to the soil fabric, and a detailed analysis of the permeability data can be found in Leroueil et al. (1992).

Values of the anisotropy ratio, $r_k = k_{h0}/k_{v0}$ have been calculated from the data shown in Figure 8.14, and the values of r_k are found to vary between 1.1 and 1.6 in the top 12 m.

Leroueil et al. (1992) and Little et al. (1992) have shown that under compression the variation of permeability, either in the vertical or horizontal direction, follows approximately a logarithmic law with void ratio, up to 25% vertical strains. The value of the permeability change index, $C_k = \Delta e/\Delta \log (k)$ was found to be approximately 0.5 times the initial void ratio, e_0, as previously found for other natural clays.

8.3 Description of the load tests

In June 1990, two reinforced concrete footings were constructed at the Bothkennar site, in order to investigate both the small and the large stress - strain behaviour of soft clay foundations under loading.

Footing A was loaded to failure over a period of 4 days, while footing B was loaded to about two thirds of the failure load of footing A, monitored over a period of over 11 years, and only then loaded to failure (denominated herein Test C).

8.3.1 Footing geometry

The footings were located in the south – west corner of the Bothkennar research site, shown in Figure 8.2 as *BRE test area*. Footing A was approximately 2.2 m x 2.2 m square and footing B 2.4 m x 2.4 m square, giving equivalent diameters of 2.48 m and 2.71 m, respectively. The footings were about 0.8 m thick, with the base at 0.8 m BGL. Based on a schematic drawing from Gildea (1990) the footings are just over 8 m apart centre to centre, about 6 m edge to edge. No further data was found in the literature regarding the spacing between the two footings

When casting the footings, a 0.6 m square hole was left in the centre of the footings in order to accommodate the instrumentation that was to be installed subsequently (Figure 8.15).

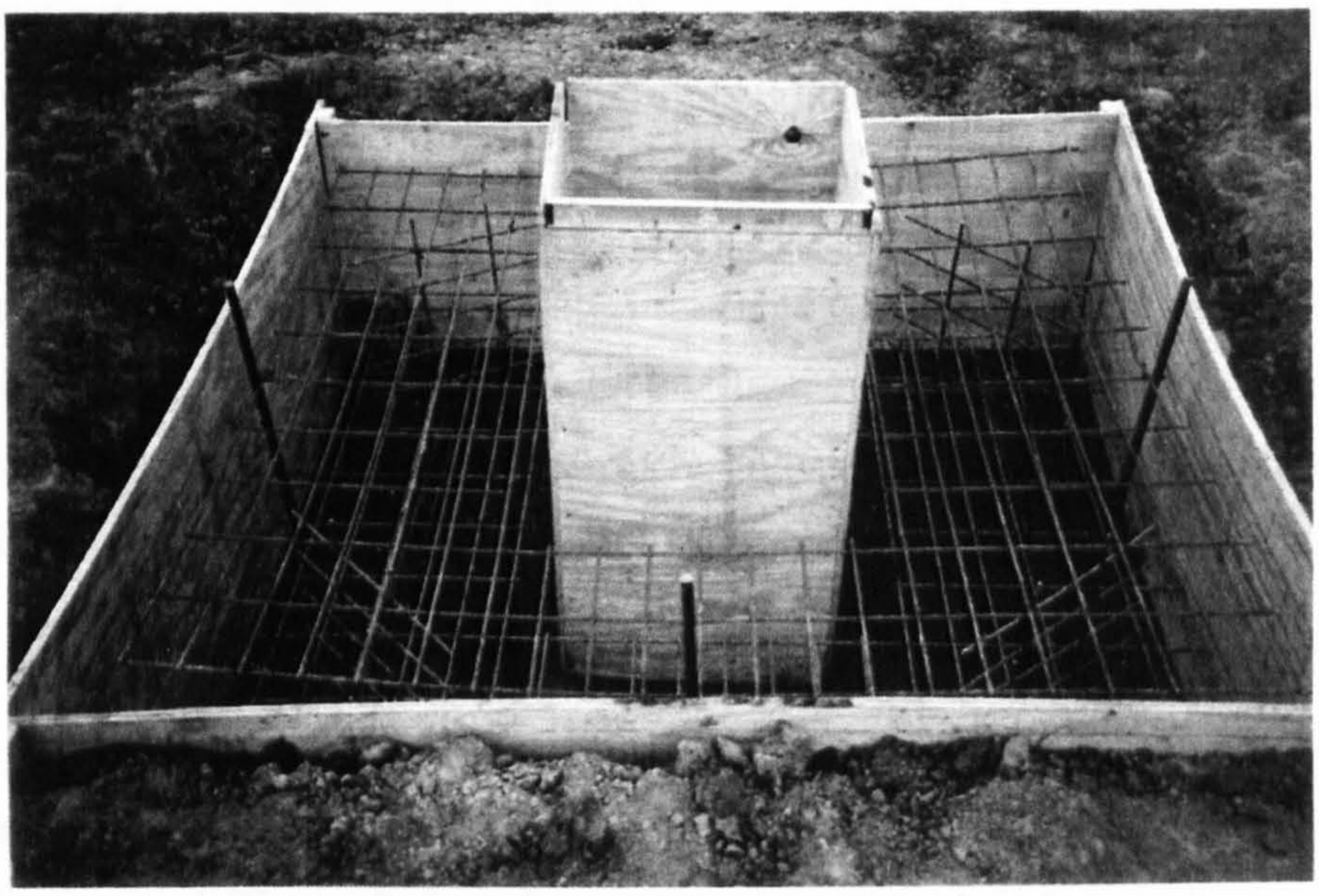

Figure 8.15: Construction of the test footings (after Gildea, 1990).

Footing A was loaded to failure in July 1990, about 40 days after the pouring of the concrete, which was considered sufficient for the concrete to cure fully. The loading of footing B started one month later.

8.3.2 Monitoring equipment

The instrumentation adopted for footings A and B is shown in Figure 8.16. The loading tests of footings A and B aimed to give complementary and partially overlapping sets of information, and the monitoring plan for the footings has been designed accordingly. Test A intended to give data on the short-term behaviour up to failure, and also involved a more detailed survey of the surrounding ground surface movements. Test B was designed to provide higher resolution data on ground strains at low loads, subsurface radial movements and data on the behaviour under maintained load.

Most of the instrumentation was installed two and a half weeks after the footings were cast. Initially the central opening was cleaned out and levelled off. The boreholes required for the installation of individual devices were formed by hand augering, with a 250 mm or 100 mm diameter auger.

The pneumatic piezometers (9), spade cells (6, combined with pneumatic piezometer units), inclinometers (2) and magnetic extensometers (3) were manufactured by Soil Instruments and Geotechnical Instruments. All transducers and read-out systems were

recalibrated before use. The spade cell readings were corrected assuming that the initial radial stresses matched the sum of the undisturbed in-situ profile of horizontal effective stress, given by Hight et al. (1992) and pore water pressures.

The extensometer installed under footing A was read using a tape measuring system that gave a nominal accuracy of 1 mm. For footing B, the measuring system was improved using fixed indexed brass bars and verniers and the system was shown to have a repeatability of about 0.1 mm. In addition, the magnetic access tubes were levelled regularly to identify and measure any movement of the relatively shallow base.

Ground surface settlement targets were installed in a total of 26 positions; locating 8 targets on the concrete pads, one at each mid-side of the footings, and 18 more into the surrounding ground. The surface settlements were monitored with a precise level, with a nominal resolution of 0.1 mm. Finally a temporary benchmark was constructed close to the test area. Its position was considered to be sufficiently distant from the loading tests not to be affected by ground movements, but at the same time close enough so that regular checks could be performed.

To enable a comparison between tests A and B, the measurements are often identified by the current mobilized load factor $L_f = q_L/q_L^{max}$, where q_L^{max} is the ultimate bearing capacity proven in test A and q_L is the current bearing pressure.

In July 2001 during the loading of footing B to failure (herein Test C), only part of the instrumentation remained operational and the elevation of the operational spade cells (SC2, SC3, SC4) and pneumatic piezometers (PZ2) was corrected based on the extensometer data. Both the two inclinometers and the two extensometers were fully functional, but as a consequence of the agreed safety criteria the monitoring of the two inclinometers and the extensometer on the edge of the footing (EXT2) had to be abandoned once the applied load reached 175 kPa. The extensometer at the centre of the footing (EXT1) was monitored up to failure. Precise levelling of the footing settlement was done remotely using graduated scales clamped to each of the levelling targets embedded in the footing.

It is noted that if nothing is stated to the contrary the data regarding the field behaviour and the monitoring data during tests A and B is from Jardine et al. (1995) and the data concerning test C is taken from Lehane & Jardine (2003).

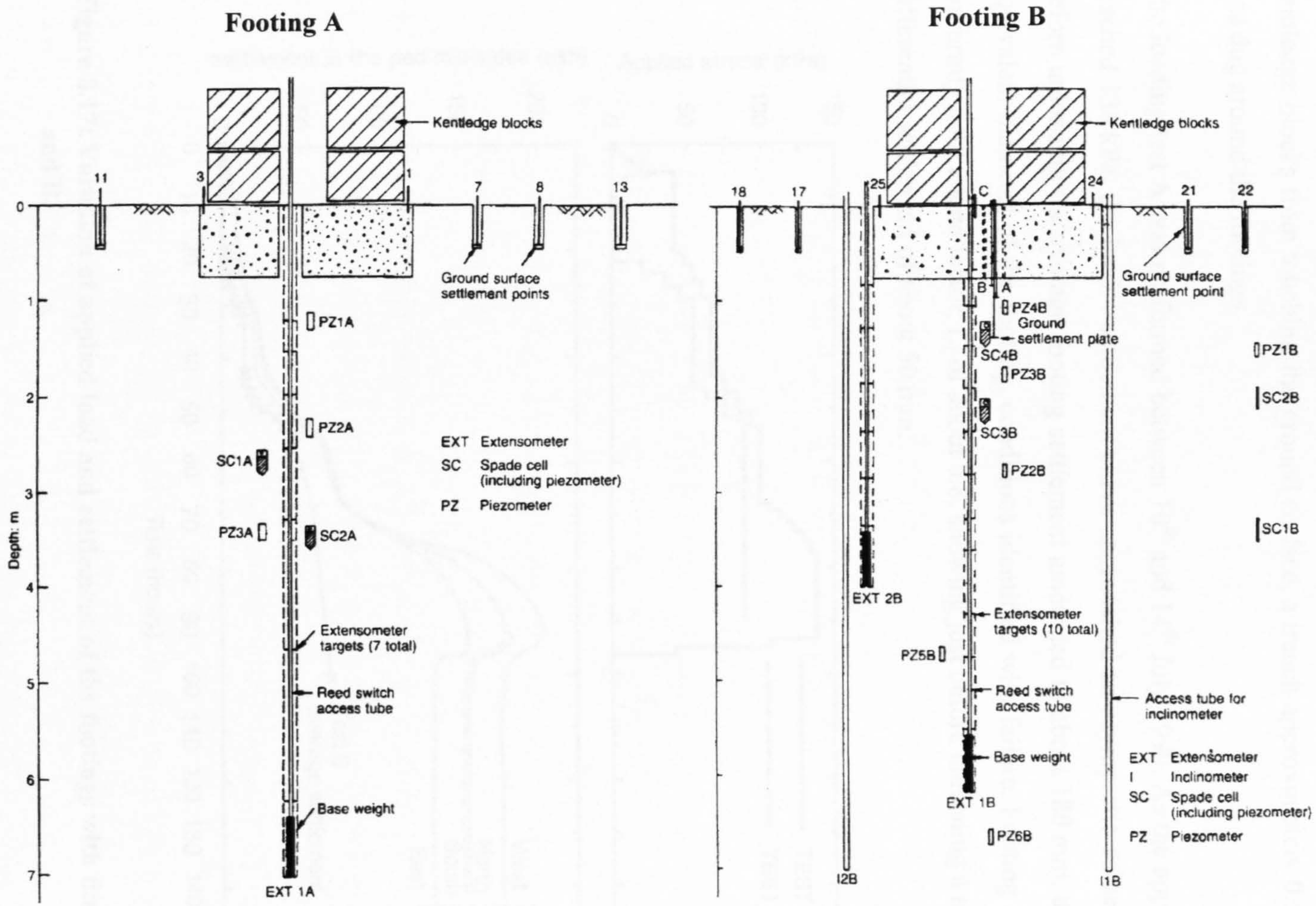

Figure 8.16: Instrumentation placed for footing A and B (after Jardine et al., 1995)

8.3.3 Loading sequence

Figure 8.17 shows the variation of applied load and footing settlement with time, during tests A and B. The kentledge consisted of concrete blocks and iron railway tracks packed into rectangular bundles, which were previously weighed and then placed by crane. It was agreed that placing of loading would cease overnight and whenever the settlement rate exceeded 8mm/h. Before the start of the testing, and to prevent the kentledge blocks from touching the ground surface, a trench approximately 0.5 m deep was dug around the footings.

The loading test A was performed between 10th and 14th July 1990. As the applied load reached 138 kPa, the load – settlement curve approached an asymptotic value and just before unloading the average footing settlement amounted to about 180 mm, 8% of the equivalent diameter of the footing, conditions identified with failure. Footing A settled uniformly until a load factor, L_f of about 0.8, showing just before unloading a maximum differential settlement of about 50 mm.

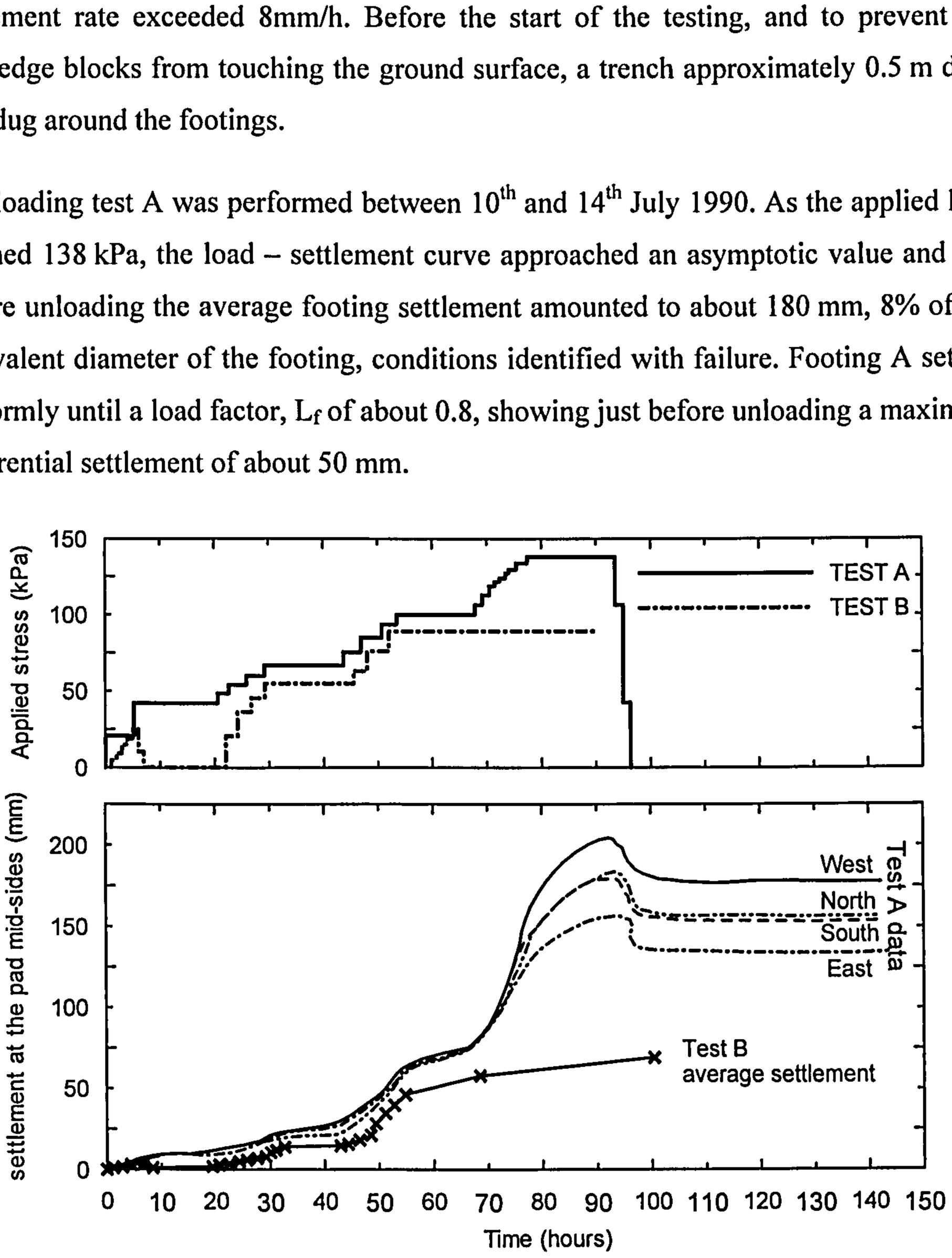

Figure 8.17: Variation of applied load and settlement of the footings with time, Test A and B.

Figure 8.18: Footing A at failure (after Gildea, 1990).

The footing was subsequently unloaded in two stages over a period of 3 hours with continuing monitoring over this period and for the following two days. The unloading of the footing caused minimal rebound suggesting that most of the settlement developed during loading resulted from plastic deformation. Figure 8.18 shows the footing A at failure, just before unloading.

The loading of footing B started one month later. At the start of the test, a small load – unloading cycle was performed to investigate the ground response at small strains. The loading of footing B was completed using the same criteria described above (not to exceed a settlement rate of 8 mm/h) up to 89 kPa, about 65% of the ultimate bearing capacity proven in footing A.

From quite an early stage, corresponding to a load factor of about 0.35, footing B showed a noticeable tilting and the footing rotated up to 0.6° as loading continued, even though some of the remaining weights were placed eccentrically to counteract the tilt. Later piezocone tests were not able to identify any local variation in the ground conditions that could explain the development of tilt from so early on. Regarding the magnitude of the tilt during test B the only information is the account given by Jardine et al. (1995), as there is no information on the individual measurements of settlements at the mid-sides of the footing.

Figure 8.19 shows the load–displacement curves for tests A and B. Despite the different pattern of tilting the agreement between the two tests in terms of bearing pressure – settlement response is very good, for the complete loading range of test B. Note that footing A did not tilt significantly up to a load factor of 0.8, that is about 110 kPa, and so the value of mean and maximum settlement are almost identical up to that load.

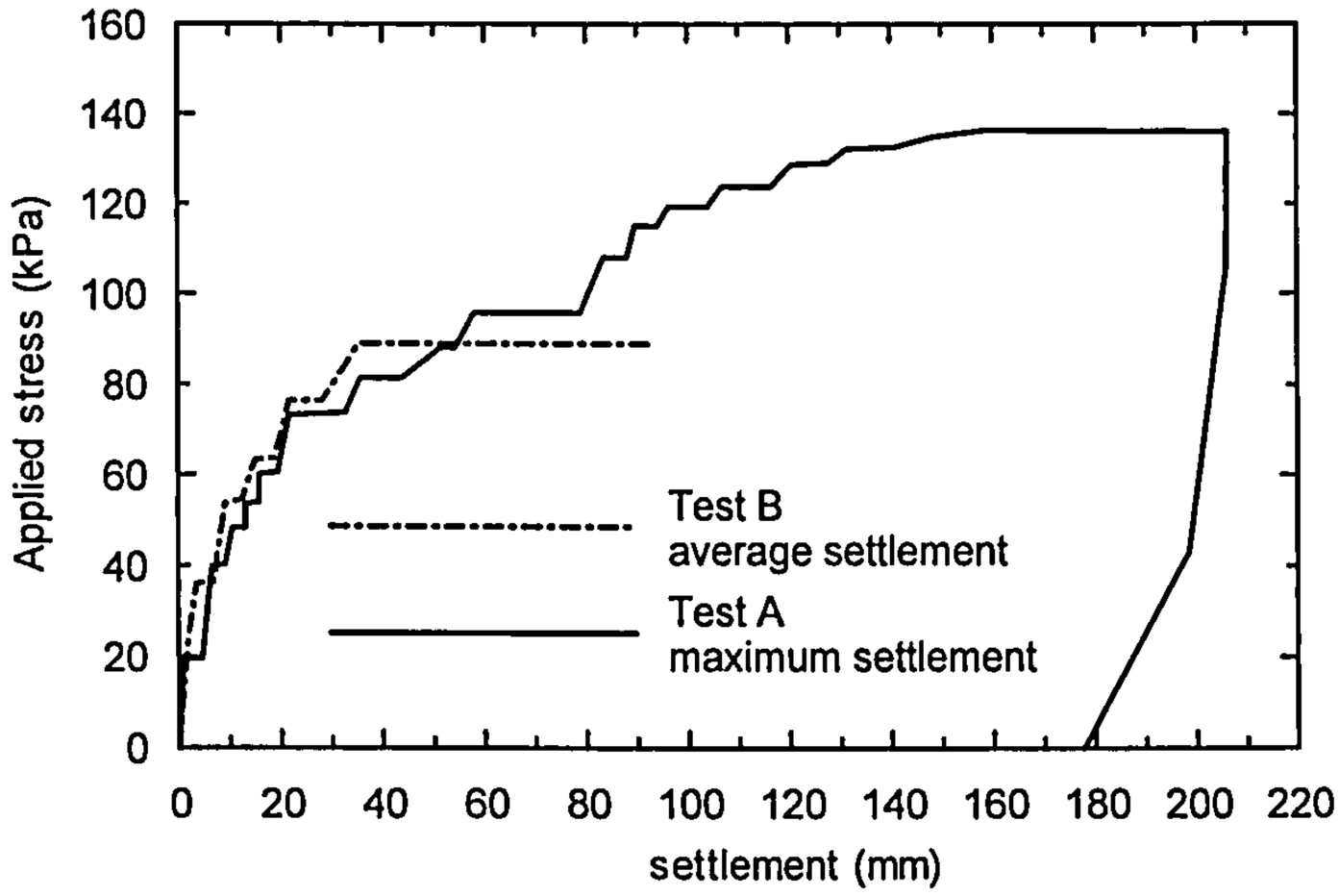

Figure 8.19: Load – displacement curves for tests A and B.

In 2001, due to the imminent closure of the Bothkennar research site it was decided to load and take to failure footing B, and in this way obtain information on the foundation stiffness and strength after such a period of preload. This experiment is herein referred to as test C. Footing B was under a constant bearing pressure of 89 kPa for more than 11 years, developing a total settlement of 230 mm by July 2001. Figure 8.20 shows the development of the footing settlement with time during the period July 1990 to July 2001.

At the start of Test C, the footing was unloaded from 89 kPa to 60 kPa to remove some less regularly shaped weights and prepare a stable loading surface. The loading of the footing was done using steel kentledge following similar loading rates to those applied in tests A and B.

Figure 8.21 shows the variation of applied load and footing settlement with time during test C. Figure 8.21 indicates that the footing started to tilt from an applied load of about 150 kPa, and that this tilt became progressively more noticeable as loading continued up to 205 kPa, even though some kentledge blocks were placed eccentrically to counteract

it. Just before unloading, the maximum differential settlement and the mean settlement of the footing both amounted to about 220 mm, about 9.2% of the equivalent footing diameter.

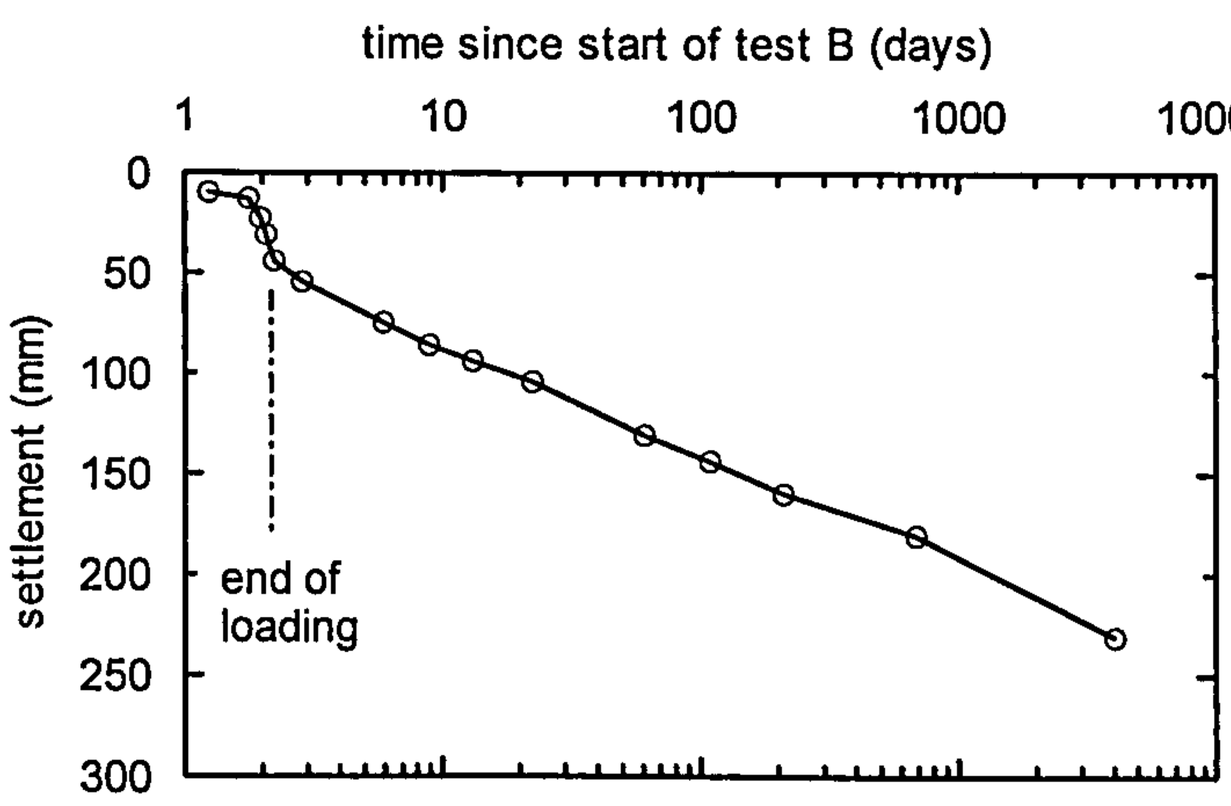

Figure 8.20: Long term settlement of footing B (July 1990 to July 2001).

Continuing to add load would have aggravated the tilting of the footing and eventually put in danger the safety of the test, and so the test was terminated at this point. Lehane & Jardine (2003) note that the settlement rate reduced quickly during the last night break and suggest that the footing was still relatively stable and could possibly sustain further load.

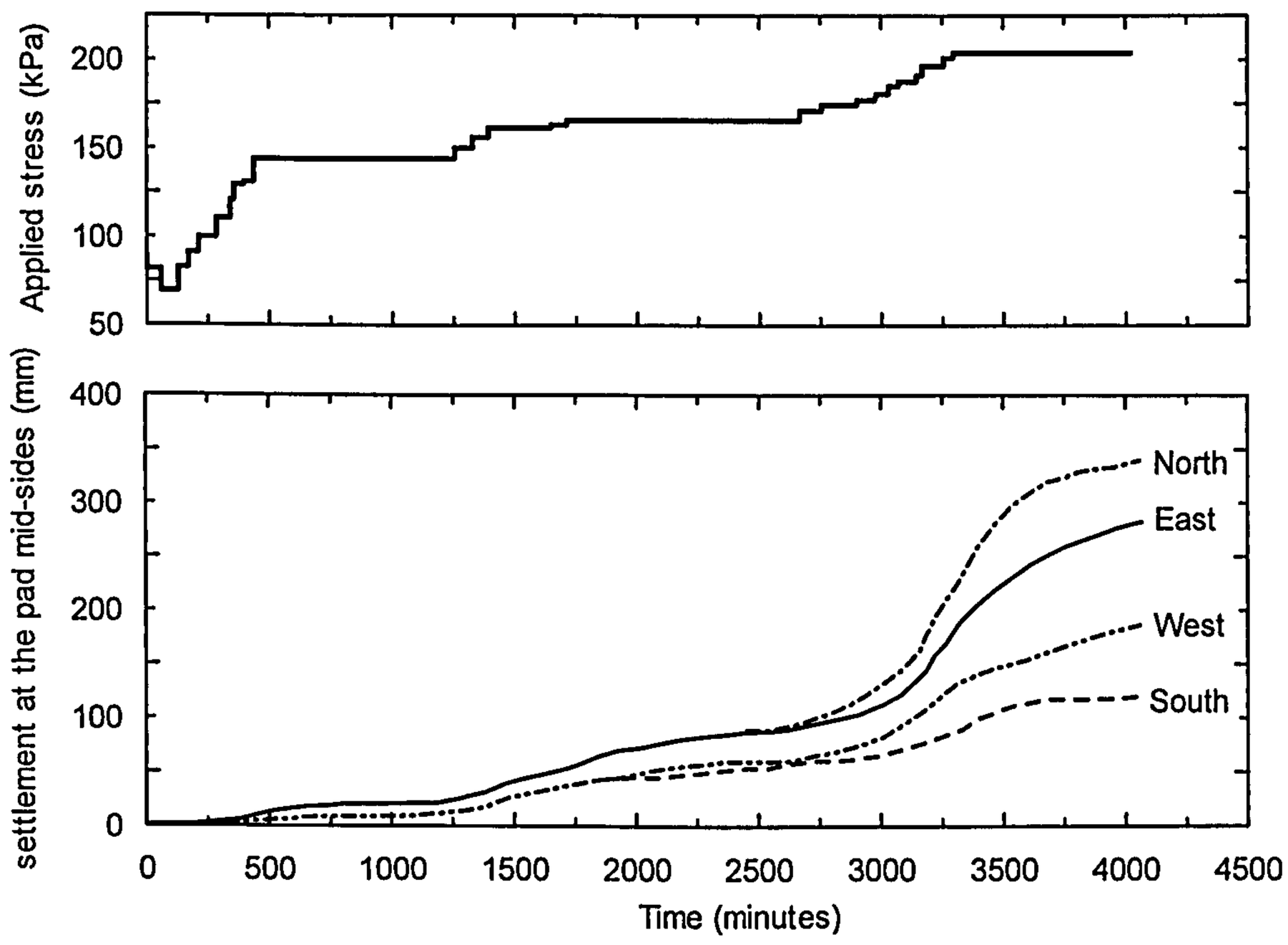

Figure 8.21: Variation of applied load and footing settlement with time, Test C.

8.4 Finite element analysis

8.4.1 Problem geometry and boundary conditions

The footings were analysed by means of axi-symmetric finite element analyses, considering circular footings of equivalent diameter, D*. Potts and Zdravkovic (2001) show that the bearing capacity of a circular footing is just 2.3% higher than that of a square footing with the same area, and the numerical calculations are considerably simplified by using an axi-symmetric analysis instead of a full three dimensional analysis.

Figure 8.22 illustrates the finite element mesh used in the analysis of footing A, which consists of 843 eight-noded solid elements, with a total of 2642 nodes. Due to symmetry considerations only half of the problem needs to be analysed and the left hand boundary constitutes the symmetry axis. The finite element mesh employed in the analyses of footing B is identical to that shown in Figure 8.22, except that the footing diameter has been changed from 2.48 m to 2.71 m. The dimensions of the mesh were defined based on previous experience such that they would not influence the analyses results.

Figure 8.22 shows schematically the displacement and the pore pressure boundary conditions specified along the mesh boundaries. The bottom of the mesh was prevented from moving in the horizontal and vertical directions, the lateral boundaries were prevented from moving in the horizontal direction only, and the ground surface was a stress free boundary.

The footings were not simulated using solid elements; instead their weight was simulated by applying an equivalent uniform stress along the boundary BC. The horizontal movements along the boundary BC were set equal to zero and the vertical displacements are made to have the same magnitude, thus mimicking the behaviour of a rough rigid footing.

The latter condition was achieved by using the *tied degrees of freedom* concept in which the movements in a particular direction, along a certain boundary, can be set to have the same magnitude, however this magnitude is not specified but is a result of the analysis. Following the excavation and the casting of the footings (grey area), the boundary AB is prevented from moving in the horizontal direction.

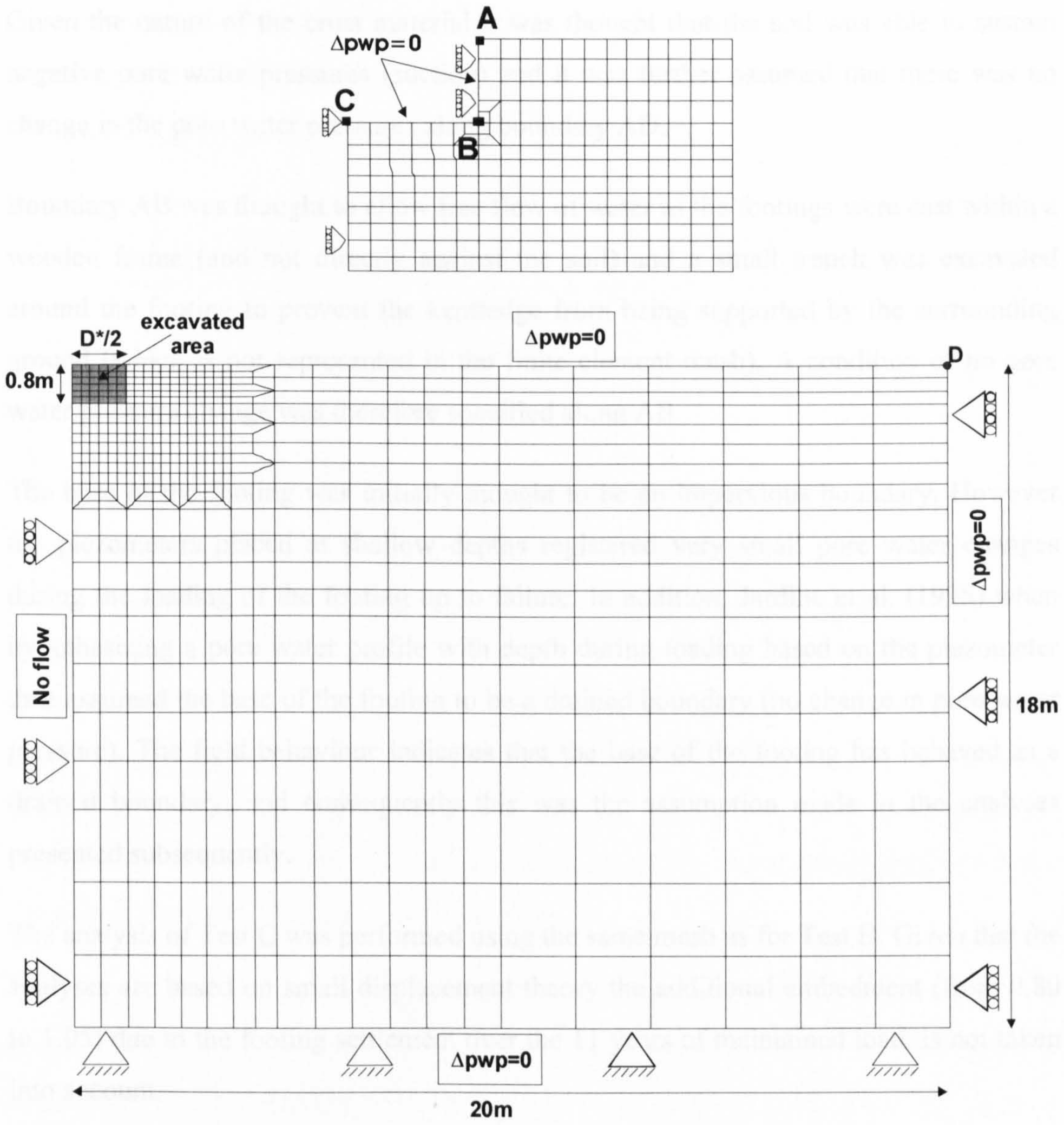

Notes: D= equivalent diameter. In test A D*= 2.48 m and in test B and C D*=2.71 m.*

Figure 8.22: Finite element mesh for footing A indicating the displacement and pwp boundary conditions.

The analyses of the footings presented in this Chapter all involve coupled consolidation and therefore it is required to specify appropriate pore pressure boundary conditions. In ICFEP the default pore pressure boundary condition is that of no flow of water and this was applied to the left hand boundary. The bottom and right hand boundaries were considered to be at a sufficient distance from the footing to have no change in pore pressure.

Given the nature of the crust material it was thought that the soil was able to sustain negative pore water pressures (suction) and it was further assumed that there was no change in the pore water pressures along boundary AD.

Boundary AB was thought to allow free flow of water as the footings were cast within a wooden frame (and not directly against the soil) and a small trench was excavated around the footing to prevent the kentledge from being supported by the surrounding ground (which is not represented in the finite element mesh). A condition of no pore water pressure change was therefore specified along AB.

The base of the footing was initially thought to be an impervious boundary. However the piezometers placed at shallow depths registered very small pore water changes during the loading of the footing up to failure. In addition, Jardine et al. (1995) when hypothesizing a pore water profile with depth during loading based on the piezometer data assumed the base of the footing to be a drained boundary (no change in pore water pressure). The field behaviour indicates that the base of the footing has behaved as a drained boundary, and consequently this was the assumption made in the analyses presented subsequently.

The analysis of Test C was performed using the same mesh as for Test B. Given that the analyses are based on small displacement theory the additional embedment (from 0.80 to 1.05) due to the footing settlement over the 11 years of maintained load, is not taken into account.

8.4.2 Geotechnical profile adopted

The geotechnical ground profile relevant for the numerical analysis of the footing tests is defined based on the extensive characterization data available for the Bothkennar research site, which was summarized in Sections 8.2.2 and 8.2.3. The ground profile is divided into four geotechnical units, as shown in Table 8.1.

Unit I consists of modern deposits of the reclaimed tidal flats. Its thickness varies throughout the site and is about 1 m thick near the footings location. Unit II corresponds to the layer of "shells within a matrix of clay" about 30 cm thick that marks the unconformity between the Carse Clay sequence and the modern deposits above. There

are no specific laboratory test data for these materials, consequently they are assumed to be similar to the Carse Clay stratum.

Table 8.1: Geotechnical units: depth, soil description, bulk modulus and permeability.

Unit	Depth (m) Top-Bottom	Soil description	Bulk unit weight (kN/m3)	Permeability (m/s)
I	0.0-1.0	Weathered clayey silt crust	18.0	$5.0x10^{-9}$
II	1.0-1.3	Shelly layer	17.0	$1.0x10^{-8}$
III	1.3-2.2	Soft clayey silt with some shell fragments	17.0	$5.0x10^{-9}$
IV	2.2-18.0	Soft black silty clay with fine mottling and occasional silt laminae	16.0	$2.0x10^{-9}$

Unit III corresponds to the weathered facies in the top of the Carse Clay sequence and it is about 0.9 m thick. This material is assumed to be similar to the main Clay sequence, as the mineralogy, composition and depositional environment are likely to be the same, and the effect of weathering on the soil response is expressed by means of appropriate values of K_0 and YSR. Unit IV comprises the Carse Clay sequence and includes in the top a transition zone of lightly weathered material.

The profile of pore water pressures with depth is assumed to be hydrostatic with the ground water level (GWL) at 0.9 m depth and assuming the soil to be able to sustain negative pore water pressure above the GWL.

In the numerical analyses shown subsequently, the foundation soil is modelled using the Equivalent Time (ET) model. The basic model parameters for the foundation soil are assumed to be identical within the four units defined above, with the variation in the stiffness and strength with depth being expressed by means of appropriate values of K_0 and YSR. The derivation of the model parameters is presented in Section 8.4.3.

Figure 8.23 shows the profile of the coefficient of earth pressures at rest and the yield stress ratio adopted in the analyses. For comparison the laboratory and in-situ test data previously shown in Figure 8.6 and Figure 8.9 are also included.

Based on in-situ and laboratory tests at the in-situ void ratio, the ratio of horizontal to vertical permeability is between 1.1 and 1.6 in the top 12 m of the clay stratum. This

permeability anisotropy was regarded to be quite small and consequently was not introduced into the numerical analyses. The values of (the isotropic) permeability adopted for each geotechnical unit are included in Table 8.1 and have been defined based on the data included in Figure 8.14, and assuming that the permeability obtained from samples may be different, in general lower, than that of the soil mass.

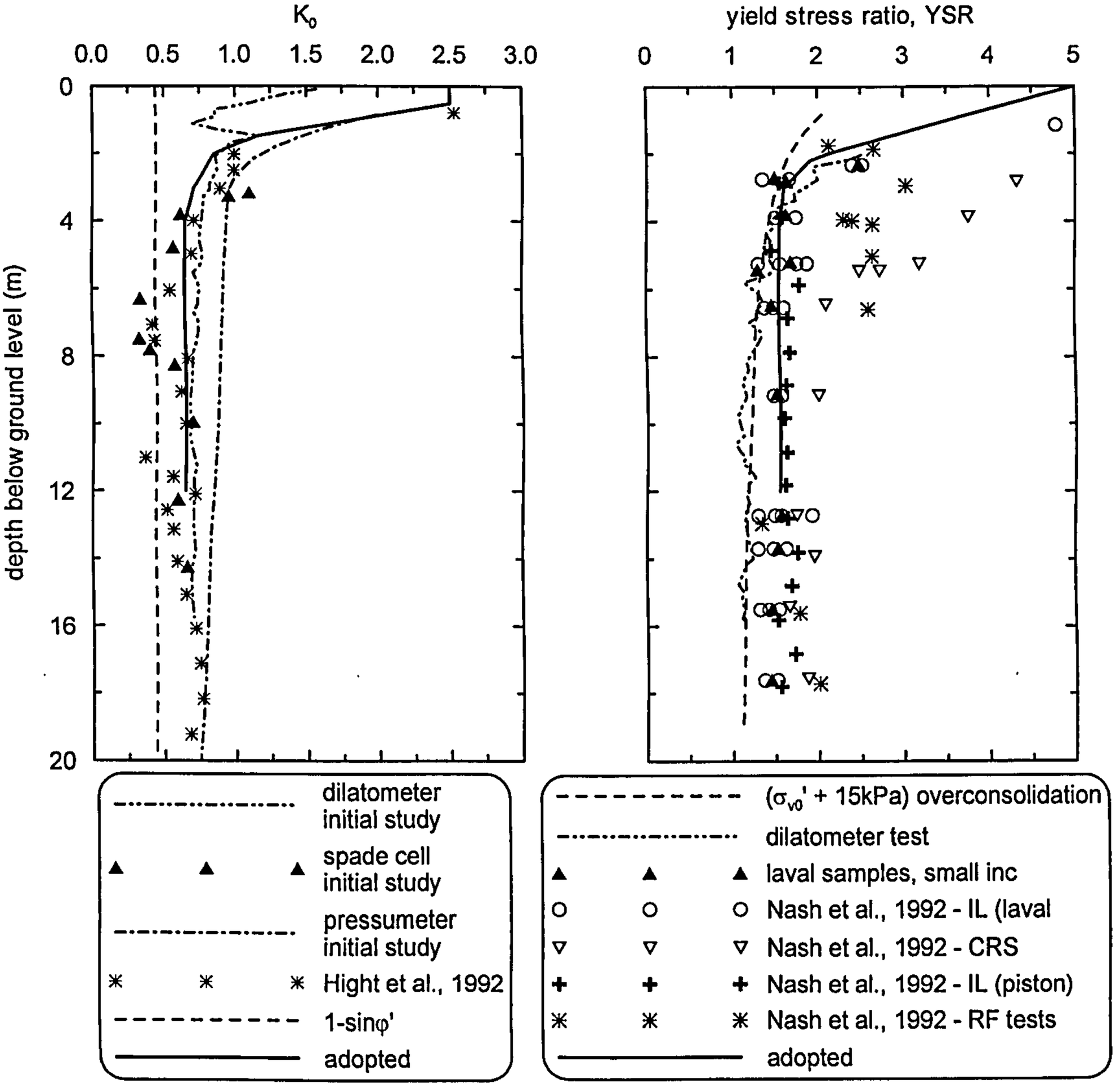

Figure 8.23: Profile of the coefficient of earth pressures at rest and yield stress ratio adopted in the analyses.

The initial effective stresses in the foundation soil are calculated using: i) the distribution of bulk unit weight with depth included in Table 8.1; ii) a hydrostatic pore water pressure profile with the GWL at 0.9 m depth and iii) the adopted K_0 profile included in Figure 8.23. The resultant profiles of vertical and horizontal effective stresses with depth are shown in Figure 8.24.

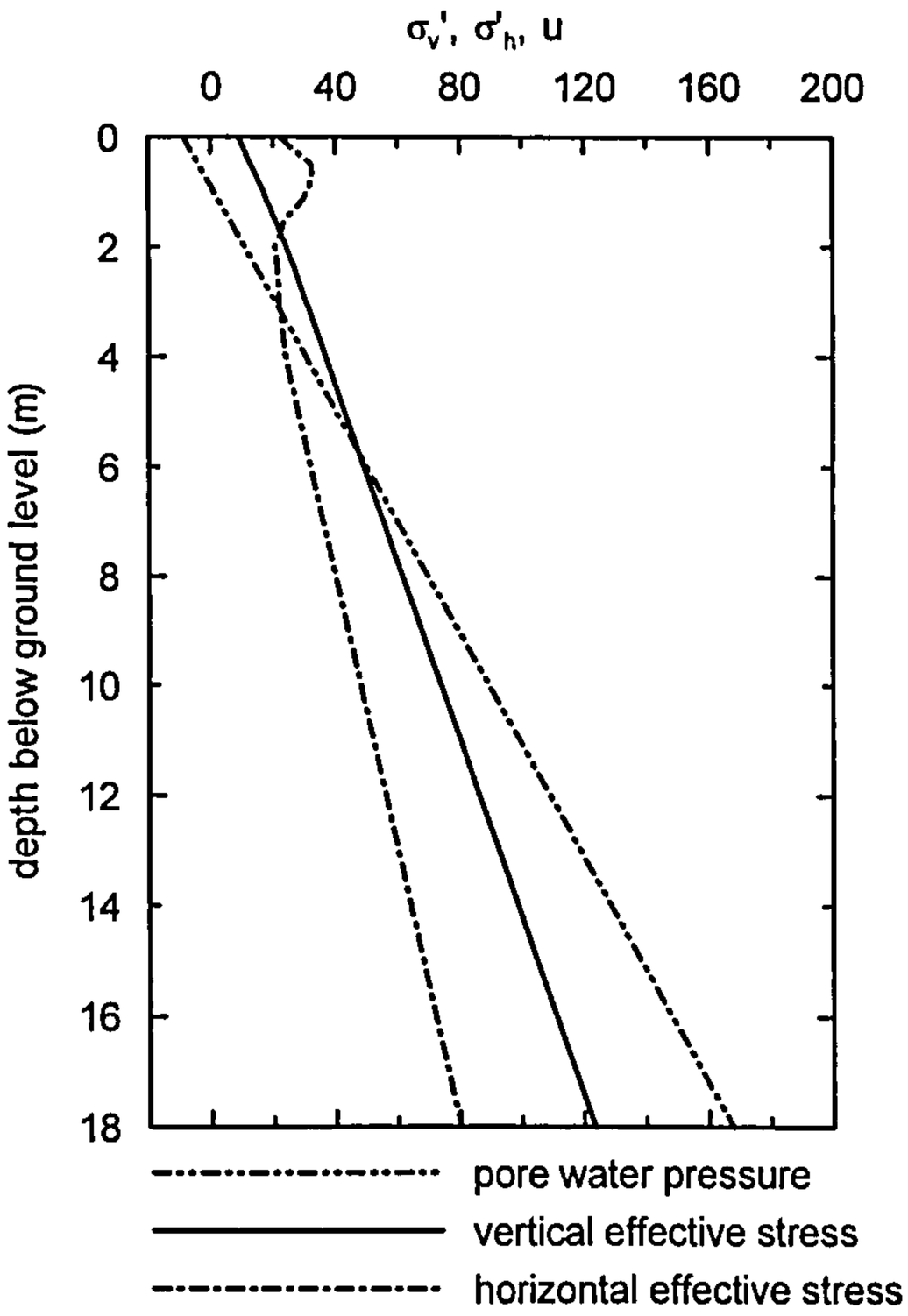

Figure 8.24: Profile of initial vertical and horizontal effective stress with depth.

8.4.3 Derivation of the model parameters for the Carse Clay at Bothkennar

8.4.3.1 Definition of the parameters values

The ET model parameters for the Carse Clay are derived based on the laboratory test data that were mostly carried out as part of the characterization project for the Bothkennar site launched by the former SERC. The samples are mainly from 5.3 to 6.2 m depth. The ET model parameters for the Carse Clay are summarized in Table 8.2, and their justification is described in the following paragraphs.

Table 8.2: Model parameter adopted in the numerical analyses.

OCR (*)	e_0	φ'	λ/V	κ/V	μ	ψ_0/V	k (**)
-	-	°	-	-	-	-	m/s
1.55	1.85	36	0.0842	0.0105	0.26	0.00378	$2x10^{-9}$
t_0	$\varepsilon^{vp}_{vol,m,Limit}$	$\alpha_g=\alpha_f$	$\mu_g=\mu_f$	p'_{mio}	p_{s0}	ρ_s	
day	-	-	-	kPa	kPa	-	
1.0	0.065	0.05	0.85	10.0	30.0	1500	

Notes:
e_0 = initial void ratio;
φ' = critical state shear angle in triaxial compression;
λ/V = slope of the reference time line in ε_v – ln p' space;
κ/V = slope of the instant time line in ε_v – ln p' space;
μ = Poisson's ratio;
ψ_0/V = creep parameter;
k = permeability;
t_0 = time on the reference time line
$\varepsilon^{vp}_{vol,m,Limit}$ = Limit for the amount of visco-plastic volumetric strain
α_f, μ_f = parameters that characterize the shape of the loading surface in p'-q plane.
α_g, μ_g = parameters that characterize the shape of the plastic potential in p'-q plane.
p'_{mio} = mean effective stress on the intrinsic reference time line at zero volumetric strain in ε_v – ln p' space
p_{s0} = initial increase in p'_{mi0} due to structure
ρ_s = destructuration parameter

(*) In the top 4 m of the ground profile the OCR is larger than 1.55 as result of e.g. weathering, fissuring, seasonal variations in the ground water level. The profile of OCR adopted in the analyses is shown in Figure 8.23.

(**) The permeability value adopted for each geotechnical unit is shown in Table 8.1; the value of $2x10^{-9}$ m/s corresponds to the value in Unit IV.

a) Critical state angle of shearing resistance in triaxial compression

Based on undrained triaxial compression tests on reconstituted samples Allman & Atkinson (1992) report a critical state angle of 34°. However, Smith (1992) notes that on natural samples the mobilized shear angle at large strains between 15-20% varies between 36° and 45°, depending on the samples facies. The value of 36° is adopted here.

b) Poisson's ratio

Rolo (2003) performed consolidated drained triaxial tests with local strain measurements on high quality samples of Carse Clay from 5.9 to 6.2 m depth. From the initial pseudo-linear range of the stress-strain curves the author deduced values of the elastic parameters and obtained Poisson's ratio values between 0.22 and 0.29, with an average value of 0.26.

c) Slope of the reference time line, λ/V

Based on IL oedometer tests on reconstituted samples from various depths Nash et al. (1992b) report values of the coefficient of primary consolidation C_c of about 0.55 at depths ranging from 5 to 6.5 m. This corresponds approximately to a value of λ of 0.24.

It is shown in Chapter 6 that the ET model should be formulated using λ/V and κ/V constant such that the reference time line and the instant time line are straight lines in the $\varepsilon_v - ln\, p'$ space. With an initial void ratio of 1.85, λ/V comes equal to 0.0842.

d) Slope of the instant time line, κ/V

The slope of the instant time line was estimated based on the first unloading increment of IL oedometer tests and a value of κ equal to 0.03 is adopted. Assuming an initial void ratio e_0 equal to 1.85 this corresponds to a value of κ/V equal to 0.0105.

As explained in Chapter 6, the elastic part of the ET model is characterized by a stress dependent bulk modulus, given by Equation 8.8 and a second elastic parameter that can be input in several ways. The second elastic parameter is set to be the Poisson's ratio and equal to 0.26, and then the elastic shear stiffness is calculated by means of Equation 8.9.

Equation 8.8

$$K' = \frac{V \cdot p'}{\kappa}$$

where p' is the current mean effective stress and κ/V is the slope of instant time line in ε_v-ln p' space.

Equation 8.9

$$G = K' \cdot \frac{3 \cdot (1 - 2\mu)}{2 \cdot (1 + \mu)}$$

where μ is the Poisson's ratio.

e) Time at the reference time line

The time at the reference line was taken to be one day, as the reference time line is made to correspond to that obtained in IL oedometer tests with 24 hours load increments.

f) Creep parameter Ψ_0/V

The creep parameter Ψ_0/V is related to the visco-plastic volumetric strain rate on the reference time line by means of Equation 8.10. Considering a visco-plastic volumetric strain rate on the reference line equal to $5x10^{-8}$ m/s, (note that according to Nash et al., 1992b this was the typical value of axial strain rate at the end of the load increments), and the values of λ and κ defined above, the parameter Ψ_0/V is found to be 0.00432.

Equation 8.10 $$\dot{\varepsilon}_{vol}^{vp} = \frac{\psi_0}{V \cdot t_0}$$

On the other hand, the parameter Ψ_0/V can be related to the coefficient of secondary consolidation, $C_{\alpha e}$ by means of Equation 8.11. Nash et al. (1992b) reported that the ratio of $C_{\alpha e}/C_{ce}$ (mathematically equivalent to ψ_0/λ) was fairly constant, and varied between 0.03 and 0.05 around the pre-consolidation pressure stabilizing in the NC range after full destructuration at about 0.045. This gives a value of $C_{\alpha e}$ about 0.025 that in turn corresponds to a value of Ψ_0/V of about 0.0378, the value employed in the following analyses.

Equation 8.11 $$\psi_0 = \frac{C_\alpha}{\ln 10}$$

g) Parameter p'_{mi0}

The parameter p'_{mi0} is the value of the mean effective stress at zero volumetric strain on the intrinsic reference time line and it is given a value of 10.0 kPa.

h) Parameters p'_{s0} and ρ_s

The parameter p'_{s0} corresponds to the initial increase in p'_{m0} (the mean effective stress at zero volumetric strain on the reference time line of the natural material) due to

structure and therefore together with p'_{mi0} defines the distance between the intrinsic and the in-situ reference time line. The parameter ρ_s defines the decay in p_s with the development of volumetric plastic strains by means of Equation 8.12. Based on the IL oedometer tests on natural samples the two parameters p'_{s0} and ρ_s are estimated to be 30 kPa and 1500, respectively.

Equation 8.12 $$\Delta p_s = -3.0 \cdot \rho_s \cdot p_s \cdot \varepsilon_d^2 \cdot \Delta\varepsilon_d$$

p_s = current increase in p'_{m0} due to structure;

$$\Delta\varepsilon_d = \left|\Delta\varepsilon_x^{vp} + \Delta\varepsilon_y^{vp} + \Delta\varepsilon_z^{vp}\right|$$

where $\Delta\varepsilon_i^{vp}$ is the visco-plastic strain increment in the i direction;

$$\varepsilon_d = \int_0^t \Delta\varepsilon_d$$

i) Limit for the amount of volumetric visco-plastic strain, $\varepsilon_{vol,m,Limit}^{vp}$

The parameter $\varepsilon_{vol,m,Limit}^{vp}$ corresponds to the value of the volumetric visco-plastic strain attained at infinite creep time and in the absence of a long-term creep test, is often taken to be $e_0/1+e_0$ which corresponds to the situation when voids no longer exist in the soil. This value causes the ET model to collapse onto a nearly linear logarithmic creep law within engineering time intervals. Smith (1992) reports creep tests on natural samples of Carse Clay that demonstrate a strong non-linearity of the creep behaviour. Based on these test results the value of $\varepsilon_{vol,m,Limit}^{vp}$ is set equal to 0.065 (10% of $e_0/1+e_0$).

j) Parameters α and μ

The parameters α and μ define the shape of the plastic potential and the loading surface in *p'-J* stress space. In this case, the plastic potential and the yield surface are given the same shape in *p'-J* stress space and $\alpha_q=\alpha_f$ and $\mu_q=\mu_f$. The value of α and μ are selected such that when assuming the model parameters included in Table 8.2 and the initial stress conditions and overconsolidation ratio described in Section 8.4.2, the model predicts the required values of peak undrained strength. Based on the consolidated undrained triaxial compression tests on samples from 5.3 to 6.2 m reported by Smith (1992) the values of α and μ are set equal to 0.05 and 0.85, respectively.

8.4.3.2 1 D compression behaviour

Finite element analyses of laboratory tests were performed to validate the derived model parameter values. Figure 8.25 shows an IL oedometer test on a reconstituted sample of Carse Clay from about 5.2 m by Smith (1992) and the ET model predictions. The results shown in Figure 8.25 are obtained using the parameter values shown in Table 8.2, except for the initial void ratio that is set to 2.4, to reflect the reconstituted nature of the soil, and the parameters related with structure are set to zero. The values of λ/V and κ/V are set such that the condition of λ=0.24 and κ=0.03 are still verified, so that a good agreement is obtained when comparing the data in *void ratio – ln p'* space. Figure 8.25 also includes the results of an IL oedometer test on a reconstituted sample reported by Nash et al. (1992b), showing the repeatability of the results from Smith (1992).

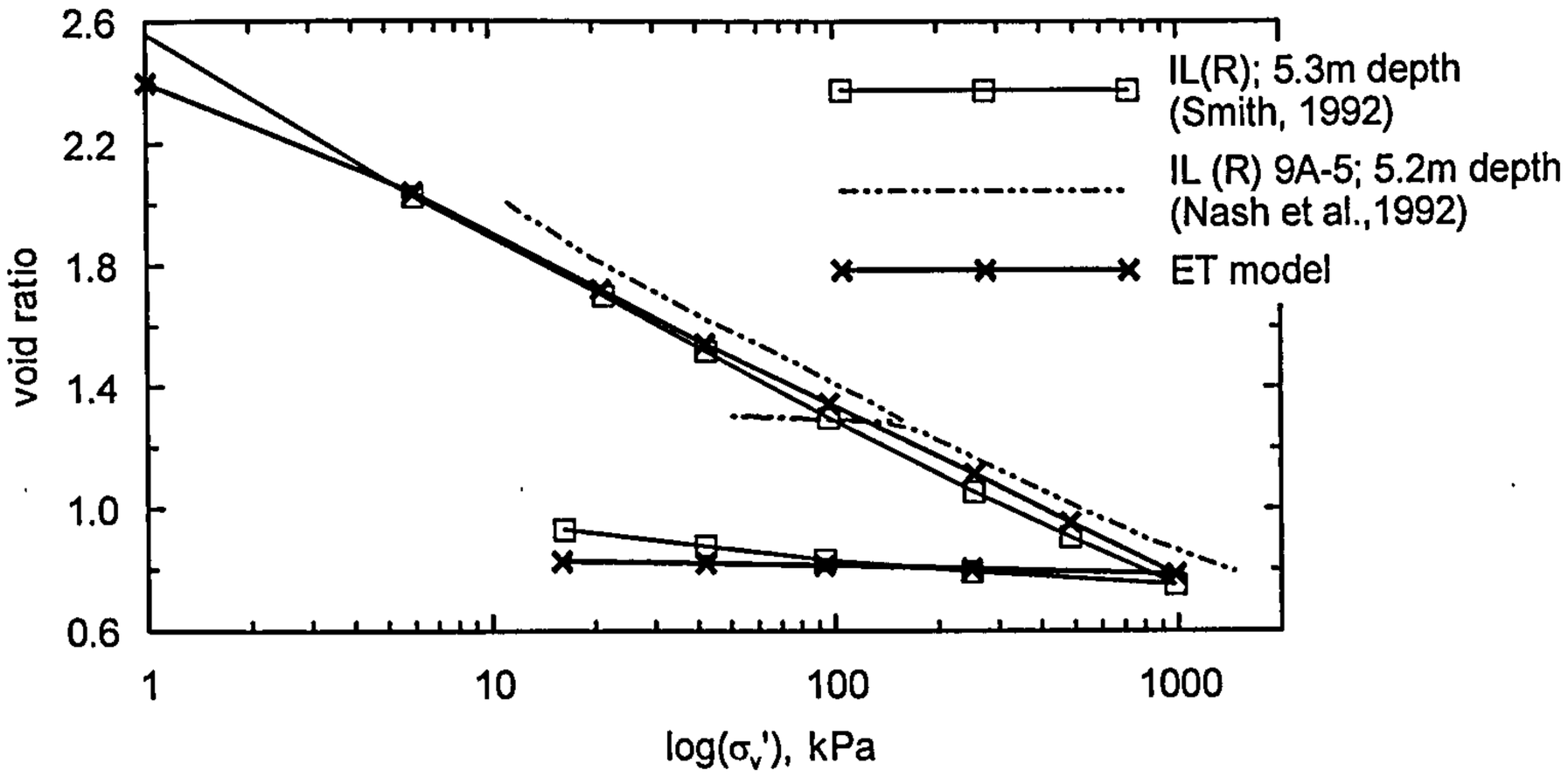

IL = incremental load oedometer test with 24h load increments; R = reconstituted sample

Figure 8.25: Incremental load oedometer tests on reconstituted samples of Carse clay; laboratory data and model predictions.

The finite element analyses of the IL oedometer tests invoke coupled consolidation so that the effect of consolidation is taken into account. The finite element mesh is therefore required to have the real dimensions of the sample and to have several elements in the direction of flow (vertically) so that a reasonable profile of pore water pressure across the sample is predicted. The author has checked that in a single drainage oedometer about 10 elements are needed in order for the number of elements not to influence the analysis results. In the model predictions, the void ratio at the end of each increment is calculated from the vertical displacement of the top of the sample, identically to the procedure in the laboratory.

a) Natural samples - structure and destructuration

Figure 8.26 shows two 24 hours IL oedometer tests on natural samples and the model predictions. The finite element analyses of the IL oedometer tests shown in Figure 8.26 are coupled consolidation analyses as discussed above, and were performed using the parameter values included in Table 8.2, with exception of the initial void ratio, e_0 that is set equal to 1.875 and 1.775 to match those of the Sherbrooke and Laval samples, respectively. The values of λ/V and κ/V have been set such that the conditions of λ=0.24 and κ=0.03 are still verified. The Laval and Sherbrooke samples are from 5.3 m and 6.2 m depth and the estimated in-situ vertical effective stresses are about 43.8 and 49.1 kPa, respectively. The FE analyses assume that the samples have an overconsolidation ratio of 1.45 in relation to the in-situ stresses, slightly reduced from the in-situ value of 1.55 due to disturbance caused during sampling, transportation and specimen preparation.

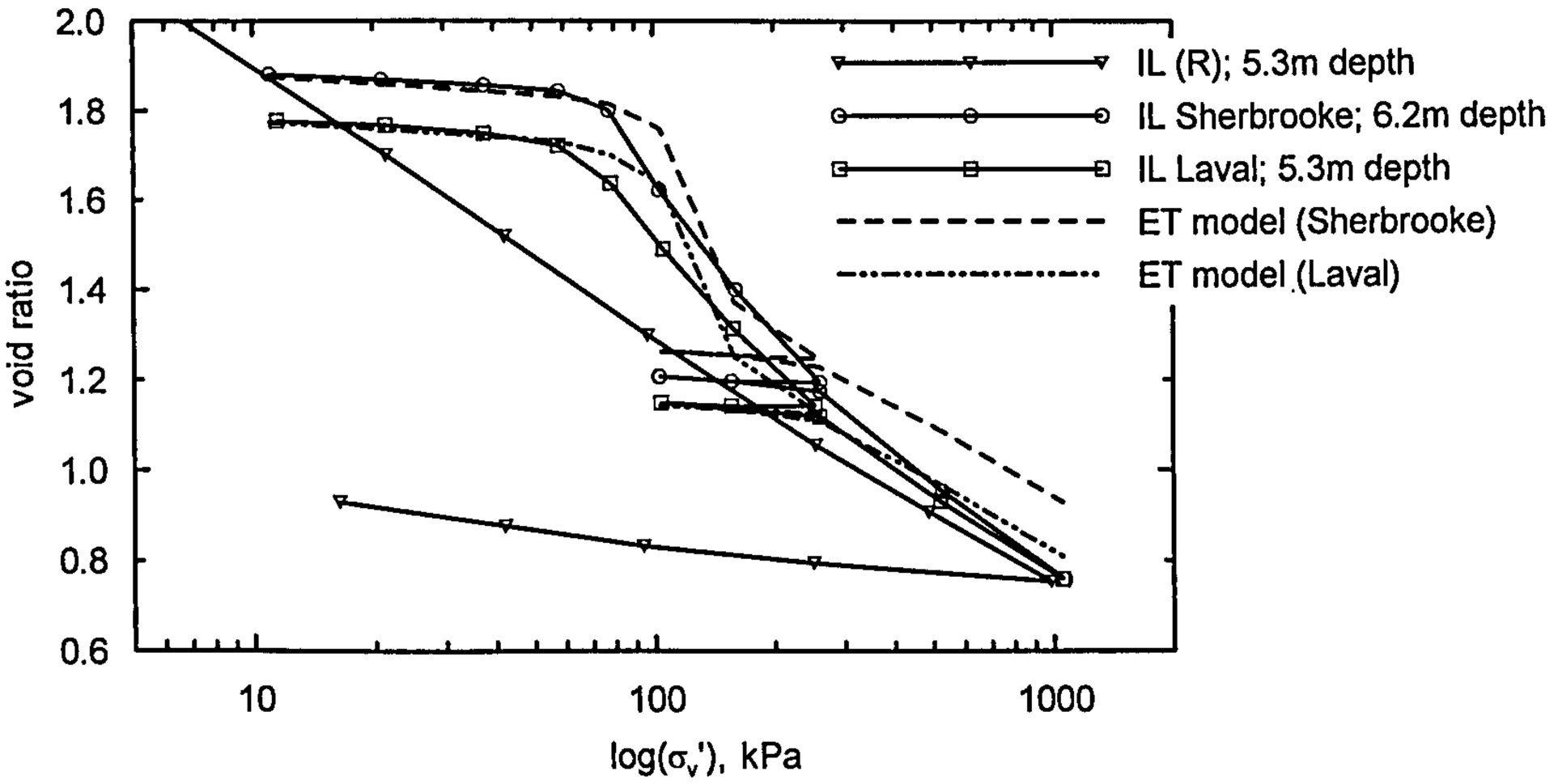

Figure 8.26: IL oedometer tests on natural samples of Carse Clay: laboratory data from Smith (1992) and model predictions.

Figure 8.26 shows a good agreement between the FE analyses predictions and the laboratory compression curves during the initial loading steps during the overconsolidated stress range. During the intermediate loading stages the FE analyses predictions are found to produce a more abrupt destructuration than that observed in the laboratory curves and from about 160 kPa on the FE analyses cease to predict any further destructuration and the predicted compression curves remain parallel to, and above, the laboratory intrinsic compression curve. This behaviour is in contrast to that

observed in the laboratory compression curves on natural samples that are found to join the intrinsic compression curve at about 1000 kPa vertical stress.

This behaviour derives from the fact that in the ET model the intrinsic and the natural compression lines are defined and their location fixed in ε_v-*lnp'* space, and thus a change in the initial void ratio causes the intrinsic and the natural reference time line to move vertically when the results are plotted in *void ratio – lnp' space*. Therefore, rather than looking at the absolute value of void ratio at a certain stress value one must consider the changes in void ratio during compression. The soil structure can be quantified as the distance between the intrinsic compression line and a parallel line passing through the yield point of the compression curve on a natural sample, noting that in the case of the FE analysis the intrinsic curve of a given soil element is a tangent to the last part of the respective compression curve. Using this definition, the model predictions shown in Figure 8.26 under predict the amount of initial structure when compared with the laboratory test data by Smith (1992).

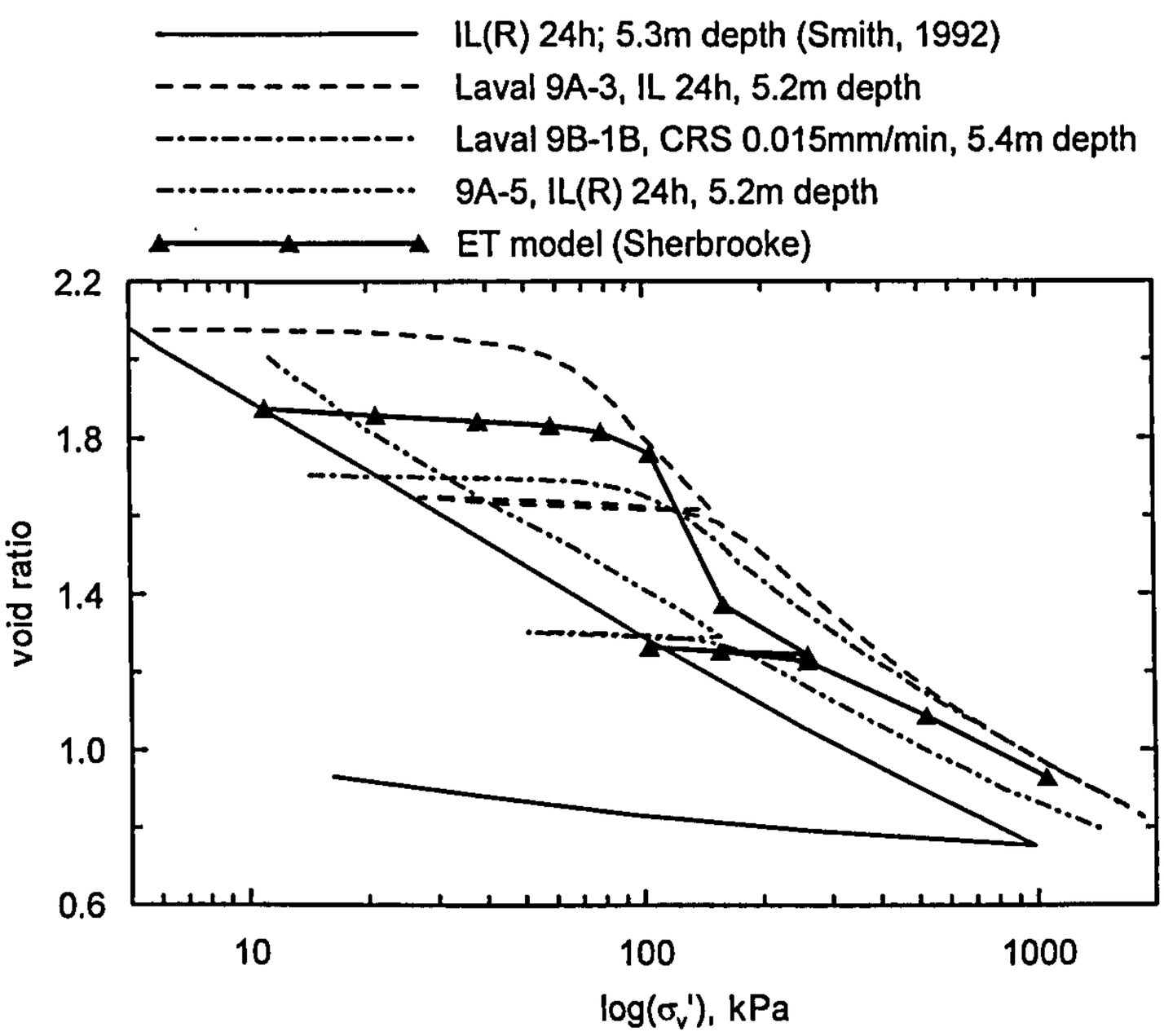

Notes: when not stated the data is this Figure is from Nash et al.(1992b).

Figure 8.27: IL oedometer on Carse Clay samples: laboratory data and model predictions.

Figure 8.27 shows oedometer tests on natural samples of Carse Clay reported by Nash et al. (1992b) and the model predictions are found to fit the general trend of the laboratory test data. Although Nash et al. (1992b) undertook an extensive study on the

1D behaviour of the intact Carse Clay, the tests from Smith (1992) are preferred as a comparison with the FE analyses, as it is only for these tests that information regarding the value of the load steps is available.

Finally it is noted that the destructuration mechanism included in the ET model was initially derived by Lagioia & Nova (1995) to reproduce the behaviour of a calcarenite in which structure occurs mainly due to cementing. In comparison, in Carse clay the structure results mainly from particle bonding and the destructuration process is found to be gradual. The limitations of the destructuration mechanism to reproduce the behaviour of the intact Carse Clay are discussed subsequently.

b) Long-term creep test

Figure 8.28 shows the variation of void ratio with time during creep tests on natural samples of Carse Clay. The laboratory procedure was to consolidate a triaxial sample under K_0 conditions and a constant axial strain rate of 1%/day up to a mean effective stress of 100 kPa, at which point the sample was allowed to creep at constant effective stress.

The model predictions are obtained from a coupled consolidation FE analysis using the model parameters in Table 8.1. In the FE analysis, the sample is assumed to have no initial structure, as at 100 kPa the sample is at an intermediate state, between intact and fully unstructured. If this structure had been accounted for, then during the creep stage the ET model would have predicted further structure loss associated with the development of volumetric visco-plastic strains, while in reality the soil structure is expected to remain stable or even to increase.

Figure 8.28 shows that, in the overall, the FE analysis predictions agree well with the two laboratory tests. The FE analysis slightly overpredicts the amount of creep during the early stages of the creep period but fits quite well the creep deformation (or void ratio change) and the creep rate at the end of the creep period, in particular for test SUD1. The initial softer response predicted by the FE analysis when compared with the laboratory data is thought to result from the different pore pressure response. Smith (1992) reports that the end of consolidation defined at 95% excess pore pressure dissipation is about 19 hours after the start of the creep, while in the FE analyses there is virtually no excess pore pressure developed during consolidation.

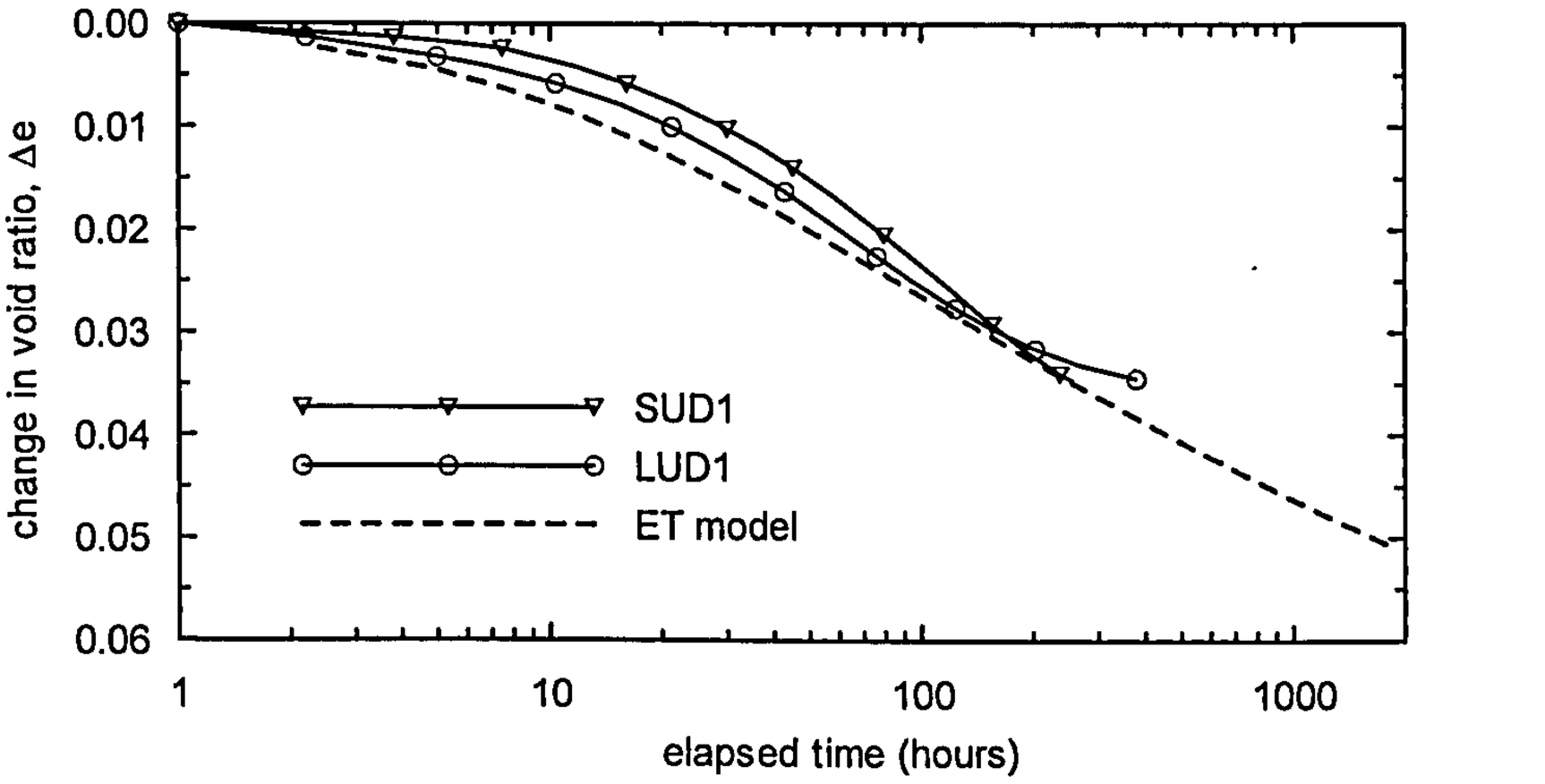

Figure 8.28: Void ratio change with time during creep: laboratory data (Smith, 1992) and model predictions.

c) Strain rate effects on the yield stress ratio

Figure 8.29 shows the variation of the yield stress ratio with the applied axial strain rate from oedometer tests on natural samples of Carse Clay and compares the laboratory data with the model predictions. The model predictions have been obtained by means of drained single element finite element analyses of constant rate of strain oedometer tests, assuming the model parameters given in Table 8.2. The ET model is found to reproduce well the variation of the YSR with strain rate of the intact Carse Clay.

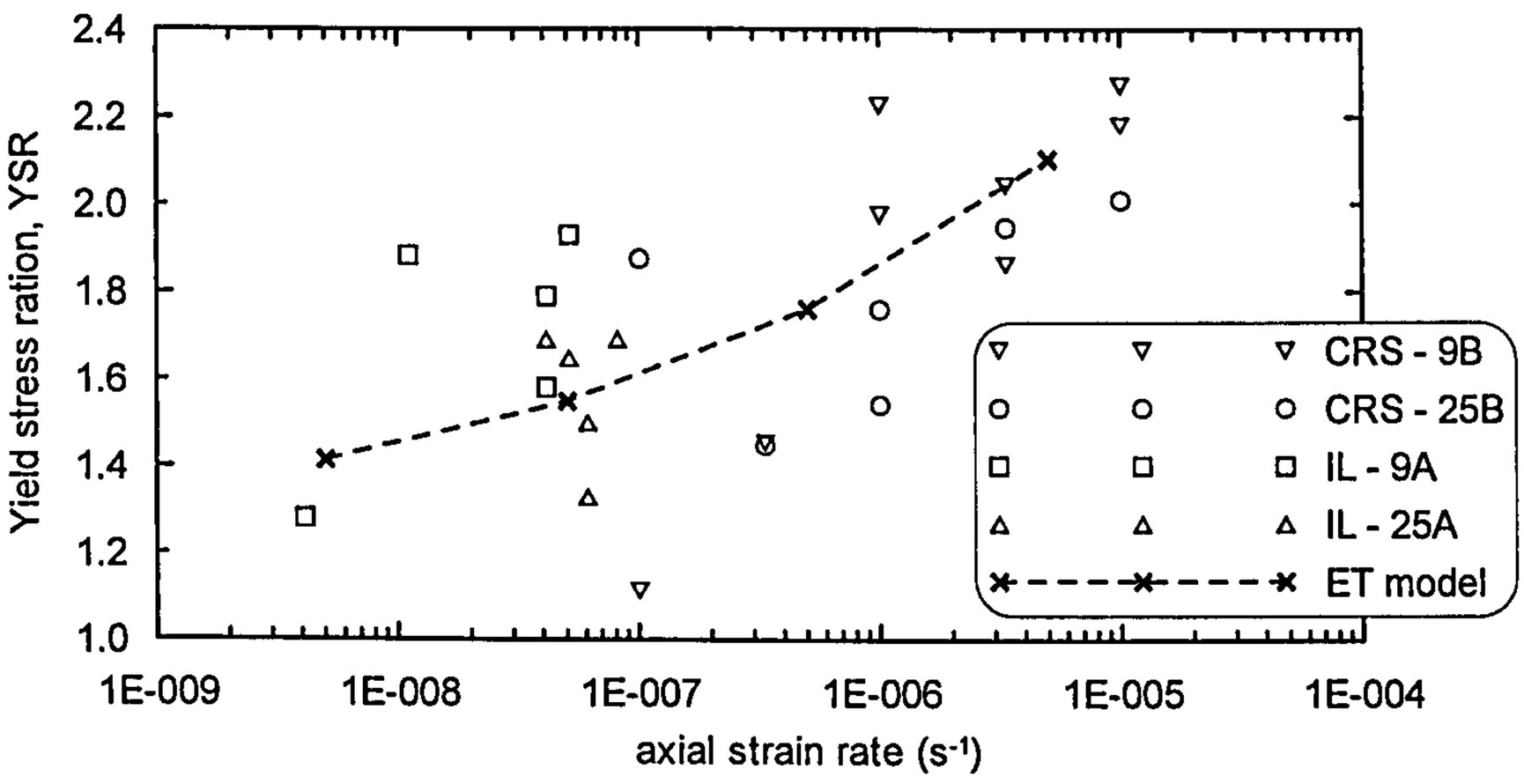

Note: in the IL oedometer tests the strain rate is that observed at the end of the relevant load increment.

Figure 8.29: Variation of the yield stress ratio with strain rate: laboratory test data (Nash et al., 1992b) and model predictions.

8.4.3.3 Consolidated undrained triaxial tests

Peak undrained strength

Figure 8.30 shows the effective stress paths of consolidated undrained triaxial tests on intact samples of Carse Clay. The Laval and Sherbrooke samples were from 5.3 and 6.2 m depth, respectively. The samples were consolidated to the estimated in-situ effective stress state following a swelling loop to mimic the recent stress history of the in-situ material. The specimens were then sheared either in compression or extension at 1%/day constant axial strain rate in tests LCU1 and LCU3 and 4.5%/day in the remaining tests. The model predictions are obtained by means of undrained FE analyses using the model parameters given in Table 8.2.

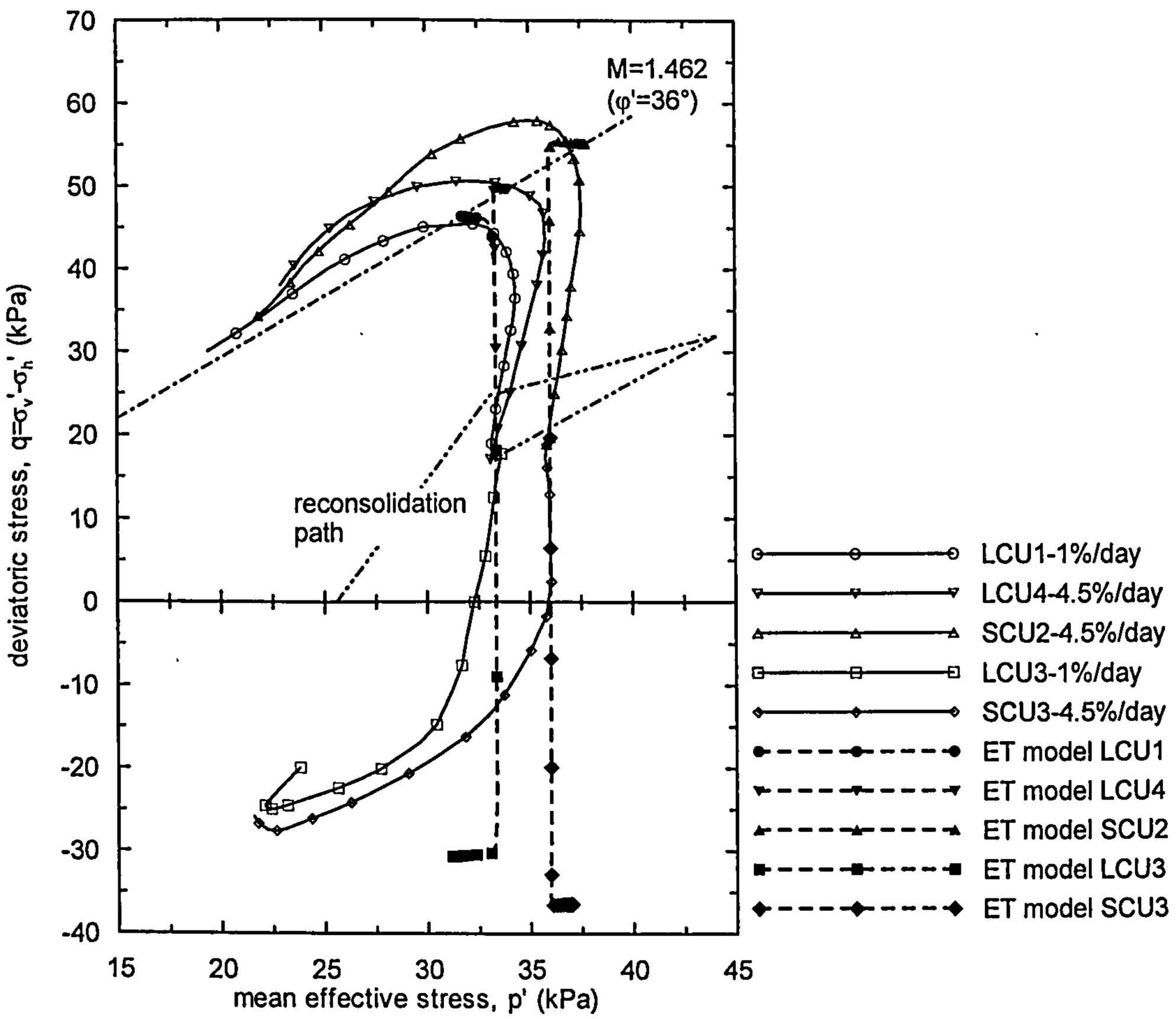

L = Laval sample; S = Sherbrooke sample.

Figure 8.30: Effective stress paths of consolidated undrained triaxial tests on intact Carse Clay samples: laboratory data and model predictions.

When reproducing the Sherbrooke and Laval samples YSR values of 1.55 and 1.5 were adopted, respectively, assuming that the Sherbrooke samples produced marginally less disturbance during sampling. As noted previously, the parameters α and μ were estimated by matching the peak undrained strengths in compression. In the ET model the extension to generalized stress space is by default done using the Matsuoka-Nakai failure criterion and it is not possible to control the shape of the loading surface and the plastic potential in the deviatoric plane. Consequently, once the undrained strength has been matched in triaxial compression the value of undrained strength under other shearing modes is set, and the ET model is found to overpredict the undrained strengths in extension.

Although the samples have an initial structure and the ET model incorporates a destructuration mechanism, the model does not predict destructuration as observed in the laboratory tests with significant loss in deviatoric and mean effective stress post peak during undrained shearing. This arises because the formulation of the destructuration mechanism in the ET model is a function of the visco-plastic volumetric strain component only. During undrained shearing the total volumetric strain is zero, implying that the elastic and the visco-plastic components have the same magnitude but opposite signs. Given that the changes in mean effective stress are small both the elastic and visco-plastic components are expected to be very small and the magnitude is not enough to produce any noticeable change in the value of p_s.

The ET model is found to capture quite well the rate dependent response in undrained shearing, as it provides a good fit to both the test data of LCU1 and LCU4.

Figure 8.31 shows the stress-strain curves for the same consolidated undrained triaxial tests. The model is found to fit reasonably well the value of the axial strain at peak, however it is not able to simulate the stiffer initial response observed in the laboratory tests, as the elastic part of the model is based on a stress dependent Bulk modulus and a constant Poisson's ratio.

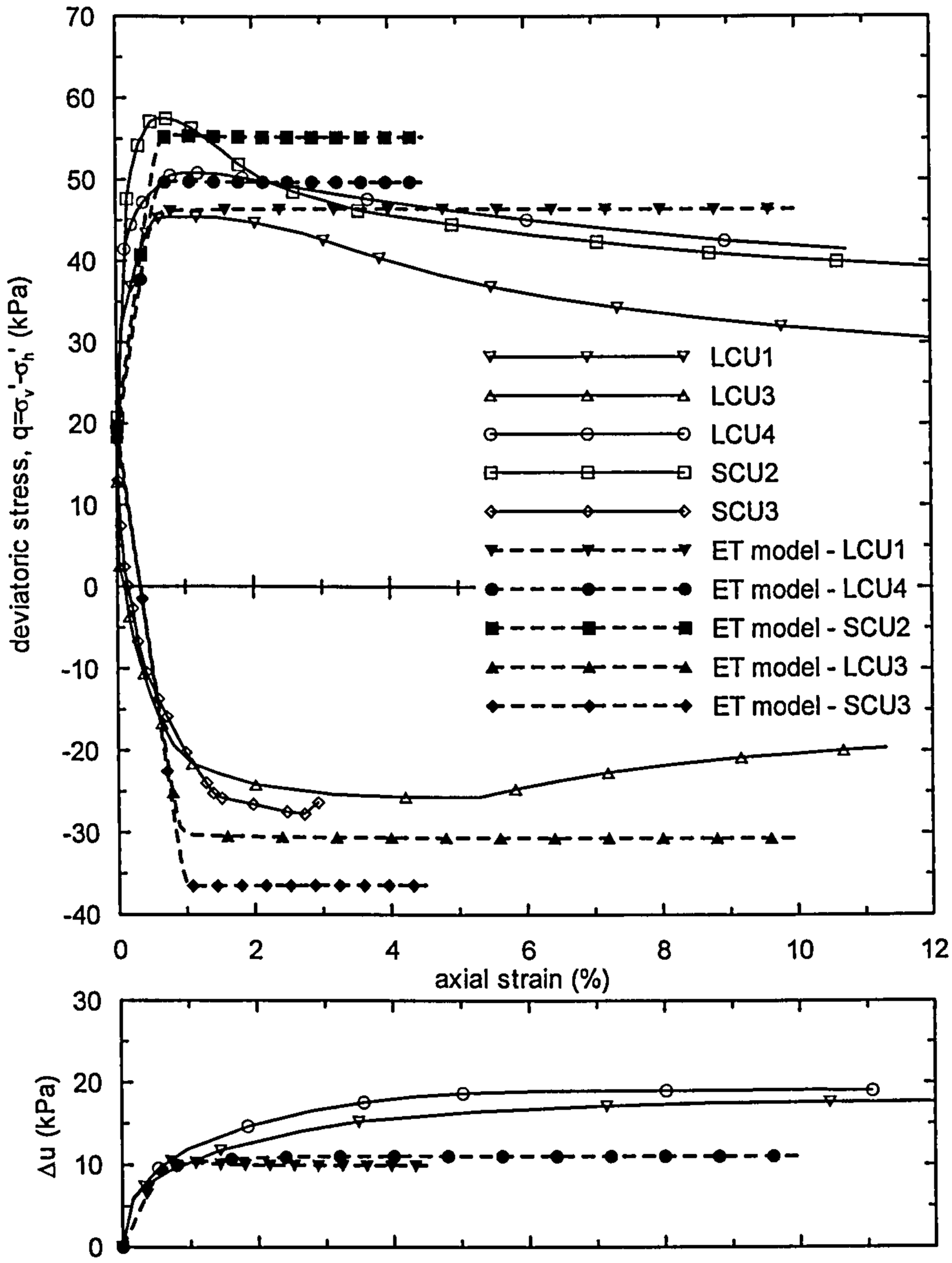

Notes: + pore water pressures are contractive; S= Sherbrooke sample; L= Laval sample.

Figure 8.31: Stress – strain curves and evolution of excess pore water pressures during consolidated undrained triaxial tests on intact Carse Clay samples: laboratory data and model predictions.

8.4.3.4 Undrained strength profile

Figure 8.32 shows the profile of peak undrained strength in triaxial compression predicted by the ET model together with the laboratory data. In the ET model, the undrained strength, S_u cannot be obtained directly from the current stress state and the model parameters as S_u is also a function of the applied strain rate. The profile of peak undrained strength with depth was obtained by means of undrained FE analyses simulating consolidated undrained triaxial compression tests at 4.5%/day axial strain, at

various depths. Each FE consolidated undrained triaxial test is performed with the appropriate initial effective stresses given in Figure 8.24 and the respective value of YSR shown in Figure 8.23.

The S_u profile predicted by the ET model fits well the laboratory data in the top 8 m. Below this depth, where there is some divergence, the strength values are unlikely to have a significant effect on the footing behaviour.

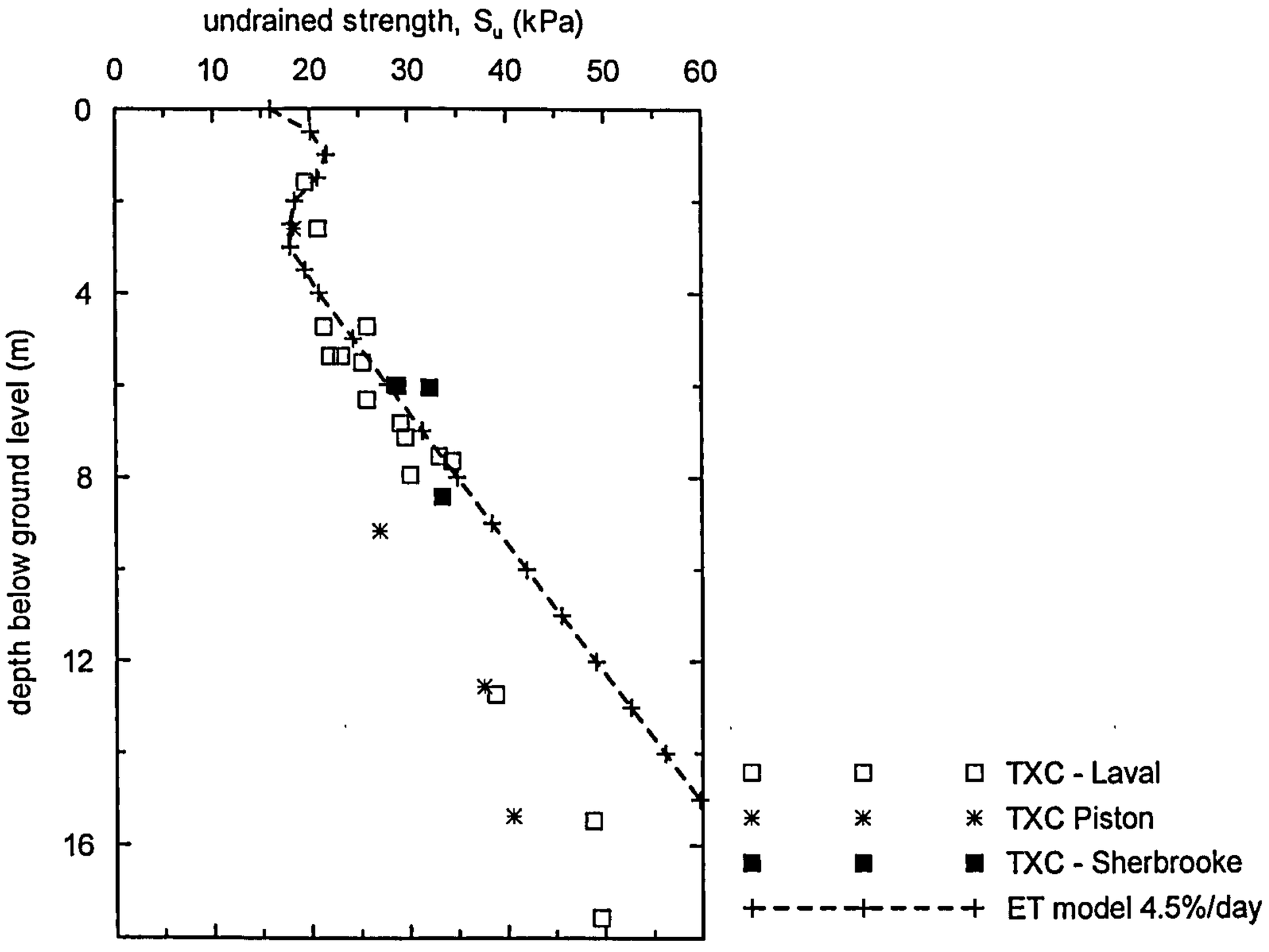

Figure 8.32: Profile of undrained strength in triaxial compression: laboratory data and model predictions.

8.4.4 Analyses of the footing tests with soil structure

Footing tests A and B are simulated by means of axi-symmetric coupled consolidation finite element analyses, considering the finite element mesh presented in Figure 8.22 and the model parameters defined in Section 8.4.3. The analyses simulate the excavation for the footing, the casting and the waiting time until the start of the loading test. Loading histories identical to those shown in Figure 8.33 (and Figure 8.17) were applied to the footings in the analyses.

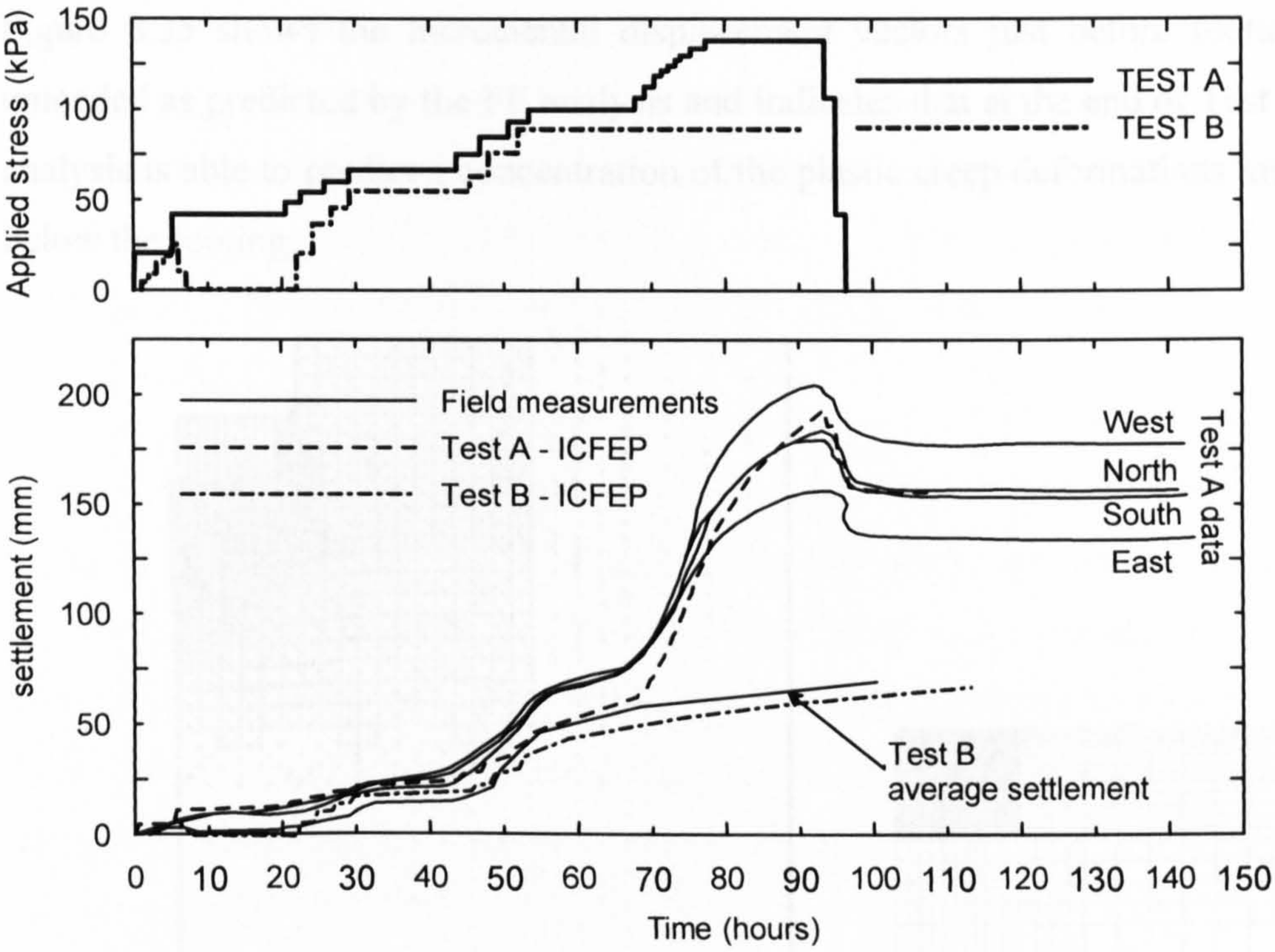

Figure 8.33: Variation of applied load and settlement with time during test A and B.

It is noted that the applied load provided by Gildea (1990), Jardine et al., (1995) and Lehane & Jardine (2003) has been interpreted as being a net bearing pressure, q_{net} as shown schematically in Figure 8.34, and considering the bulk unit weight of the concrete equal to 24 kN/m^3.

Figure 8.33 shows the applied load history and the variation of footing settlement with time, and compares the FE analyses predictions (series ICFEP) with the field data. The agreement between the FE analyses and the average measured settlement is in general excellent. In both tests, the FE analyses slightly overpredict the footing settlements during the early loading stages up to about 65 kPa and underpredict at intermediate loads between 75 and 120 kPa.

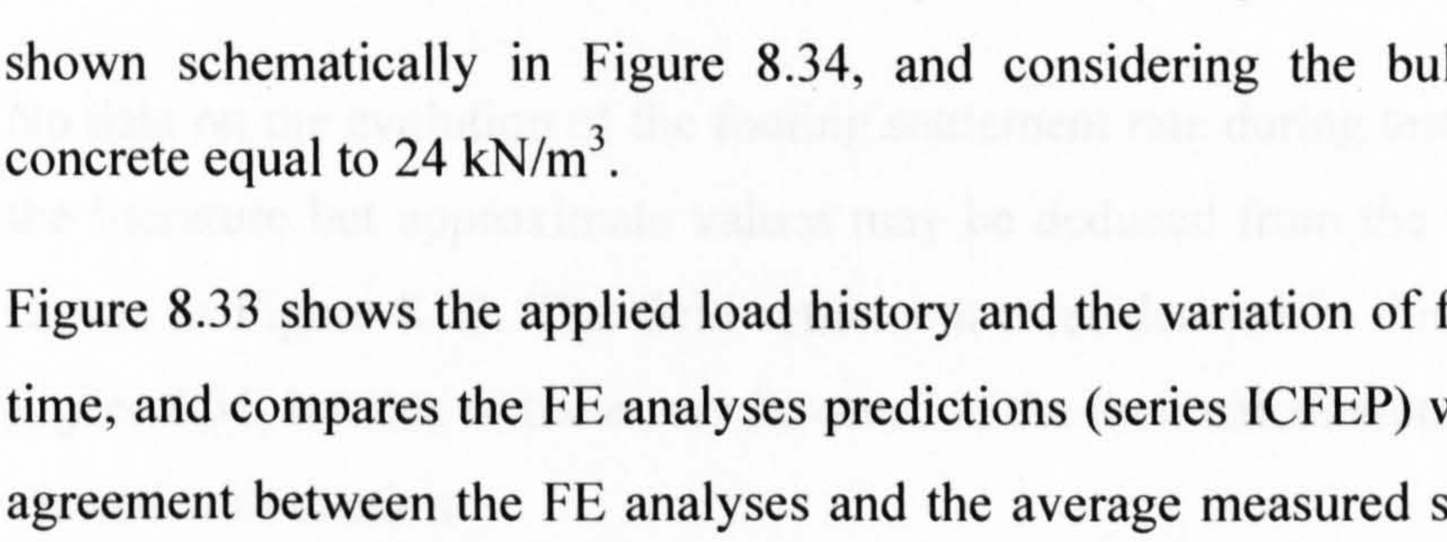

Figure 8.34: Definition of net and gross bearing pressure.

Figure 8.35 shows the incremental displacement vectors just before footing A was unloaded as predicted by the FE analysis and indicates that at the end of Test A, the FE analysis is able to predict a concentration of the plastic creep deformations immediately below the footing.

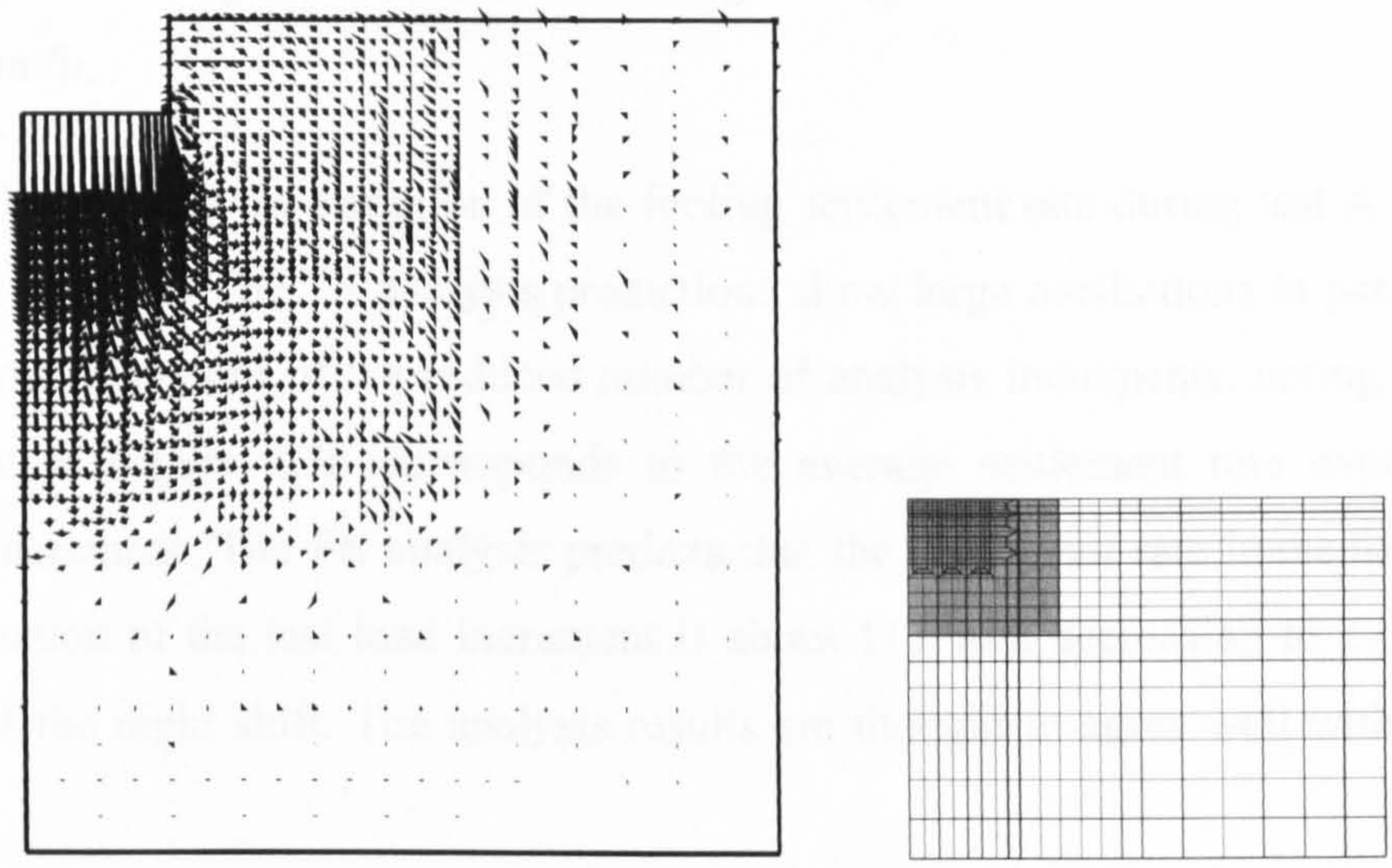

Figure 8.35: Incremental displacement vectors at failure just before the footing unloading - test A.

No data on the evolution of the footing settlement rate during test A have been found in the literature but approximate values may be deduced from the time-settlement curves shown in Figure 8.33. The field settlement rates derived in this manner are shown in Figure 8.36, but due to the errors involved in the their calculation these values should be viewed with caution.

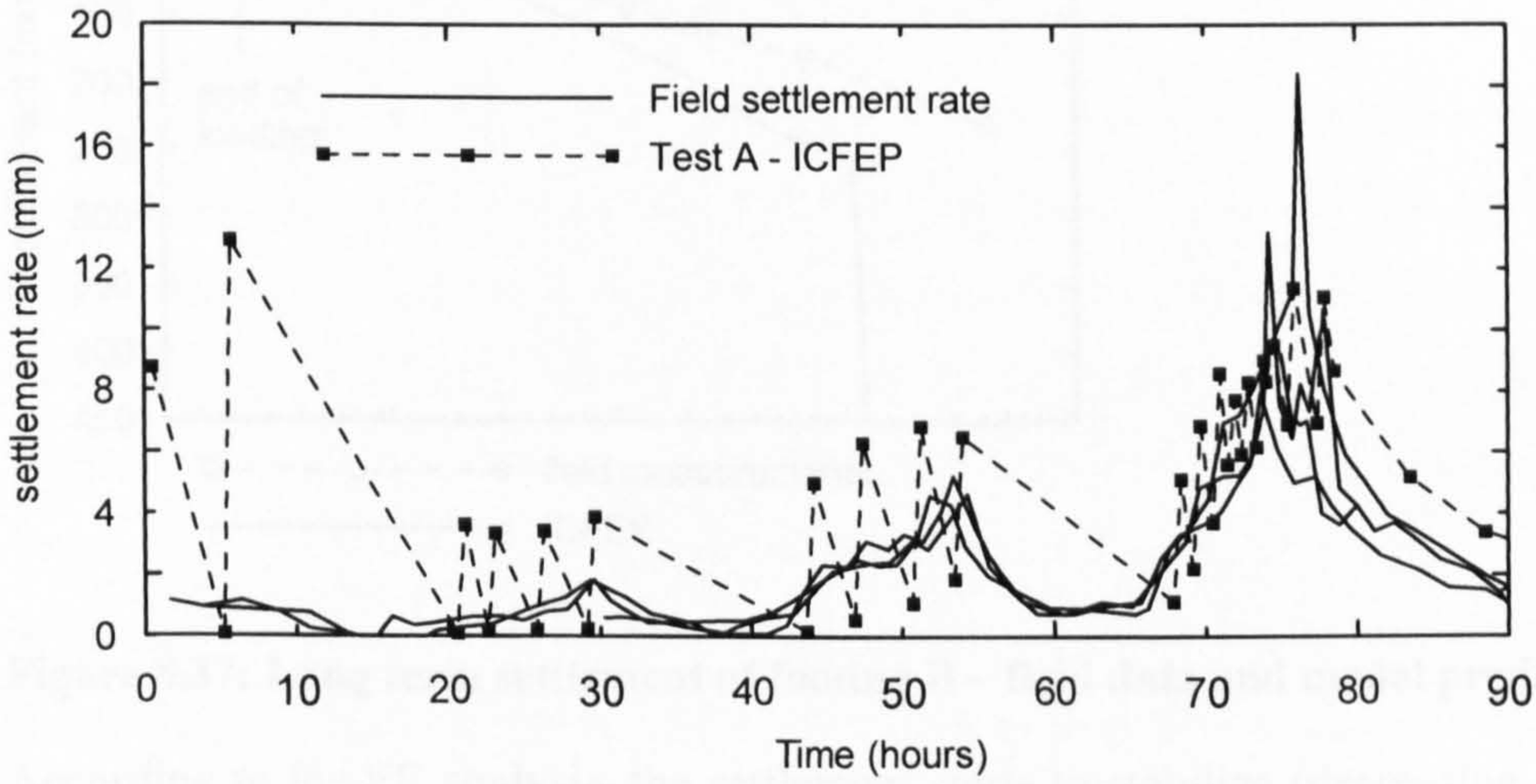

Figure 8.36: Variation of foundation settlement rate with time during test A.

The data show a wide scatter as the values vary considerably between the four targets, or footing sides, towards the end of the test due to the tilting of the footing. For example, immediately after the application of the last load increment the settlement rate is found to vary between 18 mm/h and 7 mm/h (with an average of 10.5 mm/h) depending on the target considered and during the night shift the settlement rate falls to about 1 mm/h.

Figure 8.36 includes the variation of the footing settlement rate during test A predicted by the FE analysis. The FE analysis predictions show large oscillations in particular up to t=60 hours as result of the reduced number of analysis increments, noting that each data point in Figure 8.36 corresponds to the average settlement rate over a given analysis increment. The FE analysis predicts that the settlement rate immediately after the application of the last load increment is about 11 mm/h decreasing to 2.6 mm/h at the end of the night shift. The analysis results are thought to agree well with the field data.

Figure 8.37 shows the variation of the settlement of footing B between July 1990 and July 2001, and compares the field data with the analysis predictions. The FE analysis predicts that the footing B fails during consolidation, about 1200 days after the start of the test.

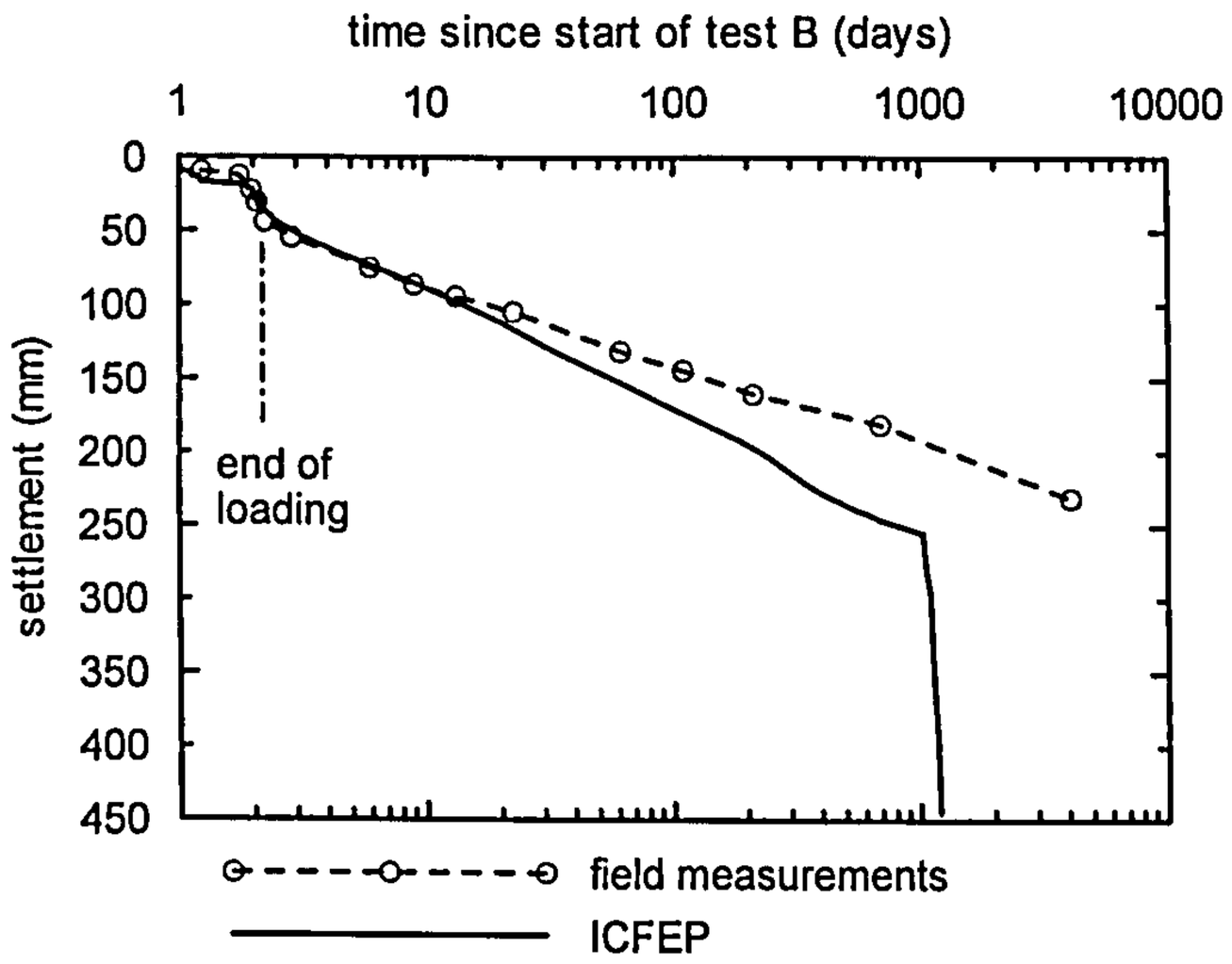

Figure 8.37: Long term settlement of footing B – field data and model predictions.

According to the FE analysis, the settlement starts to stabilize (decreasing slope of the settlement – time curve in semi-logarithmic space) between 300 and 700 days, but then

unexpectedly the footing settles a further 200 mm further between 1000 and 1200 days preceding the footing failure. Figure 8.38 shows the incremental displacement vectors at failure, which indicate a punch-through type of mechanism.

The sudden increase in the footing settlement at 1000 days and the subsequent failure can be understood by examination of Equation 8.13, which describes the change in the soil structure, p_s during the analysis.

Equation 8.13 $$\Delta p_s = -3.0 \cdot \rho_s \cdot p_s \cdot \varepsilon_d^2 \cdot \Delta\varepsilon_d$$

p_s = current increase in p'_{m0} due to structure;

$\Delta\varepsilon_d = \left|\Delta\varepsilon_x^{vp} + \Delta\varepsilon_y^{vp} + \Delta\varepsilon_z^{vp}\right|$ *Where* $\Delta\varepsilon_i^{vp}$ *is the visco-plastic strain increment in i direction;*

$$\varepsilon_d = \int_0^t \Delta\varepsilon_d$$

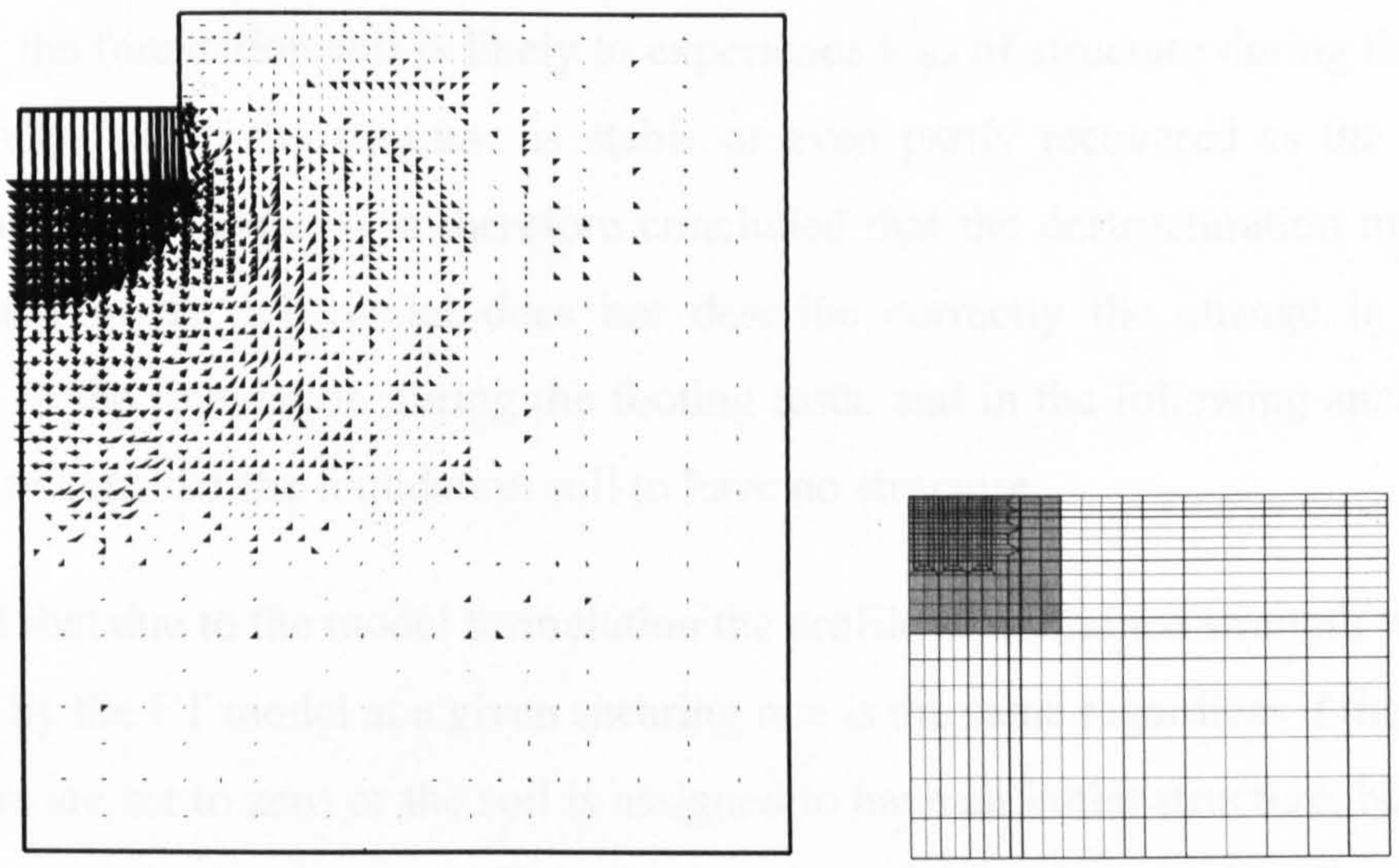

Figure 8.38: FE analysis of test B assuming soil structure - incremental displacement vectors at failure, about 1200 days after start of the test.

The change in p_s – the parameter that quantifies the current soil structure – is a function of the volumetric visco-plastic strain component only. It is noted that according to the ET model formulation, on applying a stress increment the model predicts instantaneous elastic deformations only, and the plastic deformations develop subsequently with time. In addition the foundation soil behaves quasi-undrained, at least within most of the foundation soil with the exception of a superficial layer, and most of the footing settlement at the end of loading originates from shear strains associated with the foundation yielding. Therefore in the short term, during the footing loading, the amount

of volumetric visco-plastic strains developed is likely to be relatively small, and to produce minimal or no significant change in p_s.

With time there is continuous soil deformation associated with both dissipation of the excess pore water pressure and creep. Dissipation of the excess pore water pressure generated during the footing loading is found to be mostly complete in about 200 days, and during this period the footing is found to be stable even if the predicted settlements and the settlement rate are larger than those observed in the field. The subsequent development of creep strains is thought to cause the value of the visco-plastic volumetric strain component to assume values at which there is a significant decrease in p_s, and thus loss of structure. This in turn produces exacerbated volumetric visco-plastic strains as the soil tends to the intrinsic state, and strength loss causing the footing to fail.

In reality, the foundation soil is likely to experience loss of structure during the footing loading, after which the structure is stable or even partly recovered as the soil ages under a new stress state. It is therefore concluded that the destructuration mechanism incorporated in the ET model does not describe correctly the change in structure occurring in the foundation during the footing tests, and in the following analyses it is preferred to consider the foundation soil to have no structure.

It is noted that due to the model formulation the profile of undrained strength with depth predicted by the ET model at a given shearing rate is the same regardless if the structure parameters are set to zero or the soil is assigned to have an initial structure, because the latter corresponds simply to a shift in the location of the reference time line. The fact that the soil is assigned an initial structure implies that the soil has scope for structure and consequent strength loss. Therefore, for the same set of model parameters the consideration of soil structure causes the ET model to predict that the soil, following destructuration, is weaker than the unstructured soil. The author is aware that this is in contrast with the common perception that the behaviour of a structured soil is stronger than that of the reconstituted one.

8.4.5 Analyses of the footing tests without soil structure

8.4.5.1 Footing test A

a) General load – displacement behaviour

Test A is simulated by means of an axi-symmetric coupled consolidation finite element analysis, considering the finite element mesh presented in Figure 8.22 and the model parameters defined in Section 8.4.3, with the exception of the parameters that control the soil structure and the destructuration process, p_s and ρ_s, that are set to zero The analysis simulates the excavation for the footing, the casting of the footing, and the waiting time until the start of the loading test.

A way of simulating the additional compressibility due to the loss of structure during the footing loading is to consider a higher value of λ – the slope of the reference time line. The value of λ adopted is in the upper bound of values obtained in oedometer tests on reconstituted samples of Carse Clay between 5.2 and 6.5 m depth (within geotechnical unit IV), and this value has been adopted throughout the soil profile, inclusive in the geotechnical units I to III that are expected to be stiffer. Therefore the value of λ equal to 0.24 adopted in the analyses is thought to be a good approximation to the average operational compressibility of the foundation soil.

Figure 8.39 shows the variation of applied load and footing settlement with time during test A as predicted by the FE analysis. For comparison the predictions presented in Section 8.4.4 are also included.

In a similar fashion to the analysis presented in Section 8.4.4, the FE analysis without soil structure overpredicts the footing settlement during the early stages of loading up to about 65 kPa and underpredicts at intermediate applied stresses between 75 and 120kPa, but in general the FE analysis predictions are thought to approximate well the field data, in particular when considering the average of the four settlement measurements at the mid-sides of the footing. The initial softer behaviour predicted by the FE analyses is thought to result from the adoption of an elastic bulk and shear stiffness, dependent on stress level only, that cannot reproduce the strong soil linearity at small strains.

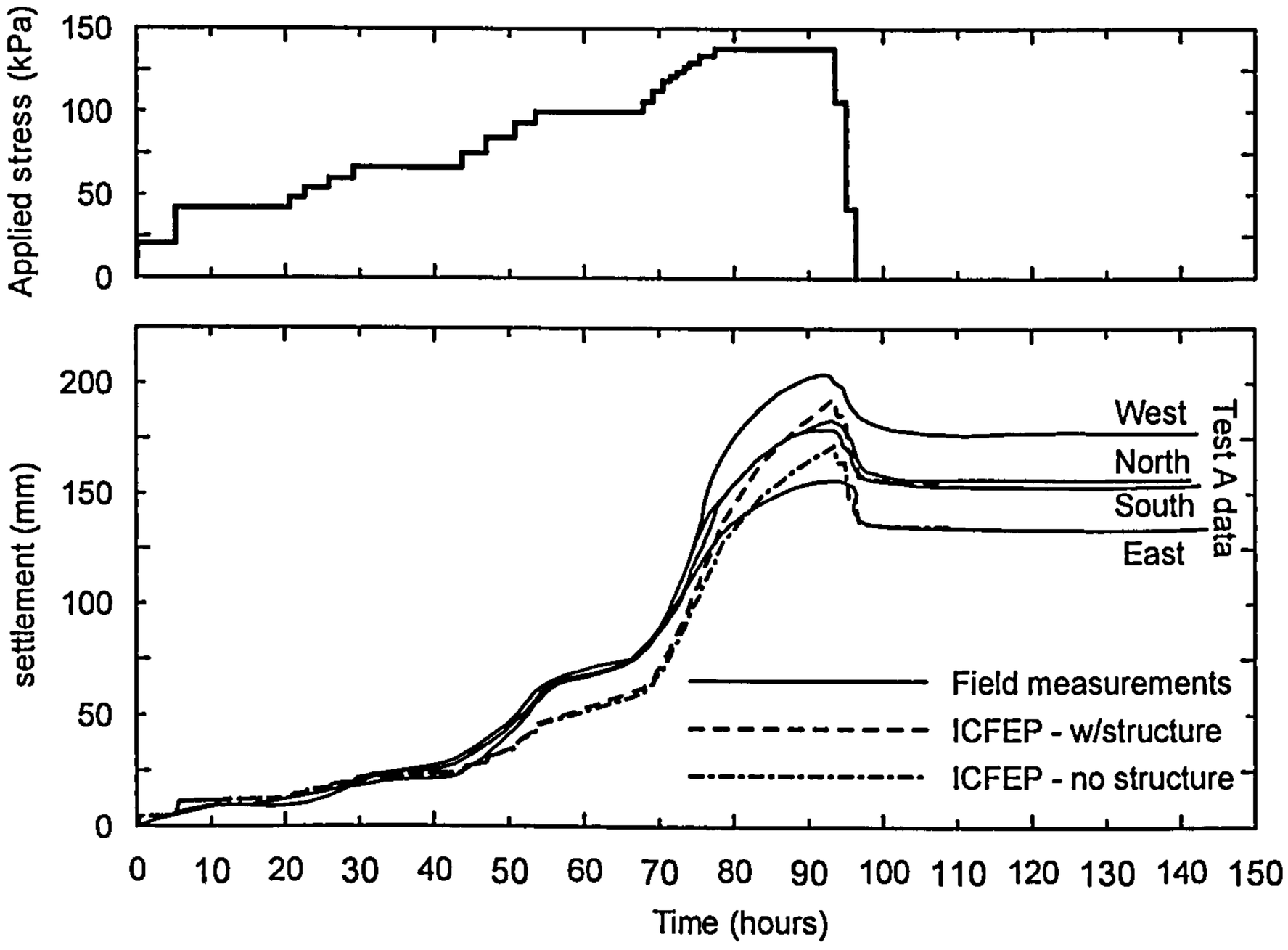

Figure 8.39: Variation of applied load and footing settlement with time during test A: field measurement and model predictions.

The variation of footing settlement with applied load predicted by both analyses is identical up to an applied stress of about 100 kPa and at failure, just before footing unloading, the consideration of soil structure accounts for an additional settlement of only 20mm, about 10% of the total footing settlement.

Figure 8.40 shows the variation of the foundation settlement rate with time, derived from the field settlement-time curves, and compares the field data with the FE analyses predictions. The consideration of soil structure in the FE analysis is found to have a minimal effect on the footing settlement rate throughout the loading test, with the analysis with structure yielding slightly higher settlement rates at the end of the test and during the night break before the footing was unloaded. As noted previously, the FE analysis yields large oscillations on the predicted footing settlement rate, in particular up to t=60 hour as a result of the reduced number of analysis increments. In any case, the agreement between the FE analysis predictions and the field data is thought to be good, particularly during the latter stages of the load test.

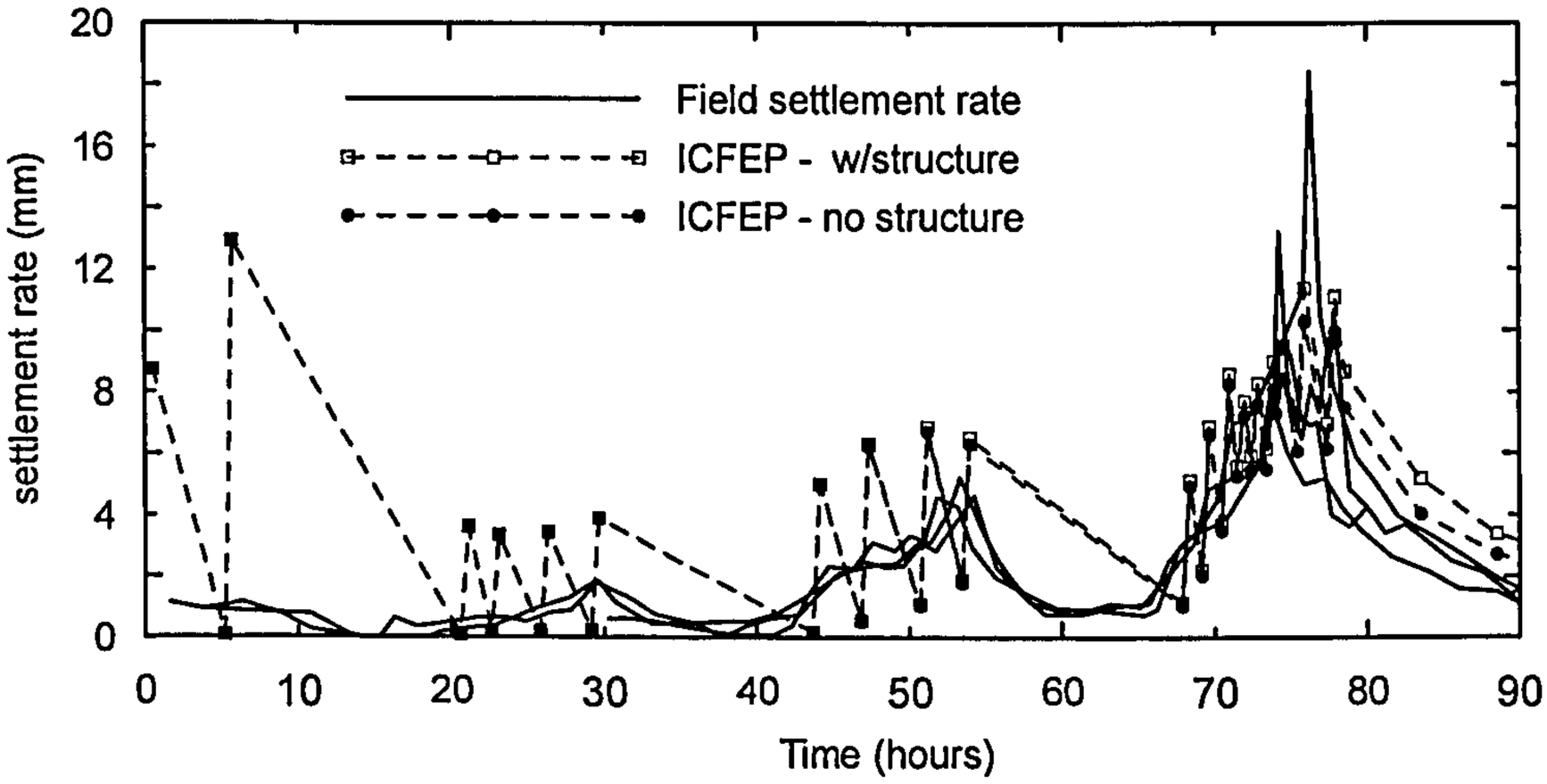

Figure 8.40: Variation of foundation settlement rate with time during test A.

Figure 8.41 shows the incremental displacement vectors occurring in the foundation soil just before the footing unloading. The FE analysis is able to reproduce a concentration of plastic deformation immediately below the footing but fails to predict a well-defined failure mechanism. In any case, the good agreement between the FE analysis and the field data in terms of the load-displacement curve and the footing settlement rates at the end of the test confirm that the FE analysis recovers well the overall behaviour of footing A.

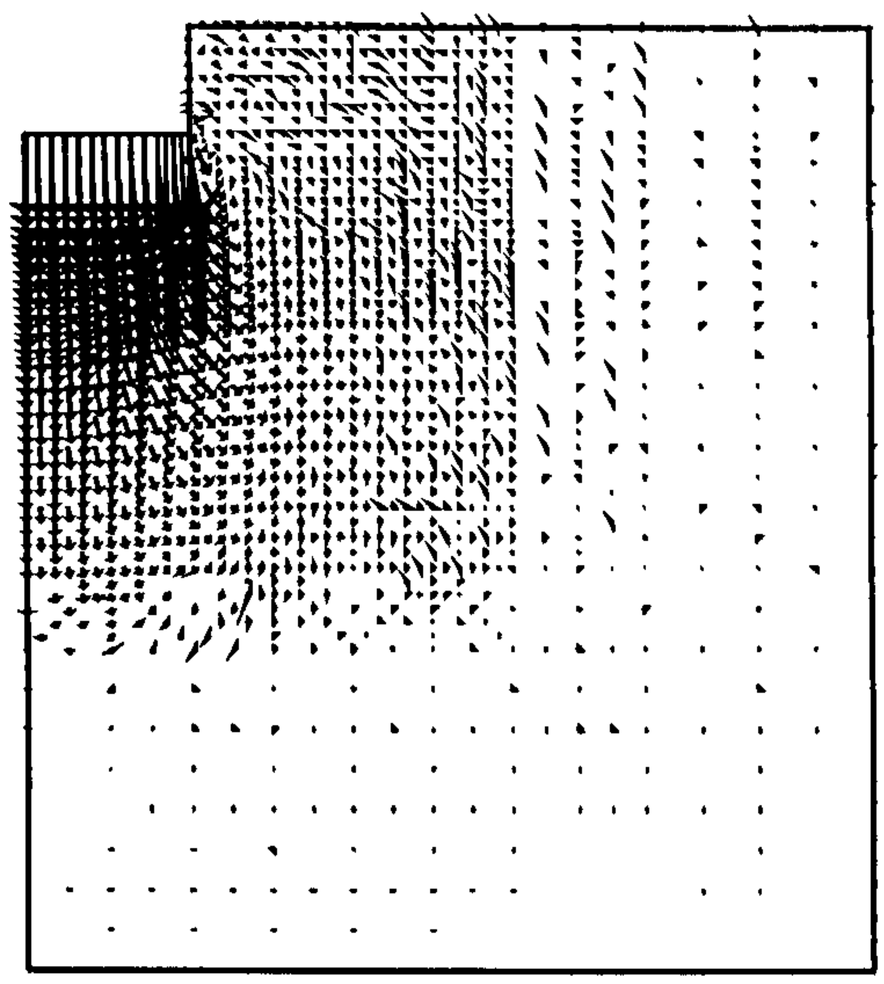

Figure 8.41: Incremental displacement vectors at failure just before the footing unloading – Test A.

b) Investigation of the failure condition of footing A

The FE analysis of test A has shown no convergence problems throughout. Therefore despite the good agreement with the field measurements in terms of the overall behaviour of the footing, it was of interest to investigate the bearing capacity predicted by the FE analysis and the shape and extent of the associated failure mechanism.

FE analyses simulating the application of further load to footing A were performed, and the respective load – settlement curves are shown in Figure 8.42. Series (a) corresponds to a coupled consolidation FE analysis during which the footing is loaded at 6 kPa/hour (a loading rate similar to that applied during hour 70 and 80, see Figure 8.39) after the last night break. The FE analysis fails to predict a well-defined failure load, and the footing is able to accommodate further loading even at very large displacements. Figure 8.43a) shows the incremental displacement vectors predicted by the FE analysis when the accumulated settlement of the footing amounted to about 800 mm.

Another analysis (not shown in Figure 8.42) was performed in which the additional load was applied immediately after the last load increment, not simulating the last night break. This analysis predicted no significant differences in the subsequent footing response, and the load-displacement curve was found to join that predicted by series (a) after 30 kPa of additional applied load.

The continuous increase of the footing bearing pressure even at very large displacements was observed in Chapter 7 when analysing strip footings using the ET constitutive model. It was postulated that this behaviour derives from the continuous soil hardening associated with the process of consolidation and the development of creep strains that occurs simultaneously with the footing loading.

In an attempt to define the footing ultimate bearing capacity an extreme situation is considered, in which the footing is further loaded after the last night break, but now under undrained conditions, such that any increase in the load carried by the footing results from the soil hardening due to the development of volumetric visco-plastic strains, only. In series (b) the footing is further loaded at 6kPa/hour and in series (c) at 12 kPa/hour. The respective load – settlement curves are shown in Figure 8.42.

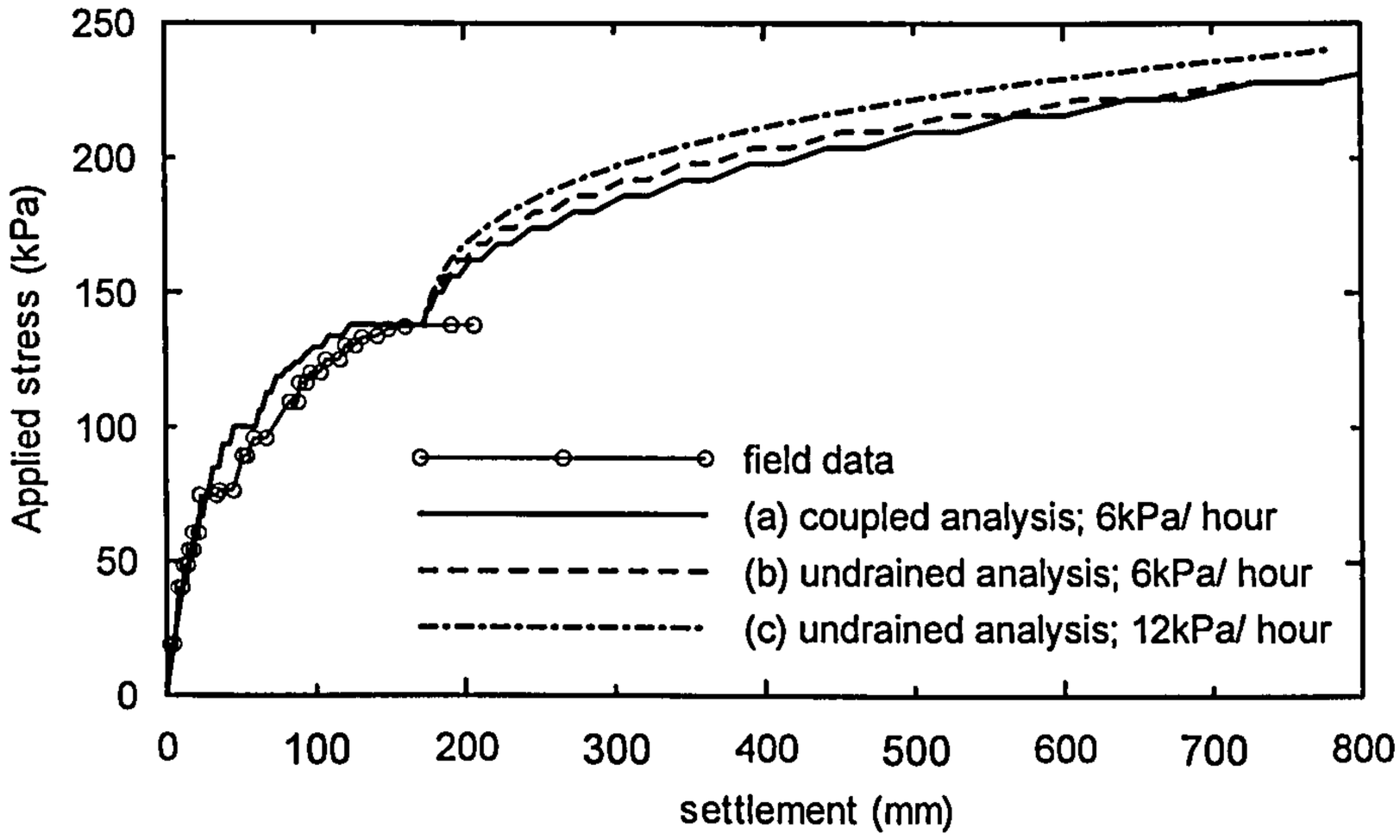

Figure 8.42: Load – displacement curves on further loading footing A.

The load-displacement curve predicted by series (b) is very similar to that predicted by series (a), with series (b) predicting a slightly larger load at the same footing settlement. This indicates that the soil hardening associated with the process of consolidation is not relevant to the observed continuous increase in the load sustained by the footing.

When in series (c) the footing is loaded under undrained conditions at double the loading rate of 12kPa/hour the resulting load-settlement curve is found to lie above the previous two, and the footing shows a stronger response. This indicates that the inability of the analyses to predict a well defined failure load results from the formulation of the ET model. As failure is approached the application of a given load increment ΔQ will produce gradually larger footing settlements, which implies an increase in the average strain rates acting in the foundation soil and so, according to the ET model formulation, an increase in the soil undrained strength is predicted. Application of a higher loading rate will result on the analyses predicting a higher undrained strength, and thus the footing is able to sustain a higher load at the same settlement value.

The continuous cycle of higher strain rate leading to higher soil undrained strength, leading back to higher strain rate is responsible for the continuous increase in the load accommodated by the footing. This is related to the fact that the ET model is not able to reproduce accelerating creep, and thus it is not possible for an increase in strain rate to occur at constant stresses.

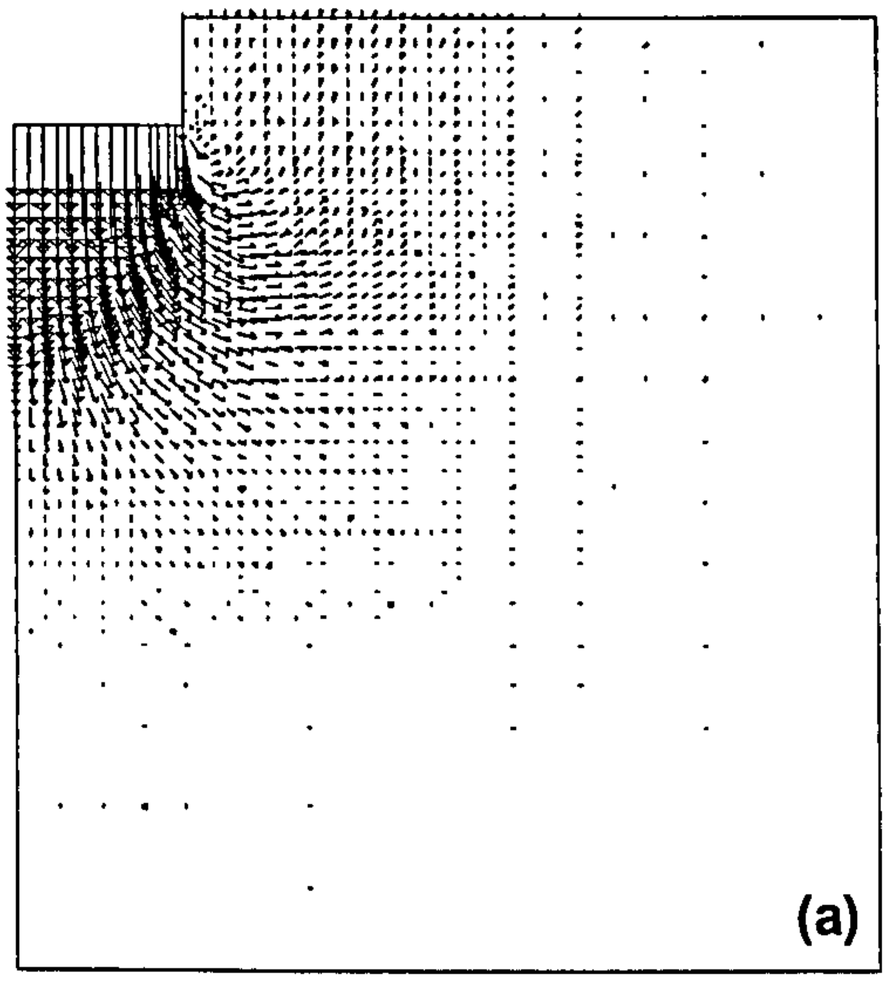

Figure 8.43: Incremental displacement vectors at large settlements predicted by a coupled consolidation FE analyses (series a).

This implies that the ET model cannot predict failure in the same way as classical plasticity theory, associated to plastic flow along a surface where the soil strength has been fully mobilized (and remains constant with further straining and time). When using the ET model, failure should be defined in a manner similar to that used in engineering practice, as a threshold value of displacement or displacement rate. However, this *serviceability type* failure condition will, in principle, be distinct for different geotechnical structures. On the other hand, the loading conditions specified in the analysis need to be comparable to those being applied to the geotechnical structure during its construction and lifetime.

In any case, it is noted that, since the ET model is unable to reproduce the post peak strength loss and it is unrealistic to consider that the peak undrained strength is mobilized simultaneously throughout the foundation soil, the average mobilized strength in the foundation in the field, at or close to the footing failure, is likely to have been substantially lower than that estimated from laboratory tests on good quality samples at peak, and which corresponds closely to that predicted by the ET model (shown in Figure 8.32).

c) Pore water pressures and radial total stresses

Figure 8.44 shows the variation of pore water pressures and radial stresses during test A as measured in the in-situ piezometers and spade cells that were installed at the footing

centreline. The piezometer PZ1A shows minimal pore water pressure changes up to the footing failure due to the high permeability of the superficial silty layers (crust). The behaviour of piezometers PZ2, PZ3 and SC1P show a very similar pattern, with modest excess pore water pressure being generated up to about 120 kPa applied load, and then, as failure is approached, the most superficial devices where larger total stress changes occur, record larger increases in pore water pressure.

The piezometer attached to the stress cell SC2 (SC2P), is only 20 cm deeper than piezometer PZ3 but registers much larger pore water pressures, right from the early stages of loading. It is not clear if this abnormal behaviour results from localized variations in the soil characteristics or a malfunction of the monitoring device. Regarding the total radial stress measurements it is noted that the spade cell SC2 registers larger increases in radial stress than spade cell SC1 located at a shallower depth. This is quite surprising, as one would expect the larger stress changes to occur at shallower depth.

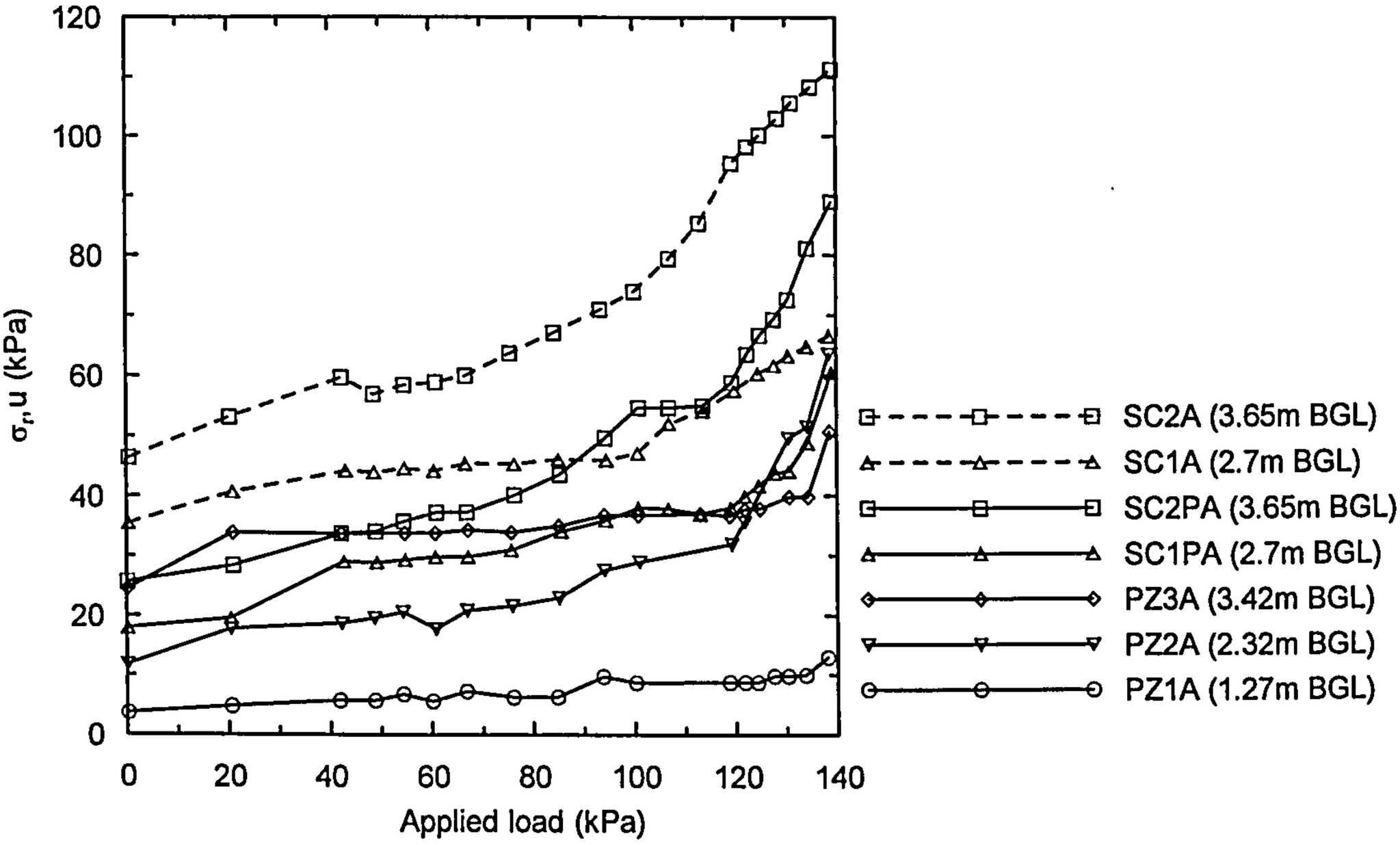

The depth of the piezometers and spade cells are from Gildea (1990). PZ = pneumatic piezometer; SC = spade cell (total radial stress reading) and when followed by P denotes the piezometer attached to the spade cell (pore pressure reading).

Figure 8.44: Variation of radial stress and pore pressure at the footing centreline during load test A – field measurements.

Figure 8.45 a) shows the variation of the pore pressure in the piezometers PZ1 PZ2 and PZ3 during test A and the analysis predictions. The FE analysis consistently overpredicts the excess pore pressure generated in the foundation. The difference between field measurements and analysis predictions decreases with the depth of the piezometer, both because the changes in total stress (and therefore the potential pore water pressure changes) are smaller and the drainage path increases.

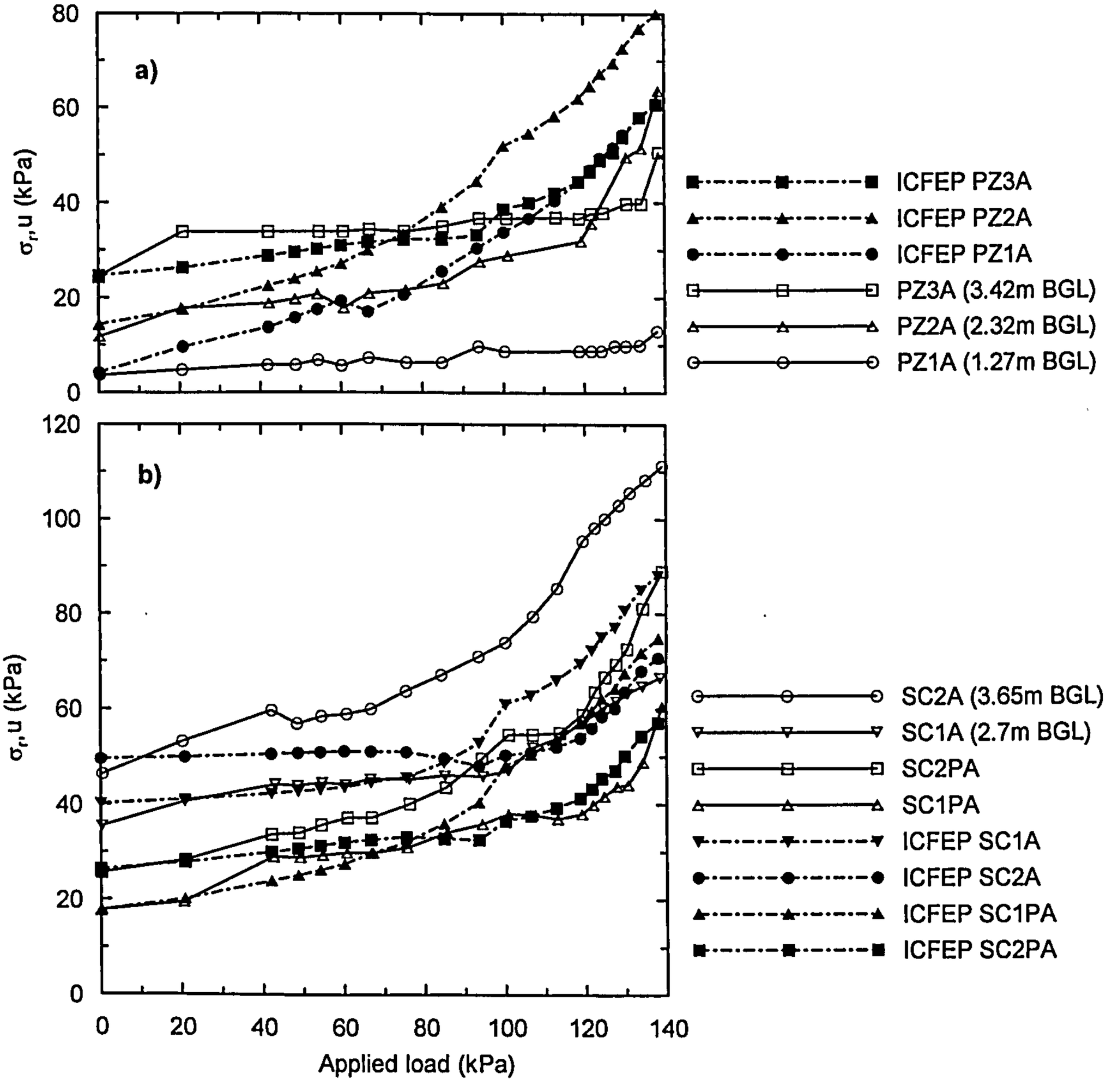

The depth of the piezometers and spade cells are from Gildea (1990). PZ = pneumatic piezometer; SC = spade cell (total radial stress reading) and when followed by P denotes the piezometer attached to the spade cell (pore pressure reading).

Figure 8.45: Variation of pore pressure and total radial stress at the footing centreline during test A: field measurements and analysis predictions.

Figure 8.45 b) shows the variation of pore pressure and total radial stress at the two spade cells during test A and the FE analysis predictions. The FE analysis predicts

reasonably well the pore pressure and total radial stresses in the spade cell SC1 up to about 80-90 kPa applied load, but it overpredicts the field measurements at larger applied loads. The FE analysis considerably under predicts the field measurements of spade cell SC2, but that is thought to result, in part at least, to its abnormal behaviour.

When comparing the FE analysis and the piezometer readings a trend can be identified that the FE analysis systematically overpredicts the excess pore pressures generated in the foundation during loading. This discrepancy is thought to derive from the adoption of lower permeability values, in the superficial layers, than those operating in the field causing the analysis to predict a response closer to undrained.

d) Centreline settlements with depth

Figure 8.46 shows the profile of settlements with depth at the footing centreline for various values of applied load during test A, and compares the field measurements with the FE analysis predictions. The FE analysis gives reasonable predictions of the settlement at the base of the footing, even if slightly lower than the field measurements, but fails to reproduce the shape of the profile of settlement with depth.

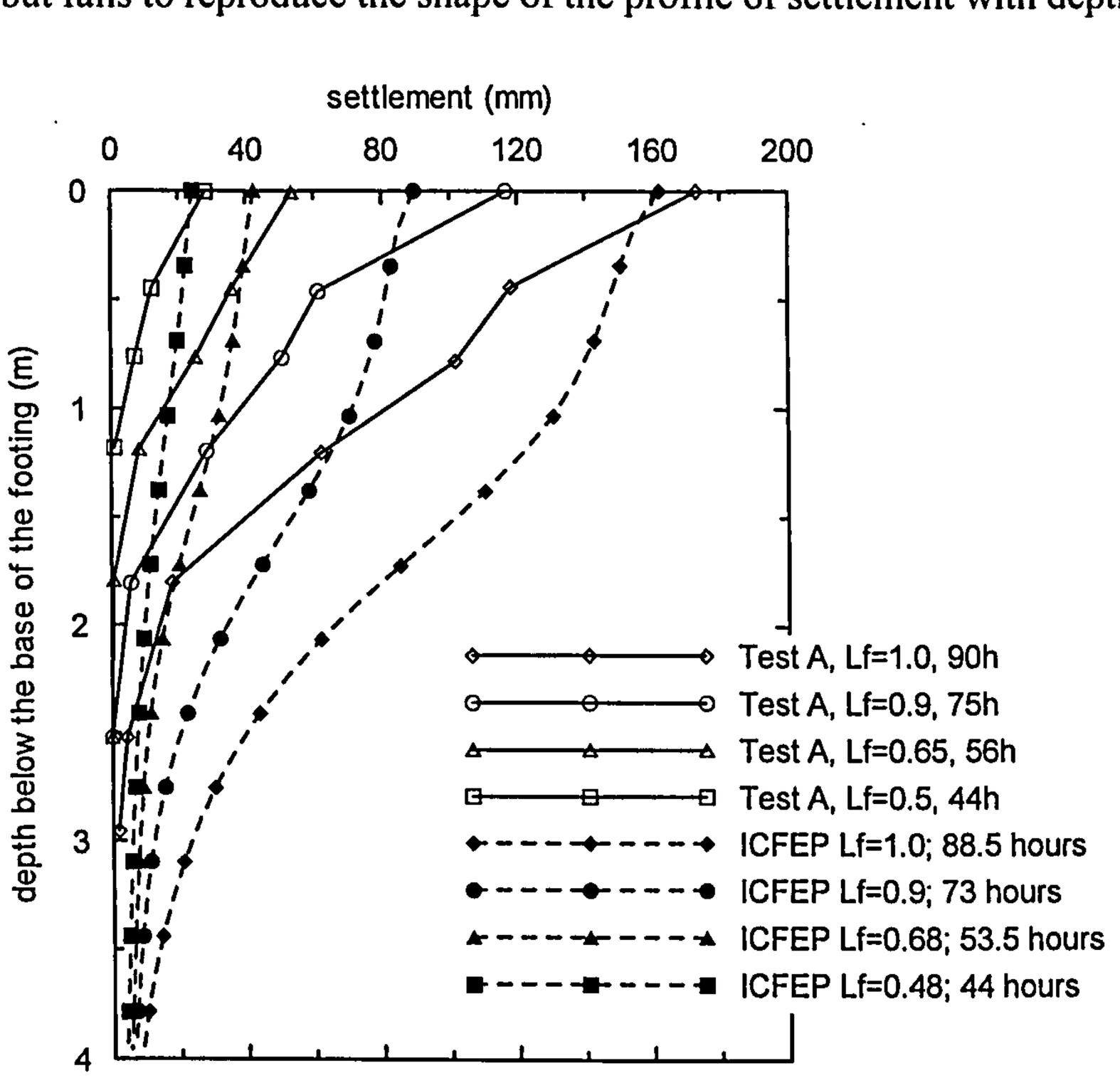

Figure 8.46: Centreline settlements during loading test A: field measurements and analysis predictions.

The settlement profile obtained from the FE analysis is much wider and extends considerably deeper than that measured in the field. This is thought to derive from the fact that the elastic part of the constitutive model adopted for the foundation soil is based on a stress dependent stiffness and cannot account for the strong soil non-linearity at small strains.

e) Ground surface settlements

Figure 8.47 shows the variation of ground settlement, δ with normalized distance from the centre of the footing, *x/D** for various values of applied load, and compares the field measurements with the analysis predictions.

The ground settlements are normalized by the maximum settlement. For the field measurements this is taken as the settlement of the footing. In the FE analysis the footing is not modelled with solid elements, instead its weight is simulated by equivalent nodal forces which are applied at the base of the footing, and the vertical side of the footing (boundary AB, see Figure 8.22) is restrained from moving in the horizontal direction and assumed to be smooth (free movement in the vertical direction). This implies that the settlement of the footing is different from that of point A (see Figure 8.22), the point at the ground surface adjacent to the footing but in the soil mass.

Figure 8.47 shows the FE results using two normalizations: (1) the settlement trough is normalized by the settlement of point A; (2) the normalization quantity is the average footing settlement, in which case the quantity δ/δ_{max} is less than unity at the edge of the footing (x/D*=0.5). When analysing the field data there wasn't this difficulty as the settlement trough around the footing was estimated on the basis of individual targets points. So the normalization (2) is thought to be the more appropriate and to be valid except for the region close to the footing (values of x/D* close to 0.5). In both cases, the settlement trough predicted by the FE is found to be wider than that in the field.

Addenbrooke et al. (1997) show the importance of incorporating the strong soil non-linearity at small strains to correctly predict the ground movements above tunnels. In particular the adoption of a linear elastic model to describe the soil behaviour at small strains is shown to produce a wider and flatter settlement trough.

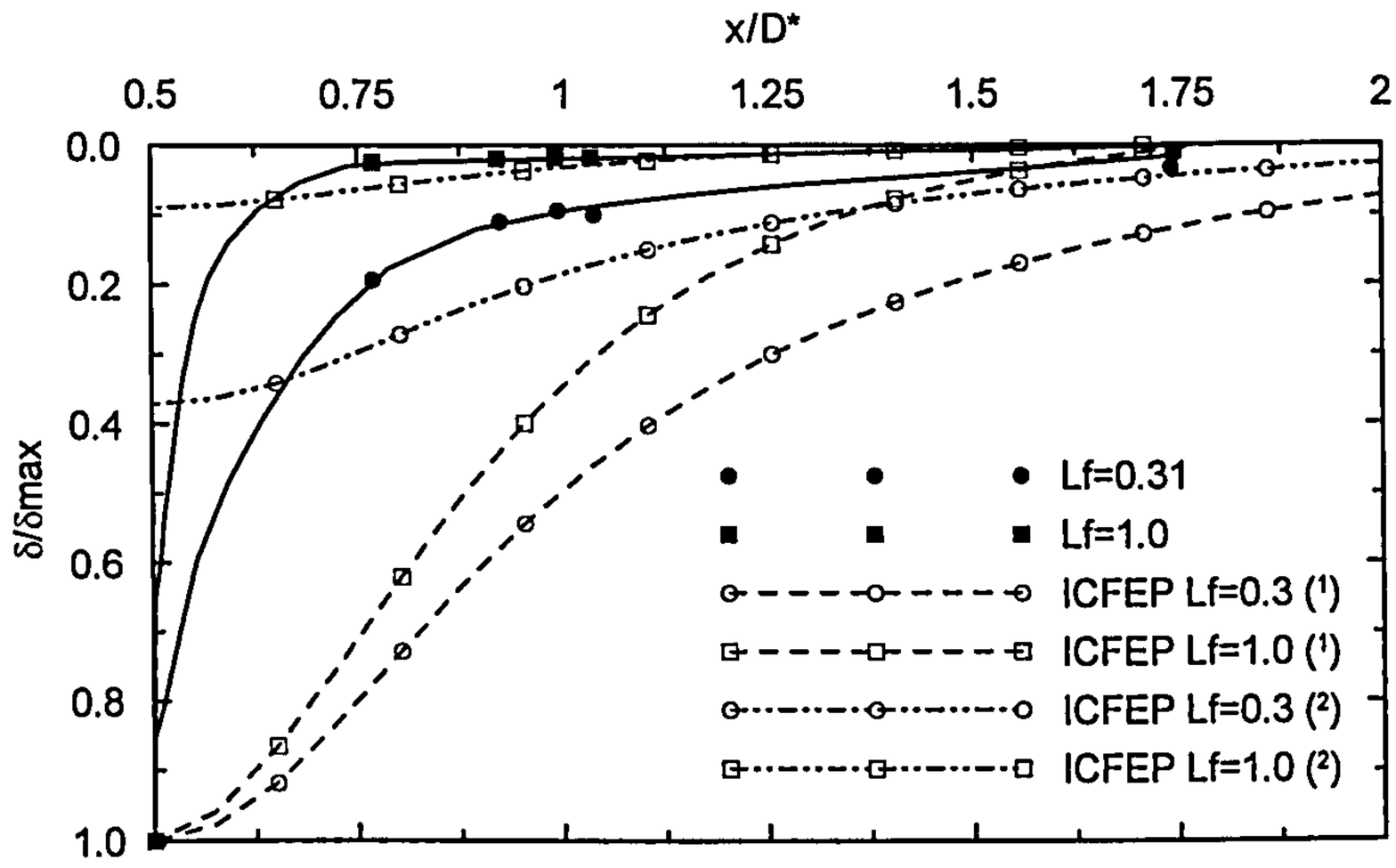

Notes: x = distance from the footing axis; D^* = equivalent diameter of the footing; δ_{max} = maximum ground settlement, in the field data taken as the settlement of the footing; δ = ground settlement at a distance x/D^*.
(1) Data are normalized by the settlement at A, the point at the ground surface adjacent to the footing but in the soil mass;
(2) Data are normalized by the average footing settlement.

Figure 8.47: Ground surface settlements during loading test A: field measurement and analysis predictions.

8.4.5.2 Footing test B

a) General load – displacement behaviour during footing loading

Test B was simulated by means of an axi-symmetric coupled consolidation FE analysis using the model parameters defined in Section 8.4.3, with the exception of the parameters that characterize the soil structure and the destructuration mechanism, p_s and ρ_s, which were set to zero. The analysis simulated the small load – unloading cycle applied to footing B at the start of the loading test to evaluate the footing and foundation soil behaviour at very small loads.

Figure 8.48 shows the variation of applied load and footing settlement with time during test B, and compares the field measurements with the FE analysis predictions. For comparison the FE analysis predictions presented in Section 8.4.4 that consider soil structure are also included. In test B, the footing is loaded up to 89 kPa, about 2/3 of the bearing capacity proven in test A and then left to consolidate. Over this load range the effect of loss of soil structure during loading is insignificant and both FE analyses provide a good match to the field data.

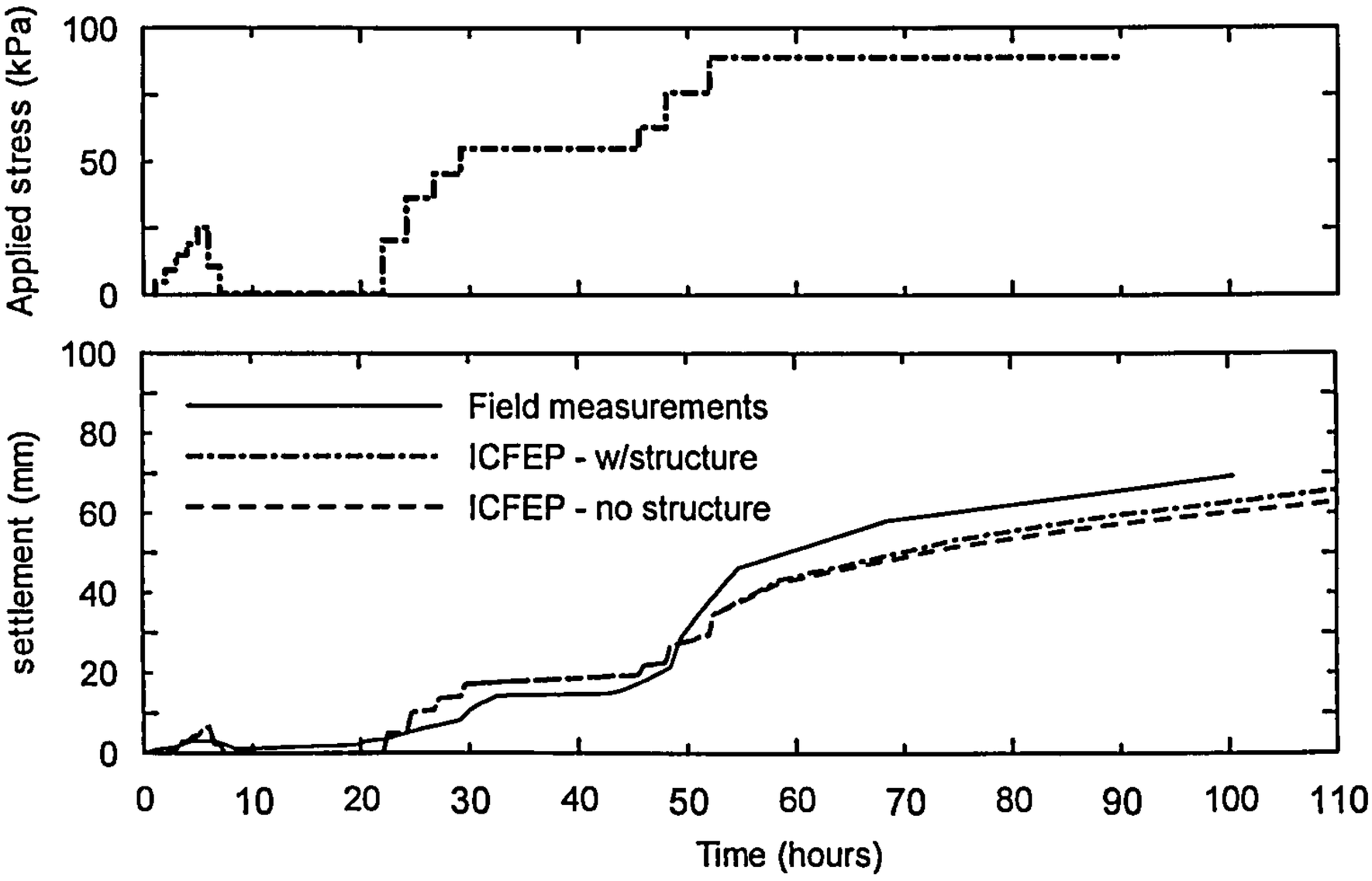

Figure 8.48: Variation of the applied load and footing settlement during test B – field measurements and model predictions.

Figure 8.49 shows the variation of footing settlement with applied load during tests A and B. The general load – settlement behaviour of tests A and B during loading is similar, and as a result what has previously been noted for test A is applicable to test B at the same load factor, L_f values. Consequently, when presenting the results of the FE analysis of test B particular attention is given to the long-term behaviour.

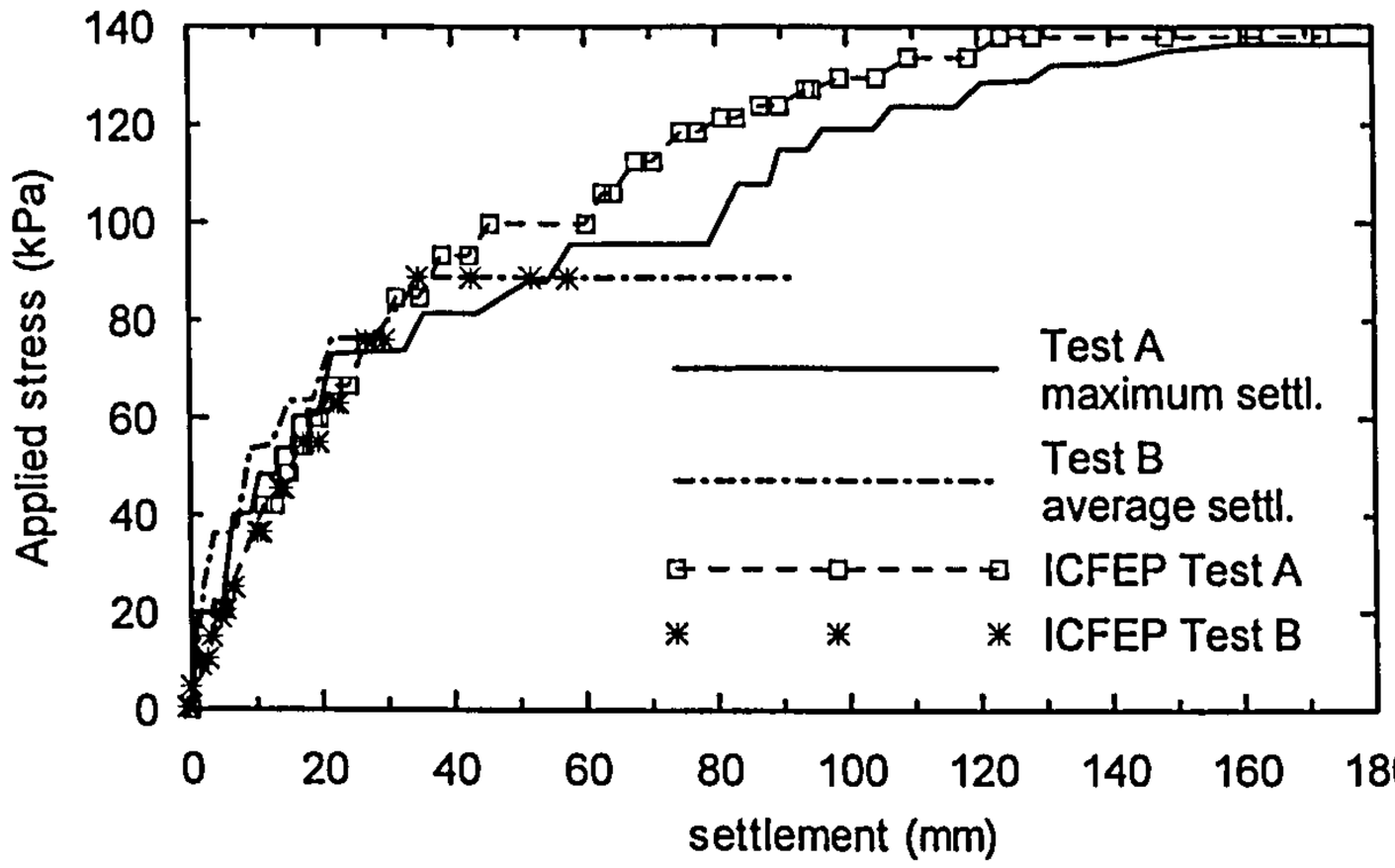

Figure 8.49: Applied load versus footing settlement during test A and B.

b) Long-term settlements

From the *settlement-time curve* it is not possible to identify a period of primary consolidation (or pore water pressure dissipation), and the curve of footing settlement with time (in semi-logarithmic space) shows a fairly constant slope throughout. From about 60 days on, the field data shows a slight tendency for the settlement rate to decrease, which is well recovered by the FE analysis. The last two readings are over 9 years apart and the Bothkennar research site was abandoned for most of that period, therefore the last field reading, that deviates considerably from the trend, should be treated with caution.

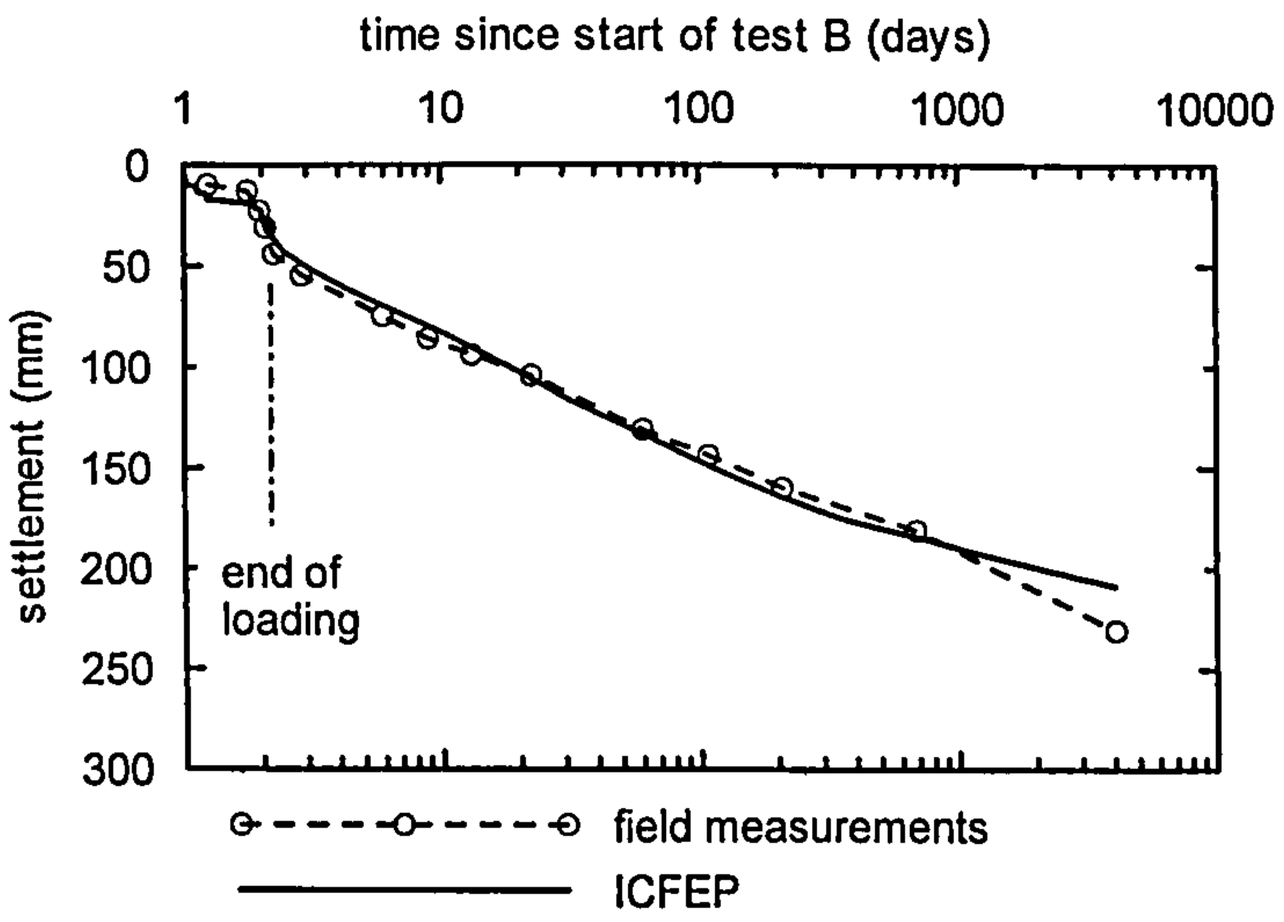

Figure 8.50: Long term settlements of footing B.

c) Pore water pressures in the foundation

Figure 8.51 shows the variation of pore water pressure and total radial stress in the foundation soil, from the end of loading until the Bothkennar site was decommissioned nearly two years later, recorded by the pneumatic piezometers and spade cells installed in the foundation on the footing axis. According to the field measurements most of the excess pore water pressure dissipation took place within the first 1000 hours (about 42 days), and full dissipation after about 10000 hours.

At the end of the monitoring period when the pore water pressure readings are stable there are still discrepancies between the field measurements and the FE analysis data. The equilibrium pore water pressures of the FE analysis correspond to a hydrostatic profile with the ground water level at 0.9 m depth. The differences in relation to the

field data may derive from seasonal variations of the ground water level (which is unlikely to affect the piezometers at depth) or calibration errors of the instruments.

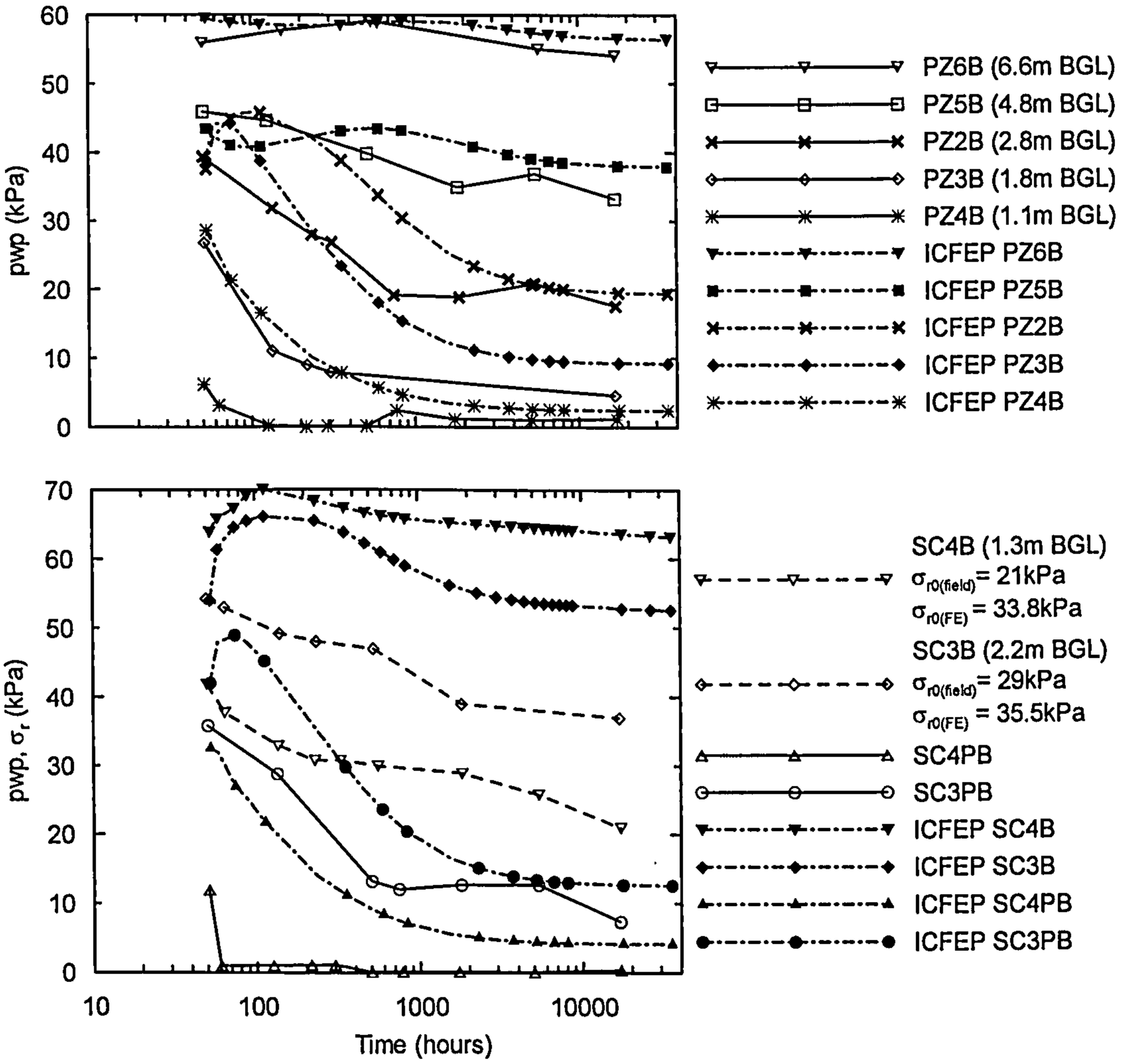

Note: The depth of the piezometers and spade cells are only approximate, they are extrapolated from Figure 8.16. Values of $\sigma_{r0(field)}$ were taken from Jardine et al. (1995)

Figure 8.51: Variation of the pore water pressures and total radial stress in the foundation soil at the footing axis, since the end of test B until the site was decommissioned.

Therefore comparisons between the field data and the FE analysis predictions should be done in terms of excess pore pressure, assuming the equilibrium value to be that obtained at the end of the monitoring period. Figure 8.52 presents the data of Figure 8.51 in terms of excess pore water pressure and changes in radial stress in relation to the stresses in repose, prior to the footing loading.

Two opposite factors influence the amount of excess pore water pressure generated at the end of the footing loading, at a certain depth. At shallow depth there are larger total

stress changes and therefore the potential pore pressure changes are larger. However a soil element located at shallower depth is closer to the drainage boundary, and the field data shows that the soil at shallow depth behaved nearly in a drained manner suggesting that at that level the soil is quite permeable. It is noted that according to the piezometer readings the time for excess pore pressure dissipation increased with depth i.e. with the distance from the drainage boundary.

Piezometer PZ6, located about 6.6 m below ground level, indicates that the excess pore pressure generated at this depth are minimal and this is recovered by the FE analysis. According to Jardine et al. (1986), the change in vertical total stress at this depth (z/D*= 2.1) is less than 10% and the change in radial total stress is practically insignificant.

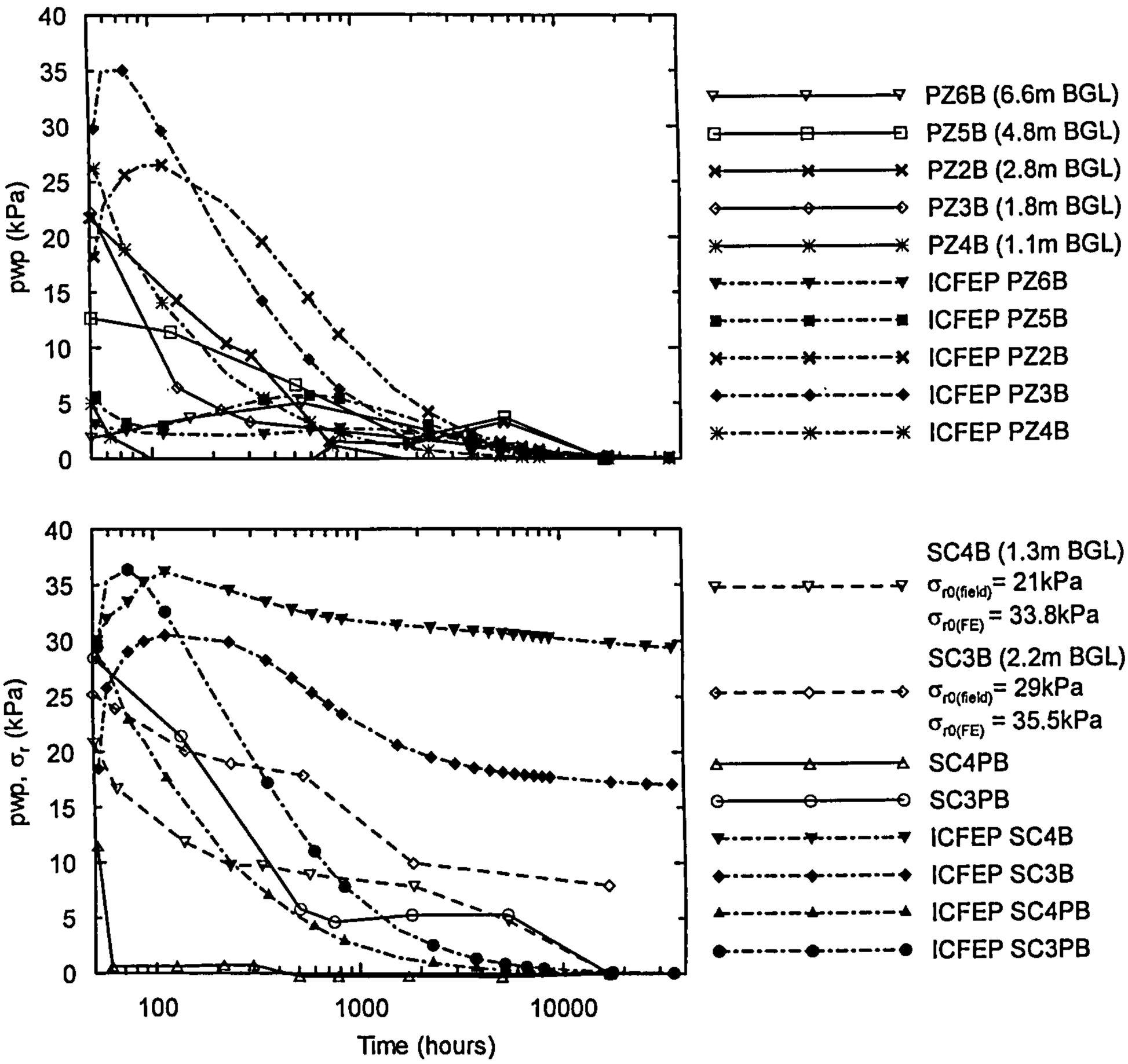

Note: The depth of the piezometers and spade cells are only approximate, they are extrapolated from Figure 8.16. Values of $\sigma_{r0(field)}$ were taken from Jardine et al. (1995)

Figure 8.52: Incremental pore water pressures and total radial stress in the foundation soil at the footing axis, since the end of test B until the site was decommissioned.

Piezometer PZ5 (4.8 m BGL) registers about 12 kPa of excess pore pressure at the end of loading, a value that is underestimated by the FE analysis. In piezometers PZ2 and PZ3 the excesses pore pressure at the end of loading are identical and around 22 kPa. In piezometer SC3PB (2.2 m BGL), the excess pore pressure is the highest and about 28 kPa at the end of loading. In piezometers PZ4 and SC4PB, the excess pore pressure at the end of loading are minimal, being dominated by the relatively high permeability at that level and the closeness to the drainage boundary.

The FE analysis systematically overestimates the excess pore pressure at the end of loading in the piezometers located in the top 2.5 m, the difference being larger at shallower depth. This can be better appreciated in Figure 8.53, which shows the profile of excess pore pressures (normalized by the applied load, equal to 89 kPa) with depth at the footing axis, at the end of loading and at two instants during the consolidation period.

The FE analysis predicts that the time for the dissipation of most of the excess pore water pressure is between 4000 and 5000 hours, about 4 to 5 times longer than in-situ. It is apparent that the FE analysis predicts the foundation soil response to be *more undrained* than that observed in the field.

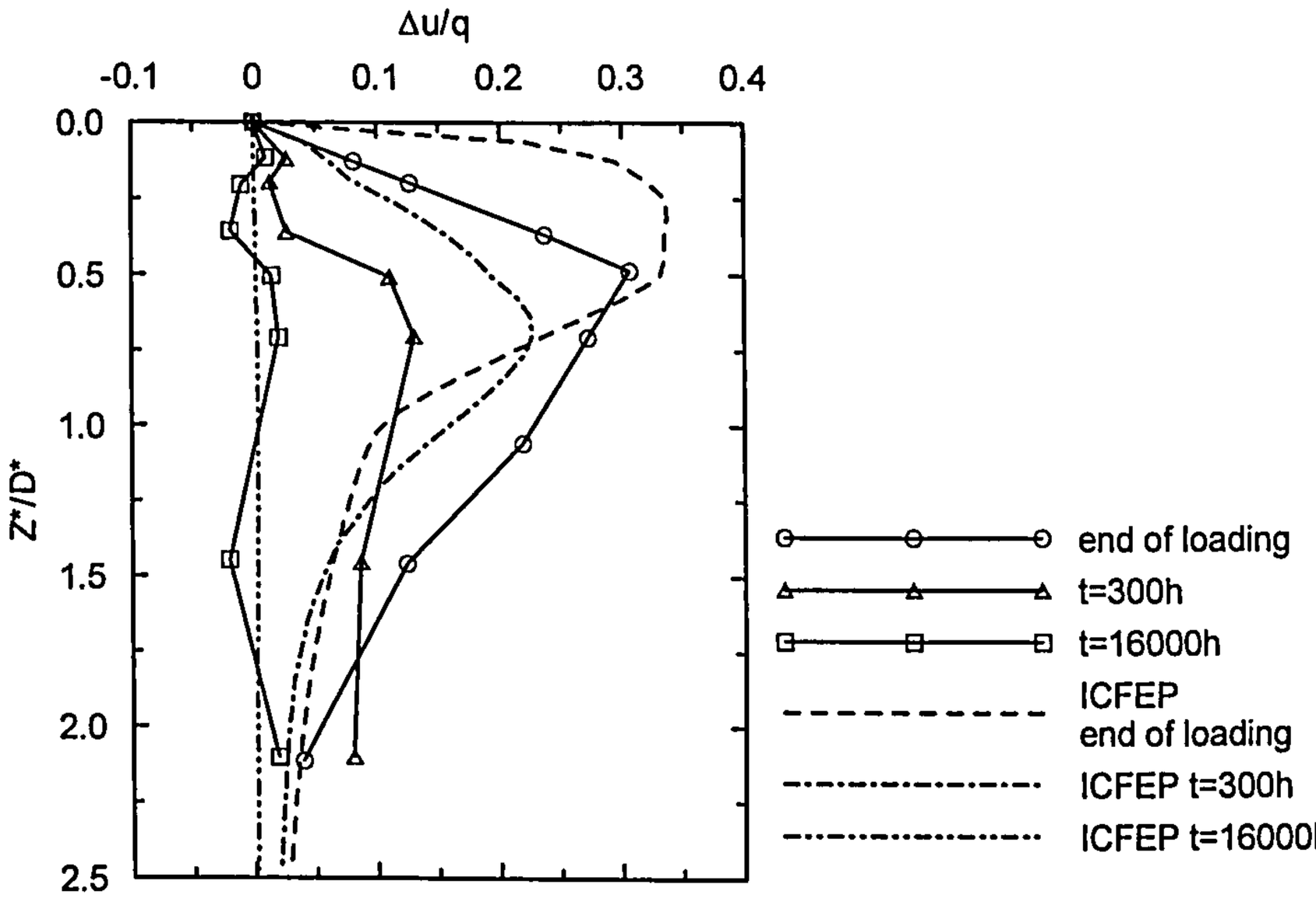

Notes: Z= depth below the base of the footing; D*= 2.71m = equivalent diameter.*

Figure 8.53: Profile of excess pore pressure with depth during consolidation – test B.

Further evidence of the exacerbated undrained conditions produced by the FE analysis are the predictions for piezometers PZ2, PZ3 and SC3PB (and to a lesser degree PZ5) that show a time delay between the end of loading and the occurrence of the maximum excess pore water pressure. This phenomenon, known as the Mandel – Cryer effect, has been reported by several authors to occur e.g. under embankments on soft soil. Mandel (1953) and Cryer (1963) have shown that when consolidation is governed by the Biot equations, it is possible for a rise in pore pressure to occur, above that set up by the loading, before the subsequent decay, in a soil element away from the drainage boundary, where undrained conditions prevail. As discussed in Chapter 6 the consideration of the time dependent nature of soils may aggravate this effect.

Comparison of the field data and the FE analysis prediction suggests that the in-situ operational permeability, up to about 5 m depth, was much higher than that used in the FE analysis. The permeability value adopted for the Carse Clay is in the upper bound of values obtained from laboratory and in-situ tests, and an increase in relation to this value may be attributed to the local occurrence of silty layers or other geological features not intercepted in the measurements mentioned above. However it is recognized that no measurements were available within the modern tidal deposits and the superficial weathered Carse Clay and the values of permeability for units I to III had to be set based on experience with similar materials.

d) Radial total stresses in the foundation

Regarding the radial total stress data, it should be noted that the interpretation of spade cell data is complex. In particular, the coefficient of earth pressures at rest, K_0 is very difficult to measure resulting in uncertainties in the values of (initial) radial stress at rest. The profile of the coefficient of earth pressures at rest used in the FE analysis is based on in-situ test data (obtained from dilatometer tests, self-boring pressumeter tests and spade cells) and simultaneously it is defined in such way as to produce, in conjunction with the remaining model parameters, an appropriate undrained strength profile. The initial total radial stresses assumed in the field measurements and in the FE analysis are therefore in general different and they are indicated in Figure 8.51.

At the end of loading, the field data gives an increase in total radial stress of about 19 and 25 kPa, in spade cell SC4B and SC3B, respectively. However, the values of total

radial stress are found to reduce during the consolidation period reaching values of total radial stress change (in relation to the value at rest) of about 0 kPa and 8 kPa, at SC4B and SC3B, respectively. These values are thought to be very low for the load values being applied to the footing and the depth of the spade cells.

At the end of loading, the FE analysis predicts an increase in total radial stress of about 30 and 18.5 kPa, at SC4B and SC3B respectively. During the consolidation period the radial total stresses are predicted to increase before converging again to a value close to that at the end of loading. This behaviour is associated with the Mandel-Cryer effect mentioned previously, with a larger additional increase in total radial stress being predicted at SC3B because it is further way from the drainage boundary.

e) Horizontal movements in the foundation soil

Figure 8.54 shows profiles of horizontal movements within the foundation during test B and the consolidation period, registered by the inclinometers I1 and I2. Comparison of the data from the two inclinometers demonstrates the accentuated tilt of the footing that developed from the early stages of loading, with horizontal movements being much smaller in inclinometer I1 than I2, at comparable times.

Figure 8.54 also includes the FE analysis predictions, which are taken at the vertical profile passing through the edge of the footing. The FE analysis predictions give a good match to the maximum horizontal displacement, overpredicting the measurements at I1 and underpredicting those at I2. However, when considering the whole profile of horizontal movements with depth there are significant discrepancies between the FE analysis and the field measurements.

It is recognized that the location of the profile adopted to take the FE analysis predictions does not exactly match the location of the inclinometers that are at a finite distance from the footing. In this respect, it is noted that all the profiles of horizontal movements predicted by the FE analysis have a common point, with zero movement at z=0.8 m, because of the displacement condition imposed at the base of the footing.

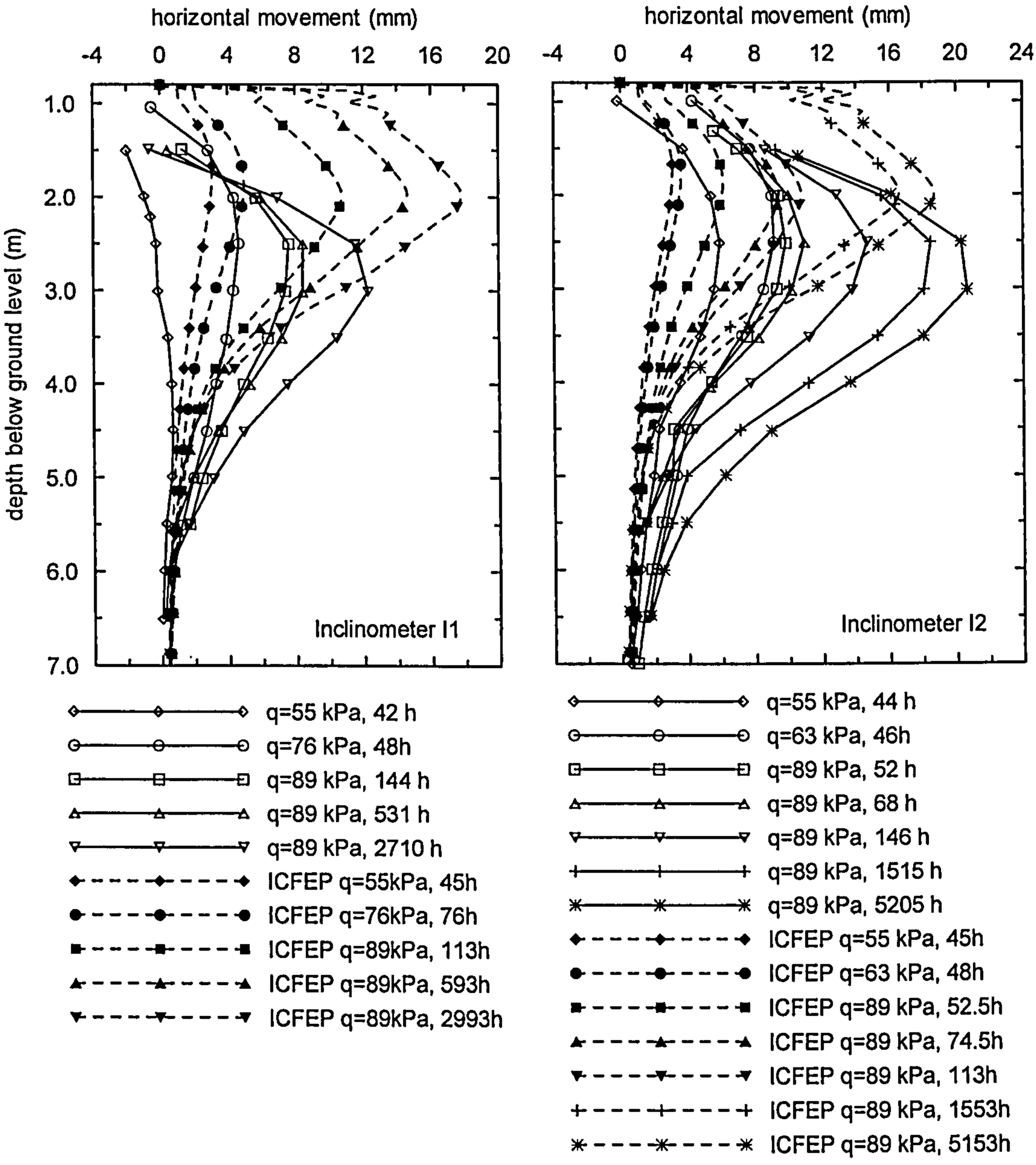

Note: the graphs are at the same scale.

Figure 8.54: Horizontal movements in the foundation at inclinometer I1 and I2 during test B and consolidation.

In general terms it can be said that the bulb of horizontal movements predicted by the FE analysis is shallower than that recovered from the field measurements. The field measurements indicate that the horizontal movements increase steadily from a modest value (in general non zero) below the footing up to about 3 m BGL where they reach their maximum. Below 3 m BGL, the horizontal movements decrease becoming almost insignificant (less than 4 mm) at about 4 m BGL during loading and at about 5.5 m BGL during the latter stages of consolidation.

In contrast, the profile of horizontal movements given by the FE analysis is characterized by large horizontal movements (about 2/3 of the maximum) just 20 mm below the footing and the maximum occurs at about 2 m BGL. The movements become almost insignificant below 3 m BGL during loading and below about 4 m during the latter stages of consolidation.

It has been shown in Figure 8.53 that the FE analysis considerably overpredicts the excess pore water pressures generated during loading in the top 2.5 m (Z*/D* of about 0.7) of the foundation, which is thought to result from considering a permeability lower than that in-situ. Despite the undrained conditions prevalent below 2.5 m up to about 5 m, and demonstrated by the pore pressure predictions (accentuated Mandel-Cryer effect), the FE analysis considerably underestimates the excess pore pressure generated at this level. Examining together the data on radial stress, pore pressures and horizontal displacements it seems that the relatively low excess pore pressures generated between 2.5 and 6.0 m reflect in fact smaller total stress changes. The FE analysis seems to concentrate most of the stress changes in the top 3.5 m, and the critical horizon is identified to be about 2.0 m BGL, corresponding to the larger excess pore pressure and horizontal movements.

The field data indicates significant stress changes up to about 4.5 to 5.0 m BGL and the maximum horizontal movement is at about 3.0 m BGL perhaps indicating the location of a pre-failure mechanism. Examining the profile of undrained strength predicted by the ET model in Figure 8.32 the minimum value of undrained strength is predicted to occur between 2.5 and 3.0 m depth. However the gradient of the undrained strength is quite small between 2 and 3 m, and this may cause the failure mechanism associated with the lowest resistance to pass about 2.0 m BGL. In addition, the ET model does not recover the post peak strength loss, which while it would be minimal in the materials that constitute the modern tidal deposits and the superficial weathered Carse Clay, it is expected to be important in the competent unweathered soft Carse Clay. The post peak strength loss may cause the weakest horizon to move deeper and to about 3.0 m BGL.

f) Centreline settlements

Figure 8.55 shows the profile of settlements with depth at the footing axis, for two values of applied load, for test A and B, demonstrating that despite the accentuated

tilting of footing B from the early stages of loading the behaviour of test A and B during loading is still comparable. Figure 8.55 also includes the FE analysis predictions for test B, that are found to give a good match for the settlement at the base of the footing but fail to recover the distribution of settlements with depth.

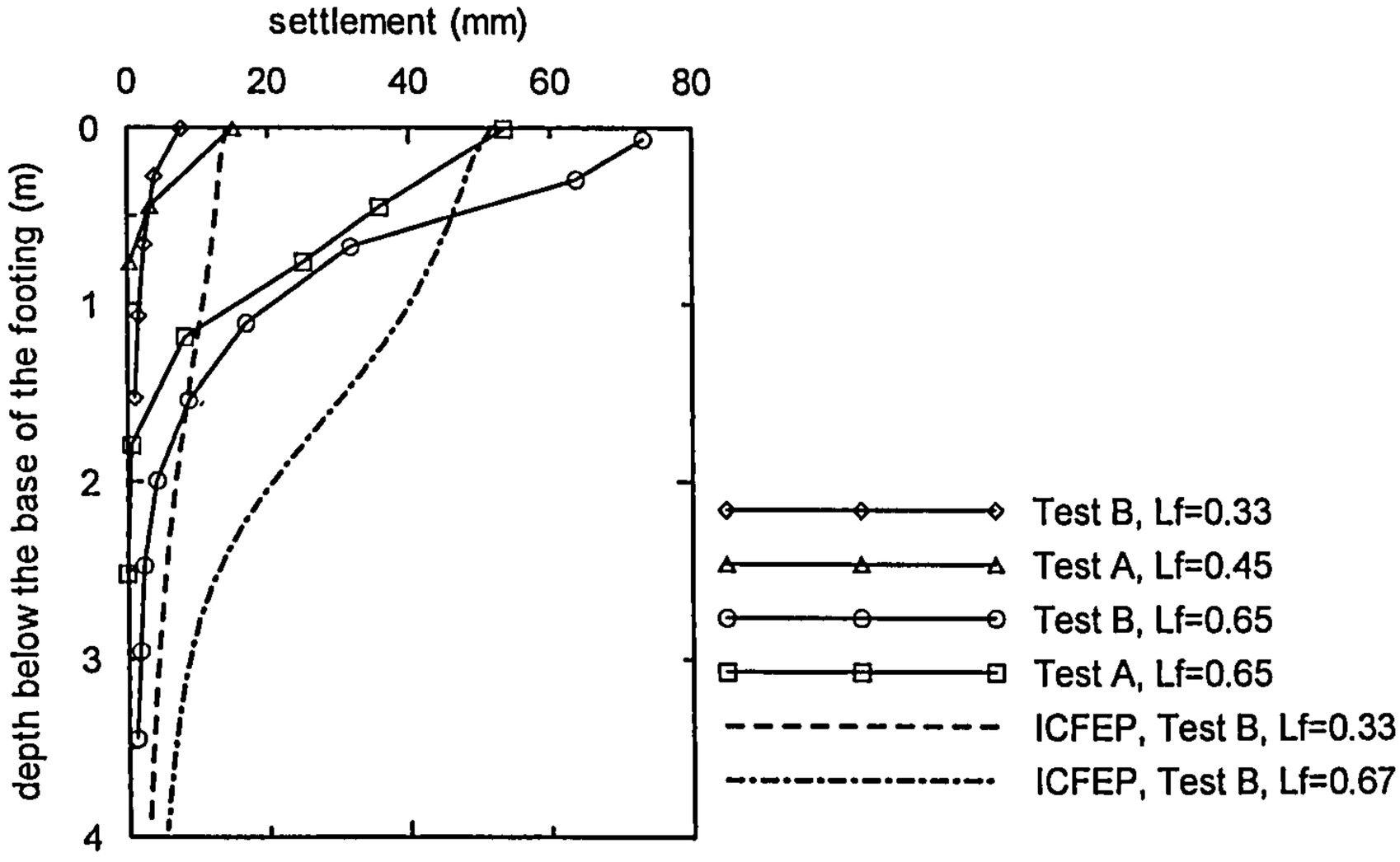

Figure 8.55: Profile of settlements with depth at the footing axis during loading – comparison between test A and B.

The profile obtained from the FE analysis is wider and extends significantly deeper than that measured in the field. As discussed when presenting the data for test A, this is thought to result mainly from the fact that the elastic part of the ET model is based on a stress dependent stiffness and cannot account for the strong soil non-linearity at small strains. Therefore the FE analysis is expected to diverge from the field measurements particularly within the zones of the foundation that have undergone small stress changes, in which the soil behaviour is dominated by the elastic component.

Figure 8.56 shows the profile of settlements with depth at the footing axis since the end of loading and during the consolidation period, for about 210 days, and compares the field measurements with the FE analysis predictions. Again the FE analysis is able to give a good prediction of the settlement at the base of the footing but cannot recover the shape of the settlement profile with depth.

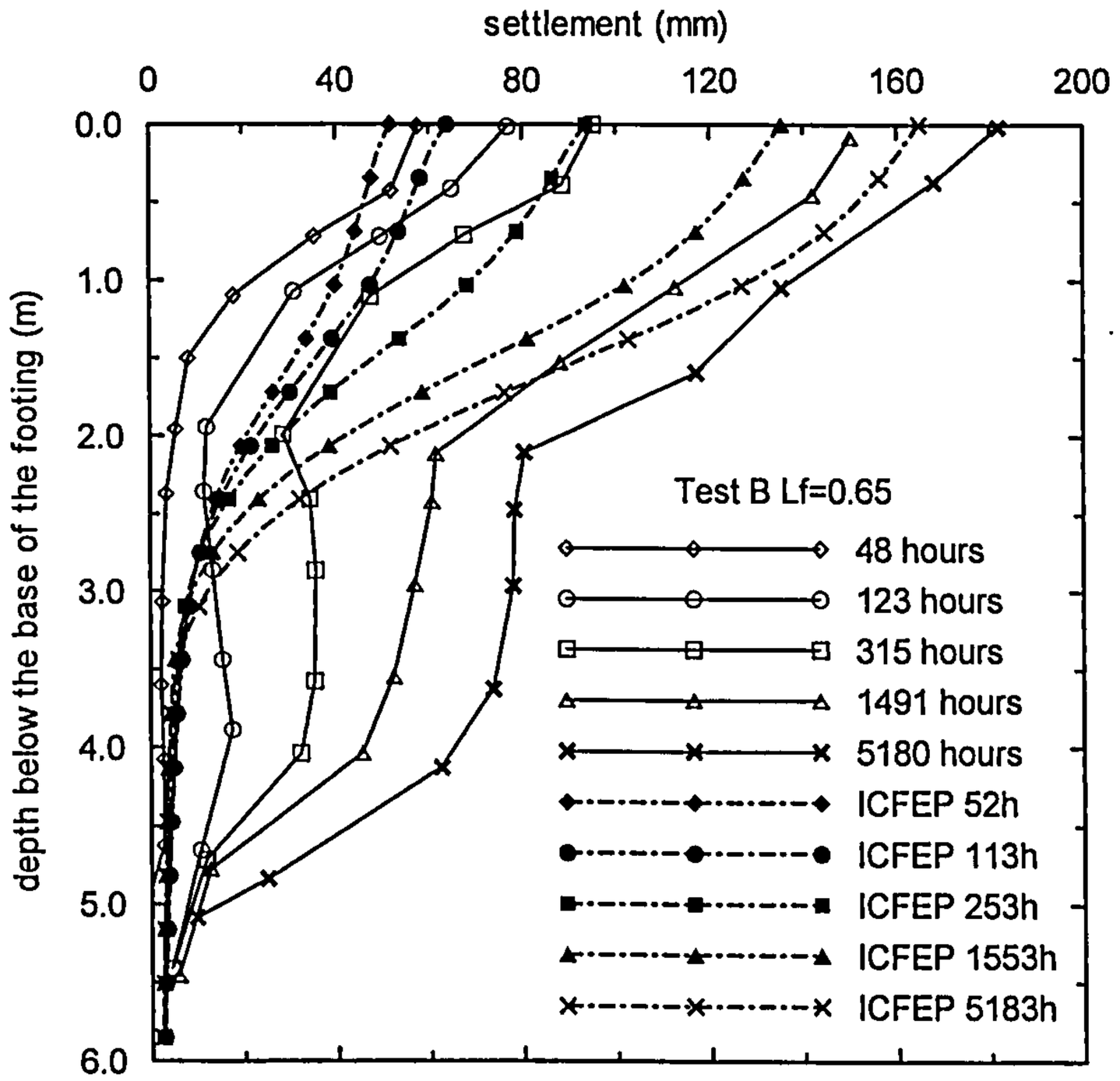

Figure 8.56: Profile of settlement with depth at the footing axis during consolidation – test B.

The field measurements indicate that during loading the settlements are almost insignificant below Z*=1.5 to Z*= 2.0 m, where Z* is the depth below the base of the footing. In contrast during the consolidation period most of the additional settlement occurs between Z*= 2.5 m and Z*=5 m, contributing at the end of the monitoring period about 80 mm, about 44% of the total settlement at the ground surface.

The FE analysis is not able to recover this behaviour and predicts minor settlements below Z*=3 m. In the FE analysis, the same model parameters are used throughout the profile; in contrast the field measurements indicate that most of the delayed settlement occurred below Z*=2 m and therefore it would be relevant to adopt distinct parameters for the superficial units I to III especially those which control the time dependent behaviour and stiffness. It is noted that the predicted response is consistent with the observation that the FE analysis predicts minimal stress changes below 3 m BGL and therefore there is little scope for the development of delayed settlements.

8.4.5.3 Footing test C

a) General load – displacement behaviour

Test C corresponds to the loading to failure of footing B in July 2001, which had been under maintained load since July 1990. Test C was simulated by means of an axi-symmetric coupled consolidation finite element analysis using the same finite element mesh and model parameters employed in the analysis of test B described in Section 8.4.5.2.

The initial conditions for test C is the stress – strain distribution obtained in the analysis of Test B at the end of the consolidation period. The FE analysis simulates the unloading of the footing from 89 kPa to about 70 kPa for the rearrangement of the kentledge blocks, and this gave the chance to access the behaviour of the foundation at small strains after a period of 11 years of consolidation.

Figure 8.57 shows the variation of footing settlement and applied load with time during test C, and compares the field measurements with the FE analysis predictions. The footing settlement series "North", "East", "West" and "South" refer to the measurements at the mid sides of the footing at the respective orientation, and the large differences between the four series indicate the accentuated tilt of the footing since the very early stages of loading.

The FE analysis predicts about 160 mm of footing settlement just after the last load increment was applied, increasing during the night to about 260 mm, just before the footing was unloaded, which is about 9.7% of the equivalent diameter of the footing (a condition usually identified with failure). The FE analysis recovers the general load – settlement behaviour of the footing when compared against the average of the measurements at the four mid sides. In particular, the FE analysis is able to recover the observed field behaviour that indicates that during the initial unloading – loading loop the footing settlement is completely reversible, and that up to about 160 kPa the footing response is stiff, identical to that observed during the initial stages of test A and B.

This can be better appreciated in Figure 8.58 which shows the variation of the footing settlement with applied load during test A, B and C, and compares the field measurements with the FE analysis. The response predicted by the FE analysis is still

softer than that observed in the field during the early stages of loading, up to about 160 kPa, where the soil response is dominated by the elastic component. This derives from the fact that the elastic part of the ET model is based on a stress dependent stiffness only and cannot account for the strong soil non-linearity at small strains.

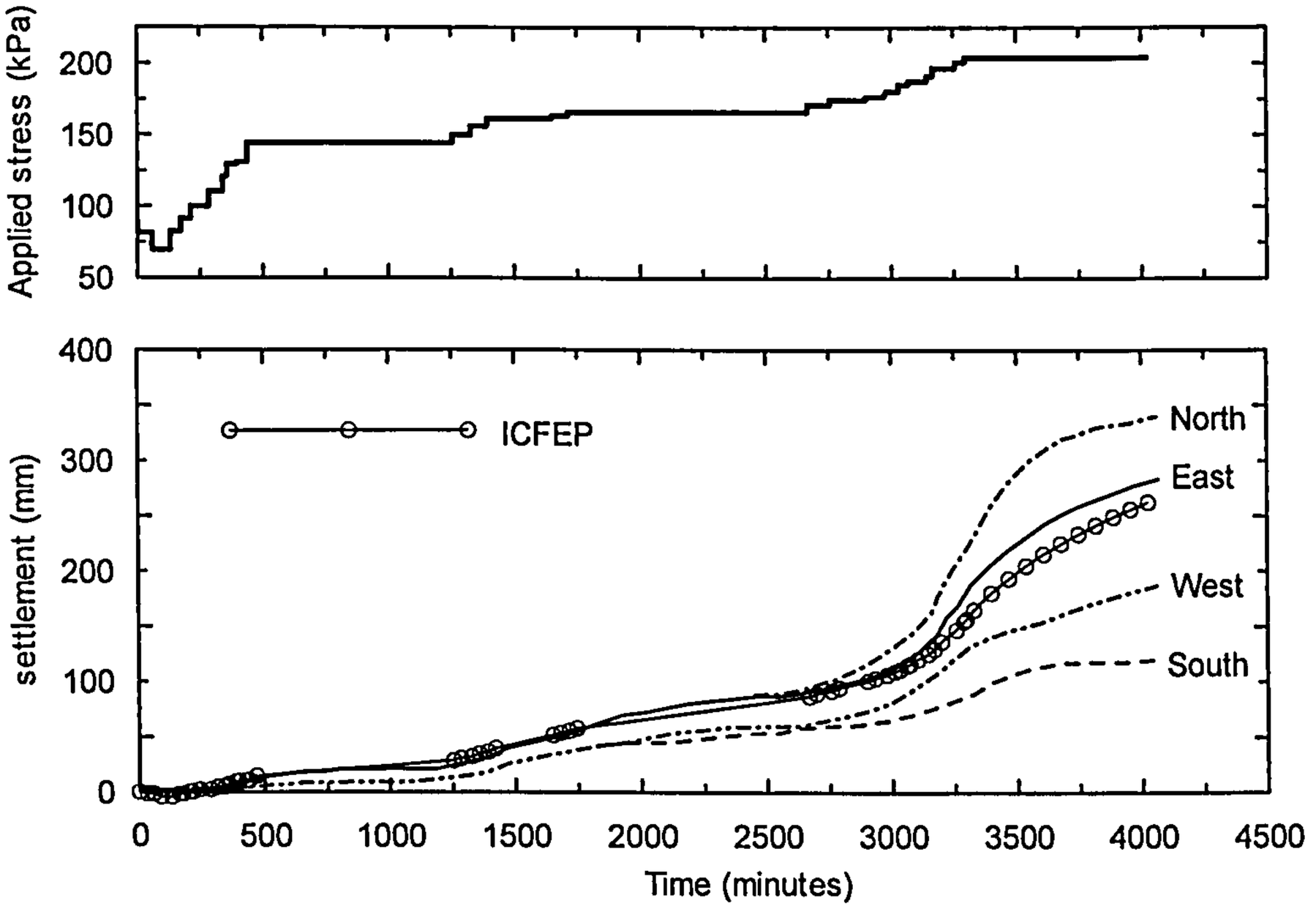

Figure 8.57: Variation of the applied and footing settlement during test C – field measurements and analysis predictions.

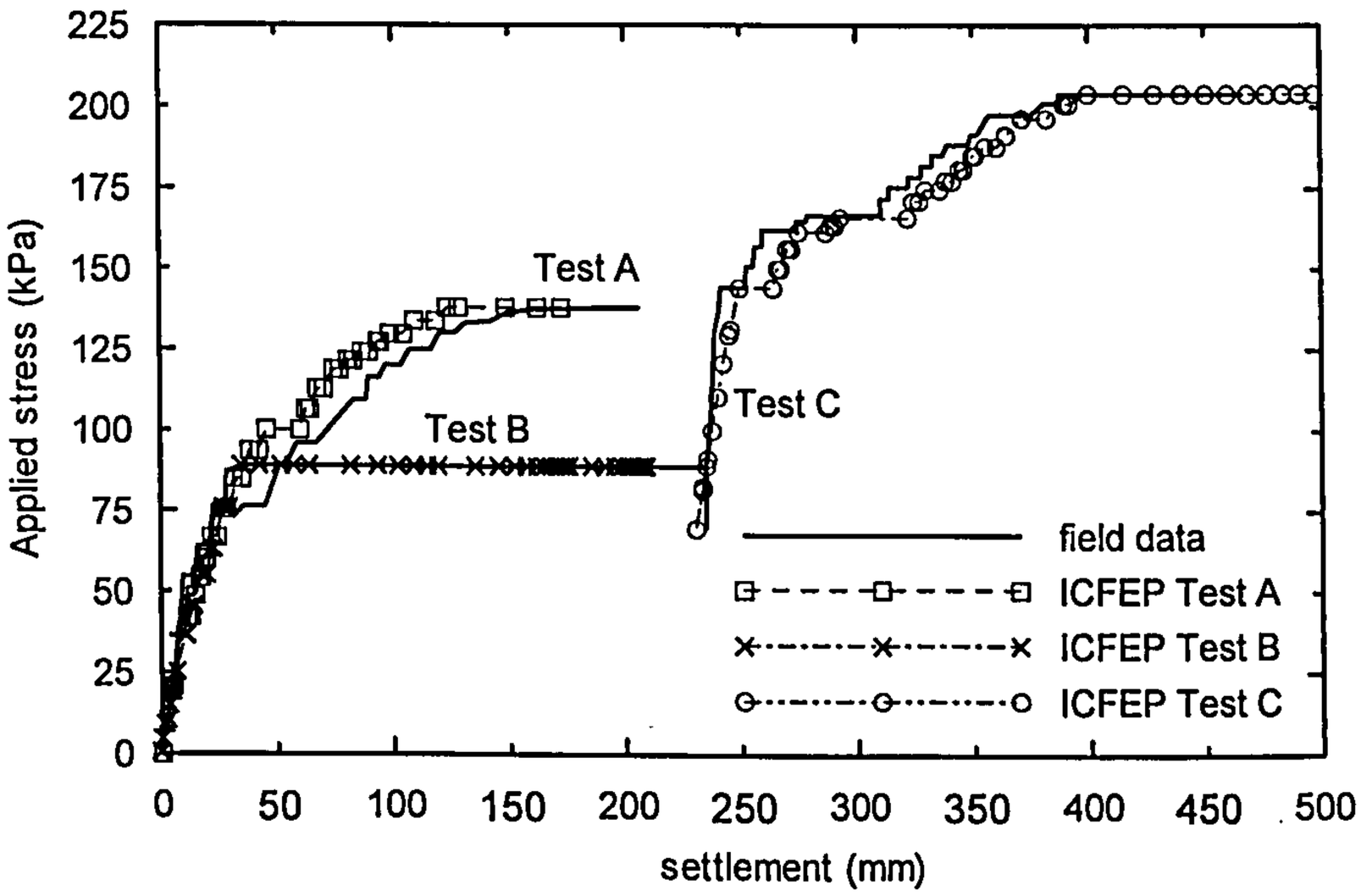

Figure 8.58: Variation of settlement with applied load during test A, B and C.

Figure 8.59 shows the variation of the footing settlement rate with time during test C and compares the field measurements (from Lehane & Jardine, 2003) with the FE analysis predictions. The agreement between the two data sets is very good, in particular towards the end of the test from t=2500 minutes onwards. The FE analysis recovers the variation and magnitude of the settlement rate during the latter stages of loading, predicting a maximum settlement rate of about 16 mm/h immediately after the application of the last load increment. According to the field data the settlement rate reduced to about 3.6 mm/h at the end of the night shift, a value that compares well with the value 5.5 mm/h predicted by the FE analysis.

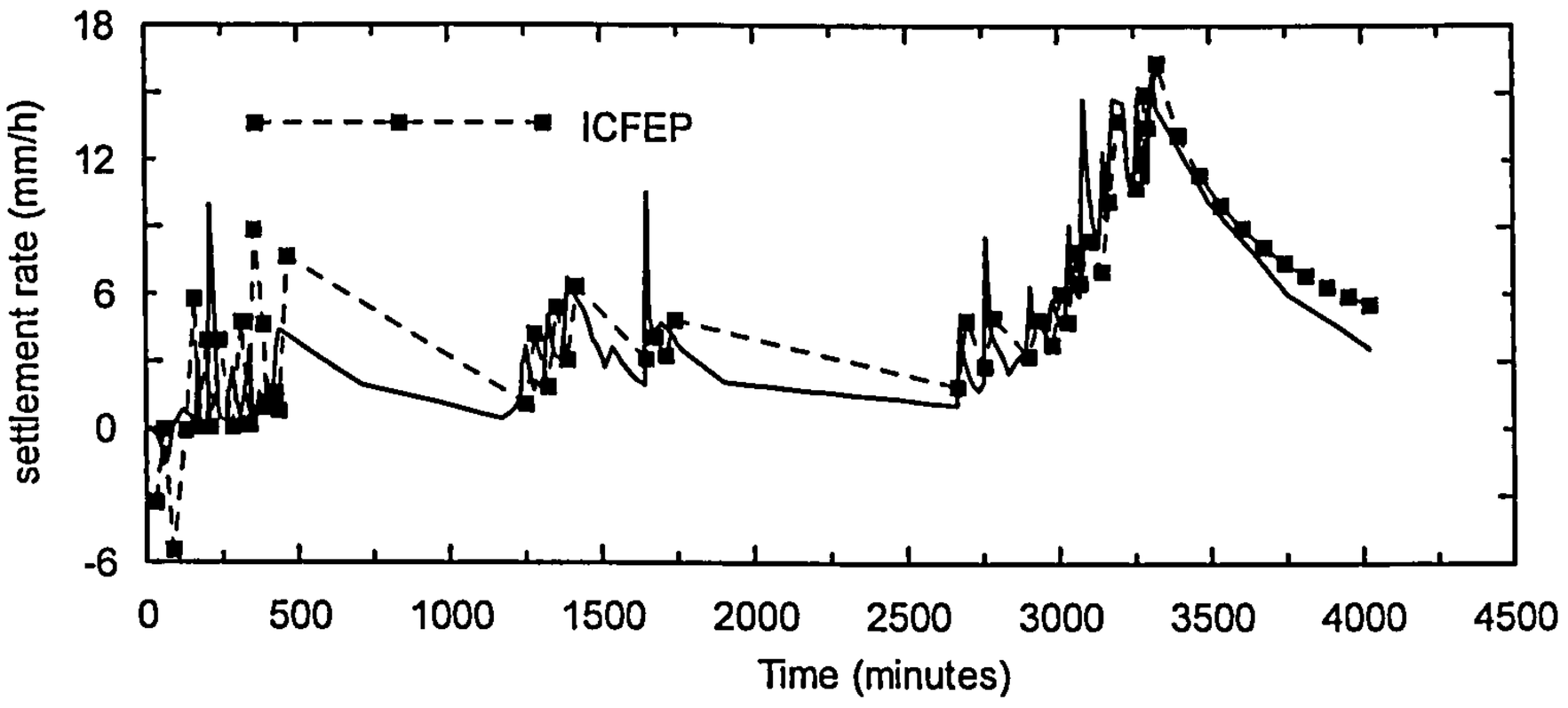

Figure 8.59: Variation of the foundation settlement rate with time during test C.

Figure 8.60a) shows the incremental displacement vectors in the foundation soil just before the footing was unloaded indicating that there is a concentration of plastic deformation below the footing, but no signs of a well defined failure mechanism.

It is remembered that the loading of the footing came to a halt due to the severe tilt of the footing that jeopardized the safety of the test. Lehane & Jardine (2003) when summarizing the loading test data concluded that the foundation could sustain marginally more load, based on the rapid decay of the footing settlement rate during the last night shift.

However, when comparing the field settlement rates during tests A and C, it is concluded that higher settlement rates are recorded in test C during the last loading stages, and that the settlement rate decay during the night break is similar in the two tests (marginally faster in test A) which is recovered by the FE analyses (Figure 8.61). Thus, it is anticipated that the stability conditions at the end of the loading tests are

similar in the two cases, with test C being marginally less stable. To investigate the stability conditions of the footing at the end of test C and assess how they compare with those at the end of test A, FE analyses simulating the application of further load on footing C have been carried out.

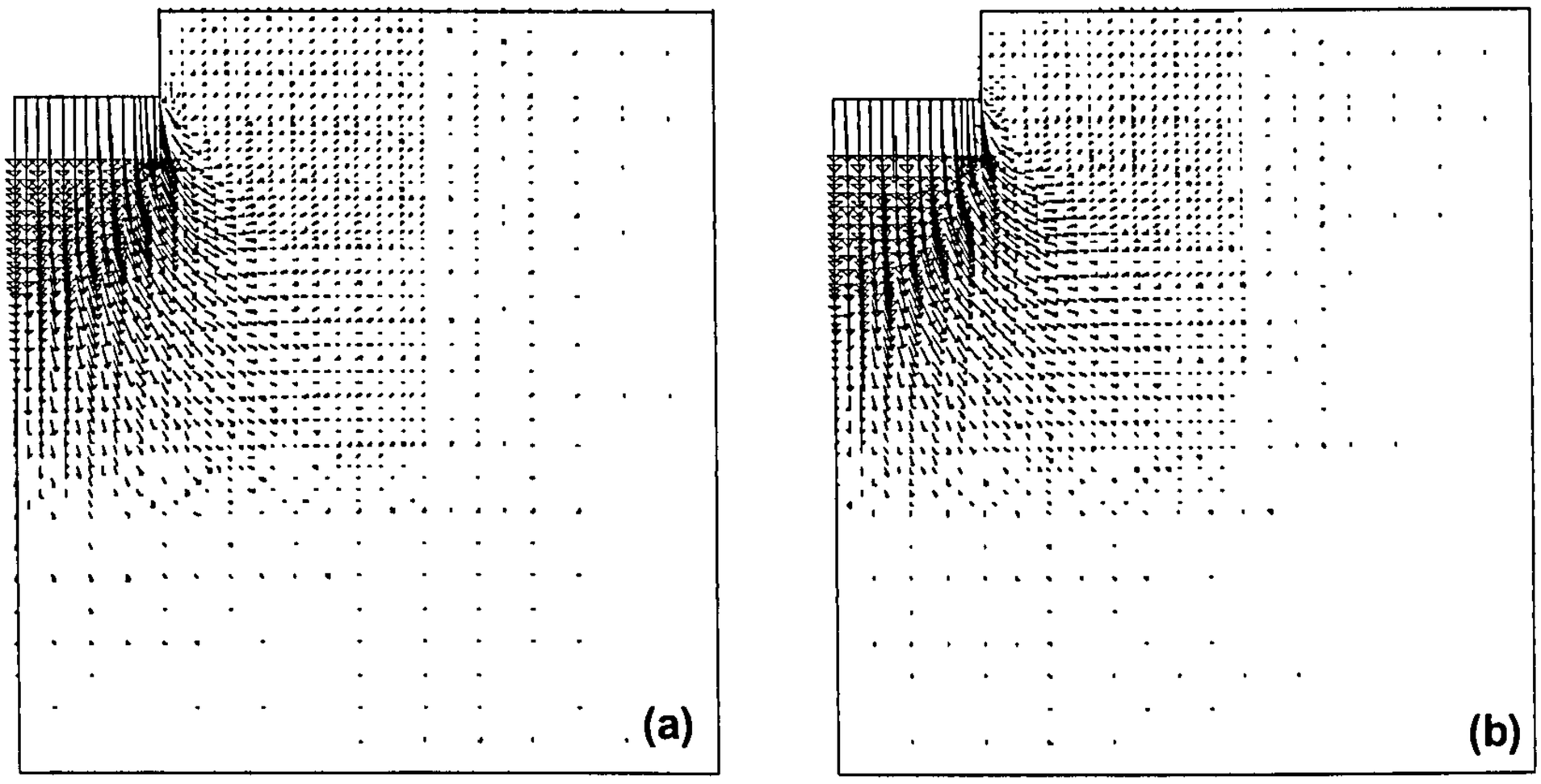

Figure 8.60: Incremental displacement vectors predicted by the FE analysis: a) just before the footing unloading; b) after further loading at very large settlements.

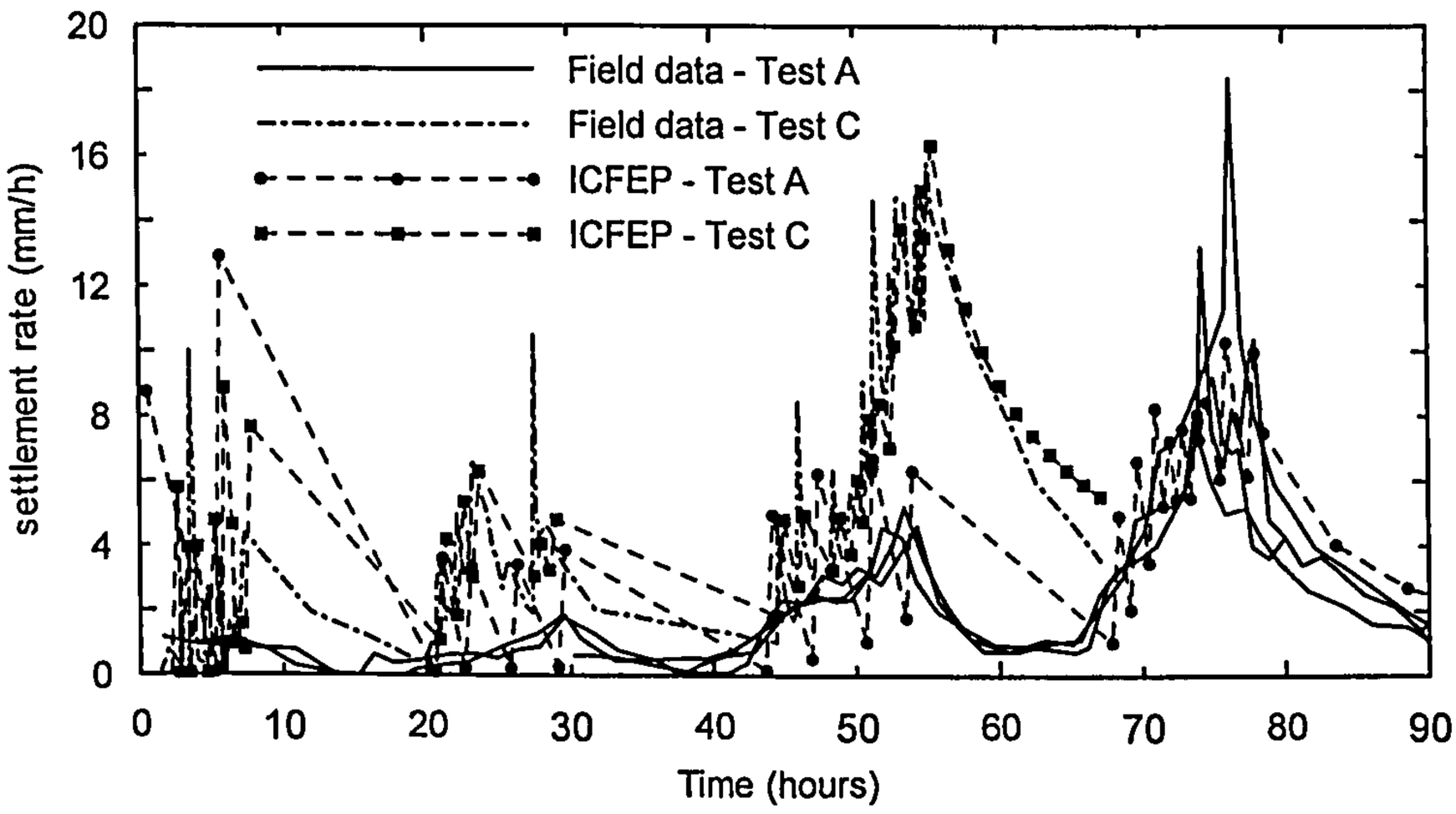

Figure 8.61: Comparison of the footing settlement rate during test A and C.

Figure 8.62 shows the load-displacement curve predicted by a couple consolidated FE analysis when additional load is applied to the footing at a rate of 6 kPa/hour after the last night break. Similar to the behaviour predicted in Section 8.4.5.1 when applying additional load to footing A (series (a) in Figure 8.42), the FE analysis fails to predict a

well-defined failure load for footing C. When comparing the load-displacement curves predicted by the FE analyses on applying further load to footings A and C, it is noticeable that the initial response of footing C at identical values of additional load is softer than that of footing A, indicating that the former footing is less stable. Figure 8.60b) shows the incremental displacement vectors predicted by the FE analysis at very large settlements, denoting an insipient punch-trough type mechanism.

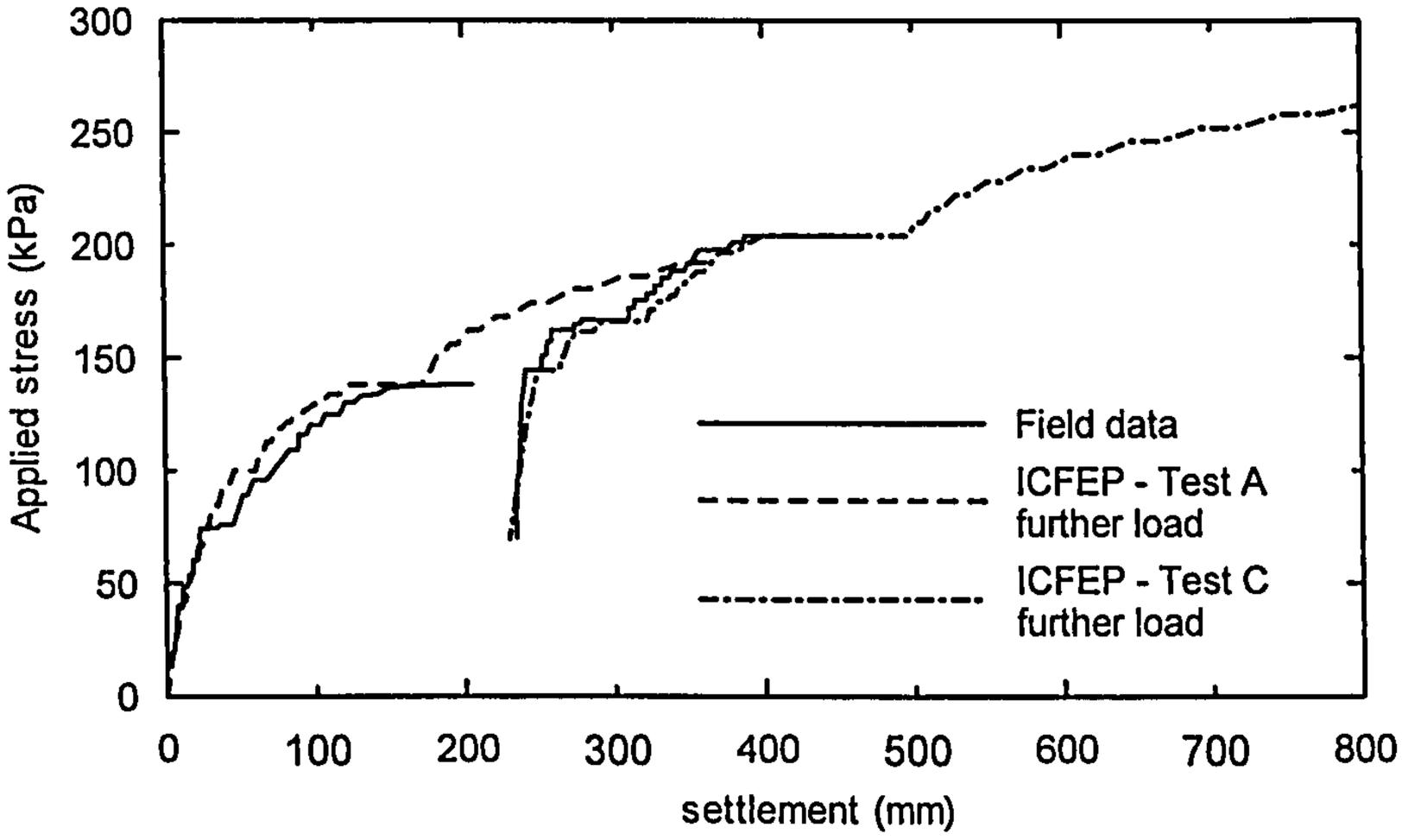

Figure 8.62: Load-displacement curves on further loading of footing A and C.

b) Pore pressures and total radial stresses in the foundation

Figure 8.63 shows the variation of pore pressures and total radial stresses with time during test C at the footing axis, and compares the field measurements with the FE analysis predictions. It is noted that during the consolidation period, especially since the Bothkennar site was decommissioned, some of the monitoring devices became faulty and therefore there is relatively less data during test C than test B.

Piezometer PZ2 registers a systematic increase in pore pressure from the start of loading, reaching about 70 kPa of excess pore pressure just before the unloading of the footing. The FE analysis recovers quite well the behaviour of piezometer PZ2 throughout the test. The field measurements indicate that at the location of the piezometer SC3P there are very small excess pore pressure throughout the test, reaching a maximum of about 15 kPa just after the application of the last load increment. This behaviour has been attributed to the existence of silty layers at shallow depth with

relatively high permeability, such that the conditions at this level during loading are partially drained. As discussed in the previous section, the FE analysis is not able to recover the significant drainage within the upper 2.5 m and large excess pore pressure are predicted by the FE analysis at SC3P.

Regarding the radial total stress measurements, the FE analysis is found to predict reasonably well the field measurements at SC4 and SC3 throughout the test. The differences between FE analysis predictions and field measurements increase towards the last stages of loading but they are regarded as reasonable, taking into account the uncertainties associated with the reading and interpretation of the spade cells devices.

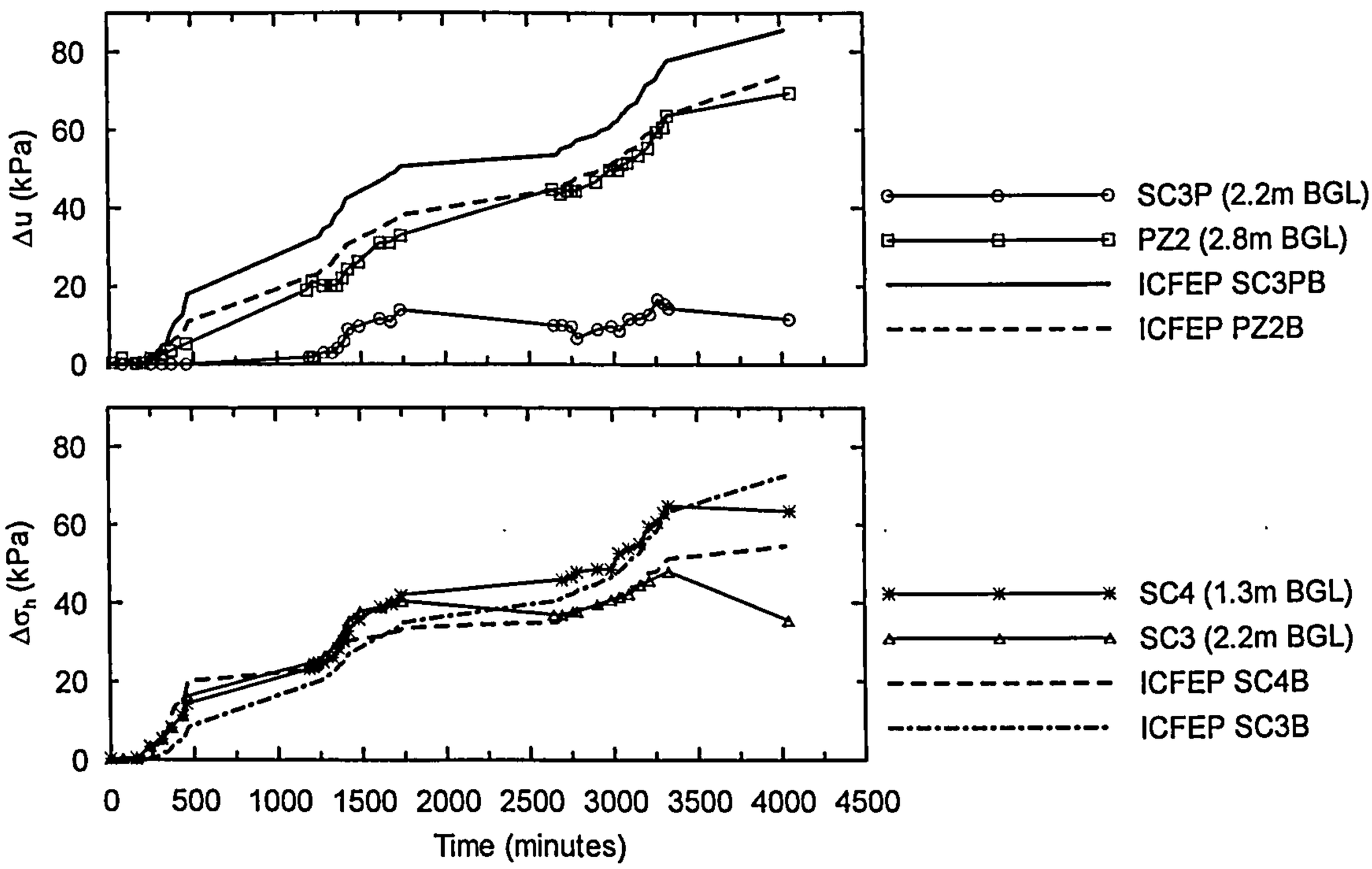

Figure 8.63: Variation of pore water pressure and radial total stresses in the foundation at the footing axis during test C.

c) Centreline settlements

Figure 8.64 shows the profile of settlement with depth at the footing axis, at several times during test C, and compares the field measurements with the FE analysis. The field measurements indicate that above an applied load of 172 kPa the soil is in tension between Z*=1.5 m and Z*=2.5 m (being Z* the depth below the base of the footing), which is clearly illogical. Lehane & Jardine (2003) suggest that these measurements

have been affected by the distortion of the access tube as the foundation tilt increased or deterioration of the target anchors over time, and therefore they should be disregarded.

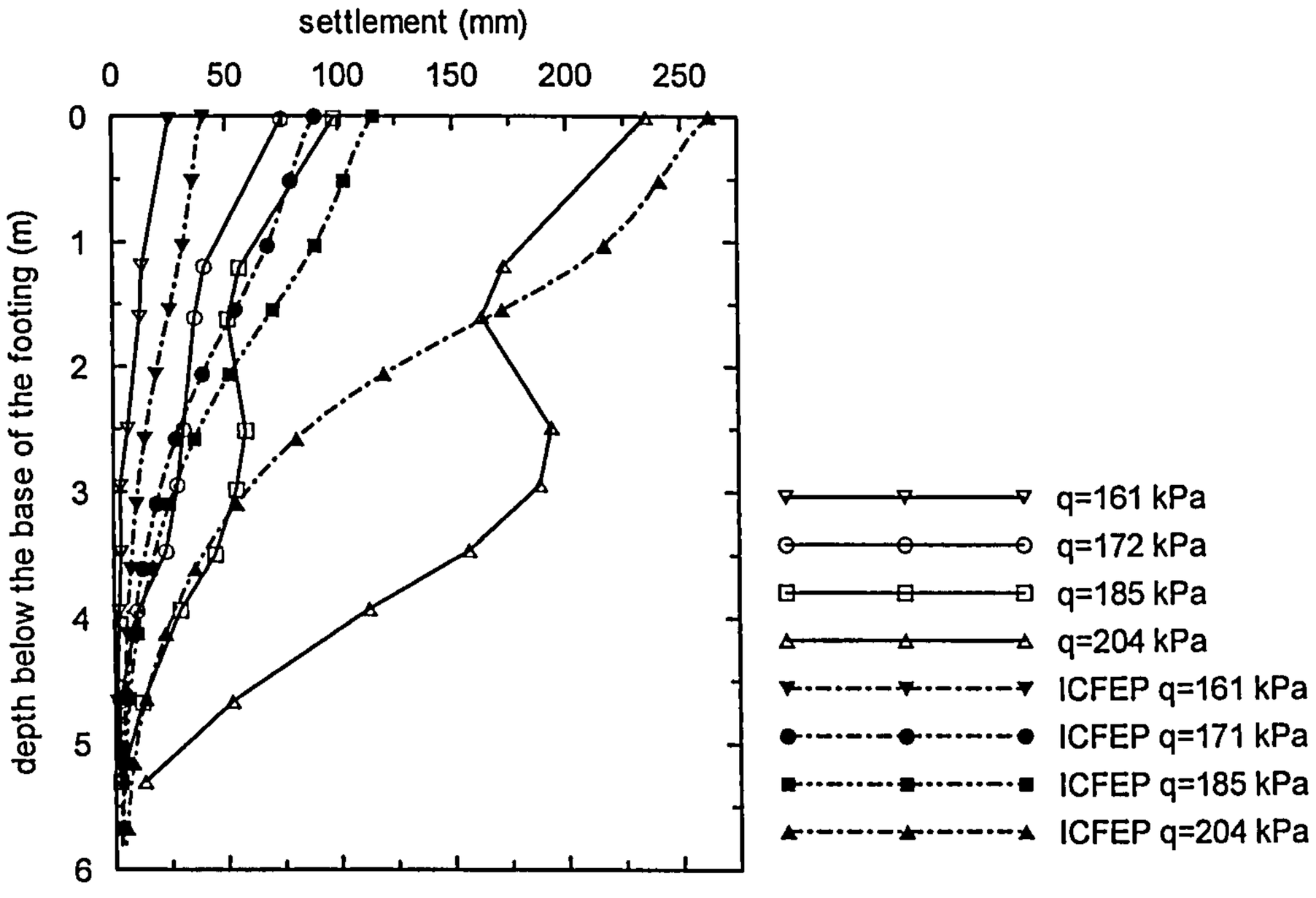

Figure 8.64: Profile of settlement with depth at the footing axis during test C.

In any case, the field measurements indicate that as failure is approached most of the footing settlement (at Z*=0) results from straining between Z*=2.5 m and Z*=5 m, and the vertical strains remain relatively small in the upper 2 m. This contrasts with the behaviour observed in test A at failure (see Figure 8.46) in which the straining is limited to the upper 2 m, and becomes insignificant below that.

However, as predicted by Zdravkovic et al. (2003), pre-loading causes a gain in strength especially in the upper layers where larger stress changes have occurred, and therefore on further loading there is a shift of the bearing capacity mechanism downwards in order to intercept the weakest layers.

The FE analysis predicts reasonably well the settlement at the base of the footing (Z*=0) during test C, but fails to recover the distribution of settlements with depth. According to the FE analysis, vertical straining occurs mainly between 1 and 3.5 m, at much shallow depths than observed in the test, and the FE analysis is not able to recover the differences between the settlement profile at failure in test A and test C. The overprediction of settlements during the early stages of loading, say at q=161 kPa,

demonstrates the inability of the model to recover the strong soil non-linearity at small strains.

d) Horizontal movements in the foundation

Figure 8.65 shows the profile of horizontal displacements with depth during test C as recovered by the inclinometer I1 and I2, and compares the field measurements with the analysis predictions. The horizontal movements, Y are normalized by the respective maximum, Y_{max} and the values of maximum horizontal displacements are plotted against the mean footing settlement in the small graph inset. Lehane & Jardine (2003) report that despite the severe tilting of the footing the two inclinometers located 0.15 m to the east and the west side of the footing indicate very similar lateral displacements up to an applied load of about 176 kPa when measurements of the inclinometers had to be abandoned due to safety reasons.

The field measurements indicate that the shape of the profile of lateral displacements with depth does not change with the level of applied load. The maximum lateral displacement occurs at Z*= 1.2 m (about 2 m BGL). The lateral displacement then decreases to about 20% of the maximum value at about Z*=4 m.

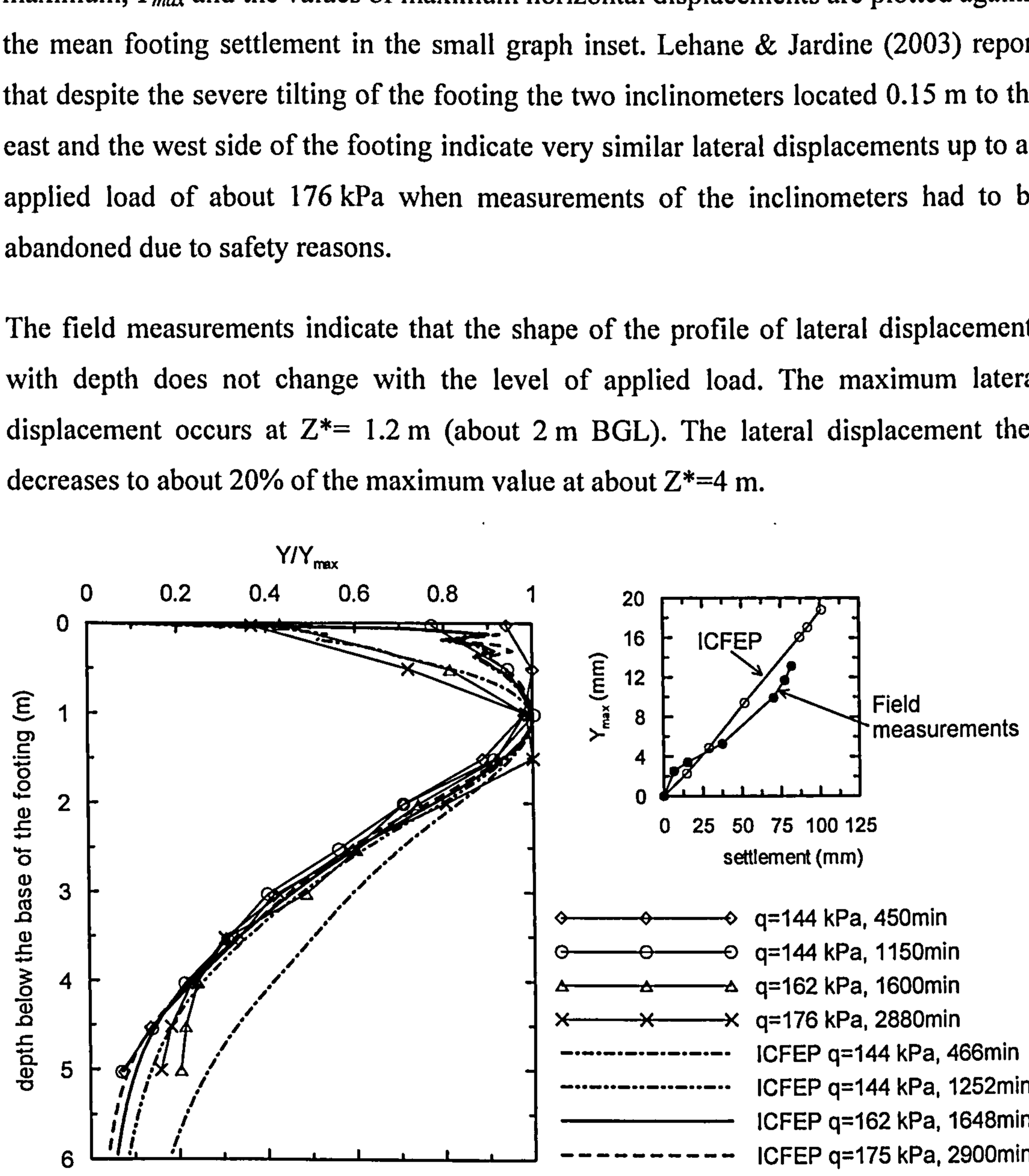

Figure 8.65: Profile of horizontal movements with depth in the foundation at the inclinometers location during test C.

The FE analysis recovers reasonably well the maximum horizontal movement and the shape of the profile of horizontal movements with depth during test C, up to an applied load of 176 kPa. However given the large vertical strains that developed in the foundation below Z*=3 m, close to failure (see Figure 8.64), it is thought that the profiles shown in Figure 8.65 are not representative of the behaviour at failure.

Figure 8.66 compares the profile of undrained strength available on the footing axis just before test C with the in-situ values available before tests A and B, both predicted by the ET model under triaxial compression at 4.5%/day axial strain. The increase in foundation undrained strength during the consolidation period is associated both with the dissipation of the excess pore pressures generated during the initial loading and the development of creep strains. The FE analyses predict a significant increase in the available undrained strength to about 4 m BGL. The profile of undrained strength just before test C is characterized by an almost constant value of undrained strength of about 33 kPa in the top 2 m, decreasing to about 23 kPa at 4.5 m BGL where it attains its minimum. Below 5 m BGL there is no significant change in the available undrained strength in relation to the initial value.

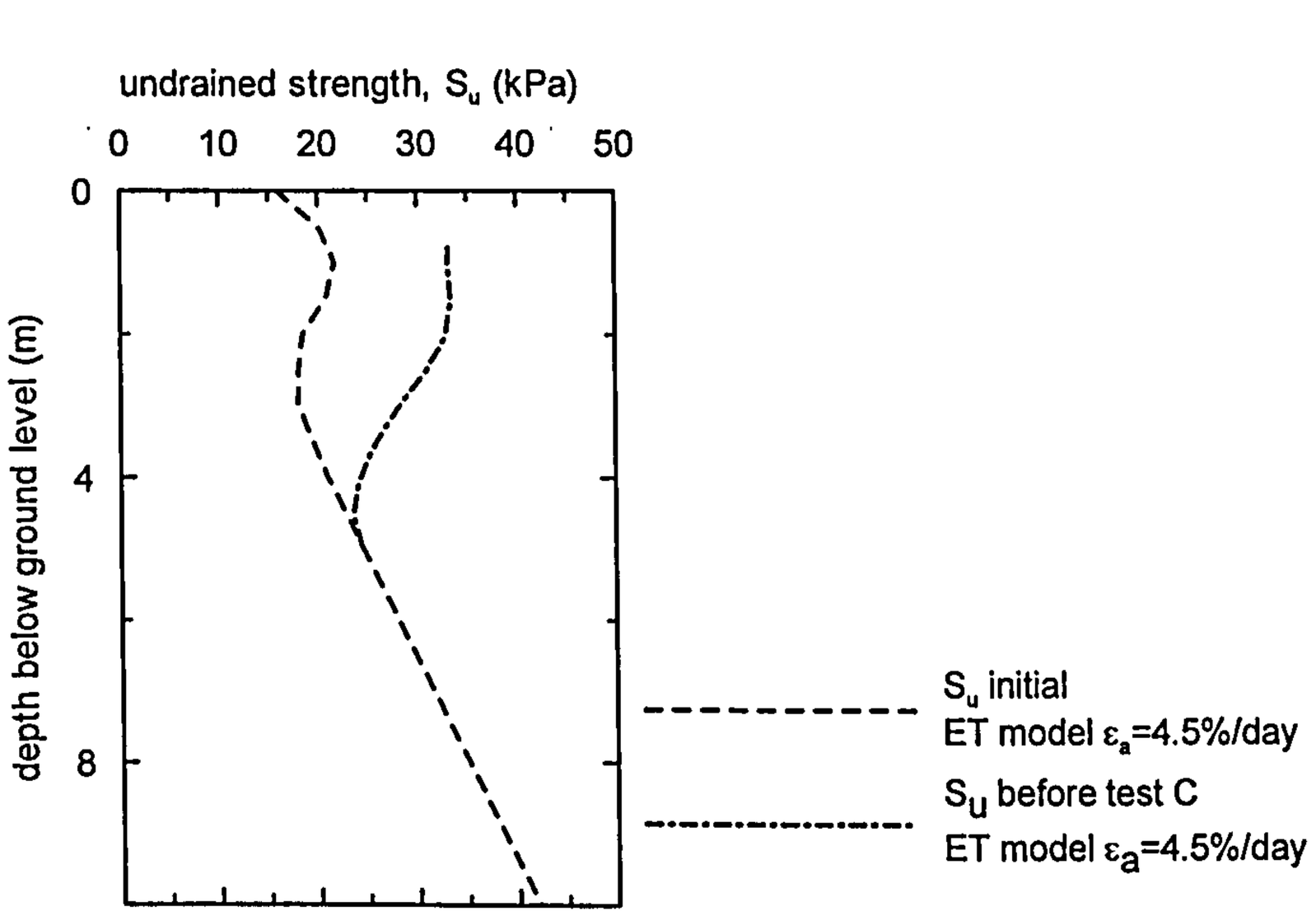

Figure 8.66: Profile of undrained strength in undrained compression predicted by the ET model at the footing centreline just before test C (at an axial strain rate of 4.5%/day).

The field measurements indicate that on taking to failure the preloaded footing, the failure mechanism has moved downwards with most of the vertical straining occurring between Z*=3 and Z*=5 m close to failure, which coincides with the horizon with the

lowest undrained strength values as predicted by the FE analyses. However, according with the FE analysis data presented regarding settlements and horizontal movements in the foundation the lowest resistance horizon seems to remain at about Z*=2 m, suggesting that the gradient in undrained strength between 2 and 4 m BGL is not sufficient to move the failure mechanism downwards.

This implies that the profile of in-situ available undrained strength before test C is different from that shown in Figure 8.66 derived from the FE analyses. Discrepancies are thought to result from:

a) During test B (application of preload) the FE analysis predicts that most of the stress changes are confined to the upper 3.5 m (see Figure 8.53); in contrast the field measurements indicate significant stress changes to larger depth;

b) During the consolidation period the FE analysis failed to predict the large vertical straining between Z*=2.5 m and Z*=5 m at the footing axis that was identified in the field. The zone where larger delayed vertical straining has occurred is expected to have the largest gains in undrained strength.

c) The ET model is not able to mimic the post peak strength loss associated with the soil destructuration during shearing which is likely to be most significant within the unweathered Carse Clay (below 2.5 m BGL). During the initial loading (test B), the foundation soil is likely to have undergone significant destructuration, which would not be (completely) recoverable during the consolidation period. If that is the case, the available undrained strength in the foundation is lower than that predicted by the FE analysis.

d) The ET model is an isotropic model and the state boundary surface predicted by the model is always symmetric in relation to the mean effective stress axis. Smith (1992) has performed an extensive programme of laboratory triaxial tests and mapped the state boundary surface of the intact Carse clay, concluding it to be strongly anisotropic. In-situ, the soil's state boundary surface is in general approximately symmetric in relation to the K_0-stress axis and when consolidated to a different stress state the state boundary surface is found to rotate towards the new stress state (a phenomenon often called *evolving anisotropy*). This causes the state boundary surface to expand around the current stress state. In the preloaded footing this means that there would be an additional increase in the

foundation undrained strength associated with the rotation of the state boundary surface in relation to the new stress state imposed by the preload, which can not be captured by the ET model. It is noted that when calibrating the ET model against the laboratory data on Carse Clay the parameters were selected such that the model would best predict the soil behaviour at the in-situ stresses.

8.4.6 Consideration of non-linear behaviour at small strains

The results from the FE analyses presented in the previous section show, in general, good agreement with the field measurements, in terms of the overall load-displacement behaviour of the footings. However, when looking at the displacements within the foundation soil there are discrepancies. Some of them have been attributed to the fact that the elastic part of the ET model is based on a bulk stiffness dependent on mean stress only and a constant Poisson's ratio value, and cannot reproduce the soil's strong non-linearity at small strains. In principle, this could be overcome by incorporating a small strain stiffness model, which then describes the elastic part of the ET model.

One such model is the small strain stiffness model proposed by Jardine et al. (1986) in which the tangent bulk and shear modulus are described by trigonometric functions and vary both with stress level and strain values, and are given by Equation 8.14 and Equation 8.15, respectively.

Equation 8.14
$$\frac{K}{p'} = R + S \cdot \cos\left(\delta \cdot Y^{\mu}\right) - \frac{S \cdot \delta \cdot \mu \cdot Y^{(\mu-1)} \sin\left(\delta \cdot Y^{\mu}\right)}{2.303} \qquad \text{with}$$

$$Y = \log_{10}\left(\frac{|\varepsilon_{vol}|}{T}\right)$$

R, S, T δ, μ are model parameters

Equation 8.15
$$\frac{G}{p'} = \frac{A}{3} + \frac{B}{3}\cos\left(\alpha \cdot X^{\gamma}\right) - \frac{B \cdot \alpha \cdot \gamma \cdot X^{(\gamma-1)} \sin\left(\alpha \cdot X^{\gamma}\right)}{6.909} \qquad \text{with}$$

$$X = \log_{10}\left(\frac{E}{\sqrt{3}C}\right)$$

A, B, C, α, γ are model parameters

The model parameters can be derived from degradation curves of the bulk and shear stiffness during drained and undrained triaxial tests provided there is data in the small strain range, i.e. axial, shear or volumetric strain less than 0.1%.

However, it was soon realized that such a model could not be combined with the ET model formulation, at least when implemented as described in Chapter 6. In the ET model the visco-plastic multiplier, Φ that determines the magnitude of the visco-plastic strain increment is given by Equation 8.16 which requires the calculation of the quantities ε_{vm} and ε_{vm}^{ref}.

Equation 8.16

$$\Phi = \frac{\psi_0}{V \cdot t_0} \cdot \left(1 + \frac{\varepsilon_{vol,m}^{ref} - \varepsilon_{vol,m}}{\varepsilon_{vol,m,Limit}^{vp}}\right)^2 \cdot \exp\left[\frac{V}{\psi_0} \frac{\varepsilon_{vol,m}^{ref} - \varepsilon_{vol,m}}{\left(1 + \frac{\varepsilon_{vol,m}^{ref} - \varepsilon_{vol,m}}{\varepsilon_{vol,m,Limit}^{vp}}\right)}\right] \cdot \frac{1}{\left|\frac{\partial P}{\partial p'}\right|_{\substack{p'=p'_m \\ J=0}}}$$

The value of ε_{vm} is calculated by Equation 8.17, which corresponds to moving the current stress point (p_i', J_i) to the equivalent stress state $(p_m', 0)$ along the elastic wall. According to the initial formulation of the model the quantity κ/V is constant, and thus the elastic or instant line is a straight line in $\varepsilon_{vol} - lnp'$ space. This is compatible with the elastic response of the model that is described by the bulk modulus, K' given by Equation 8.18 and a second elastic parameter in this case chosen to be the Poisson's ratio, μ, such that the shear stiffness is given by Equation 8.19.

Equation 8.17

$$\varepsilon_{vm} = \varepsilon_v + \frac{\kappa}{V} \cdot \ln\left(\frac{p'_m}{p'_i}\right)$$

Equation 8.18

$$K' = \frac{V \cdot p'}{\kappa}$$

Equation 8.19

$$G = \frac{K' \cdot 3 \cdot (1 - 2\mu)}{2 \cdot (1 + \mu)}$$

The adoption of a small strain stiffness model of the type described above causes the quantity K'/p' to be strain dependent. If Equation 8.17 is still employed to evaluate the quantity ε_{vm} then there are two options, to use either the quantity κ/V that has been introduced in the input parameters of the ET model or the current value $(\kappa/V)_{equiv}$ that is related to the current bulk modulus by Equation 8.18.

The use of Equation 8.17 assumes that the elastic line is a straight line in $\varepsilon_{vol} - lnp'$ space. This is no longer true when using a small strain stiffness model, as the quantity

$(\kappa/V)_{equiv}$ is a function on the current accumulated volumetric strain and so to obtain the *true* value of ε_{vm} the integral in Equation 8.20 must be evaluated.

Equation 8.20

$$\int_{p_i'}^{p_m'} d\varepsilon_v = \varepsilon_v - \varepsilon_{vm} = \int_{p_i'}^{p_m'} \frac{dp'}{K\left[f\left(p', \varepsilon_{vol}\right)\right]}$$

The implications of using Equation 8.17 can be better appreciated in Figure 8.67. The difference in ε_{vm} arising from using either of the two previous options may seem small however it becomes important for stress states close to the reference time line when this difference is of the same order of magnitude as the quantity ($\varepsilon_{vm} - \varepsilon_{vm}^{ref}$), that controls the magnitude of the visco-plastic multiplier.

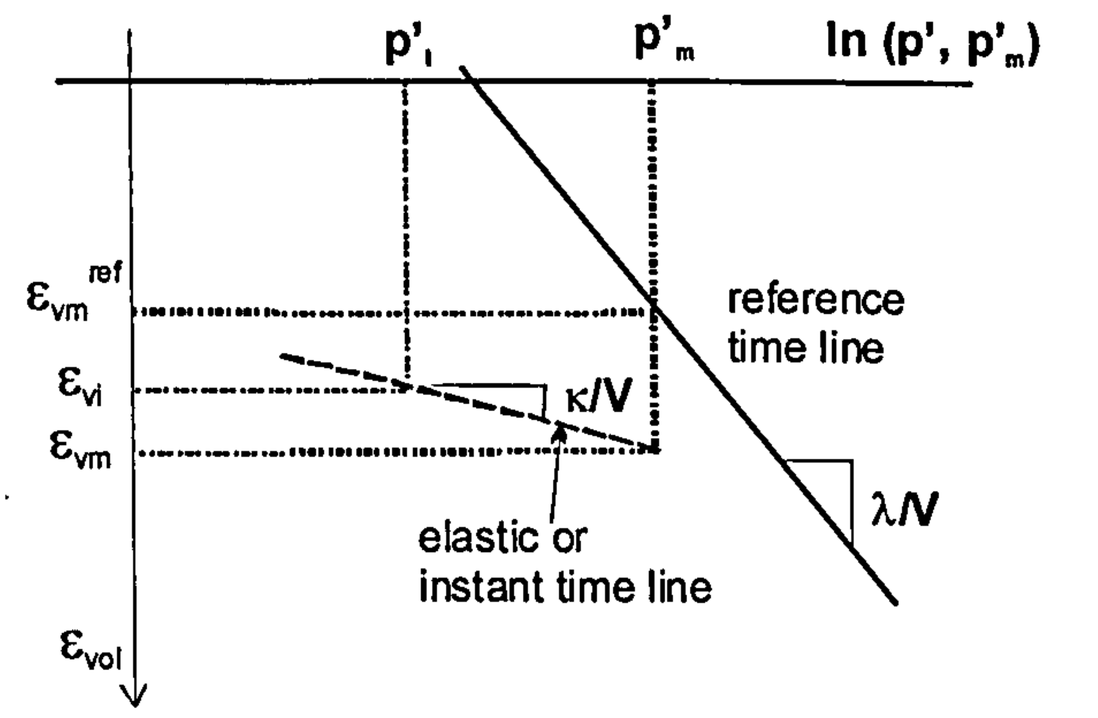

Figure 8.67: Schematic calculation of the value of ε_{vm}: a) in the basic formulation of the ET model with stress dependent only bulk modulus; b) with an elastic small strains stiffness model.

8.5 Concluding remarks

This Chapter presents numerical analyses of the loading tests performed on two instrumented surface footings at the Bothkennar research site. The loading tests highlight the importance of incorporating the viscous time dependent behaviour of soils to correctly predict the long-term settlement and the increase in bearing capacity of preloaded footings.

In the numerical analyses presented herein, the foundation soil is modelled using the Equivalent Time constitutive model that is described extensively in Chapter 6, and which has been shown to reproduce well the phenomena of primary and secondary creep, stress relaxation and the effect of strain rate on the stress-strain soil response, associated with isotach viscosity.

The time dependent part of the model requires three parameters which are derived ideally from a one-dimensional oedometer test (or isotropic consolidation tests), either of the incremental load or constant rate of strain type, and a long creep test. The remaining parameters can be determined from undrained triaxial compression and extension tests on samples consolidated both on the dry and wet side of the critical state.

The numerical analyses show, in general, good agreement with the field measurements in terms of the overall load displacement behaviour of the footings. The agreement is particularly good regarding the long-term settlements of the preloaded footing. However when looking at the displacements within the foundation soil there are discrepancies, which are thought to derive from the following aspects:

a) The same stiffness and time dependent characteristics are assumed throughout the soil profile, as there is no specific characterization data within the superficial materials; the model parameters are derived from data on competent unweathered Carse Clay, which is expected to be softer and more prone to the development of time delayed strains/movements;

b) The elastic part of the ET model is characterized by a bulk modulus dependent on mean effective stress only and a constant Poisson's ratio value, and it cannot reproduce the strong stiffness non-linearity at small strains; when trying to incorporate a small strain stiffness model to describe the elastic part of the ET

model it was soon realized that it is not compatible with the model formulation, at least as the model is implemented at present.

c) The mechanism that is incorporated in the ET model to describe soil structure and the destructuration process with plastic straining has been initially derived to describe a calcarenite (Lagioia & Nova, 1995) and is best suited to mimic the soil structure associated with cementing, in which the loss of structure is quite abrupt and loading conditions are drained. Therefore, it cannot adequately describe the soil structure of clayey soils that derives mainly from particle bonding, in which the loss of structure tends to be gradual, with the full destructuration requiring large plastic strain values, and therefore no structure has been considered in the analyses. In addition, the ET model cannot describe the increase in soil structure, associated with either bonding or cementing, during a creep period. The materials more prone to post peak strength loss and destructuration due to plastic straining are within the competent unweathered Carse Clay, which occur below 2.5 m to 3 m BGL, and this is likely to have caused the lowest operational undrained strength to move slightly downwards in relation to the profile of undrained strength in-situ, following the application of preload.

d) The ET model is an isotropic model and therefore cannot mimic the rotation of the state bounding surface during consolidation under a new stress state. This is likely to be significant when analysing the final loading of the preloaded footing (Test C) as the preload has imposed considerable levels of strength mobilization within the foundation.

To investigate the importance of considering the soil creep non-linearity an additional analysis of footing B was carried out, exactly as the analysis described in Section 8.4.5.2 with the exception of the parameter $\varepsilon^{vp}_{vol,m,Limit}$ that was set equal to 0.6, which is the volumetric strain required to bring the soil to a state when there are no voids left. It has been shown that the adoption of such value causes the ET model to yield predictions very close to a logarithmic creep law.

The results of the analysis in terms of the variation of the footing settlement with time, during both the application of the preload and the 11 years of consolidation are shown

in Figure 8.68, and is denoted as *ICFEP (2)*. Figure 8.68 also includes the field data and the predictions presented previously in Figure 8.50 that assume a value of $\varepsilon^{vp}_{vol,m,Limit}$ equal to 0.06 derived based on the laboratory test data.

It can be seen that the two analyses yield very similar predictions up to about 100 days, recovering very well the field data. After t=100 days the predictions given by the two analyses diverge. The analysis that accounts for the soil creep non-linearity recovers well the field data (the exception being the last field measurement, whose accuracy is in any case dubious as previously discussed) while the analysis that assumes a linear creep law overestimates the footing settlements. After 11 years of consolidation the difference between the two analyses is about 55 mm, about 25% of the footing total settlement. This emphasizes the need to incorporate the soil creep non-linearity if good predictions of the long-term settlements of geotechnical structures are to be made.

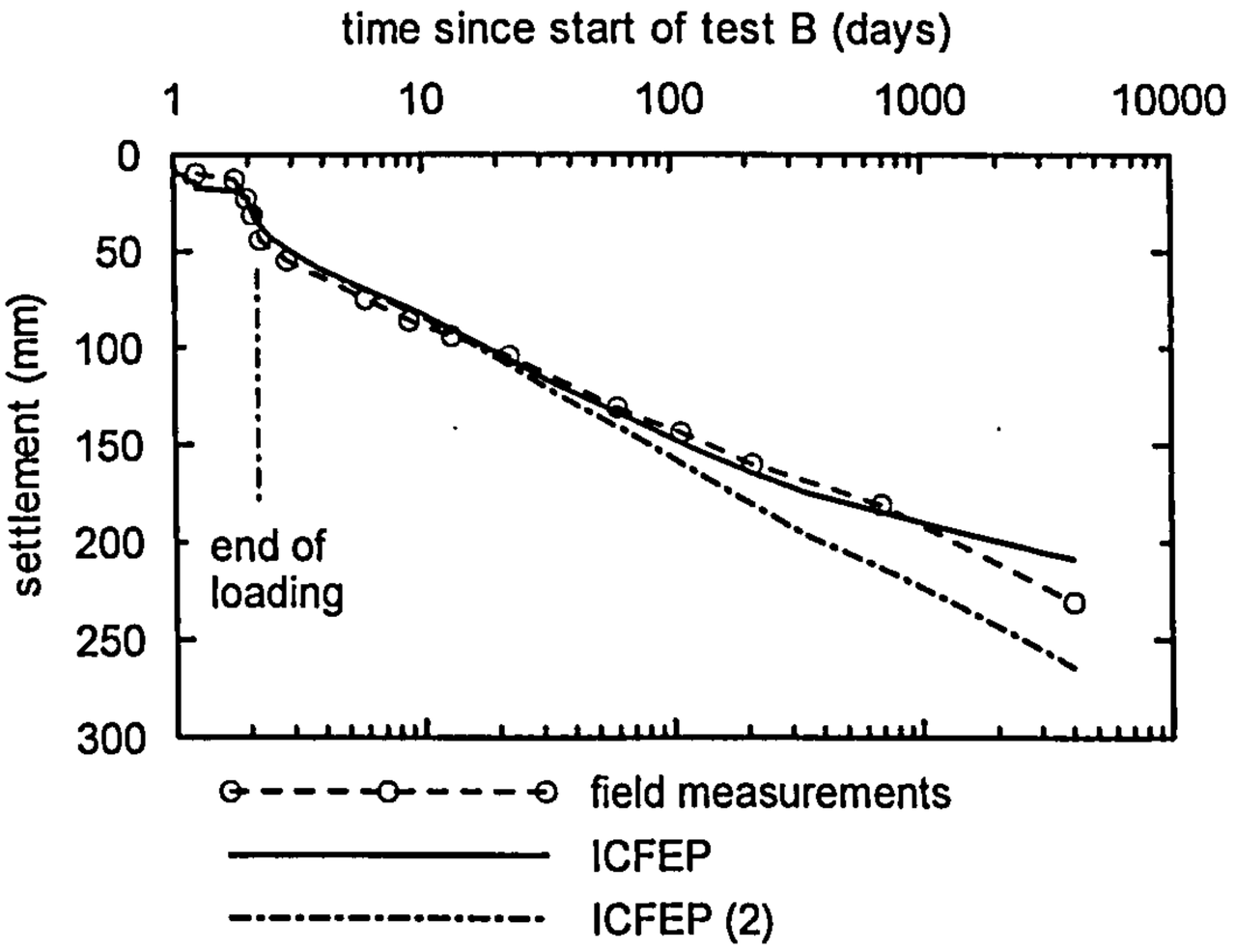

Notes: ICFEP (2) corresponds to an anal

Figure 8.68: Long term settlement of footing C – influence of adopting a non-linear logarithmic law.

Analyses were carried out to evaluate the undrained bearing capacity of footing A predicted by the ET model. However, it was concluded that due to its formulation the ET model is not able to predict failure as it is defined in plasticity theory – plastic flow along a surface where the soils strength has been fully mobilized (and remains constant with further straining or time). This derives from the fact that the ET model is not able to predict accelerating creep and thus it is not possible for an increase in strain rate to occur at constant stresses.

When using the ET model the failure condition should be defined in a similar way to that done in engineering practice, i.e. as a threshold value of settlement or settlement rate. It would be of interest to evaluate the ultimate bearing capacity that would be predicted by an analysis of the same boundary value problem that uses instead a conventional plasticity model e.g. Modified Cam Clay model, and consider how this value compares with the load predicted by the ET model at settlement and settlement rates identified in practice with failure. However, the user should be aware that this *serviceability type* failure condition will be, in principle, distinct for different boundary value problems, and thus experience needs to be gained in analysing other boundary value problems.

9 CONCLUSIONS AND RECOMMENDATIONS

9.1 Introduction

The research presented in this thesis can be divided into two main parts. The first part involved the development of two generalized elastic visco-plastic constitutive models to describe the viscous behaviour of clays. The main difference between the two models lies in the adopted law to describe the variation of the creep deformation with time. The models were implemented in the Imperial College Finite Element Program (ICFEP) and validated through a series of simple finite element analyses simulating common laboratory tests.

The second part of the research comprises the application of one of the models (the Equivalent Time model) to a typical engineering problem. The model was first employed in a parametric study to evaluate the bearing capacity of a 2 m wide preloaded strip footing. The study considers different values of the coefficient of secondary compression, the effect of creep non-linearity and the effect of the adopted loading rate. Comparison of the results of this study with those reported by Zdravkovic et al. (2003), who investigated the same problem but modelled the foundation soil with the time independent Modified Cam-Clay model, highlights the significance of considering the time dependent nature of soils in engineering practice, and in particular, in the design of shallow foundations.

The constitutive model was then employed in the numerical analyses of the loading tests performed on two rigid footings at the Bothkennar clay test site (Jardine et al., 1995; Lehane & Jardine, 2003), for which there is a large amount of data regarding both the footings performance during the tests and the soil characterization. The results of the analyses are compared with the monitoring data published in the literature, and the capabilities and limitations of the model to mimic the behaviour of this real boundary value problem investigated in detail.

The conclusions from this research are presented in more detail in the following sections.

9.2 Two generalized time dependent models for saturated clays

Two elasto visco-plastic constitutive models were developed during this research and were presented in this thesis. The two models are based on the overstress theory as described by Perzyna (1963) and the concept that the total deformation of a soil element can be divided into an instant and a delayed component. The instant strain component is elastic, reversible and time independent and can be calculated from the models elastic parameters. The delayed strain component is irreversible and rate dependent. The models differ essentially in the calculation of the delayed component, in particular on the adopted law to describe the variation of creep deformation with time.

Creep Model 1 is based on the Modified Cam Clay model and assumes a linear law for the variation of the visco-plastic volumetric strain with the logarithm of time during a drained creep period under constant effective stresses, i.e. a constant coefficient of secondary compression.

Using a similar approach to that followed by other researchers, the extension to general stress space was initially carried out assuming, based on the experimental observation made by Tavenas et al. (1978), that a given loading surface was a locus of constant volumetric visco-plastic strain rate and that the remaining strain components could be calculated from a potential surface. In this form the model is referred to as the *Basic* Creep Model 1. However, when adopting the above assumption it was found that the model was not able to predict critical state conditions. This was shown to be a consequence of the above assumption and implies that many theoretical models described in the literature, which are based on this assumption, are flawed.

The formulation of the model in general stress space was subsequently modified such that a given loading surface is a locus of constant visco-plastic scalar multiplier. In this form the model is referred to as the *Modified* Creep Model 1. It was shown that the above two formulations yield very similar predictions for stress levels below about 0.7, however only the latter approach is able to simulate critical state conditions.

The loading and plastic potential surfaces are assumed to have the ellipse shape of the Modified Cam Clay model in *J-p'* stress space. This means that once the effective stress strength parameters (i.e. the angle of shearing resistance at critical state) are set the undrained strength predicted by the model at a given stress state and strain rate is fixed.

To account for the influence of the intermediate principal stress in the deviatoric plane the loading surface can be described by either the Mohr Coulomb hexagon or by a flexible function that can describe a wide range of shapes. The plastic potential is also described by the above flexible function. This means that after specifying the stress ratio at critical state under a given shearing mode, say triaxial compression, the user has various options on how to specify the value of the critical state stress ratio under different shearing modes.

The parameters of the Creep Model 1 can be derived from one IL 24 hour oedometer test and one, ideally two, consolidated undrained triaxial tests, one in compression and the other in extension. The model requires two additional parameters in relation to the MCC constitutive model, ψ and $\dot{\varepsilon}_{ref}^{vol}$. The parameters ψ and $\dot{\varepsilon}_{ref}^{vol}$ are shown to be equivalent to the more common set of parameters $C_{\alpha e}$ and t_0, where $C_{\alpha e}$ is the coefficient of secondary compression defined in terms of void ratio and t_0 is the real time associated with the reference line. If the value of t_0 is set equal to 1day=24 hours, as the reference time line is usually defined based on IL 24hour oedometer tests, then the model only requires one additional parameter in relation to the MCC model.

The model was implemented in ICFEP and was then validated by means of single element analyses simulating common laboratory tests. Regarding the model's performance under common laboratory stress paths the following was observed:

- The model simulates primary and secondary compression under 1D conditions, however it cannot reproduce the tertiary compression phase that corresponds to an increase in the value of the current coefficient of secondary compression with time, and which has been observed experimentally by some authors (e.g. den Haan, 1994).

- The model reproduces a reduction in the soil's vertical effective stress during a period of stress relaxation under 1D stress conditions, reproducing well the relaxation phenomenon in soils as reported by Lacerda & Houston (1973).

- The model predicts that the compression behaviour under 1D conditions is rate dependent and the effects of strain rate are persistent, replicating isotach type viscosity.

- In undrained triaxial compression tests, the model predicts an increase in the soil's undrained strength with increasing applied axial strain rate. The differences in the predicted undrained strength are associated with differences in the predicted excess pore water pressures as the effective stress failure envelope remains unchanged. The model is able to mimic the shearing behaviour of samples that are on the wet and on the dry side of the critical state. Normally and lightly overconsolidated samples are contractive and the stress ratio is seen to increase monotonically up to the critical state. Heavily overconsolidated samples are initially contractive, reaching a stress ratio well in excess to that at critical state, and then the behaviour becomes dilative as the stress state tends to the critical state line. An increase in the OCR value and the applied strain rate results in an increase of the soil's pseudo-elastic stress range.

The Modified Creep Model 1 was shown to have good predictive capabilities. However the fact that the model includes a linear logarithmic creep law is, in particular when predicting the long-term creep settlements under an engineering structure, a significant limitation. The creep behaviour of soils is found to be in general non-linear logarithmic (corresponding to a reduction of C_α with time) and the use of a linear logarithmic creep law results in that case on a significant overestimation of soil's settlement. This problem is overcome by the Equivalent Time model, which includes a limit to the magnitude of the volumetric creep deformation, and can therefore capture the soil's creep non-linearity.

The Equivalent Time Model described in this thesis includes a hyperbolic law to describe the variation of the visco-plastic volumetric strain with the logarithm of time during an isotropic drained creep period, described by Yin et al. (1999).

Based on the findings reported in Chapter 5 the Equivalent Time model is extended to general stress space by assuming that a given loading surface is a locus of constant visco-plastic scalar multiplier. The loading and the plastic potential surfaces are defined by a flexible equation that can reproduce a wide range of shapes, in J-p' stress space. This means that once the effective stress strength parameters are set, the user can adjust the shape of the above surfaces so that the model yields the required value of undrained strength, under a particular shearing mode.

The influence of the intermediate principal stress on the shapes of the yield and plastic potential surfaces in the deviatoric plane is accounted for using the Matsuoka-Nakai failure criterion. This means that after specifying the stress ratio at critical state under a given shearing mode, say triaxial compression, the stress ratio at critical state under other shearing modes is fixed. When analysing a boundary value problem the user should ensure that the model recovers well the soil strength under the mode of shearing that is likely to dominate in that particular problem (i.e. in an excavation problem the model should predict well the soil strength in triaxial extension, and data from extension tests are should be used to determine the model parameters M, μ and α).

The model requires 13 parameters to completely characterize an unstructured soil; six of these parameters are related to the definition of the loading and plastic potential surfaces in J-p' stress space and can be derived by fitting an undrained triaxial compression stress path, three are time dependent parameters and can be derived from an IL 24 hour oedometer test for which there is consolidation data, and which ideally has one longer creep period, and the remaining parameters are analogous or equivalent to parameters of the MCC model and can be derived from the above two laboratory tests. The model was implemented in ICFEP and was then validated by means of simple finite element analyses. The validation can be divided into three parts:

a) Simulation of common laboratory tests

The conclusions given above regarding the performance of the Modified Creep Model 1 also apply to the Equivalent Time Model. In addition:

- The ability of the ET model to predict a non-linear logarithmic law for the variation of creep deformation with the logarithm of time was investigated. If the model parameter $\varepsilon^{vp}_{vol,m,Limit}$ - the limit for visco-plastic volumetric strain - is given a value close to or larger than the volumetric strain that causes the soil to have no voids left, then the model yields predictions very close to those given by a linear logarithmic creep law, for time intervals of interest to engineering practice. Smaller values of the parameter $\varepsilon^{vp}_{vol,m,Limit}$ cause the model to predict a non-linear logarithmic creep law, the non-linearity increasing as $\varepsilon^{vp}_{vol,m,Limit}$ decreases.

- The model is able to mimic the behaviour of samples that are on the wet and on the dry side of the critical state, sheared under drained conditions. Samples at the same initial effective stress state are found to reach the same critical state shear strength, independently of their initial state (dry or wet in relation to the critical state). Normally consolidated and lightly overconsolidated samples are predicted to have contractive behaviour and a monotonic increase in the shear stress up to critical state, which is reached at very large strains. Heavily overconsolidated samples show an initial contractive phase up to peak strength, which is well in excess of the strength at critical state, and then the behaviour becomes dilative as the deviatoric stress decreases to the rate and time independent critical state strength, which is attained at very large strains. Again an increase in OCR and the applied axial strain rate causes an increase in the sample's pseudo-elastic stress range.

b) Consolidation of samples with different thickness

The consolidation curves predicted by the ET model for three oedometer samples with different thicknesses, 20, 10 and 2 cm respectively, subjected to a load increment $\Delta\sigma_v'$=40 kPa were compared. The ET model predicts that the vertical strain at the end of primary consolidation (defined as 95% degree of pore water pressure dissipation) depends on the thickness of the consolidating layer, increasing with the layer thickness. The implications are that when estimating the vertical strain (or deformation) of a consolidating layer in the field, which will be much thicker than the element of soil investigated in the laboratory, the non-consideration of the rate effects may lead to a substantial underestimation of the magnitude of the settlement at EOP. In this respect, as noted in Chapter 2, the effects of the difference in the temperature between the field and the laboratory, and sample disturbance, will have the opposite effect on the magnitude of predicted settlements and may partially mask the role of rate effects.

In addition, it is noted that Terzaghi's solution for 1D consolidation can be used to evaluate the average degree of settlement, independently of the consolidating layer thickness. However, the degree of pore water pressure dissipation is in principle different. For a thick layer consolidating in the field (where due to the length of the drainage path the soil deforms at rates much lower than those experienced in the laboratory), the degree of excess pore water pressure dissipation is expected to be

smaller than the degree of settlement, an issue of major importance, e.g. in staged construction of embankments.

c) Simulation of laboratory tests on Hong Kong marine deposits

Overall the ET model is found to capture well the behaviour of the Hong Kong Marine Deposits under a variety of stress conditions. Most of the discrepancies may be attributed to the fact that the elastic part of the ET model is characterized by stress dependent elastic bulk modulus and therefore cannot incorporate the soil's strong non-linearity at small strains, and the progressive yielding of the soil, as observed experimentally. The analyses of undrained triaxial creep tests have highlighted the limitation of the overstress theory in general, and of the ET model in particular, that it cannot mimic tertiary (accelerating) creep, and therefore cannot reproduce undrained creep rupture.

Although it has been stated that the consideration of structure was beyond the scope of this thesis a structure mechanism as described by Lagioia & Nova (1995) was incorporated in the Equivalent time model, providing the possibility of investigating the coupling between soil structure and viscosity in the same constitutive model. To characterize a structured soil two additional parameters are required, which can be derived by fitting the compression data from an oedometer test on a natural sample. One parameter characterizes the soil initial structure and the other the destructuration rate. However, because the destructuration is a function of the visco-plastic volumetric strain component only very little loss of structure is predicted during undrained conditions.

Finally a comparison between the two models has shown that the two formulations can be made to be equivalent by a suitable choice of parameters. However the ET model presents advantages in relation to the Modified Creep Model 1, and is therefore the model employed for the analyses of the boundary value problems described in the thesis. Two of these advantages are:

- The ET model has a limit to the amount of visco-plastic volumetric strain during creep at constant effective stress. Therefore, the model can reproduce the soil creep non-linearity that has been reported by some researchers, Aboshi (2004). Simultaneously, if required, the ET model can mimic a linear creep law for limited creep periods, which is often relevant to engineering practice.

- In the ET model the loading and the plastic potential surfaces are defined by a flexible equation that can reproduce a wide range of shapes, in J-p' stress space. In contrast, in the Creep Model 1 the loading and plastic potential surfaces are given by the ellipse shape of the MCC model. This means that in the ET model once the effective stress strength parameters are set, the user can adjust the shape of the above surfaces so that the model yields the required value of undrained strength, under a particular shearing mode.

9.3 Influence of considering the soil viscous effects in the analysis of geotechnical structures

9.3.1 Shallow foundations

In this thesis the influence of the viscous effects on the behaviour of shallow foundations was investigated through two series of finite element analyses.

The first series consisted of a parametric study to evaluate the bearing capacity of a 2 m wide preloaded strip footing. Following on from the study presented by Zdravkovic et al. (2003) which investigated the increase in bearing capacity of a pre-loaded strip footing due to consolidation, this study considers the bearing capacity of the same pre-loaded strip footing when, in addition, the soil hardening associated with the development of creep strains is taken into account. The study considers the effect of the value of the coefficient of secondary compression, the creep non-linearity and the adopted loading rate. From this study the following conclusions can be drawn:

- The study highlights the importance of considering soil viscous effects in the design of geotechnical structures, and in particular the design of preloaded shallow foundation. The long term bearing capacity of a surface footing with an initial factor of safety on load of 2 is about 1.15 times the initial one, when only the effect of consolidation is considered (Zdravkovic et al., 2003). When, in addition, the development of creep strains is considered, the predicted bearing capacity is found to be between 1.3 and 1.6 times the initial one, the value depending on the amount of secondary compression considered.

- The adoption of a large coefficient of secondary consolidation C_α, may be conservative when estimating the long term settlement of an engineering

structure, however it is unsafe when considering the soil hardening with time, which in this study is directly related to the current bearing capacity of the preloaded footing.

- The adoption of a non-linear logarithmic creep law becomes more significant at larger consolidation times, and in particular when considering serviceability limit states. For the case examined, when the creep law non-linearity is taken into account, the total long-term settlement (after about 100 years) is found to reduce by up to a third.

- Based on the work of Randolph et al. (2004), and some additional analyses not included herein, it is anticipated that the results obtained in this study on a strip footing could be applied to footings of similar dimensions but different geometry.

- The study considered a typical soft clay soil profile, two values for the coefficient of secondary consolidation and various consolidation times relevant to engineering practice. The study is sufficiently general to enable the results to be directly incorporated in the design of existing foundations.

The second study comprised numerical analyses of the loading tests performed on two rigid footings at the Bothkennar test site (Jardine et al., 1995; Lehane & Jardine, 2003). The model parameters were derived based on the large amount of laboratory and in-situ test data published in the literature and the analyses results were compared with the available monitoring data. From this series of analyses the following conclusions can be drawn:

- The results of the numerical analyses highlight the importance of incorporating the effect of soil hardening associated with the development of creep strains to correctly predict the increases in bearing capacity of preloaded footings, and it validates the application of the parametric study in engineering practice.

- The numerical analyses show, in general, good agreement with the field measurements in terms of the overall load displacement behaviour of the footings. The agreement is particularly good regarding the long-term settlements of the preloaded footing.

- However, when looking at the displacements within the foundation soil, there are discrepancies that are related to the following aspects: a) the same basic model parameters were adopted throughout the soil profile, for the competent unweathered Carse Clay, the weathered Carse Clay and the recent deposits at the surface; b) the ET model cannot incorporate the non-linearity of stiffness at small strains; c) the destructuration mechanism included in the ET model can not appropriately describe the gradual loss of structure associated with both volumetric and deviatoric straining and d) the ET model being an isotropic model cannot mimic the rotation of the state bounding surface during consolidation under a new stress state, that would be of particular relevance for the analyses of footing C.

- When investigating the failure conditions of footing A it was concluded that due to the ET model formulation the model is not able to predict failure as it is defined in conventional plasticity theory. This derives from the fact that the ET model is not able to predict accelerating creep and thus it is not possible for an increase in strain rate to occur at constant stresses. When using the ET model the failure condition should be defined in a similar way to that done in engineering practice, i.e. as a threshold value of settlement or settlement rate.

- The elastic part of the ET model is characterized by a bulk modulus dependent on mean effective stress only and a constant Poisson's ratio value, and it cannot reproduce non-linearity of stiffness at small strains; when trying to incorporate a small strain stiffness model to describe the elastic part of the ET model it was soon realized that it is not compatible with the model formulation, at least as the model is implemented at present.

- The analyses emphasize the importance of considering the creep soil non-linearity to correctly predict the long-term settlements of geotechnical structures. The adoption of a constant coefficient of secondary compression is likely to overestimate the magnitude of the long-term settlements.

9.3.2 Embankments

Though not shown in this thesis, the ET model was employed by Losacco (2007) to analyse the behaviour of two instrumented test embankments built on the river Thames

estuary. The analysis of one of the embankments focused on the prediction of the long-term settlements and the FE analyses were found to recover well the field measurements. The other embankment had been taken to failure and the analysis focused on the simulation of the embankment failure and the various options for reconstruction and raising of the embankment, once failure had occurred. Similarly to that reported in this thesis regarding the analysis of the footings at the Bothkennar test site, Losacco (2007) was not able to predict the failure conditions of the embankment, as a well defined ultimate embankment height associated with a very large and accelerating horizontal displacement at the toe.

9.4 Recommendations for further research

9.4.1 Constitutive modelling

Based on the above discussion it is thought that the predictive capabilities of the Equivalent Time constitutive model could be improved in the following respects:

- Incorporate a flexible function to describe the failure and plastic potential surfaces in the deviatoric plane, similarly to that included in Creep Model 1. This would allow mimicking the soil strength under various shearing modes, simultaneously.

- Most existing constitutive models are based on the behaviour of isotropically consolidated soils. However, in most cases in practice, soils are anisotropically consolidated and the in-situ soil's yield surface is found to be rotated in relation to the K_0 stress axis. This implies that both the yield and the plastic potential surfaces should be rotated in J-p' stress space, and the model should be able to reproduce the rotation of the yield and plastic potential surfaces due to further loading.

- Modify the model formulation such that the ET model can be combined with a small strain stiffness model to describe the elastic part of the model.

- Following the formulation used by other researchers (e.g.; Rouainia & Muir Wood, 2000; Kostinen et al., 2002; Baudet & Stallebrass, 2004) incorporate a structure mechanism in which the destructuration law is a function of both the

deviatoric and the volumetric visco-plastic strain component, so that structure loss is predicted both during drained and undrained stress conditions.

9.4.2 Numerical studies

The implementation of the above two models into the ICFEP allowed the analysis of shallow foundations and embankments, taking into account the viscous properties of the soil. Further work could include:

- Further research into the definition of failure of shallow foundations when the ET model is employed. It has been suggested that when using the ET model the failure condition should be defined in a similar way to that done in engineering practice, i.e. as a threshold value of settlement or settlement rate. It would be of interest to evaluate the ultimate bearing capacity that would be predicted by an analysis of the same boundary value problem that uses a conventional plasticity model (e.g. Modified Cam Clay model) and consider how that value compares with the load predicted by the ET model at settlement and settlement rates identified in practice with failure.

- Extend the above study to other geotechnical structures, and in particular embankments, where the application of the ET model is seen as advantageous e.g. the analyses of staged construction, construction and long term settlements.

- Within this thesis the soils modelled with the ET model were exclusively soft normally consolidated clays. This was the case as soft normally consolidated clays are more prone to viscous effects i.e. undergo larger delayed settlements and have larger rate effects on the stress-strain response. However, it would be of interest to use the ET model to mimic the behaviour of other soils types that show isotach viscosity.

REFERENCES

Aboshi H (2004), "Long-term effect of secondary consolidation on consolidation settlement of marine clays", *Advances in Geotechnical Engineering: The Skempton Conference*, 2004, Thomas Telford, London.

Adachi T, Oka F and Mimura M (1987), "Mathematical structure of an overstress elasto-viscoplastic model for clay", *Soils and Foundations*, Vol.27, No.3, 31-42.

Adachi T and Oka F (1982), "Constitutive equations for normally consolidated clay based on elasto-viscoplasticity", *Soils and Foundations*, Vol.22, No.2, 57-70.

Adachi T, Oka F and Mimura M (1996), "State of the Art: Modelling aspects associated with time dependent behaviour", *Measuring and Modelling Time Dependent Behaviour of Soils, ASCE, Geotechnical Special Publication*, N.61, 61-95.

Addenbrooke TI, Potts DM & Puzrin AM (1997), "The influence of pre-failure soil stiffness on numerical analysis of tunnel construction", *Geotechnique*, Vol.47, No.3, 693-712.

Allman MA & Atkinson JH (1992), "Mechanical properties of reconstituted Bothkennar Clay", *Geotechnique*, Vol.42, No.2, 289-301.

Al-Tabbaa A & Wood DM (1989), "An experimentally based "bubble" model for clay", *Proceeding 3rd Int Conference Numerical Models in Geomechanics*, 91-00.

Anderson DG and Stokoe KHI (1978), "Shear Modulus: a time dependent soil property", *Dynamic Geotechnical Testing*, ASTM, STP654, 66-90.

Arulanandan K, Shen CK and Young RB (1971), "Undrained creep behaviour of a coastal organic silty clay", *Geotechnique*, Vol.21, No.4, 359-375.

Augustesen A, Liingaard M & Lade PV (2004), "Evaluation of the time-dependent behaviour of soils", Int Journal of Geomechanics, Vol.4, No.3, 137-156.

Baudet B & Stallebrass S (2004), "A constitutive model for structured clays", *Geotechnique*, Vol.54, No.4, 269-278.

Bjerrum L (1967), "Engineering geology of Norwegian normally-consolidated marine clays as related to the settlements of buildings", *Geotechnique*, 17, 81-118.

Booker JR & Small JC (1975), "An investigation of the stability of numerical solutions of Biot's equations of consolidation", *Int. Journal Solids Structures*, Vol.11, 907-917.

Borja R I & Kavazanjian E (1985), "A constitutive model for the stress-strain-time behaviour of "wet" clays", *Geotechnique*, Vol.35, No.3, 283-298.

Bransby MF (2002), "The undrained inclined load capacity of shallow foundations after consolidation under vertical load", *Proc Int. Conf. On Numerical Methods in Geomechanics*, Rome, 431-437.

Browne MAE, Graham DK & Gregory DM (1984), *"Quaternary deposits in the Grangemouth area, Scotland"*, Report 16/3. Edinburgh: British Geological Survey.

Buisman K (1936), "Results of long duration settlement tests", *Proceedings 1st ICSMFE*, Cambridge, Vol.1, 103-107.

Burland JB (1990), " On the compressibility and shear strength of natural clays", *Geotechnique*, Vol.40, 329-378.

Clayton CRI, Hight DW & Hopper RJ (1992), "Progressive destructuration of Bothkennar clay: implications for sampling and reconsolidation procedure", *Geotechnique*, Vol.42, No.2, 219-239.

Cotecchia F (1996), *"The effects of structure on the properties of an Italian Pleistocene clay"*, PhD Thesis, Imperial College, University of London.

Cryer CW (1963), "A comparison of the three dimensional theories of Biot and Terzaghi", *Journal Mech. Appl. Math.*, Vol.16, 401-412.

den Haan E J (1994), *"Vertical compression of soils"*, PhD thesis, Technical University of Delft, The Netherlands.

den Haan E J & van den Berg P (2001), "*Evaluation of creep models for soft soils under axially symmetric conditions*", Report CO-710203/21, GeoDelft, The Netherlands.

Di Benedetto H, Ibraim E and Cazacliu B (1999), "Time dependent behaviour of sand", *Proceedings of the 2nd International Symposium on the Pre-failure deformation characteristics of Geomaterials,* Torino, Jamiolkowski, Lancellotta & Lo Presti (eds), Balkema, Rotterdam, 459-466.

Feda J (1992), "*Creep of soils and related phenomena*", Developments in Geotechnical Engineering, 68, Elsevier Publishers.

Garlanger JE (1972), "The consolidation of soils exhibiting creep under constant effective stress", *Geotechnique*, Vol.22, No.1, 71-78.

Gasparre A (2005), *"Advanced laboratory characterization of London Clay"*, PhD Thesis, Imperial College, University of London.

Gildea PA (1990), *"An investigation into the yielding of soft clay"*, MSc Dissertation, Imperial College, University of London.

Gnanendran C T, Manivannan G & Lo S-C R (2006), "Influence of using a creep, rate, or an elasto-plastic model for predicting the behaviour of embankments on soft soils" *Canadian Geotechnical journal*, Vol.43, 134-154.

Grammatikopoulou A (2004), *"Development, implementation and validation of kinematic hardening models for overconsolidated clays"*, PhD Thesis, Imperial College, University of London.

Hight DW, Bond AJ & Legge JD (1992), "Characterization of the Bothkennar Clay: an overview", *Geotechnique*, Vol.42, No.2, 303-347.

Institute of Civil Engineers (1992), "Bothkennar soft clay test site", Symposium in Print, *Geotechnique*, Vol.42, N.2.

Jackson C, Zdravkovic L & Potts DM (1997), "Bearing capacity of pre-loaded surface foundations on clay", *Proceedings of the 9th Int. Conf. Computer Methods and Advances in Geomechanics,* Yuan (ed.), Balkema, Rotterdam, 745-750.

Jaky (1944), "The coefficient of earth pressures at rest" *J. Society Hungarian Architects and Engineers*, 355-358.

Jardine RJ, Lehane BM, Smith PR & Gildea PA (1995), "Vertical loading experiments on rigid pad foundations at Bothkennar", *Geotechnique*, Vol.45, N.4, 573-597.

Jardine RJ, Potts DM, Fourie AB & Burland JB (1986), " Studies of the influence of non-linear stress-strain characteristics in soil-structure interaction", *Geotechnique*, Vol.36, N.3, 377-396.

Kavazanjian E and Mitchell (1977), "A general stress-strain-time formulation for soils", *Proceedings 9th ICSMFE, Tokyo 1977, Speciality Session 9. Constitutive equations of soils*. 113-120.

Komoto N, Tatsuoka F and Nishi T (2003), "Viscous stress-strain properties of undisturbed Pleistocene clay and its constitutive modelling", *Proceedings 3rd International Symposium on the Deformation Characteristics of Geomaterials*, Lyon, 579-587.

Kostinen M, Karstunen M & Wheeler SJ (2002), "Modelling destructuration and anisotropy of a natural soft clay", *Proceeding 5th European Conf Numerical Methods in Geotechnical Eng.*, Paris, France, 11-19.

Kovocevic N (1994), "Numerical analyses of rockfill dams, cut-slopes and road embankments", PhD Thesis, Imperial College, University of London.

Kutter B L & Sathialingam N (1992), "Elasto-viscoplastic modelling of the rate dependent behaviour of clays", *Geotechnique*, Vol.42, No.3, 427-441.

Lacerda W A & Houston W N (1973), "Stress relaxation in soils", *Proceedings of the 8th ICSMFE,* Moscow, 1/34, 221-227.

Lade PV (1977), "Elasto-plastic stress-strain theory for cohesion less soil with curved yield surfaces", Int Journal Solids Structures, Vol.13, pp 1019-1035.

Lagioia R & Nova R (1995), "An experimental and theoretical study of the behaviour of a calcarenite in triaxial compression", *Geotechnique*, Vol.45, No,4, 633-648.

Lagioia R, Puzrin AM & Potts DM (1996), "A new versatile expression for yield and plastic potential surfaces", *Computers and Geotechnics*, Vol.19, No. 3, 171-191.

Lehane BM & Jardine RJ (2003), "Effects of long-term pre-loading on the performance of a footing on clay", *Geotechnique*, Vol.53, N.8, 689-695.

Leroueil S, Tavenas F, Samson L and Morin P (1983), "Pre-consolidation pressure of Champlain clays. Part II. Laboratory determination." *Canadian Geotechnical Journal*, Vol.20, 803-816.

Leroueil S, Kabbaj M, Tavenas F and Bouchard R (1985), "Stress-strain-time rate relation for the compressibility of sensitive natural clays", *Geotechnique*, Vol.35, No.2, 159-180.

Leroueil S & Vaughan PR (1990), "The general and congruent effects of structure in natural soils and weak rocks", *Geotechnique*, Vol.40, 467-488.

Leroueil S, Lerat P, Hight DW & Powell J J M (1992), "Hydraulic conductivity of a recent estuarine silty clay at Bothkennar", *Geotechnique*, Vol.42, No.2, 275-288.

Leroueil S (1995), "Could it be that clays have no unique way of behaving during consolidation?" *Compression and Consolidation of Clays*, Yoshikuni & Kusakabe eds., Balkema, 1039-1048.

Leroueil S, Perret D and Locat J (1996), "Strain rate and structuring effects on the compressibility of a young clay", *Measuring and Modelling Time Dependent Behaviour of Soils*, ASCE, Geotechnical Special Publication, N.61, 137-150.

Leroueil S & Marques MES (1996), "State of art: Importance of strain rate and temperature effects in Geotechnical Engineering", *Measuring and Modelling Time Dependent Behaviour of Soils*, ASCE, Geotechnical Special Publication, N.61, 1-60.

Liigaard M, Augustesen A and Lade PV (2004), "Characterization of models for the time dependent behaviour of soils", *Int. Journal of Geomechanics*, Vol.4, No.3, 157-177.

Little JA, Muir Wood D, Paul MA & Bouazza A (1992), "Some laboratory measurements of permeability of Bothkennar Clay in relation to soil fabric", *Geotechnique*, Vol.42, No.2, 355-361.

Lohani TN, Imai G, Tani K and Shibuya S (2001), "G_{max} of fine-grained soils at wide void ratio change, focusing on time-dependent behaviour", *Soils and Foundations*, Vol.41, No.5, 87-102.

Lo Presti DCF, Jamiolkowski M, Pallara O and Cavallaro A (1996), "Rate and creep effects on the stiffness of soils", *Measuring and Modelling Time Dependent Behaviour of Soils*, ASCE, Geotechnical Special Publication, N.61, 166-180.

Losacco N (2007), "*Raising of embankments on soft clay*", MSc Thesis, Department of Civil and Environmental Eng., Imperial College, London.

Mair RJ, Hight DW & Potts DM (1992), "*Finite element analyses of settlements above a tunnel in soft ground*", Contractors Report 265, Transport and Road Research Laboratory, Crowthorne, England.

Mandel J (1953), "Consolidation des sols", *Geotechnique*, Vol3, N.7, 287-299.

Matešić L & Vucetic M (2003), "Strain rate effect on soil secant shear modulus at small cyclic strains", *Journal Geotechnical and Geoenvironmental Eng.*, ASCE, Vol.129, N.6, 536-549.

Mesri and Godlewski (1977), "Time and stress compressibility relationships", *J Geotechnical Eng.*, Vol.103, No.5, 417-430.

Mesri G & Castro A (1987), "C_α/C_c concept and K_0 during secondary compression", *J Geotechnical Engineering*, 113 (3), 230-247.

Mesri G & Choi Y K (1985), "The uniqueness of the end of primary void ratio - effective stress relationship", *Proceedings of the 11Th ICSMFE*, San Francisco, Vol.2, 587-590.

Mesri G, Lo D O K & Feng T W (1994), "Settlement of embankments on soft clays", *Vertical and horizontal deformations of foundations and embankments*, Geotechnical Special Publication No.40, ASCE, Vol.1, 8-56.

Mitchell J K (1960), "Fundamental aspects of thixotropy in soils", *J Soil Mechanics and Foundations Div.,* ASCE, Vol.83, N.3, 19-52.

Mitchell J K (1993), *"Fundamentals of soil behaviour"*, John Wiley & Sons, Inc., London, 2nd Edition.

Murayama S, Michihiro K and Sakagami T (1984), "Creep characteristics of sands", *Soils and Foundations*, Vol.24, No.2, 1-15.

Nash DFT, Powell JJM & Lloyd IM (1992a), "Initial investigations of the soft clay test site at Bothkennar", *Geotechnique*, Vol.42, No.2, 163-181.

Nash DFT, Sills GC & Davison LR (1992b), "One-dimensional consolidation testing of soft clay from Bothkennar", *Geotechnique*, Vol.42, No.2, 241-256.

Paul MA, Peacock JD & Wood BF (1991), "*The engineering geology of the estuarine deposits at the national soft clay research site, Bothkennar*" Report to the Science and Engineering Research Council.

Paul MA, Peacock JD & Wood BF (1992), "The engineering geology of the Carse Clay of the national soft clay research site, Bothkennar", *Geotechnique*, Vol.42, No.2, 183-198.

Perzyna P (1963), "The constitutive equations for work-hardening and rate sensitive plastic materials", *Proc of vibrational problems*, Vol.4, No.3 281-290.

Potts DM & Gens A (1994), "The effect of the plastic potential in boundary value problems involving plane strain deformations", *Int. Journal Numerical Analytical Methods Geomechanics*, Vol. 8, 259-286.

Potts DM & Zdravkovic L (1999), "*Finite element analysis in geotechnical engineering: Theory*", Thomas Telford, London.

Potts DM & Zdravkovic L (2001), "*Finite element analysis in geotechnical engineering: Application*", Thomas Telford, London.

Randolph M.F., Jamiolkowski M.B. & Zdravkovic L. (2004), "Load carrying capacity of foundations", A*dvances in Geotechnical Engineering. Proceedings of the Skempton Memorial Conference*. Pub Thomas Telford, London, Vol. 1, 227-240.

Rolo R (2003), "*The anisotropic stress-strain-strength behaviour of brittle sediments*" PhD Thesis, Imperial College, University of London.

Rouainia M & Muir Wood D (2000), "A kinematic hardening model for natural clays with loss of structure", Geotechnique, Vol.50 No.2, 153-164.

Santucci de Magistris F and Tatsuoka F (1999), "Time effects on the stress-strain behaviour of Metramo silty sand", *Proceeding of the 2nd International symposium on the Pre-failure deformation characteristics of Geomaterials*, Jamiolkowski, Lancellotta & Lo Presti (eds), Balkema, Rotterdam, 555-564.

Santucci de Magistris F, Sato T, Koseki J and Tatsuoka F (1998), "Effects of strain rate and ageing on small strain behaviour of a compacted silty sand", *The geotechnics of hard soils - soft rocks*, Evangelista & Picarelli (eds), Balkema Rotterdam, 843-854.

Skempton AW and Northey RD (1952), "The sensitivity of clays", *Geotechnique,* Vol.3, No.1, 30-53.

Shibuya S, Mitachi T, Hosomi A and Hwang SC (1996), "Strain rate effects on stress-strain behaviour of clay as observed in monotonic and cyclic triaxial tests", *Measuring and Modelling Time Dependent Behaviour of Soils*, ASCE, Geotechnical Special Publication, N.61, 214-227.

Singh A & Mitchell J K (1968) "General stress-strain-time function for soils" *Journal Soils Mechanics and Foundations Division*, ASCE, Vol.94, No.1, 21-46.

Smith PR (1992), "*The behaviour of natural high compressibility clay with special reference to construction on soft ground*", PhD Thesis, Imperial College, University of London.

Smith PR, Jardine RJ & Hight DW (1992), "The yielding of Bothkennar Clay", *Geotechnique*, Vol.42, No.2, 257-274.

Sissons JB, Cullingford RA & Smith DE (1966), "Late-glacial and post-glacial shorelines in southeast Scotland", *Trans. Instn. British Geographers* 39, 9-18.

Soga K and Mitchell JK (1996), "Rate-dependent deformation of structured natural clays", *Measuring and Modelling Time Dependent Behaviour of Soils*, ASCE, Geotechnical Special Publication, N.61, 243-257.

Sorensen KK (2006), "*Influence of viscosity and ageing on the behaviour of clays*", PhD Thesis, University of London.

Sorensen KK, Baudet BA and Simpson B (2007), "Influence of structure on the time-dependent behaviour of a stiff sedimentary clay", *Geotechnique*, Vol.57, No.1, 113-124.

Stallebrass SE & Taylor RN (1997), "The development and evaluation of a constitutive model for the prediction of ground movements in overconsolidated clays", Geotechnique, Vol.47, No.2, pp 235-254.

Suklje L (1957), "The analysis of the consolidation process by the isotaches method", *Proceedings of the 4th ICSMFE*, Vol.1, 200-206.

Tavenas F and Leroueil S (1977), "Effects of stress and time on yielding of clays", *Proceedings of the 9th ICSMFE*, Vol.1, 319-326.

Tavenas F, Leroueil S, La Rochelle P & Roy M (1978), "Creep behaviour of an undisturbed lightly overconsolidated clay", *Canadian Geotechnical Journal* 15, 402-423.

Tatsuoka F, Santucci de Magistris F, Hayano K, Koseki J and Momoya Y (1998), "Some new aspects of time effects on the stress-strain behaviour of stiff geomaterials", *The geotechnics of hard soils – soft rocks, Proceedings 2nd Int Symposium hard soils soft rocks*, Napoli, 1285-1371.

Tatsuoka F, Maruyama N, Santucci de Magistris F and Momoya M (1999), "Isotach behaviour of geomaterials and its modelling", *Proceeding of the 2nd International*

symposium on the Pre-failure deformation characteristics of Geomaterials, Jamiolkowski, Lancellotta & Lo Presti (eds), Balkema, Rotterdam, 491-499.

Tatsuoka F, Ishihara M, Di Benedetto H Kuwano R (2002), "Time – dependent shear deformation characteristics of geomaterials and their simulation", *Soils and Foundations*, Vol.42, No.2, 103-129.

Tatsuoka F, Di Benedetto H Nishi T (2003), "A framework for modelling time effects on the stress-strain behaviour of geomaterials", *Proceedings 3rd International Symposium on the Deformation Characteristics of Geomaterials*, Lyon, 1135-1143.

Tatsuoka F (2006), "Keynote Lecture: Inelastic deformation characteristics of geomaterial", *Soil stress-strain behaviour: measurement, modelling and analysis. Proceedings of the Geotechnical Symposium in Rome*, 2006.

Terzaghi K and Peck RB (1967), *"Soil mechanics in engineering practice"*, Wiley, 2nd Edition.

Vaid YP and Campanella RG (1977), "Time-dependent behaviour of undisturbed clay", *Journal of the Geotechnical Eng. Division*, Vol.103, No.7, 693-709.

Vermeer PA & Neher HP (1999), "A soft soil model that accounts for creep", Beyond 2000 in Computational Geotechnics - 10 years of Plaxis international. Balkema, Rotterdam.

Xin YC (1988), " Experimental study on the elasto-plastic model of loess", *Proceedings of the 3rd National conference on numerical analysis methods in geomechanics*, Zuhai, China, Vol.1, 193 (in Chinese).

Yin J-H (1999), "Non-linear creep of soils in oedometer tests", *Geotechnique*, Vol.49, No.5, 699-707.

Yin J-H and Graham J (1989), "Viscous-elasto-plastic modelling of one-dimensional time-dependent behaviour of clays", *Canadian Geotechnical Journal*, Vol.26, 199-209.

Yin J-H and Graham J (1994), "Equivalent times and one-dimensional elastic visco-plastic modelling of the time-dependent stress-strain behaviour of clays", *Canadian Geotechnical Journal*, Vol. 31, 42-52.

Yin J-H & Graham J (1999), "Elastic viscoplastic modelling of the time-dependent stress-strain behaviour of soils", *Canadian Geotechnical Journal*, Vol.36, 736-745.

Yin J-H, Zhu J-G & Graham J (2002), "A new elastic visco-plastic model for time-dependent behaviour of normally and overconsolidated clays: theory and verification", *Canadian Geotechnical Journal*, 39, 157-173.

Zdravkovic L, Potts DM & Jackson C (2003), "Numerical study of the effect of preloading on undrained bearing capacity", *Int. Journal of Geomechanics*, Vol.3, No. 1, 1-10.

Zhu JG (2000), "*Experimental study and elastic visco-plastic modelling of the time dependent stress-strain behaviour of Hong-Kong marine deposits*", PhD Thesis, The Hong Kong Polytechnic University, Hong Kong.

APPENDIX A

Settlement – load curves obtained on reloading for all the cases investigated in the parametric study

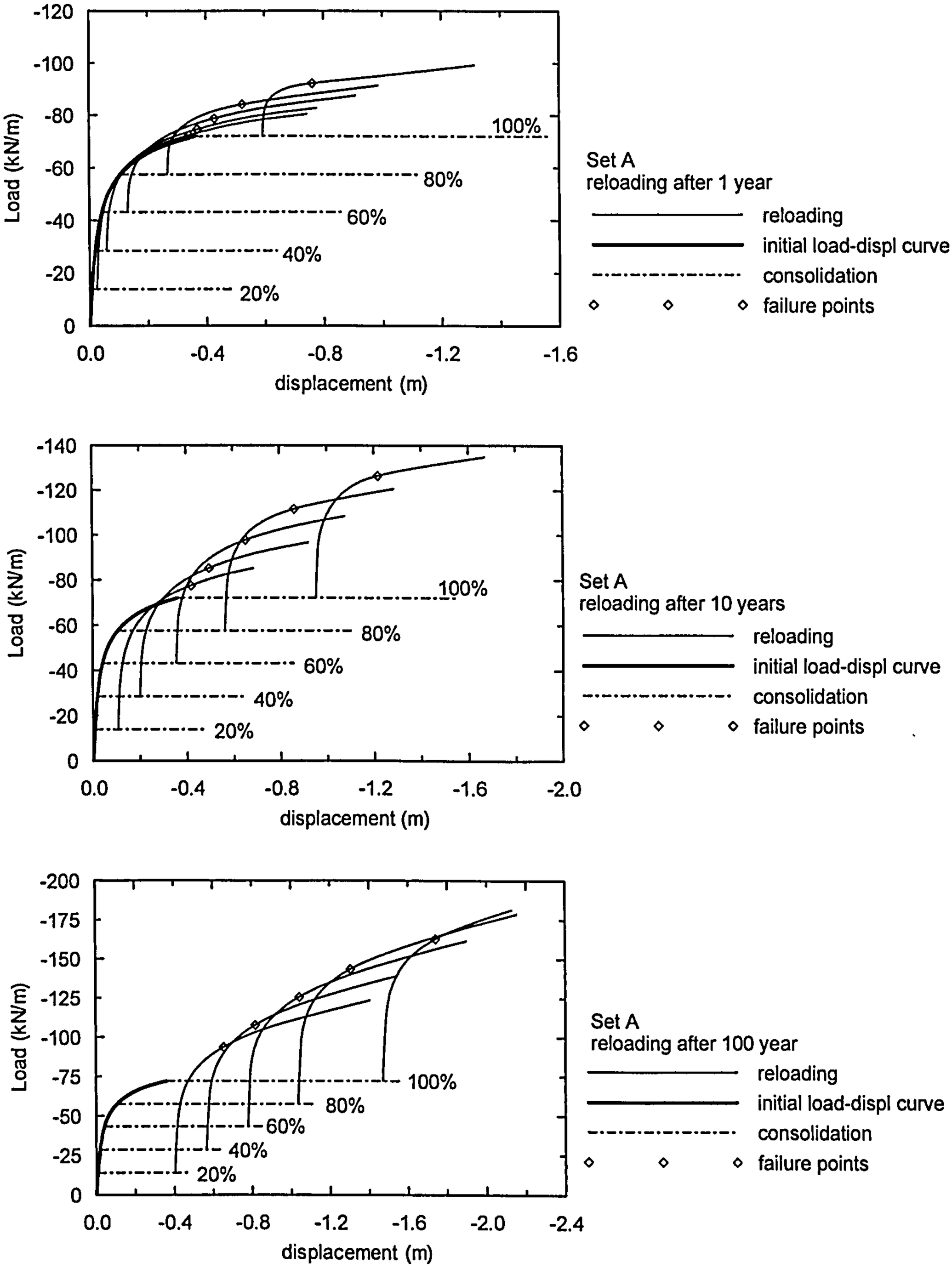

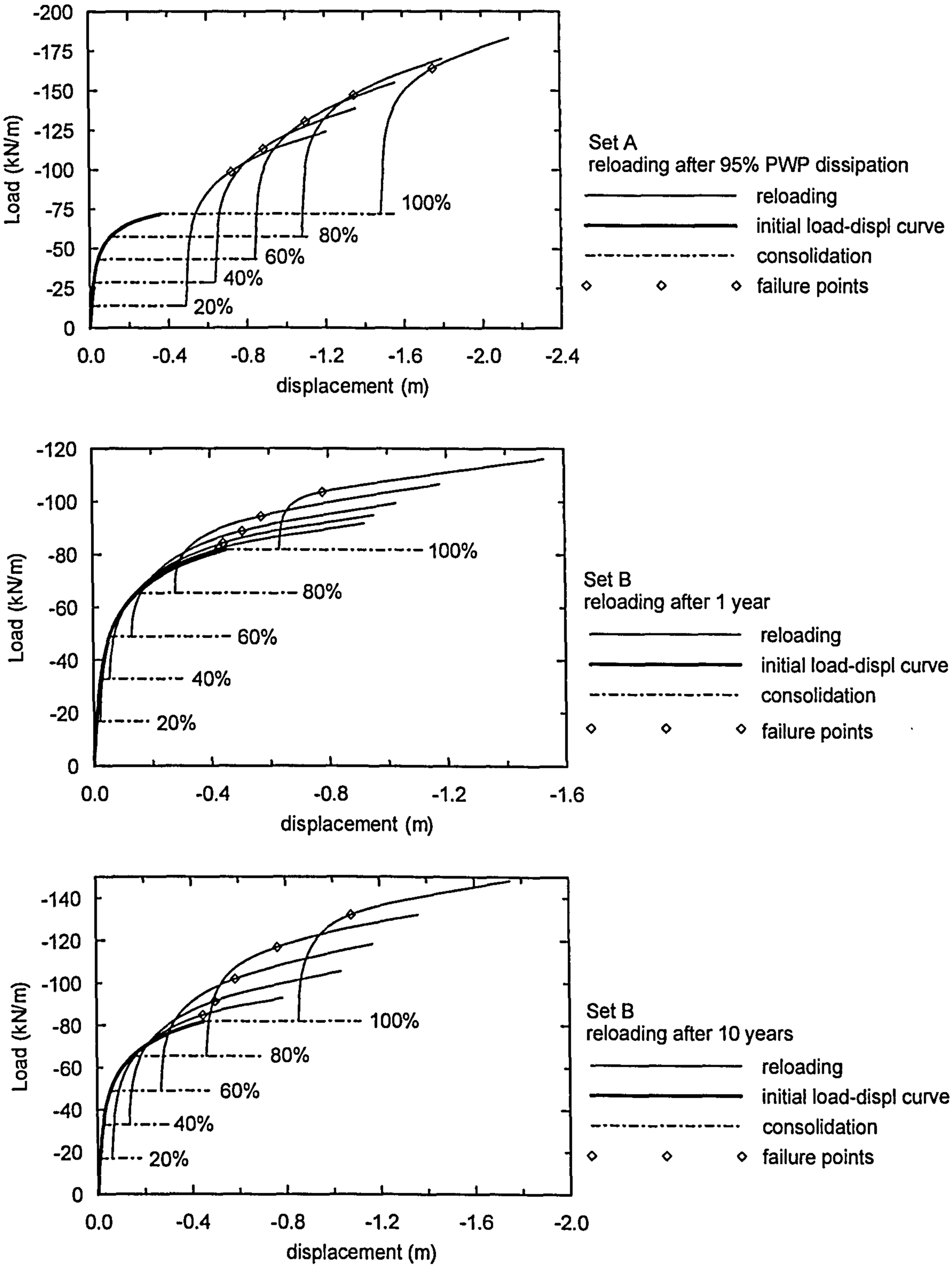
Load (kN/m)
displacement (m)
100%
80%
60%
40%
20%
Set A
reloading after 95% PWP dissipation
reloading
initial load-displ curve
consolidation
failure points
Set B
reloading after 1 year
Set B
reloading after 10 years

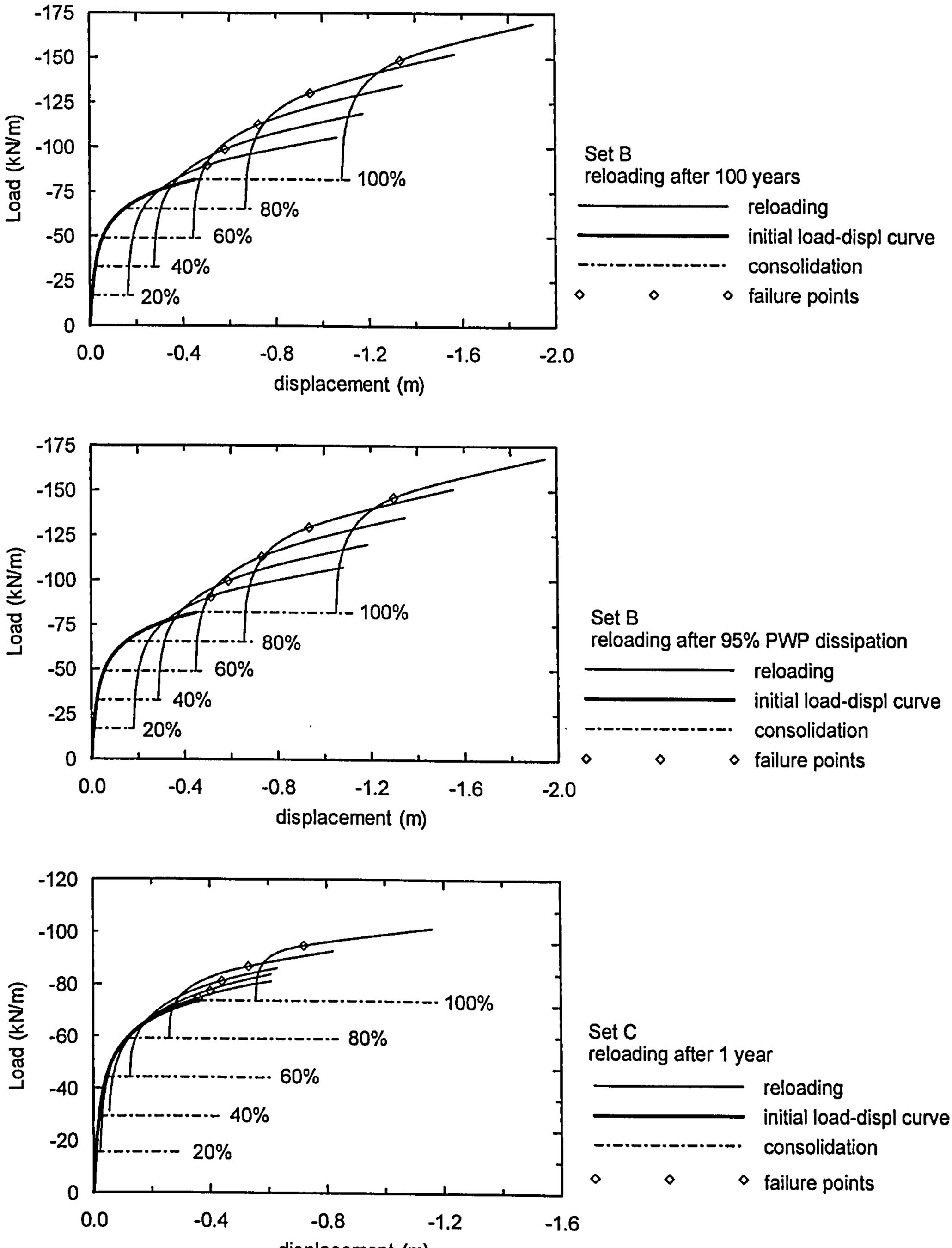
Load (kN/m)
-175
-150
-125
-100
-75
-50
-25
0
0.0
-0.4
-0.8
-1.2
-1.6
-2.0
displacement (m)
100%
80%
60%
40%
20%
Set B
reloading after 100 years
reloading
initial load-displ curve
consolidation
failure points
Load (kN/m)
-175
-150
-125
-100
-75
-50
-25
0
0.0
-0.4
-0.8
-1.2
-1.6
-2.0
displacement (m)
100%
80%
60%
40%
20%
Set B
reloading after 95% PWP dissipation
reloading
initial load-displ curve
consolidation
failure points
Load (kN/m)
-120
-100
-80
-60
-40
-20
0
0.0
-0.4
-0.8
-1.2
-1.6
displacement (m)
100%
80%
60%
40%
20%
Set C
reloading after 1 year
reloading
initial load-displ curve
consolidation
failure points

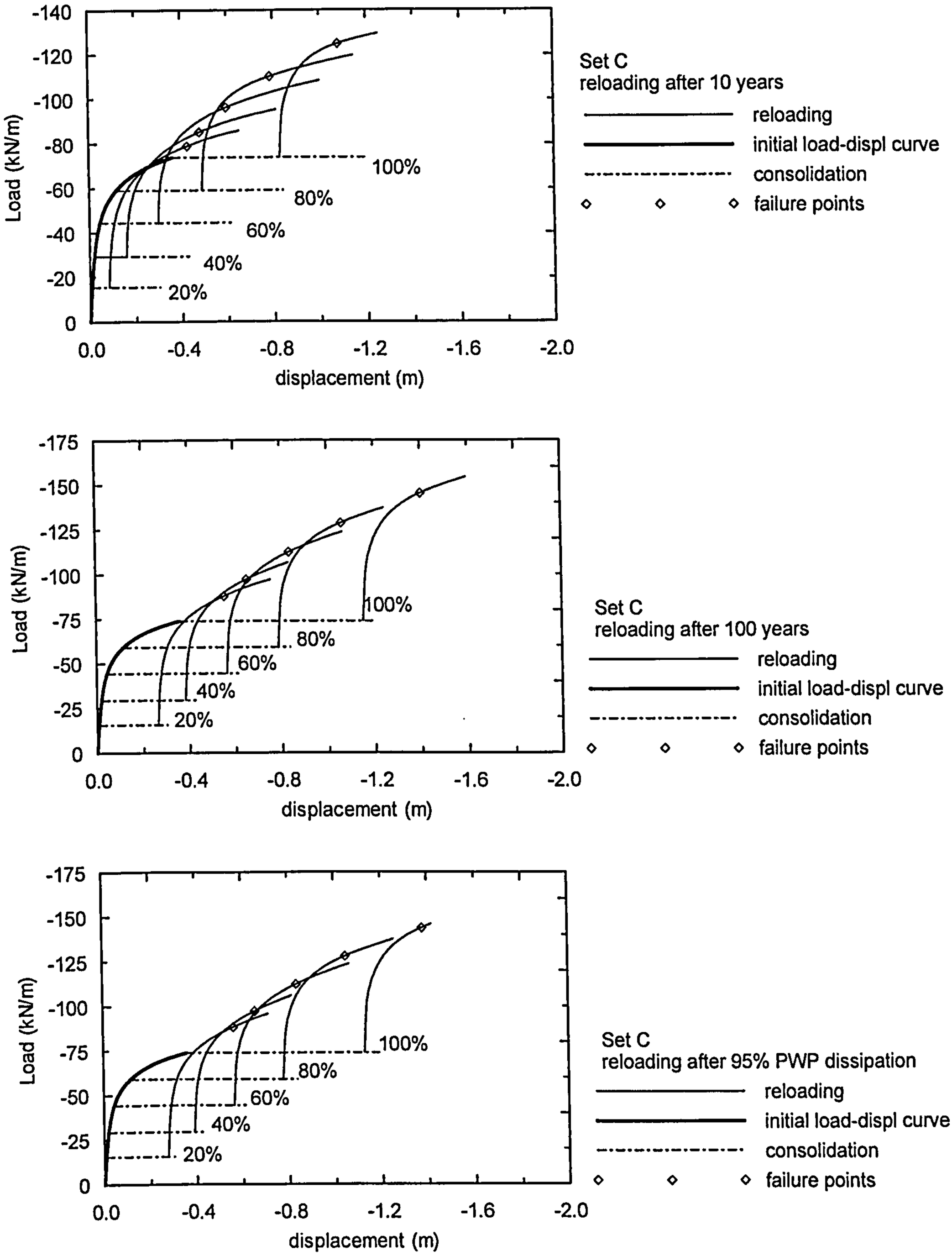
Load (kN/m)
-140
-120
-100
-80
-60
-40
-20
0
100%
80%
60%
40%
20%
0.0
-0.4
-0.8
-1.2
-1.6
-2.0
displacement (m)
Set C
reloading after 10 years
reloading
initial load-displ curve
consolidation
failure points
Load (kN/m)
-175
-150
-125
-100
-75
-50
-25
0
100%
80%
60%
40%
20%
0.0
-0.4
-0.8
-1.2
-1.6
-2.0
displacement (m)
Set C
reloading after 100 years
reloading
initial load-displ curve
consolidation
failure points
Load (kN/m)
-175
-150
-125
-100
-75
-50
-25
0
100%
80%
60%
40%
20%
0.0
-0.4
-0.8
-1.2
-1.6
-2.0
displacement (m)
Set C
reloading after 95% PWP dissipation
reloading
initial load-displ curve
consolidation
failure points